Magmatic-hydrothermal volatile exsolution and mineralisation in Tasmanian Sn granites

by

Wei Hong (BSc, MSc)

Submitted in fulfilment of the requirements for the degree of

Doctor of Philosophy

December, 2016

UNIVERSITY OF TASMANIA

CODES

ARC CENTRE OF EXCELLENCE IN ORE DEPOSITS

Declaration of Originality

This is thesis contains no material which has been accepted for any other degree or diploma by the university or any other institution, and to the best of my knowledge and belief, contains no material previously published or written by another person, except where due reference is made in the text of the thesis, nor does the thesis contain any material that infringes copyright.

Signature: Date: 16-05-2017

Authority of Access

This thesis may be made available for loan and limited copying and communication that are permitted in accordance with the *Copyright Act 1968*.

Signature: Date: 16-05-2017

Statement and regarding published work

Part of Chapter 4 and Chapter 5 was published in the journal of *American Mineralogist* in April of 2017. Chapter 3 and part of Chapter 9 was published in the journal of *Gondwana Research* in 2017. The publishers of the papers comprising the chapters mentioned above hold or will hold the copyright for that content, and access to the material should be sought from the journals. The remaining non-published content of the thesis may be made available for loan and limited copying in accordance with the *Copyright Act 1968*.

Signature: Date: 16-05-2017

Abstract

Large volumes of granites were emplaced across Tasmania in the mid-Palaeozoic. Many of them have distinctive magmatic – hydrothermal features, and some of them produced world class Sn-W deposits. In eastern Tasmania, the weakly metaluminous George River Granodiorite, Grant Point Granite and Mt Pearson Granite have zircon U-Pb ages ranging from 405 to 396 Ma, and intruded prior to the Tabberabberan Orogeny. The peraluminous Coles Bay Granite has a U-Pb age of 388 ± 7 Ma, emplaced simultaneously with the Tabberabberan Orogeny in Tasmania at ~390 Ma. Granites in western Tasmania are moderately to strongly fractionated, including the Housetop, Meredith, Pine Hill, Heemskirk and Pieman Heads. They intruded from 374 to 360 Ma, after the Tabberabberan Orogeny. Initial Pb isotopic compositions of K-feldspars from the Palaeozoic granites vary from 17.638 to 20.658 ($^{206}Pb/^{204}Pb$), 15.549 to 15.739 ($^{207}Pb/^{204}Pb$) and 37.903 to 38.940 ($^{208}Pb/^{204}Pb$), defining a narrower range than the corresponding whole-rock Pb isotopes. These isotopic results, combined with previous studies, suggest that differentiated granites in Tasmania were strongly contaminated by crustal rocks, and that western Tasmanian granites had a crustal source with different isotopic characteristics to that of eastern Tasmania. The tin-mineralised granites in Tasmania (e.g., the Housetop, Meredith, Pine Hill and Heemskirk granites) formed in a post-collisional extensional setting, a favourable environment for the production of Sn-rich melts from the lower crust. Prolonged fractional crystallisation, low oxygen fugacity, and enrichments of volatiles were crucial factors that promoted Sn enrichment in magmatic – hydrothermal fluids exsolved from these felsic magmas.

Distinctive tourmaline- and quartz-rich magmatic – hydrothermal features characterise the Heemskirk and Pieman Heads granites of western Tasmania. They include tourmaline-rich patches, orbicules, miarolitic cavities, veins, and unidirectional solidification textures (USTs). Tourmaline cavities and USTs were only observed in the Heemskirk Batholith, and not in the Pieman Heads Granite. These textural features occur in discrete layers in the roof zone of granitic sills within the Heemskirk and Pieman Heads granites. Tourmaline patches in the Heemskirk Granite occur below a tourmaline orbicule-rich granitic sill. Tourmaline-filled cavities have typically developed above the tourmaline orbicules in the White phase of the Heemskirk Granite. Both the tourmaline orbicules and cavities commonly occur below the UST layers. Tourmaline-quartz veins were developed throughout both granites, locally cutting tourmaline orbicules, cavities or USTs.

Scanning electron microscope-backscattered electron images recognise three types of compositional zones in tourmalines from the western Tasmanian granites: (1) oscillatory zoning, (2) concentric zoning, and (3) radial zoning. The tourmalines are mostly schorl (Fe-rich) and foitite, with an average end-member component of $schorl_{45}\,dravite_{6}\,tsilaisite_{1}\,uvite_{0}\,Fe\text{-}uvite_{3}\,foitite_{31}\,Mg\text{-}foitite_{4}\,olenite_{10}$. Element substitutions within tourmaline were controlled by $FeMg_{-1}$, $^{Y}Al^{X}\square(R^{2+}Na)_{-1}$, and minor $^{Y}AlO(R^{2+}OH)_{-1}$ (where R^{2+} = Fe^{2+} + Mg^{2+} + Mn^{2+}) exchange vectors. Tourmalines from the Heemskirk Granite are enriched in Fe, Na,

Li, Be, Sn, Ta, Nb, Zr, Hf, Th, and rare earth elements relative to the tourmalines from the Pieman Heads Granite, but depleted in Mg, Mn, Sc, V, Co, Ni, Pb, Sr, and most transition elements. These results imply that bulk compositions of the host granites exerted a major control on the chemical variations of tourmalines. There is a progressive decrease of most transition and large ion lithophile elements, and a gradual increase of most high field strength elements in tourmaline grouped from tourmaline patches, through orbicules and cavities, to veins. Trace element ratios (e.g., Zn/Nb, Co/Nb, Sr/Ta and Co/La) and Sn concentrations in tourmaline can distinguish the productive Heemskirk Granite from the barren Pieman Heads Granite.

Scanning electron microscope-cathodoluminescence analyses reveal that different types of CL textures developed in quartz from the tourmaline-rich features, USTs and Pb-Zn veins in the Heemskirk and Pieman Heads granites. CL-bright quartz cores are typically cut by dark to gray CL patches, CL-dark streaks and healed fractures, offset by cobweb-like networks and jigsaw puzzle pieces, and/or overprinted by gray to bright CL growth zones. Al, Li, Ti, Na, K, Fe, Ge, and Rb are the most abundant trace elements in quartz. Trace element substitutions in quartz were mainly controlled by the $[AlO_4/M^+][Si^{4+}]_{-1}$ ($M^+ = H^+$, Li^+, Na^+, K^+, Rb^+) vector. Trace elements in UST quartz are consistent with those in tourmaline orbicules and cavities, whereas aplitic quartz intergrown with UST quartz has similar trace element contents to quartz in tourmaline patches from the Heemskirk Granite. Ge/Ti and Al/Ti ratios of quartz in the Heemskirk Granite (0.01–1.0 and 3.0–100) define wider ranges than those from the Pieman Heads Granite (0.01–0.2 and 2.0–306), suggesting a higher extent of fractional crystallisation of the Heemskirk Granite. High Sb concentrations (up to 100 ppm) in quartz may be an indicator of low temperature base metal mineralisation related to granitic intrusions.

Melt and fluid inclusions observed in tourmaline patches, orbicules, cavities and/or veins provide unambiguous evidence for their precipitation from magmatic – hydrothermal fluids. Liquid-rich (type I), vapour-rich (type II) and halite-bearing (type III) fluid inclusions have been identified in quartz from these tourmaline-rich textural features. Microthermometric measurements show that fluid inclusions have homogenisation temperatures and salinities ranging from 156 ° to 460 ℃ and 2 to 15 wt % NaCl equiv (type I), 334 ° to 550 ℃ and 6 to 8 wt % NaCl equiv (type II), and 170 ° to 530 ℃ and 31 to 56 wt % NaCl equiv (type III). Combined microthermometry and Ti-in-quartz geothermometry demonstrate that tourmaline patches, orbicules and cavities formed at temperatures of 500 ° to 565 ℃ and lithostatic pressures of 0.6 to 1.3 kbars (depth of 2.8 to ≥ 5 km). Tourmaline veins formed at 310 ± 20°C and 400° to 410 ℃ for the Heemskirk and Pieman Heads granites, respectively, at hydrostatic pressures of 0.1 to 0.3 kbars (depth of ca. 1 km). Pb-Zn quartz veins from the Heemskirk Granite precipitated under lower temperature-pressure conditions (280 ± 40 ℃; hydrostatic pressure of 80 bars).

In situ SIMS analyses show that boron isotopic compositions ($\delta^{11}B_{Tur}$) of tourmaline range broadly from –21.7 ‰ to +4.1 ‰. Oxygen isotopes ($\delta^{18}O_{Tur}$) of tourmaline vary between +6.5 ‰ and +14.9 ‰, similar to the $\delta^{18}O$ range of quartz ($\delta^{18}O_{Qtz}$ = +5.0 ‰ to +16.1 ‰) intergrown with tourmaline. Temperature-corrected boron and oxygen isotopic fluid compositions indicate that tourmaline-rich assemblages were precipitated from magmatic – hydrothermal fluids derived locally from their host

intrusions. In combination with fluid inclusions data, the boron and oxygen isotopic variations illustrate that decompression, decreasing temperature, and/or mixing with external water could all have played positive roles in the generation and precipitation of the tourmaline-quartz-rich features. Six initial $^{87}Sr/^{86}Sr$ compositions of tourmaline from the Heemskirk and Pieman Heads granites range from 0.719525 to 0.750317, indicating that their parental magmas were strongly contaminated by continental crust.

Both boron and oxygen isotopic compositions of tourmaline increase sequentially from patches to orbicules and cavities in the Heemskirk and Pieman Heads granites. These isotopic and trace element variations in tourmaline and quartz among different tourmaline-rich textures are interpreted to have been caused by volatile exsolution and fluxing of aqueous boron-rich fluids that separated from the granitic melts during the emplacement of S-type magmas into the shallow crust (4 to 5.5 km). Volatile-rich hypersaline fluids separated from the crystallising aluminosilicate magmas due to liquid immiscibility, ascending and coalescing between grain boundaries of the crystallising melts via tube plumes and/or spanning clusters. Rayleigh fractionation modelling indicates that approximately 60 % to 77 % of the boron was removed from the initial felsic melt to produce tourmaline patches, whereas higher degrees of fractional crystallisation of the initial granitic melt (up to 90 %) led to exsolution of boron-rich hypersaline fluids from which the tourmaline orbicules and miarolitic cavities precipitated.

The tin-mineralised Heemskirk and barren Pieman Heads granites from western Tasmania were emplaced simultaneously around 365 Ma. They have similar geochemical signatures and tourmaline-rich textural features. More abundant evidence for volatile exsolution (e.g., tourmaline-filled miarolitic cavities and USTs), a higher degree of fractional crystallisation, a lower redox state and higher volatile element contents characterised the Heemskirk Granite, and are considered to have made the Heemskirk Batholith to be highly fertile, producing world class Sn deposits and numerous Pb-Zn-Ag veins.

Acknowledgements

The ARC Centre of Excellence in Ore Deposits (CODES) and University of Tasmania are thanked for granting a PhD scholarship to me, covering the tuition fee and living allowance during my PhD candidature. This PhD study was financially supported by the ARC Centre of Excellence in Ore Deposits, and the ARC funded Industrial Transformation Research Hub for Transforming the Mining Value Chain, and the Hugh E. McKinstry Fund from Society of Economic Geologists, with some external analytical work provided by Geoscience Australia.

I would like to thank my principle supervisor Professor David Cooke who proposed the initial idea of this PhD project, granting me an opportunity at CODES in Tasmania, the best place to study geology in the world. Dave generously provided his enthusiasm, expertise and encouragement to guarantee me on the right track over the four years. His inspiring, critical and insightful conversations refreshed my brain at each supervisory meeting, with regards to field work, laboratory analysis, data interpretation, talk preparation and chapter drafting. Dave has shown enormous patience, particularly in 'lavishing red ink' over my thesis chapters and papers for polishing my linguistic English in the recent years.

Many thanks also go to my co-supervisors, Dr Lejun Zhang and Dr Nathan Fox. Lejun and his wife Haibo provided warm-hearted assistance for my living and study in Hobart, especially in the first year after I arrived in Tasmania. I enjoyed many dinners and parties with his family over the previous years. Lejun helped me significantly to complete the geological mapping and sample collecting in the field. He also provided stimulating suggestions to my laboratory analysis, and insightful discussions to my thesis drafting. Nathan generously passed me his knowledge and microanalytical techniques regarding tourmaline chemistry (major, trace elemental and isotopic compositions), allowing me being well trained over the years. He provided positive feedback on the data reduction, presentation preparation and paper drafts, making this PhD study forward smoothly.

Stephanie Sykora, Qiuyue Hong, Evan Orovan, Erin Lawlis, Angela Escolme, Jose Piquer, Carlos Jimenez, Chengbiao Leng, Wenbo Li, Jing Chen, Aleksandr Stepanov and Wasim Hashmi are thanked for their assistance of mapping and sampling the tourmaline-rich features and granites in the field. Travis Holmes is thanked for providing drillhole samples of the Meredith Granite. I am also debited to James Xie from Huanglong Mining Ltd. who allowed me to take drillhole samples of the Red Heemskirk Granite. Andrew McNeil and other people from Mineral Resource Tasmania kindly provided previous reports of Tasmanian geology and mineral deposits, and I am benefited from discussing the genesis of Tasmanian granites and tin mineralisation with them.

Alexander (Al) Cuison and Michele Chapple-Smith did excellent sample polishing, including rock thin sections, fluid inclusion thin sections and laser mounts to this PhD project. Dr Karsten Goemann and Dr Sandrin Feig from Central Science Laboratory are acknowledged for assisting with backscattered electron and cathodoluminescence imaging, and microprobe analysis. I am debited to Professor Mostafa Fayek and Mr Ryan Sharpe who gave kind assistance and discounted charges when I conducted the SIMS

boron and oxygen isotopes of tourmaline at the University of Manitoba, Canada. Dr David Huston invited me to visit Geoscience Australia, and nicely provided funds to carry out radiogenic isotopic study. Dr Roland Maas from the University of Melbourne is appreciated to complete the radiogenic isotopic analysis. David Huston, Roland Maas and Sebastien Meffre have critically edited parts of this thesis and provided beneficial discussions with regards to understanding radiogenic isotopic compositions. A number of analytical jobs in the thesis are done by LA-ICP-MS at CODES, including zircon U-Pb dating, trace elements of tourmaline and quartz. Gratitude is owned to Jay Thompson, Sarah Gilbert and Leonid Danyushevsky for their help and discussion throughout the analysis. Professor Dima Kamenetsky gave help to recognise melt and fluid inclusions and subsequent microthermometric measurements. Rayleigh fractionation modelling of boron isotope is largely benefited from the discussion with Ping-ping Liu when she visited CODES.

Other people inside and outside CODES and Earth Science Discipline, including Noel White, Ron Berry, Garry Davidson, Bruce Gemmell, Chun Kit Lai, Jocelyn McPhie, Anya Reading, Jane Higgins, Deborah Macklin, Helen Scott, Indrani Mukherjee, Nathan Chapman, Joe Knight, Charles Makoundi, Steve Calladine, Ian Little, Peter Cornish, Zanke Li, Xiaoye Jin, and unlisted persons are appreciated for their assistance and support during my PhD study.

Last but not least, I would like to thank my parents, brothers and other relatives who encouraged and supported me to leave home and pursue my PhD in Tasmania. Xiaoqing (Kelly) Peng came into my life in the past few years, and I wish to thank her encouragement and understanding when I drafted the thesis.

Table of Contents

List of Figures

Chapter 1

Chapter 2

Chapter 3

Chapter 4

Chapter 5

Chapter 6

Chapter 7

Chapter 8

Chapter 9

List of Tables

Chapter 8

List of Appendices

Chapter 1 Introduction

1.1 Preamble

As the most abundant igneous rocks in the continental crust, granitoids not only form some of the most spectacular geological landscapes, but can also be well-endowed with a wide range of economically significant metal resources (e.g., Cu, Mo, Au, W, Sn and rare earth elements; Sillitoe, 2010; Solomon and Groves, 2000). In Tasmania, economically significant granites were emplaced in the Devonian and Carboniferous period, during and after the cratonisation of eastern Australia during via Tabberabberan Orogeny (Black et al., 2010). The granitic intrusions occupy over 6% of Tasmania's landmass. There are more than 80 individual plutons with variable compositions (McClenaghan, 2006a; Fig. 1.1). Large volumes of granitoids crop out in northeastern Tasmania, where several batholiths range in composition from garnet-cordierite-biotite granites, to biotite granites, and hornblende-biotite granodiorites. SHRIMP zircon U-Pb dating indicates that the northeast Tasmanian intrusions were emplaced between 400 and 376 Ma (Black et al., 2005; Kositcin and Everard, 2013).

The most economically important granitoids in Tasmania crop out in western Tasmania, and are concentrated in the Dundas and Dial Range troughs (Fig. 1.1). In contrast to the granitoids of eastern Tasmania, the western Tasmanian granites are less voluminous, mainly consisting of biotite granites, and hornblende-biotite granodiorites. Available U-Pb ages range from 373 to 350 Ma (Black et al., 2005; Kositcin and Everard, 2013), younger than the plutons in eastern Tasmania. Economic Sn-W mineralisation is associated with several western Tasmania granites, including the Meredith, Housetop, Pine Hill, and Heemskirk granites. Tin, Cu, and Ag-Zn-Pb vein-type deposits occur both proximal and distal to the western Tasmanian granitoids, defining world class zoned mineral districts (e.g., Zeehan, Dundas) and Sn deposits (e.g., Renison Bell, Bischoff, and Cleveland Sn deposits; Weston-Dunn, 1922; Groves, 1972a; Solomon, 1981; Kitto, 1994; Halley and Walshe, 1995; Jackson et al., 2000; Zaw and Singoyi, 2000; Walshe et al., 2011; Green, 2012; Fig. 1.1).

Tasmanian granite-related Sn-W deposits can be divided into four broad types: (1) carbonate-replacement Sn deposits, (2) vein-type Sn-W deposits, (3) greisen-type Sn deposits, and (4) magnetite-scheelite skarn deposits (Solomon, 1981). Numerous high-grade but small-size Ag-Zn-Pb vein-type deposits occur in the Zeehan-Dundas mineral field, and the Waratah area. They are considered to be the distal products of the Heemskirk and Meredith granites, respectively (e.g., Both and Williams, 1968; Both et al., 1969).

In addition to significant mineralisation, several of the western Tasmanian granites (e.g., Heemskirk, Pieman Heads) are characterised by spectacular magmatic – hydrothermal features, such as tourmaline orbicules, tourmaline veins, miarolitic cavities and unidirectional solidification textures (Fig. 1.2). It is well-established that abundant volatiles and hydrous fluids can exsolve from crystallising melts emplaced

into the shallow crust (e.g., Burnham, 1979; Burnham and Ohmoto, 1980). The formation of magmatic – hydrothermal mineral deposits fundamentally depends on the release of volatiles and fluids during the final stages of fractionation and crystallisation of felsic magmas. Evidence for fluid exsolution and volatile accumulation in the apical regions of granitoids are provided by magmatic – hydrothermal features and related hydrothermal alteration. Such textures have been described across a wide spectrum of magmatic – hydrothermal ore deposits, including granite-related Sn-W, porphyry Cu-Mo-Au, and even barren granitic systems (Shannon et al., 1982; Kirkham and Sinclair, 1988; Candela and Blevin, 1995; Lowenstern and Sinclair, 1996; Kirwin and Seltmann, 2002; Lickfold et al., 2003; Wilson et al., 2003; Harris et al., 2004; Cannell et al., 2005; Lickfold et al., 2007). Detailed analyses of magmatic – hydrothermal features can potentially help to unravel the nature of magmatic – hydrothermal fluid evolution from granitoids. They could potentially help to inform understanding as to why some granitoids are fertile and can produce economic ore deposits, whilst others are barren, exsolving fluids but not causing mineralisation.

Recent research into magmatic-hydrothermal systems has been heavily biased towards oxidised magmas that produce porphyry Cu-Au-Mo deposits (Sillitoe, 2010, and references therein). In contrast, reduced granitic systems related to Sn-W mineralisation have received comparably little attention over the past few decades (e.g., Solomon, 1981; Blevin and Chappell, 1995; Mao et al., 2013). The well-exposed Sn-W deposits and related granites in Tasmania present an excellent opportunity to study the processes of fluid exsolution and mineralisation associated with large, reduced granitoids.

More than 35 historical Sn-W workings are located within and adjacent to the composite Heemskirk Granite, such as Federation, Sweeney's, Globe Mine, St. Dizier, Queen Hill, Severn, and Montana (Fig. 1.1; Table 1.1). The latter four tin deposits are currently owned and explored by Stellar Resources Limited and are undergoing exploration. Small high-grade Ag-Zn-Pb veins distal to the Heemskirk Granite were mined in the late 1860s-1900s, and are mostly mined out. None are currently under exploration or operation. Recently, the Avebury Ni deposit was discovered in the contact aureole of the Heemskirk Granite. It is unusual because it appears to be granite-related (Seymour et al., 2007; Keays and Jowitt, 2013). The Heemskirk Granite is therefore an excellent example of a fertile granitic pluton, producing proximal Sn (and Ni) deposits and distal Pb-Zn-Ag veins (Fig. 1.1; Tables 1.1 and 1.2).

In contrast to the Heemskirk Granite, no mineralisation has been discovered to be associated with the Pieman Heads Granite (Fig. 1.1), despite its geological similarities and proximity to the Heemskirk Granite. Both the granites are characterised by distinctive magmatic – hydrothermal textures including tourmaline-quartz orbicules and tourmaline-rich veins (Fig. 1.2). The Heemskirk Granite also has unidirectional solidification textures (USTs; e.g., Kirkham and Sinclair, 1988), tourmaline-filled miarolitic textures.

Most of the Tasmanian granitoids have been historically dated by K-Ar and/or Rb-Sr methods (McDougall and Leggo, 1965), but these ages have been affected largely by radiogenic Sr and Ar loss. Black et al. (2005) and Kositcin and Everard (2013) partially resolved this problem, providing a large database of precise SHRIMP zircon U-Pb results for the Tasmanian granites. However, some Tasmanian granites still lack precise zircon U-Pb ages, including the George River Granodiorite, Mt. Pearson Granite,

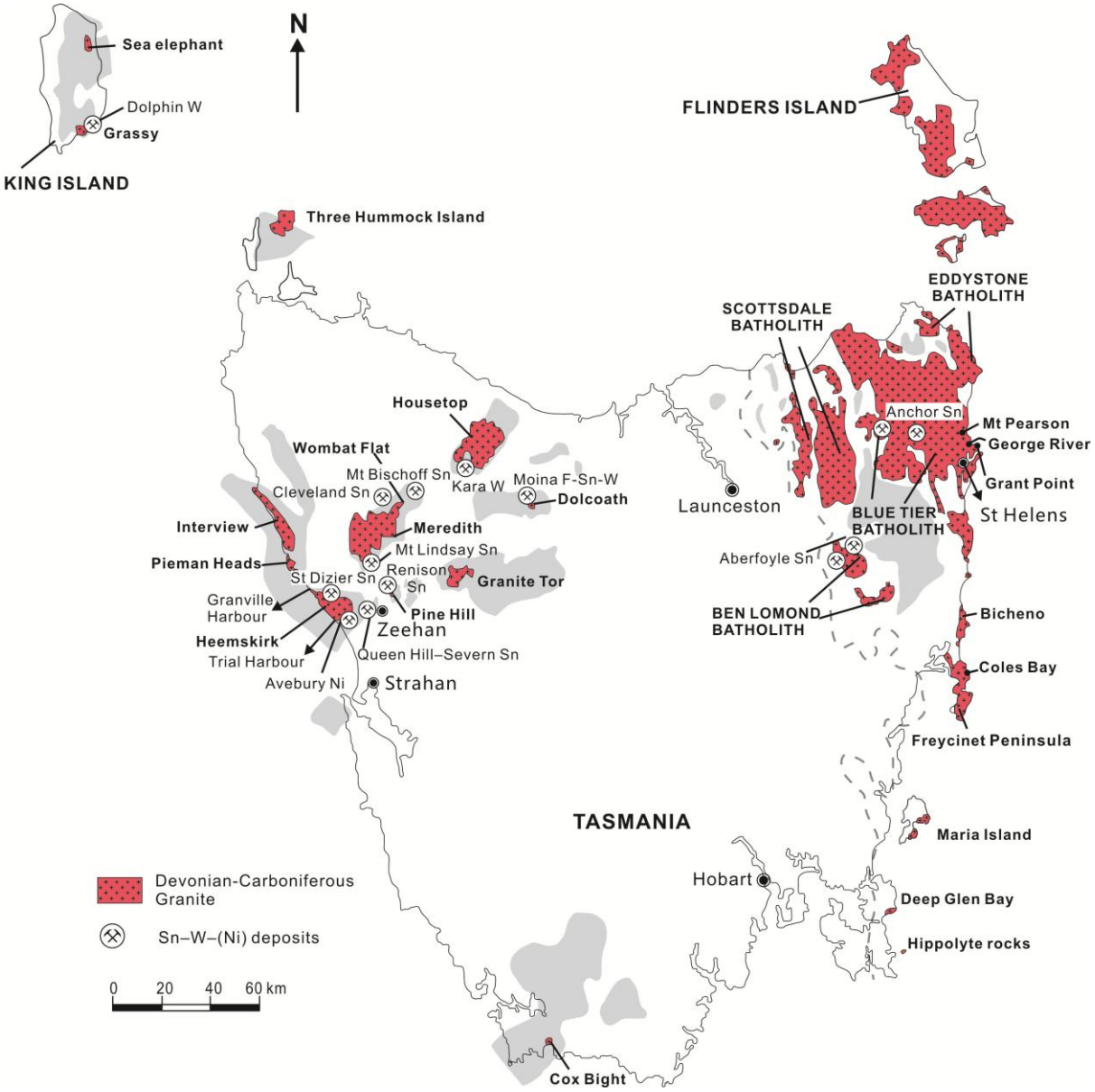

Figure 1.1 Simplified map showing granitic intrusions and main Sn-W-Ni deposits in Tasmania and neighbouring regions. The grey areas and dashed lines represent surface batholiths (2 km isobaths) for mid-Palaeozoic granites (after Leaman and Richardson, 2003).

Grant Point Granite and Coles Bay granites in eastern Tasmania, and the Pine Hill, Meredith and Pieman Heads granites in western Tasmania (Fig. 1.1).

Previous radiogenic studies of Tasmanian granites mostly focused on the relationships between granite genesis and source rocks in Tasmania (e.g., Cocker, 1982; Turner et al., 1986; Mackenzie et al., 1988; Sun and Higgins, 1996; Black et al., 2010), and did not consider metal fertility. Some eastern Tasmanian granites (e.g., the Lottah, and Ben Lomond), and most of the western Tasmanian granites are spatially associated with economic Sn-W deposits, but only a few studies have attempted to unravel their genetic relationships (e.g., Groves and McCarthy, 1978; Bajwah et al., 1995). Therefore, geological controls on Sn-W mineralisation related to Tasmanian granites still need to be elucidated.

Table 1.1 Sn, W, Fe and Ni deposits associated with the Heemskirk Granite, western Tasmania

Field	Deposit	Commodity	Tonnage (Mt)	Grade	Reference
South Heemskirk	Tenth Legion	Sn-Fe	0.9 6.0	0.4 - 0.5 % Sn 60 % Fe	Purvis (1989)
	Colemans	Sn	0.5	0.2 % Sn	
	Sweeneys	Sn	0.5	0.6 % Sn	
	Federation Globe	Sn	> 1.5	0.5 - 0.6 % Sn	
	Avebury	Ni	29.3	0.9 % Ni	Keays and Jowitt (2013)
North Heemskirk	St. Dizier	Sn-W-Fe	~2.6	0.5 % Sn 0.05 % WO_3	Seymour et al. (2007)
Zeehan	Severn	Sn	4.17	0.98 % Sn	Callaghan (2013)
	Montana	Sn	0.51	1.91 % Sn	
	Queen Hill	Sn	3.6	1.2 % Sn	Seymour et al. (2007)
	Oonah	Sn	1.0	0.7- 1 % Sn	Purvis (1989)

1.2 Aims of the project

Magmatic – hydrothermal processes involve the interaction of magmas and the hydrothermal fluids that are derived from them. They include processes such as phase separation, unmixing, vein formation and metasomatism/hydrothermal alteration. They can produce a range of textural features such as USTs, miarolitic cavity, pegmatites, vein dykes, veins, alteration patches and halos, etc. This thesis examines evidence for such phenomena in the western Tasmanian Sn granites.

The main aim of this PhD project is to conduct a comparative study of the geological and geochemical characteristics of the fertile (Heemskirk) and barren (Pieman Heads) granites in Tasmania. This study aims to determine the origin of magmatic – hydrothermal transition textures (e.g., USTs, tourmaline-quartz orbicules, and tourmaline cavities) associated with both the mineralised and barren granites. Secondly, the PhD project will evaluate how the magmatic – hydrothermal fluid (i.e., hydrothermal fluid of magmatic origin) evolution influenced Sn-W mineralisation associated with Tasmanian granites, particularly the Heemskirk Batholith and Pieman Head Granite. Last but not least, based on whole-rock geochemistry, radiogenic Pb-Sr isotopes and U-Pb geochronology, this study will explore possible geodynamic and geochemical controls on tin mineralisation associated with Tasmanian granites, with a comparative analysis of the eastern and western Tasmanian granitoids through time.

1.3 Exploration history

Table 1.2 Production records of Ag and Pb from the Zeehan mineral field (from Both and Williams, 1968)

Deposit or prospect	Lead (tons)	Silver (oz.)	Production years
Argent No.2	1,750	207,347	1899-1925
Argent No. 5	1,100	170,000	1915-1917
Argent No. 6	1,398	183,763	1920-1925
Austral Valley	800	33,000	1907-1913
Florence	10,200	1,400,000	1900-1910
Colonel North	1,534	127,225	1890-1909
Junction	15	8,728	1888-1906
Maxim	60	10,000	1890-1910
Montana No.1	115	1,500	1887-1984
Montana Silver-Lead	2,304	279,348	1899-1958
Mt. Zeehan	1,540	166,850	1883-1893
Nike	2,149	225,830	1896-1954
Nubeena	325	42,000	1894-1910
Oceana	14,902	614,981	1893-1960
Oonah	11,724	2,050,135	1888-1925
Queen	16,532	1,973,746	1902-1929
Silver King	5,000	350,000	1887-1908
Britannia	41,700	6,456,674	1893-1923
Sunrise	36	4,760	1892-1910
Tasmanian Crown	113	15,737	1893-1956
Victoria Zeehan	15	850	
Watt & McAuliffes & North Austral	250	50,000	1901-1905
Zeehan Bell	600	27,500	1890-1908
Zeehan Montana	49,580	7,058,122	1892-1936
Zeehan Western	26,300	4,800,000	1901-1928
Comstock & South Comstock	545	57,096	1888-1952
Silver Stream	165	9,200	1888-1903
Boss	70	6,500	1888-1916
Susannite	20	3,500	1888-1923
Sylvester	274	16,560	1893-1950
Doric	0.5	30	1928
T.L.E	200	30,000	1888-1911
Stonehenge	30	2,700	1888-1894
Swansea	1,319	35,630	1925-1929
Tasmanian (including North Tasmanian)	720	41,229	1893-1953
Total	193,385.5	26,460,541	

Exploration activities related to the Heemskirk Granite date back to 1876 when a government surveyor, C.P. Sprent, found alluvial Sn on the western flank of the Heemskirk Mountain. Many vein-type, skarn and greisen cassiterite deposits and occurrences, including Federation, Sweeney's, Globe, Cornwall, Prince George, Kelvin, Victoria, and Cliff (Table 1.1; Fig. 3.5), were discovered between 1879 and 1890 (Waterhouse, 1916; Blissett, 1962; Table 1.1). Over 15 batteries were subsequently erected in the south Heemskirk region (Blissett, 1962). However, the exploration boom collapsed during the 1890s, due to the irregular occurrence of cassiterite, coupled with high cost of erecting batteries, inaccessibility of the district, and partially with mistaking tourmaline and hematite for cassiterite (Hajitaheri, 1985).

Detrital cassiterite was discovered in 1901 at Mayne's, ca. 4 km south of Mt. Agnew (Blissett, 1962). Federation Tin Mine Limited re-opened some of the Sn deposits in 1928, but terminated the production by 1934, largely due to lack of capital for further development. A few tons of cassiterite ores were produced at western Federation between 1934 and 1942, and at Coleman between 1942 and 1953. The Electrolytic Zinc Co. Ltd., and the Renison Limited conducted geological investigations in the south Heemskirk region during the early 1950s, and late 1970s, respectively, and both the companies concluded that the Sn mineralisation in this district was not economically minable. Blissett (1962) estimated that at least 814 tons of tin was extracted out from the south Heemskirk Granite up to the 1950s. The Heemskirk tin field was estimated to host at least 0.03 Mt of tin (Purvis, 1989; Seymour et al.. 2007; Table 1.1). The unusual hydrothermal Avebury deposit was discovered in 1997 at the contact between the southern edge of the Heemskirk Granite and ultramafic-mafic rocks. It contains a resource of 29.3 Mt at 0.9 % nickel (Keays and Jowitt, 2013; Table 1.1).

The Zeehan mineral field is located east of the Heemskirk Granite (Fig. 2.5). Frank Long discovered silver-lead vein mineralisation in the Zeehan field in 1882. Intense prospecting and mining of silver-lead veins from the Zeehan mineral field occurred through the late 1880s to early 1900s, and ceased in 1914 (Both and Williams, 1968). As the Montana Ag-Pb deposit was discovered, and the Oceana mine re-developed in the late 1940s, silver, lead, and zinc were mined again from this district until the early 1960s (Both and Williams, 1968). Approximately 0.2 million tons of lead, 826 tons of Ag and 2,700 tons of Zn had been extracted from ca.50 individual mines (Blissett, 1962; Both et al., 1969; Table 1.2).

Minor cassiterite was found in 1937 on Queen Hill as a part of the Stormsdown Lode. The Zeehan Tin Development NL which owned the Stormsdown mine produced approximately 5.4 tons of tin between 1937 and 1960 (Blissett, 1962). Placer and Minops Limited commenced modern exploration in the mid-1960s, and estimated 'total reserves' in the Oonah lode with 674 000 tons of 1.1 % Sn, 1.25 % Cu and 115 g/t Ag (Purvis, 1989; Table 1.1). Sulphide-cassiterite mineralisation was discovered at Queen Hill and Montana between 1965 and 1971, with subsequent discovery of the larger cassiterite-sulphide Severn deposit in 1975. Aberfoyle Limited conducted a program of 89 drills in the Zeehan mineral field from 1970s to 1992. Stellar Resources Limited conducted drilling programs between 2010 and 2013 at Queen Hill, Severn and Montana orebodies, defining a combined indicated and inferred resource of 72000 tons of tin at 0.98 to 1.91 % (Callaghan, 2013; Seymour et al., 2007; Table 1.1).

1.4 Previous work

Waterhouse (1916) described the geology and petrology of the Heemskirk Granite, and the tin exploration activities within and distal to the granite. He noted the white and pink colours of the Heemskirk Batholith. Green (1964) conducted geological mapping along the Trial Harbour coast. He recognised magnetite skarn and related magnetite veins, and the relationships between the Heemskirk Granite, and Neoproterozoic metasedimentary rocks and Cambrian ultramafic rocks. Brooks and Compston (1965) and Brooks (1966) divided the Heemskirk batholith into a Red phase and two White phases (white A and white B). They reported that the Heemskirk Granite has highly radiogenic strontium

isotopic compositions, ranging from 0.705 to 0.734, with an Rb-Sr age of 354 ± 7 Ma. Heier and Brooks (1966) argued that low K/Rb ratios reflected highly fractionated feature of the Heemskirk Granite, and that abundant tourmaline, cassiterite and sulphide in the white Heemskirk were products of a vapour phase accumulating in the roof of the intrusion. Klominsky (1972) conducted a detailed mapping of the Heemskirk Batholith, and divided the granite into two main phases, the White and Red phases based on geological, petrographic and geochemical studies. Subsequent whole-rock geochemical, fluid inclusion and stable isotopic investigations were carried out by Hajitaheri (1985) on the south of the Heemskirk Granite, providing insights into physicochemical conditions prevailing in the batholith during cassiterite-sulphide mineralisation.

The Pieman Heads Granite has drawn less attention than the Heemskirk Granite, largely due to a lack of known mineralisation. The granite intruded the Neoproterozoic Rocky Cape Group, and is overlain by Tertiary and Quaternary sedimentary rocks. Brooks (1966) reported an Rb-Sr age of 353 ± 7 Ma and high $^{87}Sr/^{86}Sr$ ratios (0.7354 ± 0.0018), similar to the white Heemskirk Granite. Sawka et al. (1990) grouped the Pieman Heads Granite (Conical rocks) as part of the 'Sandy Cape Suite', and reported a whole-rock Rb-Sr isochron age of 344 ± 5 Ma, K-feldspar Ar-Ar plateau ages of 350 to 340 Ma, and a biotite Ar-Ar plateau age of 353 ± 5 Ma for the granite.

Regional investigations on western and eastern Tasmanian granites and related mineralisation were conducted by McDougall and Leggo (1965), Groves (1972a), Groves and MaCarthy (1978), Cocker (1982), Turner et al.(1986), Mackenzie et al. (1988), Sawka et al. (1990), Sun and Higgins (1996), McClenaghan (2006a), Black et al. (2005, 2010), and Kositcin and Everard (2013). Their findings are reviewed in Chapter 2.

1.5 Location and access

The Heemskirk Granite is exposed west of the Zeehan Township, on the western coastline of Tasmania. The landscape associated with this intrusion includes the Heemskirk Range to the east, and the coastal plain to the west. The margins of the granite are easily accessible through roads to Trial Harbour and Granville Harbour, both of which are in good condition. Trial Harbour is ca. 20 km west of Zeehan, and can be accessed via Trial Harbour Road. Distinctive tourmaline-rich magmatic – hydrothermal features crop out near Trial Harbour at E145°09′23.93″and S 41°55′20.64″ (elevation = 22 m; Figs. 1.2a-b). Access from Trial Harbour involves walking on rough rocky beaches that expose Neoproterozoic sedimentary rocks, ultramafic-mafic rocks, magnetite skarn, and the contact of the Red and White phases of the Heemskirk Granite. Granville Harbour is situated northwest of Zeehan, and can be accessible by the 38 km-long Zeehan – Granville Harbour Road. There are excellent exposures of magmatic – hydrothermal textures in the south side of Granville Harbour (E145°01′40.47″, S 41°48′34.80″, elevation = 1 m), where a northern apophysis of the Heemskirk Granite has intruded the metasedimentary Oonah Formation (Fig. 1.2c). Distinctive magnetite-bearing unidirectional solidification textures, tourmaline-quartz orbicules, and tourmaline-filled miarolitic cavities can be observed at this locality.

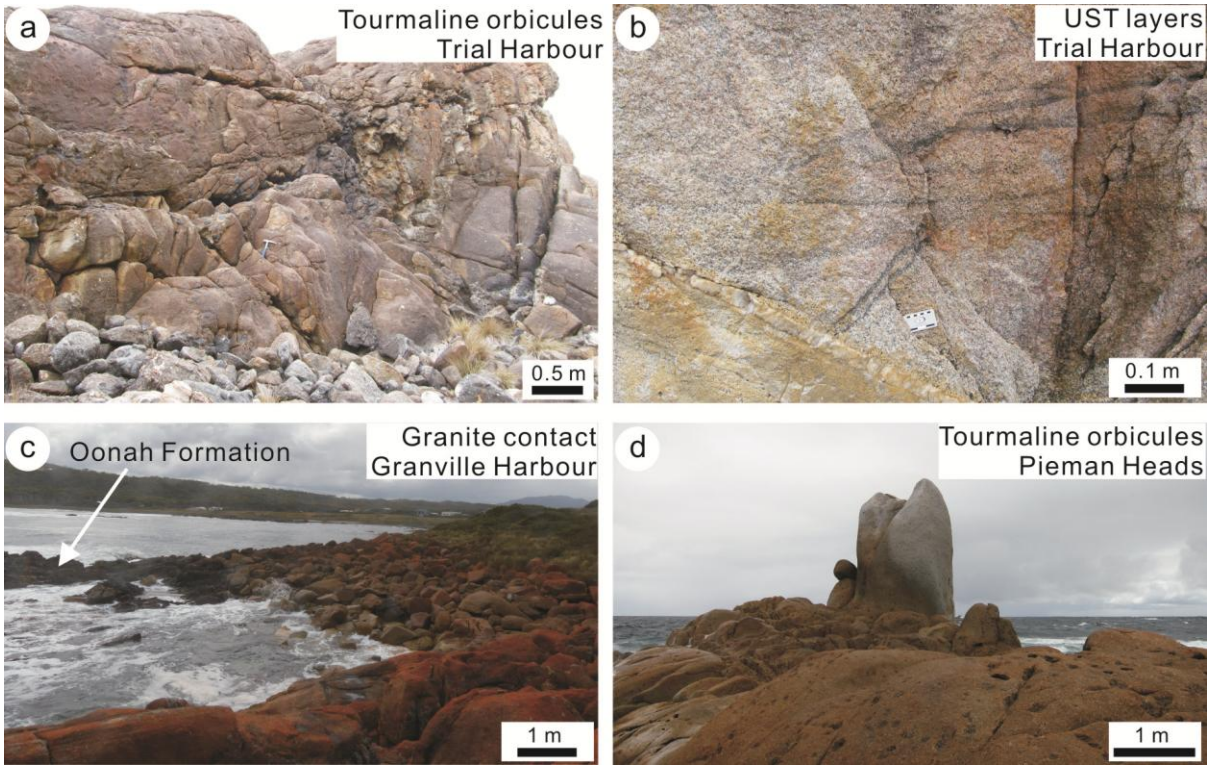

Figure 1.2 Photos showing outcrops of the Heemskirk and Pieman Heads granites from western Tasmania. (a) Tourmaline-rich features exposed in the Heemskirk Granite at Trial Harbour. (b) A quartz-rich UST layer is bounded between the Red phase (right up) and the White phase (left down) of the Heemskirk Granite at Trial Harbour. (c) Contact of the Heemskirk Granite and Oonah Formation at Granville Harbour (view from the intrusion to NW direction). (d) Tourmaline orbicules and patches in the Pieman Heads Granite.

The Pieman Heads Granite crops out approximately 20 km north of the Heemskirk Granite. The granite (sampling coordinate: E144°55′40.01″, S41°43′15.00″; Fig. 1.2d) is located on the southern side of the Pieman River, immediately to the south of the Interview River Granite. Access to the Pieman Heads Granite is difficult. A 4 WD coastal track that extends north through sand dunes from the Granville Harbour proves the most direct access. This track is in poor condition, and locally encounters forests, creeks, beaches and steep sandy slopes.

The George River Granodiorite, Mt Pearson Granite and Grant Point Granite crop out in the Binalong Bay area, eastern Tasmania, approximately 13 km northeast of St. Helens. The George River Granodiorite (sampling coordinate: E148°18′32.23″, 41°14′58.28″; Fig. 1.3a) and Grant Point Granite (sampling coordinate: E148°18′50.63″, S41°14′58.97″; Fig. 1.3b) crop out extensively on Binalong Beach, on the southern side of Binalong Bay. The Mt Pearson Granite (sampling coordinate: E148°17′32.57″, S41°14′33.11″) is well exposed on the northern side of Binalong Bay (Fig. 1.3c). These three granitic intrusions are easily accessible via walking tracks along the beaches.

The Bicheno Granite has a number of outcrops on the foreshore around Bicheno in eastern Tasmania. This granite is best exposed at Bicheno Blowhole (sampling coordinate: E148°18′46″, S41°52′30″; Fig. 1.3d). Several granitic plutons are exposed on the Freycinet Peninsula on the central eastern coast of Tasmania. One felsic intrusion (the Coles Granite) was sampled from Friendly Beach (sampling coordinate: E148°17′00.31″, S42°01′23.43″), approximately 30 km south of Bicheno. All of the eastern

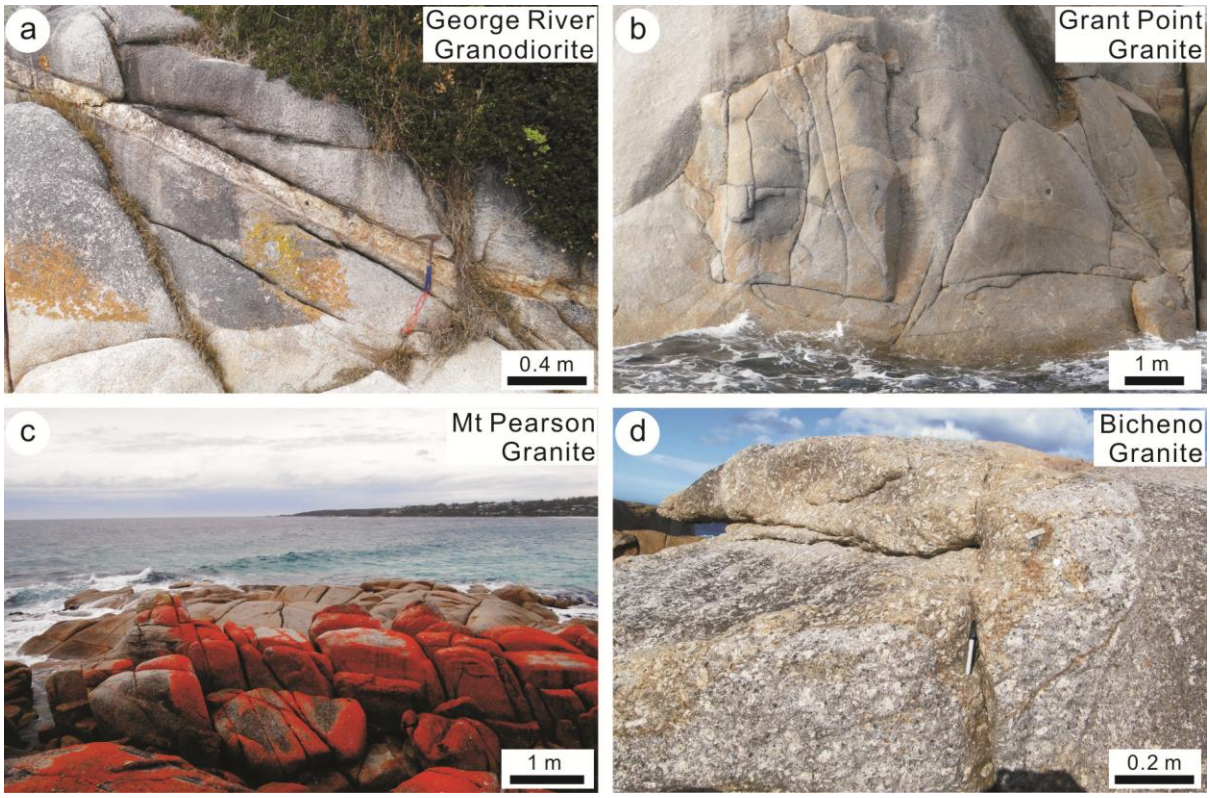

Figure 1.3 Photos showing outcrop of granitic intrusions from eastern Tasmania. (a) An aplitic dyke cuts the George River Granodiorite at Binalong Bay. (b) The Grant Point Granite exposed at Binalong Bay. (c) Weathered Mt Pearson Granite with red skin. (d) The Bicheno Granite contains megacrystic K-feldspar grains.

Tasmanian sampling sites are easily accessible via the A3 Tasmanian highway and other local roads.

1.6 Thesis organisation

In addition to this introduction, this PhD thesis contains another eight chapters.

Chapter 2 briefly reviews the geological evolution of Tasmania and neighbouring regions since the Mesoproterozoic (ca. 1.45 Ga). This chapter also describes the main features of granitic rocks in Tasmania, including the Neoproterozoic, Cambrian, and Devonian – Carboniferous granites, with emphasis on documenting the characteristics, geochronology and petrogenesis of Tasmanian Devonian – Carboniferous granites. This chapter also reviews economically important tin-tungsten mineralisation in Tasmania that are intimately associated with the Devonian – Carboniferous granites.

Chapter 3 presents petrography, major- and trace element data, LA-ICP-MS zircon U-Pb ages, and Pb isotopes for K-feldspar of eastern and western Tasmanian granites, including the George River, Mt. Pearson, Grant Point, Bicheno and Coles Bay granitoids from eastern Tasmania, and the Housetop, Meredith, Pine Hill, Heemskirk, and Pieman Heads granites from western Tasmania. This chapter discusses the granite petrogenesis, geodynamic evolution of mid-Palaeozoic Tasmania, and space-time correlations with other granite provinces in the Lachlan Fold Belt of southeastern Australia.

Chapter 4 documents the detailed geological and mineralogical characteristics of tourmaline- and quartz-rich magmatic – hydrothermal features, including tourmaline patches, orbicules, miarolitic cavities, veins and unidirectional textures from the Heemskirk and Pieman Heads granites from western Tasmania. A brief discussion of spatial-temporal relationship and origins of these features concludes the chapter.

Chapter 5 presents backscattered imaging, electron microprobe and laser ablation inductively coupled plasma mass spectrometry (LA-ICP-MS) analyses of tourmaline grains from magmatic – hydrothermal features in western Tasmanian granites documented in Chapter 4. These techniques reveal remarkable growth zones, and major and trace element variations between different textural types of tourmalines crystals. Possible geological controls that affect compositional variations between tourmaline types from western Tasmania are discussed, and a preliminary model is proposed for the formation of the magmatic – hydrothermal textural features.

Chapter 6 presents scanning electron microscope-cathodoluminescence and LA-ICP-MS analytical results of quartz crystals from tourmaline-rich magmatic – hydrothermal features. The chapter discusses the main factors causing chemical variations in magmatic – hydrothermal quartz, and fluid evolution based on quartz chemistry. The potential usefulness of trace concentrations and ratios in quartz for exploration is evaluated.

Chapter 7 determines the physicochemical conditions of tourmaline- and quartz-rich magmatic – hydrothermal features in the Heemskirk and Pieman Heads granites, including temperature, pressure, depth and salinity, in combination with fluid inclusion data and Ti-in-quartz geothermometry.

Chapter 8 presents boron and oxygen isotopes of tourmaline and quartz analysed by secondary ion mass spectrometry, and strontium isotopes of tourmaline analysed by multi-collector ICP-MS. These analytical results are used to elucidate possible fluids or source reservoirs that relate to the formation of the tourmaline-rich magmatic – hydrothermal features. Geological factors and modelling that illustrate isotopic variations between different textural features conclude the chapter.

Chapter 9 presents a genetic model describing the geodynamic evolution of Tasmanian granitoids during the mid-Palaeozoic, and a model highlighting the origins of tourmaline-rich magmatic – hydrothermal features in the Heemskirk and Pieman Heads granites. Geological and geochemical controls on Sn-W mineralisation associated with Tasmanian granites are discussed, and recommendations for future work are provided.

Chapter 2 Tasmanian granitoids and related mineralisation

2.1 Introduction

Tasmania has experienced a complex geological evolution from the Mesoproterozoic to the Quaternary, especially in the western Tasmanian terrace (Seymour et al., 2007). This chapter briefly reviews the history of Precambrian and Palaeozoic rocks that crop out in Tasmania and neighbouring regions, and geological events that they have witnessed. The main emphasis is on granitic intrusive activity that leads to Sn-W mineralisation in Tasmania. This chapter therefore describes the main exposures and characteristics of the Sn granites. Devonian – Carboniferous granites are distributed widely in Tasmania, and have been studied in detail during the past several decades (McDougall and Leggo, 1965; Groves, 1972a; Cocker, 1982; Higgins et al., 1985; Mackenzie et al., 1988; Williams et al., 1989; Sun and Higgins, 1996; Solomon and Groves, 2000; McClenaghan, 2006a; Black et al., 2005, 2010), largely because they are intimately associated with world class Sn-W deposits. This chapter reviews the types, characteristics, and genesis of Sn-W mineralisation related to Devonian – Carboniferous granites in Tasmania, based on primarily previous research.

2.2 Geological background

Situated off the southeastern corner of mainland Australia, Tasmania is principally composed of two distinctive geological domains: the western and eastern Tasmanian terranes (Fig. 2.1). These two geological fragments are bounded by the Tamar Fracture System (Williams, 1978). The eastern terrane is Palaeozoic, comprising an Ordovician to Lower Devonian marine quartzwacke turbidite sequence (Mathinna Supergroup) that has been intruded by abundant Palaeozoic granitoids (Seymour et al., 2007). In contrast, a broad variety of sedimentary sequences ranging from Mesoproterozoic to Triassic crop out across the western two-thirds of the island (Seymour et al., 2007). The long history of sedimentation with intermittent volcanism, in turn, demonstrates that the western Tasmanian terrane has experienced a relatively complicated tectonic evolution and history when compared to the eastern Tasmanian terrace. The western terrace is underlain by Proterozoic sequences, and has been intruded by Precambrian, Cambrian and Devonian – Carboniferous granitoids.

2.2.1 Geological evolution

2.2.1.1 Proterozoic

The oldest known rocks in Tasmania are metasedimentary units of the lower to middle Rocky Cape Group, which have detrital zircon and authigenic monazite U-Pb ages of ~ 1450 to 1330 Ma (Halpin et al., 2014; Fig. 2.1). Stratigraphically equivalent Mesoproterozoic metasedimentary rocks crop out on King

Island (e.g., Surprise Bay Formation; Black et al., 2004). The largest exposed area of Meso- to Neoproterozoic rocks is the Tyennan region in central-southwestern Tasmania (Fig. 2.1). The polydeformed metamorphic assemblages include greenschist-facies metaquartzite, graphitic and chloritic metapelite, and garnet-bearing schist, amphibolite-bearing quartzite, and eclogite facies mafic rocks. This Proterozoic basement of Tasmania is interpreted to have been attached to the Transantarctic Mountains of East Antarctica until 580 Ma (Berry et al., 2008), and the Mesoproterozoic successions are interpreted to have been deposited between proto-Australia and Laurentia during the rifting of the Columbia (or Nuna) supercontinent (Halpin et al., 2014).

Neoproterozoic shallow marine shelf sedimentation produced the upper section of Rocky Cape Group siliciclastics, and the Oonah Formation and their correlates in western Tasmania (Fig. 2.1). In contrast to the laminated siltstones and sandstones that dominate lower-middle sections of the Rocky Cape Group, the upper parts of the Proterozoic succession contain more fine-grained quartz arenite and quartzite with abundant cross-bedding (Calver et al., 2014a), probably with a depositional age of < 1010 Ma (Halpin et al., 2014). The Oonah Formation, previously named the Burnie Formation and Badger Head Group (Fig. 2.1), is a thick quartzwacke turbidite sequence with various metamorphic grades. It is widely distributed in Northwest Tasmania (Fig. 2.1), and was probably deposited between 1070 and 750 Ma, according to the youngest detrital zircon ages and the ages of overlying strata (Seymour et al., 2007).

Neoproterozoic sedimentation was interrupted by a low angle regional unconformity, when rift-related granite emplacement took place around 777 – 760 Ma on King Island (Cape Wickham Granite; Fig. 2.1) and Northwest Tasmania (Bowry Formation Granite; Fig. 2.3), perhaps being a response to the Rodinia Supercontinent breakup (Turner et al., 1998; Holm et al., 2003). Another cycle of sedimentation on the passive continental margin then produced the Togari Group and its correlates, until the Early Cambrian (~ 520 Ma; Seymour et al., 2007). These tholeiitic volcanic and sedimentary sequences consist of early-phase siliceous conglomerate, sandstone and volcaniclastics intercalated with basaltic lava flows as well as late-phase siliciclastics and dolomite (Fig. 2.1). A second phase of rifting away from the East Antarctic margin probably occurred around 580 Ma, as indicated by the extensive eruption of tholeiites (Meffre et al., 2004). At this time, the western Tasmanian terrane had separated from the Cambrian Ross-Delamerian Orogen (Berry and Bull, 2012).

2.2.1.2 Cambrian

The Cambrian Tyennan Orogeny in western Tasmania was triggered by an arc-continent collision from the early to middle Cambrian. In the first stage (515 – 510 Ma), the collisional event led to the emplacement of voluminous allochthonous blocks, including obducted mafic and ultramafic complexes (mainly ophiolite) in northwestern Tasmanian (Fig. 2.1; Berry and Crawford, 1988). The widely distributed Mt Read volcanic rocks and associated volcanic-hosted massive sulphide (VHMS) deposits were generated within the Dundas Trough and neighbouring regions at ~ 505 Ma, as the Tyennan Orogeny evolved to a post-collisional volcanism and extension stage (Crawford and Berry, 1992). The western Tasmania then underwent basin inversion in the late Cambrian, causing extensive and complex

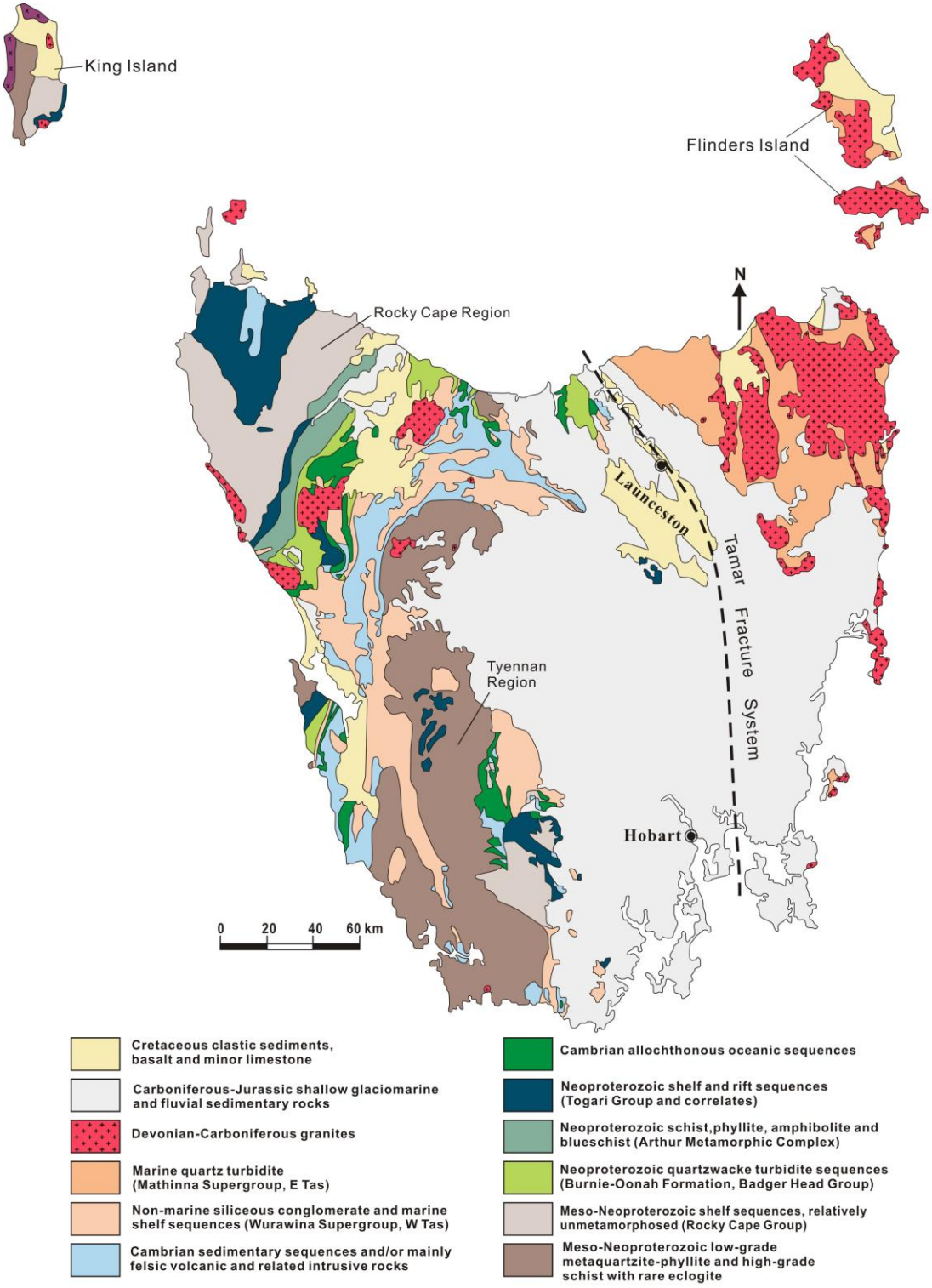

Figure 2.1 Simplified geological map of Tasmania (modified from Seymour et al., 2007), including the King Island and Flinders Island. The lower-middle sections of the Rocky Cape Group have been constrained to be Mesoproterozoic (~ 1450 Ma; Halpin et al., 2014). The location of the Tamar Fracture System is approximate (from Williams, 1978).

unconformities within the siliciclastic Owen Group, as the micro-continent was accreted back onto the Gondwana margin (Berry and Bull, 2012).

2.2.1.3 Late Cambrian-Devonian

Contrasting sedimentary sequences accumulated in the western and eastern Tasmanian terranes during the Palaeozoic (Fig. 2.1). As the late Cambrian basin inversion and E-W compression resulted in major reverse faults and uplifting in the Tyennan region, voluminous coarse siliciclastic conglomerates of the Owen Group were deposited within a half-graben in western Tasmania, disconformably resting on older sequences (Seymour et al., 2007). West of the Machinery Fault, the Ordovician – Early Silurian Gordon Group unconformably overlies the Owen Group sequences, whereas east of this structure, the relationships between these two groups are transitional and conformable. The intertidal to shallow marine Gordon Group units are dominated by micritic, dolomitic limestone, and gradually thinned from the central-south to western Tasmania (Calver et al., 2014b). The carbonate-rich sequences are overlain conformably to unconformably by thick siliciclastics sediments of the Silurian to early Devonian Eldon Group (Fig. 2.1). The depositional setting of the Eldon Group changed from initial shallow-marine quartz sandstone to younger shelf-facies shale with minor carbonate (Banks and Baillie, 1989). The Owen, Gordon and Eldon Groups compose the Wurawina Supergroup, which is exposed over significant areas in western Tasmanian terrane (Fig. 2.1).

In the eastern Tasmanian terrane, Palaeozoic sedimentation produced the Mathinna Supergroup which consists mainly of deep marine quartzose, and feldspathic turbidites with graptolites and shelly fossils. They are the oldest rocks exposed in the eastern Tasmania, forming the pre-Carboniferous basement of the region (Seymour et al., 2011; Fig. 2.1). The Mathinna Supergroup is correlated with the lower Palaeozoic turbidites of the Lachlan Fold Belt of Victoria, especially with the Melbourne Trough (Powell, 1992; Cayley, 2011). The eastern Tasmania terrace appears to have been separated from the rest of Tasmania at the time of Mathinna Supergroup deposition, and did not amalgamate with the older western Tasmanian terrane until the Middle Devonian orogeny (Williams et al., 1989; Powell, 1992; Seymour et al., 2007).

Extensive felsic magmatism began in Tasmania around 400 Ma with relatively mafic I-type granodiorites emplaced in northeast Tasmania (Fig. 2.3). The granitic rocks became progressively younger westward across the whole Tasmanian terrane (McDougall and Leggo, 1965; Black et al., 2005; Kositcin and Everard, 2013), with the youngest plutons exposed on King Island (~ 350 Ma; Fig. 2.3). A series of NNW-oriented folds and fault systems throughout Tasmania characterise the Tabberabberan Orogeny. This is the most widespread Palaeozoic deformation event in eastern Australia, and affected the entire Lachlan Fold Belt in New South Wales and Victoria, in addition to the Tasmanian terrace (Fig. 2.2). At least two compressional deformation events, which are largely interpreted by reactivation of older structures, occurred in Tasmania during this Middle Devonian orogeny (Seymour et al., 2007, and references therein). On the basis of NW-directing foliations dominated in individual granites of northeast Tasmania, Black et al. (2005) precisely constrained the deformation induced by the Tabberabberan Orogeny at ~ 390 Ma for north-eastern Tasmania. The Tabberabberan Orogeny in Tasmania was probably a response to the collision and amalgamation of the western and eastern Tasmanian terranes (Black et al., 2005, 2010).

2.2.1.4 Carboniferous

The Kanimblan Orogeny is a Middle Devonian to Early Carboniferous deformation event that influenced parts of the Lachlan Fold Belt. It is interpreted to be related to the initiation of post-Tabberabberan extension, which caused local rifting (Meakin and Morgan, 1999; Lyons et al., 2000; Wormald et al., 2004). Clastic (mostly continental) sedimentation and widespread I-, S- and A-type granites were emplaced during this orogeny (Chappell and White, 1992; Glen et al., 2004). The recognition of the Kanimblan Orogeny in Tasmania is principally restricted to felsic magmatic events. McDougall and Leggo (1965) noted that granitic plutons with ages around 340 Ma may correlate with the Kanimblan Orogeny identified in Victoria and New South Wales, although these ages were not particularly accurate. Recent zircon SHRIMP U-Pb dating confirmed the presence of Early Carboniferous granites in western Tasmania (Black et al., 2005), including the Sandy Cape Granite (362 ± 2 Ma), the White phase of the Heemskirk Granite (361 ± 2 Ma), the Red phase of the Heemskirk Granite (360 ± 2 Ma), and the Grassy Granite on King Island (351 ± 2 Ma; Fig. 2.3).

2.2.1.5 Post-Carboniferous

Considerable erosion followed the termination of Devonian – Carboniferous magmatism and orogeny. Sedimentation occurred in the Tasmania basin from the Late Carboniferous to the Late Triassic. The basin is generally subdivided into several widespread lithological sequences, including the Lower and Upper Parmeener Supergroups. The former is composed of marine-glacial and subordinate terrestrial sediments, whereas fluvial and lacustrine sediments comprise the latter association (Clarke and Forsyth, 1989). The Parmeener Supergroups and Jurassic tholeiitic dolerite intrusions largely obscure the Tamar Fracture System, which is considered as the boundary between the eastern and western Tasmanian terranes (Fig. 2.1). Large volumes of Jurassic dolerite currently crop out over half of Tasmania. Their emplacement resulted from tensional strains between continental blocks, and this was one of the precursors to the breakup of Gondwanaland (Baillie, 1989). With continuous rifting of Australia from Antarctica, numerous extensional sedimentary basins developed in Tasmania from the Late Mesozoic to Neogene.

2.2.2 Granitic intrusions

2.2.2.1 Pre- Cambrian and Cambrian granitoids in Tasmania

Three major episodes of granite emplacement affected Tasmania and adjacent regions. The Cape Wickham and Loorana granites (760 ± 12 Ma and 762 ± 14 Ma) on King Island, and an unnamed granite (777 ± 7 Ma) that intruded the Bowry Formation in northwest Tasmania are the only known Precambrian felsic intrusions in the Tasmanian region (Fig. 2.3). They are characterised by foliated or sheared K-feldspar-dominated porphyritic monzonites with considerate enrichments of high field strength elements, and have been attributed to the breakup of Rodinia (Holm et al., 2003), and/or with a small-scale deformation event (the Wickham Orogeny; Turner et al., 1998).

The second period of granite emplacement occurred in the Cambrian. These granites sparsely crop out at Beulah, Dove River, Mt Murchison, Mt Darwin, Elliot Bay and South West Cape (McDougall and

Leggo, 1965; Williams et al., 1989; Black et al., 2005; Fig. 2.3). The Dove Granite is exposed in the Forth and Mersey rivers, and is characterised by a hornblende granodiorite and quartz monzodiorite. The Murchison Granite is a strongly altered and deformed hornblende-bearing adamellite, about 5 km long by 1.6 km wide, elongated N-S. This granite has been recently dated by isotope dilution thermal ionization mass spectroscopy, which yielded a precise U-Pb zircon age of 497.3 ± 0.86 Ma (Mortensen et al., 2015).The Darwin Granite is a coarse-grained pink to white pluton with a non-bulbous pipe-shape (Jones, 1993). The Elliot Bay Granite intruded the extension of the Cambrian volcanic rocks at Low Rocky Point on the southwest coast of Tasmania, and comprises a large composite body and two satellite intrusions with a zircon U-Pb age of 499 ± 3.3 Ma (Black et al., 2005). All of these subvolcanic felsic intrusions are geochemically comparable to typical of oxidised I-type magnetite series granites, and have strongly compositional and temporal affinities with the Cambrian Mt Read volcanics (Crawford et al., 1992; Perkins and Walshe, 1993). The South West Cape Granite is an unusual body, yielding a zircon U-Pb age of 498 ± 3.3 Ma (Black et al., 2005), crudely synchronous with the Mt Read volcanics (Mortensen et al., 2015). However, this intrusion is characterised by a more reduced, peraluminous S-type composition, and was emplaced into Proterozoic sequences (Fig.2.3). These features distinguish it from the Cambrian felsic plutons that intruded the Cambrian volcanics. The Murchison and Darwin granites may have contributed magmatic – hydrothermal components to the formation of Cu-Au-rich group of VHMS deposits hosted in the coeval Mt Read volcanic rocks (Large et al., 1992; Huston et al., 2011).

2.2.2.2 Granite provinces in the Lachlan Fold Belt

Abundant granitic intrusions crop out widely in the Lachlan Fold Belt of eastern Australia (Fig. 2.2), including eastern and western Tasmania. These granitoids have been classified into I- and S-type granites, which originated from meta-igneous (or infracrustal) and meta-sedimentary (or supracrustal) protoliths, respectively (Chappell and White, 1974, 2001). Based on geochemical investigation, ten granite provinces (or basement terranes) have been delineated, including the Bathurst, Bega, Kosciusko, Wagga, Howqua, Melbourne, Stawell, Grampians-Stavely, Bassian, and Taswegia Basement Terranes (Chappell et al., 1988; Fig. 2.2). According to age determinations (Gray, 1997; Black et al., 2005; Fergusson, 2014), these Palaeozoic granites in Lachlan Fold Belt have been revealed to emplace in four periods: Late Silurian – Early Devonian (430 - 400 Ma), mid-Devonian (400 - 385 Ma), Late Devonian – Early Carboniferous (380 - 350 Ma), and Carboniferous (350 - 320 Ma; Fig.2.2).

The granites exposed in eastern Tasmania are major components of the Bassian Province. The granite province encompasses the area east of the Tamar Fracture System, including the large granitoid batholiths on Flinders Island and northeast Tasmania, and continues southward to Maria Island (Fig. 2.2). This granite province extends northward across Bass Strait to Wilsons Promontory in mainland Australia (Fig. 2.2). Granitic plutons in this province were mostly emplaced during the mid-Palaeozoic (400 - 385 Ma). The granitoids exposed west of the Tamar Fracture System in Tasmania are grouped into the Taswegia Province (Fig. 2.2). This granitic province includes King Island, and possibly stretches across Bass Strait

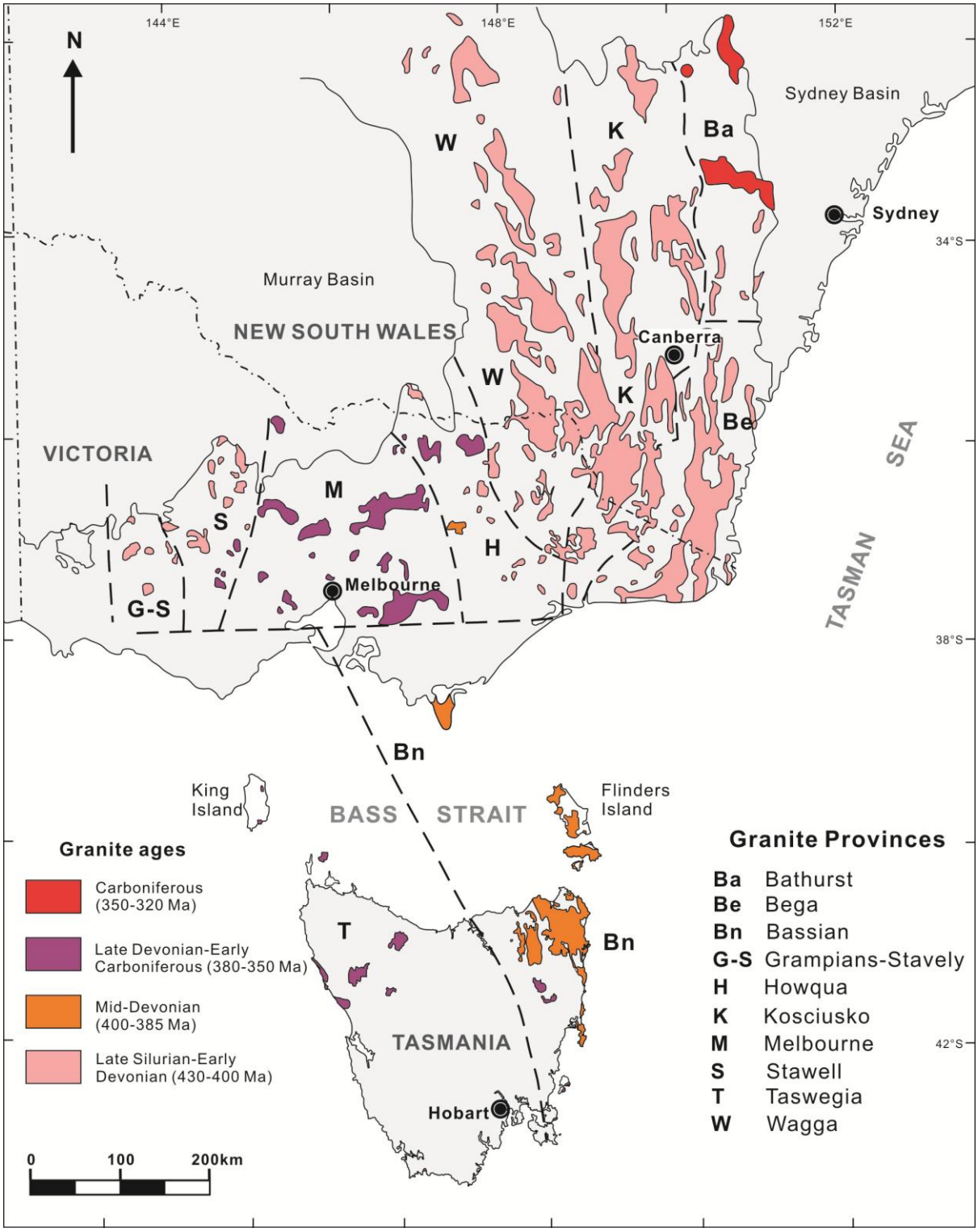

Figure 2.2 Generalised geological map showing the major distributions of granitoids and granite provinces in the Lachlan Fold Belt, southeastern Australia (after Chappell et al., 1988; Gray, 1997; Fergusson, 2014).

to beneath Cape Otway (Chappell et al., 1988). These felsic intrusions were emplaced during the Late Devonian - Early Carboniferous (380 - 350 Ma), younger than the granitoids in eastern Tasmania (Fig. 2.2).

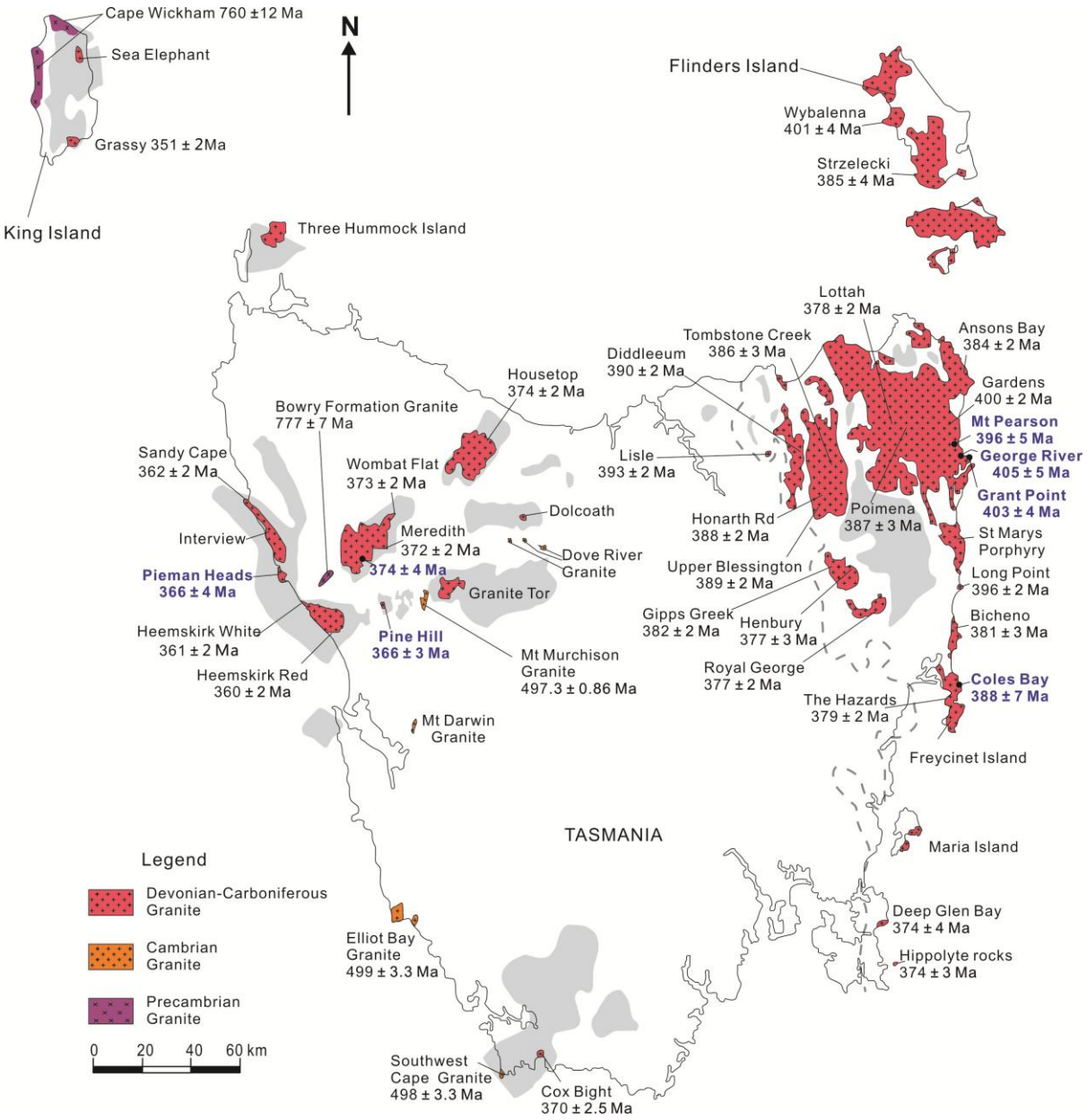

Figure 2.3 The major outcrops of granitic rocks in Tasmania and neighbouring islands. According to their ages, these granitoids can be divided into Precambrian, Cambrian, and Devonian – Early Carboniferous (reproduced from Williams et al., 1989; McClenaghan, 2006a). Zircon U-Pb ages of granitoids are compiled from Turner et al. (1998), Black et al. (2005), Kositcin and Everard (2013), Mortensen et al. (2015) and this study (blue bold). The grey areas and dashed lines (East Tasmania) represent surface batholiths (2 km isobaths) for Devonian – Early Carboniferous granites (after Leaman and Richardson, 2003). The site is approximate for the Precambrian Bowry Formation Granite.

2.2.2.3 Middle Palaeozoic granitoids

The most significant period for granitic magmatism in Tasmania was the Devonian – Carboniferous, with substantial volumes of granitic bodies exposed widely in the eastern and western terranes (McDougall and Leggo, 1965; Williams et al., 1989; Black et al., 2005, 2010; McClenaghan, 2006a; Kositcin and Everard, 2013; Fig. 2.3). Three huge composite granite batholiths have been identified on mainland Tasmania based on the three-D gravity model (Leaman and Richardson, 2003); one in the east, another in the west, and the third primarily unexposed beneath the southwest (Fig. 2.3).

The Cox Bight Granite is the only intrusion in southwest Tasmania that has been mapped and documented in detail; it has only limited exposures (<1 km^2). The pluton is a medium to fine-grained, leucocratic granite to monzogranite, mainly consisting of quartz, K-feldspar, biotite and rare muscovite (McClenghan, 2006a). The pluton is moderately fractionated and has a felsic S-type composition (74 - 76 wt % SiO_2) with a U-Pb age of 370 ± 2.5 Ma (Black et al., 2005). Gravity investigations indicate that the granite batholith underlying southwestern Tasmania may cover an area more than 1700 km^2 at depths of > 2 km (Leaman and Richardson, 2003). Black et al. (2005) argued that the strong gravity anomaly may be caused by subsurface Cambrian rocks rather than Devonian granites.

The largest granitoid batholith in Tasmania is exposed in the eastern terrace, comprising hundreds of individual granitic bodies with diverse chemical compositions and crystallisation ages (McDougall and Leggo, 1965; Black et al., 2005, 2010; McClenaghan, 2006a; Kositcin and Everard, 2013). Several large batholiths have been recognised, including the Eddystone Batholith in the extreme northeast corner of the state, and the Blue Tier, Scottsdale and Ben Lomond Batholiths in central-east Tasmania (Fig. 2.3). There are also granites exposed on Flinders Island and sporadic plutons along the eastern coast (Fig. 2.3). There is a geochemical trend from old, mafic unfractionated granodiorites, throughout felsic, weakly fractionated I- and S-type monzogranites towards young, felsic highly fractionated I- and S-type leucogranites (Black et al., 2005; Kositcin and Everard, 2013). Mafic granodiorites with SiO_2 < 70 wt %, including the Gardens and the Long Point from the Blue Tier Batholith, as well as the Wybalenna Granite (Finders Island), are associated with the oldest known plutons (~ 400 Ma). These unfractionated I-type granites were affected by the mid-Devonian deformation, and were associated with the onset of the Tabberabberan Orogeny. They were followed by unfractionated to weakly fractionated granodiorites and monzonites with zircon U-Pb ages of 390 – 387 Ma, postdating deformation associated with the Tabberabberan Orogeny in Tasmania. These granites are significant constituents of the Eddystone, Blue Tier and Scottsdale Batholiths. Highly fractionated I- and S-type leucogranites, cropping out at Lottah, Mt Paris, and Henbury, and Royal George (Ben Lomond Batholith), yielded the youngest U-Pb ages with 378 – 377 Ma, 10 m.y. after the Devonian deformation event. These reduced, felsic leucogranites are associated with economic Sn (-W) deposits and occurrences (e.g., Aberfoyle, Storeys Creek, and Anchor Sn deposits; Fig. 2.4).

In contrast to the huge granite batholiths in eastern Tasmania, felsic plutons in western Tasmanian terrane are scattered, with relatively small exposures. The major granites include Housetop, Dolcoath, Heemskirk, Pine Hill, Meredith, Pieman Heads, Interview, and Granite Tor in mainland Tasmania, and the Grassy Granite on King Island (Fig. 2.3). McDougall and Leggo (1965) noticed that these western Tasmanian granites are apparently younger than their eastern counterparts, although their reported ages were inaccurate largely due to radiogenic Sr and Ar loss, and thermal resetting by later geological deformation. Precise U-Pb zircon dating of these granites demonstrated that they intruded between 373 to 350 Ma (Black et al., 2005; Kositcin and Everard, 2013), and identified a westward younging pattern (Fig. 2.3). The western Tasmanian intrusions are dominated by highly fractionated felsic I- and S-type granites (Williams et al., 1989; McClenaghan, 2006a), and are geochemically distinct from most of the eastern

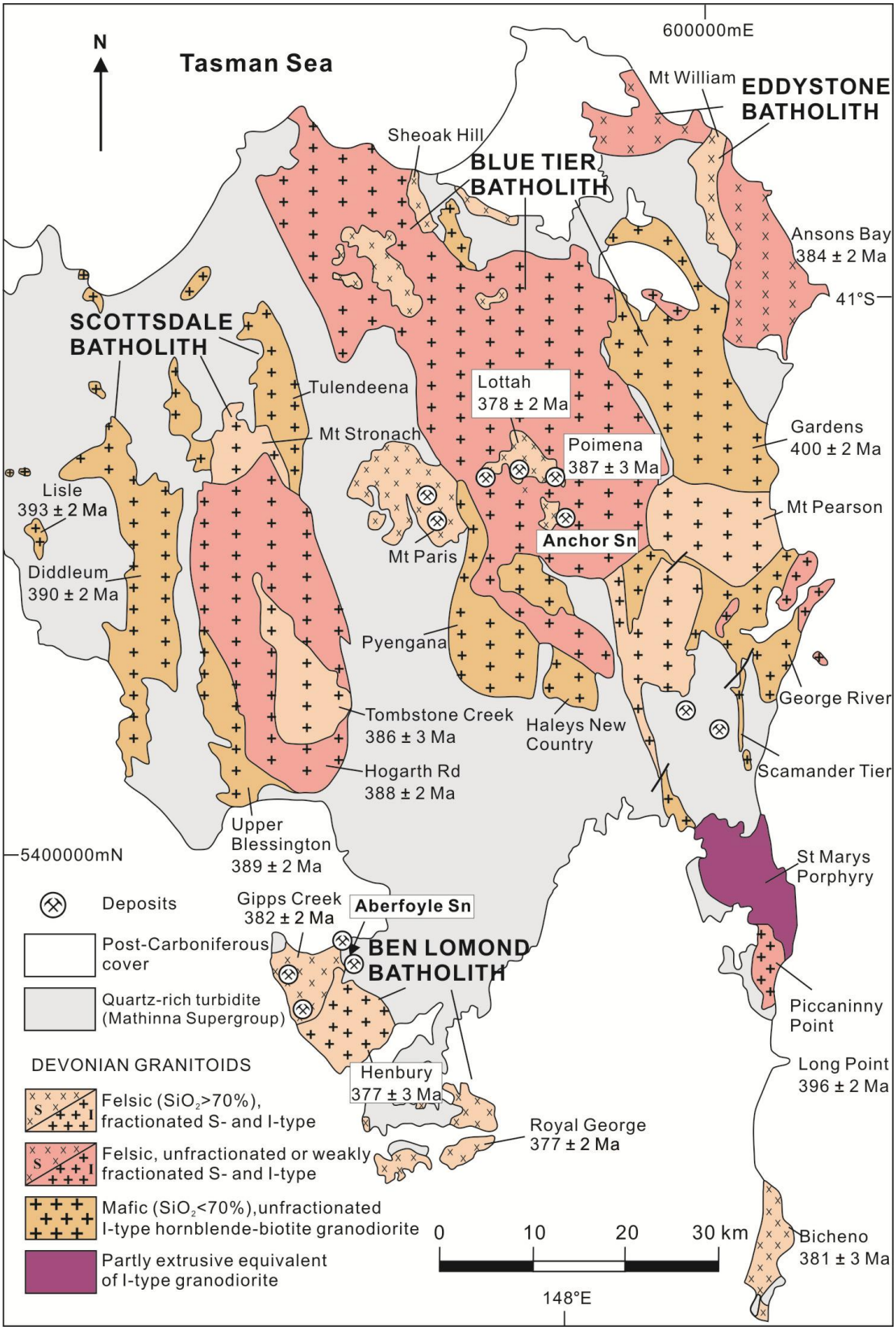

Figure 2.4 Simplified geological map of northeast Tasmania showing granite outcrops and major Sn deposits (after Solomon and Groves, 2000; Black et al., 2005; Kositcin and Everard, 2013).

Tasmanian granites. Most of the western Tasmanian granites are fertile, being genetically related to world class Sn-W deposits (Solomon, 1981; Williams et al., 1989; Solomon and Groves, 2000; Green, 2012).

2.3 Mineralisation associated with granites

Tasmania contains many economic mineral deposits (Seymour et al., 2007). There have been at least four important metallogenic episodes since the Proterozoic (Green, 2012). The most significant deposits economically are the Cambrian Mt Read volcanic-hosted massive sulphide (VHMS) deposits, and the world-class Devonian – Carboniferous granite-related tin-tungsten deposits. The Cambrian VHMS belt is the most important massive sulphide deposit cluster in Australia (Large, 1992; Large et al., 1996; Huston et al., 2011), with pre-mining resources of 8.1 Mt Zn, 3.0 Mt Pb, 3.3 Mt Cu, 9.1 kt Ag and 278 tonnes Au (Seymour et al., 2007). The granite-related Sn-W deposits have been the dominant Sn-W producer in Australia, yielding more than 0.65 Mt Sn, 0.2 Mt WO_3 and other by-products (Fe, Ni, CaF_2; Seymour et al., 2007). The Sn and W deposits are mostly concentrated in the western Tasmanian terrane, aligning in two parallel NNW-trending zones in the central west, known as the Northern and the Southern Sn-W zones (Solomon and Groves, 2000; Fig. 2.5). In contrast, Sn-W deposits in eastern Tasmania are sporadically distributed, smaller in size (Fig. 2.4), and mostly have been mined out.

2.3.1 Sn-W deposits in eastern Tasmania

The eastern Tasmania tin province (Fig. 2.4) produced about 0.09 Mt Sn (of which 65 tonnes were alluvial resources), 14, 000 metric tonnes of WO_3, and by-produced kaolinite (Solomon and Groves, 2000). The main types of primary Sn deposits are extra-granitoid vein systems (e.g., Aberfoyle, Storeys Creek, Scamander), and endo-granitoid greisens (e.g., Anchor, Rex Hill; Fig. 2.4; Table 2.1).

2.3.1.1 Sn deposits associated with the Blue Tier Batholith

The greisen-type Anchor Sn deposit (Table 2.1) is hosted in the Lottah leucogranite (Fig. 2.4), which intruded larger bodies of the Poimena adamellite. These two intrusions constitute substantial portions of the Blue Tier Batholith. Tin mineralisation also crops out in the Mt Paris area, northwest of the Lottah Granite (Fig. 2.4). The Mt Paris and Lottah granites may be joined at depth, based on their similar textures and compositions (McClenaghan and Williams, 1982). The greisenised pluton and greisens are mostly localised in the cupolas of the K-feldspar granite, although some greisenisation has occurred at the contact with the Poimena adamellite (Groves, 1972a). At Anchor, disseminated cassiterite is associated with muscovite, topaz, fluorite, and minor chalcopyrite, bornite, molybdenite and wolframite. Highest tin, silver and copper grades are concentrated in the most intensively greisenised part of the leucogranite, confined to the upper 50 m-thick layer. Greisenisation and contemporaneous tin mineralisation are interpreted to have resulted from interaction between the host granite and post-magmatic residual fluids at temperatures of 350 °to 300 ℃ (Williams et al., 1989; and references therein).

The petrogenesis of the Lottah Granite and neighbouring intrusions within the Blue Tier Batholith has been hotly debated. Groves and MaCarthy (1978) argued that in-situ fractional crystallisation in the Blue Tier Batholith progressively generated granodiorites, adamellites, and leucogranites as well as associated tin mineralisation. This model was challenged by Cocker (1982) and Higgins et al. (1985), who noted chemical and isotopic variations between the Pyengana granodiorite and Poimena monzogranite. The

Lottah leucogranite may have been evolved from the Poimena adamellite via extreme Rayleigh-type fractionation (Higgins et al., 1985). Subsequent chemical and radiogenic investigations demonstrated that the Lottah and Poimena granites display chemical discontinuities for certain elements and oxides, different εNd ranges, and diverse U-Pb ages and initial Sr isotopes (Mackenzie et al., 1988; Sun and Higgins, 1996; Black et al., 2005, 2010). These later authors agreed that mafic magmas assimilating large amounts of sedimentary components were probably responsible for the development of the Lottah magma. In the late stage of Lottah Granite crystallisation, large volumes of vapour and fluids were concentrated in the apical regions of the southern parts of the granite, generating greisen alteration, and cassiterite and sulphide mineralisation at Anchor (Solomon and Groves, 2000).

2.3.1.2 Sn deposits associated with the Ben Lomond Batholith

Three sheeted vein-type Sn (-W) deposits, Aberfoyle, Storeys Creek, and Lutwyche, are hosted in quartzwacke turbidite sequences of the Mathinna Supergroup, overlying the apical region of the Ben Lomond Granite in the Rossardon area (Table 2.1; Fig. 2.4). The granite is mostly a coarse-grained, porphyritic intrusion, consisting of quartz, K-feldspar, albite, and minor biotite, muscovite, tourmaline and topaz. The Royal George Granite is thought to be the southward continuation of the Ben Lomond Batholith, due to their similar mineral assemblages and compositions (Williams et al., 1989). Zircon U-Pb dating indicates that the intrusion was emplaced at 377 ± 3 Ma (Black et al., 2005; Kositcin and Everard, 2013). The stanniferous veins mostly occur in the Mathinna beds, but some veins continue upwards from the greisenised cupolas of the Ben Lomond Granite to the overlying metasedimentary units. The early-formed veins are dominated by cassiterite, wolframite, muscovite, topaz, apatite, fluorite, stannite and other sulphides. They are overprinted by later quartz, fluorite, galena, tetrahedrite, scheelite, siderite, calcite, and native bismuth (Solomon and Groves, 2000; and references therein). Three types of fluid inclusions were recognised in quartz, cassiterite and other minerals: (1) a CO_2-rich multi-phase fluid, (2) a hypersaline multi-phase fluid with various daughter minerals at room temperature, and (3) a vapour-dominant low salinity fluid. Homogenization temperatures range from 500 ℃ for the hypersaline brine, down to 200 ° – 100 ℃ associated with the low salinity fluid responsible for late scheelite mineralisation (Halley, 1982). $\delta^{18}O$ values of vein quartz suggest the equilibrated water has $\delta^{18}O$ compositions of + 6.7 to + 8.1 ‰, typical of magmatic water mixed with minor groundwater; $\delta^{34}S$ values of sulphides (+ 3.6 to -3.3 ‰) imply a magmatic sulphur component circulated into the ore-forming fluids (Solomon and Groves, 2000; and references therein).

2.3.1.3 Mineralisation in the Scamander field

Minor economic vein-type mineralisation occurs in the Scamander field of northeastern Tasmania. The mineralised field exhibits spatial metal zonings from proximal W ± Mo to Sn, through Cu, outwards to distal Ag + Pb + Zn (Groves, 1972b; Fig. 2.4). The mineralised veins occur in the Mathinna beds up to 10 km east and southeast from the Constable Creek and Echo granites (parts of the Mt Pearson Granite). The deposits are mostly aligned along northeast- and southeast-striking faults. Variations in mineralogy and

temperature in the Scamander field represent elevated depths to the source granite with increasing distance from the granite outcrop (Groves, 1972b).

2.3.2 Northern Sn-W Zone, western Tasmania

The Northern Sn-W zone in western Tasmania extends westward from the S-type Interview Granite, through the I-type Meredith Batholith, and then eastward to the I-type Housetop Granite (Fig. 2.5). The host rocks include high-grade metamorphic sequences.

2.3.2.1 Sn-W deposits associated with the Meredith Granite

The cassiterite deposit at Mt Bischoff (Table 2.1) was the first Sn deposit discovered in Tasmania, in 1871. It is also one of the richest Sn deposits (10.54 Mt @ 1.1 % Sn; Seymour et al., 2007). Tin mineralisation at Mt Bischoff is genetically and spatially related to a radial porphyritic dyke swarm that intruded Proterozoic sandstones and dolomites. The dykes have steep dips, are up to 30 m thick, and contain topaz. The dykes are explained to be evolved melts derived from the underlying Meredith Batholith prior to albite crystallisation and subsolidus albitisation (Solomon and Groves, 2000). In addition to abundant K-feldspar and quartz, tourmaline and muscovite are locally observed to occur as phenocrysts in the dykes, and are considered to be products of extensive post-magmatic greisen alteration. These minerals also occur in hydrothermal breccias associated with dyke emplacement (Halley and Walshe, 1995). Three principal types of stanniferous ores have been mined: (1) stratabound massive pyrrhotite-rich Sn ore which is predominant in the metasomatic Proterozoic dolomite; (2) greisen ore that consists of pyrite, sphalerite, cassiterite, tourmaline, topaz, muscovite and minor wolframite, and occurs in altered porphyritic dykes and especially on the dyke margins (Wright and Kwak, 1989); (3) steeply dipping vein-type ore that consists of quartz, cassiterite, arsenopyrite, sulphides, fluorite, topaz, siderite and wolframite. Some of the veins cut the carbonate replacement ores, while thin veinlets extend into sandstones beneath the dolomite in places.

The replacement-style carbonate-hosted ore contains two distinctive mineral assemblages: high-temperature and low-temperature associations, respectively. The high-temperature assemblage comprises chondrodite, pyrrhotite, magnetite and minor apatite and fluorite, and contains aqueous salt-bearing and vapour-rich fluid inclusions. The fluid inclusions show high homogenisation temperatures (460 °– 400 °C) and relatively high salinities (30 – 36 wt. % NaCl equiv; Halley and Walshe, 1995). In contrast, the low-temperature assemblage is marked by the presence of cassiterite, associated with talc, pyrrhotite, carbonates, arsenopyrite, chalcopyrite, sphalerite, and quartz. It is the most abundant alteration assemblage, hosting the bulk of the carbonate replacement ore. It is characterised by vapour-rich, and CO_2-bearing fluid inclusions that have lower homogenisation temperatures of 370 °–200 °C, and lower salinity (12 – 14 wt. % NaCl equiv). Ore precipitated due to pH increase during carbonate replacement and unmixing of brines and vapours under hydrostatic conditions (Wright and Kwak, 1989; Halley and Walshe, 1995). Greisen-hosted cassiterite ore precipitated at temperatures of 420 °– 230 °C and in highly saline (30 – 50 wt. % NaCl equiv) fluids containing CO_2 and hydrocarbons, possibly being products of

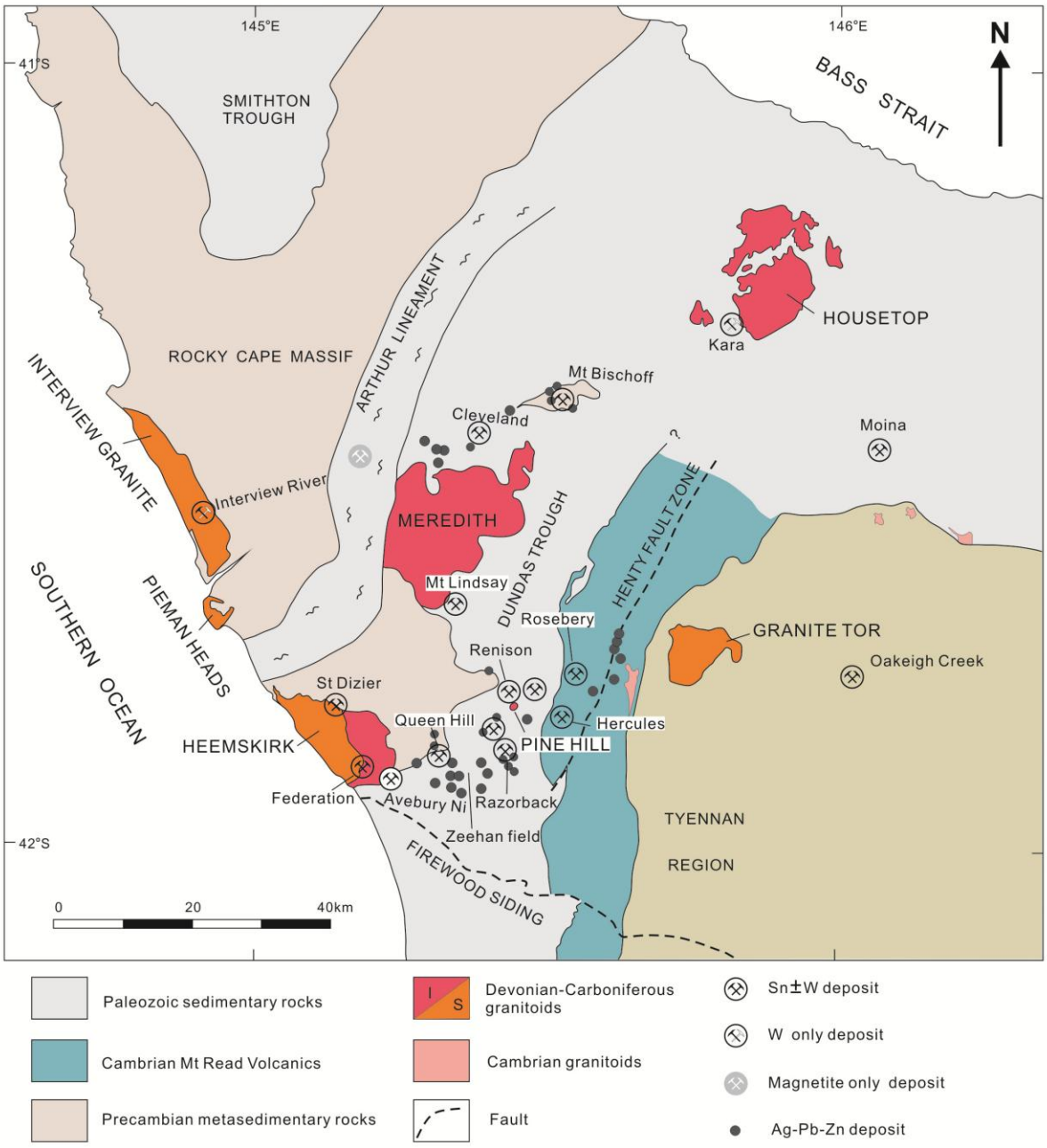

Figure 2.5 Simplified geological map of northwest Tasmania and major granite-associated Sn-W deposits (after Solomon and Groves, 2000).

boiling (Wright and Kwak, 1989). These stanniferous fluids originated from the porphyry dykes, which acted as conduits to transport magmatic-hydrothermal fluids from the Meredith Granite. During the emplacement of the granite batholith and related dykes, Sn-bearing fluids moved upwards along the margins of the dykes and breccias, and permeated into adjacent dolomites and non-reactive sedimentary rocks.

Table 2.1 Characteristics, types, tonnages, grades, host hocks and associated granites of major Sn-W deposits in Tasmania

Deposit	Type	Economic product	Tonnage (Mt)[ξ]	Grade[ξ]	Host rocks	Associated granite	Granite type	Granite age*	References
Aberfoyle, eastern Tasmania	Vein-type	Sn	2.1	0.91 % Sn, 0.05 % WO_3	Ordovician to Devonian quartzwacke turbidite sequences of the Mathinna Supergroup	Ben Lomond	highly fractionated, reduced granite with both I- and S-types	377 ± 3 Ma	Halley (1982), Williams et al. (1989)
Lutwyche, eastern Tasmania	Vein-type	Sn	not available	not available	Ordovician to Devonian quartzwacke turbidite sequences of the Mathinna Supergroup				Williams et al. (1989), Solomon and Groves (2000)
Storeys Creek, eastern Tasmania	Vein-type	Sn-W	1.1	0.18 % Sn, 1.09 % WO_3	Ordovician to Devonian quartzwacke turbidite sequences of the Mathinna Supergroup				Williams et al. (1989), Solomon and Groves (2000)
Anchor, eastern Tasmania	Greisen-type	Sn	2.39	0.28 % Sn	Lottah Granite	Lottah	strongly fractionated, reduced S-type granite	378 ± 2 Ma	Solomon and Groves (2000)
Mt Bischoff, western Tasmania	Sulphide skarn	Sn	10.54	1.1 % Sn	Neoproterozoic quartzite, shale, sandstone and dolomite, correlated with Oonah Formation	porphyry dikes, Meredith	strongly fractionated, potassic quartz-feldspar porphyry dykes	373 ± 2 Ma for Wombat Flat Granite	Wright and Kwak (1989), Halley and Walshe (1995)
Cleveland, western Tasmania	Sulphide skarn	Mo, W, Sn	12.4	0.61 % Sn, 0.25 % Cu	Neoproterozoic succession of spilitic basalt, mafic pyroclastic, argillite, and limestone, correlated with Crimson Creek Formation	Meredith	reduced, moderately to strongly fractionated I-type granite	375 ± 4 Ma for Meredith	Collins (1981), Jackson et al. (2000)
Mt Lindsay, western Tasmania	Sulphide skarn	Sn-W-F-Be	not available	not available	Neoproterozoic Crimson Creek Formation comprising mudstone quartzite, volcanic flows and a number of marble units				Kwak (1983)
Kara, western Tasmania	Calcic skarn	W, Fe	5.2 Mt Fe_3O_4, 0.3Mt WO_3	> 30 % Fe, and 0.52 % WO_3	Ordovician Gordon Limestone and Moina Sandstone	Housetop	moderately fractionated, moderately to strong oxidised I-type granite	374 ± 2 Ma	Zaw and Singoyi (2000), Singoyi and Zaw (2001)
Renison Bell, western Tasmania	Sulphide skarn	Sn	24.54	1.41 % Sn	Neoproterozoic dolomitised limestone beds (Success Creek Group and Red Rock group)	Pine Hill	reduced, moderately to strongly fractionated I-type granite	367 ± 3 Ma	Patterson et al. (1981), Kitto (1994), Bajwah et al. (1995)

Table 2.1 (continued)

Deposit	Type	Economic product	Tonnage (Mt)[ξ]	Grade[ξ]	Host rocks	Associated granite	Granite type	Granite age*	References
Severn, western Tasmania	Sulphide skarn	Sn	4.17	0.98 % Sn	Neoproterozoic Oonah Formation consisting of shales, siltstones and quartzite and Cambrian Montana beds	Heemskirk	Strongly fractionated reduced magnetite and ilmnite series granites	White Granite: 361 ± 2 Ma; Red Granite: 360 ± 2 Ma	Williams et al. (1989), Solomon and Groves (2000)
Queen Hill, western Tasmania	Sulphide skarn	Sn	3.6	1.2 % Sn	Neoproterozoic Oonah Formation consisting of shales, siltstones and quartzite and Cambrian Montana beds				Williams et al. (1989), Solomon and Groves (2000)
Montana, western Tasmania	Sulphide skarn	Sn	0.51	1.91% Sn	Neoproterozoic Oonah Formation consisting of shales, siltstones and quartzite				Williams et al (1989), Solomon and Groves (2000)
Federation, western Tasmania	Greisen	Sn	not available	not available	Heemskirk Granite- White phase				Hajitaheri (1985)
St. Dizier, western Tasmania	Silicate skarn	Sn-W-Fe	~2.6	0.5 % Sn, 0.05% WO_3	Neoproterozoic tourmalinised turbiditic quartzite intercalated with discontinuous dolomite (Oonah Formation)		Strongly fractionated reduced magnetite and ilmnite series granite		Williams et al. (1989)
Avebury, western Tasmania	Skarn or hydrothermal-altered magmatic deposit	Ni	29.3	0.9 % Ni	Cambrian ultramafic adjacent to structurally overlying basalt and mudstone-lithicwacke-minor carbonate sequences		Strongly fractionated, reduced, White granite		Keays and Jowitt (2013)
Moina, western Tasmania	Skarn, distal Au ± Bi ± Cu skarn	Fe, F, minor Sn, W	18	26 % CaF_2, 0.1 % Sn, 0.1 % WO_3	Ordovician Gordon limestone calcareous siltstone and Moina sandstone	Dolcoath	strongly fractionated, moderately reduced I-type granite	no precise U-Pb age	Kwak and Askins (1981)
Dolphin, Bold Head, western Tasmania	Calcic skarn	W	23.8	0.66 % WO_3	Late Neoproterozoic Grassy Group consisting of biotite hornfels, metavolcanic units, shale and dolomite	Grassy	moderately oxidised unfractionated I-type granodiorite	351 ± 2 Ma	Kwak and Tan (1981)

ξ: tonnage and grade of the deposits are mainly from Seymour et al. (2007), except that those of Avebury from Keays and Jowitt (2013), and those of Severn, Queen Hill and Montana from Callaghan (2013);
*: new ages of granites are mostly referred from Black et al. (2005), whereas the U-Pb ages for Meredith and Pine Hill granites are from this study (see Chapter 3).

The Meredith Granite was a very productive felsic intrusion in terms of Sn mineralisation. In addition to the Mt Bischoff Sn mine, it generated the Cleveland tin skarn, north of the Meredith Granite (Collins, 1981; Jackson et al., 2000; Table 2.1; Fig. 2. 5), and the Mt Lindsay Sn-W-F (-Be) skarn, south of the Meredith Granite (Kwak, 1983; Table 2.1), as well as numerous Pb-Zn-Ag vein systems between Mt Bischoff and Cleveland (Solomon and Groves, 2000).

2.3.2.2 W-Fe deposits associated with the Housetop Granite

The Kara magnetite-scheelite skarn deposit is located southeast of the Housetop Granite, which intruded the Ordovician Gordon limestone and Moina sandstone at 374 ± 2 Ma (Black et al., 2005; Table 2.1). At least four paragenetic stages of skarn-related assemblages have been identified at Kara (Singoyi and Zaw, 2001), which can be divided roughly into two groups, (1) a high-temperature anhydrous assemblage consisting of clinopyroxene, garnet, vesuvianite, wollastonite, magnetite and scheelite, and (2) a low-temperature hydrous assemblage comprising magnetite, amphibole, epidote, chlorite, scheelite, carbonates, quartz, fluorite, hematite and minor sulphides. Although magnetite and scheelite have been observed in the early anhydrous and late hydrous stages, abundant Fe and W mineralisation mostly appear to have deposited with the low-temperature hydrous minerals (Zaw and Singoyi, 2000). Fluid inclusion microthermometry has shown that the prograde clinopyroxene-garnet-vesuvianite association formed at very high temperature (locally > 500 ℃) with salinities ranging from 10 to 17.8 wt. % NaCl equiv. Subsequent retrograde metasomatism occurred when temperature dropped to < 300 ℃, and fluid salinity decreased from 19.8 to 2.0 wt. % NaCl equiv, possibly indicating mixing of hypersaline magmatic fluids with low temperature and low salinity meteoric waters (Singoyi and Zaw, 2001). Oxygen and carbon isotopes imply that skarn development and Fe-W ore precipitation resulted from interaction of external fluids with magmatic – hydrothermal fluids during infiltration metasomatism (Zaw and Singoyi, 2000).

2.3.3 Southern Sn-W Zone, western Tasmania

Ore deposits in the Southern Sn-W Zone of western Tasmania (Fig. 2.5) are intimately associated with granitic batholith that includes the Heemskirk Granite (western), Pine Hill Granite (central), and Granite Tor (eastern). These granitic intrusions are interpreted to connect at depths > 2 km in an E-trending batholith, based on gravity modelling (Leaman and Richardson, 2003).

2.3.3.1 Sn deposits associated with the Heemskirk Granite

The Heemskirk Granite is a composite intrusion, consisting of I-type and S-type variants. The I-type Red granite overlies and was intruded by the S-type White granite (Klominsky, 1972; Hajitaheri, 1985; Fig. 2.5). Precise zircon U-Pb dating cannot distinguish the Red granite (360 ± 2 Ma) from the White granite (361 ± 2 Ma; Black et al., 2005). The Heemskirk Granite was a highly productive pluton in terms of mineralisation, with more than 30 historical mine workings within and around the batholith (Hajitaheri, 1985). These deposits and occurrences can be divided into three types: (1) skarn (e.g., St. Dizier silicate skarn), (2) greisen (e.g., Federation), and (3) vein-type (e.g., Globe, Sweeney's; Table 2.1).

Cassiterite is disseminated in greisen veins, pipes and irregular zones at the Federation deposit, where it is associated with quartz-topaz-muscovite-tourmaline alteration in the argillised Red granite along the Red and White granite contact. The stanniferous sulphide-rich pipes are enclosed by argillic alteration zones. Hajitaheri (1985) argued that Federation and other tin deposits in the southern Heemskirk Granite were generated by magmatic – hydrothermal fluids sourced from the White granite that interacted with minor groundwater.

The St. Dizier stanniferous magnetite skarn deposit is hosted by the Oonah Formation rocks on the northern contact of the Heemskirk Granite. The host sequence is composed principally of black shale and tourmalinised quartzite intercalated with discontinuous dolomite. Magnesian skarn minerals were produced by metasomatic replacement of dolomite during interaction with granite-related hydrothermal fluids. They are intergrown with magnetite, pyrrhotite with pyrite, minor sphalerite and chalcopyrite, and rare wolframite and scheelite. Tin is hosted in a variety of minerals, including cassiterite, hulsite and schoenfliesite, and also occur as a trace element in skarn silicate minerals (Williams et al., 1989).

Other Sn deposits, including Queen Hill, Severn, and Montana, occur in the centre of the Zeehan Ag-Pb-Zn field. They are genetically linked to the concealed Heemskirk Batholith (Solomon and Groves, 2000; Fig. 2.5). Magmatic – hydrothermal fluids from the granite also appear to have led to formation of the unusual Avebury Ni deposit (Keays and Jowitt, 2013; Fig. 2.5).

2.3.3.2 Sn deposits associated with the Pine Hill Granite

The Pine Hill Granite has a very small outcrop in central western Tasmania (Fig. 2.5). It is a highly fractionated, reduced felsic granite (Bajwah et al., 1995; Table 2.1). This intrusion is temporally and genetically related to the Renison Bell cassiterite deposit, the largest primary Sn deposit in Australia, with about 0.4 Mt Sn (Patterson et al., 1981; Kitto, 1994). Stratabound cassiterite mineralisation occurs in dolomitised limestone beds of the Success Creek Group, overlain by the Red Rock sequence. Stanniferous veins are formed in major fault zones (especially the Federal-Bassett Fault) with carbonate replacement. Minor tin ores are developed in recrystallised sandstones (Patterson et al., 1981). Cassiterite and silicates were formed early by replacement, whereas main stage mineralisation were characterised by cassiterite, pyrrhotite, arsenpyrite, silicates, minor sulphides and iron oxides (Kitto, 1994). Late sideritic alteration of dolomites and tourmalinisation of clastic sediments is also present. The cassiterite and abundant sulphides (galena, sphalerite, and pyrite), quartz, fluorite and carbonates are inferred to have deposited late in the vein and fault zones. Fluid inclusion and stable isotope studies show that mineralisation took place at relatively high temperatures (400 ° to 300°C) at low fO_2 and low pH in reduced fluids exsolved from the Pine Hill Granite (Patterson et al., 1981; Kitto, 1994). Cassiterite deposition occurred due to fluid-rock interaction accompanied by redox changes, and by increasing pH due to carbonate dissolution (Kitto, 1994).

Two mineralised clusters are located outside of the two western Tasmanian Sn-W zones. The Sn-Cu deposits at Moina are proximal to the Dolcoath Granite (Fig. 2.5; Kwak and Askins, 1981; Table 2.1).

World-class scheelite skarn deposits are associated with the I-type Grassy Granite on King Island (Kwak and Tan, 1981; Table 2.1).

2.4 Summary

The eastern and western Tasmanian terranes evolved independently until the mid-Devonian (Seymour et al., 2007, and references therein). The western Tasmanian terrane has Mesoproterozoic basements (e.g., the Tyennan Region), whereas the basement of the eastern terrace probably did not form until the Ordovician (Mathinna Supergroup; Seymour et al., 2011). The two terranes docked during the mid-Devonian Tabberabberan Orogeny (Williams et al., 1989; Black et al., 2005; Seymour et al., 2007). Abundant post-orogenic granitoids were emplaced into both terranes, defining an older and a younger granite province in eastern and western Tasmania, respectively. Significant Sn-W mineralisation is closely associated with each province of Devonian – Carboniferous intrusions. Most of the granites have experienced exhumation to differing extents. Numerous alluvial cassiterite ores were historically discovered and mined around or distal to the granite batholiths in eastern Tasmania. Although there are much larger granite outcrops in eastern Tasmania, the granites in western Tasmania are apparently endowed with larger Sn-W deposits (Table 2.1). There is a broader variety of reactive host rocks, such as dolomite, limestone and ultramafic rocks in western Tasmania. The differences in metal endowment may relate to a lack of reactive host lithologies, and/or a greater degree of unroofing of granites in eastern Tasmania (Solomon and Groves, 2000).

Based on geochemical investigations of granites and their associated mineralisation in the Lachlan Fold Belt, Blevin and Chappell (1992, 1995) noted that Sn mineralisation is preferentially associated with both I- and S-type magmas that are reduced (low Fe^{3+}/Fe^{2+} ratios) and have experienced high degrees of fractional crystallisation. In contrast, Cu ± Au mineralisation appears to be associated with relatively unevolved, oxidised, intermediate I-type magmas. W is associated with a variety of granite types and displays little dependence on the magmatic redox state (Blevin and Chappell, 1992). However, the King Island scheelite deposits and the Kara magnetite-scheelite deposit in Tasmania were formed by moderately or highly oxidised granitoids (Kwak and Tan, 1981; Zaw and Singoyi, 2000). Most Sn ± W deposits in Tasmania contain quartz with CO_2- and hydrocarbon-bearing fluid inclusions, and have pyrrhotite-cassiterite mineral assemblages, further evidencing that these deposits were generated by relatively reduced hydrothermal fluids. In addition to feldspar-dominated crystal fractionation and oxidation states, the volatile compositions of the crystallising magmas may exert a significant control on formation of specific types of mineralisation, because some volatiles can enhance metal solubilities and/or decrease the viscosity of melts (Cooke et al., 2009). Kitto (1994) found that in Tasmania, the major Sn deposits are associated with both boron- and fluorine-rich granites, whereas Sn-W deposits are closely related to granitic intrusions containing fluorine-rich phases. W-dominant deposits are commonly associated with granites that lack appreciable boron and fluorine.

There has been a complex geological evolution and several granitic intrusive events in Tasmania. The Sn-W mineralisation is associated with Devonian – Carboniferous granitoids, which are extensively

exposed in both eastern and western Tasmanian terraces. Based on geological mapping and sampling in field, the next chapter will present and discuss petrographic features, whole-rock and radiogenic geochemical data, and geochronological data from a number of Tasmanian granites. Key locations have been selected for this PhD study, e.g., the Binalong Bay granites (East Tasmania), the Heemskirk and Pieman Heads granites (West Tasmania), in order to understand their petrogenesis and possible controls on magma fertility.

Chapter 3 Granite petrography, geochemistry and geochronology

3.1 Introduction

3.1.1 Purpose of this study

This chapter investigates the geochemistry and geochronology of granitic rocks from eastern and western Tasmania, including the George River Granodiorite, Mt. Pearson Granite and Grant Point Granite at Binalong Bay in St. Helens area, and Bicheno Granite and Coles Bay Granite along the eastern coast (Fig. 3.1). The Pieman Heads, Pine Hill, Heemskirk, Housetop and Meredith granites from the western Tasmania were also investigated. Most of these granites have been not dated precisely by modern techniques. This chapter provides petrography, major- and trace-element analyses, zircon U-Pb dating, and Pb isotopic K-feldspar analyses for selected Tasmanian granites, in order to elucidate granite petrogenesis and space-time correlations with other granite provinces in the Lachlan Fold Belt of southeast Australia (Fig. 2.2), as well as to evaluate possible controls on Sn mineralisation.

3.1.2 Previous work

Previous reports on radiogenic isotope analyses from Tasmanian granites focused primarily on the eastern intrusions (Cocker, 1982; Turner et al., 1986; Mackenzie et al., 1988; Sun and Higgins, 1996; Black et al., 2010), with only limited data available for western Tasmania (e.g., Brooks, 1966; Sawka et al., 1990; Black et al., 2010). The systematic radiogenic isotopic studies of Tasmanian granites by Black et al. (2005, 2010) provided high-quality SHRIMP age determinations and Sr-Nd-Pb isotopic data. In contrast, only limited Pb isotopic analyses are available for the Tasmanian granites and associated mineralisation (e.g., Gulson and Porritt, 1987; Hughes, 1995; Innes, 1995).

Most of these previous studies focused on the relationships between granite petrogenesis and source rocks, and did not consider metal fertility. A large number of the earlier radiogenic isotopic datasets generated for Tasmanian granites were used whole-rock samples (e.g., Brooks, 1966; Cocker, 1982; Turner et al., 1986; Mackenzie et al., 1988; Sawka et al., 1990; Sun and Higgins, 1996; Black et al., 2010).

3.2 Granite petrography

3.2.1 Granitoids in eastern Tasmania

3.2.1.1 Granitoids in the St. Helens area

Several granitic rocks crop out in the St. Helens area of eastern Tasmania, including the George River Granodiorite, Grant Point Granite, Mt Pearson Granite, Akaroa Granodiorite, and Scamander Tier granodiorite (Fig. 3.1; Cocker, 1971). The George River Granodiorite, Grant Point Granite and Mt Pearson Granite have been investigated in this study. They are mainly exposed in the Binalong Bay district. These

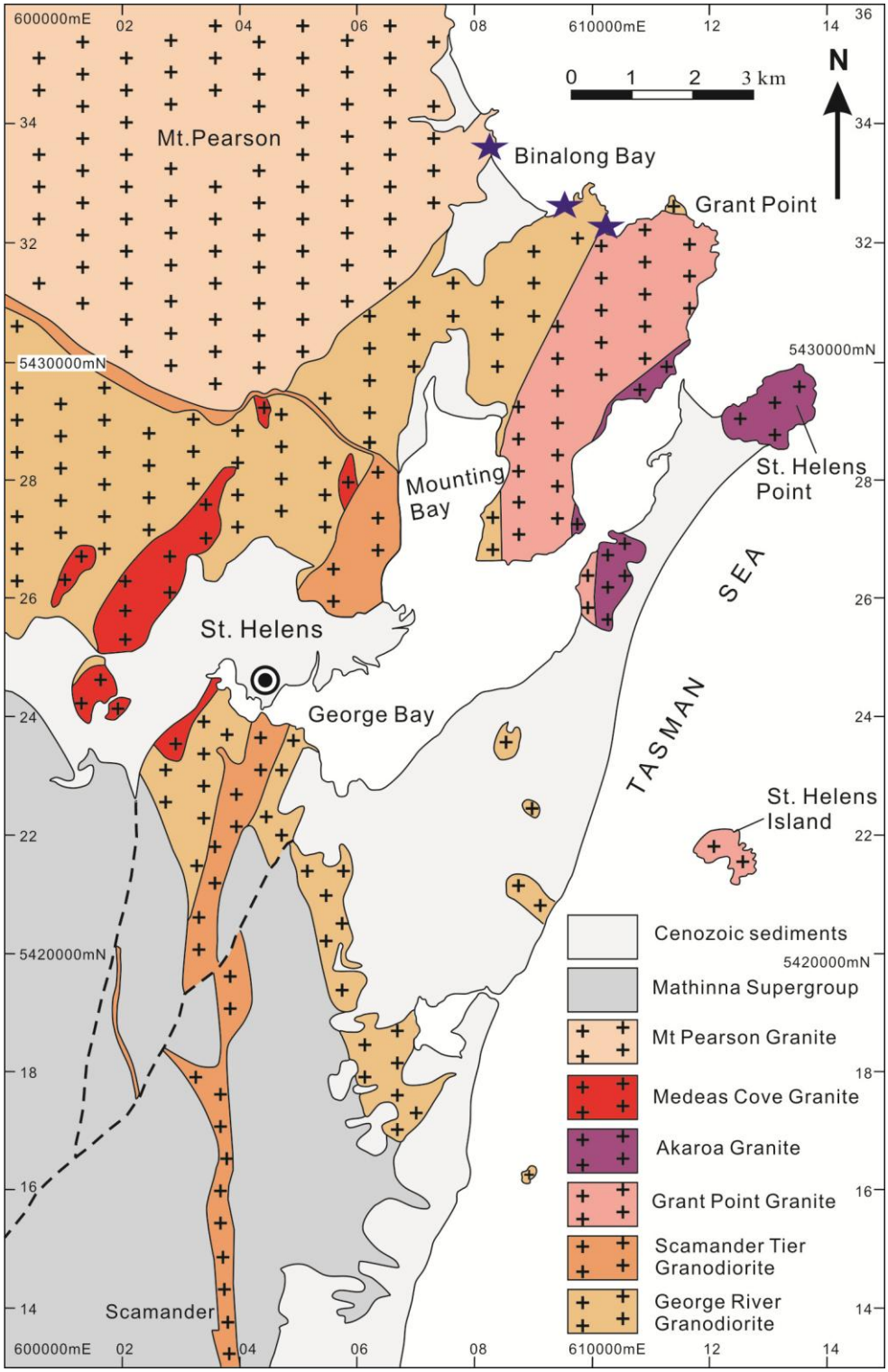

Figure 3.1 Simplified geological map showing the outcrop of granitic rocks in St. Helens area, eastern Tasmania (modified from McClenaghan, 2006b). Sample locations were marked as stars.

plutons compose the southeastern parts of the Blue Tier Batholith, which is the largest batholith exposed in eastern Tasmania (Fig. 2.4).

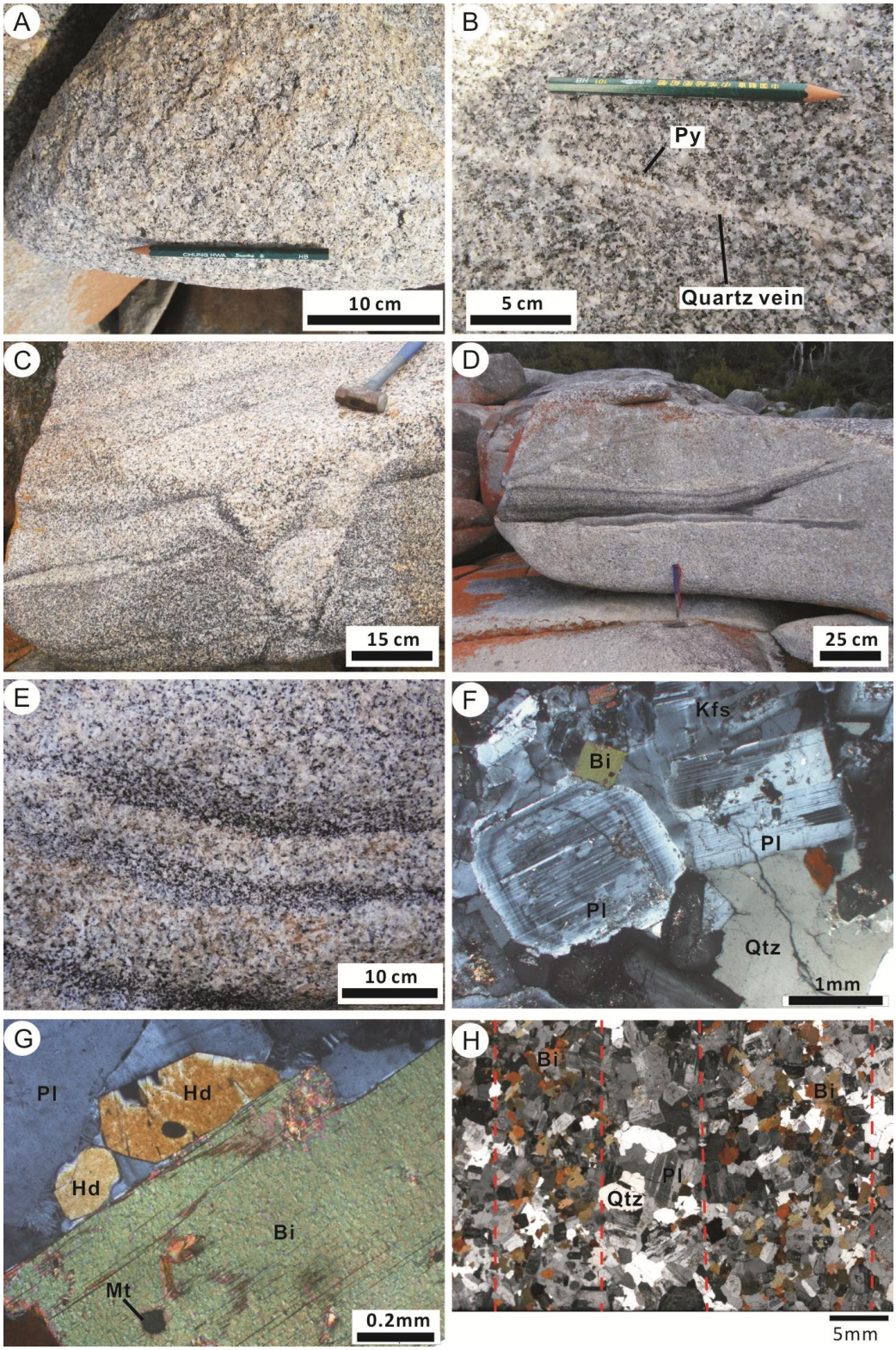

Figure 3.2 Photographs and photomicrographs showing features of the George River Granodiorite, eastern Tasmania. (A) Medium- to coarse-grained phase of the George River Granodiorite. (B) Pyrite-filled quartz vein cut across the granodiorite. (C, D, E) Trough-like, fish-tail and multiple-layer biotite schlieren occur in the granodiorite. (F) Euhedral biotite and granular quartz filled interstitially to euhedral plagioclase and minor K-feldspar with typical multiple twins. (G) Hornblende associated with plagioclase and biotite. (H) Abundant biotite crystals occur in the schlieren relative to in the granodiorite. All photomicrographs taken under cross polarised light. Bi = biotite, Kfs = K-feldspar, Pl = plagioclase, Py = pyrite, Qtz = quartz. Sample coordinate: E148°18′23.51″, S41°15′05.28″.

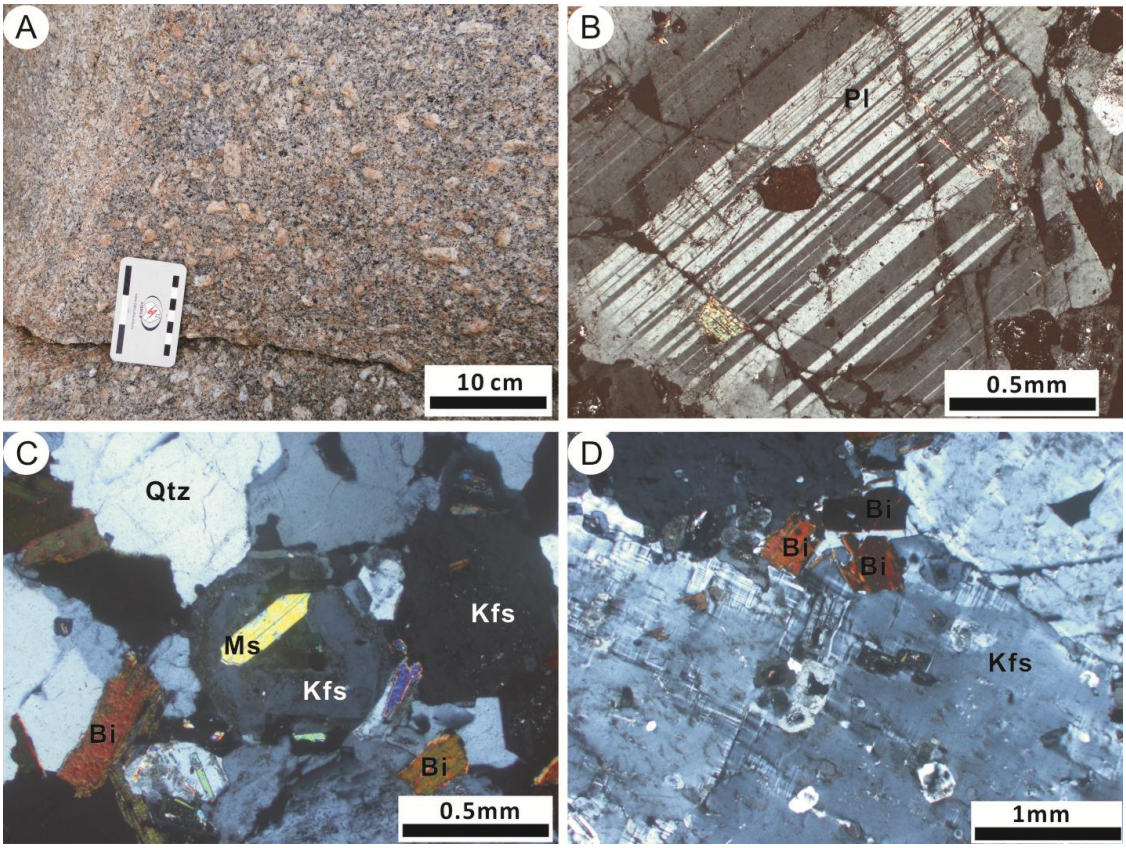

Figure 3.3 Photographs and photomicrographs showing features of the Grant Point Granite, eastern Tasmania. (A) The porphyry phase of the Grant Point Granite is rich in plagioclase phenocrysts. (B) Phenocrystic plagioclase presents typical multiple twins. (C) Euhedral muscovite associated with quartz, K-feldspar and biotite. (D) Mega-grained K-feldspar contains biotite inclusions. All photomicrographs taken under cross polarised light. Bi = biotite, Kfs = K-feldspar, Ms = muscovite, Pl = plagioclase, Qtz = quartz. Sample coordinate: E148°18′50.63″, S41°14′58.97″.

George River Granodiorite

The George River Granodiorite, together with the Pyengaga, Gardens and Long Point granitoids, compose the main biotite-hornblende-bearing phase of the Blue Tier Batholith (Fig. 2.4; McClenaghan, 2006a). These hornblende-bearing granodiorites were foliated during the mid-Palaeozoic Tabberabberan deformation (Black et al., 2005). The George River pluton is bounded by the Mt Pearson Granite to the west, and has a transitional boundary with the Grant Point Granite to the east (McClenaghan, 2006a). To the south, the George River Granodiorite was intruded by the later, non-foliated Scamander Tier granodioritic dykes (McClenaghan, 2006b; Fig. 3.1).

The George River Granodiorite is a grey dark, medium- to coarse-grained intrusion (Fig. 3.2A). It consists mainly of euhedral to anhedral plagioclase, biotite and hornblende (~5%; Fig. 3.2G), and granular K-feldspar and quartz. Plagioclase is volumetrically more than K-feldspar, and both of them have undergone minor muscovite alteration. The plagioclase crystals are characterised by multiple twins, with Ca-rich cores (Fig. 3.2F). Trace amounts of accessary minerals, e.g., apatite, titanite, magnetite, zircon, monazite and allanite, locally occur as solid inclusions in main minerals, or are interstitially filled between massive minerals. In some places, quartz veins cut across the granodiorite, and minor sulphides (pyrite, molybdenite, chalcopyrite etc.) are localised at the centre of the quartz halos (Fig. 3.2B).

Spectacular biotite schlieren are developed in coastal outcrops of the George River Granodiorite at Binalong Bay (Figs. 3.2C, D, E). The biotite schlieren define sub-horizontal biotite-rich layers in this granodiorite (Cocker, 1971). Biotite crystals are concentrated in the bands, associated with minor feldspar and quartz (Fig. 3.2H). These biotite-rich layers extend continuously or discontinuously for 5-10 m, locally over 60 m. They typically occur as multiple irregular layers (Fig. 3.2E), but locally display trough-like (Fig. 3.2C), and fish-tail structures (Fig. 3.2D) in the host granite. The biotite schlieren in the granodiorite have locally been truncated by the coarse-grained Grant Point Granite.

Grant Point Granite

The small Grant Point pluton crops out east of the George River Granodiorite (Fig. 3.1). It is a medium- to coarse-grained intrusion, and locally has a porphyritic phase. The Grant Point Granite may have a transitional boundary with the George River granodiorite (McClenaghan, 2006a). However, compared to the latter intrusion, it is generally coarser in grain size and lighter in colour (Fig. 3.3A). This granite is mainly composed of plagioclase, K-feldspar, quartz, and minor biotite which are intergrown with euhedral muscovite (Fig. 3.3C); the intrusion lacks hornblende. Plagioclase shows typical polysynthetic twinning (Fig. 3.3B), and has a similar abundance to K-feldspar. K-feldspar locally occurs as megacrysts containing abundant biotite and muscovite inclusions (Fig. 3.3D).

Mt Pearson Granite

The Mt Pearson Granite has a relatively large outcrop west of the George River Granodiorite (Fig. 3.1). At its southeastern margin near St. Helens, the intrusion has a pink-reddish appearance partly due to strong weathering (e.g., Fig. 3.4A). The Mt Pearson Granite is coarse to very coarse grained, sparsely porphyritic, and characterised by abundant K-feldspar megacrysts up to several cm in diameter (Fig. 3.4A). This granite consists of K-feldspar, plagioclase, quartz, and biotite (Fig. 3.4B), as well as trace numbers of zircon, monazite, apatite or magnetite. In the Binalong Bay area, K-feldspar is coarsely perthitic, and volumetrically more abundant than plagioclase.

3.2.1.2 Bicheno Granite

The Bicheno Granite is exposed on the central coast of eastern Tasmania (Fig. 2.3). The southern flank of the granitic body intruded small inliers of the Mathinna Supergroup (Fig. 2.4). This granite has fault contacts with the Jurassic dolerite (Cocker, 1977). This granite is commonly porphyritic and very coarse-grained (Fig. 3.4C). Large volumes of K-feldspar megacrysts (up to 5 cm) characterise the intrusion, which consists of quartz, muscovite, biotite and minor plagioclase and tourmaline. The K-feldspar megacrysts commonly contain inclusions of biotite, muscovite, quartz and plagioclase (Fig. 3.4D). Accessory minerals include zircon, apatite, ilmenite, monazite, and xenotime. Trace amounts (< 0.5 %) of garnet and/or cordierite occur in the Bicheno Granite, both of which have been replaced by pale green biotite (Cocker, 1977). Minor tourmaline-rich cavities, orbicules and quartz veins crop out in some localities, including the exposure near Bicheno town area.

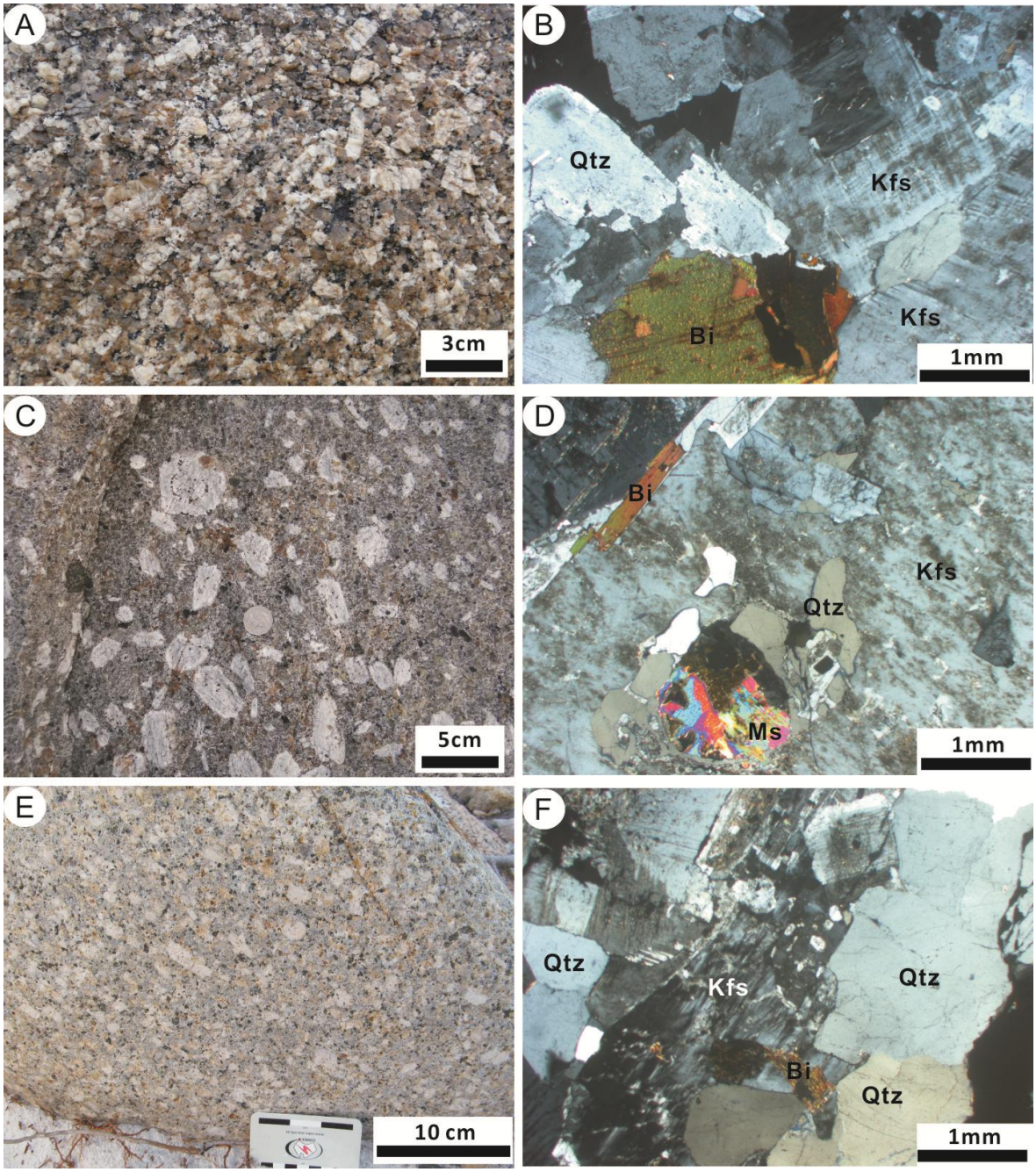

Figure 3.4 Photographs and photomicrographs showing features of the Mt Pearson, Bicheno and Coles Bay granites from eastern Tasmania. (A) The Mt Pearson Granite contains abundant mega-grained K-feldspar crystals. (B) Quartz, biotite and K-feldspar with hatchback twins comprise the major component of the Mt Pearson Granite. (C) Abundant mega-grained K-feldspar phenocrysts characterise the porphyritic Bicheno Granite. (D) Biotite, muscovite, quartz and feldspar occur as inclusions in K-feldspar megacrysts. (E) Coarse-grained K-feldspar phenocrysts develop in porphyritic Coles Bay Granite. (F) Quartz, K-feldspar and biotite comprise the Coles Bay Granite. All photomicrographs taken under cross polarised light. Bi = biotite, Kfs = K-feldspar, Ms = muscovite, Qtz = quartz. Sample coordinates: Mt Pearson Granite, E148°17′32.57″, S41°14′33.11″; Bicheno Granite, E148°18′46″, S41°52′30″; Coles Bay Granite, E148°17′00.31″, S42°01′23.43″.

3.2.1.3 Coles Bay Granite

A number of granitic plutons are exposed on the Freycinet Peninsula in the central eastern coast of Tasmania. These intrusions range from granodiorite to alkali-feldspar granite (McClenaghan, 2006a). The dominant phase is medium- to coarse-grained alkali-feldspar granite. It is commonly porphyritic, with

megacrystic K-feldspar (Fig. 3.4E). The area of the Coles Bay Granite investigated in this study crops out on the coast to the north of the Freycinet Peninsula (Fig. 2.3). This granite consists of quartz, K-feldspar, albite, biotite, and minor muscovite (Fig. 3.4E), together with trace amounts of zircon, monazite, apatite, fluorite, tourmaline and rare cassiterite (Everard, 2001). The K-feldspar has simple zoned twins that have commonly experienced weak to intermediate muscovite alteration.

3.2.2 Granites in western Tasmania

3.2.2.1 Heemskirk Granite

The semi-cauldron shaped Heemskirk Batholith is a composite Late Devonian – Early Carboniferous intrusion that is exposed over 140 km^2 in western Tasmania. The batholith crops out spectacularly along the coastline, and has intruded the Neoproterozoic Oonah Formation to the north and east. On its southern edge, the Heemskirk Batholith has steep intrusive contacts with the Oonah metasedimentary rocks, and has also intruded Cambrian volcanics, gabbro, serpentinised dunite, and Silurian – Devonian sedimentary rocks. It is covered locally by Tertiary basalt and Quaternary alluvium (Green, 1964; Fig. 3.5). The granitic batholith extends beneath the Zeehan and Dundas mineral field, and gravity modelling shows that it connects with the Pine Hill and Granite Tor granites at depths > 2 km (Leaman and Richardson, 2003; Fig. 3.5).

The Heemskirk Granite contains two main phases: the White and the Red granites (Fig. 3.5). This subdivision is based mainly on the distinctive colour of orthoclase feldspar in both units (Klominsky, 1972; Figs. 3.7D, E). The White phase of Heemskirk Granite (abbreviated as White granite) occurs as a sill over a large area. It is more than 500 m thick, extending from the western coastline to the eastern margin of the batholith. The Red phase of Heemskirk Granite (abbreviated as Red granite) is an approximately 300m-thick sill, and is confined to the eastern half of the exposed intrusion, overlying the White granite (Fig. 3.5). According to grain size variations and mineral textures, the White and Red granites can both be subdivided into coarse-grained, medium- to fine-grained and porphyritic varieties. The porphyritic Red granite can be further subdivided into biotite- and hornblende-bearing granites. Coarse-grained granites generally crop out on the rim of the batholith, while the inner parts are dominated by medium- to fine-grained phases. Porphyritic granites are of the smallest components of the batholith. They are sporadically distributed in the interiors of both the White and Red granite phases, with much smaller outcrops (Fig. 3.5).

The White and Red granites are mineralogically similar, consisting of quartz, K-feldspar, plagioclase, and minor biotite (Fig. 3.8D, E). However, biotites from the two granites are different in their colours and compositions. Brown-green pleochroism and higher Ti are typical for biotite from the Red granite, whereas biotite from the White granite displays red-brown pleochroism with higher Al (Hajitaheri, 1985). Previous studies have shown that accessory minerals such as zircon, monazite, ilmenite, apatite and fluorite occur in both granite phases. Hornblende and allanite are observed only in the Red granite, and muscovite, garnet and cassiterite only in the White granite (Heier and Brooks, 1966; Klominsky, 1972; Hajitaheri, 1985). In

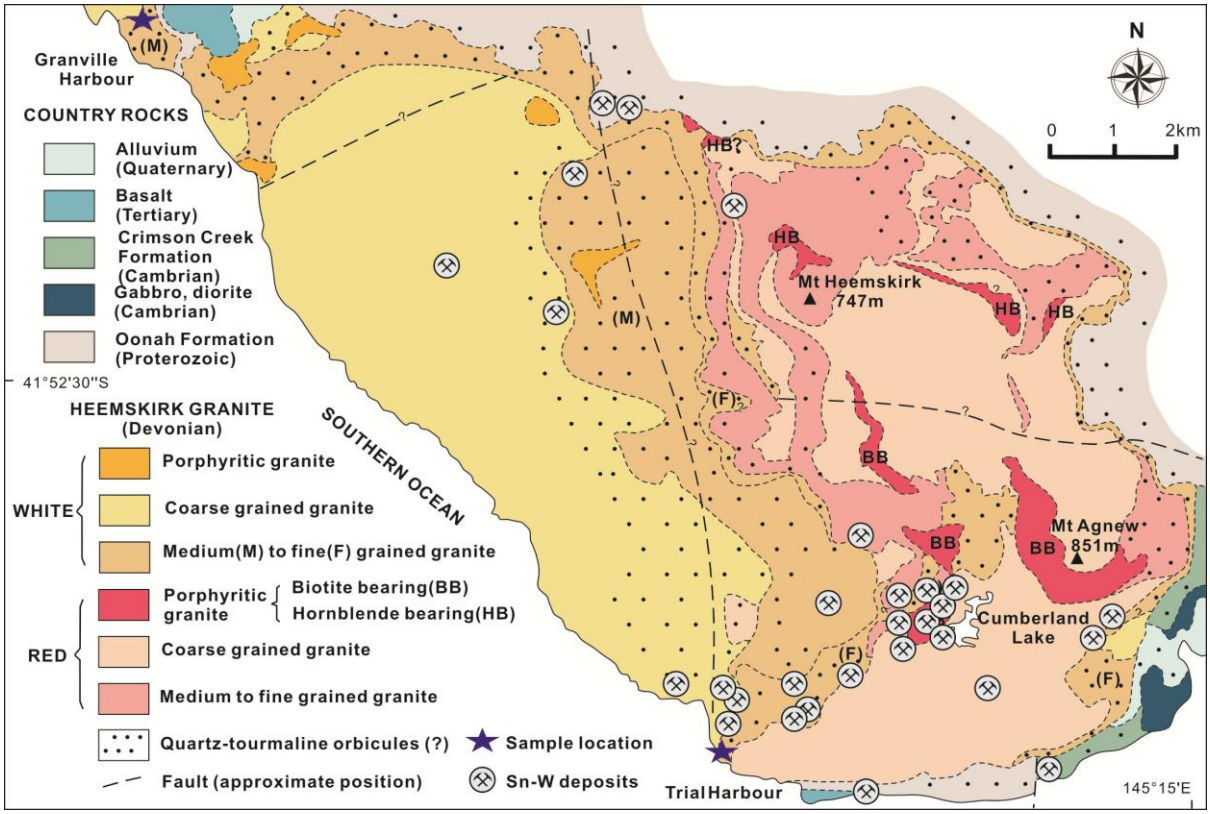

Figure 3.5 Geological map showing principal features of the Heemskirk Batholith and associated Sn–W deposits (from Klominsky, 1972; Hajitaheri, 1985). This batholith has been divided into two main granite phases, the White granite (S-type) and the Red granite (I-type).

the current study, monazite, titanite and magnetite have also been recognised in the White granite at Granville Harbour (Fig. 3.5).

The tourmaline-bearing Heemskirk batholith is a fertile intrusion, genetically associated with abundant Sn-Fe skarn and/or greisen deposits and vein-type Ag-Pb-Zn deposits, including the Federation Sn, Severn Sn, Queen Hill Sn, Montana Sn and St Dizier Sn-Fe skarn, numerous Ag-Pb-Zn deposits in the Zeehan mineral field, and also the Avebury Ni deposit (Williams et al., 1989; Solomon and Groves, 2000; Seymour et al., 2007; Keays and Jowitt, 2013; Tables 1.1 and 1.2).

3.2.2.2 Pieman Heads Granite

The Pieman Heads Granite (also known as Conical rocks; Sawka et al., 1990) crops out 20 km north of the Heemskirk Granite, and has a much smaller surface exposure (ca. 8 km^2; Fig. 3.6). This granite has not been studied in detail previously, largely because no mineralisation has been discovered within or around the intrusion, and partly because it is not easily accessible. The granite intruded the Neoproterozoic Rocky Cape Group, and is overlain by Tertiary and Quaternary sedimentary rocks (Brooks, 1966; Fig. 3.6). The Pieman Heads Granite is situated on the southern side of the mouth of the Pieman River, whereas the NNW-elongate Interview River Granite is exposed on the northern bank of the Pieman River (Fig. 3.6). These two plutons, together with the Sandy Cape Granite and Three Hummock Island Granite, were grouped as the 'Sandy Cape Suite' by Sawka et al. (1990). Geophysical investigations have shown that the

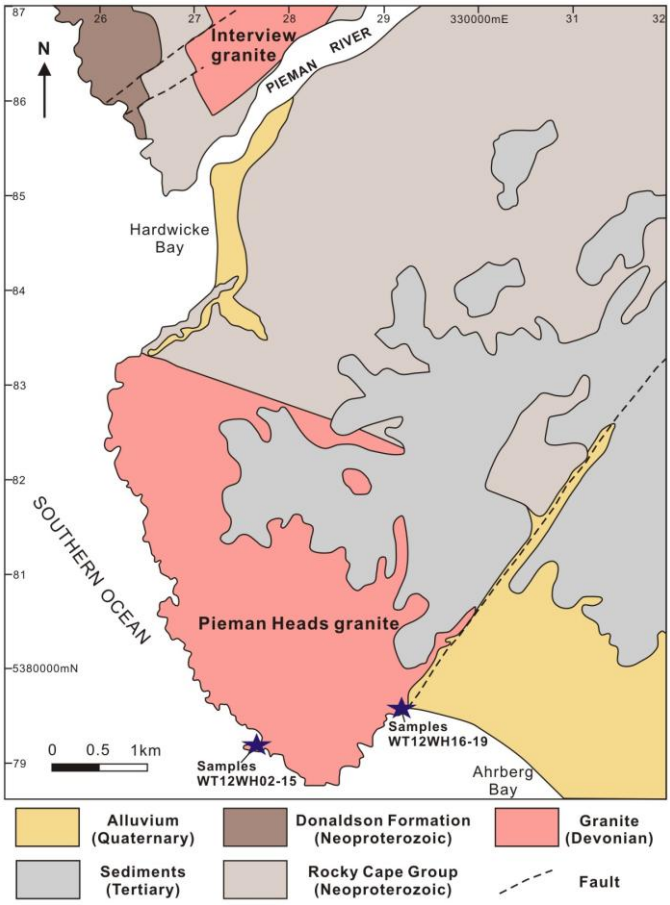

Figure 3.6 Simplified geological map of the Pieman Heads Granite (modified from Vicary, 2004). Sample locations are marked as stars in the map.

Pieman Heads Granite is probably connected to the Interview River Granite and the Sandy Cape Granite at depth of 1 km or more below the present-day surface (Leaman and Richardson, 2003). The Sandy Cape Suite, including the Pieman Heads Granite, has been considered to be petrologically similar to the White phase of the Heemskirk Granite (Brooks, 1966; Sawka et al., 1990; McClenaghan, 2006a).

The Pieman Heads Granite is coarse- to fine-grained, and equigranular to porphyritic (Fig. 3.7). It contains quartz, K-feldspar, plagioclase, biotite and muscovite (Fig. 3.8), with accessory tourmaline, apatite, zircon, monazite and titanite. This granitic pluton has undergone weak to moderate muscovite alteration. Amongst the Sandy Cape Suite, the Pieman Heads Granite is exceptional because of its distinctive tourmaline-quartz nodules (Sawka et al., 1990; McClenaghan, 2006a).

3.2.2.3 Housetop Granite

The Housetop Granite has a large exposure (> 160 km^2), 20 km south of Burnie, western Tasmania (Fig. 2.5). This granite has sharp, discordant contacts against folded Proterozoic to Palaeozoic country rocks (McDougall and Leggo, 1965). Williams et al. (1989) and Sawka (1990) identified several textural types or individual bodies in the Housetop Granite. Overall, the pluton is generally pink to reddish, and medium- to coarse-grained (Fig. 3.7A). Porphyritic textures, miarolitic cavities and thin vuggy pegmatites occur locally, and have been transgressed by aplitic, porphyritic microgranite dykes (Seymour, 1989).

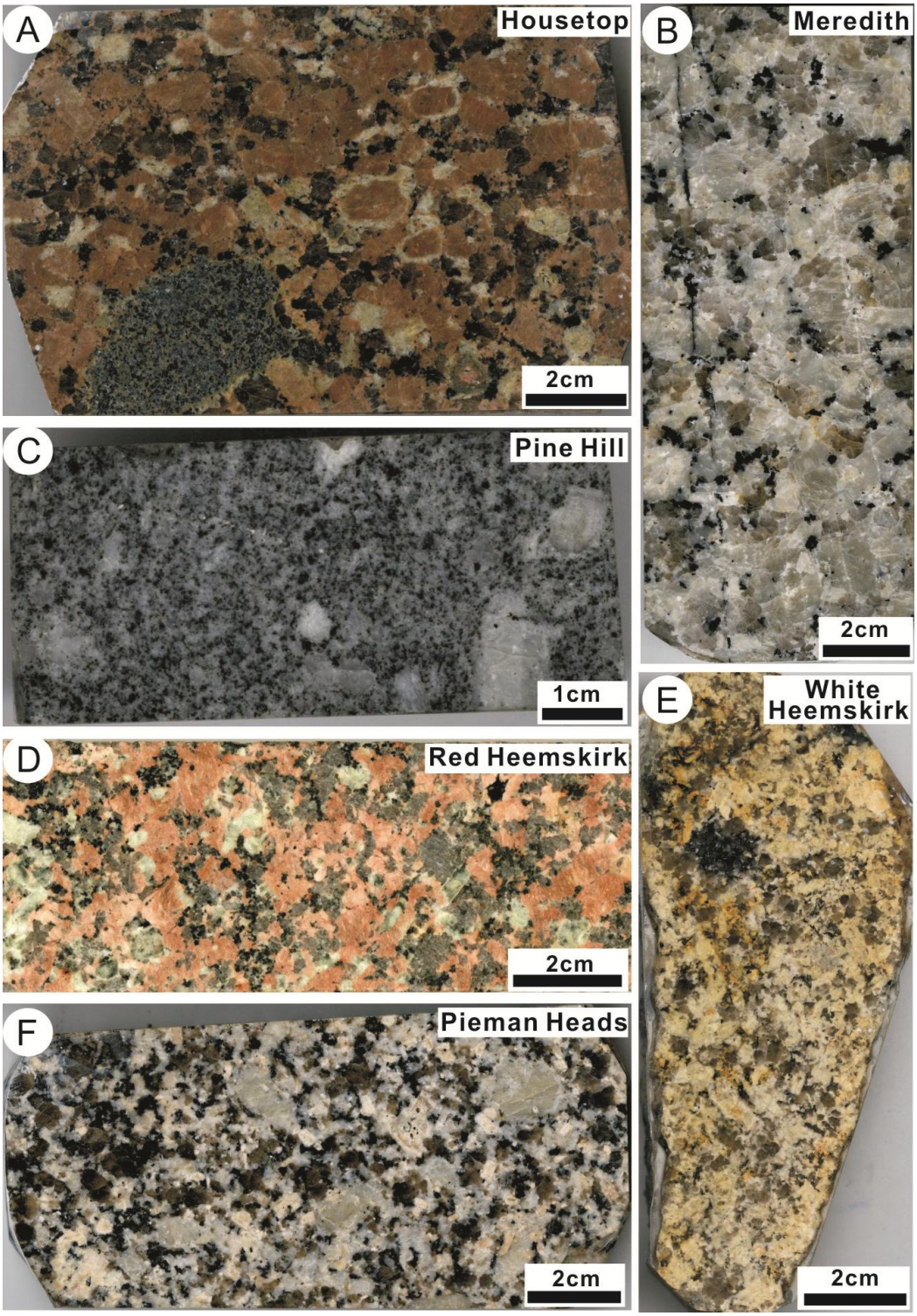

Figure 3.7 Photographs showing features of western Tasmanian granites. (A) The Housetop Granite consists of coarse-grained K-feldspar, biotite and quartz, and contains mafic enclaves locally. (B) The felsic phase of the Meredith Granite is characterised by coarse-grained K-feldspar. (C) K-feldspar phenocrysts and biotite-quartz matrix consists of a porphyritic phase of the Pine Hill Granite. (D) Red K-feldspar characterise the Red phase of the Heemskirk Granite. (E) In contrast to the Red Heemskirk Granite, the White Heemskirk Granite contains white K-feldspar. (F) The Pieman Hill Granite is mineralogically similar to the White Heemskirk Granite, consisting of white K-feldspar, biotite, quartz and minor muscovite. Sample coordinates: Housetop Granite, E145°54′44.76″, S41°11′33.10″; Meredith Granite, E145°22′10.80″, S41°39′10.21″, -233 to 240 m ; Pine Hill Granite, E145°27′53.70″, S41°48′56.42″, -1001.3m; Red Heemskirk Granite, E145°14′38.92″, S41°52′54.76″, -183m; White Heemskirk, E145°09′23.93 ″, S41°55′20.64″; Pieman Heads Granite, E144°55′40.01″, S41°43′15.00″.

Mafic enclaves dominated by biotite aggregates occur in some places (Fig. 3.7A). The granite typically consists of coarse-grained, granular K-feldspar, quartz, and minor plagioclase and biotite (up to 20 mm). Perthitic K-feldspar locally shows mosaic textures, and plagioclase crystals are zoned or polysynthetic twinned (Fig. 3.8A). Hornblende is common on the western flank of the granite, while tourmaline occurs widely in the southern part of the granite. The Kara magnetite-scheelite deposit formed in the southern contact aureole of the Housetop Granite (Singoyi and Zaw, 2001).

3.2.2.4 Meredith Granite

The Meredith Granite crops out intermittently over 280 km^2, southwest of Waratah in northwestern Tasmania (Fig. 2.5). It intruded a series of deformed Proterozoic to Palaeozoic sequences. The Meredith Granite is a composite batholith, with a smaller mafic phase in the northeast (Wombat Flat pluton) and a larger, more felsic part in the remainder (Williams et al., 1989; McClenaghan, 2006a). The Wombat Flat pluton is a fine- to medium-grained, equigranular to porphyritic monzogranite, consisting of quartz, perthitic K-feldspar, plagioclase, biotite and minor hornblende. This smaller pluton has a zircon U-Pb age of 373.2 ± 1.9 Ma (Black et al., 2005). The dominant portion of the Meredith Granite is grey to pale reddish, coarse-grained, equigranular to porphyritic, composing quartz, K-feldspar, and minor plagioclase and biotite (Figs. 3.7B, 3.8B). Accessory minerals include apatite, zircon, monazite, ilmenite, magnetite, tourmaline, topaz, fluorite, and secondary muscovite. Tourmaline-quartz orbicules, miarolitic cavities, and tourmaline-filled veins are widespread in some places. The felsic phases of the granite range from adamellite to alkali-feldspar granite (McClenaghan, 2006a). Several economically significant Sn-W deposits, including the Mt Bischoff Sn skarn and greisen, Cleveland Sn-W skarn, and Mt Lindsay Sn-W-F (-Be) skarn, together with numerous Pb-Zn-Ag veins, are genetically related to the Meredith Granite (Solomon and Groves, 2000; Seymour et al., 2007; Fig. 2.5).

3.2.2.5 Pine Hill Granite

The Pine Hill Granite has a very limited exposure, but is a part of an E-trending batholith that extends from Heemskirk Granite to Granite Tor in western Tasmania (Leaman and Richardson, 2003; Fig. 2.5). The Pine Hill Granite intruded the Proterozoic Success Creek Group and Crimson Creek Formation, and crops out 2 km southeast of the world-class Renison Bell Sn deposit. According to granite mineralogy and textures, Patterson et al. (1981) divided the Pine Hill stock into three major variants, including feldspar-porphyritic granite, quartz-feldspar porphyritic granite and quartz-feldspar porphyries. Samples in the study are relatively fresh or weakly altered, and were collected from diamond drill holes studied by Hughes (1995) and Innes (1995), and also from a more recent drill hole. The granitic samples are pale grey, medium- to coarse-grained, and have a porphyritic texture with subeuhedral quartz phenocrysts (Fig. 3.7C). The granite mainly consists of K-feldspar, quartz, plagioclase and biotite (Fig. 3.8C), as well as trace amounts of zircon, monazite, apatite, magnetite, ilmenite, allanite, titanite, tourmaline, topaz, and fluorite. Parts of the Pine Hill granite proximal to cassiterite sulphide mineralisation have experienced strong tourmalinisation, sericitisation and albitisation due to intense interaction between ore-forming fluid

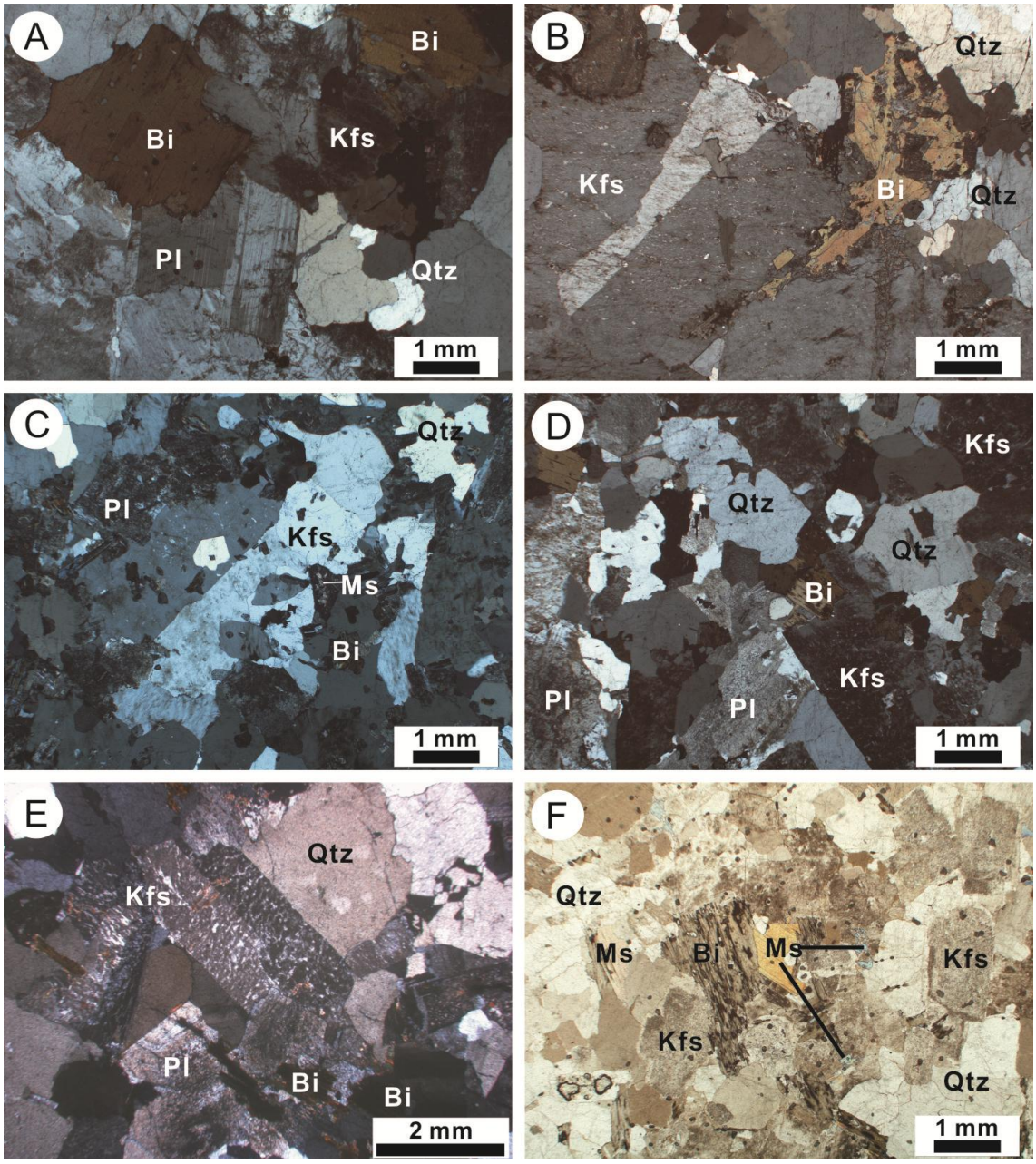

Figure 3.8 Photomicrographs showing mineralogical features of western Tasmanian granites. (A) K-feldspar, quartz and euhedral biotite coexisting with plagioclase displaying polysynthetic twins the Housetop Granite. (B) In the Meredith Granite, coarse-grained K-feldspar is associated with anhedral biotite and granular quartz. (C) K-feldspar, quartz, plagioclase and biotite and muscovite altered from K-feldspar comprise the porphyritic Pine Hill Granite. (D) Plagioclase, K-feldspar, biotite and quartz occur in the Red phase of the Heemskirk Granite. (E) In the White phase of the Heemskirk Granite, granular quartz, biotite and minor plagioclase coexisting with K-feldspar having simple twins. (F) The Pieman Head Granite contains quartz, K-feldspar, plagioclase, biotite and minor muscovite. All the photomicrographs taken under cross polarised light, except (F) under plane polarised light. Bi = biotite, Kfs = K-feldspar, Ms = muscovite, Pl = plagioclase, Qtz = quartz.

and the granitic rock (Patterson et al., 1981; Kitto, 1994; Bajwah et al., 1995).

3.3 Analytical methodologies

3.3.1 Whole-rock geochemistry

Whole-rock geochemical analyses of Tasmanian granites were completed using the analytical method LF200 at ACME Analytical Laboratories Ltd., Vancouver, British Columbia (Canada). Rock samples were crushed, split and pulverised to below 200 meshes. Apparatus was cleaned between each sample. A total of 66 elements (10 major elements and 56 trace elements) were determined by ICP-MS (inductively coupled plasma-mass spectrometry) and ICP-ES (inductively coupled plasma-emission spectrometry) analytical procedures. For each analysis, 0.2 g sample split was fused with $LiBO_2/LiB_4O_7$ and then dissovled in ICP-ES/ICP-MS analysis; 0.5 g sample for Ni using four acid digestion followed by an ICP-ES finish. The whole rock analytical results, together with detection limits, are presented in Appendix 3.1.

3.3.2 Lead isotopes

Whole rock samples of collected granites were crushed into ~ 1 mm size with a Cr-steel mortar and pestle. Over 0.5g of K-feldspar separates were hand-picked from each crushed rock under a binocular microscope, at CODES, University of Tasmania. Lead isotopic compositions of K-feldspar were analysed in the Isotope Geochemistry Laboratory, School of Earth Sciences, University of Melbourne. Approximately 80 mg of K-feldspar grains were weighed into Teflon beakers and subjected to a four-step acid leach protocol (6M HNO_3, then 6M HCl, both 20 ℃, three hours; 5M HF, then 6M HNO_3, both 60 ℃, three hours, e.g. DeWolf and Mezger, 1994). Acid leaching has become a standard procedure in Pb isotope studies since the work of Ludwig and Silver (1977) and aims to remove U-Th-rich impurities, e.g., apatite, oxides, fine-grained silicates and fracture-bound radiogenic lead. Weight loss from leaching of the Tasmanian K-feldspar is estimated to be near 75% based on visual inspection of the material. The residues were dissolved with 3:1 HF-HNO_3, followed by destruction of fluorides with concentrated HNO_3 and complete dissolution in 5M HNO_3. The resulting clear solutions were split for Pb isotope and trace element analyses. The reported Pb concentrations are adjusted for variable Pb isotopic compositions.

Lead was extracted from the dissolved residues using small anion resin columns, similar to the method by Kamber and Gladu (2009). The combined Pb processing blank was 50 ± 25 pg. Lead isotopic ratios were measured on a Nu Plasma multi-collector ICP-MS at the University of Melbourne, with sample aspiration via a Glass Expansion Opal Mist PFA nebuliser (~0.07 ml/min uptake) and a CETAC Aridus desolvator (Woodhead, 2002; Maas et al., 2005). Lead fractions were re-dissolved in 2% nitric acid doped with 10 ppb of thallium, to allow correction of instrumental mass bias using the Tl doping method (Woodhead, 2002). For samples large enough to produce sustained signals near 8-10V of total Pb (for a 6-10 minute mass spectrometer run this requires 25–30 ng of Pb), this correction protocol produces external precisions of ± 0.05–0.09 (2σ). BCR-2 averages $^{206}Pb/^{204}Pb$ = 18.758 ± 0.047, $^{207}Pb/^{204}Pb$ = 15.619 ± 0.066 and $^{208}Pb/^{204}Pb$ = 38.726 ± 0.090 (n=40, 2σ). A solution made from a Broken Hill galena averages = 16.004, 15.388 and 35.659 (n=73), with 2σ uncertainties of 0.038 %, 0.057 % and 0.076 % for $^{206}Pb/^{204}Pb$, $^{207}Pb/^{204}Pb$ and $^{208}Pb/^{204}Pb$, respectively. Both data sets are consistent with TIMS and MC-ICPMS reference values (e.g., Woodhead and Hergt, 2000; Weis et al., 2006). The Pb isotopic results are tabulated in Table 3.1.

3.3.3 Zircon U-Pb dating method

More than 100 g of granitic rocks were crushed in a Cr-steel ring mill to grain sizes < 400 micron. Non-magnetic heavy minerals were then separated using a gold pan and a Fe-B-Nd hand magnet. Zircons were hand-picked from the heavy mineral concentrates under a petrographic microscope in cross-polarised transmitted light. Selected crystals were placed on double sided sticky tape and epoxy glue was then poured into 2.5-cm diameter moulds. The mounts were cured for 12 hours and polished using clean sandpaper and a clean polishing lap. The samples were then washed in distilled water in an ultrasonic bath. Cathodoluminescence images of zircons were taken with a FEI Quanta 600 environmental SEM in the Central Science Laboratory at the University of Tasmania (UTAS).

A total of 122 U-Pb zircon analyses were performed at UTAS, using an Agilent 7500cs quadrupole ICP-MS with a 193 nm Coherent Ar-F gas laser and the Resonetics S155 ablation cell. The correction factors for $^{207}Pb/^{206}Pb$ ratios were calculated using NIST610 analysed every 15 unknowns, and corrected using the values recommended by Baker et al. (2004). The 91500 zircon of Wiedenbeck et al. (1995) was analysed to correct for Pb/U and Pb/Th mass bias, down hole fractionation, and instrument drift. Each zircon analysis began with a 30 second blank gas measurement followed by a further 30 seconds of analysis time when the laser was switched on.

Zircons were abated with 32 μm spots using the laser at 5 Hz and a density of approximately 2 J/cm^2. A flow of He carrier gas at a rate of 0.35 litres/minute carried particles ablated by the laser out of the chamber to be mixed with Ar gas, which were then carried to the plasma torch. The following secondary zircon reference materials were analysed: the Temora sample of Black et al. (2003) and Plesovice sample of Sláma et al. (2008); these were treated as unknowns and monitored for accuracy. Data reduction followed the method in Halpin et al. (2014). Uncertainties were calculated using methods similar to that outlined by Paton et al. (2010). Element abundances on zircons were calculated using the method outlined by Kosler (2001) using Zr as the internal standard element, assuming stoichiometric proportions and using the NIST610 to standard correct for mass bias and drift. The U-Pb geochronological results for Tasmanian granitoids are tabulated in Appendix 3.2.

3.4 Granite whole-rock geochemistry

3.4.1 Eastern Tasmanian granitoids

All of the granitoids from eastern Tasmania are enriched in Al_2O_3 contents (12.6 to 16 wt %), and depleted in Fe_2O_3, MgO, TiO_2, CaO, MnO and P_2O_5 (Appendix 3.1). These granitic plutons generally have peraluminous affinities, with aluminium saturation indexes above unity (Fig. 3.9), due to high Al_2O_3 relative to low CaO, Na_2O and K_2O. The peraluminous nature of these granitoids increases with higher Si contents. The loss on ignition (LOI) values of these whole-rock compositions are below 1 wt %, probably indicating limited alteration.

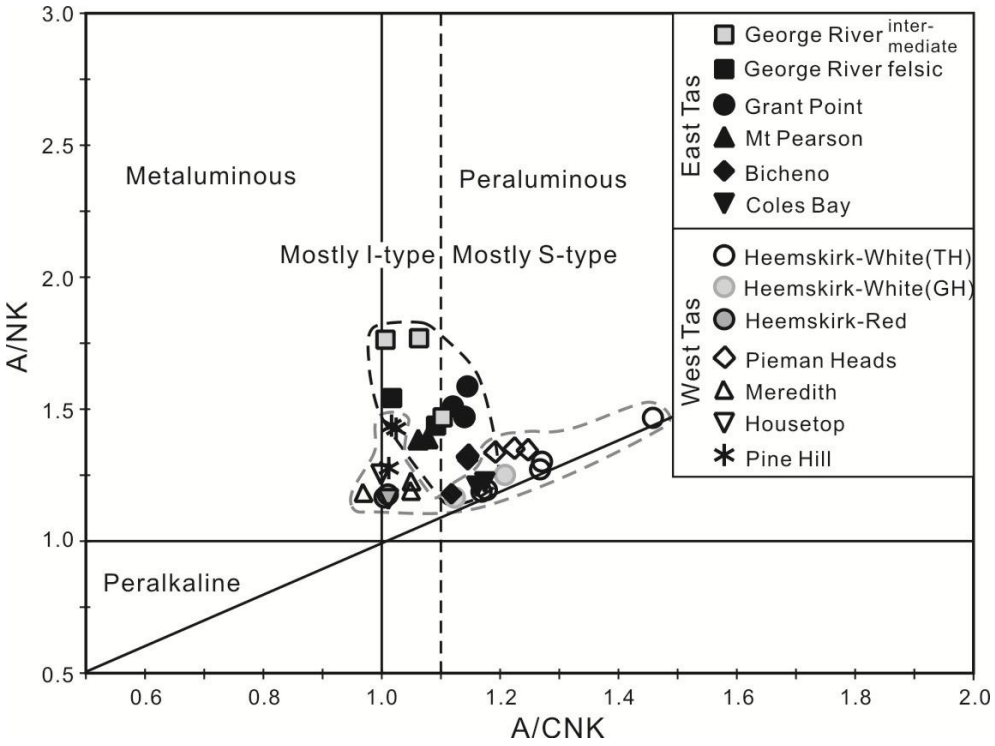

Figure 3.9 A/CNK [molar ratio $Al_2O_3/(CaO + Na_2O + K_2O)$] versus A/NK [molar ratio $Al_2O_3/(Na_2O + K_2O)$] plot for granitoids from eastern and western Tasmania. Granitoids from the two districts are delineated by black and grey dash line, respectively. All data are listed in Appendix 3.1. TH = Trial Harbour, GH = Granville Harbour.

Based on SiO_2 contents, two different phases have been recognised in the George River Granodiorite: an intermediate phase with SiO_2 < 70 wt % and a felsic phase with SiO_2 > 70 wt %, respectively (Fig. 3.10). The other analysed granitic rocks, including the Mt Pearson, Grant Point, Bicheno and Coles Bay granites in eastern Tasmania, all contain SiO_2 > 70 wt % (Fig. 3.10). The Coles Bay Granite, with SiO_2 at 77 wt %, is the most felsic of these granitic plutons. Major elements, such as Al_2O_3, Fe_2O_3, MgO, TiO_2, CaO, MnO and P_2O_5, typically show consistent depletion patterns with increasing SiO_2 contents (Fig. 3.10). Na_2O contents commonly stabilise around 3 wt % with increasing SiO_2 values, except for the George River Granodiorite and Bicheno Granite which have lower Na_2O concentrations (2.8 wt % and 2.4 wt %, respectively; Fig. 3.10D). K_2O contents show a progressive increase from intermediate (~3 wt %) to felsic compositions (6.8 wt %; Fig. 3.10E). These granitic intrusions are therefore classified as high-K to shoshonitic igneous rocks based on Peccerillo and Taylor's (1976) discrimination diagram. The Bicheno Granite is not the most felsic intrusion, but it has the highest K_2O and lowest Na_2O contents (Figs. 3.10D, E). P_2O_5 contents have a linear decrease with increasing SiO_2, except for the Bicheno Granite, which has high P concentrations that are comparable to the intermediate phase of the George River Granodiorite (0.2 wt % P_2O_5; Fig. 3.10I).

The George River Granodiorite has high Ba abundances, especially in the intermediate phase (up to 750 ppm; Fig. 3.10J). Distinct decreasing patterns with increasing SiO_2 are defined by most of the large ion lithophile elements (LILEs, e.g., Ba, Sr, Li; Figs. 3.10J, L). In contrast, Rb contents increase with increasing SiO_2 (Fig. 3.10K). Incompatible elements (e.g., Zr) decrease with increasing SiO_2 (Fig. 3.10M).

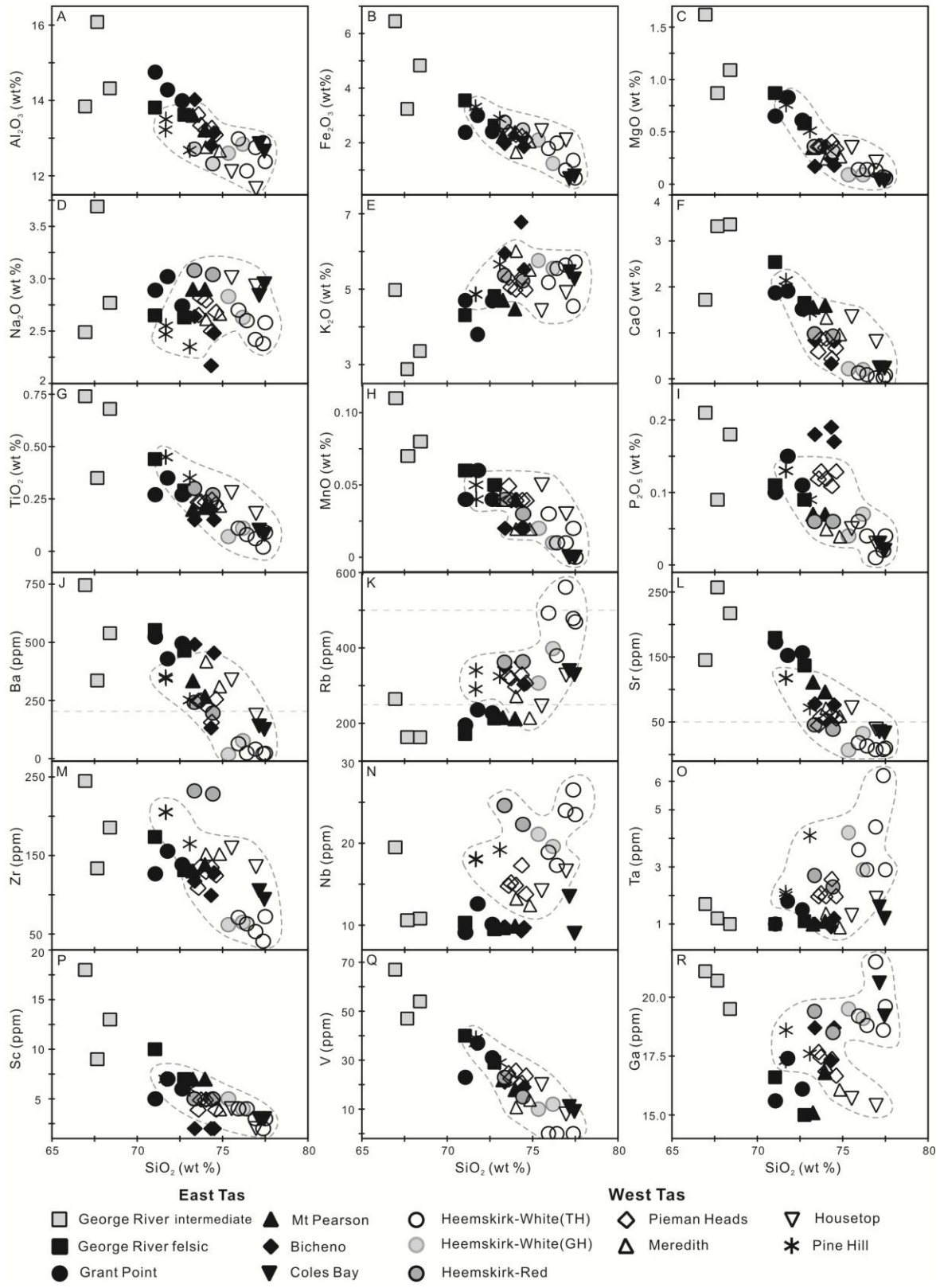

Figure 3.10 Harker diagrams for eastern and western Tasmanian granitoids. The granites from western Tasmania are delineated by dash lines. (A) Al_2O_3 vs SiO_2, (B) Fe_2O_3 vs SiO_2, (C) MgO vs SiO_2, (D) Na_2O vs SiO_2, (E) K_2O vs SiO_2, (F) CaO vs SiO_2, (G)TiO_2 vs SiO_2, (H) MnO vs SiO_2, (I) P_2O_5 vs SiO_2, (J) Ba vs SiO_2, (K) Rb vs SiO_2, (L) Sr vs SiO_2, (M) Zr vs SiO_2, (N) Nb vs SiO_2, (O) Ta vs SiO_2, (P) Sc vs SiO_2, (Q) V vs SiO_2, and (R) Ga vs SiO_2. All data are listed in Appendix 3.1. Tas = Tasmanian, TH = Trial Harbour, GH = Granville Harbour.

Many high field strength elements (HFSEs, e.g., Nb, Ta, Hf, Th) fluctuate with increasing SiO_2, which typically display a moderate decline from intermediate to felsic granitoids (Figs. 3.10N, O). Transition elements, such as Sc, V, Cr, Co, Ni etc., show progressive depletion patterns with increasing SiO_2 (Figs. 3.10P, Q). Gallium behaves differently from other transition elements. Its abundance decreases from intermediate George River Granodiorite (21 ppm) to felsic Grant Point Granite (15 ppm), whereas the Bicheno and Coles Bay granites have higher Ga abundances (17-18.7 ppm and 19-20 ppm) than these felsic intrusive rocks from St. Helens (Fig. 3.10R). Mt Pearson Granite has the lowest Sn concentration of the granitoids in eastern Tasmania (~3.5 ppm). The intermediate George River Granodiorite is slightly enriched in Sn (~7 ppm). Tin concentrations are higher in the Bicheno and Coles Bay granites, with abundances > 10 ppm (Appendix 3.1).

When plotted on mantle-normalised (McDonough and Sun, 1995) multi-element spider diagrams, granitic data from the Binalong Bay, both intermediate and felsic granitoids, show spiky patterns (Figs. 3.11A, B). These granitoids are strongly enriched in LILEs such as K, Cs, Rb and Ba relative to most HFSEs (e.g., Ta, Nb and Ti). They have positive Th and U anomalies, and negative Sr and Pb anomalies (Figs. 3.11A, B). The Coles Bay Granite displays similar trends to the granitoids at Binalong Bay, but it is more depleted in Ba, Sr and Ti (Fig. 3.11C). The Bicheno Granite has similar trace element patterns to the Coles Bay Granite, except for the notable depletion for heavy rare earth elements (HREEs; Fig. 3.11C).

The intermediate phase at George River has higher total rare earth element concentrations (∑REEs) than the felsic granite phase at Binalong Bay. ∑REE contents of the Grant Point Granite are similar to the felsic phase of the George River pluton, and lower than the Mt Pearson Granite. Granitic rocks from Binalong Bay and Coles Bay show typical spiked patterns on the spider diagram (Figs. 3.12A-C). Light rare earth elements (LREEs) define pronounced falling trends with strong negative Eu anomalies, whereas HREEs have flat trends (Figs. 3.12A-C). HREEs in the Bicheno Granite decrease in abundance from Gd to Lu (Fig. 3.12C), whereas LREEs display similar patterns to the Binalong Bay and Coles Bay granites with obvious negative Eu anomalies. Among these eastern Tasmanian granites, Eu abundances are the most depleted in the Coles Bay Granite (Eu/Eu* = 0.14 to 0.15; Fig. 3.12C).

3.4.2 Western Tasmanian granites

All of the granites investigated in western Tasmania are felsic (SiO_2 = 71–77 wt %), relatively Al_2O_3 enriched (11.6–13.6 wt %), and depleted in Fe_2O_3, MgO, CaO, TiO_2, P_2O_5 and MnO (Fig. 3.10). When plotted on an A/CNK versus A/NK diagram (Fig. 3.9), the Meredith, Housetop, Pine Hill and Red Heemskirk granites are shown to have weakly metaluminous to moderately peraluminous affinities, whereas the White phase of the Heemskirk and Pieman Heads granites are strongly peraluminous (Fig. 3.9). Some of these granites have undergone minor alteration with LOI values of ~ 1.1 wt % (i.e., the White Heemskirk and Pieman Heads granites).

Major elements (e.g., Al_2O_3, Fe_2O_3, MgO, CaO, TiO_2, P_2O_5 and MnO) mostly define progressively decreasing compositional trends with increasing SiO_2 contents (Figs. 3.10A-C, F-I). Na_2O and K_2O values decrease moderately with increasing SiO_2 (Figs. 3.10D-E). The Pine Hill Granite has the highest Fe_2O_3, MgO, CaO, TiO_2 and MnO, and the lowest SiO_2 contents among these granites. The Meredith, Housetop

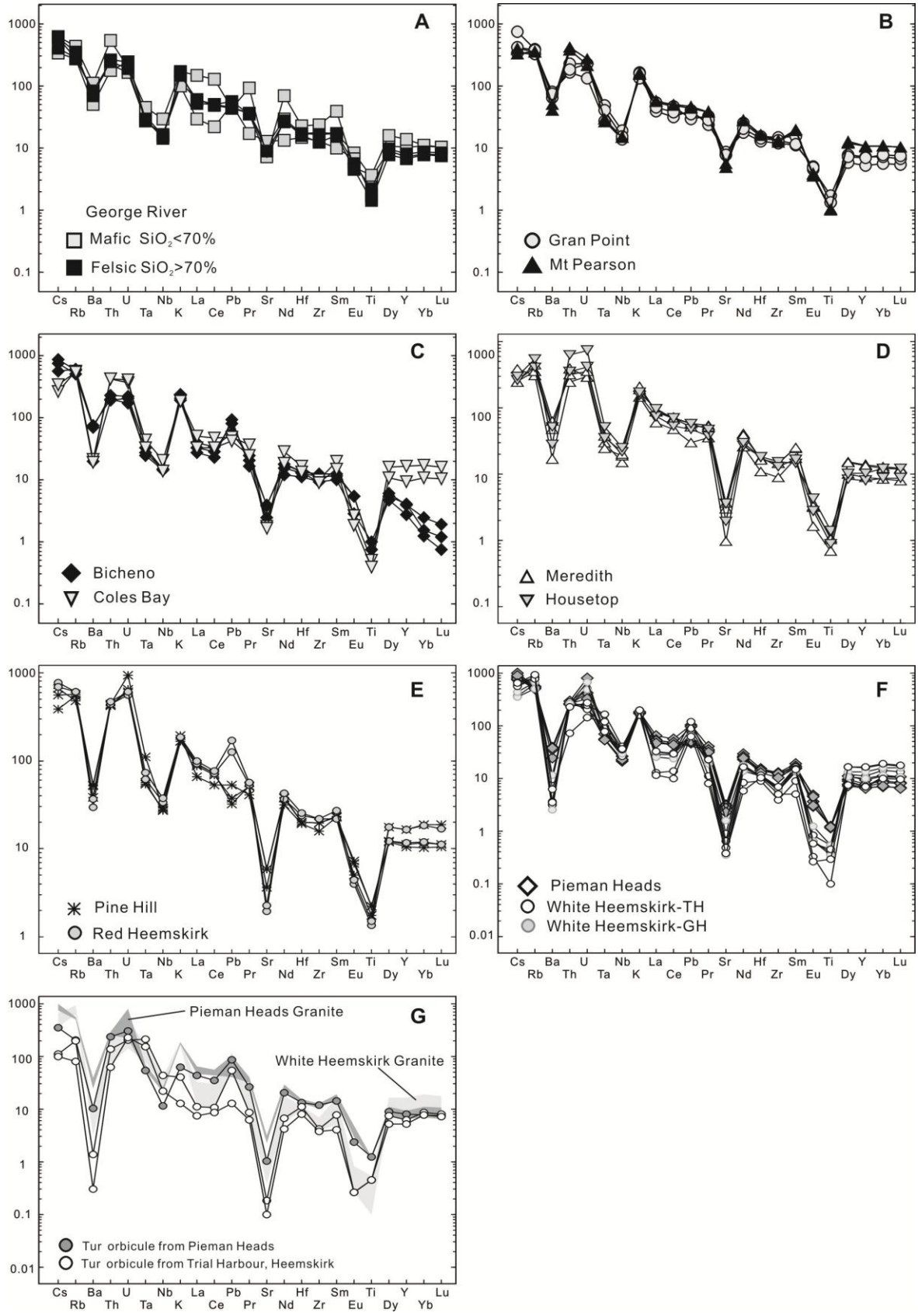

Figure 3.11 Primordial mantle-normalised multi-element plots for eastern (A, B, C), and western (D, E, F) Tasmanian granitoids, as well as tourmaline orbicules in the western granites (G). Normalising values are from McDonough and Sun (1995). All data are listed in Appendix 3.1. TH = Trial Harbour, GH = Granville Harbour, Tur = tourmaline.

and Red Heemskirk granites have similar major-element compositions to each other (Figs. 3.10 A-I). The White phase of the Heemskirk granite and the Pieman Heads granite are relatively enriched in SiO_2 (73.6–77.4 wt %) and Al_2O_3 (12.1–13.6 wt %). These western Tasmanian granites have shoshonitic features based on their high K_2O contents (> 4.4 wt % K_2O when SiO_2 > 71 %; Peccerillo and Taylor, 1976).

Most of incompatible trace elements are depleted, and a few trace elements (e.g., Rb, Ta, Nb) are enriched in the western Tasmanian granites relative to the granitic rocks in eastern Tasmania (Appendix 3.1; Fig. 3.10). LILEs (Ba, Sr, Cs, Li, Be), HFSEs (Zr, Th, U, Hf), and transition elements (Sc, V, Co, Ni, Cr) in the western Tasmanian granites decrease with increasing SiO_2 contents (Fig. 3.10). Rubidium, Nb and Ta concentrations increase linearly with elevated SiO_2 (Fig. 3.10). Gallium abundance degreases progressively from the Pine Hill Granite to the Pieman Heads Granite with increasing SiO_2, and is most enriched in the Heemskirk Granite (both the Red and White phases; 18.5–21.5 ppm). Rubidium, Nb and Ta are preferentially incorporated in the White phase of the Heemskirk Granite compared to the other granites (Figs. 3.10K, N, O), consisting with the higher degree of fractional crystallisation of this granite (e.g., Chappell and White, 1992).

When trace elements are normalised to abundances relative to primordial mantle (McDonough and Sun, 1995), all of the western Tasmanian granites display coherent depletion of Ba, Sr, Ti, Ta and Nb, and enrichment of K, Cs, Rb, Th, Pb and U (Figs. 3.11D-F). The normalised multi-element pattern for the Meredith Granite is similar to the Housetop Granite (Fig. 3.11D). Most elements define similar patterns for the Pine Hill and the Red phase of the Heemskirk granites on the primordial mantle-normalised plot, except for that Pb is enriched in the Red phase of the Heemskirk Granite (Fig. 3.11E). The multi-element plots are similar for the White phase of the Heemskirk granite and Pieman Heads granite; they have moderate Pb enrichment and subtle Ta, Nb and Sr depletion features compared to the other felsic intrusions (Fig. 3.11F).

Similar to the normalised multi-element plots, the Meredith and Housetop granites behave similarly on chondrite-normalised REE plots (Fig. 3.12D). They have moderate LREE and flat HREE fractionation patterns with negative Eu anomalies (Eu/Eu* = 0.12–0.20). The Pine Hill and Red Heemskirk granites define steep-sloped LREE and flat HREE fractionation patterns similar to the Meredith and Housetop granites, but with less negative Eu anomalies (Eu/Eu* = 0.22–0.38; Fig. 3.12E). The White phase of the Heemskirk Granite both from Trial Harbour and Granville Harbour, and the Pieman Heads Granite are characterised by typical "V"-shape REE fractionation patterns, showing weak LREE enrichments, flat HREE patterns, and pronounced negative Eu anomalies (Fig. 3.12F). The White phase of the Heemskirk Granite has the strongest negative Eu anomalies (Eu/Eu* = 0.04–0.10) of the western Tasmanian granites, consistent with a high degree of magmatic fractionation.

3.4.3 Tourmaline orbicules

Three geochemical analyses of tourmaline orbicules from the White Heemskirk and Pieman Heads granites show that they are enriched in Al_2O_3 (13.91–15.25 wt %), Fe_2O_3 (4.77–6.99 wt %) and MgO (0.22–0.82 wt %) contents, and moderately to weakly depleted in Na_2O (0.71–2.22 wt %) and CaO (0.08–0.27

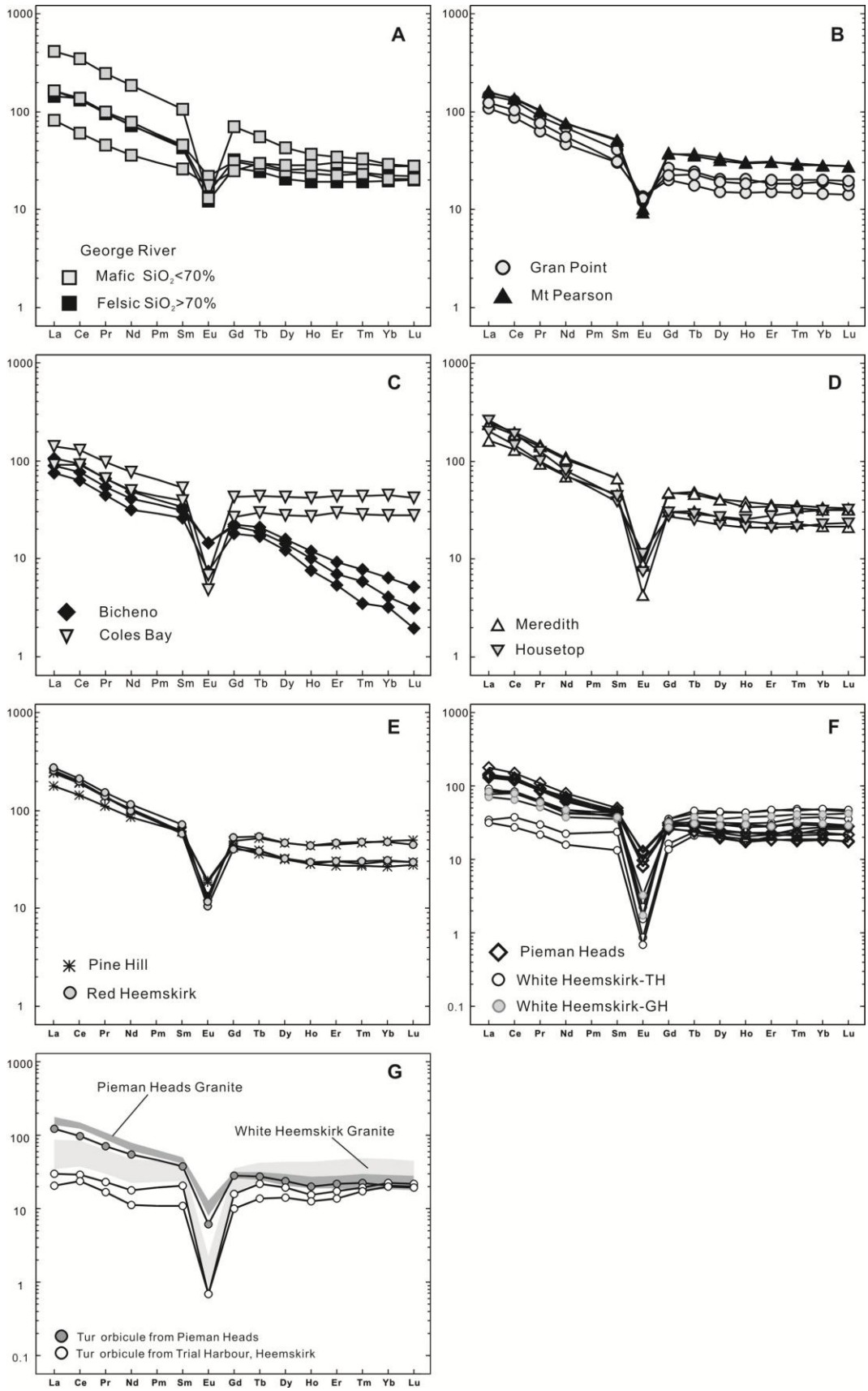

Figure 3.12 Chondrite-normalised rare earth element plots for eastern (A, B, C), and western (D, E, F) Tasmanian granitoids, as well as tourmaline orbicules in the western granites (G). Normalising values are from Sun and McDonough (1989). All data are listed in Appendix 3.1. TH = Trial Harbour, GH = Granville Harbour, Tur = tourmaline.

wt %), but strongly depleted in K_2O (K_2O/Na_2O = 0.52–0.81; Appendix 3.1). SiO_2, TiO_2, MnO and P_2O_5 contents are similar between the granitic hosts and tourmaline orbicules (Appendix 3.1). Higher concentrations of Al and ferromagnesian elements relate to the presence of abundant tourmaline which also caused the depletion of K, Na and Ca in tourmaline orbicules.

Boron is preferentially enriched in tourmaline orbicules due to the large volumes of tourmaline crystals. Lithium is depleted in tourmaline orbicules, whereas Be does not show any preference between the hosts and tourmaline orbicules (Appendix 3.1). The tourmaline orbicules have noteworthy depletion in Ba, Sr and Pb, and they are obviously depleted LILEs relative to the host granites (Fig. 3.11G). The REE pattern of tourmaline orbicules is similar to those in their respective hosts (Fig. 3.12G), but the tourmaline orbicules have lower total rare earth element abundances and more negative Eu anomalies (Fig. 3.12G).

Most HFSEs (e.g., Zr, Nb, Hf, Th, U) appear to be slightly or moderately depleted in tourmaline orbicules, whereas Ta concentrations tend to be enriched in tourmaline orbicules from the Heemskirk Granite (Fig. 3.11G; Appendix 3.1). The tourmaline orbicules have preferential enrichments of Sc and Ga, whereas V, Cr, Co, Ni and Zn are mostly depleted compared to the granite hosts (Appendix 3.1).

Most of the Tasmanian granites analysed here commonly contain 6–10 ppm Sn (Appendix 3.1). One aplitic granite sample hosting tourmaline orbicules from Trial Harbour, Heemskirk Granite has an anomalously high Sn concentration (850 ppm), which may be due to the presence of cassiterite or other stanniferous minerals. The tourmaline orbicule from the Pieman Heads Granite does not display any preferential enrichment of Sn (7 ppm). In contrast, the tourmaline orbicules from the White phase of the Heemskirk Granite have higher Sn concentrations (19–31 ppm) than their granitic hosts (Appendix 3.1).

3.5 Granite geochronology

3.5.1 Cathodoluminescence imaging of zircons

The zircons from Tasmanian granites are colourless and transparent, ranging from idiomorphic to hypidiomorphic (Fig. 3.13). Zircon grains separated from the George River Granodiorite and Grant Point Granite are mostly short prismatic, and rarely long prismatic, with length to width ratios varying 1:1 to 3:1, whereas the zircons from other granitic plutons commonly display long prismatic shapes, with length to width ratios ranging from 2:1 to 6:1 (Fig. 3.13). Cathodoluminescence (CL) images reveal that most of these zircons present strong to weak oscillatory or planar zonings (Fig. 3.13). Some zircons contain dark-luminescent inherited cores, which are commonly overgrown by bright-luminescent oscillatory rims. A few of the analysed zircons have dark-luminescent oscillatory rims surrounding irregular grey-luminescent cores (Figs. 3.13B-D). These features are mostly consistent with the zircons of magmatic origin (Corfu et al., 2003). However, a small amount of zircon grains from the Coles Bay Granite exhibit subround to elliptical morphologies, and grey to bright luminescent sector zoning (e.g., Fig. 3.13D). A xenocrystic origin is inferred for the unusual zircons. LA-ICP-MS U-Pb analyses reveal that these ovoid zircon grains have Ediacaran ages, older than the Palaeozoic emplacement age of this pluton.

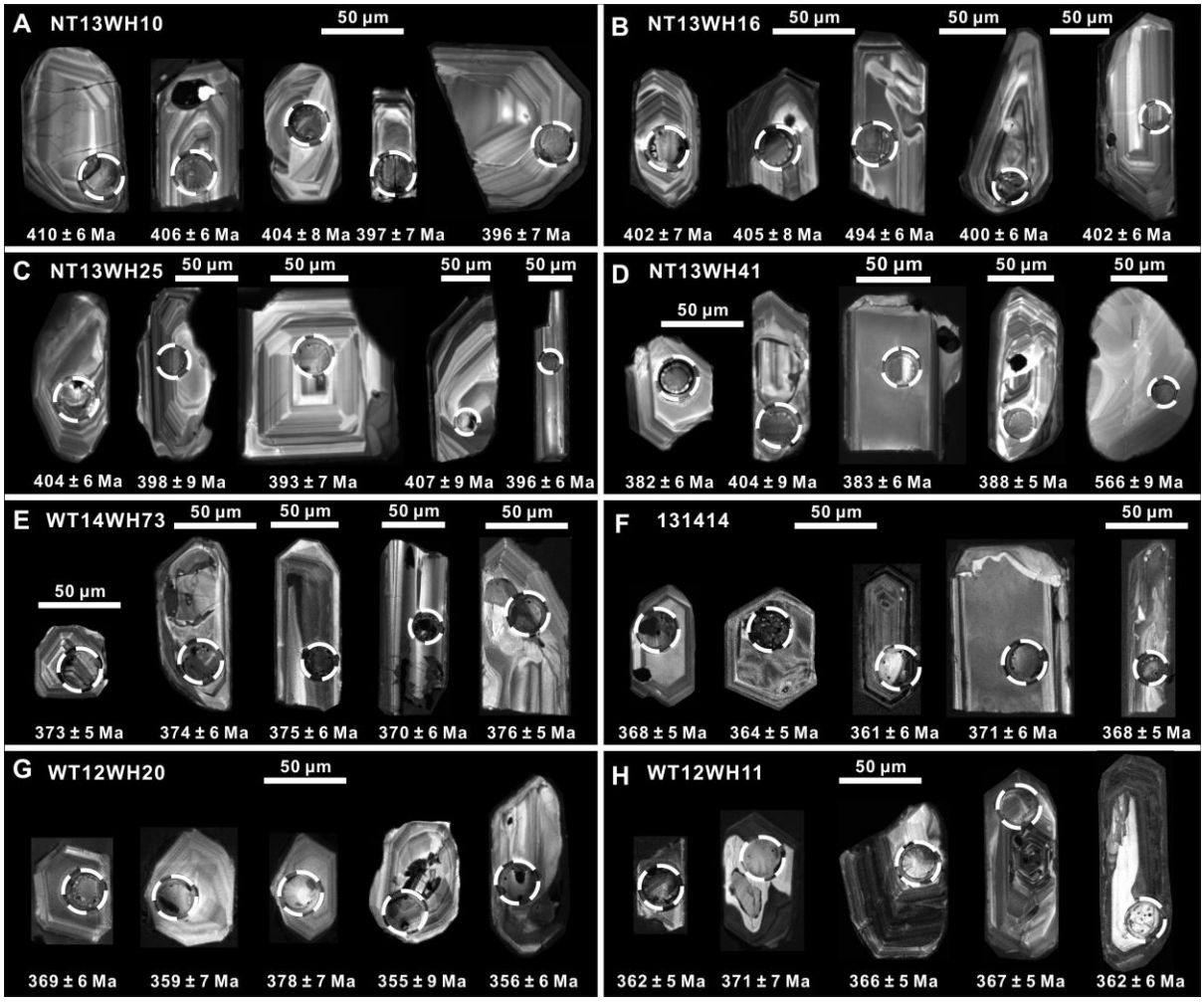

Figure 3.13 Representative CL images of zircons for U-Pb chronology from Tasmanian granitoids. (A) George River Granodiorite, (B) Grant Point Granite, (C) Mt Pearson Granite, (D) Coles Bay Granite, (E) Meredith Granit, (F) Pine Hill Granite, (G) White phase of Heemskirk Granite, (H) Pieman Heads Granite. Note that laser craters and corresponding ages are annotated. Sample coordinates are listed in Figs. 3.3, 3.4 and 3.7.

3.5.2 Zircon U-Pb dating results

3.5.2.1 Eastern Tasmanian granitoids

George River Granodiorite

The George River and Gardens plutons are significant mafic components of the Blue Tier Batholith, northeastern Tasmania, and are grouped as hornblende-biotite-bearing granodiorites. Previous biotite Rb-Sr isochron dating roughly constrained the George River Granodiorite with an age of 395 ± 3 Ma (Cocker, 1982), 10 m.y. older than the Gardens Granodiorite with an average Rb-Sr age of 383 ± 3 Ma (Cocker, 1982). In the current study, 11 zircon U-Pb LA-ICP-MS analyses yield a weighted mean age of 405.3 ± 5.2 Ma (MSWD = 1.6) for the crystallisation of the George River Granodiorite (Fig 3.14A). Two younger, U-rich (> 800 ppm) discordant grains gave ages of ca. 340 and 351 Ma, mostly likely due to small amounts of Pb loss. The two grains and one slightly older grain (425 Ma) were excluded from the age calculation.

Grant Point Granite

No previous geochronological data have been generated for the Grant Point intrusion. Eleven zircon U-Pb LA-ICP-MS analyses gave a weighted mean age of 402.6 ± 3.8 Ma (MSWD = 1.2) for the Grant Point Granite (Fig. 3.14B). One younger grain (ca. 356 Ma) has been discarded as it had an anomalous $^{207}Pb/^{206}Pb$ ratio (~0.11). One slightly older grain (ca. 443 Ma) has not been included in the age calculation. The analyses also identified several Meso- to Neo-proterozoic grains with U-Pb ages ranging from 1273 to ca. 921 Ma (Appendix 3.2), which are likely to be zircons inherited from Proterozoic sequences.

Mt Pearson Granite

The Mt Pearson Granite has been dated previously, with an average biotite Rb-Sr age of 389 ± 19 Ma (Cocker, 1982) and an average biotite K-Ar age of 386 ± 1.2 Ma (McClenaghan and Higgins, 1993). In the current study, a total of 12 zircon U-Pb LA-ICP-MS analyses yielded a weighted mean age of 396.2 ± 4.8 Ma (MSWD = 1.4) for this granite (Fig. 3.14C). The age calculation excluded two Meso- and Neo-proterzoic grains (ca.1707 Ma and ca. 927 Ma) that were probably inherited from Proterozoic units. One slightly older grain (ca. 411 Ma) was also excluded from the age calculation.

Coles Bay Granite

The felsic Coles Bay Granite located on the central-eastern coast of Tasmania was previously dated by the biotite Rb-Sr method, yielding an average age of 375 ± 3 Ma (Cocker, 1982). Kositcin and Everard (2013) reported a zircon SHRIMP U-Pb of 379 ± 2 Ma for the Hazards Granite, a fractionated I-type intrusion that is located on the western side of Freycinet Peninsula. The current study analysed 15 zircon grains, six of which produce a weighted mean age of 388.4 ± 7.4 Ma (MSWD = 1.4, probability = 0.21) for the emplacement of the Coles Bay Granite (Fig. 3.14D). Four zircon grains yield a secondary age of 580 ± 29 Ma (MSWD = 0.13; Fig. 3.14D), which have a similar range to ages of detrital zircons from the Palaeozoic Mathinna Supergroup. Three younger grains (probably Pb loss), and one Neoproterozoic grain (with mixing age domains) were discarded for the age calculation (Fig. 3.14D).

3.5.2.2 Western Tasmanian granites

Meredith Granite

McDougall and Leggo (1965) generated a mean biotite K-Ar age of 350 ± 10 Ma for the Meredith Granite in western Tasmanian terrace. Brooks (1966) reported an Rb-Sr isotopic age of 353 ± 7 Ma for the emplacement of the Meredith Granite, which is in agreement with the Rb-Sr whole-rock dating results (352.6 ± 10 Ma) of Sawka et al. (1990), who also obtained a hornblende Ar-Ar isochron age of 364.2 ± 1.7 Ma. In the current study, 14 zircon U-Pb LA-ICP-MS analyses yield a weighted mean age of 374.5 ± 4.2 Ma (MSWD = 1.4) for the crystallisation of the Meredith Granite (Fig. 3.14E), which is consistent with the zircon U-Pb age of 372 ± 2 Ma obtained by Kositcin and Everard (2013). Two high U zircon grains with Pb loss were not used in the age calculation (Fig. 3.14E).

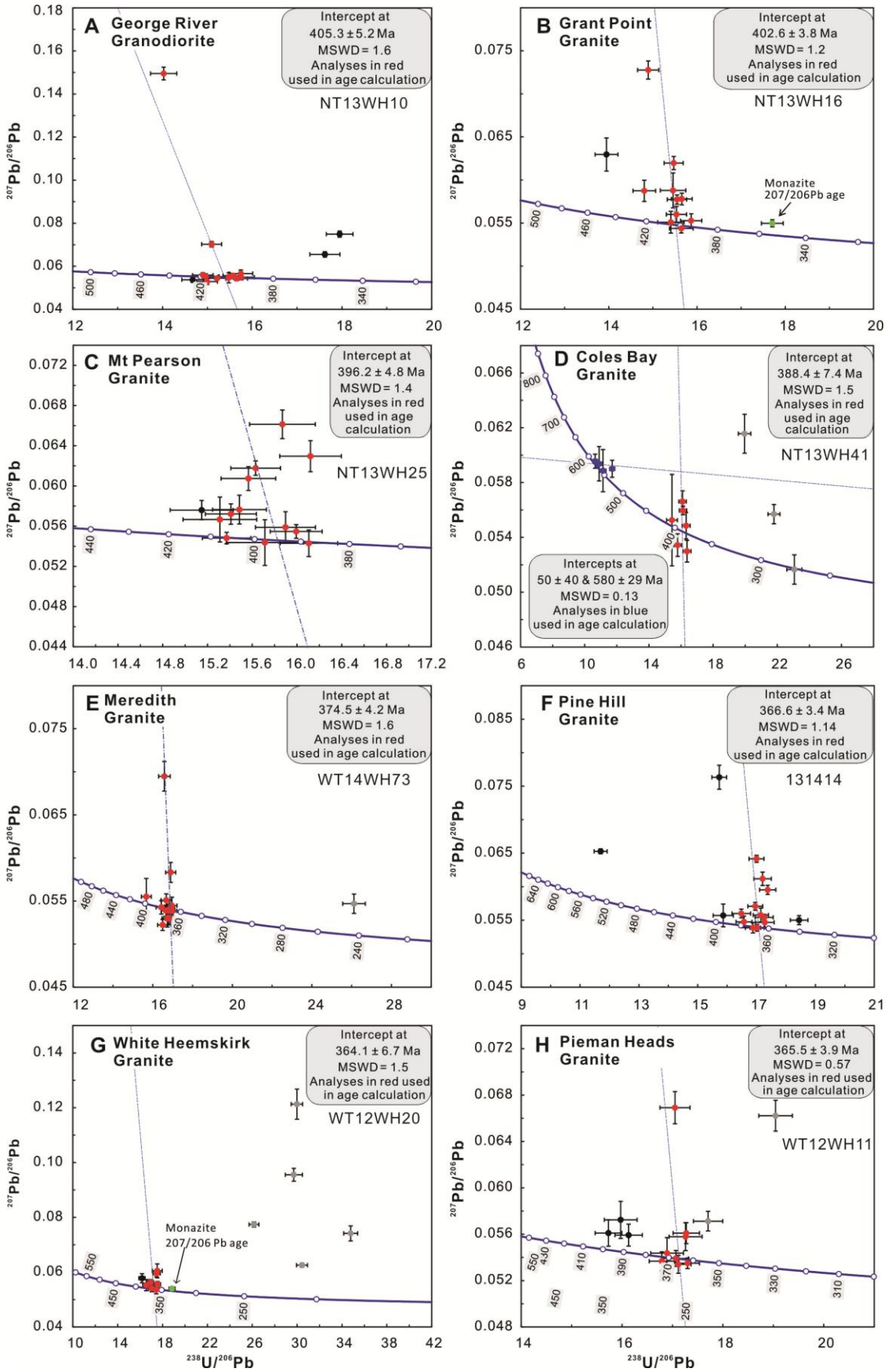

Figure 3.14 Zircon U-Pb concordia diagrams for Tasmanian granitoids. (A) George River Granodiorite, (B) Granit Point Granite, (C) Mt Pearson Granit, (D) Coles Bay Granite, (E) Meredith Granite, (F) Pine Hill Granite, (G) White phase of Heemskirk Granite, (H) Pieman Heads Granite.

Pine Hill Granite

Brooks (1966) acquired a whole-rock Rb-Sr isotopic age of 355 ± 4 Ma (Fig. 3.15) for the porphyritic phase of the Renison (Pine Hill) Granite. The current study yields a weighted mean age of 366.6 ± 3.4 Ma (MSWD = 1.14) for the crystallisation of the Pine Hill Granite using 11 zircon U-Pb LA-ICP-MS analyses (Fig. 3.14F). Two slightly younger grains (ca. 340 and ca. 319 Ma) were excluded as they are suspected to have been affected by Pb loss. In addition to one Cambrian grain (ca. 524 Ma), several older grains ranging from ca. 393 to ca. 387 Ma were not included in the age calculation (Fig. 3.14F).

Heemskirk Granite–White phase

The Heemskirk Granite has been dated extensively. A minimum emplacement age (mica K-Ar 340 ± 5 Ma) for the Heemskirk Granite was suggested by McDougall and Leggo (1965). Brooks and Compston (1965) generated mean whole-rock Rb-Sr ages of 357 ± 7 Ma and 350 ± 6 Ma for the White and Red phases, respectively. Sawka et al. (1990) gave an average biotite whole rock Rb-Sr age of 336 Ma ± 15 for the Heemskirk Granite. Precise zircon U-Pb SHRIMP ages of 360 ± 2 Ma and 361 ± 2 Ma obtained for the crystallisation of the Red and White phases of the Heemskirk Granite, respectively (Black et al., 2005; Fig. 3.15). Despite the two ages being indistinguishable, according to field relationships, the Red Heemskirk Granite was intruded by the White phase, and thus is formed earlier than the latter.

The current study analysed zircons from the White Heemskirk Granite by LA-ICP-MS. Eight spot analyses yield a weighted mean age of 364.1 ± 6.7 Ma (MSWD = 1.5) for the formation of this granite (Fig. 3.14G), which is within analytical error of the SHRIMP age from Black et al. (2005). Five younger, discordant grains contain high uranium concentrations (0.2 to 0.5%), and have variable isotopic ratios in the time resolved ICP-MS analysed, indicating Pb loss and common Pb gain. These grains and one slightly older grain were not used in the age calculation (Fig. 14G).

Pieman Heads Granite

The Pieman Heads Granite was previously thought to have been emplaced at around 356 ± 9 Ma based on whole-rock and mineral Rb-Sr isotopic measurements (Brooks, 1966). Later detailed work done by Sawka et al. (1990) provided several methods to constrain the forming age of the Pieman Heads Granite (Conical rocks), including a whole-rock Rb-Sr isochron age of 343.8 ± 4.9 Ma, K-feldspar Ar-Ar plateau ages of 350 to 340 Ma, and a biotite Ar-Ar plateau age of 353.3 ± 5 Ma (Fig. 3.15). These isotopic ages are discordant, largely due to various degrees of Ar and Sr loss.

A total of eight zircon U-Pb LA-ICP-MS spot analyses reveal a weighted mean age of 365.5 ± 3.9 Ma (MSWD = 1.5) for the formation of the Pieman Heads Granite (Fig. 3.14H). Two slightly younger discordant grains are suspected to have scattered Pb loss. In addition to these two grains, one Mesoproterozoic grain (ca. 1055 Ma) and three slightly older Palaeozoic grains (ca. 397 to ca. 382 Ma) were excluded from the age calculation (Fig. 3.14H).

3.6 Lead isotopic results

Data for a total of 13 Pb isotopic analyses of K-feldspar separates from Tasmanian granites are listed in Table 3.1. Initial Pb isotopic compositions have been calculated based on the ages of their host granites (Table 3.1), and the measured $^{238}U/^{204}Pb$ and $^{232}Th/^{204}Pb$ ratios of the feldspars. As shown in Figure 3. 17, western Tasmania granites are significantly more radiogenic than eastern Tasmanian granites. With the exception of the Grant Point Granite, the eastern Tasmanian granites are characterised by a relatively restricted range in all initial Pb isotope ratios, with $^{206}Pb/^{204}Pb_i$, $^{207}Pb/^{204}Pb_i$ and $^{208}Pb/^{204}Pb_i$ values between 18.092–18.342, 15.592–15.611 and 38.147–38.245, respectively. The Grant Point Granite has much less radiogenic values of $^{206}Pb/^{204}Pb_i$ = 17.638, $^{207}Pb/^{204}Pb_i$ = 15.549 and $^{208}Pb/^{204}Pb_i$ = 37.903. There is little difference in Pb isotopic signatures between K-feldspar from the intermediate and felsic phases of the George River Granodiorite (Fig. 3.16). K-feldspar from the neighbouring Mt. Pearson Granite has slightly more radiogenic Pb than the George River Granodiorite (Fig. 3.16). K-feldspar grains from the Bicheno and Coles Bay granites have similar $^{207}Pb/^{204}Pb_i$ and $^{208}Pb/^{204}Pb_i$ ratios to those from the Mt. Pearson Granite, but moderately higher $^{206}Pb/^{204}Pb_i$ values (Table 3.1).

In contrast, Pb isotopic ratios of K-feldspars from western Tasmanian granites are more variable and more radiogenic (Table 3.1; Fig. 3.16). Like the eastern Tasmanian granite data, the majority (five out of seven) of the western Tasmanian granite analyses have a restricted range in values, with most $^{206}Pb/^{204}Pb_i$, $^{207}Pb/^{204}Pb_i$ and $^{208}Pb/^{204}Pb_i$ values between 18.631–18.803, 15.617–15.644 and 38.554–38.667. Of these five results, the two K-feldspar results from Pine Hill Granite have the least radiogenic Pb isotopic compositions ($^{206}Pb/^{204}Pb_i$ = 18.631–18.632, $^{207}Pb/^{204}Pb_i$ = 15.642–15.644, and $^{208}Pb/^{204}Pb_i$ = 38.571–38.624; Fig. 3.16). Three other results, from the Red Heemskirk, Meredith and Housetop granites have narrow variations of Pb isotopic ratios of 18.745–18.803 for $^{206}Pb/^{204}Pb_i$, 15.617–15.638 for $^{207}Pb/^{204}Pb_i$, and 38.554–38.667 for $^{208}Pb/^{204}Pb_i$. The Pieman Heads and White Heemskirk granites yield significantly more radiogenic $^{206}Pb/^{204}Pb_i$ (> 20.4) and $^{207}Pb/^{204}Pb_i$ (> 15.7) ratios, but variable $^{208}Pb/^{204}Pb_i$ ratios (37.97–38.94).

3.7 Discussion

3.7.1 Geochemical classification

The mineralogical and geochemical compositions of Tasmanian granitoids confirm that no A-type granites occur in Tasmania (Sawka et al., 1990; McClenaghan, 2006a; this study). Instead, the Tasmanian granites can be grouped into I-type and S-type granitic rocks (e.g., Chappell and White, 1974, 2001). In eastern Tasmania, the metaluminous George River Granodiorite contains a hornblende-biotite-plagioclase assemblage, typical features of I-type granites. The Mt Pearson Granite at St. Helens is characterised by voluminous megacrystic K-feldspar and felsic composition (SiO_2 > 73 wt %), similar to an alkali-feldspar granite. Adamellitic equivalents of this granite have been reported to crop out in other places (McClenaghan, 2006a). The metaluminous signature (Fig. 3. 9), less fractionated REE patterns (Fig. 3.12) and mineral assemblages (K-feldspar + plagioclase + quartz + biotite) indicate that the Mt Pearson Granite

is I-type. The sampled Coles Bay Granite has very felsic (> 77 wt %), peraluminous characteristics, positive Y, Th and U correlations with increasing SiO_2, implying that it is I-type (cf. Chappell, 1999).

Cordierite and garnet are diagnostic minerals of S-type granites (Chappell and White, 2001). They have been reported to occur in the Bicheno Granite (McClenaghan, 2006a). Secondary muscovite aggregates that occur as inclusions in megacrystic K-feldspar phenocrysts (Fig. 3.4D) are interpreted to have resulted from magmatic-hydrothermal alteration of cordierite. The whole-rock composition of the Bicheno Granite, particularly its peraluminous character, and a positive correlation of P_2O_5 and negative correlations of Th, U and Y with increasing SiO_2, indicate that it is an S-type granitoid (Chappell, 1999).

The Grant Point Granite was thought to be a felsic variant of the George River Granodiorite (McClenaghan, 2006a), but whole-rock results in this study show that the two granitoids are compositionally distinct (Figs. 3.9, 3.10, and 3.11). The peraluminous affinity (A/CNK > 1.1; Fig. 3.9), low Fe and high K contents (Fig. 3.10), together with common muscovite-biotite-feldspar-quartz assemblage (Fig. 3.3C), suggest that the Grant Point Granite is an S-type granitoid rather than an I-type intrusion as categorised by previous studies (e.g., McClenaghan, 2006a).

In western Tasmania, the Pieman Heads and the White phase of the Heemskirk batholith are classified as S-type granites, mainly based on their strongly peraluminous signatures (Fig. 3.9), and muscovite + biotite + K-feldspar (-garnet) mineral associations. In contrast, the metaluminous affinities (Fig. 3.9), biotite + K-feldspar + plagioclase (+ hornblende) assemblages and trace element patterns with increasing SiO_2 (Fig. 3.10) indicate that the Pine Hill, Meredith, Housetop and Red phase of the Heemskirk, granites are I-type granitic plutons, although some of these granites show compositional features comparable to S-type granites largely due to extensive fractional crystallisation.

Chappell and White (1992) noted that fractionated granites in Lachlan Fold Belt commonly contain Rb > 250 ppm, Sr < 50 ppm and Ba < 200 ppm. Granites with Rb > 500 ppm have undergone strong fractional crystallisation, which may obscure the compositional line between I-type and S-type granites (Chappell, 1999; Chappell and White, 2001). According to these chemical criteria outlined, the I-type George River Granodiorite is the least fractionated Tasmanian granite investigated in the current study. This intrusion is compositionally similar to other unfractionated granodiorites in eastern Tasmania (e.g., Gardens, Pyengana, Wybalenna; McClenaghan, 2006a; Black et al., 2010). The Mt Pearson, Grant Point and Bicheno plutons are weakly fractionated granites, whereas the Coles Bay Granite is moderately (to strongly) fractionated, with Rb ≈ 335 ppm and Sr ≈ 34 ppm. Most of the western Tasmanian granites, e.g., the Meredith, Housetop, Red Heemskirk and Pine Hill granites are moderately to strongly fractionated (Rb > 250 ppm, Sr < 50ppm). The S-type White phase of the Heemskirk Granite (Rb > 500 ppm) is more strongly fractionated than the Pieman Heads Granite (Fig. 3.10). The Meredith and Pine Hill granites, which are associated with world class Sn-W deposits, are considered as the most fractionated of the western Tasmanian granites (Kwak et al., 1983; Bajwah et al., 1995; McClenaghan, 2006a; this study).

Table 3.1 K-feldspar lead isotopic compositions of Tasmanian granites.

Granite name	Sample No.	Mineral	Age (Ma)	± 2σ	^{238}U (ppm)	^{232}Th (ppm)	Pb (ppm)	$^{238}U/^{204}Pb$	$^{232}Th/^{204}Pb$	$^{206}Pb/^{204}Pb(m)$	$^{207}Pb/^{204}Pb(m)$	$^{208}Pb/^{204}Pb(m)$	$^{206}Pb/^{204}Pb(i)$	$^{207}Pb/^{204}Pb(i)$	$^{208}Pb/^{204}Pb(i)$
Eastern Tasmania															
George River mafic	NT13WH02	K-feldspar	405	5	0.36	0.69	7.49	0.36	6.1	18.288	15.604	38.270	18.092	15.593	38.147
George River felsic	NT13WH10	K-feldspar	405	5	0.10	0.06	12.2	0.10	0.3	18.184	15.594	38.156	18.149	15.592	38.150
Grant Point	NT13WH16	K-feldspar	403	4	0.21	2.83	0.63	0.21	320.3	19.135	15.631	44.355	17.638	15.549	37.903
Mt. Pearson	NT13WH25	K-feldspar	396	5	0.12	0.07	13.7	0.12	0.3	18.200	15.612	38.227	18.164	15.611	38.220
Bicheno	NT13WH34	K-feldspar	381	3	0.57	20.5	18.7	0.57	73.2	18.461	15.614	39.599	18.342	15.607	38.206
Coles Bay	NT13WH41	K-feldspar	388	7	0.05	0.49	4.18	0.05	7.6	18.346	15.610	38.393	18.299	15.607	38.245
Western Tasmania															
Pieman Heads	WT12WH11	K-feldspar	366	4	0.29	3.09	0.33	72.6	796.6	24.897	15.967	52.525	20.658	15.739	37.966
White Heemskirk	WT12WH20	K-feldspar	364	7	0.52	1.99	2.39	14.8	58.1	21.283	15.776	39.997	20.422	15.730	38.940
Red Heemskirk	WT14WH68	K-feldspar	360	2	0.15	2.11	3.56	2.7	39.7	18.949	15.628	39.380	18.793	15.620	38.667
Meredith	WT14WH73	K-feldspar	375	4	0.05	0.83	2.19	1.5	25.2	18.834	15.643	39.055	18.745	15.638	38.584
Housetop	134237	K-feldspar	373	2	0.01	0.07	0.88	1.1	5.3	18.867	15.621	38.653	18.803	15.617	38.554
Renison	2012160086	K-feldspar	367	4	1.35	0.46	16.7	6.02	2.04	18.984	15.663	38.661	18.631	15.644	38.624
Renison	2012160087	K-feldspar	367	4	0.31	0.15	22.6	1.00	0.48	18.690	15.646	38.580	18.632	15.642	38.571

Note: $^{206}Pb/^{204}Pb$ (m) represents measured lead isotopes, $^{206}Pb/^{204}Pb$ (i) represents initial lead isotopes corrected to granite ages.

3.7.2 Geochronological evolution

3.7.2.1 Age variations in granitoids across Tasmania

The zircon U-Pb age of the George River Granodiorite (405.3 ± 5.2 Ma) within analytical error, overlaps with zircon U-Pb SHRIMP ages for the Gardens Granodiorite of the Blue Tier Batholith (400 ± 2 Ma; Black et al., 2005), and the Wybalenna Granodiorite on Flinders Island (401 ± 4 Ma; Black et al., 2005), demonstrating that they intruded contemporaneously. These I-type least fractionated biotite-hornblende granodiorites (including the Pyengana Granodiorite) therefore represent the earliest mid-Palaeozoic intrusive event (~ 400 Ma) in Tasmania.

The Grant Point Granite has a zircon U-Pb age (402.6 ± 3.8 Ma) similar to the adjacent George River Granodiorite. It is the oldest S-type granitoid known in Tasmania during Palaeozoic, and was emplaced coevally with the oldest I-type granodiorites.

The Mt Pearson Granite was previously considered to be the eastward extension of the Poimena Granite (McClenaghan, 2006a). However, the zircon U-Pb age of the Mt Pearson Granite reported in this study (396.2 ± 4.8 Ma; Fig. 14.C) is almost 9 m.y. older than the U-Pb SHRIMP results of the Poimena Granite (386.8 ± 2.5 Ma; Black et al., 2005), indicating that the former is a separate felsic pluton of the Blue Tier Batholith.

The LA-ICP-MS U-Pb determination of 388.4 ± 7.4 Ma age for the Coles Bay Granite overlaps with the SHRIMP zircon U-Pb analyses of the Poimena Granite (386.8 ± 2.5 Ma; Black et al., 2005). The I-type Coles Bay Granite thus intruded contemporaneously with the I-type Poimena Granite of the Blue Tier Batholith, and the Hogarth Road Granite (388 ± 4 Ma; Black et al., 2005) and Tombstone Creek Granite (386 ± 4 Ma; Black et al., 2005) of the Scottsdale Batholith, as well as the S-type Ansons Bay Granite of Eddystone Batholith (384 ± 4 Ma; Black et al., 2005) and the S-type Strzelecki Granite on Flinders Island (385 ± 4 Ma; Black et al., 2005; Fig. 2.3). These Late Devonian suites of granitoids are the most widespread granitic rocks in northeast Tasmania. Their emplacement immediately followed the Tabberabberan Orogeny (ca.390 Ma; Black et al., 2005).

Most of the western Tasmanian granites are younger than their eastern counterparts (McDougall and Leggo, 1965; Black et al., 2005; Kositcin and Everard, 2013; this study). The oldest ages are 374.5 ± 4.2 Ma age for the southern part of the Meredith Granite (Kositcin and Everard, 2013; this study), 373 ± 2 Ma for the north of the Meredith Granite (Wombat Flat pluton, Black et al., 2005), and 374 ± 2 Ma for the Housetop Granite (Black et al., 2005; Fig. 3.15). These two mineralised I-type plutons are the oldest Palaeozoic granites in western Tasmania. They intruded at the same time as the youngest, moderately to strongly fractionated I-type and S-type granites from eastern Tasmania, e.g., the Lottah, Henbury, Deep Glen Bay and Hippolyte Rocks granites which are sporadically exposed on the southeastern Tasmania (Black et al., 2005; Fig. 3.15).

The ages of the Pine Hill Granite (366.6 ± 3.4 Ma), White Heemskirk Granite (364.1 ± 6.7 Ma) and Pine Heads Granite (365.5 ± 3.9 Ma) in western Tasmania, within analytical error, are in agreement with the SHRIMP zircon U-Pb ages of the Red Heemskirk Granite (360 ± 2 Ma), the White Heemskirk Granite (361 ± 2 Ma) and the Sandy Cape Granite (northern part of the Interview Granite, 362 ± 2 Ma) reported by

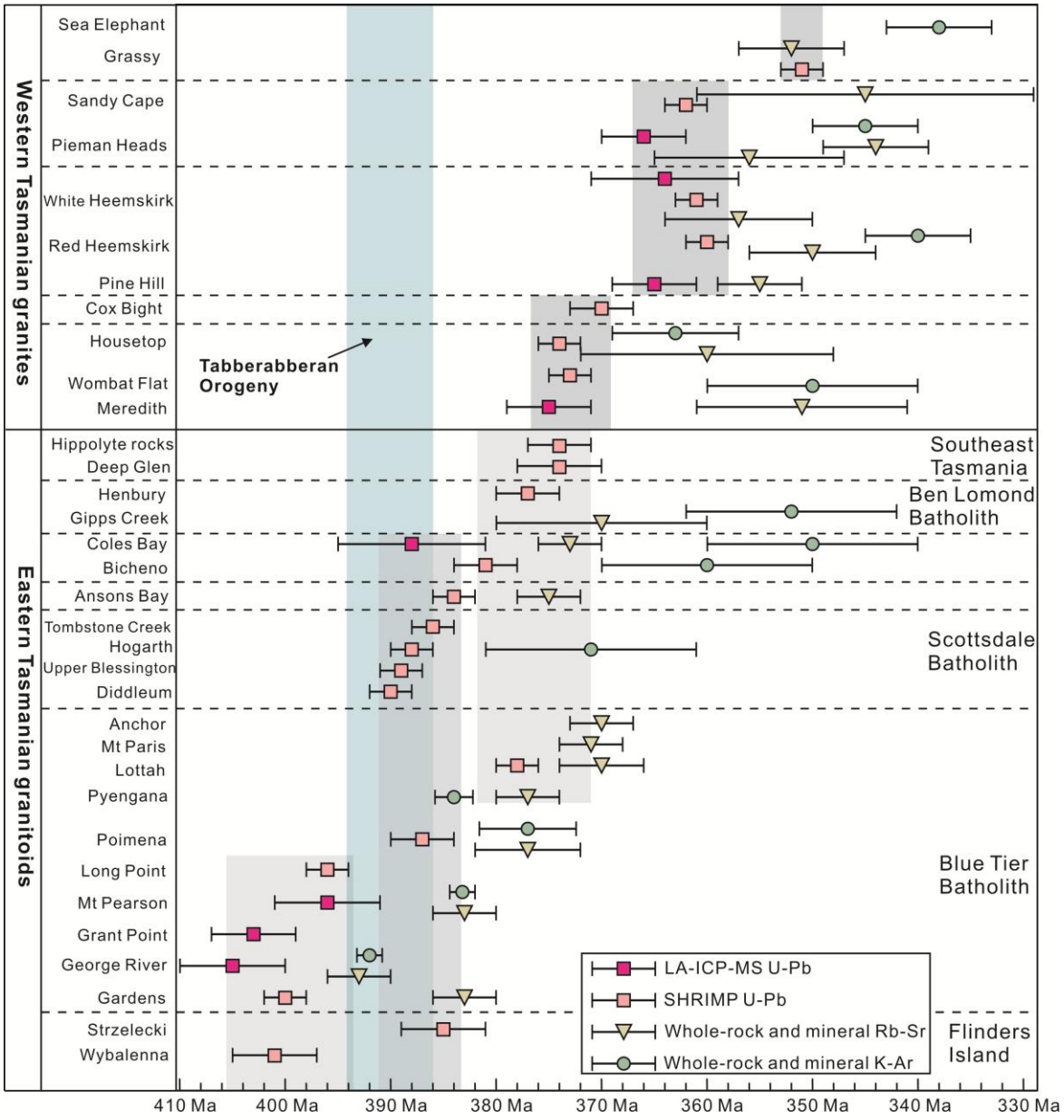

Figure 3.15 Compilations of chronological data in a timeline for granitic rocks from eastern and western Tasmania by different methods. Data sources: LA-ICP-MS zircon U-Pb ages from this study, SHRIMP zircon U-Pb ages from Black et al. (2005), whole-rock and mineral Rb-Sr and K-Ar determinations from Brooks and Compston (1965), McDougall and Leggo (1965), Brooks (1966), Cocker (1982), Mackenzie et al. (1988), McClenaghan and Higgins (1993) and Sawka et al. (1990). The gray bars represent probable time intervals for granite emplacement in Tasmania.

Black et al. (2005). These geochronological results indicate that these individual plutons were formed contemporaneously at ca. 365 – 360 Ma. These granites are approximately 8 m.y. younger than the Housetop and Meredith granites, and 10 m.y. older than the Grassy Granite which is related to world class W deposits in King Island (351 ± 2 Ma; Black et al., 2005). This implies multiple granite intrusion and mineralisation events in western Tasmania.

McDougall and Leggo (1965) reported comprehensive K-Ar and/or Rb-Sr ages of Tasmanian granites, and were first to note a progressive younging westward among Palaeozoic Tasmanian granites, although their ages were affected largely by radiogenic Sr, Ar loss and thermal offsetting by later

geological deformation or hydrothermal alteration. The LA-ICP-MS U-Pb results in the current study and the SHRIMP U-Pb data from Black et al. (2005) and Kositcin and Everard (2013) are considered to be more accurate than the K-Ar and/or Rb-Sr ages, which are generally around 10 m.y. younger (Fig. 3.15). Nevertheless, these new data have confirmed the westward younging trend between Tasmanian granites noted by McDougall and Leggo (1965).

Based on the accurate geochronological results, granite emplacement in eastern Tasmania and adjacent regions is concluded to have occurred in three major time intervals (Fig. 3.15). Unfractionated or weakly fractionated granodiorites intruded around 405–400 Ma. They were followed by widespread weakly to moderately fractionated I- and S-type granites and minor mafic granodiorites emplaced between 390–385 Ma. Moderately to highly fractionated felsic I- and S-type granites were emplaced between 380 and 374 Ma, and are sparsely distributed in eastern Tasmania. Granite emplacement in western Tasmania occurred around at 374 Ma, 365–360 Ma and 351 Ma (Fig. 2.3). Overall, there was more than 50 m.y. of granitic magmatism in the Late Palaeozoic evolution of Tasmania, beginning at ca. 405 Ma and ending at 350 Ma.

3.7.2.2 Chronological correlation with Lachlan Orogen granites

A large volume of zircon U-Pb ages have been determined for granites in southeastern Australia over the past two decades (Elburg, 1996; Arne et al., 1998; Keay et al., 1999; Bierlein et al., 2001; Kemp et al., 2005; Lennox et al., 2005; Ickert and Williams, 2011). As similar in Tasmania, these U-Pb ages are considerably older but more precise than previously published K-Ar and $^{40}Ar/^{39}Ar$ ages (Richards and Singleton, 1981). Recent zircon U-Pb dating results (Kemp et al., 2005; Lennox et al., 2005; Ickert and Williams, 2011) have revealed that granites in New South Wales were emplaced from the mid-Silurian (435–410 Ma; Fig. 2.2) to Early Devonian (401–385 Ma). In northeastern Victoria, Middle to Late Silurian I- and S-type granites (U-Pb ages from 430 to 410 Ma) intruded Ordovician sedimentary rocks in the Tallangatta region (Keay et al., 1999; Fig. 2.2). In central Victoria, a number of I- and S-type granites are well-exposed in the northeastern Bendigo and the Stawell Zone, and they have SHRIMP U-Pb ages ranging from 413 to 393 Ma (Arne et al., 1998; Bierlein et al., 2001; Fig. 2.2). The granites exposed in the central Bendigo Zone, with U-Pb ages between 396 and 367 Ma (Bierlein et al., 2001), are significantly younger than those in the northeastern Bendigo and the Stawell Zone. The granites in Melbourne Zone have a slightly narrower range of U-Pb ages (395 to 374 Ma) than those in Bendigo Zone (Elburg, 1996; Bierlein et al., 2001; Fig. 2. 2), and they are in age mostly similar to the eastern Tasmanian granites (400–374 Ma). Given that the Ordovician–Devonian Mathinna Supergroup turbidites deposited in northeastern Tasmania resemble the lower Palaeozoic turbidites of the Melbourne Trough (Powell, 1992; Cayley, 2011), the new ages of granites in this study and those from Black et al. (2005) strengthen the argument that eastern Tasmania is closely correlated with the Melbourne Zone in Victoria.

Rossiter (2003) classified the S-type Wilsons Promontory Granite in southern Victoria as parts of the Central Superprovince, which consists of the Melbourne zone, the Bendigo Zone, the Stawell Zone and northeastern Tabberabbera Zone, rather than into the Bassian Basement Terrane of Chappell et al. (1988).

The U-Pb ages of the Grant Point Granite (402.6 ± 3.8 Ma) and the Mt Pearson Granite (396.2 ± 4.8 Ma) largely overlap with that of the S-type Wilsons Promontory Granite (U-Pb age 395 ± 4 Ma; Elburg, 1996). This chronological similarity, together with the similar chemical compositions of these granites, possibly provides evidence that the 400–395 Ma magmatic event extended across Bass Strait from northeastern Tasmania to southern Victoria.

In contrast to eastern Tasmania, the western Tasmanian granites do not correlate with any granite province on mainland Australia (Fig. 2.2). These E-trending batholiths define a unique and highly productive metallogenic event in the geodynamic evolution of Australia. It is unclear whether their orientations imply an N-directed subduction system beneath southern Tasmania from 375 to 350 Ma, or if they have formed along cross-arc structures related to the previously active W-directed subduction system beneath eastern Tasmania.

3.7.3 Implications of Pb isotopes

3.7.3.1 Variations between eastern and western Tasmanian granites

Initial Pb isotope ratios calculated both from whole-rock and K-feldspar data are very scattered, although the K-feldspar data are less scattered than the fields defined by whole rock data (Fig. 3.16). This suggests post-emplacement and other processes have affected some or all of the Pb isotopic results. These processes can include both post-depositional isotopic disturbance caused by thermal events and/or water-rock interaction, and the inclusion of Th- and/or U-rich minerals such as monazite within the analysed K-feldspar separates. The former can be indicated by petrographic evidence of alteration (muscovite alteration of K-feldspar), whereas latter can be indicated by high $^{232}Th/^{204}Pb$ or $^{238}U/^{204}Pb$ ratios. Hence, the K-feldspar data have been culled to remove samples with evidence of post emplacement alteration (observed in the White Heemskirk and Pieman Heads granite samples), or with $^{232}Th/^{204}Pb$ and/or $^{238}U/^{204}Pb$ ratios above 10. Use of these criteria has eliminated two of six analyses from eastern Tasmanian granites, and four of seven analyses from western Tasmanian granites.

Although culling has significantly reduced the dataset, it has also decreased the variability in the isotopic ratios when eastern and western Tasmanian granites are considered separately (Fig. 3.17). Most of the remaining results are supported as being initial ratios from other evidence. For example, the two initial ratios estimated for the Pine Hill Granite are within error of each other for $^{206}Pb/^{204}Pb$ and $^{207}Pb/^{204}Pb$, and very similar for $^{208}Pb/^{204}Pb$ (Table 3.1; Fig. 3.16). More importantly, these initial ratios are also within error of two analyses of galena intergrown with arsenopyrite and cassiterite from the Renison Sn deposit (Fig. 3.17; Huston et al., unpublished data), which is interpreted to have been sourced from this granite (Kitto, 1994). Of the remaining four analyses of eastern Tasmanian granites, three yielded model ages using the Lachlan crustal model of Carr et al. (1995) within 10 million years of their emplacement ages. Hence, the culled dataset best approximates the initial Pb ratios of Tasmanian granites.

This culled dataset indicates important differences in the lead isotopic characteristics between eastern and western Tasmanian granites. The initial ratios of the eastern Tasmanian granites partly overlap the initial ratios determined for the Mathinna Supergroup (corrected to 380 Ma; Black et al., 2010; Fig. 3.16),

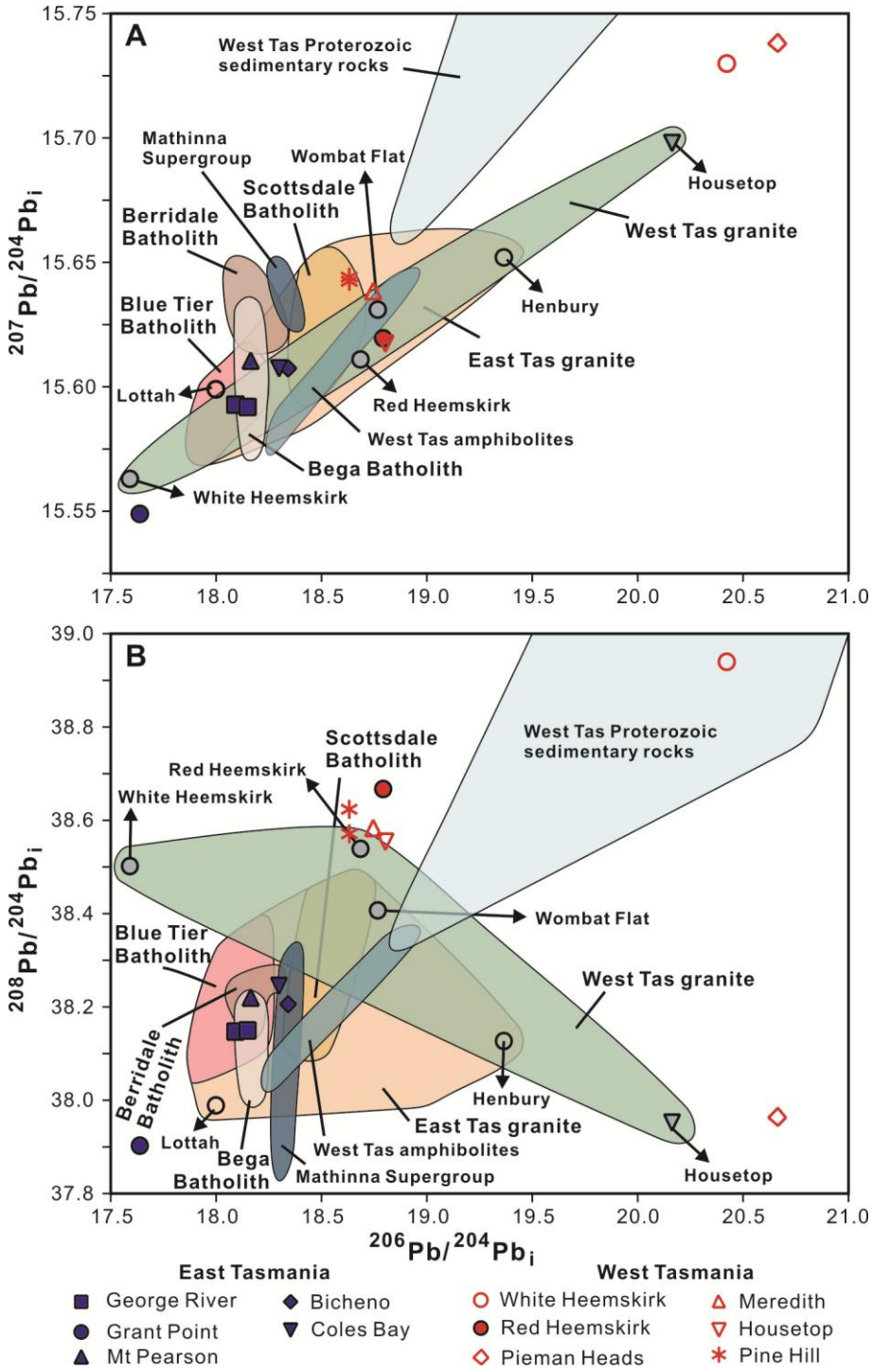

Figure 3.16 (A) Initial ^{207}Pb/^{204}Pb versus ^{206}Pb/^{204}Pb, and (B) Initial ^{208}Pb/^{204}Pb versus ^{206}Pb/^{204}Pb plots of K-feldspars from Tasmanian granitoids. The whole-rock Pb isotopes of Tasmanian granites, sedimentary and mafic rocks in Tasmania are from Black et al. (2010), and the areas for Pb isotopes of Bega Batholith and Berridale Batholith (SE Australia) referred from McCulloch and Woodhead (1993).

into which most of these granites intruded. The eastern Tasmanian granites are compatible with the Lachlan crustal growth curve of Carr et al. (1995; Fig. 3.17), and the eastern Tasmanian granite ratios overlap the fields defined by the slightly older (420–400 Ma) Bega and Berriedale Batholiths in the Lachlan Orogen (Fig. 3.16). These observations are consistent with the interpretation that the East Tasmanian Terrane, into which these granites are emplaced, has affinities to the Lachlan Orogen.

In contrast, western Tasmanian granites are significantly more radiogenic than their eastern Tasmanian and Lachlan Orogen counterparts. The initial isotopic ratios of these granites do not directly match potential source rocks in western Tasmania. Although the $^{206}Pb/^{204}Pb$ values are similar to the more radiogenic end-member of the field defined by west Tasmanian amphibolites (Fig. 3.16), values of both $^{207}Pb/^{204}Pb$ and $^{208}Pb/^{204}Pb$ are higher than those of these rocks. Moreover, the initial ratios of western Tasmanian granites approach, but do not match the field of western Tasmanian Proterozoic sedimentary rocks (e.g. Oonah, Fraser and Port Sorell formations; Black et al., 2010), which is even more radiogenic than the western Tasmanian granites. These differences suggest that either western Tasmanian granites had additional Pb sources, or the ratios upon which these source rock fields are based have been disturbed, or both. The Pine Hill K-feldspar and Renison galena results plot at the most radiogenic end-member of an array defined mostly by coeval Devonian fissure vein Pb-Ag-Zn deposits (this array is defined entirely by high-precision galena analyses; Fig. 3.17). This array trends towards the less radiogenic eastern Tasmanian granite K-feldspar analyses.

3.7.3.2 Correlations with neighbouring regions

The isotopic difference between eastern and western Tasmanian granites are consistent with the observation that initial ratios from Cambrian deposits in the West Tasmanian Terrane (square symbols in Fig. 3.17) are significantly more radiogenic than those of Cambrian deposits in western Victoria and New South Wales in South Australia (diamond symbols in Fig. 3.17; Huston et al., 2016). These results suggest fundamentally different Pb isotopic sources for granites in the East and West Tasmanian terranes.

Huston et al. (2016) modelled variations in Pb isotopes in southeast Australia as the result of mixing between two provincial isotopic systems, a less radiogenic 'proto-Australia' system (red lines in Fig. 3.17) and a more radiogenic 'proto-Pacific' system (blue lines in Fig. 3.17). The basis of these isotopic systems is the Lachlan crustal (upper red evolution curve) and Lachlan mantle (lower blue evolution curve) models of Carr et al. (1995). Most of the variation in the Lachlan Orogen can be modelled as mixing between the two curves of Carr et al. (1995), but some deposits in southeast Australia cannot be accounted for by this simple model, in particular the Cambrian Ponto and Mount Ararat deposits in the Koonenbery Province and Grampian-Stavely Zone, respectively, which yield unrealistically old ages, and the Cambrian deposits in the Mount Read Volcanics of the West Tasmanian Terrane, which yield unrealistically young model ages (Fig. 3.17).

By decreasing μ (i.e., inferring a more juvenile source) from the Carr et al. (1995) Lachlan crustal model, Huston et al. (unpublished) produced model ages for the Ponto and Mount Ararat deposits about 30 million years older than their independently constrained mineralisation ages. Similarly, by increasing μ associated with the Lachlan mantle model, the ages of the Cambrian deposits were modelled to between 505 and 460 Ma, close to their independently established ages, and the Devonian deposits to between 375 to 310 Ma, again close to their independently constrained ages. Although there are issues that remain to be resolved, this model of two isotopic systems can account for the vast majority of Pb isotope data from southeast Australia. Tectonically, these two isotopic systems could represent the over-riding plate (proto-

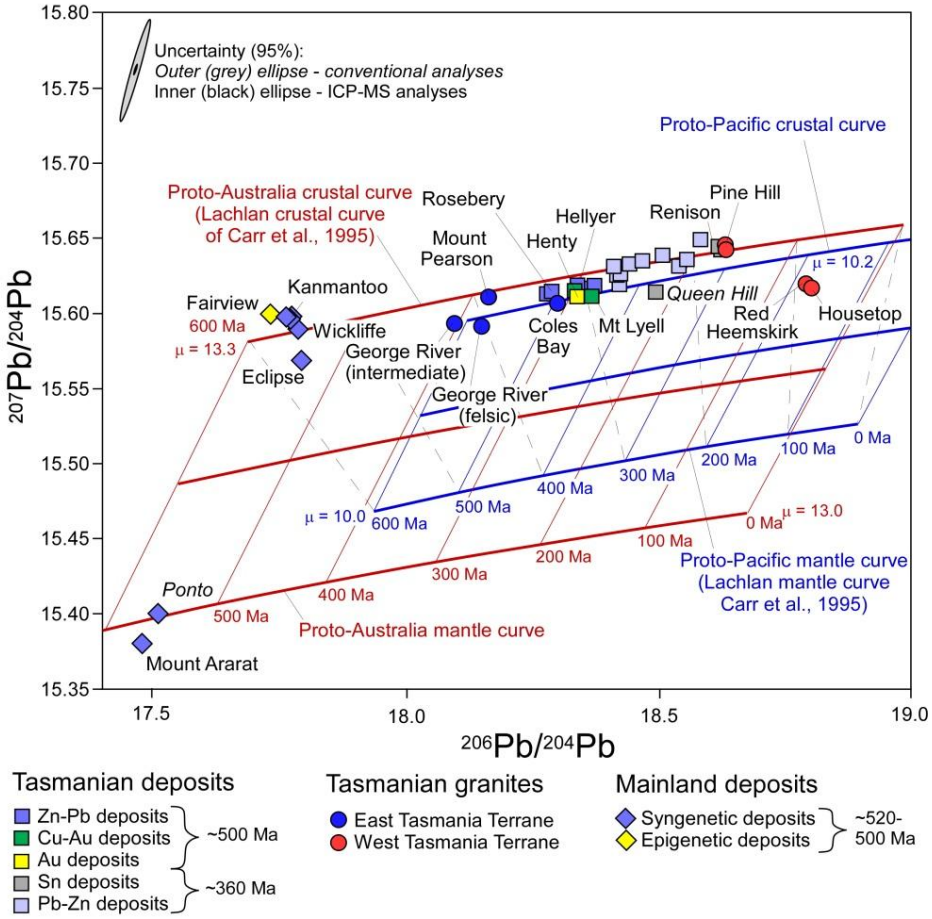

Figure 3.17 $^{207}Pb/^{204}Pb$ versus $^{206}Pb/^{204}Pb$ diagram showing Pb isotopic growth curves of Tasmanian and Lachlan Orogen in southeast Australia. The evolution curves were calculated using Cumming and Richards (1975) model ($\varepsilon = 0.0795 \times 10^{-9}$), and constrained by modelling curves from Carr et al. (1995), Huston et al. (2016) and Huston et al. (unpublished data).

Australia system) and the subducting plate (proto-Pacific system) during dominantly west-dipping subduction along the eastern Australian seaboard during the Palaeozoic.

Similar fundamental differences have been observed by Münker (2000) in the Takaka Terrane in New Zealand, where extremely radiogenic isotopic data from the Devil River Volcanics differ from interlayered, much less radiogenic rocks of the Haupiri Group. Münker (2000) interpreted the New Zealand data to indicate the presence of two lead sources, a highly radiogenic source (the proto-Pacific system), possibly linked to the presence of Archaean crust, and a less radiogenic source (the proto-Australia system), possible linked to the presence of Proterozoic crust.

3.8 Conclusions

The eastern Tasmanian granites were emplaced in three periods in the late Palaeozoic: (1) 405 – 395 Ma (pre-collision), (2) 390 – 385 Ma (syn-collision), and 380 – 375 Ma (post-collision; Fig. 3.15). The Grant Point Granite is found to be the earliest S-type pluton emplaced coevally with pre-collisional, I-type

hornblende-bearing granodiorites in the eastern Tasmania. Sn mineralisation in eastern Tasmania is associated with extremely reduced and highly fractionated post-collisional granites.

The western Tasmanian granites are moderately to strongly fractionated, reduced I- and S-type granites that are associated with several world-class Sn–W deposits. These granites, and the highly fractionated granites in eastern Tasmania, appear to have emplaced in a post-collisional setting in three intervals, 375 Ma, 365 – 360 Ma and 350 Ma.

The K-feldspar Pb isotopic compositions of highly fractionated Tasmanian granites define a narrower isotopic range than the corresponding whole-rock Pb isotopes (Fig. 3.16). K-feldspar Pb isotopes suggest that these moderately to strongly differentiated granites in western Tasmania had been highly contaminated by crustal rocks, including the Proterozoic amphibolites from the lower crust, and Neoproterozoic to Cambrian upper-crusted sedimentary rocks.

The following Chapter 4 documents the characteristics of magmatic – hydrothermal textures (e.g., USTs and tourmaline-rich assemblages) from western Tasmanian granites. The origins and exploration application of these magmatic – hydrothermal textures will be discussed in Chapters 5, 6 and 7.

Chapter 4 Magmatic – hydrothermal textures

4.1 Introduction

Spectacular magmatic – hydrothermal textures are exposed in the Heemskirk Batholith, particularly around the contact of the White and Red granites, northwest of Trial Harbour (Fig. 3.5). Similar features crop out at Granville Harbour where the batholith intruded the Proterozoic Oonah Formation. The Pieman Heads Granite, located tens of km north of the Heemskirk Granite, also contains abundant tourmaline-rich textural features, in some ways comparable to these in the Heemskirk Batholith. This chapter describes magmatic – hydrothermal textures (formed by hydrothermal fluids of magmatic origin) from these three key locations. Emphasis is placed on documenting geological and mineralogical features that can help to determine relative sequences of tourmaline- and quartz-rich textures and their origins.

4.2 Magmatic – hydrothermal textures

Tourmaline nodules in the Heemskirk Batholith were first described by Heier and Brooks (1966), Klominsky (1972), and Hajitaheri (1985). In the Heemskirk Granite, tourmaline is considerably more abundant in the White granite than the Red granite. Around the contacts between the two granite types, and the contacts of the White granite with local country rocks, abundant magmatic – hydrothermal textures dominated by quartz and tourmaline have developed. In the current study, these textures are divided into (1) tourmaline patches, (2) tourmaline-quartz orbicules, (3) tourmaline-filled cavities and (4) tourmaline-quartz veins, largely according to their morphology, size, mineral assemblages and contact relationship with host granites (Table 4.1; Fig. 4.1). In addition to the four main variants of tourmaline-bearing textures, unidirectional solidification textures (USTs, cf. Shannon et al., 1982) are exposed in the upper part of the Heemskirk Granite. This granite is associated with abundant Sn, Pb, Zn, Ag and Ni deposits (Tables 1.1 and 1.2; Seymour et al., 2007).

Within the Sandy Cape Suite, the Pieman Heads Granite is exceptional for its distinctive tourmaline-quartz ‘nodules’ (Sawka et al., 1990; McClenaghan, 2006a). These magmatic – hydrothermal textures are very similar to those that occur within the Heemskirk Batholith. In this current study, they have been subdivided into tourmaline patches, orbicules and tourmaline-quartz veins (Table 4.1). However, tourmaline-filled miarolitic textures and USTs have not been observed in the Pieman Heads Granite, and the granite is not associated with any known mineralisation.

4.2.1 Tourmaline patches

4.2.1.1 Tourmaline patches in the Heemskirk Granite

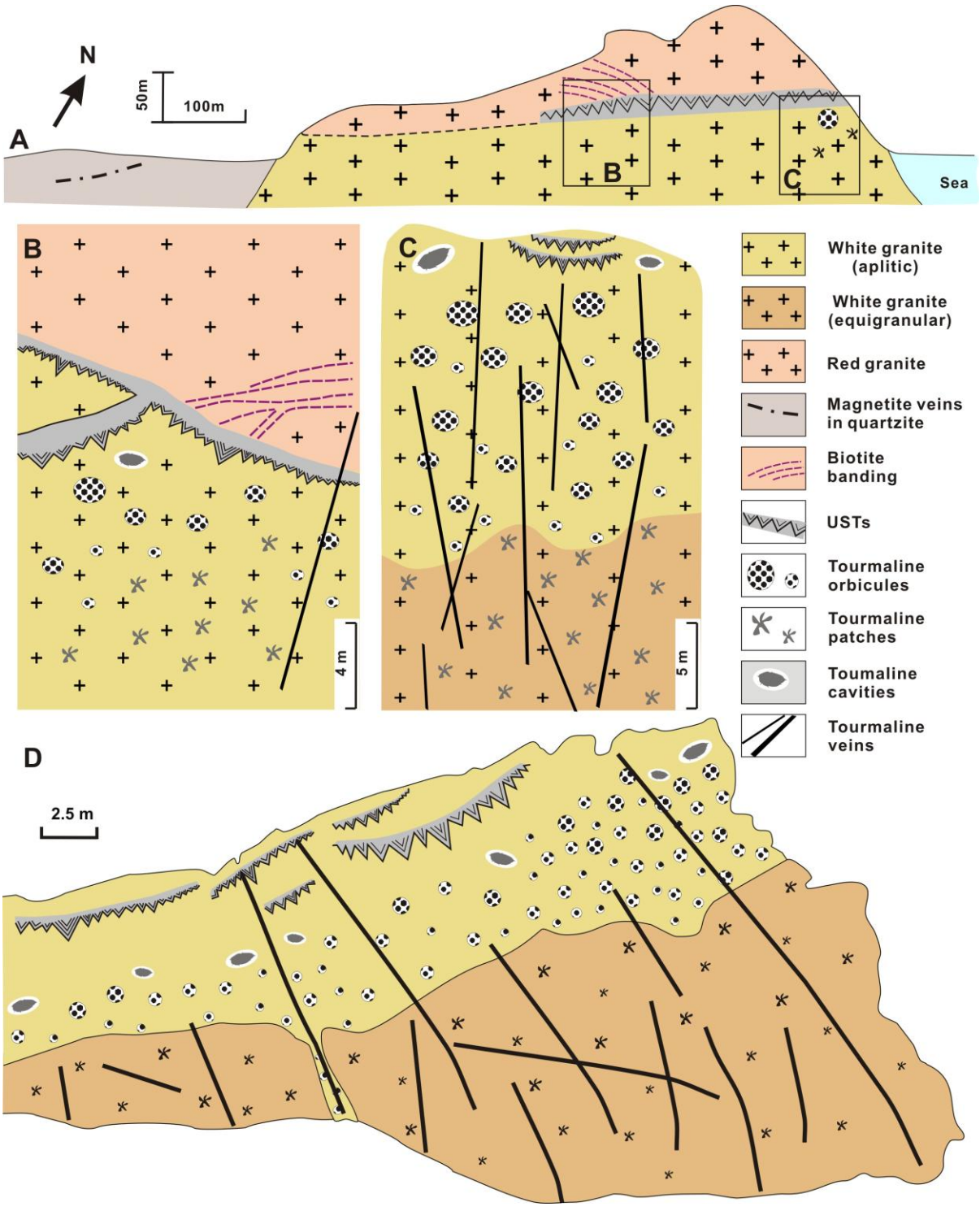

Figure 4.1 (A) Simplified cross-section describing the geological outcrop at Trial Harbour, south of the Heemskirk Batholith, where tourmaline-rich textured features, unidirectional solidification textures (USTs) and biotite bands occur around the contact between the White and Red granites. (B) USTs mark the boundary of the White and Red granites, and truncate biotite-rich bands within the Red granite (Fig. 4.7F). Tourmaline veins locally cut the UST quartz layer. (C, D) Sketched cross-sections showing relative spatial distributions of tourmaline patches, orbicules, cavities and veins that typical crop out in the White granite, and they are commonly beneath the quartz-dominated UST layers. The tourmaline patches that are hosted by equigranular granite commonly occur below an orbicule-rich aplitic granite sill, whereas the USTs usually appear in upper level of the granite, higher than the tourmaline patches and orbicules. Tourmaline-quartz veins occur in all exposed levels of the granite and have cut the orbicules, cavities and/or USTs locally.

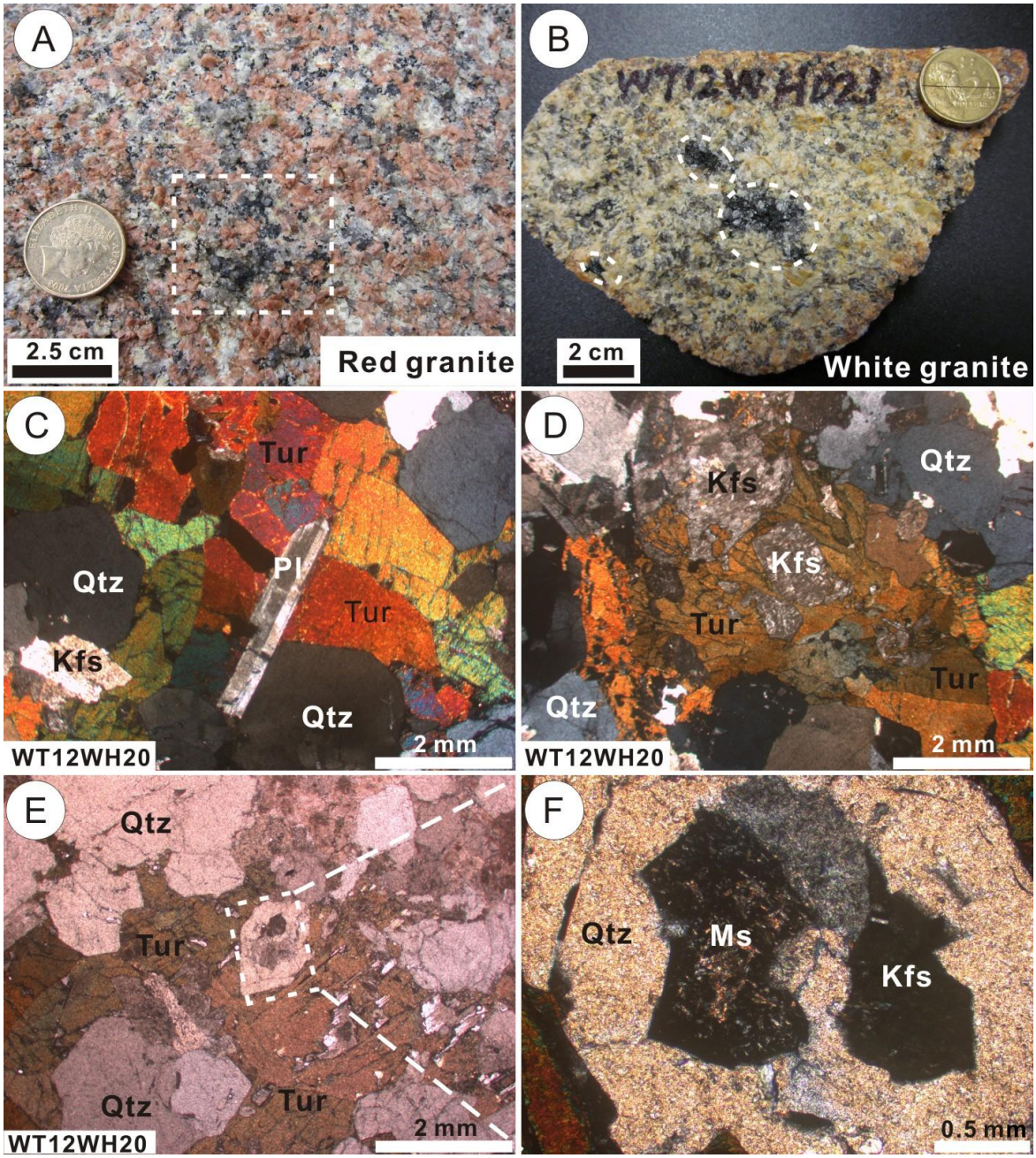

Figure 4.2 Photographs and photomicrographs showing textural and mineralogical features of tourmaline patches hosted in equigranular (A) Red granite and (B) White granite at Trial Harbour. (C) Euhedral plagioclase with polysynthetic twins in massive tourmaline and quartz. (D) Residual K-feldspar in tourmaline has zigzag contacts. (E) Tourmaline filled interstitially between subeuhedral quartz grains. (F) Muscovite-altered K-feldspar residue in quartz. (D) and (E) taken under cross polarised light, whereas (F) and (G) taken under plane polarised light. Abbreviation: Kfs = K-feldspar, Pl = plagioclase, Qtz= quartz, Ms = muscovite, Tur = tourmaline. Outcrop and sample (WT12WH20, 21) location: E145°09′23.93″, S41°55′20.64″, elevation = 3 m.

Tourmaline patches are typically disseminated in lower exposure levels within the Heemskirk Granite (Fig. 4.1). They are commonly 0.5-3 cm in diameter, and exhibit irregular and dendritic morphologies (Figs. 4.2A, B). Tourmaline patches have been observed in both the Red and White granites, extending from the White granite upwards to the Red granite at Trial Harbour (Fig. 4.1B). They are more common in the lower layers of the White granite. In either granite phase, the host granite is typically equigranular, and locally porphyritic.

Tourmaline patches contain smoky quartz (> 50 %; 1-10 mm diameter) intergrown with coarse-grained tourmaline (10-30 %; 5-20 mm), K-feldspar (20-30 %; 2-10 mm), plagioclase (10-15 %; 2-10 mm) and biotite (5-10%; 1-5 mm; Fig. 4.2). Contacts between tourmaline patches and the host granite are relatively smooth (Fig. 4.2C), implying that the patches are primary components in the granite. Tourmaline grains are typically interstitial to subeuhedral quartz and anhedral feldspar, and are characterised by vivid red-brown to yellow-green pleochroism under cross polarised light (Figs. 4.2C, D). Quartz and alkali feldspar grains occur in massive tourmaline aggregates (Fig. 4.2D). K-feldspar is volumetrically more abundant than plagioclase in the tourmaline patches, and plagioclase with polysynthetic twins are observed locally within massive tourmaline (Fig. 4.2C). K-feldspar has irregular contacts with tourmaline, and has typically undergone weak muscovite alteration (Figs. 4.2E, F). Accessory minerals, including anhedral zircon, monazite or titanite, and/or apatite are recognised locally in tourmaline patches (Table 4.1).

4.2.1.2 Tourmaline patches in the Pieman Heads Granite

Tourmaline patches in the Pieman Heads Granite are mineralogically and texturally similar to those in the Heemskirk Batholith. They are extensively developed in the upper portion of the felsic pluton, and hosted by equigranular, fine- to coarse-grained phases. The tourmaline patches commonly range in diameter from a few millimeters to centimeters, and mostly display a dendritic morphology (Fig. 4.7A; Table 4.1). The main components of the patches are quartz (> 50 %), tourmaline (10-30 %), K-feldspar (20-30 %), plagioclase (10-15%) and minor biotite or muscovite (< 5 %), representing a coarse-grained texture in the granite. Tourmaline grains are typically interstitial to quartz and K-feldspar, and locally have a wedge-like shape (Fig. 4.8A). These tourmalines have vivid pleochroism ranging from brown to deep green (cross polarised light). Massive tourmaline locally contains small granular quartz inclusions. K-feldspars display simple twins or cross-hatched twins, and volumetrically more than plagioclases in the tourmaline patches. Minor primary biotite and muscovite are locally associated with tourmaline. A small amount of irregular zircon, monazite, apatite and titanite are sparsely distributed in the patches. The granite adjacent to tourmaline patches is weakly altered, with perthitic K-feldspar partly replaced by muscovite (Fig. 4.8A).

Figure 4.3 (next page) Photographs showing the textural characteristics of tourmaline orbicules in the Heemskirk Granite at Trial Harbour. (A) Clusters of tourmaline orbicules underneath the quartz-rich USTs in the White granite. (B, C) Clusters of spherical to elliptical tourmaline orbicules hosted in aplitic granite. Locally two or more orbicules can be connected to form a larger, irregular mass. (D) A sub-spherical 8 cm-diameter tourmaline orbicule with inner and outer growth zones. (E) Tourmaline orbicule-rich aplitic sill overlying the equigranular granite hosting tourmaline patches. (F) Subvertically oriented tourmaline orbicule-bearing aplitic dyke that fed the overlying aplite sill intruded the equigranular White granite. (G) A subround tourmaline orbicule cut by a 1 cm-wide tourmaline vein in the weathered, aplitic White granite. Outcrop location: E145°09′23.93″, S41°55′20.64″, elevation ranging from 3 to 30 m. Tur = tourmaline.

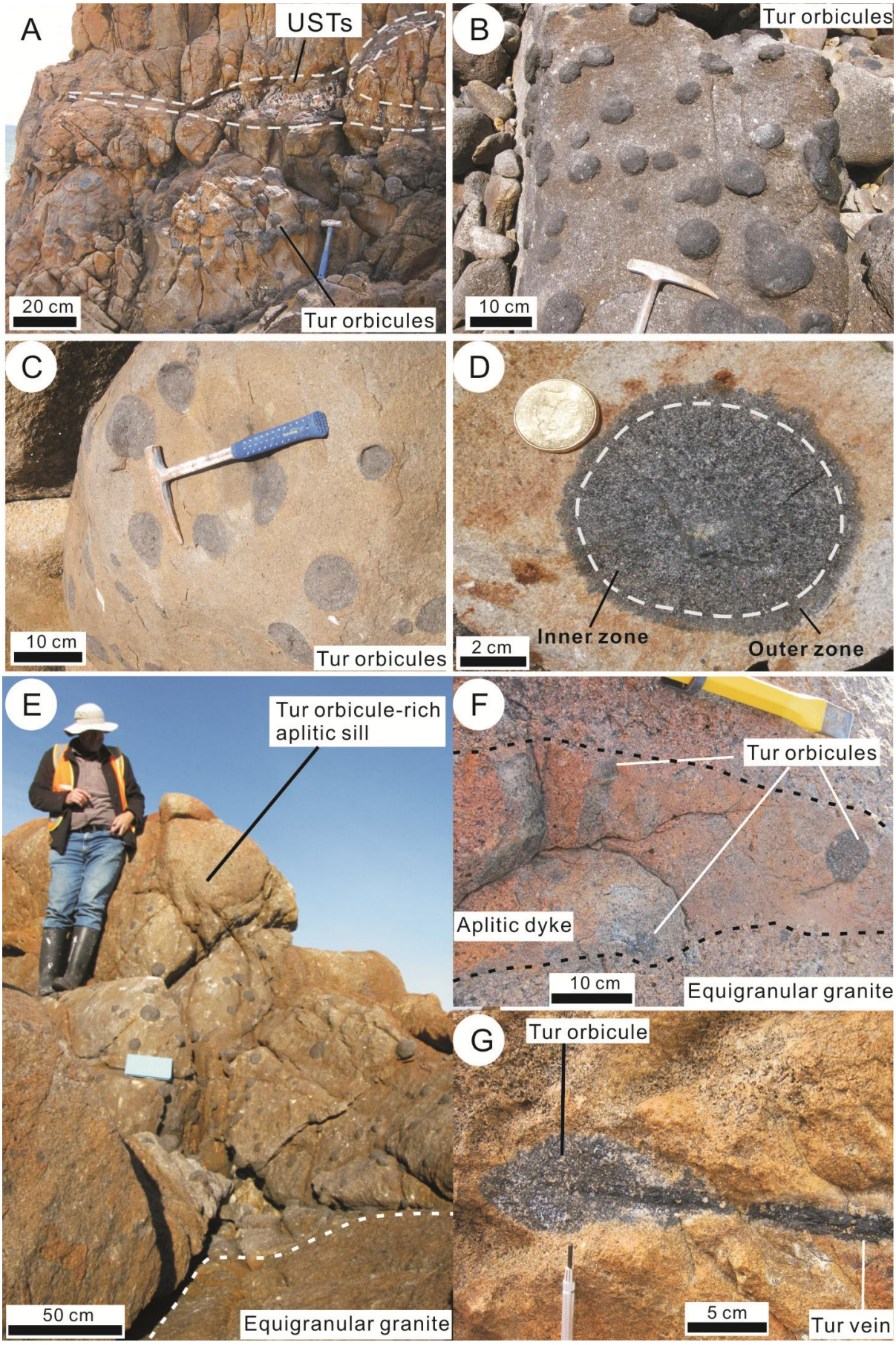
A
USTs
20 cm
Tur orbicules
B
Tur orbicules
10 cm
C
10 cm
Tur orbicules
D
2 cm
Inner zone
Outer zone
E
Tur orbicule-rich
aplitic sill
50 cm
Equigranular granite
F
Tur orbicules
Aplitic dyke
10 cm
Equigranular granite
G
Tur orbicule
5 cm
Tur vein

4.2.2 Tourmaline orbicules

4.2.2.1 Tourmaline orbicules in the Heemskirk Granite

Compared with tourmaline patches, the tourmaline orbicules in the Heemskirk Granite are much larger, ranging from 3 to 15 cm in diameter, and are located near the walls and roof of individual sills (Fig. 4.1C), where they locally comprise 15-20 % by volume of the local granitic body (Fig. 4.3; Table 4.1). The orbicules are typically characterised by spherical or elliptic shapes (Fig. 4.3). Locally, two or more orbicules are connected to generate larger, more irregular tourmaline masses (Fig. 4.3B). Both the Red and White phases of the Heemskirk granites have developed tourmaline orbicules, but the orbicules are more common in the White granite. Tourmaline orbicules are intensely distributed near the contact between the White and Red granites. They are most common in the roof zone of the White granite, and decrease progressively in abundance and size with increasing depth. Tourmaline orbicules also occur some meters into the base of the Red granite; however, their abundance decreases dramatically away from the contact with the White granite.

Tourmaline orbicules are particularly well-developed around the contact between the White and Red granites at Trial Harbour (Fig. 4.1), where they are commonly hosted by a porphyritic aplite phase of the White granite. The tourmaline orbicules consist mainly of quartz (> 55 %; 1-5 mm) and tourmaline (~ 45%; 0.5-2 mm) with rare muscovite (< 3 %). An orbicule-bearing subvertical aplite dyke (20 cm wide) has cut the equigranular White granite (Fig. 4.3F). The aplite dyke is a feeder to a laterally extensive tourmaline orbicule-rich granitic sill (> 3 m thick) that overlies the equigranular White granite (Fig. 4.3E), and that occurs immediately below the Red granite.

Tourmaline orbicules at Granville Harbour are, in contrast, hosted by equigranular or porphyritic granite adjacent to the Oonah Formation, rather than by porphyritic aplite. They typically consist of quartz (35-45 %; 0.5- 5 mm), tourmaline (30-40 %; 0.2-10 mm), K-feldspar (10-20%; 0.5-5 mm) partly replaced by muscovite, and minor plagioclase (< 10 %) and biotite (< 5 %). Trace amounts of zircon, monazite and titanite have been identified in tourmaline orbicules from both Trial Harbour and Granville Harbour, but apatite only occurs in the orbicules from Granville Harbour.

Many tourmaline orbicules surrounded by aplitic granite are internally zoned. Tourmaline is more abundant than quartz in the melanocratic outer zone, whereas the leucocratic inner zone is rich in fine-grained quartz with lesser tourmaline (Fig. 4.3D). The ovoid outer zone of tourmaline orbicules typically exhibit cryptic, protruding contacts with the neighbouring leucocratic host granite (Fig. 4.3D), possibly due to high temperature hydrothermal alteration. The leucocratic inner zone is absent in some orbicules which are entirely melanocratic. The textures and colours of tourmaline in internally zoned orbicules vary across different growth zones. Tourmalines with deep blue to orange pleochroism (under cross polarised light) occur in the outer zone, and they are 1-2 cm in diameter, as irregular veinlets, stringers or stockworks, interstitial to quartz, K-feldspar and plagioclase (Fig. 4.4). The K-feldspar (possible perthite) and albitic plagioclase have been partially or totally replaced by tourmaline and/or muscovite (Figs. 4.4B and C). The inner zone of the tourmaline orbicules typically displays mosaic textures, where euhedral to subeuhedral quartz grains are intergrown with massive tourmaline that has greenish-blue to deep blue

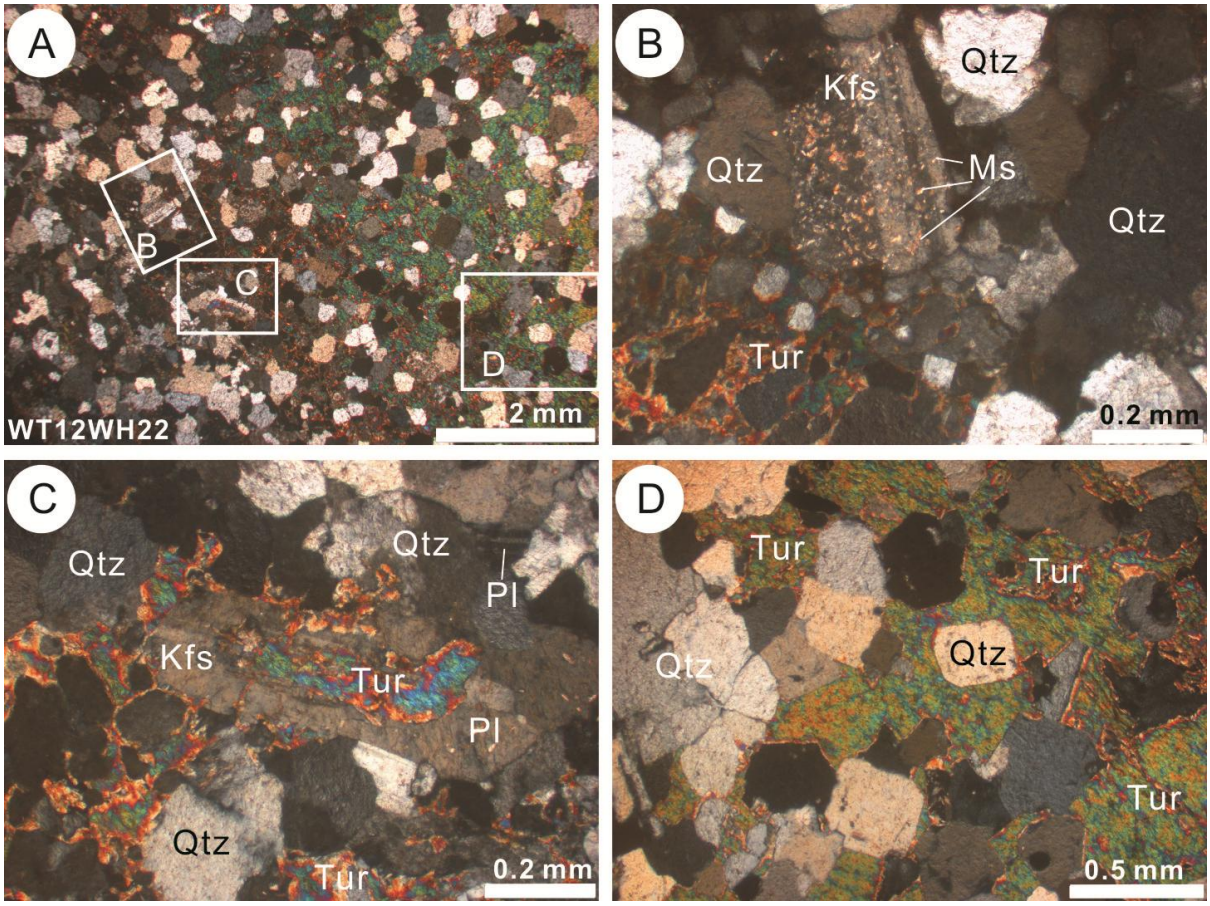

Figure 4.4 Photomicrographs showing mineralogical features of tourmaline orbicules in the Heemskirk Granite at Trial Harbour. (A) Tourmaline displays different pleochroism and textures between inner and outer growth zones. (B) Tourmaline in the outer zone occurs interstitially between quartz and muscovite-altered K-feldspar with simple twins. (C) Blue-orange pleochroic tourmaline has partially replaced K-feldspar and plagioclase in the outer zone. (D) In the inner zone, sub- and euhedral quartz occur in a mosaic of greenish to blue pleochroic tourmaline. All photomicrographs taken under cross polarised light. Abbreviation: Kfs = K-feldspar, Ms = muscovite, Pl = plagioclase, Qtz = quartz, Tur = tourmaline. Sample (WT12WH22) location: E145°09′23.93″, S 41°55′20.64″, elevation = 3 m.

pleochroism (Fig. 4.4D). The inner zone consists only of quartz and tourmaline, typically 5-6 cm in diameter, and limited alterations have been observed. These textural features are similar to tourmaline-quartz orbicules described from the Seagull Batholith from Yukon Territory, Canada (Sinclair and Richardson, 1992).

Tourmaline orbicules hosted by the coarse-grained granite with equigranular textures at Granville Harbour typically lack any internal zonation. Apart for their large size and sub-spherical shape, the tourmaline orbicules hosted by equigranular granite are texturally similar to the tourmaline patches. There is a gradual transition from the tourmaline patches in lower sills of the granite to tourmaline orbicules occurring in higher layers of the intrusion (Fig. 4.1).

4.2.2.2 Tourmaline orbicules in the Pieman Heads Granite

Tourmaline orbicules developed in the Pieman Heads Granite are very similar to those exposed in the Heemskirk Batholith at Granville Harbour, both of which are hosted by equigranular to porphyritic granite.

Table 4.1 Tourmaline- and quartz-rich textured features in the Heemskirk and Pieman Heads granites

Type	Granite locations	Host granite	Mineral association	Morphology	Distribution, mineral zone, alteration
Tourmaline patches	Heemskirk Granite at Trial and Granville Harbour, Pieman Heads Granite	Equigranular, locally porphyritic	Quartz, K-feldspar, plagioclase, tourmaline, biotite, muscovite, zircon, monazite, titanite, or apatite	Irregular, dendritic, 0.5-2 cm in diameter	Disseminated in the carapace of the host granites; no mineral zones; weak to moderate muscovite alteration; beneath the orbicule-rich aplitic and/or equigranular sill or UST layers; apatite only occurs at Granville Harbour and Pieman Heads Granite
Tourmaline orbicules	Heemskirk Granite at Trial and Granville Harbour, Pieman Heads Granite	Equigranular, locally porphyritic, and aplitic at Trial Harbour	Quartz, K-feldspar, plagioclase, tourmaline, muscovite, zircon, monazite, titanite, or apatite	Spherical, elliptic, 3-15 cm in diameter	Locally composing 15-20 % by volume of the local granitic cupolas; internal tourmaline-rich rimed by tourmaline-quartz intergrowths or K-feldspar-quartz; weak muscovite alteration; commonly occur in aplitic sills (~ 30 m thick) and also in orbicule-hosted aplitic feed dykes at Trial Harbour, or in the equigranular granite at Granville Harbour and Pieman Heads, locally in a higher granitic sill than the patches
Tourmaline cavities	Heemskirk Granite at Trial and Granville Harbour	Equigranular, locally porphyritic and aplitic	Quartz, tourmaline, muscovite, zircon, monazite, titanite	Spherical, subround, 2 cm up to 2 m in diameter	Typically having a central tourmaline-rich zone and a quartz-rich rim; develop intensive muscovite-quartz alteration halo; occur in high levels of the orbicule-rich equigranular and/or porphyritic granite, or aplitic sill at Trial Harbour
Tourmaline veins	Heemskirk Granite at Trial and Granville Harbour, Pieman Heads Granite		Quartz, tourmaline, muscovite, zircon, titanite, xenotime, or apatite	Discrete chains, several cm to m wide	Central tourmaline-quartz zone rimed by quartz and muscovite halo; intense muscovite-quartz alteration; occur in all exposed levels of the two granites, and have cut the orbicules, USTs and/or cavities locally; apatite only occurs in the Pieman Heads Granite
Unidirectional solidification textures (USTs)	Heemskirk Granite, particularly Trial and Granville Harbour	Equigranular and aplitic	Quartz, K-feldspar, plagioclase, biotite, tourmaline, muscovite, magnetite, chlorite, zircon, monazite, or rutile	Comb, crenulate layer; coarse-grained quartz up to 5 cm; locally hundreds of meters long	Occurring in higher sills than the tourmaline orbicules and/or cavities in the upper carapace of an intrusion; commonly alternating with aplitic layers; marking the boundary of the overlying red-phase and underlying white-phase granites; locally crosscut by tourmaline-quartz veins; experienced K-feldspar and/or muscovite alteration, and selective chlorite alteration around magnetite in the USTs at Granville Harbour

No aplite-hosted tourmaline orbicules have been observed in the Pieman Heads pluton, in contrast to the Heemskirk Granite at Trial Harbour. At Pieman Heads, the orbicules are locally concentrated in the exposed stock, where they account for 15-20 % by volume of the granitic body (Fig. 4.7C). The tourmaline-rich orbicules have relatively spherical morphologies, and comparatively large sizes (5-15 cm diameters; Figs. 4.7B, C and D; Table 4.1). The tourmaline orbicules mainly consist of quartz (40-45 %), tourmaline (30-40 %), K-feldspar (10-20 %), plagioclase (5-10 %) and minor biotite or muscovite (< 5 %). Minerals within the orbicules have grain sizes from a few mm to a few cm. Tourmaline is typically intergrown with quartz in the centre of the orbicules (Figs. 4.7B, D).

At Pieman Heads, two types of tourmaline orbicules have been recognized based on mineralogy and textures. The first orbicule type is more spherical in shape and larger in size. Coarse-grained tourmaline and quartz define the orbicules, typically 6-10 cm in diameter. These tourmaline-quartz intergrowths are typically rimmed by a pronounced leucocratic feldspar-rich halo (red-brown) in the granite that is 1-3 cm wide (Fig. 4.7D). Coarse-grained feldspar has been partly altered to be muscovite. Two or more orbicules locally coalesced to form a calabash-like body (Fig. 4.7 C).The second variety of tourmaline orbicules is smaller in size (up to 8 cm in diameter), in which quartz and tourmaline are graphically intergrown in the orbicule (Fig. 4.8B). It is surrounded by a narrow leucocratic rim comprising of abundant quartz and minor feldspar, in which biotite is volumetrically much less than that in neighbouring granite (Fig. 4.7B). This orbicular texture is very similar to that formed in tourmaline orbicules from the Seagull Batholith, Yukon Territory, Canada (cf. Sinclair and Richardson, 1992).

4.2.3 Tourmaline cavities

The tourmaline-filled miarolitic cavities are dominated in tourmaline and quartz, similar to tourmaline orbicules hosted in porphyritic aplite. The cavities have diameters varying from 2 cm up to several meters (Fig. 4.5; Table 4.1). Most of the tourmaline cavities have similar sizes to tourmaline orbicules, but are concentrated in a upper-level granitic sill within the white Heemskirk Granite at Trial Harbour, and are much less abundant than the orbicules. They occur in both the White and Red aplitic granites, but are more common in the former. The cavities also occur locally in coarse-grained granite at Granville Harbour.

The tourmaline cavities are characterised by internal growth zones (Figs. 4.5A, B, and C), in which columnar tourmaline crystals radiate inwards from the margin to the centre of the cavities (Fig. 4.5D). The radial tourmaline crystals are intergrown with rare quartz, forming a black central zone from 2 to 6 cm in diameter (Fig. 4.5C). Klominsky (1972) described these radial tourmaline aggregates as ‘tourmaline suns’. The walls of tourmaline cavities are typically fringed by abundant anhedral quartz with widths of 1-2 cm (Figs. 4.5B, C). Anhedral orange-brown to blue pleochroic tourmalines are interstitial to the granular quartz grains (Fig. 4.5E). Prismatic tourmaline grains project into the core, surrounded by anhedral quartz aggregates. These tourmaline crystals typically develop optical zonation patterns (Fig. 4.5F) that have not been observed in other tourmaline-textured variants. The centres of the cavities are commonly dominated by planar tourmalines that locally contain round to subround quartz inclusions (Fig. 4.5G). Narrow altered

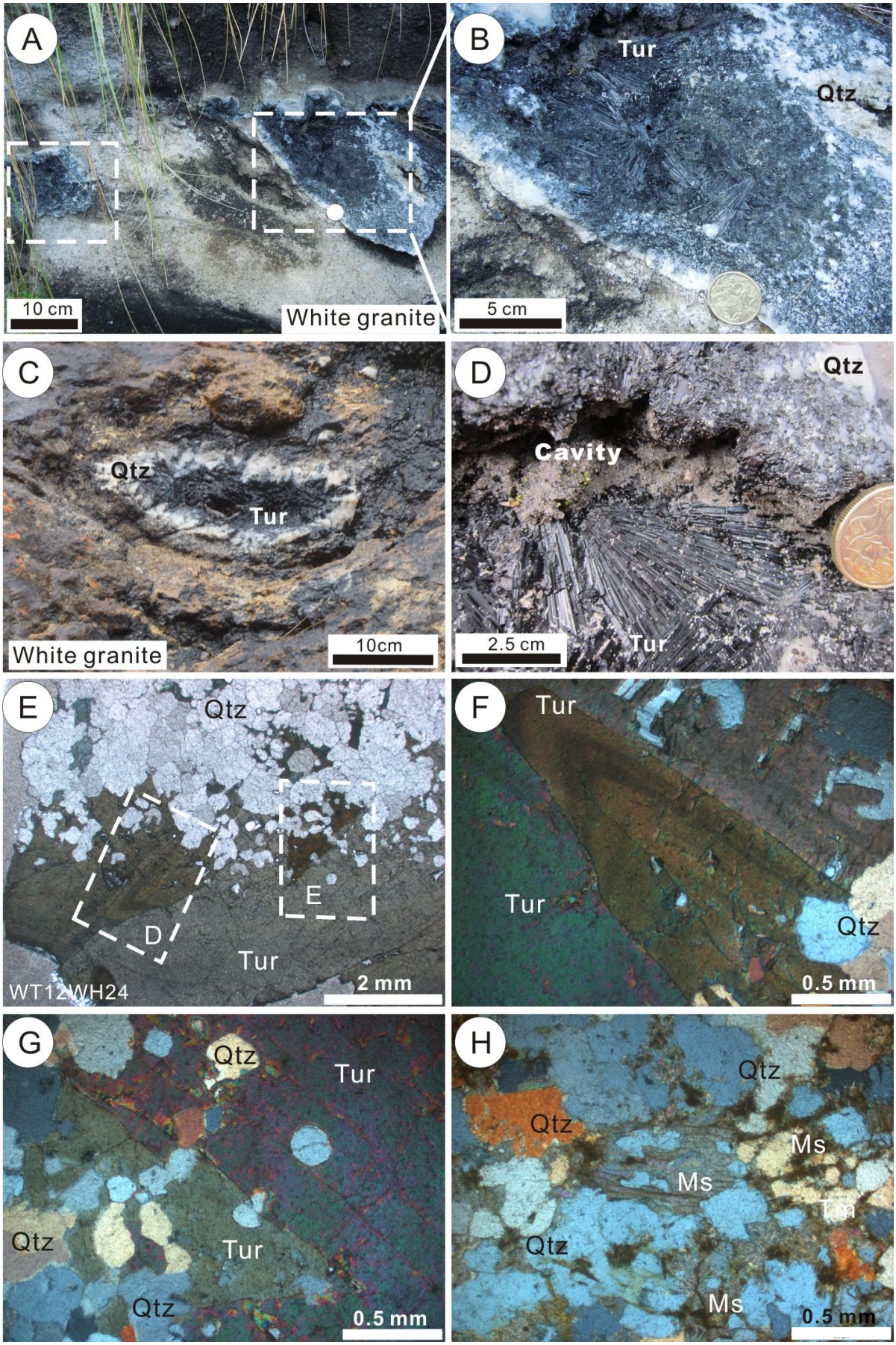
A
10 cm
White granite
B
Tur
Qtz
5 cm
C
Qtz
Tur
White granite
10cm
D
Qtz
Cavity
2.5 cm
Tur
E
Qtz
D
E
Tur
WT12WH24
2 mm
F
Tur
Tur
Qtz
0.5 mm
G
Qtz
Tur
Qtz
Tur
Qtz
0.5 mm
H
Qtz
Qtz
Ms
Ms
Tur
Qtz
Ms
0.5 mm

Figure 4.5 Photographs and photomicrographs showing miarolitic textures defined by tourmaline and quartz in the Heemskirk Granite at Trial Harbour. (A, B) tourmaline-rich miarolitic cavities consisting of radiating tourmaline centres and quartz rims in the White granite. (C) A tourmaline-filled cavity with typical growth zones of outer quartz and inner tourmaline. (D) Long, prismatic tourmaline crystals radiating inward from the wall to the centre of a miarolitic cavity. (E) Prismatic tourmaline intergrown with quartz on the edge of a tourmaline cavity. Irregular tourmaline grains have different pleochroism, and are interstitial to quartz (plane polarised light). (F) Massive tourmaline crystals displaying orange-brown to blue pleochroism, and greenish zones associated with sub-euhedral quartz grains (cross polarised light). (G) Round to subround quartz grains included in massive grey blue to deep blue-reddish pleochroic tourmaline (cross polarised light). (H) K-feldspar partially altered to muscovite in an alteration halo surrounding a tourmaline cavity (cross polarised light). Abbreviation: Ms = muscovite, Qtz = quartz, Tur = tourmaline. Outcrop and sample (WT12WH24) location: E145°09′23.93″, S 41°55′20.64″, elevation ranging from 3 to 30 m.

leucocratic granite altered halos (several cm wide) typically surround the tourmaline-filled miarolitic cavities. K-feldspar has been totally or partly replaced by muscovite, and muscovite occurs as veinlets between quartz grains (Fig. 4.5H).

4.2.4 Tourmaline-quartz veins

4.2.4.1 Tourmaline veins in the Heemskirk Granite

Quartz-tourmaline veins are intensely developed in the apical portion of the Heemskirk Granite, and have penetrated from the White granite into the overlying Red granite (Fig. 4.1; Table 4.1). The veins typically have sub-vertical orientations (Fig. 4.6), and extend up to several hundred meters along NNE-, WNW-, N-, NE- and W-orientations. The most significant vein sets are oriented NNE and WNW (Klominsky, 1972).

The alteration halos are 1-10 cm wide around the tourmaline-quartz veins. They consist of prismatic tourmaline, anhedral muscovite (Fig. 4.6C), and granular to embayed quartz (Fig. 4. 6D). Tourmaline-quartz veins are typically enriched in accessory minerals. Irregular mineral aggregates consisting of monazite, xenotime, zircon and titanite, have been identified by energy dispersive X-ray spectroscopy (EDS). Their crystal morphologies and spongy textures are distinct from those crystallising in magmatic environments. These vein-hosted REE-rich accessory minerals are interpreted to have precipitated from hydrothermal fluids (e.g., Hoskin, 2005; Schaltegger et al., 2005). Tourmaline-quartz veins have internal growth bands, and the adjacent rocks have undergone relatively strong muscovite alteration. The sub-vertical tourmaline veins have locally cut tourmaline patches and orbicules (Figs. 4.3G and 4.6B), indicating that the tourmaline veins are late-stage products of hydrothermal alterations.

Tourmaline-rich veins are of economic significance as they host most of the cassiterite in the low-grade tin deposits in the Heemskirk Granite (Hajitaheri, 1985; Solomon and Groves, 2000). Cassiterite has not been observed in the tourmaline-quartz veins studies here, possibly because the sample locations are unmineralised, being located a few km away from the old Sn mine workings (Fig. 3.5).

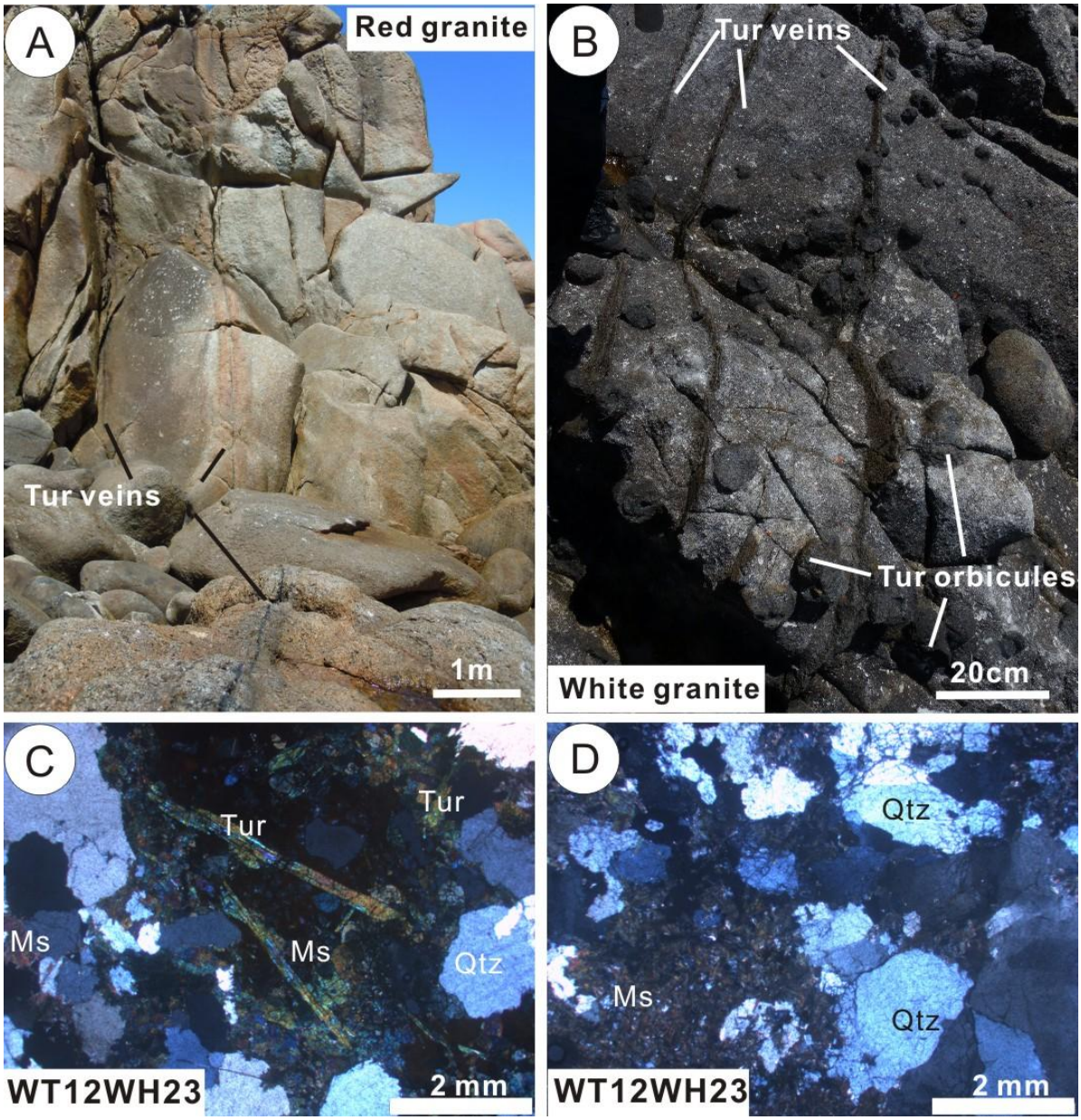

Figure 4.6 Photographs and photomicrographs showing the features of tourmaline-quartz veins from the Heemskirk Granite, Trial Harbour. (A) Sub-vertical veins extending up from the White granite towards the Red granite, over tens of meters. (B) Multiple tourmaline veins associated with tourmaline orbicules in the White granite. In the upper left corner of the photo, tourmaline-filled veins cut across the orbicules. (C) Euhedral elongated tourmaline grains occur in the centre of the veins, overgrown by quartz-muscovite halo (cross polarised light). (D) Quartz-muscovite alteration halo with granular quartz and primary feldspar that had been totally replaced by muscovite (cross polarised light). Abbreviation: Ms = muscovite, Qtz = quartz, Tur = tourmaline. Outcrop and sample (WT12WH23) location: E145°09′23.93″, S 41°55′20.64″, elevation ranging from 3 to 20 m.

4.2.4.2 Tourmaline veins in the Pieman Heads Granite

Sub-vertical to vertical tourmaline-filled quartz veins are developed extensively in the Pieman Heads Granite (Fig. 4.7F). They extend for tens to hundreds of meters from lower layers to the upmost region of the exposed pluton. These veins are typically several mm to cm wide (Fig. 4.7E), and locally can be up to tens of cm wide. Tourmaline-filled veins in the Pieman Heads Granite locally have cut across tourmaline orbicules (Figs. 4.7C, E). The veins are zoned, with central zones dominated by anhedral quartz and

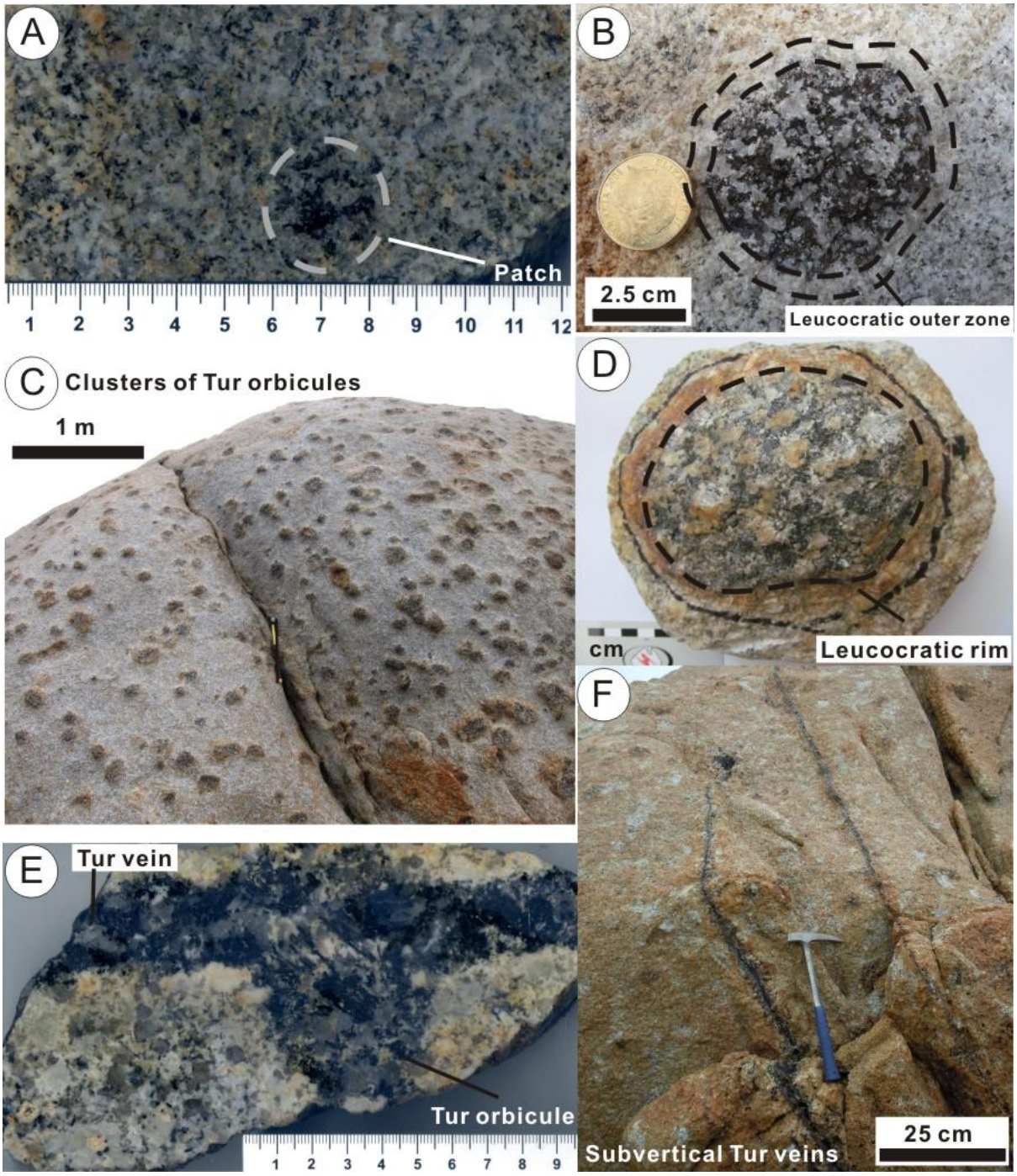

Figure 4.7 Photographs showing tourmaline-rich textured features in the Pieman Heads Granite. (A) Small, dendritic tourmaline patch hosted in medium-grained granite. (B) Sub-spherical tourmaline orbicule consisting of a quartz-tourmaline core and a leucocratic rim. (C) Clusters of tourmaline orbicules occurring in the Pieman Heads Granite. Note that some orbicules have coalesced to form larger mass, and some orbicules are cut by tourmaline veins. (D) A tourmaline orbicule composed of coarse-grained quartz and tourmaline intergrowths, surrounded by a red-brown leucocratic K-feldspar and quartz halo. (E) A small tourmaline orbicule cut by a 2-3 cm wide tourmaline-filled vein. (F) Subvertical tourmaline quartz-veins in the Pieman Head Granite. Tur = tourmaline. Outcrop locations: photos (A, B and E), E144°53′37.87.01″, S 41°43′13.75″, elevation = 3 m; photos (C, D and F), E144°55′40.01″, S 41°43′15.00″, elevation = 10 m.

euhedral tourmaline (Fig. 4.8C). The tourmaline-quartz veins have quartz-muscovite alteration halos (0.5 to 5 cm wide), while K-feldspar has been partly replaced by muscovite (Fig. 4.8D). Trace amounts of zircon, apatite, monazite and titanite are sporadically distributed in tourmaline veins at Pieman Heads.

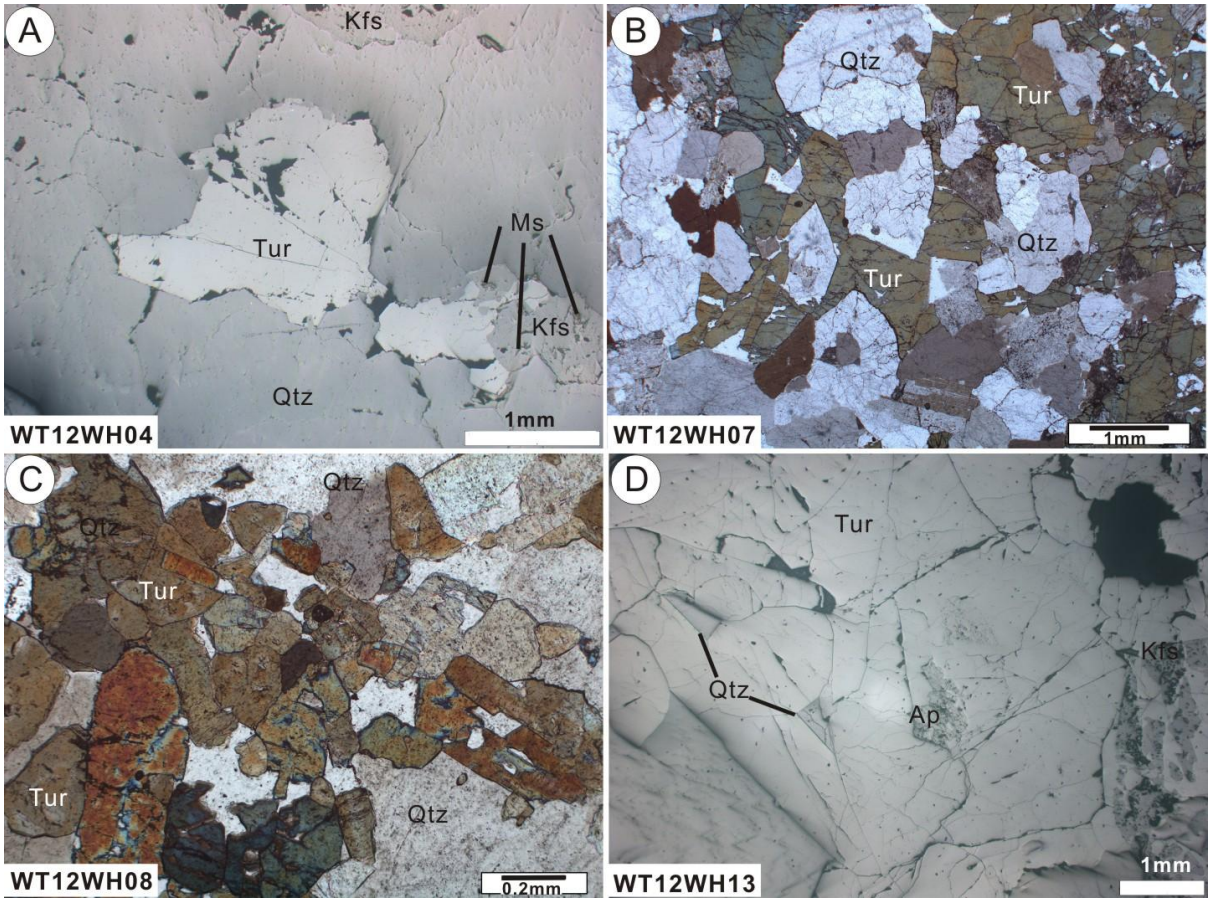

Figure 4.8 Photomicrographs showing mineralogical features of tourmaline-rich textures in the Pieman Heads Granite. (A) Typical tourmaline patches within coarse-grained quartz, and K-feldspar partially altered by muscovite (reflected light). (B) Brown to blue pleochroic tourmaline grains interstitial to quartz crystals in a tourmaline orbicule. A few fine-grained quartz inclusions in the massive tourmaline (plane polarised light). (C) Orange to deep blue pleochroic tourmaline aggregates in tourmaline-quartz veins (cross polarised light). (D) Small quartz, muscovite-altered K-feldspar and apatite grains in a massive tourmaline-filled vein (reflected light). Abbreviation: Ap = apatite, Kfs = K-feldspar, Ms = muscovite, Qtz = quartz, Tur = tourmaline. Samples (WT12WH04, WT12WH 07 and WT12WH 08) location: E144°55′40.01″, S 41°43′15.00″, elevation = 10 m; Sample (WT12WH13) location: E144°53′37.87.01″, S 41°43′13.75″, elevation = 3 m.

4.2.5 Unidirectional solidification textures

Unidirectional solidification textures (USTs) are defined morphologically as igneous crystals grown in one direction from a solid groundmass (Shannon et al., 1982). USTs can be divided into many sub-types, among which crenulate layers, also known as comb quartz layers, are the most common type in porphyry and other intrusion-related ore deposits (Shannon et al., 1982; Kirkham and Sinclair, 1988; Lowenstern and Sinclair, 1996). UST-quartz layers occur in the roof zone and on the margins of the White and Red granites. They are exposed spectacularly at Trial Harbour and Granville Harbour, and also crop out at Mt. Agnew and other locations within the Heemskirk Batholith. The USTs are defined mostly by euhedral quartz crystals up to 5 cm in length. Individual quartz grains are normally 0.2 to 30 mm in diameter, much coarser grained than the phenocrysts (normally ≤ 0.2 mm) in adjacent aplitic rocks. Some layers may be easily misrecognised as pegmatite or stockscheider (cf. Schmitz and Burt, 1990) due to the megacrystic grain sizes (Figs. 4.9B, F). There is commonly more than one layer of comb quartz in outcrop, with each layer alternating with aplitic granite (Fig. 4.9). In some cases, thick quartz UST layers have

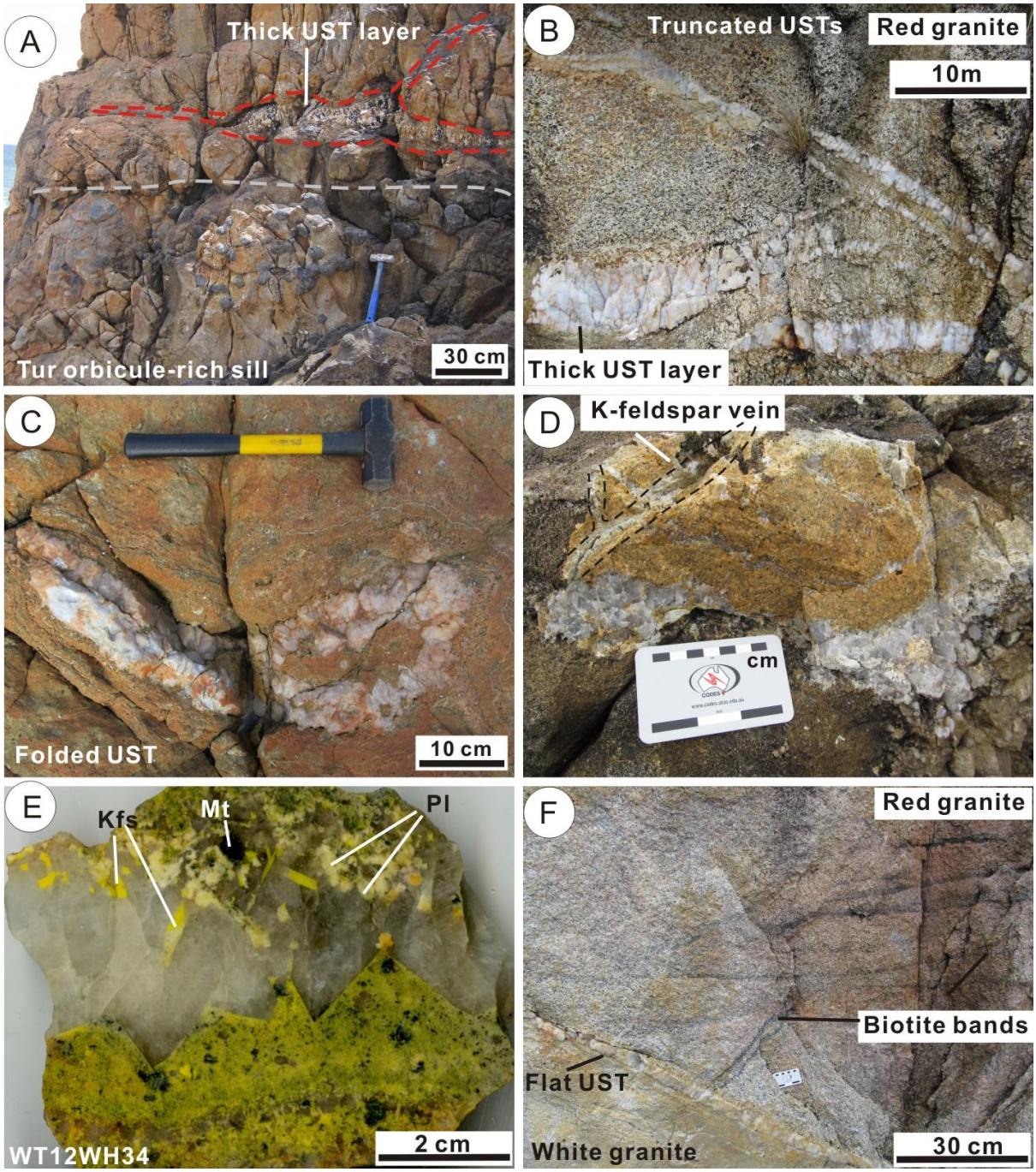

Figure 4.9 Photographs showing textural features of unidirectional solidification textures (USTs) in the Heemskirk Granite. (A) A thick UST layer consisting of quartz, feldspar and minor tourmaline overlying the tourmaline orbicule-rich sill in the White granite at Trial Harbour. (B) Multiple UST-quartz layers at Trial Harbour, locally truncating and alternating with thin aplitic bands. (C) A folded quartz UST layer defining a "necklace" texture at Granville Harbour. (D) Multiple sinuous UST quartz layers are transgressed by K-feldspar veinlets at Trial Harbour. (E) Magnetite-bearing USTs (stained cobaltinitrate) consisting of K-feldspar (yellow), plagioclase, quartz and minor biotite from Granville Harbour. (F) A long, flat UST-quartz layer truncating biotite bands (schlieren) in the Red granite. These USTs mark the contact between the Red and underlying White granites. Abbreviation: Kfs = K-feldspar, Mt = magnetite, Pl = plagioclase. Outcrop locations: photos (A, D), E145°09′23.93″, S 41°55′20.64″, elevation = 10 m; photos (B, F), E145°09′30.49″, S41°55′23.94″, elevation = 7.1 m; photos (C, E), E145°01′40.47″, S 41°48′34.80″, elevation = 1 m.

locally bifurcated into two or more narrow UST-quartz bands (Fig. 4.9B). Comb quartz layers typically range in thickness from several millimeters to centimeters. They can extend along a strike continuously for

more than tens of meters as subhorizontal bands (Fig. 4.9F), but more commonly occur as discontinuous, sinuous chains. Quartz layers are locally bent intensively, and can be folded completely into a "necklace" style (Fig. 4.9C). Several ten-meter long quartz layers may disappear suddenly, re-emerge in nearby areas, and continue for tens or hundreds of meters.

The long axes of quartz crystals are generally aligned nearly perpendicularly to the plane of each UST layer, and parallel to aplitic intergrowths (Figs. 4.9B, D, E). Anhedral quartz generally has crystallised from the top of the overlying aplite layers, and grew downwards onto a volatile-rich pocket trapped below the aplite layers (e.g., Lowenstern and Sinclair, 1996). In the lower, coarse-grained part of the UST, quartz crystals have euhedral hexagonal terminations (Fig. 4.9E), whereas the alkali-feldspars exhibit nearly square morphologies, locally with identical cross-hatched or sector twins (Fig. 4.9B). K-feldspar, plagioclase and biotite are locally concentrated on the top of USTs (Fig. 4.9A), but they are much less abundant than quartz. On the top layer of the aplite, fine-grained alkali-feldspars have locally grown towards the direction of quartz USTs terminations (Fig. 4.9A). The trigonal K-feldspar array overgrown by anhedral quartz is a cryptic, thin UST-layer dominated by K-feldspar (Fig. 4.9C), which formed prior to the main UST-quartz layer. The bottoms of USTs contain euhedral coarse-grained quartz crystals that have apparently smooth contacts with underlying aplite alternated in hand specimens (Fig. 4.9E). However, petrographic observations reveal that the hexagonal quartz grains have been corroded and overgrown by very fine-grained quartz, feldspar and biotite (Figs. 4.9E, F). Quartz-feldspar overgrowths on the lowermost UST-quartz contacts locally display granophyric textures (Fig. 4.9F), indicating that the aplite crystallised rapidly after UST growth, probably due to undercooling conditions (Kirkham and Sinclair, 1988). Minor biotite is intergrown with K-feldspar on the top of undulating USTs (Fig. 4.10A). Biotite also occurs as inclusions in coarse-grained quartz layers (Fig. 4.10D). Some USTs contain minor tourmaline (e.g., Trial Harbour; Fig. 4.9A), whereas on the margin of the granite batholith, USTs locally contain a small amount of discrete magnetite grains (e.g., Granville Harbour; Fig. 4.9E). The magnetite grains are generally rimed by secondary chlorite, whereas alkali-feldspar crystals are partly replaced by muscovite. No sulphides have been found during this study in USTs within the Heemskirk Batholith. Trace amounts of zircon, monazite, and rutile occur sparsely as isolated grains in quartz-dominated USTs.

The UST-bearing granitic sill is commonly underlain by an aplitic sill enriched in tourmaline orbicules in the apical region of the white Heemskirk Granite (Fig. 4.9A). Both sills overlie a domain enriched in tourmaline patches in the White granite. Tourmaline-rich veins have cut quartz-dominated USTs locally (Fig. 4.1). Within individual UST layers, K-feldspar veinlets have locally crosscut the UST-quartz layer and penetrated into overlying aplitic granite (Fig. 4.9D). At Trail Harbour, a flat, quartz-rich UST layer extends continuously for a few tens of meters, abruptly truncates biotite-rich bands in the Red granite, and points downwards into the underlying White granite (Figs. 4.1B and 4.9 F). Hajitaheri (1985) mistakenly documented this contact as a quartz vein. This UST actually provides unambiguous evidence that the Red granite was intruded by the underlying White granite (cf. Shannon et al., 1982).

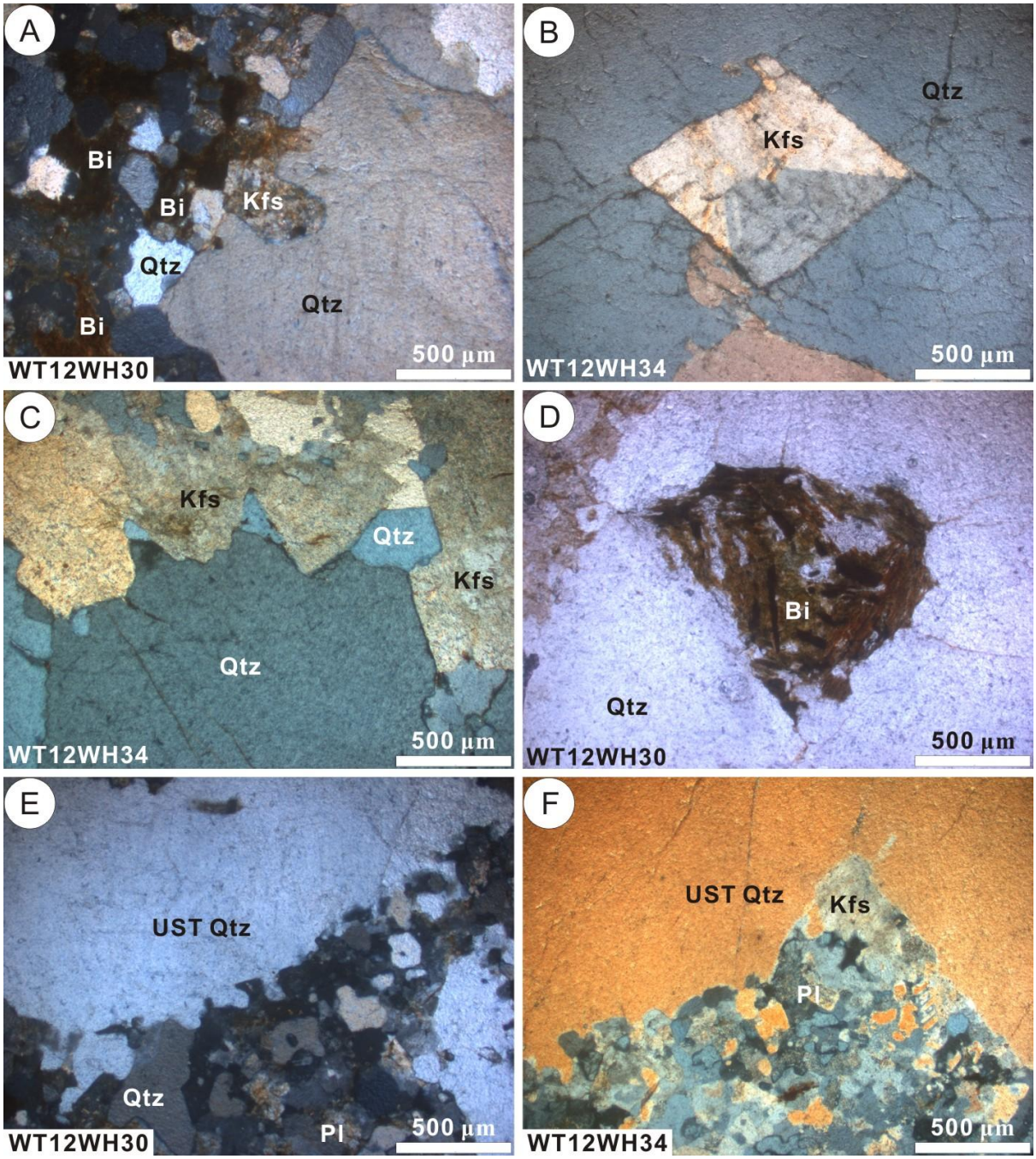

Figure 4.10 Photomicrographs showing mineralogical features of USTs in the Heemskirk Granite. (A) On the top of USTs, biotite and K-feldspar are intergrown with coarse-grained quartz (Trial Harbour). (B) K-feldspar in coarse-grained quartz displaying roughly square morphologies and identical sector twins (Granville Harbour). (C) On the top of a UST, coarse-grained quartz is partly overgrown by a thin band of trigonal alkali-feldspar (Granville Harbour). (D) Irregular biotite occurs as inclusions in coarse-grained quartz. (E, F) On the bottom of a quartz UST, coarse-grained quartz has been corroded by mineral overgrowths, while quartz overgrowths in contiguous aplite locally exhibit granophyric textures. All photomicrographs taken under cross polarised light, except (D) under plane polarised light. Abbreviation: Bi = biotite, Kfs = K-feldspar, Mt = magnetite, Pl = plagioclase, Qtz = quartz. Sample locations: WT12WH30, E145°09′23.93″, S 41°55′20.64″, elevation = 20 m; WT12WH34, E145°01′40.47″, S 41°48′34.80″, elevation = 1 m.

4.3 Discussion

4.3.1 Spatial-temporal relationship

Tourmaline- and quartz-rich textural features have systematic spatial relationships in the apical portions of sills in the Heemskirk and Pieman Heads granites (Fig. 4.1). Tourmaline patches in the aplitic White granite occur beneath an orbicule-rich sill of the Heemskirk Granite at Trial Harbour (Fig. 4.1). Tourmaline orbicules are contained in equigranular and porphyritic granites in the Heemskirk Granite at Granville Harbour, and also in the Pieman Heads Granite. At Granville Harbour, tourmaline orbicules underlie an equigranular granitic layer enriched in comb quartz-rich USTs that locally contains magnetite adjacent to the contact between the granite and Proterozoic Oonah Formation. Tourmaline-filled miarolitic cavities developed in the upper layer of the White granite, particularly at Trial Harbour and Granville Harbour. The miarolitic cavities occur locally below UST layers, but above the tourmaline orbicules (Fig. 4.3A).

At each locality studied, tourmaline veins extend from the lowest exposure level up to the uppermost part of the granite (Figs. 4.1, 4.6 and 4.7). The veins have locally cut across tourmaline orbicules (Fig. 4.3G), USTs and/or tourmaline cavities. Dick (1980) argued that tourmaline orbicules were fracture-controlled and recharged by tourmaline veins in the Seagull Batholith, Yukon Territory. This interpretation is not valid for the formation of tourmaline orbicules in the Heemskirk and Pieman Heads granites. The tourmaline orbicules appear to be boron-rich "balls" that crystallised in the granitic rocks and were then locally cut by the late-stage veins (Fig. 4.3G). Figure 4.1 systematically illustrates the spatial association of tourmaline-rich textures, USTs and biotite schlieren at Trial Harbour, Heemskirk Granite. At Trial Harbour, tourmaline orbicules are concentrated in an aplite dyke that fed a granitic sill overlying a layer of equigranular White granite that is enriched in tourmaline patches (Figs. 4.3E, F).

Based on documenting the cross cutting relationships, tourmaline-quartz veins formed after all of the tourmaline-bearing textural features. Given that quartz crystal terminations of USTs grow from the top of carapace of a granite stock inwards, they typically point downwards to a younger granitic layer (Shannon et al., 1982). The tourmaline patches, orbicules and cavities are therefore interpreted to postdate the overlying USTs. The crystallisation relationships between the tourmaline patches, orbicules and cavities are difficult to ascertain, since no obvious crosscutting or overprinting relationships were presented. Tourmaline can precipitate from an aqueous vapour phase derived from felsic plutons, and its formation relates to a boron-rich vapour phase separating from aluminosilicate magmas and ascending buoyantly to the apex of crystallising magma (Scaillet et al., 1995). According to the bubble-laden plume model of Candela (1991, 1997), small bubbles can merge into large masses during their ascent, as large volumes of volatiles separate from a magma. The small and large boron-rich bubbles are supposed to have produced the tourmaline patches and orbicules, respectively, in the Heemskirk and Pieman Heads granites. The tourmaline patches might therefore form earlier than the tourmaline orbicules at a time when spanning clusters of bubbles have not yet formed, causing patchy diffusive tourmaline growth in situ in the crystallising granite. At Trial Harbour, tourmaline orbicule-rich aplitic dykes and sills cut and overlie the tourmaline patch-bearing equigranular phase of the Heemskirk Granite, confirming that the orbicules

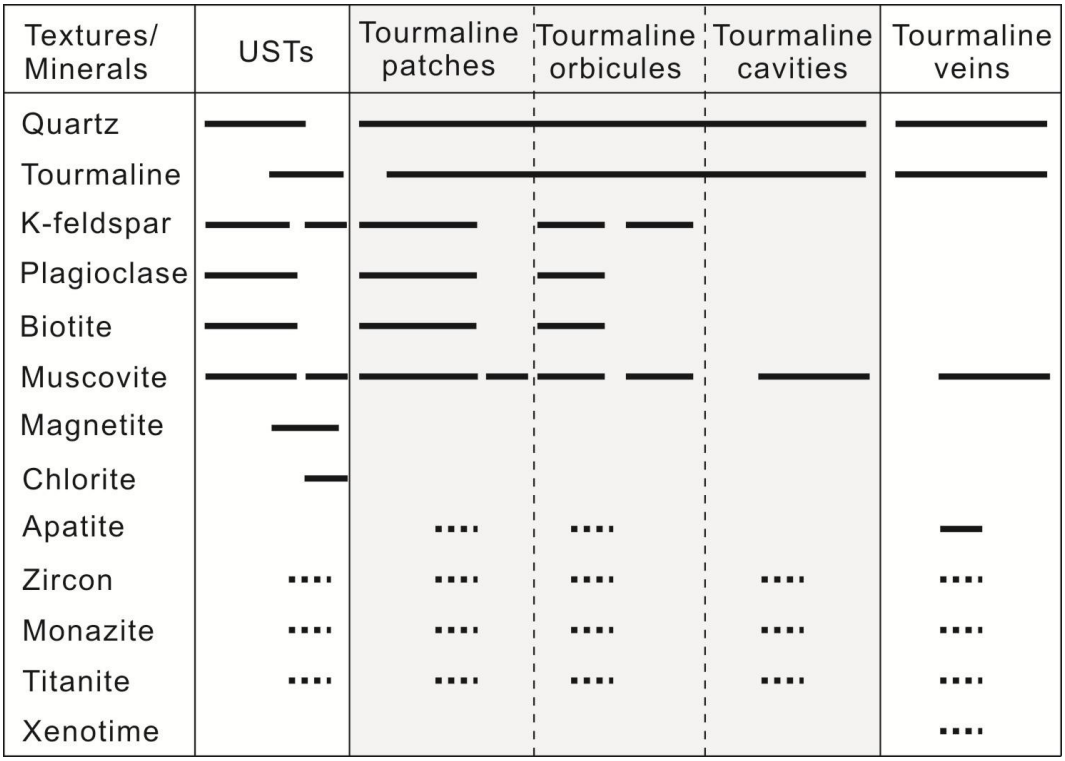

Figure 4.11 Paragenetic sequences of tourmaline- and quartz-rich textures in the Heemskirk and Pieman Heads granites from western Tasmania. Note that apatite has been only observed at Granville Harbour and Pieman Heads Granite.

precipitated later than the tourmaline patches. Tourmaline cavities occur in a granitic sill commonly overlie the tourmaline orbicules at Trial Harbour, and have experienced intense quartz-muscovite alteration (Fig. 4.5). The tourmaline-filled miarolitic cavities tend to have generated later than the orbicules if a temporal sequence could be distinguished between the two tourmaline-rich associations. Therefore, the paragenetic sequence is interpreted to be USTs → tourmaline patches → orbicules → cavities → veins (Fig. 4.11).

4.3.2 Alteration types

Tourmaline patches and orbicules have undergone weak to intermediate muscovite alteration (Table 4.1; Figs.4.2, 4.3). Perthitic K-feldspar and albitic plagioclase have been selectively replaced by secondary muscovite around the rims of tourmaline patches and orbicules. Secondary muscovite grains are also disseminated in massive feldspar due to partial alteration. At the centre of tourmaline orbicules hosted by the aplitic sill at Trial Harbour, muscovite is rarely intergrown with quartz and tourmaline. Tourmaline alteration has locally developed in the rim of some of these tourmaline patches and orbicules, where tourmaline occurs as veinlets and partially replaces feldspars (e.g., Fig. 4.3).

No topaz has been discerned in tourmaline cavities or veins based on petrographic and short wavelength infra-red (SWIR) spectral investigations. Rinds around tourmaline cavities and tourmaline vein halos have, however, experienced intense quartz-muscovite alteration (Figs. 4.5, 4.6). Tourmaline cavities are interpreted to have been pockets of boron-rich magmatic-hydrothermal fluids that were trapped in

crystallised granite sills. The growth zones consisting of tourmaline, quartz and muscovite are the products of evolution of the boron-rich fluids and hydrothermal reaction with the granitic host, where strong quartz-muscovite alteration has occurred around the cavities. The tourmaline cavities are thus explained to have been fluid-saturated relative to the tourmaline patches and orbicules. Euhedral prismatic tourmaline crystals which project from the walls to the centres of cavities were precipitated by the volatile pockets that produced appropriate space for them growing in cavities. Tourmaline-quartz veins commonly have quartz + muscovite alteration halos (e.g., Fig. 4.6). Acicular tourmaline is commonly intergrown with quartz in the centre of the veins. The alteration selvages consist of granular muscovite and quartz, and range in width from several centimeters up to meters locally.

Magnetite-bearing USTs have locally undergone selective chlorite alteration. Granular chlorite has typically overgrown around isolated magnetite grains in hexagonal quartz. Magnetite and chlorite may have scavenged Fe from the adjacent Oonah Formation rocks at Granville Harbour. Coarse- grained K-feldspar crystals in the top of individual UST are commonly altered to be secondary muscovite. K-feldspar-filled veins have typically cut across some quartz-rich UST layers (Fig. 4.9). The precipitation of comb-quartz layers overlying the crystallising magma implies the magmatic-hydrothermal water and volatiles accumulated in the UST layers during crystallisation (cf. Lowenstern and Sinclair, 1996). When the vapour pressure exceeded the overlying lithostatic load, the USTs layers and granitic carapace would have undergone brittle fracturing. This sudden pressure collapse could have led to the release of volatiles and water influx into adjacent wallrocks, which subsequently produces K-feldspar (or muscovite) alteration in the UST layers and/or fractures crosscutting the USTs, as well as tourmaline-bearing veins in the overlying granitic sills.

4.4 Conclusions

Distinctive magmatic-hydrothermal features, including tourmaline patches, orbicules, cavities and veins, together with quartz-rich and rare magnetite-bearing unidirectional solidification textures (USTs), are products of magmatic crystallisation and fluid exsolution phenomena during emplacement of the western Tasmanian granites. Most of these textural features typically occur in discrete layers in the roof of individual granite sills, particularly at the contact between the White and Red phases of the Heemskirk Granite, or on the margins of the intrusions (Table 4.1). Tourmaline cavities and USTs have only been observed in the Heemskirk Batholith, and not in the Pieman Heads Granite. The granites have experienced quartz-muscovite, tourmaline, muscovite, K-feldspar, and/or rarely chlorite alteration during magmatic-hydrothermal evolution.

Origins of different types of magmatic – hydrothermal textures in the western Tasmanian granites are further evaluated through major and trace element micro-analysis (Chapter 5 and Chapter 6), fluid inclusion study (Chapter 7), and in-situ SIMS boron and oxygen isotopes (Chapter 8).

Chapter 5 Tourmaline mineral chemistry

5.1 Introduction

Tourmaline is a mineral supergroup with more than 20 end members (Hawthorne and Henry, 1999; Henry et al., 2011). It can form in diverse geologic settings, but most commonly occurs in meta-sedimentary, pegmatitic and granitic rocks (van Hinsberg et al., 2011a). Tourmaline grains can display distinctive optical, chemical and isotopic zonations that record the geological conditions under which they precipitate. Tourmaline is exceptionally refractory, and can preserve its composition during the physical and chemical changes associated with sedimentary, metamorphic and igneous activity, due to low element diffusion rates in its crystal structure (van Hinsberg et al., 2011a, 2011b). Thus, it can be considered as an ultra-stable mineral, similar to zircon and rutile. These characteristics potentially make tourmaline a petrological 'forensic' mineral, since it can record and preserve informative conditions in igneous, sedimentary, metamorphic and hydrothermal settings (Henry and Guidotti, 1985; van Hinsberg et al., 2011a, 2011b).

This chapter presents electron microprobe (EMPA) and laser ablation inductively coupled plasma mass spectrometry (LA-ICP-MS) analyses of major and trace element concentrations in tourmaline. These data are used to investigate the formation of magmatic-hydrothermal features developed in western Tasmanian granites.

5.1.1 Tourmaline end-members

Owing to its complicated crystal arrangement and flexible structure, tourmaline can incorporate many different cations and anions, leading to a diverse association of tourmalines that can be subdivided in terms of chemical compositions, by the determination of particular chemical constituents at known crystallographic sites (Hawthorne and Dirlam, 2011).

There are many variants in the tourmaline supergroup (Table 5.1). They share the common chemical formula:

$$X\ Y_3\ Z_6\ (T_6\ O_{18})\ (B\ O_3)_3\ V_3\ W \quad \textbf{(equation 5.1)}$$

The X site is generally occupied by Na^{+}, K^{+}, Ca^{2+}, and Pb^{2+}, or else it is vacant. Elements such as Li^{+}, Mg^{2+}, Fe^{2+}, Mn^{2+}, Fe^{3+}, Al^{3+}, and Ti^{4+}, occupy the Y site. The Z site can contain Mg^{2+}, Fe^{2+}, Fe^{3+}, Al^{3+}, and Cr^{3+}. The T site is a six-fold ring of tetrahedra that consists mainly of Si^{4+}, B^{3+}, and Al^{3+} (Fig. 5.1). The V and W sites are anion sites that are usually accommodated by OH^{-} or O^{2-} (or both) at the V site, and OH^{-}, F^{-}, or O^{2-} at the W site (Henry and Guidotti, 1985; Hawthorne and Henry, 1999; van Hinsberg et al., 2011b; Table 5.1). Al, Ca, Fe, and Mg are the most significantly and commonly exchangeable elements.

Tourmaline is usually classified in terms of its common end-member constituents. To a large extent, most natural tourmalines are subdivided into two completely miscible solid solution series: schorl-dravite

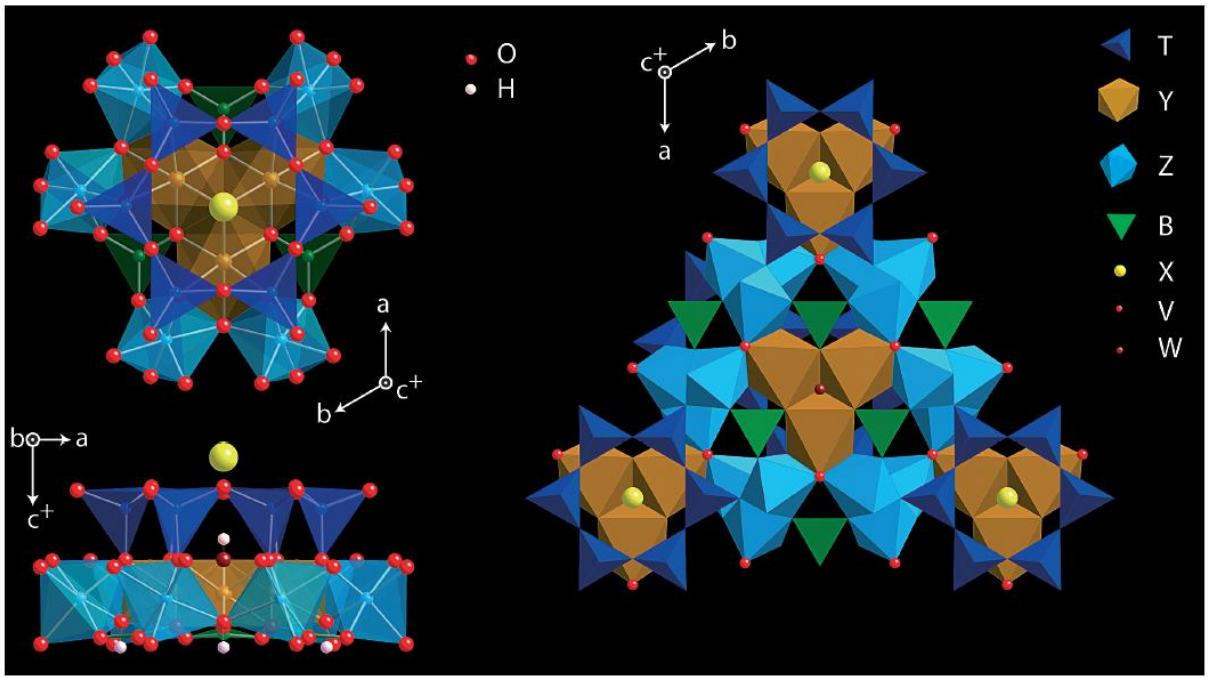

Figure 5.1 The crystal structure of tourmaline, comprising a six-fold ring of tetrahedra on the top of a plane including three Y polyhedra enclosed by six Z polyhedra (modified from van Hinsberg et al., 2011a).

and schorl-elbaite, although there is a conspicuous miscibility gap between dravite and elbaite (Henry and Guidotti, 1985). Tourmalines are therefore typically described with respect to their position in the schorl-dravite or schorl-elbaite series. Other types of tourmaline are also recognised on the basis of the dominant elements at the Y or X site (equation 5.1). For example, uvite is enriched in both Ca and Mg, whereas Mn-rich tsiliasite can be significant in tourmalines defined as the elbaite-schorl solid solution series (Table 5.1). Most natural tourmalines that are characterised by alkali-vacancies at the X site are commonly termed foitite. Those tourmalines containing large amounts of Fe^{3+}, Cr^{3+}, or V^{3+} will have appreciable buergerite or ferridravite, chromium-dravite, or vanadium-dravite constituents (Table 5.1).

5.1.2 Tourmaline in different geological environments

Variations in tourmaline chemistry can be influenced by the bulk composition of the host rock, the composition of co-existing minerals, and the prevailing P-T-fO_2 conditions at the time of crystallisation (Henry and Guidotti, 1985; van Hinsberg et al., 2011a). When taking into consideration on their mechanically and chemically refractory signatures, tourmaline grains have the potential to provide insights into the geological environments in which they formed. Henry and Guidotti (1985) proposed Al-Fe(tot)-Mg and Ca-Fe(tot)-Mg ternary plots that can discriminate protoliths based on tourmaline chemistry (Fig. 5.2). These diagrams can distinguish Li-poor or Li-rich granitoids, hydrothermally altered granites, Al-saturated or Al-unsaturated metasediment and metapelites, calc-silicates, low-Ca metaultramafics, and metacarbonate rocks.

Metasedimentary or metavolcanic rocks typically contain Mg-rich dravite, whereas tourmalines from granitoids have elevated Fe contents (Bebout and Nakamura, 2003; Marschall et al., 2006, 2008; Fig. 5.2). Tourmalines hosted in granites are also characterised by low uvite + feruvite contents and relatively high

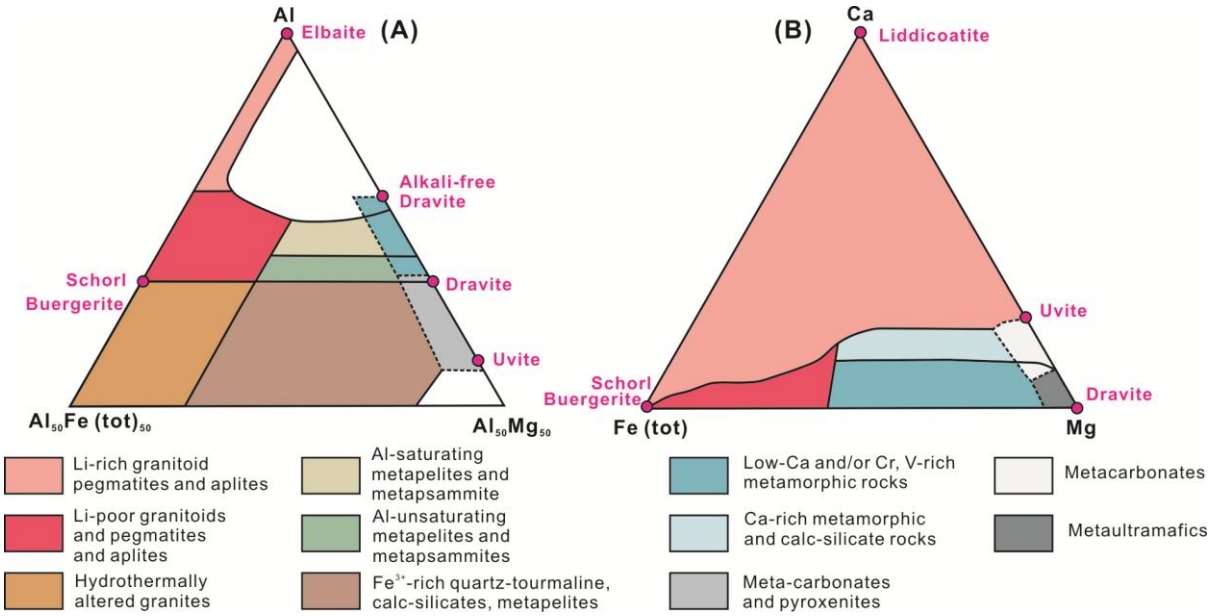

Figure 5.2 (A) Al-Fe (tot)-Mg and (B) Ca-Fe (tot)-Mg diagrams (atoms per formula unit) for discriminating tourmalines from various geological environments (modified from Henry and Guidotti, 1985).

alkali-free components, compared with tourmalines from metamorphic basement rocks (Pesquera et al., 2005, 2013; Trumbull et al., 2008; Fig. 5.2). Magmatic tourmalines from granitoids are typically classified as schorl (Trumbull and Chaussidon, 1999; Trumbull et al., 2008; Balen and Broska, 2011), although elbaite is common in Li-bearing pegmatites (Fig. 5.2). Tourmalines in pegmatites and hydrothermal veins typically have higher Al and Fe proportions relative to those in the parental granitic intrusions (Fig.5. 2). One limitation of Henry and Guidotti's (1985) classification scheme is that it did not consider tourmaline associated with mineral deposits. Tourmaline is a common gangue mineral in certain types of ore deposits (e.g., Taylor and Slack, 1984; Plimer and Lees, 1988; Slack et al., 1993; London and Manning, 1995; Slack, 1996; Yavuz et al., 1999; Jiang et al., 1999; Williamson et al., 2000; Mlynarczyk and Williams-Jones, 2006; Jiang et al., 2008; Xavier et al., 2008; Slack and Trumbull, 2011; Mercadier et al., 2012; Tornos et al., 2012). The compositions of hydrothermal tourmaline are more variable than those in igneous, metamorphic and sedimentary rocks, possibly due to multiple fluid generations and changeable physicochemical environments.

Tourmalines related to submarine massive sulphide deposits typically belong to the dravite, or Mg-rich dravite-schorl series (Taylor and Slack, 1984; Plimer and Lees, 1988; Palmer and Slack, 1989; Slack et al., 1993), whereas tourmalines that formed adjacent to submarine vents or have been overprinted by later granite-derived fluids have compositions of Fe-rich dravite or schorl (e.g., Rosebery Cu-Pb-Zn deposit, Plimer and Lees, 1988; Slack et al., 1993). Tourmalines associated with reduced granite-related Sn-W deposits are relatively enriched in Fe and thus mainly belong to schorl group (London and Manning, 1995; Jiang et al., 1999; Williamson et al., 2000; Mlynarczyk and Williams-Jones, 2006; Jiang et al., 2008). Tourmalines with schorl-dravite solid solution series can be associated with porphyry Cu-Mo-Au deposits (Slack, 1996). Those tourmalines associated with oxidized porphyry magmas often have a wide range of compositions, e.g., small proportions of uvite and/or povondraite have been detected in porphyry

Table 5.1 General structural formulae for tourmaline supergroup and their end-member compositions based on X-site classification (modified from Hawthorne and Dirlam, 2011; Henry et al., 2011).

General formula	$XY_3Z_6(T_6O_{18})(BO_3)_3V_3W$
alkali group	
Dravite	$NaMg_3Al_6(Si_6O_{18})(BO_3)_3(OH)_3(OH)$
Schorl	$NaFe^{3+}{}_2Al_6(Si_6O_{18})(BO_3)_3(OH)_3(OH)$
Chromium-dravite	$NaMg_3Cr_6(Si_6O_{18})(BO_3)_3(OH)_3(OH)$
Vanadium-dravite	$NaMg_3V_6(Si_6O_{18})(BO_3)_3(OH)_3(OH)$
Fluor-dravite	$NaMg_3Al_6(Si_6O_{18})(BO_3)_3(OH)_3F$
Fluor-schorl	$NaFe^{3+}{}_2Al_6(Si_6O_{18})(BO_3)_3(OH)_3F$
K-dravite*	$KMg_3Al_6(Si_6O_{18})(BO_3)_3(OH)_3(OH)$
Tsilaisite*	$NaMn^{2+}{}_3Al_6(Si_6O_{18})(BO_3)_3(OH)_3(OH)$
Elbaite	$Na(Li_{1.5}Al_{1.5})Al_6(Si_6O_{18})(BO_3)_3(OH)_3(OH)$
Fluor-elbaite*	$Na(Li_{1.5}Al_{1.5})Al_6(Si_6O_{18})(BO_3)_3(OH)_3F$
Povondraite	$NaFe^{3+}{}_3(Mg_2Fe^{3+}{}_4)(Si_6O_{18})(BO_3)_3(OH)_3O$
Cr-Al-povondraite	$NaCr_3(Mg_2Al_4)(Si_6O_{18})(BO_3)_3(OH)_3O$
Oxy-dravite*	$NaAl_3(Mg_2Al_4)(Si_6O_{18})(BO_3)_3(OH)_3O$
Oxy-schorl*	$NaAl_3(Fe^{2+}{}_2Al_4)(Si_6O_{18})(BO_3)_3(OH)_3O$
K-povondraite*	$KFe^{3+}{}_3(Mg_2Fe^{3+}{}_4)(Si_6O_{18})(BO_3)_3(OH)_3O$
Buergerite*	$NaFe^{3+}{}_3Al_6(Si_6O_{18})(BO_3)_3(O)_3(OH)$
Fluor-buergerite	$NaFe^{3+}{}_3Al_6(Si_6O_{18})(BO_3)_3(O)_3F$
Olenite	$NaAl_3Al_6(Si_6O_{18})(BO_3)_3(O)_3(OH)$
Fluor-olenite*	$NaAl_3Al_6(Si_6O_{18})(BO_3)_3(O)_3F$
calcic group	
Uvite	$CaMg_3(Mg_1Al_5)(Si_6O_{18})(BO_3)_3(OH)_3(OH)$
Fluor-uvite	$CaMg_3(Mg_1Al_5)(Si_6O_{18})(BO_3)_3(OH)_3F$
Feruvite	$CaFe^{2+}{}_3(Mg_1Al_5)(Si_6O_{18})(BO_3)_3(OH)_3(OH)$
Fluor-feruvite*	$CaFe^{2+}{}_3(Mg_1Al_5)(Si_6O_{18})(BO_3)_3(OH)_3F$
Liddicoatite*	$Ca(Li_2Al)Al_6(Si_6O_{18})(BO_3)_3(OH)_3(OH)$
Fluor-liddicoatite	$Ca(Li_2Al)Al_6(Si_6O_{18})(BO_3)_3(OH)_3F$
vacant group	
Foitite	$X^{\square}(Fe^{2+}{}_2Al)Al_6(Si_6O_{18})(BO_3)_3(OH)_3(OH)$
Magnesio-foitite	$X^{\square}(Mg_2Al)Al_6(Si_6O_{18})(BO_3)_3(OH)_3(OH)$
Rossmanite	$X^{\square}(LiAl_2)Al_6(Si_6O_{18})(BO_3)_3(OH)_3(OH)$

Note: * currently not accepted by the IMA-CNMNC.

Cu systems (Lynch and Ortega, 1997; Yavuz et al., 1999). Some IOCG deposits contain tourmalines that have compositions very similar to those in porphyry Cu deposits (Xavier et al., 2008; Tornes et al., 2012).

5.2 Methodology

5.2.1 Electron microprobe analysis

Tourmaline samples, including patches, orbicules, cavities, and veins from the Heemskirk and Pieman Heads granites, were mounted and polished in epoxy resin. Most of the polished planes were oriented perpendicular or parallel to the long axis (c axis) of tourmaline grains. Tourmaline grains were marked for analysis under a normal optical microscope. Backscattered electron images of the selected tourmaline

grains were conducted with a FEI Quanta 600 environmental SEM in the Central Science Laboratory at the University of Tasmania (UTAS). Compositional analyses were acquired on a Cameca SX100 electron microprobe equipped with five tunable wavelength dispersive spectrometers in the Central Science Laboratory. Operating conditions were 40 degrees takeoff angle, with beam energy of 15 kV. A probe current of 10 nA and a 10 micrometer diameter beam size were applied during the analytical procedure. The counting time was 10 seconds for Na, Si, K, Cl, 15 seconds for Ca, 20 seconds for Mg, Ti, Ba, Al, P, Mn, Fe, 30 seconds for Sr, Cr, and 45 seconds for F. The detection limits at 3σ above mean background varied from 0.01 to 0.05 wt % for these components with 99 % confidence.

Elements were acquired using analysing crystals LLIF for Cr, Mn, Fe, PET for Ba, K, Ca, Ti, LPET for Cl, P, Sr, PET for Ba, K, Ca, Ti, TAP for Al, Mg, Na, Si, and PC0 for F. Lithium was not detected by electron microprobe analysis (EMPA) due to low concentrations in the analysed tourmalines. Oxygen was calculated by cation stoichiometry and included in the matrix correction. Oxygen equivalent from halogens (F/Cl/Br/I) was subtracted in the matrix correction. Boron was calculated 0.09677 atoms relative to 1.0 atom of oxygen by stoichiometry. All microprobe analyses of tourmalines were internally calibrated by standard schorl Harvard (E6). In this study, Fe contents are all assumed as Fe^{2+} at the Y-site when calculating the formula of tourmaline. The structural formulae of tourmaline were calculated in an Excel spreadsheet by normalizing to 31 anions including 15 cations in the tetrahedral and octahedral sites (T+Z+Y), and assuming stoichiometric compositions with regard to three B atoms per formula unit (apfu), four (OH+F) apfu (Henry and Dutrow, 1996).

5.2.2 LA-ICP-MS analyses

Trace element analyses of tourmalines were acquired by LA-ICP-MS at the ARC Centre of Excellence in Ore Deposits (CODES), UTAS. An Agilent 7500cs quadrupole ICP-MS coupled with a Resonetics Resolution S-155 ablation system with a 193nm ArF excimer laser was used in the study. The laser microprobe was equipped with a large format, two-volume ablation cell with the inside holder large enough to fit 20 epoxy rounds. Ablation took place in a helium gas atmosphere flowing at 0.35 l/min carrying the ablated aerosol was mixed with argon (1.05 l/min) immediately after the ablation chamber. For spot analyses, the aerosol and gas mixture was passed through a pulse-homogenizing device (the 'squid' from Laurin Technic, Australia) where the stream of ablated aerosol is split into 10 tubes with differing residence times before being recombined to one tube before entering the ICP-MS plasma. Mineral grains were sampled on 34 micron spots using the laser at 10 Hz and an energy density of approximately 3.5 J/cm^2.

The Excel spreadsheet Laser Template (CODES, UTAS; unpublished) was employed for data reduction which used the NIST612 measured at 89 micron spots as the primary standard for quantification and drift correction. Aluminium was used as the internal standard element for tourmaline as measured by EMPA. External reproducibility was measured on the USGS glass GSD-1g (secondary standard) measured ten times throughout the session, with most elements being below 5% relative standard deviation (RSD), except Be, Cr, Cd, Sn, Au, Tl and Th which are between 6 and 9% RSD (1 σ). The LA-ICP-MS spectra of

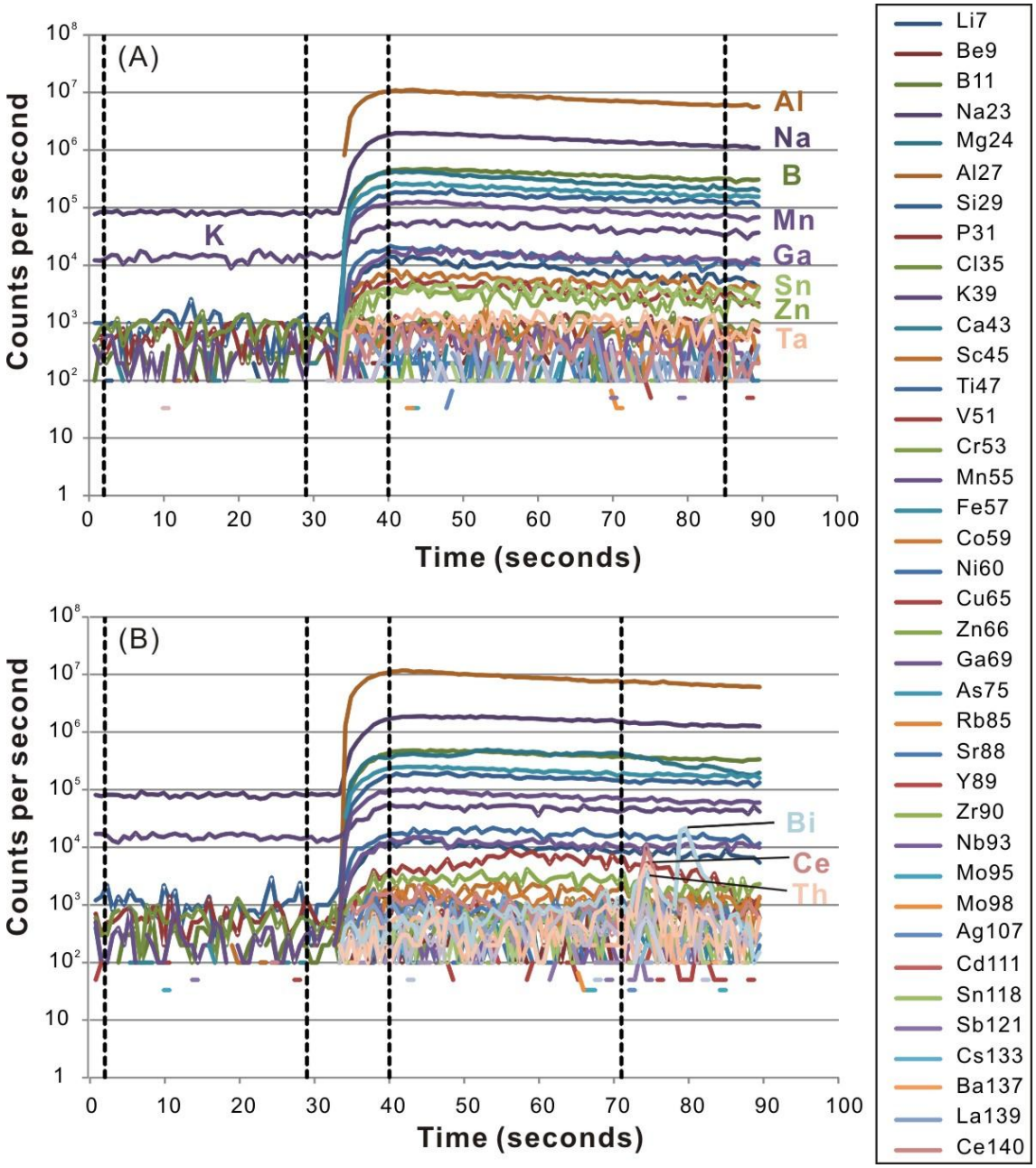

Figure 5.3 Time-resolved signals from laser ablation ICP-MS analysis of tourmalines, showing signal curves for most elements. The background measurement starts at 2s and ends at 29s, when the laser is switched on. Subsequent tourmaline ablation starts at 34s and ends at 90s. (A) Most tourmaline grains present smooth LA-ICP-MS spectral signals to the spot analysis of WT12WH20-3-1, and the chosen interval for data reduction varies from 40s to 85s. (B) Spot analysis of tourmaline WT12WH33-2-1-1 shows spiked spectra between 73s and 80s, due to ablating of a solid inclusion containing higher Th, Ce, U, Pb and Bi concentrations in tourmaline. In this case, the interval for data reduction was selected from 40s to 71s, avoiding the interference of the solid inclusion**.**

tourmalines were mostly stable, and thus these spectra were typically chosen to start at 40s and end at 85s during data reduction (Fig. 5.3A). In some cases, solid or fluid inclusions in tourmalines were accidently ablated. These spectra have anomalous spikes that were avoided during data processing (Fig. 5.3B). Only three analyses were rejected due to contamination by inclusions from a total of 135 LA-ICP-MS analyses of tourmaline. Detection limits for most trace elements were in the range of 0.01 to 0.5 ppm, depending on

the element. For some specific elements, the detection limits were typically higher, e.g., 1 ppm for Be, 2 ppm for Cr, 0.68 ppm for Ni, 0.8 ppm for Zn, 1 ppm for Cu, 1.2 ppm for As. Li, Ga, Zn, Sn, Sc, Ta, Co, V, Nb, and Ce have average analytical errors below 10 % RSD (1 σ), and Be, P, Pb, Sr, La and Pr between 10 and 24 % RSD (1 σ). The analytical errors of other elements on average exceed 30 %, up to 100 % RSD (1 σ), and their values are mostly below detection limits (Table 5.4).

5.3 Analytical results

5.3.1 Backscattered images of tourmaline growth zones

Tourmaline typically displays distinct optical and chemical zonation patterns that can record compositional information pertinent to the melts or fluids from which it precipitated (van Hinsberg et al., 2011a). Optical zoning of tourmaline that can be easily discerned by an optical microscope has only been observed in this study from the tourmaline-filled miarolitic textures from the western Tasmanian granites (Figs. 4.5E, F). Compositional zoning patterns in all varieties of tourmalines have been revealed and investigated in scanning electron microscope-backscattered electron (SEM-BSE) images. In general, three types of compositional zones have been recognised: 1) oscillatory zoning, 2) concentric zoning, and 3) radial zoning (Fig. 5.4). Hourglass zones in sections parallel to the c-axis described in metamorphic tourmaline (e.g., van Hinsberg et al., 2006) are absent in the tourmalines from western Tasmanian granites.

Oscillatory zoning patterns have mainly been identified in tourmaline grains from cavities and veins. This type of zoning typically defines a dull grey core rimmed by bright, alternating intergrowths in SEM images (Figs. 5.4A-D). In contrast, concentric zoning patterns are defined by a simple dull grey core surrounded by a bright rim, in which alternating growth zones are absent (Figs. 5.4E-G). Concentric growth zones have been observed in all of the tourmaline-rich textures (e.g., cavities, veins, patches, and orbicules). Minor radial zoning patterns (Figs. 5.4H, I) have been detected in tourmaline from orbicules and patches. The radial zones are defined by light-colour laths intergrown with dark grey-colour laths. Radial zoning is somewhat similar to the bright and dark grey rims of oscillatory zoned tourmaline. These compositional zoning patterns are influenced by the orientations of the section cut through individual tourmaline crystals (cf. van Hinsberg et al., 2006). The oscillatory zoning and concentric zoning patterns are apparent on planes perpendicular or parallel to the c-axis, whereas radial zoning patterns are largely observed in sections oblique to the long (c) axis. Since sections perpendicular or parallel to the c axis are the best planes to depict the zoning features of tourmalines, concentric and oscillatory zoning patterns are considered to be most indicative of the compositional zones of tourmaline crystals in the western Tasmanian granites.

Qualitative element maps collected by field emission SEM show concentric and oscillatory zoning patterns comparable to those detected via BSE imaging. These maps have revealed three categories of major element distributions in planes perpendicular or parallel to the c-axis. Most tourmaline cores are enriched in Al and Si, whereas the rims are generally dominated by Fe, Mg, Na and Ti (Figs. 5.5A-D). The oscillatory rims are typically characterised by Fe alternating with Mg (and Al in places). A few tourmaline grains from veins within the Pieman Heads Granite have a Fe (-Al)-rich core and Mg (-Na-Ti)-rich rims

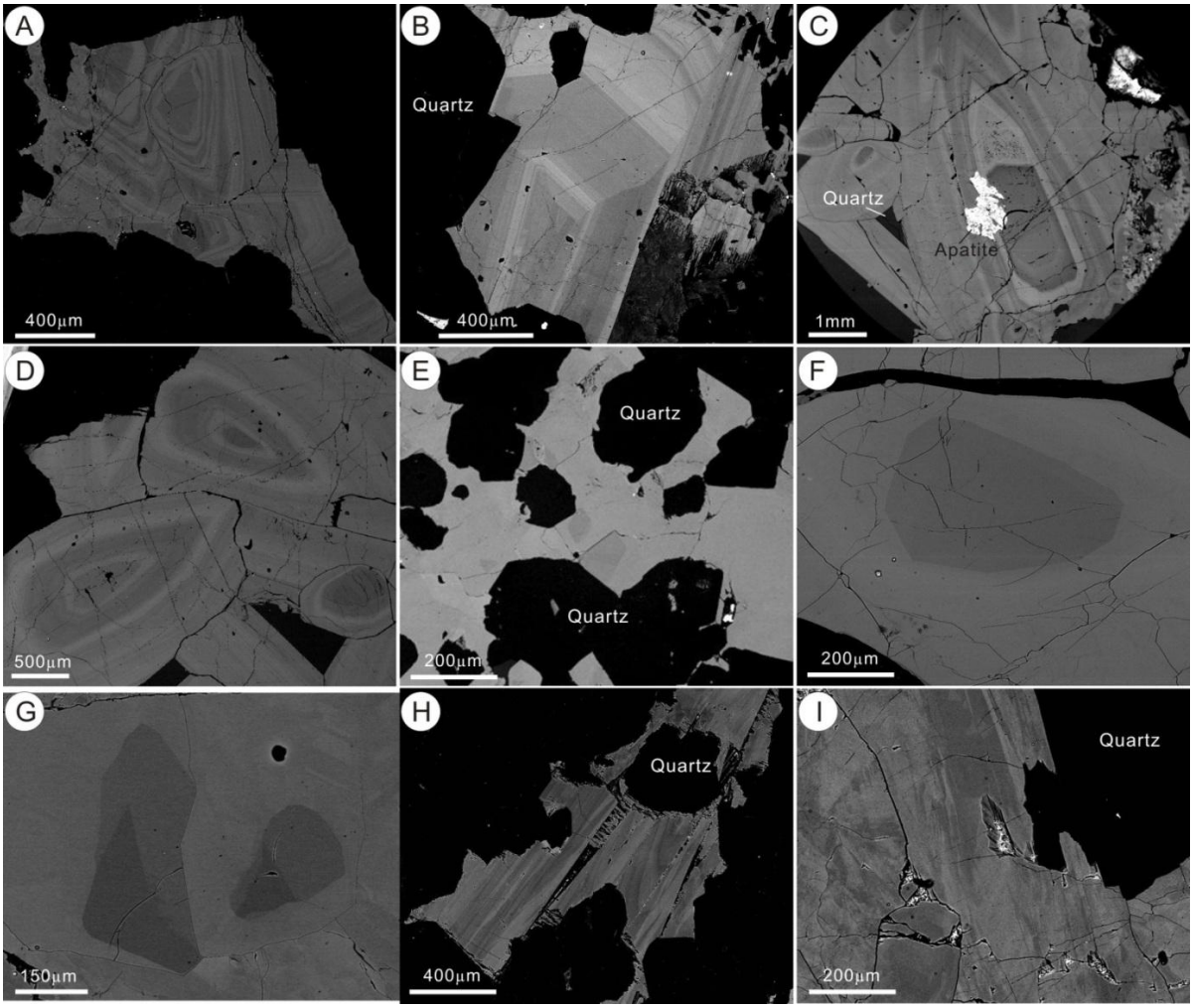

Figure 5.4 Representative BSE images show distinct growth zonations in tourmaline from the western Tasmanian granites. Oscillatory zoning is commonly identified in tourmalines in cavities (A, B, Sample WT12WH35) from Granville Harbour, Heemskirk Batholith, and tourmalines in veins (C, D, Sample WT12WH13-1) from the Pieman Heads Granite. Concentric zoning is typically discerned in tourmalines from orbicules (E, Sample WT12WH28-3) at Trial Harbour, Heemskirk Batholith, as veins (F, Sample WT12WH13-1) from the Pieman Heads Granite, and from patches (G, Sample WT12WH20) at Trial Harbour. Radial zoning is mainly observed in tourmaline hosted in orbicules (H, I, Sample WT12WH28-4) from Trial Harbour. Most grains are sectioned in a plane perpendicular or parallel to the c-axis except for the Tourmaline grain (B, H or I) oblique to the c-axis. Detailed descriptions of these compositional zones in tourmaline are provided in the text.

Figure 5.5 (next page) Representative qualitative element maps for tourmaline grains showing typical core-rim compositional patterns in patches (A, Sample WT12WH20), tourmaline-filled miarolitic textures (B, Sample WT12WH24-2; C, Sample WT12WH24-3) from Trial Harbour, Heemskirk Batholith, and in veins (D-F, Sample WT12WH13) from the Pieman Heads Granite. Most tourmaline grains are sectioned perpendicular to the c-axis, whereas the grain in (F) has been cut parallel to the c-axis. The brighter area represents the higher concentration of the element. Three types of major element distribution patterns are illustrated through the qualitative maps of tourmaline grains. In most tourmaline crystals (A-D), the Al-and Si-rich cores are surrounded by Fe, Mg, Na and Ti-rich rims in which Fe is normally alternated with Mg (or rarely Al). The tourmaline grain (E) associated with muscovite in a quartz vein has a Fe- and Al-rich core which is rimmed by Mg, and minor Na and Ti. An anomalous Mn- and Al-rich core is recognised in a tourmaline grain from a quartz vein at Pieman Heads (F). An apatite inclusion occurs at the boundary between the core and a Fe-rich inner rim, which have subsequently been enclosed by an Mg-rich outer rim.

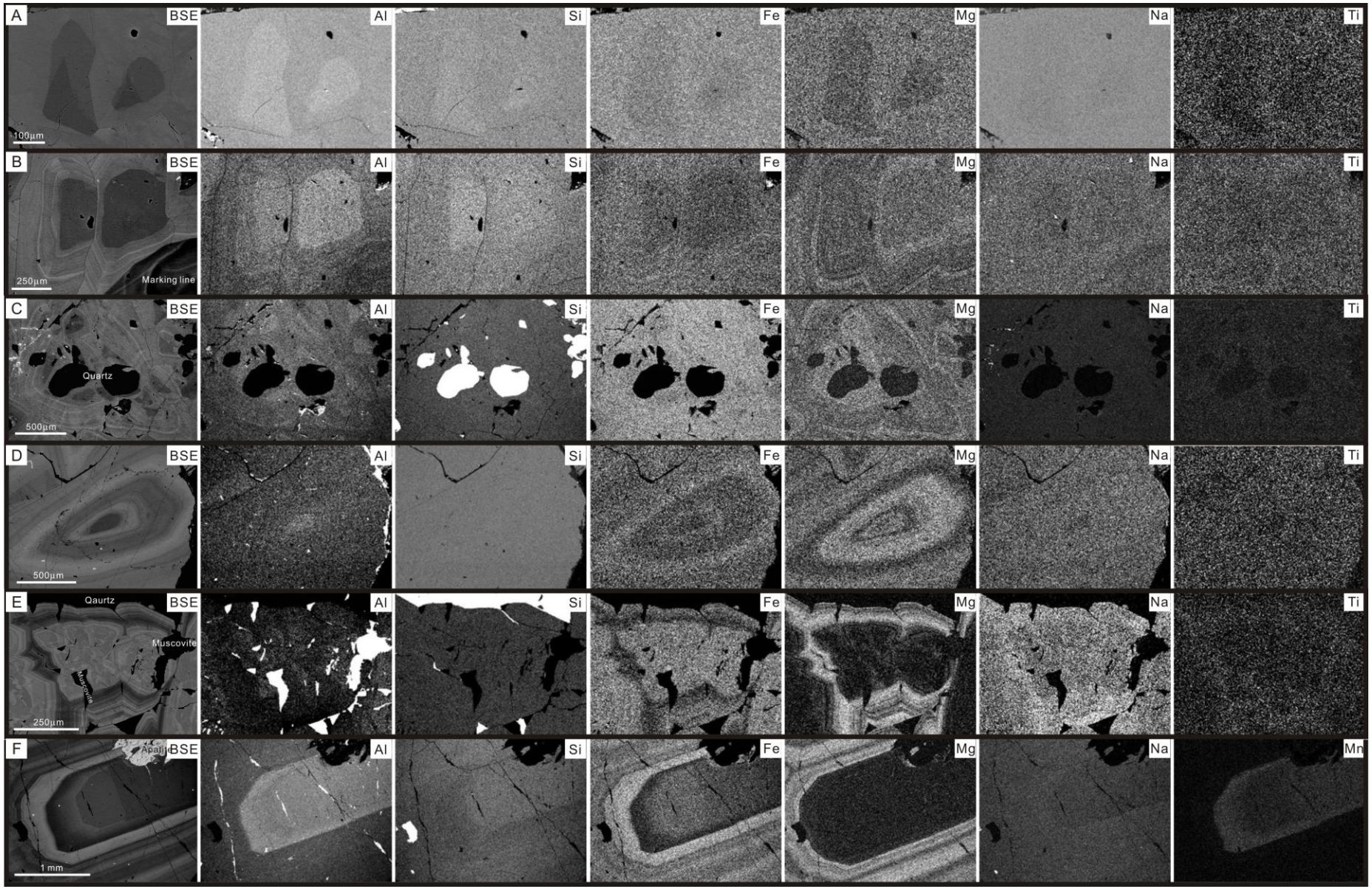
A
BSE
Al
Si
Fe
Mg
Na
Ti
100µm
B
BSE
Al
Si
Fe
Mg
Na
Ti
250µm
Marking line
C
BSE
Al
Si
Fe
Mg
Na
Ti
Quartz
500µm
D
BSE
Al
Si
Fe
Mg
Na
Ti
500µm
E
Qaurtz
BSE
Al
Si
Fe
Mg
Na
Ti
Muscovite
Muscovite
250µm
F
Apatite
BSE
Al
Si
Fe
Mg
Na
Mn
1 mm

(Fig. 5.5E). Quartz, muscovite and apatite inclusions can be found in these tourmaline crystals.

A unique tourmaline grain from a tourmaline vein in the Pieman Heads Granite has very distinctive compositional zones (Fig. 5.5F). The core is extremely enriched in Al and Mn, and has a diffuse boundary outwards to a Fe-rich growth zone. An anhedral apatite inclusion occurs between these two zones (Fig. 5.5F). The Fe-rich growth zone commonly surrounds the Mn-rich core, but locally the Fe-rich bands coalesce into a pyramidal core (Fig. 5.4C). The Fe-rich growth zone has been overgrown by an Mg-rich rim where minor Fe-rich bands alternate with Mg-rich bands. This growth pattern defined by a Fe-rich zone and Fe-Mg rim is similar to core-rim zoning detected in other tourmaline grains from quartz veins (e.g., Fig. 5.5E, F).

5.3.2 EMPA results

A total of 347 electron microprobe analyses have been obtained from tourmaline crystals. The average compositions of tourmalines from different locations are tabulated in Table 5.2, and the detailed results for each analysis are documented in Appendix 5.1. According to the nomenclature of Henry et al. (2011), most of the tourmalines belong to the alkali group with (Na+K) > 0.5 atom per formula (apfu). Only a few tourmalines are divided into the X-site vacant group with $^{\square}X \approx 0.5$ apfu (Fig. 5.6). The compositions of these tourmalines are characterised by Fe enrichment at the Y-site, and these samples plot close to the schorl field, and overlapped slightly with the foitite field, with Fe/ (Fe + Mg) and $^{\square}X$/ (Na + K + $^{\square}X$) ratios in the range of 0.65 – 1.0 and 0.18 – 0.66, respectively (Figs. 5.6A, D). The Z-site is entirely occupied by Al, with six apfu. Both Si and Al are accommodated at the T-site, in which Si is dominated with 5.32 – 5.81 apfu among total six apfu (Appendix 5.1). The average mole fractions of end-member compositions of tourmalines from the Heemskirk and Pieman Heads granites are tabulated in Table 5.3, and were calculated using the Excel spreadsheet of Morgan (2016).

5.3.2.1 Heemskirk Batholith

Tourmalines analysed from Trial Harbour were taken from patches, orbicules, cavities and veins, whilst only tourmalines from orbicules and cavities were analysed from Granville Harbour samples. Tourmaline grains in the Heemskirk Granite at Trial Harbour and Granville Harbour display mean mole fractions of end-member components of $schorl_{51}$ $dravite_4$ $Fe\text{-}uvite_3$ $foitite_{30}$ $Mg\text{-}foitite_2$ $olenite_8$ and $schorl_{46}$ $dravite_6$ $Fe\text{-}uvite_3$ $foitite_{31}$ $Mg\text{-}foitite_4$ $olenite_9$ (Table 5.3), respectively. The tourmalines all have similar compositions, with Fe/ (Fe + Mg) ratios (abbreviated as #Fe) ranging from 0.82 to 1.0 (Fig. 5.6A), indicating that Fe is dominantly hosted in the Y-site. Tourmaline grains at Granville Harbour have lower #Fe values than tourmalines from equivalent textures at Trial Harbour (Fig. 5.6A); however, Al, Na, Ti and F have similar concentrations from both sites (Figs. 5.6, 5.7).

The comparatively linear relationship in the Mg-Fe plot (Fig. 5.7A; $r^2 = 0.22$) indicates that schorl-dravite substitution is prevailing in the Heemskirk tourmalines ($FeMg_{-1}$ vector; Henry et al., 2011). The values of $\sum$ (Fe + Mg) < 3 apfu suggest that substantial accounts of Al (up to 0.72 apfu) have been incorporated into the Y-site. Based on the total Al versus $^{\square}X$ (apfu) plot (Fig. 5.7C), Al^{3+} is supposed to

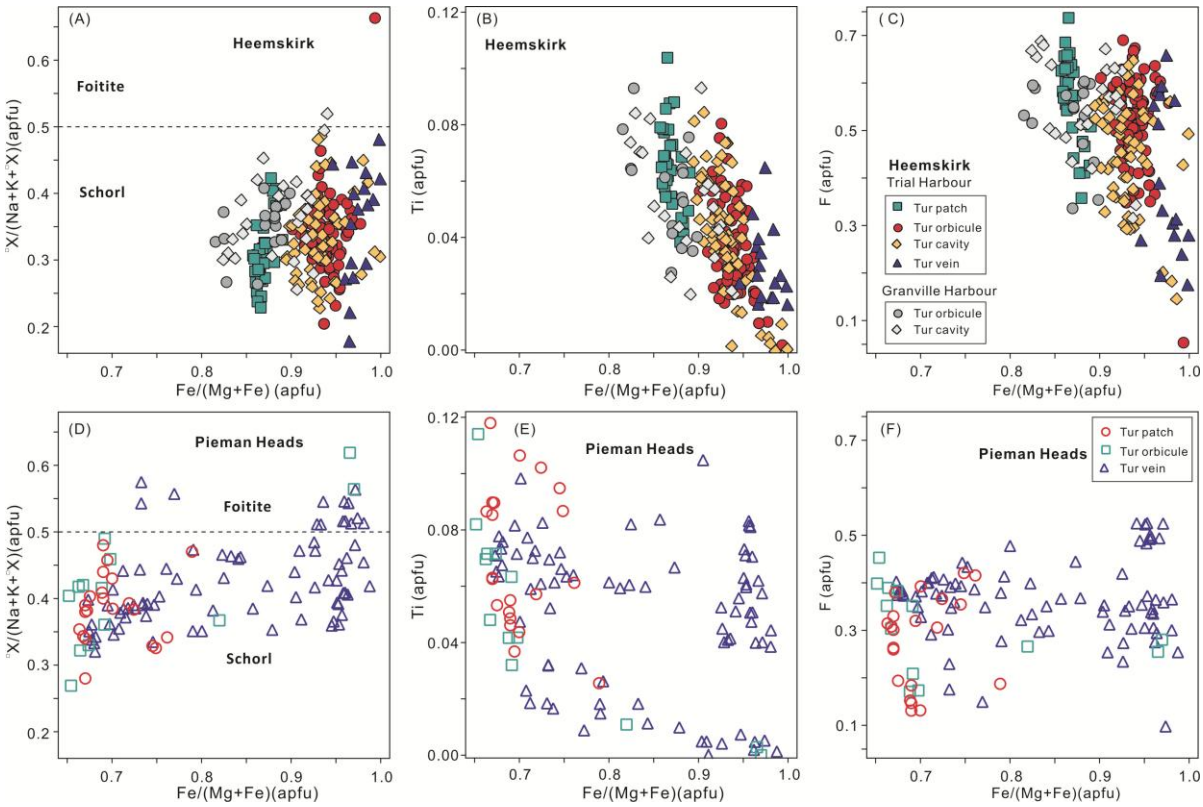

Figure 5.6 Selected binary plots showing the compositional variations of tourmalines from the Heemskirk Batholith (A, B, C), and from the Pieman Heads Granite (D, E, F). $^{\square}$X represent the proportions of vacancies at X-site. Tur = tourmaline.

substitute for Fe^{2+} (and minor Mg^{2+}, Mn^{2+}) at the Y-site, with a vacant X-site maintaining the charge balance. This substitution relates to the vector $^{Y}Al^{\square X}(R^{2+}Na)_{-1}$ where R^{2+} = (Fe + Mg + Mn); this is known as the foitite exchange (Henry et al., 2011). A number of deviations from the foitite exchange trend are apparent in the total Al versus $^{\square}$X plot (Fig. 5.7C). According to previous studies (Trumbull et al., 2008; Henry et al., 2011; Pesquera et al., 2013), the subtle diversion from foitite exchange in the Al^{tot} -$^{\square}$X plot accounts for the olenite substitution, expressed as the vector $^{Y}AlO(R^{2+}OH)_{-1}$.

Tourmalines from Heemskirk Batholith contain minor Ti and F contents at the Y-site (0.01 – 0.10 apfu) and at the W-site (0.05 – 0.74 apfu), respectively (Appendix 5.1). Titanium values decrease strongly with increasing #Fe values (r^2 = 0.457; Fig. 5.6 B); this appears to be controlled by the $FeTi_{-1}$ replacement. Fluorine contents have a poor negative correlation with #Fe values (r^2 = 0.167; Fig. 5.6 C), and a strong negative trend with ^{Y}Al (r^2 = 0.444). Correspondingly, F contents tend to increase strongly with rising Na (r^2 = 0.431), and gently with increasing Ti (r^2 = 0.331), Mg (r^2 = 0.204) and Ca (r^2 = 0.293). Negative correlations between Fe and F, and positive correlations between Mg, Ti and F (Fig. 5.6) probably relate to the differences of fluid compositions during the precipitation of tourmaline. Manganese, Ca and K are minor components of tourmalines from the Heemskirk Batholith, generally lower than 0.05 apfu (Appendix 5.1).

There are some chemical variations between tourmalines from different textures at Trial Harbour (Figs. 5.6, 5.7). Tourmalines in patches have the lowest #Fe values (average 0.87), whereas the highest values were observed from tourmaline veins, and the tourmalines in orbicules and cavities have inter-

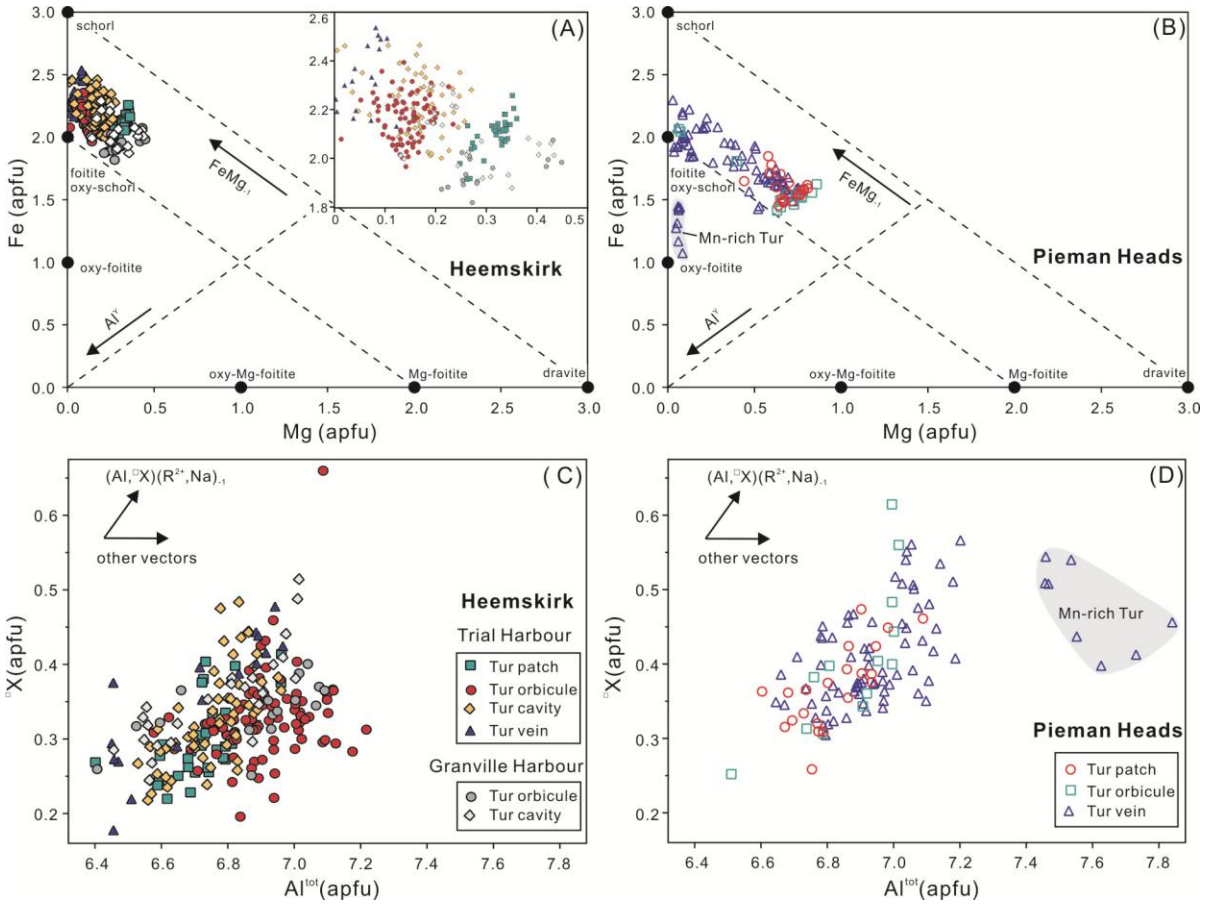

Figure 5.7 Binary plots showing main exchange vectors and compositional variations in tourmalines from the Heemskirk Batholith (A, C), and from the Pieman Heads Granite (B, D). R^{2+}= Fe + Mg + Mn, and Fe rich in R^{2+}. Tur = tourmaline.

mediate values (average 0.94 and 0.93, respectively; Table 5.2). Tourmalines in orbicules and cavities from Granville Harbour have similar #Fe values (average 0.87 and 0.88, respectively; Table 5.2). Titanium contents decrease steadily from tourmaline patches (average 0.07 apfu), orbicules (average 0.04 apfu), through cavities (average 0.04 apfu), to veins (average 0.03 apfu), although their compositional fields overlap partially (Fig. 5.6B). Fluorine contents also display clear variations between different tourmaline-rich textures (Fig. 5.6C). Fluorine tends to have higher concentrations in tourmaline patches (0.36 – 0.74 apfu) than in tourmaline veins at Trial Harbour (0.18 – 0.66 apfu). The Al and Na contents in tourmaline from different textures largely overlap (Figs. 5.6A, 5.7C). However, Na is slightly enriched in tourmaline patches, whereas tourmalines in orbicules and cavities have more Al incorporated into the Y-site (Table 5.2). Overall, tourmalines in patches and veins generally have contrasting compositions. The major element compositions of tourmaline from orbicules and cavities are intermediate to the end-member components defined by patches and veins.

In a zoned tourmaline orbicule (WT12WH28; ca.10 cm in diameter), the Mg contents in tourmalines have a wider range in the rim (0.01 – 0.23 apfu) than in the core (0.10 – 0.2 apfu). In the same sample, Fe contents show larger variability in the core than in the rim. In general, the cores of tourmaline orbicules appear to be slightly enriched in Fe, Ti, Na and F, and depleted in Al, Mg and Ca, relative to the rims (Fig. 5.8; Appendix 5.1). These analytical results explain that the differences in pleochroism of tourmalines vary

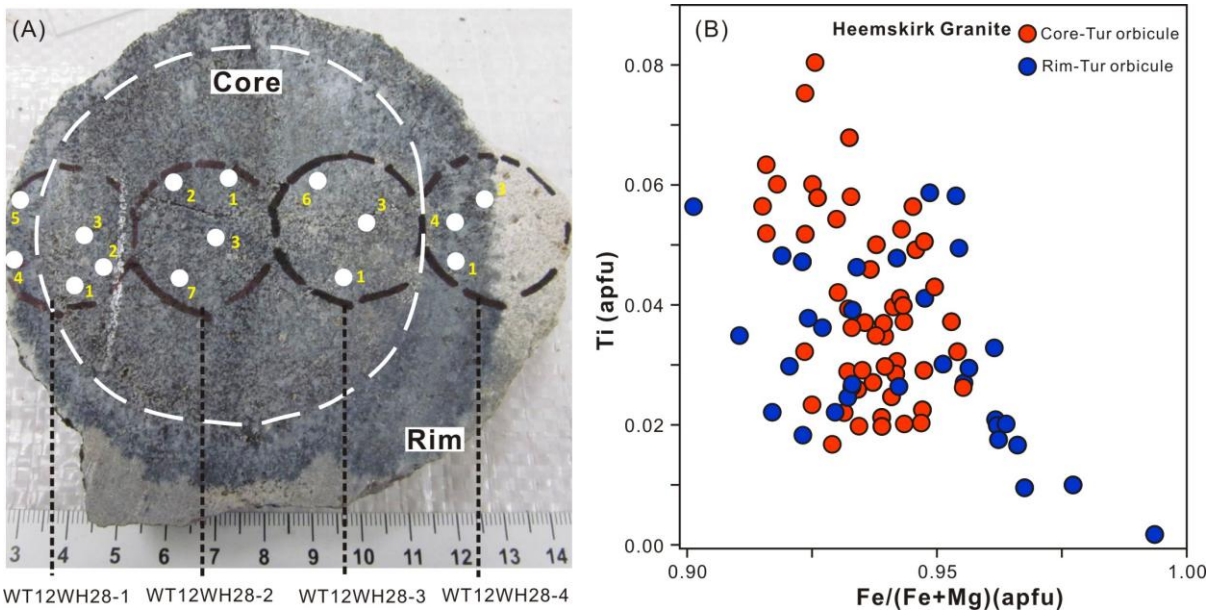

Figure 5.8 A zoned tourmaline orbicule from the Trial Harbour, Heemskirk Granite. (A) Features of the zoned tourmaline orbicule, and analysed EMPA sites are marked in the photo. These labelled numbers are paired with those in Appendix 5.1. (B) Fe/ (Fe + Mg) versus Ti plot showing chemical variations in tourmaline across different zones of the orbicule. Tur = tourmaline.

from greenish (Mg-rich) in the rim to yellow-brownish (Fe-rich) in the core (Fig. 4.4, 5.8).

5.3.2.1 Pieman Heads Granite

Compared with tourmalines from the Heemskirk Batholith, tourmalines associated with the Pieman Heads Granite are relatively enriched in Mg and depleted in Fe, and have a wider range of # Fe values (0.65 – 0.99; Appendix 5.1). These tourmalines possess an average mole fraction of end-member compositions of $schorl_{35}$ $dravite_{9}$ $Fe\text{-}uvite_{2}$ $foitite_{32}$ $Mg\text{-}foitite_{8}$ $olenite_{11}$ (Table 5.3). Na contents in tourmaline from this pluton are less than in tourmaline from the Heemskirk Batholith, implying that there are greater degrees of vacancies at the X-site of tourmaline from Pieman Heads. Correspondingly, more of the tourmalines have been classified as foitites on the Fe/ (Fe + Mg) and $^{\square}X$/ (Na + K + $^{\square}X$) diagram (Fig. 5.6D), with some classified as parts of the oxy-foitite group (Fig. 5.7B). According to the Mg versus Fe and total Al versus $^{\square}X$ plots (Figs. 5.7B, D), the compositional variations of tourmalines from the Pieman Heads Granite are jointly constrained by $FeMg_{-1}$, $^{Y}Al^{\square}X(R^{2+}Na)_{-1}$, and minor $^{Y}AlO(R^{2+}OH)_{-1}$ substitution mechanisms.

Some tourmalines in veins at Pieman Heads have moderately deviated from the known exchange vectors above (Figs. 5.7B, D). These anomalous tourmalines exhibit extraordinary enrichment of Mn contents (0.19 – 0.34 apfu), approximately one order of magnitude higher than all other tourmalines analysed in this study (generally Mn < 0.05 apfu; Fig. 5.9; Appendix 5.1). This indicates the existence of additional exchange mechanism, such as a $FeMn_{-1}$ vector, in order to explain the occurrences of these tourmalines. In addition to extremely high Mn, the anomalous tourmalines are also characterised by comparatively higher ^{Y}Al (nearly 1 apfu), with substantial depletion of Fe (~1.5 apfu) and Mg (< 0.1 apfu). These uncommon componential trends imply distinct fluid compositions, particularly enriched in Mn and

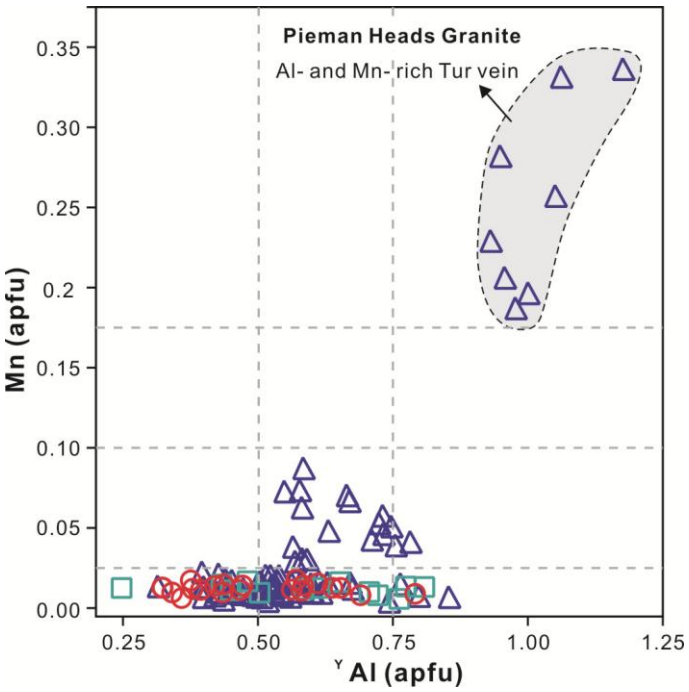

Figure 5.9 ^{Y}Al versus Mn plot shows the extremely Mn- and Al-rich tourmalines from veins associated within the Pieman Heads Granite. Symbols are same as those in Fig. 5.6. The tourmalines have extraordinary enrichment of Mn (0.19 – 0.34 apfu), much higher than other tourmaline grains (generally Mn < 0.05 apfu). Tur = tourmaline.

Al contents.

Ti contents in tourmalines from the Pieman Heads Granite (~0.01 – 0.12 apfu) have a similar range to those in the Heemskirk Batholith (Figs. 5.6).Titanium in most tourmalines (except for the Mn-rich samples) appears to correlate negatively with increasing #Fe values (Fig. 5.6E; r^2 = 0.175). Fluorine contents in tourmalines associated with the Pieman Heads Granite are lower than in tourmalines from the Heemskirk Batholith (average = 0.34, 0.51 apfu, respectively). There are no clear correlations between F and Fe/ (Fe + Mg) ratios in the tourmalines from the Pieman Heads Granite (Fig. 5.6F). However, F contents increase systematically with increasing Na (r^2 = 0.167), Fe (r^2 = 0.076) and Ti (r^2 = 0.191) in tourmalines (Appendix 5.1), and decrease slightly with increasing ^{Y}Al (r^2 = 0.107), as also noted for the Heemskirk Batholith.

Tourmalines at Pieman Heads have slight compositional variations between different types of tourmaline-rich textures. Tourmaline in patches tends to have the highest Mg and Ti, and the lowest Fe, whereas tourmaline in veins has the highest Fe, and lowest Mg and Ti concentrations (Figs. 5.6, 5.7). The average #Fe values of tourmalines increase from patches (0.73), through orbicules (0.70), to veins (0.84). Most of the major elements in tourmaline from orbicules have similar concentrations to those from patches, but have much lower Fe and Al, or higher Mg and Ti concentrations than tourmaline from veins at Pieman Heads.

Tourmaline crystals in veins from Pieman Heads have relatively complex major elemental compositions, highlighted by the extreme Mn and Al concentrations in some tourmaline grains (Fig. 5.9). In addition to higher #Fe values, the Mn-rich tourmalines contain higher Ti than other tourmaline in veins (Fig. 5.6E). Fluorine contents are similar between the patches, orbicules and veins, but the Mn-rich tourmalines in veins tend to contain more F (nearly 0.5 apfu) relative to other tourmalines (Fig. 5.6F).

Table 5.2 Average major element compositions of tourmalines from the Heemskirk and Pieman Heads granites, analysed by EMPA

Location	Trial Harbour, Heemskirk								Granville Harbour, Heemskirk				Pieman Heads Granite					
Feature	Patch (n=34)		Orbicule (n=85)		Cavity (n=57)		Vein (n=17)		Orbicule (n=16)		Cavity (n=24)		Patch (n=13)		Orbicule (n=21)		Vein (n=80)	
	Av.	SD	Av.	SD	Av.	SD	Av.	SD	Av.	SD	Av.	SD	Av.	SD	Av.	SD	Av.	SD
SiO_2 wt%	33.07	0.38	32.87	0.52	33.03	0.48	33.99	0.29	33.70	0.53	33.76	0.38	34.57	0.26	34.02	0.42	33.35	0.56
TiO_2	0.51	0.11	0.29	0.12	0.33	0.17	0.24	0.10	0.45	0.14	0.42	0.16	0.40	0.27	0.56	0.20	0.39	0.21
Al_2O_3	33.56	0.65	34.47	0.73	33.44	0.72	33.63	1.21	34.84	1.20	34.16	1.06	35.26	0.78	34.72	0.77	35.29	1.38
FeO	14.77	0.47	15.21	0.58	15.61	0.77	16.48	0.87	13.91	0.43	14.81	0.79	11.70	1.49	11.41	0.72	12.52	1.71
MgO	1.25	0.12	0.56	0.15	0.65	0.23	0.25	0.14	1.22	0.31	1.09	0.36	2.46	1.08	2.75	0.36	1.45	1.03
CaO	0.17	0.06	0.19	0.08	0.19	0.09	0.07	0.02	0.21	0.06	0.18	0.05	0.20	0.11	0.26	0.09	0.13	0.08
MnO	0.16	0.03	0.14	0.06	0.08	0.03	0.10	0.02	0.14	0.05	0.11	0.03	0.09	0.02	0.09	0.02	0.33	0.53
Na_2O	1.99	0.13	1.90	0.15	1.88	0.15	1.91	0.25	1.90	0.11	1.86	0.18	1.72	0.27	1.78	0.12	1.69	0.17
K_2O	0.05	0.02	0.05	0.02	0.04	0.02	0.04	0.01	0.05	0.02	0.04	0.01	0.04	0.01	0.05	0.02	0.03	0.02
F	1.05	0.16	0.97	0.18	0.84	0.21	0.75	0.30	0.99	0.16	1.05	0.19	0.59	0.17	0.53	0.18	0.68	0.15
*H_2O	2.99	0.09	3.04	0.09	3.07	0.12	3.17	0.17	3.09	0.09	3.04	0.11	3.33	0.09	3.32	0.10	3.21	0.09
*B_2O_3	10.13	0.06	10.13	0.07	10.06	0.08	10.21	0.11	10.31	0.07	10.26	0.09	10.46	0.07	10.36	0.08	10.24	0.08
Total	99.71	0.45	99.82	0.56	99.24	0.45	100.83	0.50	100.80	0.53	100.77	0.49	100.81	0.38	99.84	0.72	99.32	0.47
Si (T) [§]apfu	5.68	0.05	5.64	0.07	5.71	0.05	5.78	0.03	5.68	0.09	5.72	0.05	5.74	0.04	5.71	0.04	5.66	0.09
Al (T)	0.32	0.05	0.36	0.07	0.29	0.05	0.22	0.03	0.32	0.09	0.28	0.05	0.26	0.04	0.29	0.04	0.34	0.09
Al (Z)	6.00	0.00	6.00	0.00	6.00	0.00	6.00	0.00	6.00	0.00	6.00	0.00	6.00	0.00	6.00	0.00	6.00	0.00
Al (Y)	0.46	0.10	0.60	0.10	0.51	0.11	0.53	0.16	0.60	0.14	0.54	0.14	0.64	0.15	0.58	0.12	0.72	0.18
Ti (Y)	0.07	0.01	0.04	0.02	0.04	0.02	0.03	0.01	0.06	0.02	0.05	0.02	0.05	0.03	0.07	0.03	0.05	0.03
Mg (Y)	0.32	0.03	0.14	0.04	0.17	0.06	0.06	0.04	0.31	0.08	0.28	0.09	0.61	0.27	0.69	0.09	0.37	0.26
Mn (Y)	0.02	0.00	0.02	0.01	0.01	0.00	0.01	0.00	0.02	0.01	0.02	0.00	0.01	0.00	0.01	0.00	0.05	0.08
Fe (Y)	2.12	0.08	2.18	0.09	2.26	0.13	2.35	0.15	1.96	0.07	2.10	0.13	1.63	0.22	1.60	0.10	1.78	0.25
Ca (X)	0.03	0.01	0.04	0.01	0.03	0.02	0.01	0.00	0.04	0.01	0.03	0.01	0.04	0.02	0.05	0.02	0.02	0.01
Na (X)	0.66	0.04	0.63	0.05	0.63	0.05	0.63	0.09	0.62	0.04	0.61	0.06	0.55	0.09	0.58	0.04	0.56	0.06
K (X)	0.01	0.00	0.01	0.01	0.01	0.00	0.01	0.00	0.01	0.00	0.01	0.00	0.01	0.00	0.01	0.00	0.01	0.00
vac.(X)	0.29	0.05	0.32	0.06	0.32	0.07	0.35	0.09	0.33	0.04	0.35	0.07	0.40	0.10	0.37	0.06	0.41	0.07
F (W)	0.57	0.09	0.53	0.10	0.46	0.12	0.41	0.16	0.53	0.09	0.56	0.11	0.31	0.09	0.28	0.10	0.37	0.08
OH	3.43	0.09	3.47	0.10	3.54	0.12	3.59	0.16	3.47	0.09	3.44	0.11	3.69	0.09	3.72	0.10	3.63	0.08
B	3.00	0.00	3.00	0.00	3.00	0.00	3.00	0.00	3.00	0.00	3.00	0.00	3.00	0.00	3.00	0.00	3.00	0.00

* H_2O and * B_2O_3 calculated by stoichiometry; [§]apfu, tourmaline structure formulae calculations based on 31 anions including 15 cations at T, Z, and Y sites (Henry and Dutrow, 1996). Abbreviations: Av. = average, SD = standard deviation.

Table 5.3 Average mole fractions of end-member components for tourmalines from the Heemskirk and Pieman Heads granites

Location	Feature	Schorl	Dravite	Tsilaisite	Uvite	Fe-Uvite	Foitite	Mg-Foitite	Olenite
Trial Harbour, Heemskirk Granite	Patch	0.53	0.08	0.01	0.00	0.03	0.26	0.04	0.06
	Orbicule	0.50	0.03	0.01	0.00	0.03	0.30	0.02	0.10
	Cavity	0.53	0.04	0.00	0.00	0.03	0.30	0.02	0.07
	Vein	0.55	0.01	0.00	0.00	0.01	0.34	0.01	0.07
	Mean	0.51	0.04	0.01	0.00	0.03	0.30	0.02	0.08
Granville Harbour, Heemskirk Granite	Orbicule	0.45	0.07	0.01	0.01	0.03	0.29	0.04	0.11
	Cavity	0.48	0.06	0.01	0.00	0.03	0.31	0.04	0.07
	Mean	0.46	0.06	0.01	0.00	0.03	0.31	0.04	0.09
Pieman Heads Granite	Patch	0.34	0.12	0.00	0.01	0.03	0.29	0.11	0.10
	Orbicule	0.35	0.14	0.00	0.01	0.03	0.26	0.11	0.09
	Vein	0.36	0.07	0.02	0.00	0.02	0.34	0.07	0.12
	Mean	0.35	0.09	0.01	0.01	0.02	0.32	0.08	0.11

5.3.3 LA-ICP-MS analyses

In this study, more than 40 trace elements in tourmaline from the western Tasmanian granites have been determined by LA-ICP-MS at CODES, UTAS. The ranges and medians of these elements are documented in Table 5.4, whereas the detailed data for each analysis are tabulated in Appendix 5.2. The median concentrations for most trace elements fall with the range of 0.1 to 10 ppm. Lithium, Zn and Ga have the highest median concentrations amongst these elements, up to hundreds of ppm. Vanadium, P, Sc, V, Co and Sn show median values of tens of ppm. Chromium, Ni, Ta, Nb, Sr, Pb and light REEs have median concentrations of several ppm, whereas heavy REEs, Rb, Y, Mo, Cs, Sb, Ba, Hf, W, Au, Bi, Th and U all have median concentrations < 1 ppm (Table 5.4). Many trace elements have large variations in concentrations, over several orders of magnitude (Table 5.4; Fig. 5.10). Anomalous spikes of Au are mostly due to remnants of Au-coating from the SIMS B-isotope analyses. A number of trace elements have concentrations below detection limit (bdl), and the numbers of analyses of bdl vary between 0 and 96 % (Table 5.4).

Lithium and Be concentrations in tourmalines from the Pieman Heads Granite tend to have a broader range than in tourmalines from the Heemskirk Batholith, although tourmalines in the Heemskirk Batholith have higher average Li and Be contents (Fig. 5.10). The tourmalines at Granville Harbour have Li and Be contents have the narrowest range (74.64 – 154.3 ppm) but the highest median (131.4 ppm) for Li content. Most transition elements, e.g., Sc, V, Co and Ni, are preferentially enriched in tourmaline from the Pieman Heads Granite relative to tourmaline from the Heemskirk Batholith (Fig. 5.10).

The most enriched trace elements in tourmaline are Zn and Ga, up to 420 and 790 ppm, respectively (Table 5.4). They have similar average compositions in the Heemskirk and Pieman Heads granites, but the highest values for both elements are from the latter pluton. Large ion lithophile elements (LILEs) exemplified as Sr and Pb exhibit significant variations from < 1 ppm to several ppm, or rarely to tens of ppm. They are slightly depleted in tourmaline from the Heemskirk Batholith compared to the Pieman

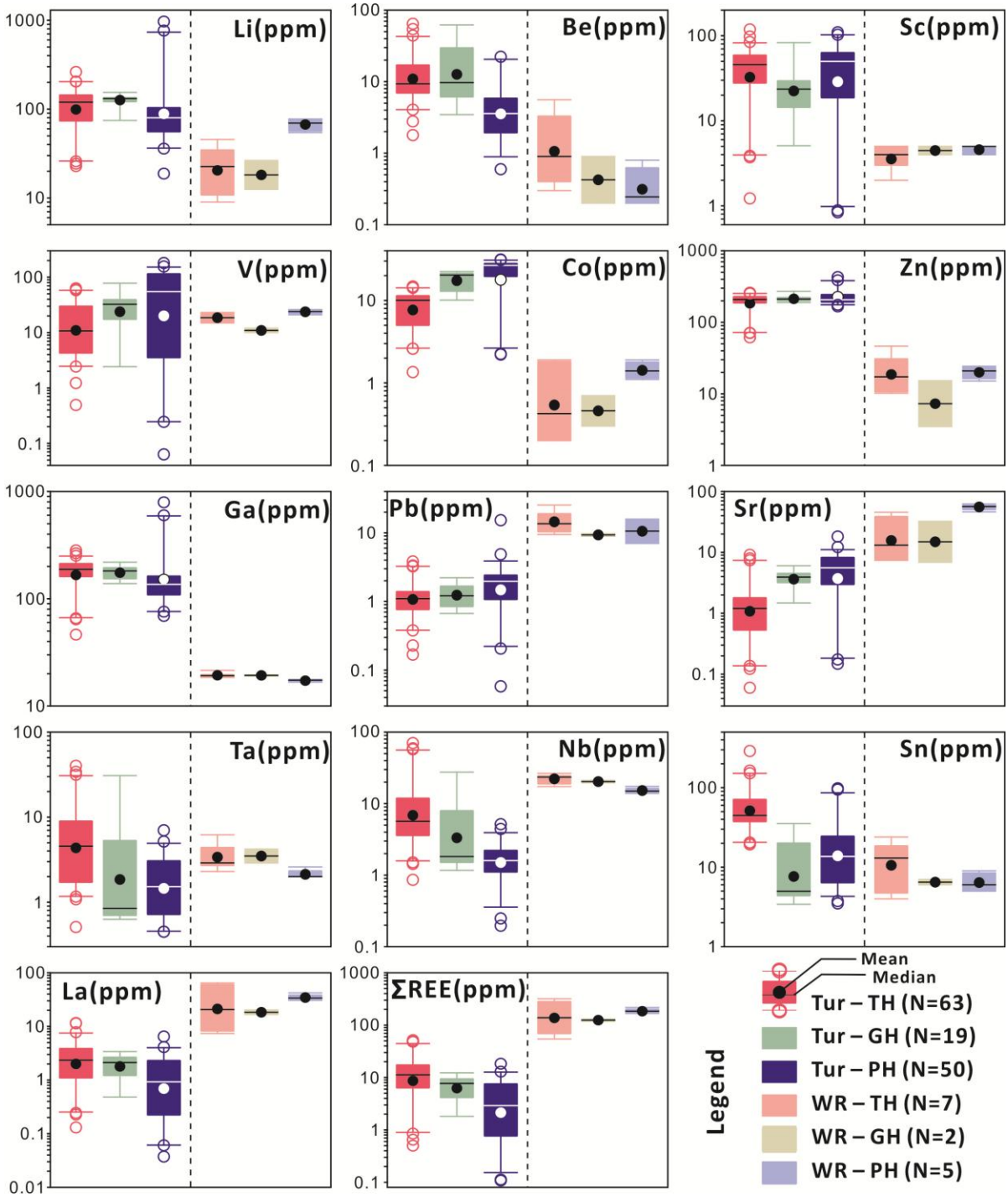

Figure 5.10 Percentile boxes and whisker plots showing comparisons of representative trace elements in tourmalines and host granites from western Tasmania. Tur = tourmaline, WR = whole rock, TH = Heemskirk Granite at Trial Harbour, GH = Heemskirk Granite at Granville Harbour, PH = Pieman Heads Granite. Tourmalines and whole rocks were analysed by LA-ICP-MS and ICP-ES/ICP-MS, respectively. Analytical numbers of each group are annotated in the brackets. The geochemical compositions of tourmaline reflect the fluids from which they precipitated. Tourmalines are preferentially enriched and depleted in special trace elements compared to their host rocks, such as Li, Be Sn, Sc, V, Co, Zn and Ga enriched and Pb, Sr, Ta, Nb and REEs depleted in tourmaline.

Heads Granite. Most rare earth elements (REEs) were undetectable in tourmaline grains, except for La, Ce, Pr and Nd (Table 5.4; Fig. 5.10). These REEs are typically enriched in tourmaline from the Heemskirk Batholith relative to the Pieman Heads Granite. Similarly, high field strength elements (HFSEs), such as

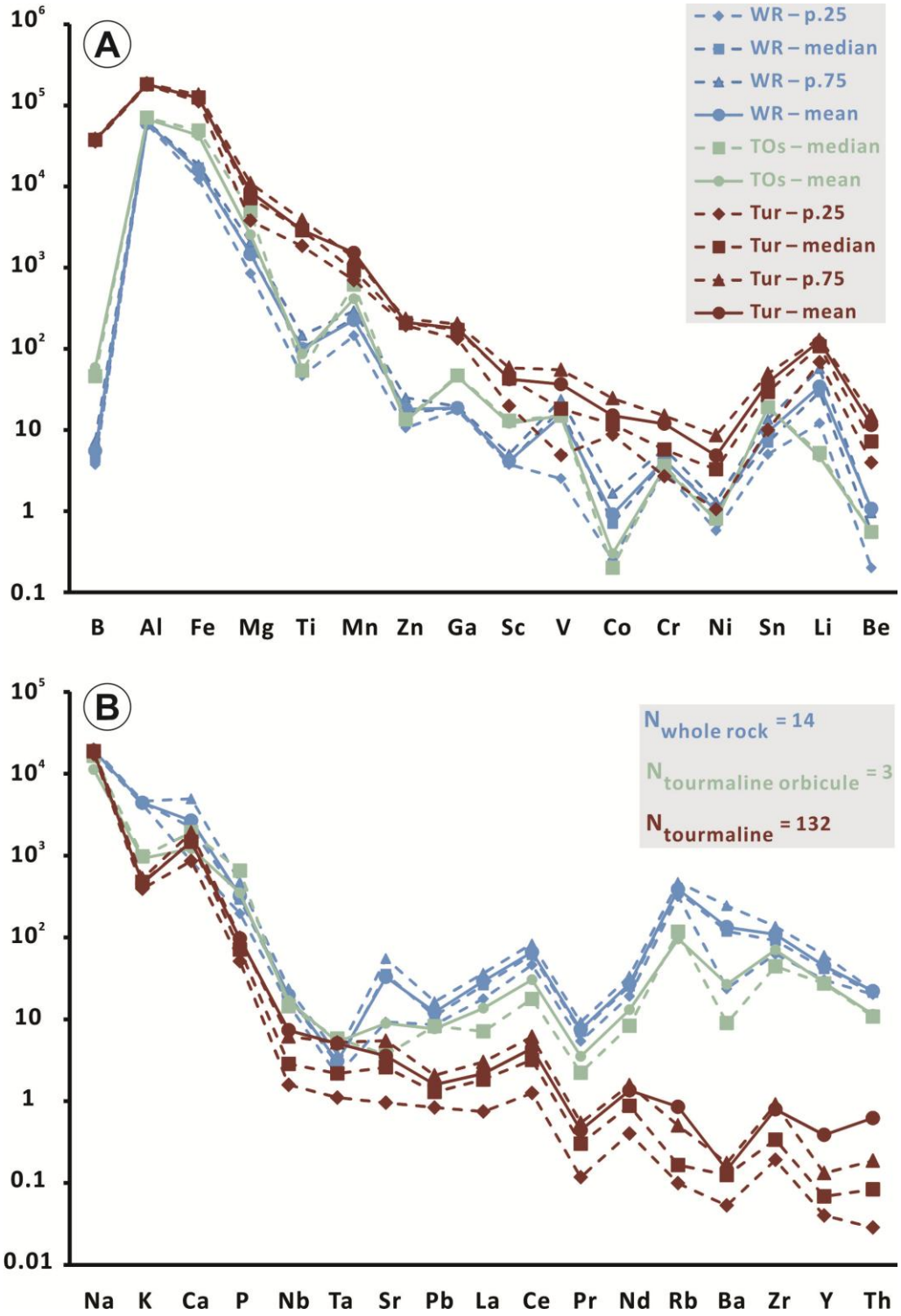

Figure 5.11 Comparisons of whole-rock, tourmaline orbicule and tourmaline LA-ICP-MS geochemical data, showing mean, median, 25th and 75th percentile results. (A) Elements that are preferentially incorporated in tourmaline. (B) Elements that are relatively depleted in tourmaline relative to the host granites. Note that transition elements (e.g., Zn, Co), Li, Be and Sn are relatively enriched in tourmaline, whereas Sr, Pb, Rb, Ba, Zr, Th and rare earth elements are depleted in tourmaline by several orders of magnitude relative to the host granites. WR = whole rock, TOs = tourmaline orbicules, Tur = tourmaline.

Ta, Nb (Zr, Hf and Th), have consistently higher concentrations in tourmaline from the Heemskirk Batholith (Table 5.4; Fig. 5.10).

Table 5.4 Summary of trace element compositions of tourmalines from the Heemskirk and Pieman Heads granites, analysed by LA-ICP-MS

	Heemskirk Batholith			Heemskirk Batholith			Pieman Heads Granite (n=50)		
	Trial Harbour (n=63)			Granville Harbour (n=19)					
Elements	Range	Median	% bdl	Range	Median	% bdl	Range	Median	% bdl
Li	22.82 - 262.3	119.8	0	74.64 - 154.3	131.4	0	18.80 - 968.4	79.83	0
Be	1.79 - 64.51	9.36	2	3.46 - 62.09	9.71	0	0.89 - 22.32	3.69	24
P	40.69 - 512.1	81.49	25	41.37 - 284.7	73.11	26	48.15 - 189.1	81.59	22
Sc	1.22 - 118.6	45.61	0	5.10 - 83.10	23.63	0	0.84 - 109.9	49.92	0
V	0.49 - 62.97	10.73	3	2.42 - 78.04	32.49	0	0.24 - 180.6	60.51	4
Cr	0.23 - 19.29	7.9	60	2.59 - 74.28	20.75	5	1.05 - 40.65	6.4	60
Co	1.35 - 14.73	10.05	0	10.11 - 22.39	20.33	0	2.21 - 31.33	26.61	0
Ni	0.23 - 6.54	1.41	33	2.01 - 9.69	6.08	5	0.28 - 14.86	10.1	20
Cu	0.84 - 10.31	2.44	59	1.23 - 9.86	2.02	58	0.71 - 8.80	1.55	82
Zn	61.57 - 260.2	208.1	0	189.5 - 271.8	211.0	0	166.6 - 430.0	206.9	0
Ga	46.34 - 282.6	187.9	0	138.5 - 219.0	181.3	0	69.20 - 792.8	136.3	0
As	0.30 - 10.59	2.47	56	0.30 - 1.22	0.65	68	0.34 - 3.03	0.82	76
Rb	0.04 - 13.64	0.5	51	0.08 - 0.37	0.12	68	0.10 - 0.72	0.13	86
Sr	0.06 - 9.12	1.2	0	1.47 - 6.03	3.92	0	0.15 - 18.20	5.57	2
Y	0.01 - 8.77	0.08	27	0.02 - 0.14	0.05	47	0.01 - 0.54	0.06	42
Zr	0.12 - 6.64	0.39	5	0.03 - 1.51	0.33	21	0.02 - 3.46	0.28	24
Nb	0.86 - 70.38	5.67	0	1.17 - 27.52	1.82	0	0.20 - 5.16	1.6	0
^{95}Mo	0.08 - 1.71	0.42	57	0.09	0.09	95	0.07 - 0.44	0.16	90
^{98}Mo	0.06 - 1.34	0.32	54	0.04 - 0.12	0.08	89	0.09 - 0.31	0.24	92
Ag	0.06 - 0.09	0.07	87	0.08	0.08	95	0.03 - 0.06	0.05	96
Cd	0.21 - 4.60	0.44	87	0.19 - 0.30	0.25	89	0.13 - 0.45	0.19	86
Sn	19.33 - 289.2	44.8	0	3.42 - 35.29	4.97	0	3.50 - 98.18	13.65	0
Sb	0.10 - 1.09	0.17	81	0.19	0.19	95	0.07 - 0.19	0.16	92
Cs	0.01 - 19.38	0.16	37	0.02 - 0.26	0.05	53	0.01 - 0.69	0.11	64
Ba	0.04 - 0.80	0.1	56	0.09 - 0.24	0.13	63	0.05 - 0.75	0.16	52
La	0.13 - 11.60	2.34	0	0.48 - 3.39	2.12	0	0.04 - 6.48	0.93	6
Ce	0.29 - 25.35	4.2	0	0.87 - 6.23	3.98	0	0.07 - 8.83	1.68	6
Pr	0.03 - 3.36	0.39	3	0.08 - 0.59	0.32	0	0.01 - 0.78	0.17	16
Nd	0.13 - 9.78	1.23	10	0.19 - 1.52	0.79	0	0.03 - 1.97	0.52	28
Sm	0.03 - 4.52	0.33	30	0.05 - 0.39	0.14	26	0.03 - 0.28	0.1	56
Eu	0.01 - 0.10	0.03	57	0.02 - 0.14	0.07	32	0.01 - 0.25	0.09	48
Gd	0.03 - 1.79	0.21	37	0.03 - 0.20	0.1	53	0.02 - 0.25	0.06	58
Dy	0.01 - 0.75	0.09	52	0.01 - 0.10	0.03	58	0.01 - 0.16	0.05	64
Er	0.01 - 2.14	0.03	56	0.01 - 0.04	0.02	68	0.01 - 0.11	0.02	68
Yb	0.02 - 9.49	0.05	54	0.02 - 0.10	0.05	58	0.02 - 0.08	0.03	70
Hf	0.04 - 1.78	0.21	33	0.01 - 0.59	0.13	53	0.01 - 0.79	0.09	42
Ta	0.51 - 40.21	4.55	0	0.63 - 30.83	0.85	0	0.45 - 7.01	1.52	0
W	0.01 - 6.77	0.28	35	0.06 - 0.38	0.15	58	0.04 - 14.07	0.17	56
Au	0.03 - 29.48	0.1	63	0.10 - 1.11	0.23	79	0.02 - 18.70	0.14	76
Tl	0.01 - 0.15	0.03	75	0.01 - 0.03	0.02	79	0.01 - 0.05	0.02	86
Pb	0.17 - 3.82	1.1	0	0.67 - 2.22	1.21	0	0.06 - 15.25	1.96	0
Bi	0.01 - 0.66	0.08	37	0.01 - 2.25	0.12	32	0.03 - 14.26	0.3	38
Th	0.01 - 22.43	0.13	6	0.01 - 2.85	0.12	26	~0.01 - 2.49	0.03	32
U	0.01 - 4.22	0.08	38	0.01 - 3.44	0.02	53	~0.01 - 0.16	0.02	46

In contrast to remarkable variations between the Heemskirk and Pieman Heads granites, the trace element concentrations in tourmaline also show subtle variations amongst tourmaline-rich textures from

each intrusion. Tourmalines from orbicules and patches at Trial Harbour have slightly higher Li and Be contents than the veins from the same location (Appendix 5.2; Fig. 5.15). However, at Pieman Heads, Li and Be tend to be preferentially incorporated into tourmaline from the veins relative to the patches and orbicules (e.g., Fig. 5.15D). Tourmaline in miarolitic cavities appear to be the most depleted in Li and Be of the different tourmaline-bearing assemblages at Trial Harbour (Fig. 5.15D).

A number of transition elements (e.g., V, Co) appear to commonly occur in tourmaline from patches, whereas tourmaline from veins typically contains the lowest concentrations of these trace elements (Figs. 5.15A, B). Gallium and Zn concentrations in tourmaline largely overlap between patches, orbicules and cavities, and their contents decrease sharply in tourmaline from veins at Trial Harbour (up to 70 and 50 ppm, respectively; e.g., Fig. 5.15C). However, some anomalous tourmalines in veins from the Pieman Heads Granite have high concentrations of Ga and Zn (up to 700 and 400 ppm, respectively; Fig. 5.15C; Appendix 5.2). In the Heemskirk Batholith, Sc tends to be concentrated in tourmalines from patches and orbicules, and varies widely in tourmalines from miarolitic cavities and veins (Appendix 5.2). LILEs (e.g., Pb, Sr) are depleted in tourmalines from orbicules, but are enriched in tourmaline veins associated with the Heemskirk Batholith. In contrast, Pb and Sr tend to be enriched in tourmaline from patches and orbicules relative to veins at Pieman Heads (Figs. 5.15E, G). HFSEs exemplified as Ta, Nb (Th and Hf), together with Sn, are relatively enriched in tourmaline from the veins, and weakly depleted in tourmalines from patches and orbicules (Figs. 5.15F, I; Appendix 5.2), whereas REEs commonly have lower concentrations in tourmaline veins than tourmaline orbicules and cavities (Fig. 5.15H).

Tin concentrations up to 280 ppm were detected in tourmalines from the Sn-mineralised Heemskirk Batholith. These values are much higher than the average concentrations in tourmalines from the barren Pieman Heads Granite (median 13.7 ppm; Table 5.4; Fig. 5.10). Most of the high Sn values in tourmalines come from the Heemskirk Batholith at Trial Harbour (Fig. 5.10). Except for a few tourmaline grains that contain anomalously high Sn contents in tourmaline veins at Pieman Heads, average Sn concentrations in tourmalines from the Heemskirk Batholith at Granville Harbour and Pieman Heads Granite are close to or slightly higher than those of corresponding whole-rock compositions (Fig. 5.10). Tourmalines preferentially incorporates transition elements (e.g., Zn, Co; cf. Henry and Dutrow, 2001), together with Li, Be and Sn, compared to the host granites (Fig. 5.11A). This may be due to major element substitutions (e.g., Fe, Al, and Na) in tourmaline, because these elements have similar atomic radii and charges (e.g., Henry et al., 2011). The tourmalines are slightly depleted in HFSEs (e.g., Nb, Ta), and significantly depleted in LILEs (e.g., Sr, Pb) and REEs relative to their host granites (Fig. 5.11B).

Figure 5.12 (next pages) Representative combed EMPA and LA-ICP-MS profiles show chemical variations across the sector zonings of tourmalines from Trial Harbour (A, tourmaline patch; B, tourmaline orbicule; C, tourmaline cavity), Granville Harbour (D, E, tourmaline cavities), Heemskirk Batholith, and the Pieman Heads Granite (F, G, H, tourmaline veins). Major and trace elements are obtained by EMPA and LA-ICP-MS, respectively. Corresponding analysed numbers and sites are marked in the BSE images. Most tourmaline grains were sectioned approximately perpendicular to the c-axis except grain (H) which was cut parallel to the c-axis. The shaded areas in chemical plots represent the core of the grain.

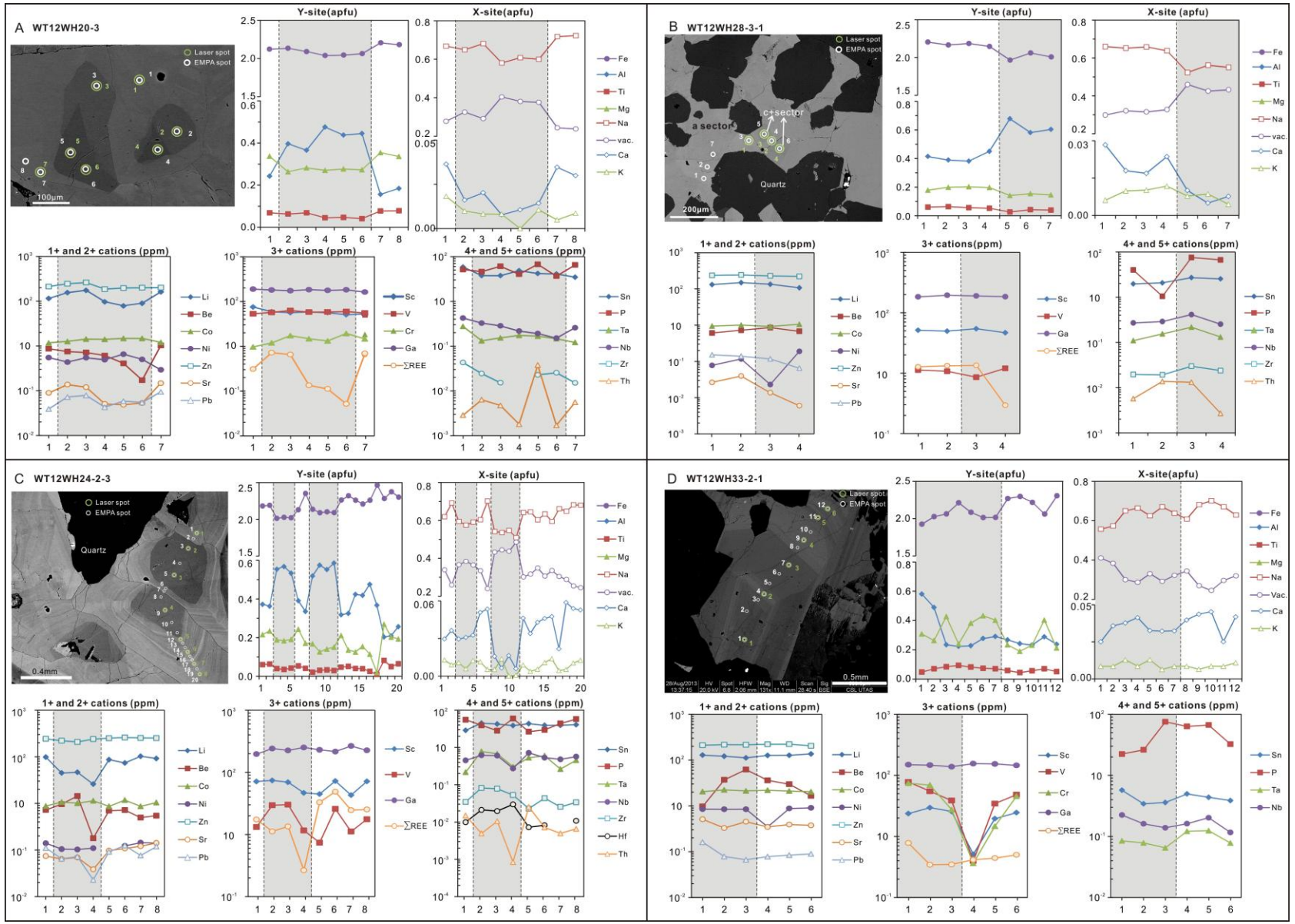
A WT12WH20-3
Laser spot
EMPA spot
100μm
Y-site(apfu)
X-site(apfu)
Fe
Al
Ti
Mg
Na
vac.
Ca
K
1+ and 2+ cations (ppm)
3+ cations (ppm)
4+ and 5+ cations (ppm)
Li
Be
Co
Ni
Zn
Sr
Pb
Sc
V
Cr
Ga
∑REE
Sn
P
Ta
Nb
Zr
Th
B WT12WH28-3-1
c+sector
a sector
Quartz
200μm
Y-site (apfu)
X-site (apfu)
1+ and 2+ cations(ppm)
3+ cations(ppm)
4+ and 5+ cations(ppm)
C WT12WH24-2-3
Quartz
0.4mm
Y-site (apfu)
X-site (apfu)
1+ and 2+ cations (ppm)
3+ cations (ppm)
4+ and 5+ cations (ppm)
Hf
D WT12WH33-2-1
0.5mm
Y-site(apfu)
X-site(apfu)
1+ and 2+ cations (ppm)
3+ cations (ppm)
4+ and 5+ cations (ppm)

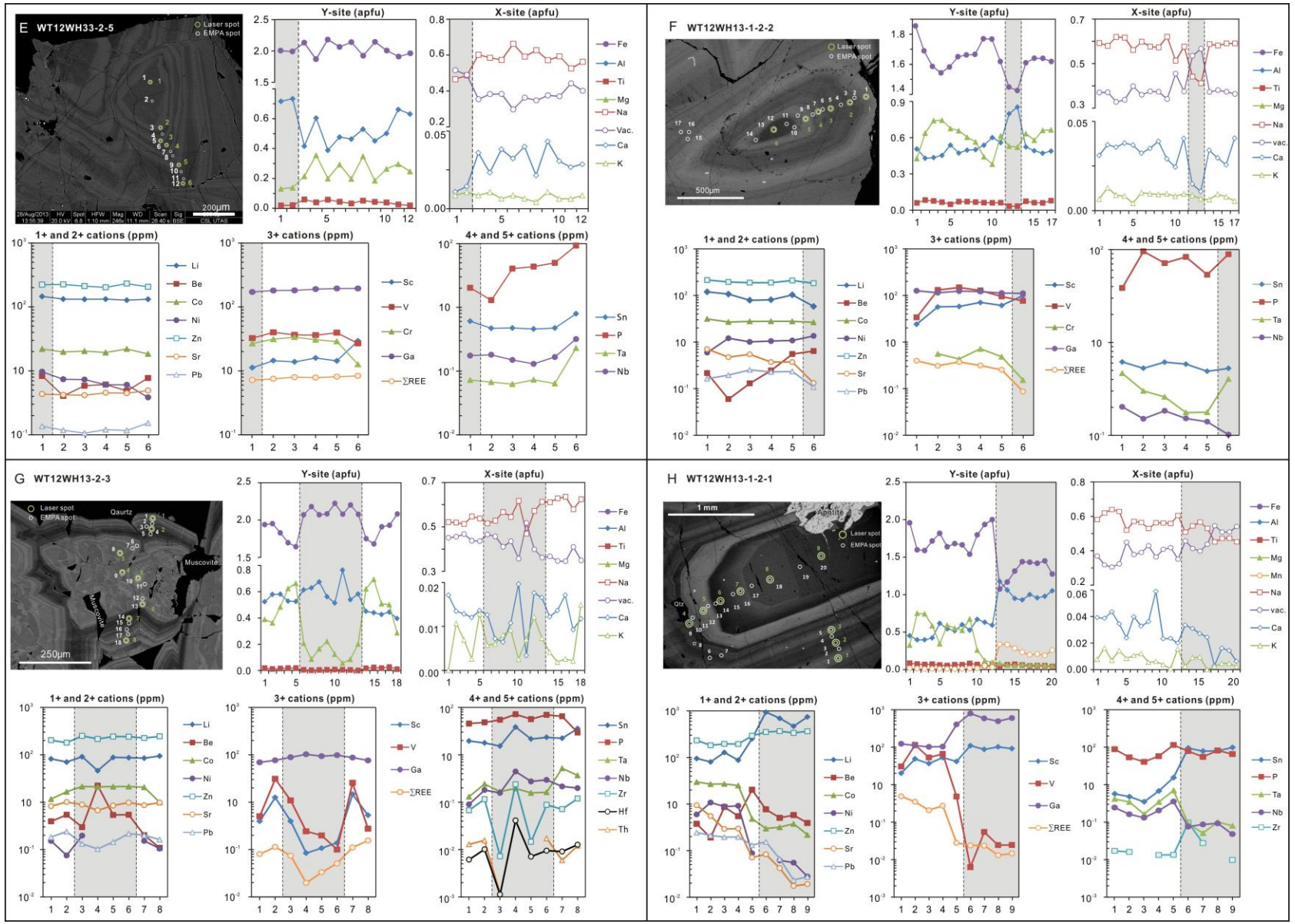
E WT12WH33-2-5
Laser spot
EMPA spot
200μm
Y-site (apfu)
X-site (apfu)
Fe
Al
Ti
Mg
Na
Vac.
Ca
K
1+ and 2+ cations (ppm)
3+ cations (ppm)
4+ and 5+ cations (ppm)
Li
Be
Co
Ni
Zn
Sr
Pb
Sc
V
Cr
Ga
∑REE
Sn
P
Ta
Nb
F WT12WH13-1-2-2
500μm
vac.
G WT12WH13-2-3
Qaurtz
Muscovite
250μm
Mn
Zr
Hf
Th
H WT12WH13-1-2-1
1 mm
Apatite
Qtz

5.3.4 Compositional variations in tourmaline sector zones

Concentric and oscillatory zoning patterns in tourmalines are commonly composed of c- and a-sectors (Henry et al., 1999; van Hinsberg et al., 2006; Marks et al., 2013). The c-sector can be divided into the c^+-sector and c^--sector due to the different poles of tourmaline's c axis. Two subsectors named as 'o-facet' and 'r-facet' can be further identified at the c-sector (Henry et al., 1999; van Hinsberg et al., 2006). In BSE images that show zoning in tourmalines from the western Tasmanian granites, the concentric cores of tourmaline are mostly c-sectors, whereas the outer matrix and oscillatory rims are inferred to correspond to a-sectors (Figs. 5.4, 5.5). Typical triangular o-facets and banded r-facets (pyramidal faces; cf. van Hinsberg et al., 2006) have been found in some c-sector planes (e.g., Fig. 5.5E), but they are uncommon. The c^--sectors display bright inner cores (e.g., Fig. 5.5E), whereas dark cores of sector zonings are inferred as c^+-sectors (Figs. 5.5A-D).

Figure 5.12 shows representative analytical profiles for tourmaline grains with sector zones based on combined EMPA with LA-ICP-MS results. Compositional variations in tourmaline growth zones from the Pieman Heads Granite are similar to those from the Heemskirk Batholith (Fig. 5. 12). However, Fe- and Al-rich cores have been only observed in Pieman Heads tourmaline (Fig. 5. 12).

Compositional profiles show that most major and trace elements in western Tasmanian tourmaline grains have different substitutions in the c-and a-sectors (Figs. 5. 12, 5.13). When compared to the neutral a-sector (Henry et al., 1999; van Hinsberg et al., 2006), the c^+ -sector is enriched in Al and the X-site vacancies, and depleted in Fe, Mg, Ca, Na, K, Ti and F (Figs. 5. 12, 5.13). Despite the limited dataset, the c^--sector appears to be enriched in Al, Fe, Ca and K compared to the a-sector, but lower in Mg, Ti, Na and F (e.g., Fig. 5.12G). Within the zoned cores (c-sector), the wedge-shape o-facet is commonly depleted in Fe, Na and Ca, but enriched in Al^Y, Mg, X-site vacancies and K relative to the laminated r-facet (e.g., Fig. 5.12G). In contrast to the relatively smooth changes in major element abundances between growth zones, most trace elements from individual tourmaline grains show variable enrichments and depletions between the c- and a-sector zonings (Fig. 5.13B). In most cases, Zn and Ga do not have any strong enrichment in each sector zone. Lithium, Sr, Pb and REEs are generally enriched in the a-sector, whereas the c-sector has pronounced enrichments of Co, Ni, V, Sc, and Th. Beryllium, Sn, Hf and Zr concentrations are slightly enriched in the c-sector, whereas Cr, Ta and Nb are higher in the a-sector (Fig. 5.12). Trace elements do not show consistent correlations between the o-facet and r-facet in the c-sector (e.g., Fig. 5.12G), possibly due to the limited numbers of analyses.

The major and trace element variations detected between the a-sectors and c-sectors typically occur by a factor of two (Fig. 5.13). However, some tourmaline grains have dramatic intra-crystalline variations, with a-sector/c-sector ratios up to 10 (Fig. 5.13). The exceptionally Mn- and Al-rich tourmaline core from a quartz vein at Pieman Heads (Sample WT12WH13-1-2-1) contains the highest Al, Mn, X-site vacancies, Li, Zn, Ga, Sc and Sn contents, and the lowest Fe, Mg, Ca, Co, Ni, Sr, Pb, V, REEs, Ta and Nb among the three tourmaline growth zones (Fig. 5.12H). The concentrations of these elements change dramatically between the core and rim, up to several orders of magnitude (Fig. 5.12H). In contrast, the compositional and textural correlations between the bright inner and grey outer tourmaline rims are similar to those

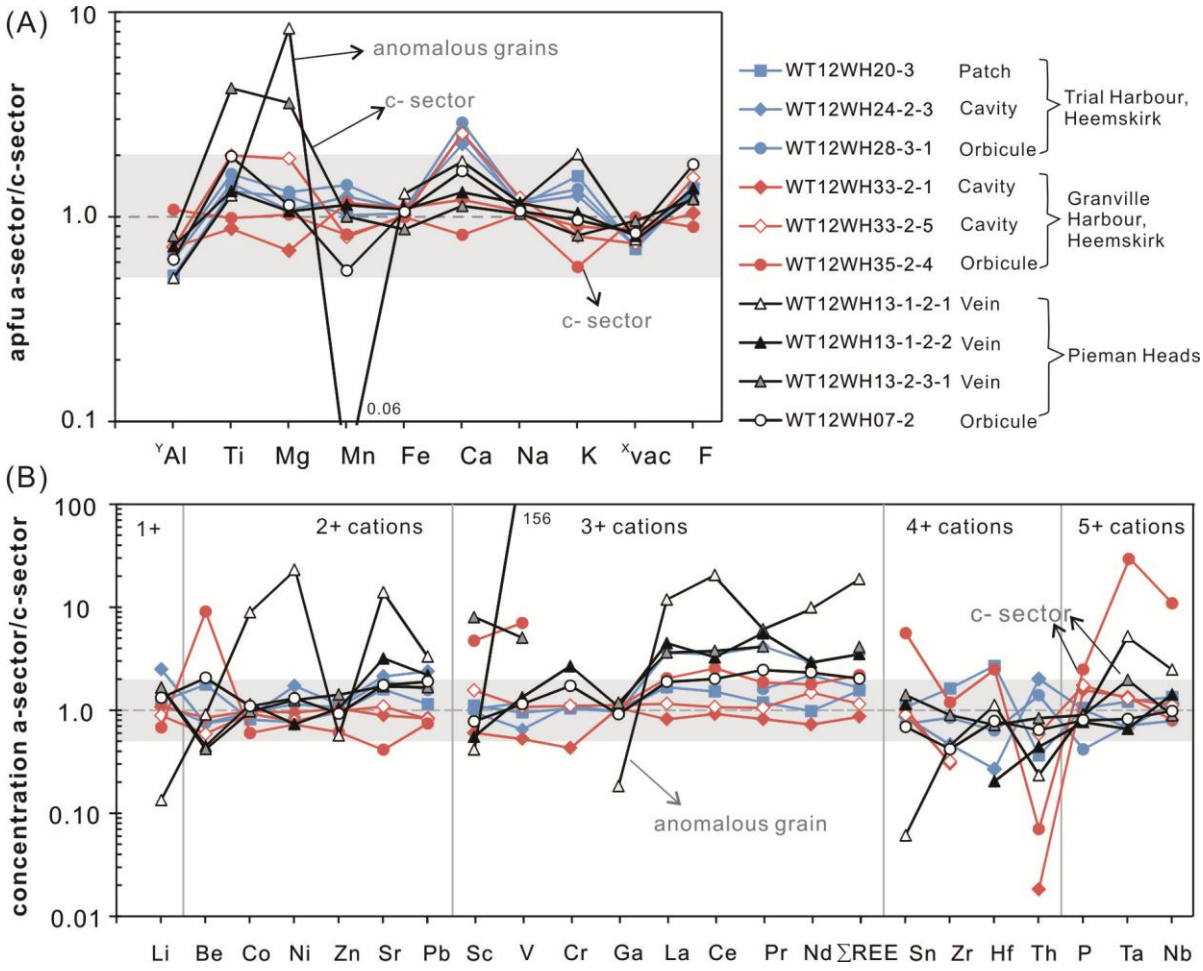

Figure 5.13 Chemical variational plots of major (A) and trace elements (B) between a- and c-sector zonings for typical tourmaline grains associated with western Tasmanian granites. The grey areas represent enrichment and depletion factors of two.

between the cores and rims of other tourmaline grains (e.g., Sample WT12WH13-2-3; Fig. 5.12G). In addition to the considerable compositional variations, the internally zoned tourmaline cores show apparent dissolution-recrystallisation textures along their contacts with the inner rims (Fig. 5. 5F). Irregular apatite grains containing zircon micro-inclusions define the boundary of the core and rim of this tourmaline grain. The apatite grain is intergrown with fine-grained tourmaline grains with BSE features similar to the tourmaline rim (Fig. 5. 5F). These chemical and mineralogical features imply that the Al-Mn-rich core and Fe-Mg-rich rim tourmalines precipitated from multiple-stages of fluids with distinctive compositions.

5.4 Discussion

5.4.1 Origin of tourmaline's sector zoning

There are many explanations for the origin of sector zones in tourmaline (cf. van Hinsberg et al., 2006). The key problem is whether sector zoning results from deposition by one or multiple fluids. Detrital cores surrounded by overgrowths had been proposed as a method for producing sector zoning in tourmaline formed under metamorphic conditions (Henry and Guidotti, 1985 and references therein). For tourmalines from the western Tasmanian granites, the chemical compositions of the refractory cores and

rims are mostly consistent with magmatic – hydrothermal tourmalines that contain higher Al, and lower Fe, Mg, Na and Ca in the cores than in the rims (Marks et al., 2013). However, some tourmaline grains display remarkable textural and chemical heterogeneities between the cores and rims (e.g., Fig. 5.12H). Those tourmalines, which represent abrupt compositional variations across different zones, may have formed via precipitation from multiple-stage fluids with distinct chemical signatures. For example, the Al-Mn-rich core was probably a pre-existing grain precipitated from a fluid remarkably different from the main-stage fluid from which the inner and outer tourmaline rims precipitated (Sample WT12WH13-1-2-1).

The explanation above cannot account for individual tourmaline grains showing evidence for progressive compositional variations from core to rim. Because of the asymmetric nature of tourmaline's crystal structure, the growth rates of individual facets of tourmaline are different, so that the morphology of the growth plane and accompanying surface charge will produce preferential incorporation of elements on specific growth facets (Henry et al., 1999; van Hinsberg et al., 2006). These factors further facilitate the polarity of individual growth directions of tourmaline crystal facets, such that more positively charged elements are preferentially adsorbed into the rims (a-sector) than the cores (c-sector) (e.g., van Hinsberg et al., 2006), or in the r-facet rather than the o-facet on the c-plane (e.g., Fig. 5.12G; Henry et al., 1999). These relationships are consistent with the detected major and trace element variations from core to rim in most tourmaline grains analysed during this study (Fig. 5.12).

Tourmaline's cores and rims are believed to grow simultaneously but in different directions (van Hinsberg et al., 2006 and references therein). Local equilibrium may be achieved between the mineral surface and its immediate surroundings; however, once the growth facet is produced, transient equilibrium can no longer be maintained (van Hinsberg et al., 2006). Accordingly, sector zoning in tourmaline is considered to routinely form under disequilibrium conditions. On the other hand, apparent variations in the types of sector zonings, such as concentric zoning versus oscillatory zoning, could depend on the planes along which individual tourmaline grains are sectioned. Real variations would probably be due to the physiochemical conditions of the tourmaline-forming fluids. Oscillatory growth zones appear to be common in tourmaline grains from the western Tasmanian granites, whereas metamorphic tourmalines typically have concentric zoning (e.g., Henry et al., 1999; van Hinsberg et al., 2006). The oscillatory zoning of tourmaline may have resulted from self-organised growth in the magmatic system, a mechanism that has been proposed for the genesis of similar textures in quartz, plagioclase, calcite and dolomite (e.g., Allègre, 1981; Shore and Fowler, 1996; Larsen et al., 2009). It may be that selective adsorption of elements caused by subtle fluctuations in temperature, pressure, pH, oxygen fugacity or progressive crystallising evolution of the granite-related magmatic-hydrothermal fluids, will give rise to the formation of rhythmic sector zoning patterns, such as these illustrated in Figure 5.12.

5.4.2 Influence of bulk composition of the host rocks

Chemical variations of tourmaline crystals are both influenced by internal factors (e.g., crystallographic sectors), and external factors such as the bulk composition of the host rock, composition of coexisting minerals and P-T-fO_2 conditions (Henry and Guidotti, 1985; van Hinsberg et al., 2011a,

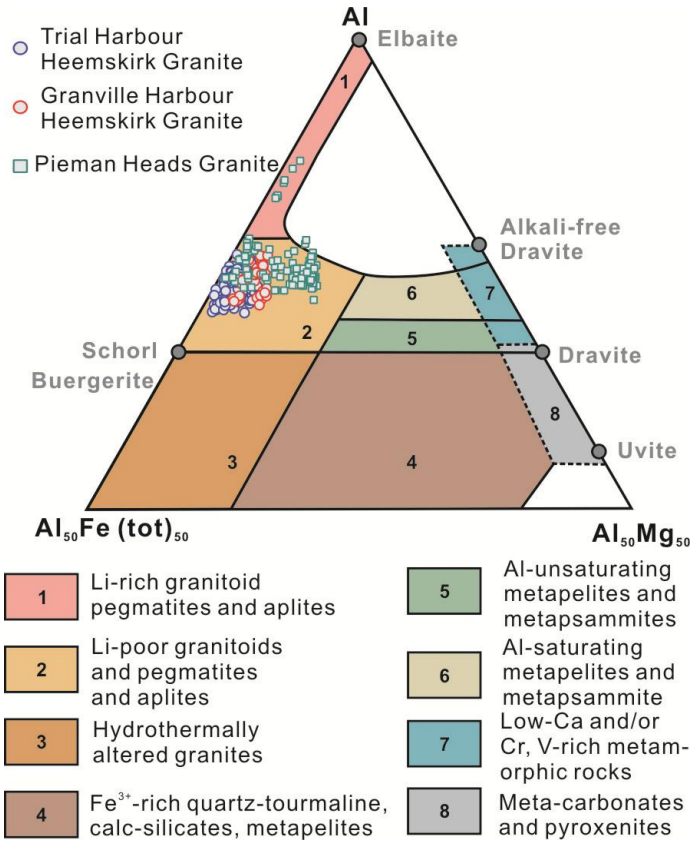

Figure 5.14 Al-Fe-Mg triplot showing tourmalines from various source rocks (modified from Henry and Guidotti, 1985). Note that tourmalines from the Heemskirk and Pieman Heads granites are plotted into the fields of Li-poor granitoids, hydrothermally altered granites and Fe-rich quartz-tourmaline rocks.

2011b; Dutrow and Henry, 2011; Marks et al., 2013). In order to diminish the effect of intra-crystalline partitioning of trace elements, it is best to compare trace elements from the neutral a-sector (van Hinsberg et al., 2006) when assessing external influences on tourmaline chemistry (Marks et al., 2013). For the western Tasmanian tourmalines, there are few differences between the a-sector data and the c-sector data (except for several anomalous results; Fig. 5.13), and chemical variations related to sector zoning are subordinate to those related to variations in host rocks and geographic locations (e.g., Figs. 5.10, 5.15).

The chemical compositions of tourmaline crystals from western Tasmanian granites plot mostly in the Li-poor granitoid field, with a few in the Li-rich granitoid field in the ternary Al-Fe-Mg diagram of Henry and Guidotti (1985; Fig. 5. 14). The contents of Al, Mg, most of the analysed transition elements (e.g., Sc, V, Co and Ni), large ion lithophile elements (e.g., Pb and Sr), and REEs are elevated in the Pieman Heads tourmalines compared to those from the Heemskirk Batholith (Fig. 5.15).

Tourmalines from the Heemskirk batholith are enriched in Sn, Na, and most high of the field strength elements (e.g., Ta, Nb, Zr, Hf and Th) relative to tourmalines associated with the Pieman Heads Granite (Fig. 5.15). Chemical heterogeneities between tourmalines are comparable to the differences in whole-rock compositions between the two granitic intrusions (Fig. 5.10). The major and trace element abundances of the tourmaline crystals are considered to be most strongly controlled by their granitic hosts, to a greater extent than by the effect of sector zoning crystallography (Fig. 5.10). This conclusion is in agreement with the assertion that tourmaline chemistry mostly reflects the compositional nature of its host melt and/or fluids (van Hinsberg, 2011).

5.4.3 Volatile exsolution influence between different textural variants of tourmalines

Tourmaline-quartz patches, orbicules and cavities are called by a variety of names, including spots, clots, ovoids, clusters and nodules. They are well-documented across a wide variety of leucocratic granites, from the Palaeoproterozoic Scruber granite in West Australia to the Late Miocene Capo Bianco aplite at Elba Island, Italy (e.g., Didier, 1973; Le Fort, 1991; Sinclair and Richardson, 1992; Samson and Sinclair, 1992; Slack et al., 1993; London and Manning, 1995; Rozendaal and Bruwer, 1995; Jiang et al., 2003; Shewfelt, 2005; Marschall and Ludwig, 2006; Buriánek and Novák, 2007; Dini et al., 2007; Perugini and Poli, 2007; Trumbull et al., 2008; Balen and Broska, 2011; Drivenes et al., 2015). Post-magmatic metasomatic alteration related to boron-rich hydrothermal fluids derived from the crystallizing granites along fractures has been proposed for the genesis of tourmaline nodules in felsic granites (Dick, 1980; Le Fort, 1991; Rozendaal and Bruwer, 1995). These tourmaline patches and orbicules are commonly distributed in the upper parts of western Tasmanian granites as disseminated masses or clusters. There is abundant field evidence that later tourmaline-filled fractures have cut across the orbicules (Fig. 4.3), disproving the hypothesis that veins play a role as conduits to feed or recharge the orbicules (cf. Dick 1980; Le Fort 1991; Rozendaal and Bruwer 1995). The observed cross-cutting relationships contradict the genetic model that tourmaline orbicules result from post-magmatic alteration by boron-rich fluids migrating along fractures. Nonetheless, the observed leucocratic outermost rims of the orbicules contain anhedral secondary muscovite and tourmaline, and K-feldspar relicts that are unambiguously caused by hydrothermal alteration, implying a minor metasomatic contribution to orbicule formation.

Tourmaline orbicules have been alternatively interpreted to be magmatic – hydrothermal textures resulting from devolatilisation, and phase separation of hydrous boron-rich fluids unmixed from granitic melts (Sinclair and Richardson, 1992; Samson and Sinclair, 1992; Jiang et al., 2003; Shewfelt, 2005; Shewfelt et al., 2005; Marschall and Ludwig, 2006; Buriánek and Novák, 2007; Dini et al., 2007; Perugini and Poli, 2007; Trumbull et al., 2008; Balen and Broska, 2011; Drivenes et al., 2015). These fluids were trapped beneath the roof of crystallising granitic sills, and also formed unidirectional solidification textures (cf. Shannon et al., 1982). This model best interprets the origins of tourmaline-rich textures formed in western Tasmanian granites.

Volatile-rich hydrous phases can exsolve from the crystallising melts during emplacement into the shallow crust due to phase separation (Burnham, 1979). In felsic magmas formed by partial melting of metapelitic rocks, boron has extremely incompatible behaviour (London et al., 1996). It can be concentrated within silicic melts, but will eventually be further partitioned into a bubble-rich aqueous phase (London et al., 1996; Dingwell et al., 1996). Experimental studies have shown that during fractional crystallisation of silicic magmas, a B-Fe-Na-rich aqueous phase can separate from the initial aluminosilicate-rich and water-rich melts due to liquid immiscibility (Veksler and Thomas, 2002; Veksler, 2004). The ASI values of the white Heemskirk and Pieman Heads granites (mostly 1.18 to 1.46), high boron contents (based on widespread tourmaline in the granites), estimated lithostatic pressures of 1 to 1.2 kbar (4 to 5.5 km depth), temperatures of 600 °-700 °C (Hajitaheri, 1985), and relatively high fluorine concentrations (EMPA on tourmaline; Table 5.2) fall largely into the field of tourmaline stability

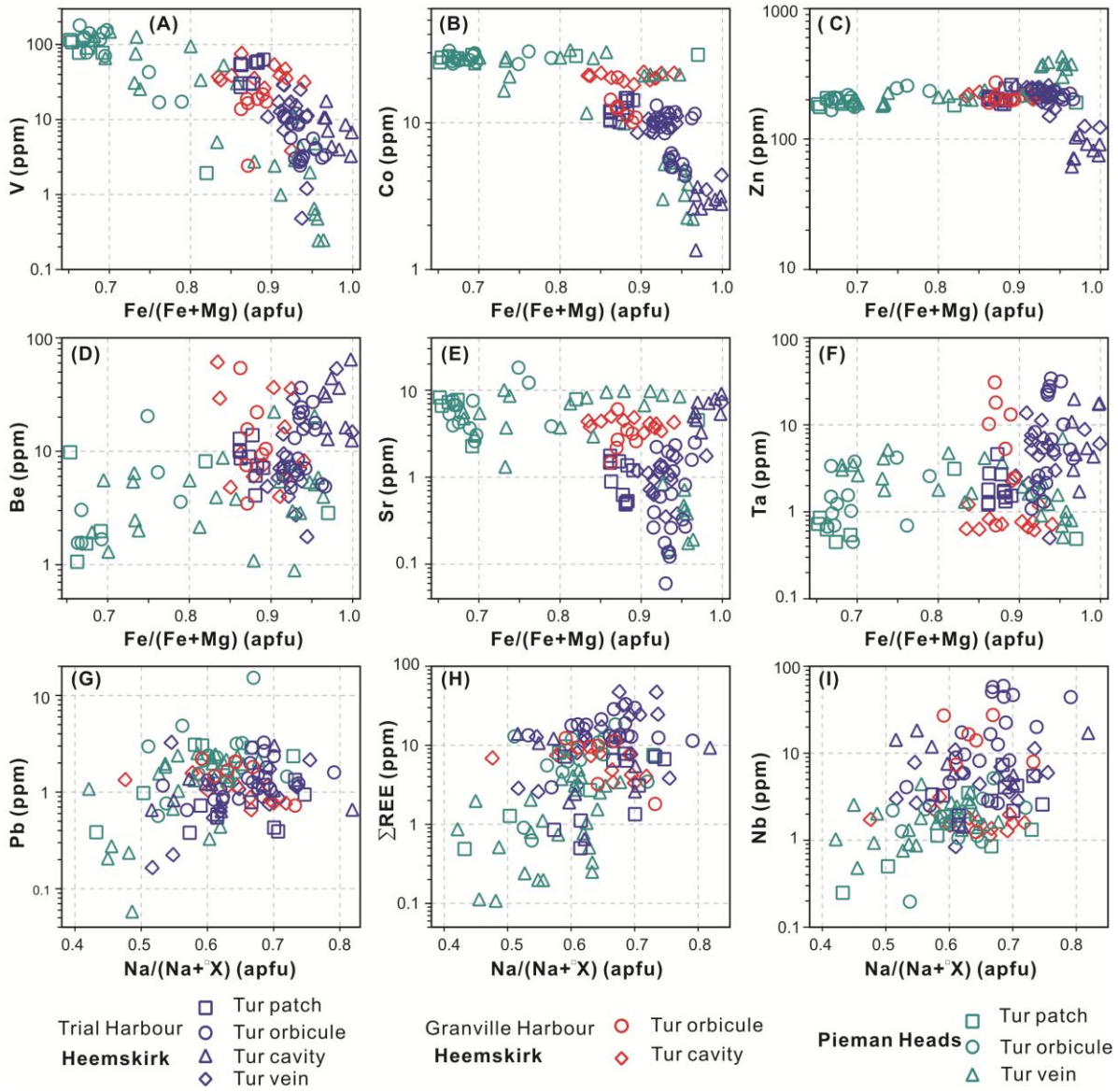

Figure 5.15 Plots showing major elements versus selective trace elements for tourmalines from western Tasmanian granites. Major and trace elements in tourmalines were analysed by EMPA and LA-ICP-MS, repectively. Fe/(Fe+Mg) ratios correlate inversely with transition elements (A, B, C) and Sr (E), but positively with Be (D) and high field strength elements (F). Na/(Na+□X) ratios appear to have a positive correlation with Pb (G), REE (H) and Nb (I). These diagrams also show that compared to tourmalines in the Pieman Heads Granite, tourmalines associated with the Heemskirk Batholith have higher concentrations of Fe, Na, Be, high field strength and rare earth elements, but lower concentrations of Mg and transition elements.

suggested by Wolf and London (1997) and London (1999). It might be that a B-Fe-Na-rich aqueous phase separated before complete crystallisation of biotite, cordierite and garnet – which is supported by absence of biotite in the granitic regions surrounding the tourmaline orbicules (Figs.4.3B-D, 4.7D), leading to a significant proportion of ferromagnesian components being available to generate the tourmaline crystals (cf. Drivenes et al., 2015). The huge volume of tourmaline developed over the 20 × 30 km areal exposure of the Heemskirk Granite shows that this intrusion was very capable of crystallising tourmaline.

The irregular tourmaline patches disseminated in western Tasmanian granites are interpreted to be tourmalinised remnants of domains that contained the small boron-rich volatile bubbles, whereas the spherical tourmaline orbicules and cavities solidified in uppermost portions of the granites are likely to be

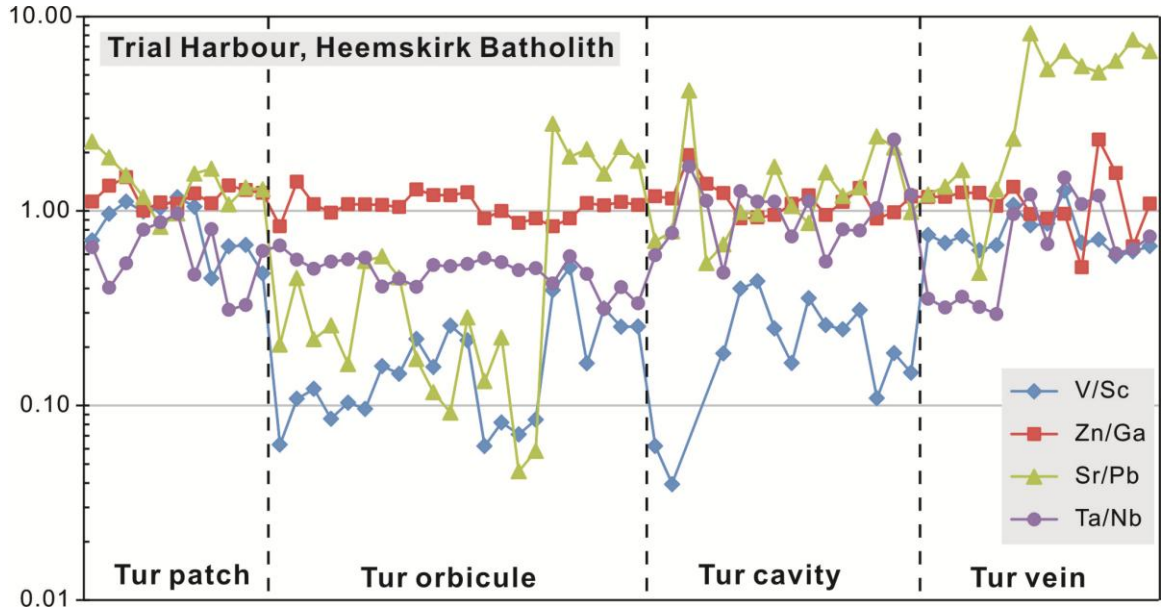

Figure 5.16 Variation plots showing representative trace element ratios in tourmalines from Trial Harbour (Heemskirk Batholith), where different tourmaline-rich textures are well-exposed. These element ratios (V/Sc, Zn/Ga, Sr/Pb, Ta/Nb) are commonly smooth due to their similar geochemical properties, but V/Sc and Sr/Pb ratios in tourmaline cavities are almost one order of magnitude higher than in tourmaline orbicules, implying that fluids responsible for the tourmaline cavities are more evolved than those for the tourmaline orbicules. Tur = tourmaline.

relicts of large trapped volatile bubbles enriched in B, Fe, Al and Na that reacted with the melt. Tourmaline grains from orbicules and cavities contain higher Fe, volatiles (Li, Be), and incompatible elements (Nb, Ta, Th, U and Pb), but lower Mg, Na, Ti, and transition elements (V, Co, Sc, Zn and Ga) than the tourmaline patches (Fig. 5.15). Strontium contents have been found to increase with incompatible elements (Nb, Ta, Th, U and Pb) and volatile elements (F, Li, Be) in the transition from tourmaline patches to orbicules and cavities (Fig. 5.15). This may be because high volatile contents (e.g., F) can promote significant Sr being preferentially incorporated into an aqueous phase (Hannah and Stein, 1990). Nevertheless, these chemical variations imply that the magmatic – hydrothermal fluids evolved compositionally, largely due to progressive crystal fractionation and high volatile contents of the parental intrusion.

The bleached leucocratic rims that are commonly observed in the outermost parts of tourmaline orbicules from the western Tasmanian granites are also common to orbicular granites worldwide (e.g., Sinclair and Richardson, 1992; Shewfelt, 2005; Buriánek and Novák, 2007; Dini et al., 2007; Trumbull et al., 2008; Balen and Broska, 2011). This feature is considered to be produced by the aqueous fluids in the volatile bubbles reacting with and altering the surrounding granites. The boron-rich aqueous fluids are predicted to be depleted in Al (Veksler et al., 2002; Thomas et al., 2003), and so the extra Al contents in tourmaline orbicules are intended to have been sourced from leaching of feldspars adjacent to the orbicules.

Tourmaline grains from orbicules and cavities largely overlap in terms of their compositions (Figs. 5.6, 5.15). However, a number of trace element ratios in tourmaline show distinct variations between tourmaline orbicules and cavities (Fig. 5.16). Higher Sr/Pb and Ta/Nb ratios are detected in tourmaline from miarolitic cavities than from orbicules in the Heemskirk Granite at Trial Harbour (Fig. 5.16). The

heterogeneity of trace element ratios, together with the obvious alteration zones of tourmaline cavities, tends to demonstrate that the tourmaline cavities may have been more evolved and water-saturated than the tourmaline orbicules.

Compared to other tourmaline-rich textures, tourmalines from quartz veins in western Tasmanian granites are relatively depleted in Na, Mg, Ti, Ca as well as transition elements (V, Co, Sc, Zn, Ga). They are enriched in Fe, Al^{Y}, Be and incompatible elements (e.g., Nb, Ta, Pb, Sr, REEs; Figs. 5.7, 5.15). The tourmalines in quartz veins are explained to have precipitated from a boron-rich aqueous fluid. During the final stage of granite crystallisation and emplacement, large amounts of boron-rich aqueous fluids are likely to have accumulated between the interface of the overlying tourmaline orbicule-bearing carapace and underlying crystallising magma. Increasing vapour pressure exceeds lithostatic pressure. This can lead to the fracture failure of the carapace and neighbouring wallrocks. Boron-rich aqueous fluids would have then migrated along these fractures, hydrothermally altering the host rocks, and eventually sealed the fractures due to mineral precipitation (e.g., Burnham, 1979). The boron-rich fluids may have coincidently cut across the early-formed tourmaline orbicules in the thin granitic carapace (e.g., Fig. 4.3G). Hydro-fracturing and sealing may have repeated until the vapour pressure dropped to the confining pressure, during which multiple phases of tourmaline-filled quartz veins can be generated (cf., Dini et al., 2008).

5.4.4 Implications for Sn enrichment and mineralisation

Some tourmaline orbicules in the Heemskirk Batholith reportedly contain cassiterite (Waterhouse, 1916). Subsequent studies have only found a few cassiterite grains in quartz-tourmaline veins, not in the tourmaline orbicules (Klominsky, 1972; Hajitaheri, 1985). No cassiterite has been found to occur within tourmaline orbicules, cavities, or veins among more than 50 thin sections and mounts examined. This is partly because the sample locations are around 1 km from the nearest historical Sn workings in the Heemskirk Granite at Trial Harbour (Fig. 3.5). Whole-rock analyses of tourmaline orbicules show that their Sn contents (average 19 ppm; Fig. 5.11A) are commonly higher than the granite host rocks (average 9.5 ppm). Tin is more abundant in the Heemskirk Batholith at Trial Harbour (10 – 31 ppm; Fig. 5.10) than from Granville Harbour (6 – 7 ppm) or the Pieman Heads Granite (5 – 9 ppm; Fig. 5.10). The White Heemskirk intrusion is more felsic and highly fractionated than the Pieman Heads Granite, with Rb/Sr ratios for the Heemskirk Batholith (28 – 62) several times higher than those for the Pieman Heads Granite (5.3 – 7.0). High degrees of fractional crystallisation are important for concentrating Sn in felsic magmas (Blevin and Chappell, 1992, 1995). Variable extents of fractionation crystallisation may have led to the different concentrations of Sn between these two intrusions. These geochemical data also show that, even in the interior of the Heemskirk Batholith, the degrees of fractionation crystallisation are not always constant, and varied from place to place (e.g., Trial Harbour versus Granville Harbour).

Volatile components of the crystallising magmas can play an important role in the formation of magmatic – hydrothermal mineral deposits. The volatiles can increase metal solubilities and decrease melt viscosities, and facilitate and transport some metals with speciation (Hedenquist and Lowenstern, 1994; Cooke et al., 2009). Tourmaline contains substantial volatile components (e.g., B, F, Li), and it is

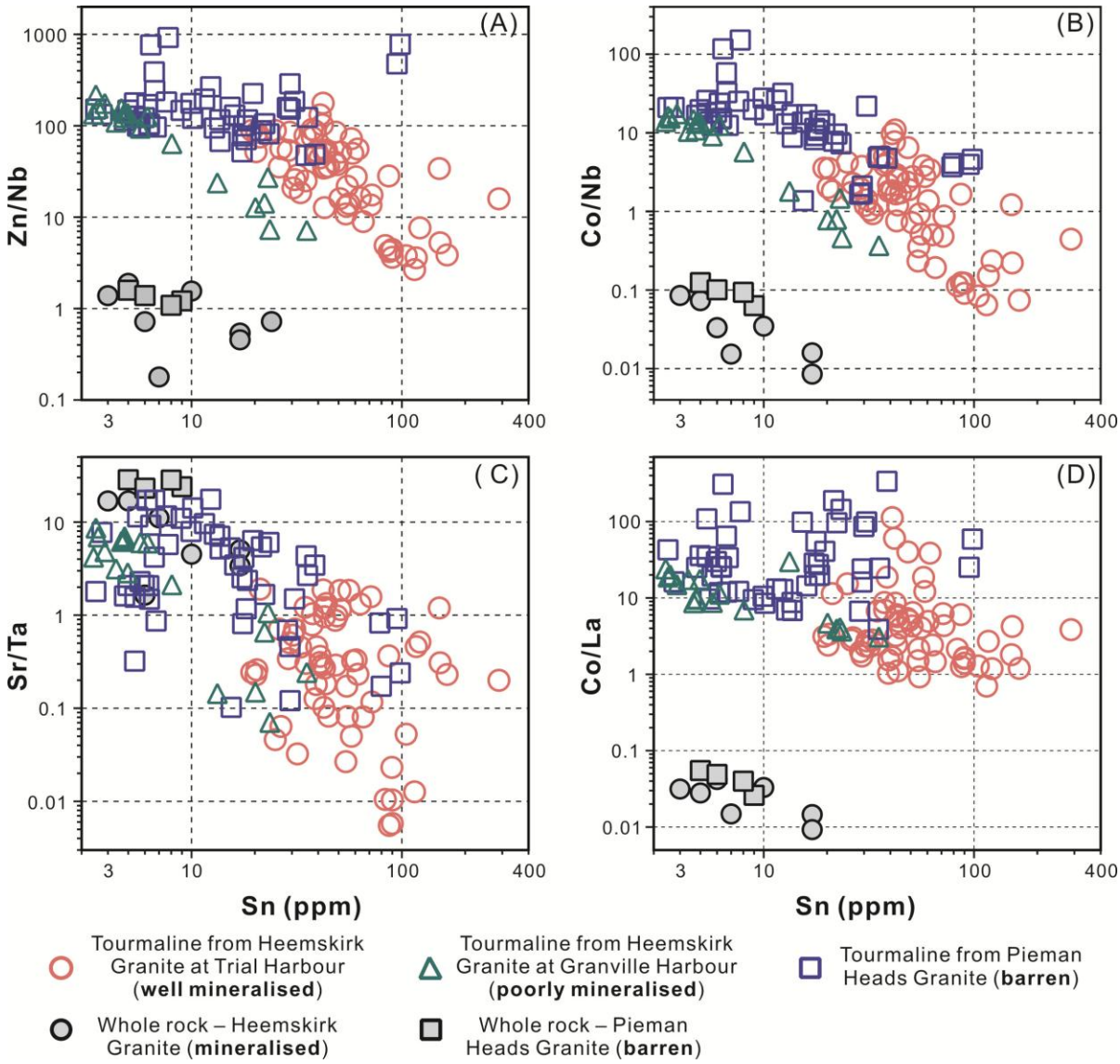

Figure 5.17 Discriminative plots showing trace element ratios versus Sn from whole rock and tourmaline LA-ICP-MS data. (A) Zn/Nb versus Sn, (B) Co/Nb versus Sn, (C) Sr/Ta versus Sn, (D) Co/La versus Sn. Compared to the whole rock geochemical data, trace element ratios versus Sn in tourmaline can typically discriminate well-mineralised (Heemskirk Granite at Trial Harbour) from barren (Pieman Heads) granites from western Tasmania.

commonly viewed as a liquidus phase in felsic magmas (Benard et al., 1985; Dingwell et al., 1996). Because tourmaline orbicules and associated tourmaline-rich textures are the consequences of volatile exsolution from the crystallising host intrusion, they have been able to concentrate Sn during granite crystallisation at Trial Harbour and to a lesser content at Granville Harbour. As a result, high Sn (up to 280 ppm), together with elevated Fe, Be,Ta, Nb, Sr, REEs and lower Mg, Ti, Sc, V, Cr, Co, were incorporated into tourmalines in the cavities and veins in the White phase of the Heemskirk Granite at Trial Harbour (Fig. 5.15).

Element ratios between enriched and depleted elements in tourmaline can amplify geochemical anomalies inherited from the host granites. Geochemical diagrams that plot element ratios (e.g., Zn/Nb, Co/Nb, Sr /Ta, and Co/La) against Sn concentrations in tourmaline clearly separate the Sn-mineralised

intrusion (Heemskirk Granite at Trial Harbour) from the barren granite (Pieman Heads Granite) from western Tasmania (Fig. 5.17). Element ratios and Sn contents in tourmaline from the Heemskirk Granite at Granville Harbour are situated in intermediate districts on these discrimination diagrams, partially overlapping with the Trial Harbour and Pieman Heads data (Fig. 5.17). Trace element ratios plotted against from tourmaline may therefore prove to be powerful tools to discriminate productive and barren granites relative to whole-rock geochemical data (Fig. 5.17).

5.5 Conclusions

Tourmaline grains from magmatic – hydrothermal features of the Heemskirk and Pieman Heads granites have been analysed by SEM-BSE, EMPA and LA-ICP-MS. These tourmaline grains commonly display distinctive compositional growth zonation patterns revealed by backscattered electron imaging, including (1) oscillatory zoning, (2) concentric zoning, and (3) radial zoning.

The tourmalines are mostly schorl (Fe-rich) and foitite, with an average end-member component of $schorl_{45}$ $dravite_{6}$ $tsilaisite_{1}$ $uvite_{0}$ $Fe\text{-}uvite_{3}$ $foitite_{31}$ $Mg\text{-}foitite_{4}$ $olenite_{10}$. Element substitutions of the tourmalines are controlled by $FeMg_{-1}$, ${}^{Y}Al^{\square}X$ $(R^{2+}Na)_{-1}$, and minor ${}^{Y}AlO(R^{2+}OH)_{-1}$ (where $R^{2+} = Fe^{2+} + Mg^{2+} + Mn^{2+}$) exchange vectors. A number of trace elements in tourmaline have consistent chemical evolutions grouped from tourmaline patches, through orbicules and cavities, to veins. There is a progressive decrease of most transition and large ion lithophile elements, and a gradual increase of most high field strength elements. These compositional variations in the different tourmaline-rich features probably relate to element partitioning occurring in these phases due to volatile exsolution and fluxing of aqueous boron-rich fluids that separated from the granitic melts during the emplacement of S-type magmas into the shallow crust (estimated depth 4 to 5.5 km; Hajitaheri, 1985).

Tourmalines from the Heemskirk Granite are enriched in Fe, Na, Li, Be, Sn, Ta, Nb, Zr, Hf, Th, and rare earth elements relative to the tourmalines from the Pieman Heads Granite, but depleted in Mg, Mn, Sc, V, Co, Ni, Pb, Sr, and most transition elements. These results imply that bulk compositions of the host granites exert a major control on the chemical variations of tourmalines. The trace element compositions of tourmalines from the Sn-mineralized Heemskirk Granite are different from those of the barren Pieman Heads Granite. Trace element ratios (e.g., Zn/Nb, Co/Nb, Sr/Ta and Co/La) and Sn concentrations in tourmaline can distinguish the productive Heemskirk Granite from the barren Pieman Heads Granite.

The following chapters further explore the genesis of the tourmaline-rich textural features from the two western Tasmanian granites using quartz mineral chemistry, fluid inclusion and stable and radiogenic isotopic data.

Chapter 6 Quartz mineral chemistry

6.1 Introduction

Quartz is one of the most abundant silica minerals on Earth. It occurs in magmatic, sedimentary and metamorphic rocks from diverse geological environments. Quartz has a simple formula of SiO_2 with an ultra-stable crystal structure (e.g., Götze, 2009). Only a few trace elements can be incorporated into the quartz lattice at low concentrations, including tetravalent ions (e.g., Ti^{4+}, Ge^{4+}) and trivalent and pentavalent ions (e.g., Al^{3+}, B^{3+}, Fe^{3+}, and P^{5+}) that pair with monovalent and bivalent ions (e.g., H^{+}, Li^{+}, Na^{+}, K^{+}, and Fe^{2+}) to substitute for Si (Weil, 1993; Götze et al., 2001, 2004; Müller and Koch-Müller, 2009). Many factors can contribute to trace element substitutions into the quartz lattice, such as the composition of the parental melt or hydrothermal fluid, degree of magma fractionation, temperature, pressure, pH, redox and growth dynamics (Götze et al., 2001, 2004; Larsen et al., 2004; Breiter and Müller, 2009; Jacamon and Larsen, 2009; Götze, 2009; Müller and Koch-Müller, 2009; Jourdan et al., 2009; Wark and Watson, 2006; Thomas et al., 2010; Huang and Audétat, 2012).

Scanning electron microscope-cathodoluminescence (SEM-CL) analysis can reveal cryptic luminescent textures in quartz that are not observed throughout transmitted light or backscattered electron imaging (Seyedolali et al., 1997; Rusk and Reed, 2002; Götze, 2009). These SEM-CL textures are interpreted to result from the differences of luminescent intensity in quartz caused by intrinsic and extrinsic defects, such as poor ordering of crystal structure, point defects, trace elements, and by the presence of solid and/or fluid inclusions (Götze et al., 2001).

Because of its relatively refractory response to fluid-rock interaction (Larsen et al., 2004), the trace elements of quartz detected by micro-analytical instruments (e.g., laser ablation inductively coupled plasma mass spectrometry), in combination with SEM-CL analysis, have been used increasingly to track the evolution of magmatic – hydrothermal systems (Larsen et al., 2004; Breiter and Muller, 2009; Jacamon and Larsen, 2009; Larsen et al., 2009; Götze, 2009; Müller and Koch-Müller, 2009; Jourdan et al., 2009; Breiter et al., 2013; Drivenes et al., 2016), especially those associated with magmatic – hydrothermal ore deposits (Rusk and Reed, 2002; Rusk et al., 2008, 2011; Landtwing and Pettke, 2005; Müller et al., 2010; Tanner et al., 2013; Maydagán et al., 2015).

Quartz is one of the major components of tourmaline-rich features from western Tasmanian granites. In this chapter, quartz grains from tourmaline patches, orbicules, cavities and veins, and unidirectional solidification textures (USTs) in the Heemskirk and Pieman Heads granites, as well as quartz from Pb-Zn mineralised veins from the Heemskirk Granite, were analysed by SEM-CL and laser ablation ICP-MS. The aims of this study are to reveal the internal luminescent textures of analysed quartz samples, and trace element variations between the different types of quartz. These data provide additional geochemical

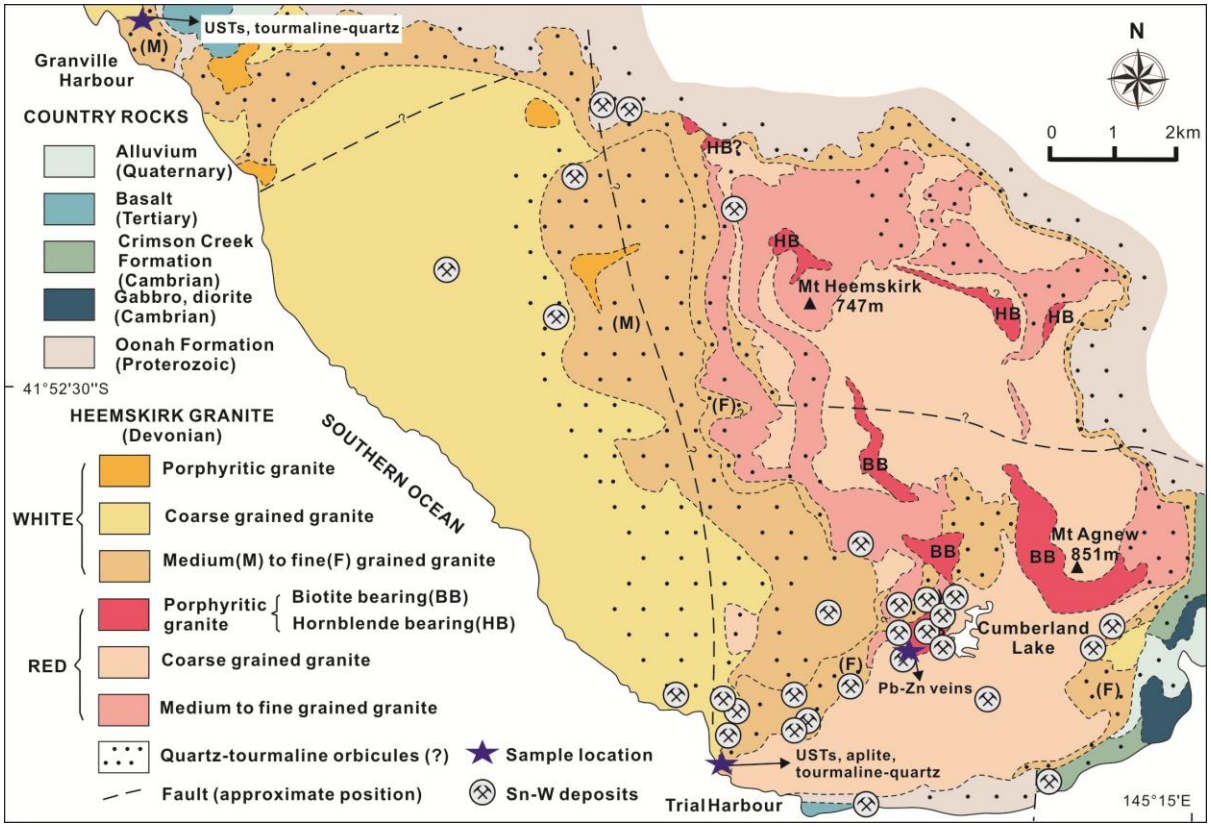

Figure 6.1 Sample locations of aplite, USTs, tourmaline-quartz textures and Pb-Zn veins from the Heemskirk Granite. All samples details listed in Table 6.1.

constraints on the formation of the tourmaline-rich assemblages and unidirectional solidification textures caused by volatile exsolution and fluid influx in the felsic magma.

6.2 Methodology

6.2.1 Scanning electron microscope-cathodoluminescence

A Cameca cathodoluminescence (CL) detector attached to a FEI Quanta 600 environmental scanning electron microscope (SEM) in the Central Science Laboratory at the University of Tasmania (UTAS) was used to generate CL images highlighting internal textures in quartz from the Heemskirk and Pieman Heads granites (Figs. 3.6, 6.1). The samples include quartz grains from tourmaline patches, tourmaline orbicules, tourmaline cavities, tourmaline-quartz veins, and USTs, together with Pb-Zn veins from the south of the Heemskirk Granite (Fig. 6.1; Table 6.1). A total of 40 carbon-coated, polished thin sections and mounts were examined using the instrument at an accelerating voltage of 20 kV and beam current of ~ 3nA.

6.2.2 Laser ablation ICP-MS

Trace elements of quartz from tourmaline-rich features, Pb-Zn veins, USTs and aplitic granite were analysed using the laser ablation (LA) ICP-MS facility at CODES. These quartz grains were measured in two runs, in April 2014 and June 2016, respectively. Quartz samples in 2014 (58 analyses) were ablated on 47 micron diameter spots using the laser at 10 Hz and an energy density of approximately 10.8 J/cm^2, and

Table 6.1 Features of quartz-bearing samples analysed in the current study

Sample name	Coordinate	Granite	Type	Mineralogy	Source
WT12WH30-1	E145°09'23.93", S41°55'20.64", 3 m	Heemskirk	Aplite	Qtz, Kfs, Bi	This study
WT12WH34-3	E145°01'40.47", S41°48'34.80", 1 m	Heemskirk	Aplite	Qtz, Kfs, Bi	This study
WT14WH58	E145°09'23.93", S41°55'20.64", 3 m	Heemskirk	Aplite	Qtz, Kfs, Bi	This study
WT12WH30-2	E145°09'23.93", S41°55'20.64", 3 m	Heemskirk	USTs	Qtz	This study
WT12WH34-4	E145°01'40.47", S41°48'34.80", 1 m	Heemskirk	USTs	Qtz, Mt	This study
WT12WH34-5	E145°01'40.47", S41°48'34.80", 1 m	Heemskirk	USTs	Qtz, Mt	This study
WT12WH20	E145°09'23.93", S41°55'20.64", 3 m	Heemskirk	Tur patch	Qtz, Tur, Kfs	This study
WT12WH21	E145°09'23.93", S41°55'20.64", 3 m	Heemskirk	Tur patch	Qtz, Tur, Kfs	This study
WT12WH22	E145°09'23.93", S41°55'20.64", 3 m	Heemskirk	Tur orbicule	Qtz, Tur	This study
WT12WH28	E145°09'23.93", S41°55'20.64", 3 m	Heemskirk	Tur orbicule	Qtz, Tur	This study
WT12WH24	E145°09'23.93", S41°55'20.64", 3 m	Heemskirk	Tur cavity	Qtz, Tur	This study
WT12WH33-2	E145°01'40.47", S41°48'34.80", 1 m	Heemskirk	Tur cavity	Qtz, Tur	This study
WT12WH35-2	E145°01'40.47", S41°48'34.80", 1 m	Heemskirk	Tur orbicule	Qtz, Tur	This study
WT12WH23	E145°09'23.93", S41°55'20.64", 3 m	Heemskirk	Tur vein	Qtz, Tur, Ms	This study
106405	E145°11'48.84", S41°54'22.65", -83m	Heemskirk	Pb-Zn vein	Flu, Sp	Hajitaheri (1985)
106410	E145°11'48.84", S41°54'22.65", -83m	Heemskirk	Pb-Zn vein	Qtz, Py, Ga	Hajitaheri (1985)
106425	E145°11'48.84", S41°54'22.65", -36 m	Heemskirk	Pb-Zn vein	Qtz, Flu, Py	Hajitaheri (1985)
WT12WH03	E144°55'40.01", S41°43'15.00", 10 m	Pieman Heads	Tur patch	Qtz, Tur, Kfs	This study
WT12WH04-1	E144°55'40.01", S41°43'15.00", 10 m	Pieman Heads	Tur patch	Qtz, Tur, Kfs	This study
WT12WH07	E144°55'40.01", S41°43'15.00", 10 m	Pieman Heads	Tur orbicule	Qtz, Tur, Kfs	This study
WT12WH13	E144°53'37.87", S41°43'13.75", 3 m	Pieman Heads	Tur vein	Qtz, Tur, Ms	This study

Abbreviation: Bi = biotite, Flu = fluorite, Kfs = alkali feldspar, Qtz = quartz, Ms = muscovite, Mt = magnetite, Tur = tourmaline, Ga = galena, Py = pyrite, Sp = sphalerite.

determined elements included Li, Na, Mg, Al, Si, K, Ca, Ti, V, Cr, Mn, Fe, Cu, Cu, Zn, Ge, As, Rb, Sr, Zr, Ag, Sb, Cs, Gd, Hf, Ta, Au, Pb, Bi, and U. The second run in 2016 (347 analyses) was ablated using 43 micron diameter spots using the same laser at 10 Hz and an energy density of approximately 13.67 J/cm^2, and analysing elements include Li, Na, Mg, Al, Si, K, Ca, Ti, V, Cr, Mn, Fe, Cu, Zn, Ge, As, Rb, Sr, Zr, Nb, Ag, Sn, Sb, Cs, Nd, Gd, Hf, Ta, Au, Pb, Bi, and U.

The primary standard NIST612 was measured using 64 micron diameter spots (10 Hz, 3.53 to 4.5 J/cm^2). Pure silica, GSD-1g and quartz standards from Audétat et al. (2015) were used as a secondary external standard (spot size 47 μm, 10 Hz, 10.8 J/cm^2), in order to compare values for a given element and to correct for differences in spot size between the primary standard and unknowns.

The Excel-spreadsheet laser template (CODES, UTAS) was employed for data reduction. A theoretical silicon value of 467,400 ppm was used as the internal standard element for quartz. The LA-ICP-MS spectral curves of quartz were commonly chosen to start at 40s and end at 85s during data reduction (Fig. 6.6a). For those analyses in which solid or fluid inclusions were accidently ablated, the anomalous spikes within the spectra were avoided during data processing (e.g., Figs. 6.6b-c). All of the reduced data for quartz grains were normalised to average values of the GSD-1g standards analysed by the same laser facility. A total of 390 analyses were retained after culling any contaminated or mixed LA-ICP-

MS spectra, with only 15 analyses rejected. Detection limits for most trace elements were in the range of 0.001 to 1 ppm (Appendix 6).

6.3 Results

6.3.1 SEM-CL textures of quartz

More than 500 SEM-CL images of quartz grains were collected from various assemblages in the Heemskirk and Pieman Heads granites. These images reveal different types of CL textures commonly developed in magmatic – hydrothermal quartz (e.g., Rusk and Reed, 2002), such as euhedral growth zones, CL-gray patches, CL-dark patches and streaks, healed fractures with non-luminescent intensity, cobweb-like networks and jigsaw puzzle pieces (Table 6.2; Figs. 6.2-6.5).

6.3.1.1 Heemskirk Granite – UST quartz

The CL textures of the aplitic quartz intercalated with USTs are dominated by homogeneous bright luminescence with minor small CL-dark patches (< 50 μm) and thin CL-dark fractures (Fig. 6.2a; Table 6.2). In some quartz grains, CL-dark cobweb and patchy textures are strongly developed within massive CL-bright quartz (Fig. 6.2b). Some of the CL-dark patches are up to several hundred μm in diameter. These features are similar to CL textures of quartz in the tourmaline patches (Figs. 6.3a-b), and contrast with the euhedral oscillatory zones of dark to bright CL intensity in the quartz grains from tourmaline veins of the Heemskirk Granite (Fig. 6.2c).

The base and apex of individual quartz grains from USTs are characterised by contrasting SEM-CL textures (Figs. 6.2d-e; Table 6.2). The bases of UST layers that have jagged contacts with host granites contain homogeneous, CL-bright quartz. Thin (1-2 μm), CL-dark fractures cut the bright-CL quartz grains (Figs. 6.2d-e). Some thicker CL-dark cracks and patches (> 10 μm), together with K-feldspar inclusions, are interstitial to quartz crystal mosaics with intense CL response (Figs. 6.2d-e). These features are similar to those in aplitic and granitic quartz grains in the Heemskirk Granite (cf. Figs. 6.2d-e, 6.3a-b).

The apexes of quartz crystals in USTs have distinctive CL-gray to CL-bright bands that define euhedral oscillatory growth zones (Figs. 6.2d-e). The growth zones are characterised by fine laminae (5 to 20 μm wide) that are parallel to grain edges, but only occur on the trigonal boundaries, and are restricted to domains of several hundred μm wide (Figs. 6.2d-e). Multiple sets of CL-dark to CL-gray fractures or anastomosing patches have locally cut the euhedral oscillatory zones (Figs. 6.2d-e). The oscillatory growth zones are similar to those observed in quartz from hydrothermal tourmaline veins (cf. Fig. 6.2c).

6.3.1.2 Heemskirk Granite – tourmaline-rich features

Quartz grains from tourmaline patches from the Heemskirk Granite are characterised by CL-bright intensities with homogeneous luminescence (Table 6.2; Figs. 6.3a-b). Thin (< 5 μm), distinct CL-dark fractures commonly have cut the CL-bright quartz. These healed fractures are generally distributed sparsely, being sub-parallel or intersecting obliquely (Figs. 6.3a-b). Irregular CL-dark patches are

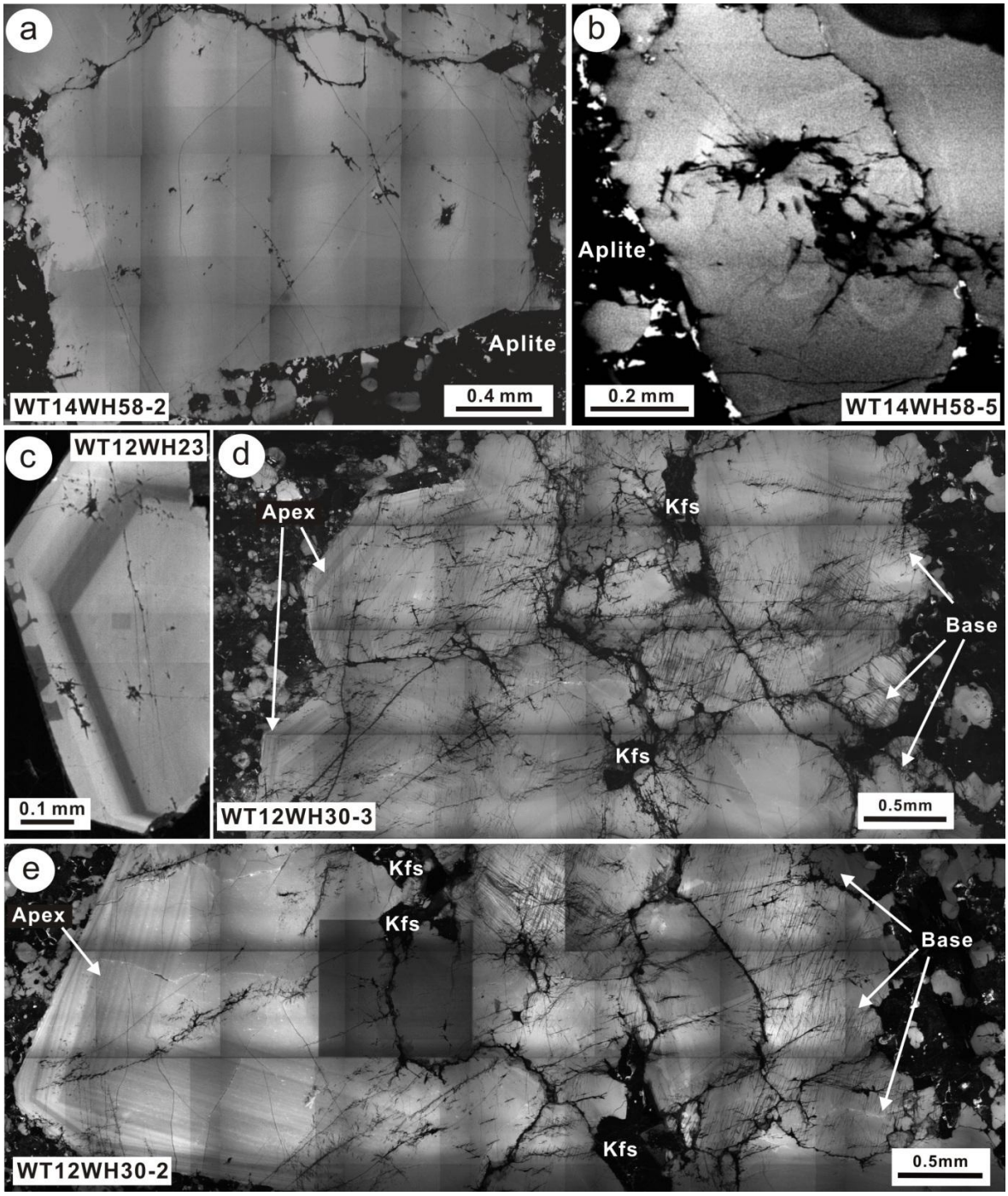

Figure 6.2 SEM-CL textures of aplitic quartz (a-b), quartz in tourmaline veins (c), and comb-layered quartz (d-e) from the Heemskirk Batholith. Kfs = K-feldspar. All sample details listed in Table 6.1 and Fig 6.1.

uncommon in this type of quartz grains. The patches are commonly connected by anastomosing thin bands and/or cracks (Figs. 6.3a-b), forming splatter and cobweb texture similar to those described by Rusk and Reed (2002). In some quartz grains, euhedral growth zones consisting of finely oscillatory laminations (1 to 10 μm wide) only occur on the grain boundaries, with CL-bright to CL-gray luminescence (Fig. 6.3b). Thin CL-gray rim rarely overgrows on the edges of massive CL-bright quartz grains (Fig. 6.3b).

Quartz in tourmaline orbicules has relatively complex SEM-CL textures (Table 6.2; Figs. 6.3c-e). These quartz grains typically contain euhedral concentric growth zones that are orientated parallel to grain

boundaries (Figs. 6.3c-d). The growth bands have subtle variations in CL intensities (bright to gray), and range from 1 to 10s of μm wide. Abundant CL-dark patches typically occur in the interior of the CL-bright quartz grains (Fig. 6.3c), whereas the dark luminescent streaks (tens of μm wide) are parallel to the edges (Fig. 6.3d). Thin CL-dark fractures (several μm) have cut the massive CL-bright quartz grains and connect the non-luminescent patches (Figs. 6.3c, e). CL-gray sectors routinely appear on the edges associated with CL-dark patches and streaks (Fig. 6.3d). However, some quartz grains have irregular CL-gray sectors within the CL-bright matrix, in which mosaics of CL-bright grains are cut by intensely developed anastomosing streaks and cracks (Fig. 6.3e). In addition to cobweb networks, rare jigsaw puzzle-like textures are defined by CL-dark fractures that have engulfed and separated brightly luminescent quartz cores (Fig. 6.3e; cf. Rusk and Reed, 2002).

CL-dark patches, healed fractures and cobweb networks have been also observed in quartz grains from the tourmaline-filled cavities (Fig. 6.3f). The weak CL features commonly cut homogenously CL-bright quartz grains (Table 6.2). Some of the miarolitic quartz grains are characterised by thick streaks (up to hundreds of μm) with intermediate CL intensities that extend from the rim to the centre of individual quartz crystals (Fig. 6.3f). CL-gray streaks contain irregular CL-dark patches and embayed CL-bright domains, which are optically continuous with the massive CL-bright quartz under plane polarised light. The CL-gray quartz band (Qtz-2) is interpreted to be a later generation product, postdating the CL-bright main quartz (Qtz-2; Fig. 6.3f).

Quartz grains from the tourmaline veins present the most complex SEM-CL textures of the tourmaline-rich associations from Heemskirk Granite (Table 6.2; Fig. 6.3g). Euhedral CL-bright quartz develops fine-scale growth zones, ranging from several to tens μm wide, with orientations commonly parallel to grain boundaries. Patchy CL-gray sectors commonly appear within the strongly luminescent quartz with relatively smooth contacts. The CL-bright and CL-gray quartz veins are typically embayed, and have been truncated by dark luminescent patches, cracks and bands (Fig. 6.3g). Irregular quartz domains with dark CL intensity in tourmaline veins can occupy ~30 to 40 % by volume of a whole quartz grain, and are volumetrically more abundant than in the other tourmaline-rich assemblages analysed (Fig. 6.3). CL-dark patches are commonly connected by thin, elongated non-luminescent cracks and streaks, producing a cobweb-like network appearance. Jigsaw puzzle-like textures with gray-dark CL intensity occur in places where the quartz has been strongly fractured and offset (Fig. 6.3g).

6.3.1.3 Pieman Heads Granite – tourmaline-rich features

Quartz grains from the various tourmaline-rich assemblages in the Pieman Heads granites display similar SEM-CL textures (Fig. 6.4) to their counterparts in the Heemskirk Granite (Fig. 6.3; Table 6.2).

Figure 6.3 (next page) SEM-CL textures of quartz from tourmaline patches (a, b), tourmaline orbicules (c-e), tourmaline cavities (f) and tourmaline veins (g) in the Heemskirk Batholith. Kfs = K-feldspar, Qtz = quartz, Tur = tourmaline. All sample details listed in Table 6.1 and Fig. 6.1.

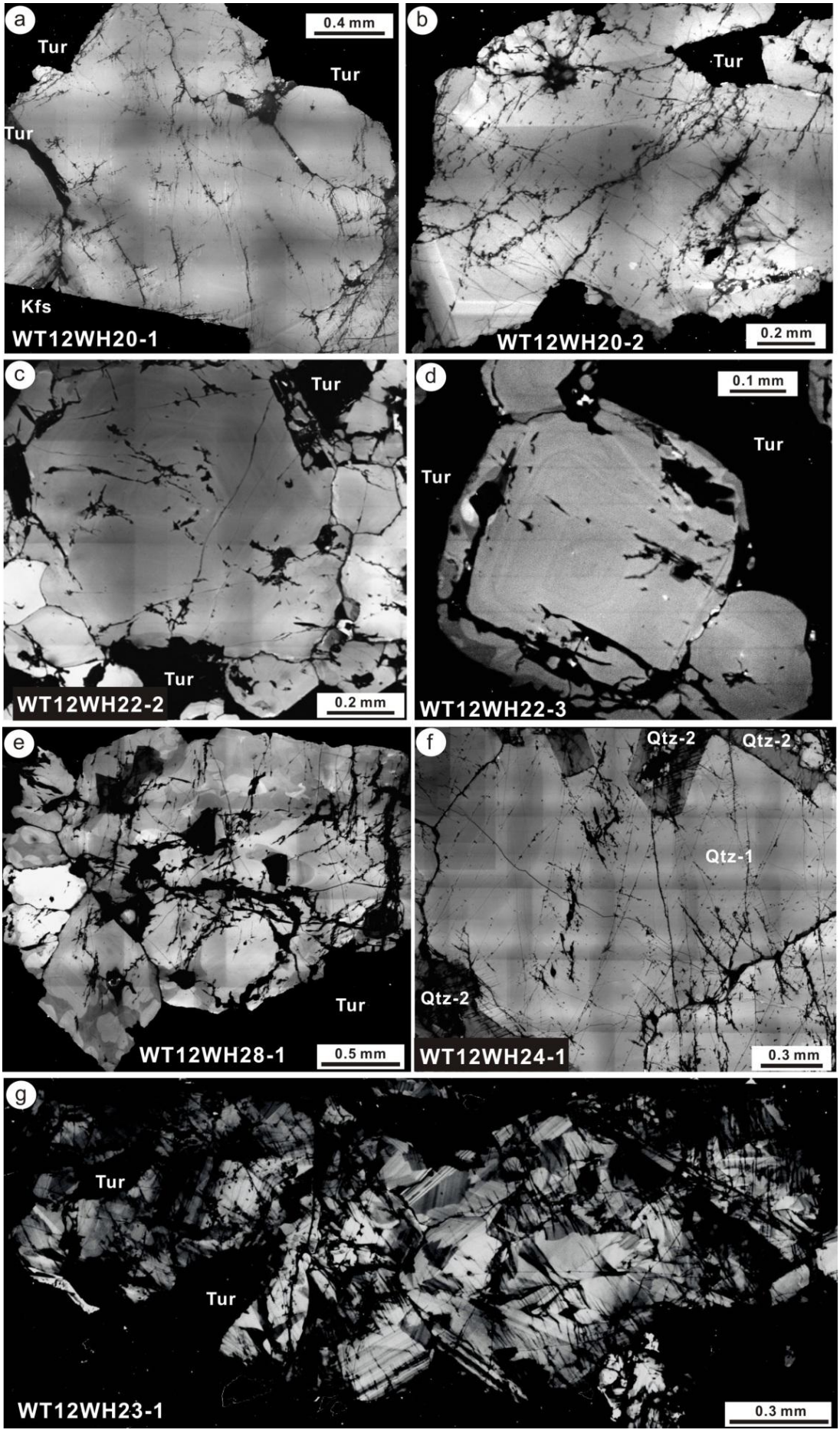
a
0.4 mm
Tur
Tur
Tur
Kfs
WT12WH20-1
b
Tur
WT12WH20-2
0.2 mm
c
Tur
Tur
WT12WH22-2
0.2 mm
d
0.1 mm
Tur
Tur
WT12WH22-3
e
Tur
WT12WH28-1
0.5 mm
f
Qtz-2
Qtz-2
Qtz-1
Qtz-2
WT12WH24-1
0.3 mm
g
Tur
Tur
WT12WH23-1
0.3 mm

SEM-CL textures in quartz from the tourmaline patches are dominated by multiple sets of healed CL-dark fractures that cut and/or offset the bright CL intensity of the main quartz grains (Fig. 6.4a). These CL-dark cracks can intersect at differing angles, and have widths ranging from several to tens of microns. In intensely fractured domains, small CL-bright quartz fragments are separated by CL-dark cracks to form jigsaw puzzle-like textures (Fig. 6.4a). Locally, cobweb network textures are defined by a few irregular CL-dark patches anastomosed by the bifurcated fractures (Fig. 6.4a). Oscillatory streaks composing fine CL-gray laminations locally grow on the edges of the CL-bright quartz (Fig. 6.4a).

CL-textures of quartz in tourmaline orbicules from the Pieman Heads Granite mostly resemble those in the tourmaline patches from the same intrusion (Fig. 6.4b; Table 6.2). These quartz grains are commonly characterised by massive, homogeneous, bright CL intensity, which have cut by numerous bifurcated CL-dark cracks in width ranging several to tens of μm. Irregular CL-dark patches are locally connected by multiple CL-dark fractures, resulting in a radiating morphology (Fig. 6.4b).

Some quartz grains from tourmaline veins have similar CL textures to those from tourmaline patches and orbicules within the Pieman Heads Granite (Figs. 6.4a-c), including a relatively homogeneous bright-CL matrix, irregular CL-dark patches, bifurcated CL-dark fractures, cobweb networks and jigsaw puzzle-like textures (Figs. 6.4c-e; Table 6.2). Thick CL-gray streaks (tens to hundred μm wide) have overgrown the massive quartz cores that have intense CL responses (Fig. 6.4d).

CL-dark fractures are more abundant in quartz from the tourmaline veins than from other quartz-rich assemblages in the Pieman Heads Granite (Fig. 6.4e; Table 6.2). The vein quartz grains are typically characterised by thick, bifurcated fractures (up to hundreds μm) that lack any CL response and separate the CL-bright quartz grains (Fig. 6.4e). Anastomosing, thin CL-dark fractures have cut some CL-dark patches. Two types of CL-gray bands and streaks have been recognised in the tourmaline veins. Most of the broad CL-gray streaks are orientated parallel to grain boundaries, and are intergrown with CL-bright quartz, both of which are truncated by CL-dark fractures and patches (Fig. 6.4e, right). The second type of CL-gray bands are closely associated with thick, sinuous CL-dark fractures (Fig. 6.4e, left), which probably resulted from dilation of CL-dark quartz into CL-bright quartz grains (cf. Rusk and Reed, 2002).

6.3.1.4 Heemskirk Granite – Pb-Zn veins

Samples of Pb-Zn quartz veins from the Sweeney Mine collected by Hajitaheri (1985; Table 6.1; Fig. 6.1) were analysed for the current cathodoluminescence study. Quartz from the Pb-Zn veins are typically characterised by the presence of euhedral oscillatory growth zones that are rhythmical parallel to grain boundaries (Table 6.2; Fig. 6.5). Fine laminations are dominated by subtle to distinct variations in CL intensity, with widths ranging from one to tens of μm. Quartz cores mostly resemble the CL intensity of oscillatory rims, but CL-bright sectors and/or small CL-dark patches have been observed locally in the central zones (Figs. 6.5a-d). The CL-dark patches are volumetrically much less abundant than those in the tourmaline-rich assemblages. SEM-CL textures of quartz in Pb-Zn veins from the Heemskirk Granite contrast markedly with quartz from the tourmaline-rich assemblages.

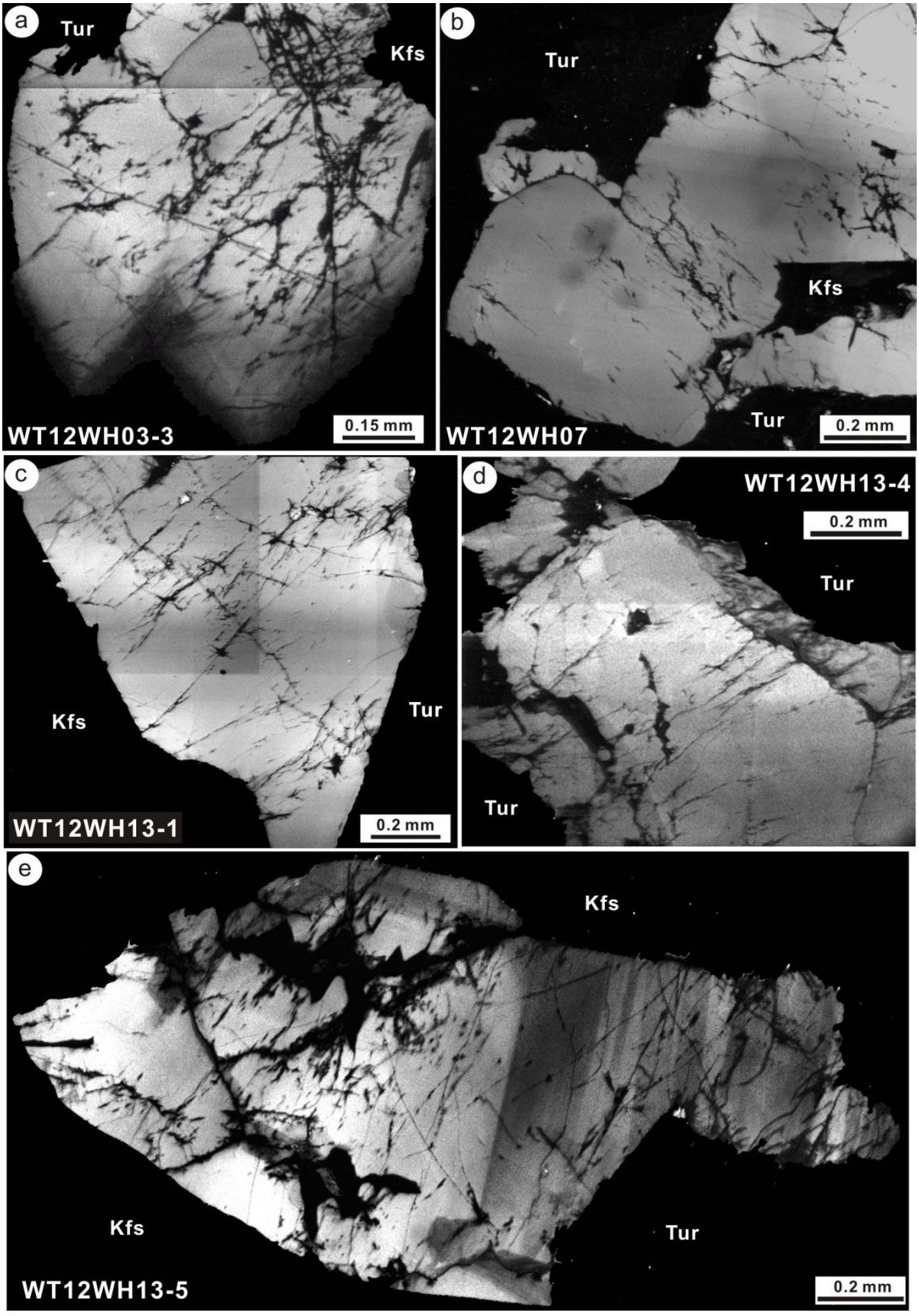

Figure 6.4 SEM-CL textures of quartz from tourmaline patches (a), tourmaline orbicules (b), and tourmaline veins (c-e) in the Pieman Heads Granite. Kfs = K-feldspar, Tur = tourmaline. All sample details listed in Table 6.1 and Fig. 3.6.

Table 6.2 CL textural characteristics of quartz from the Heemskirk and Pieman Heads granites

Type	Granite	CL textures				
		CL-bright luminescence	Euhedral growth zones	CL-dark patches and streaks	CL-dark fractures	CL-dark cobweb networks
Aplite	Heemskirk	Dominated by CL-bright luminescence	Uncommon	Minor small CL-dark patches	Minor thin CL-dark fractures	Locally developed within CL-bright quartz
USTs	Heemskirk	The bases of UST layers are characterised by homogeneous CL-bright quartz	Distinctive CL-gray to CL-bright bands occur at the apexes of UST quartz that are parallel to grain edges	Weakly to intermediately developed, and interstitial to quartz crystal mosaics with intense CL response	Thin (1-2 μm) fractures cut the bright-CL quartz grains at the base and the oscillatory zones at the apex	Uncommon developed
Tourmaline patches	Heemskirk, Pieman Heads	The most prominent characteristic in this type of quartz	Weakly developed, only occur on the grain boundaries	Uncommon; locally connected by thin cracks or bands	Weakly to intermediately developed fractures cut and offset CL-bright quartz grains	Locally developed in intensely fractured domains
Tourmaline orbicules	Heemskirk, Pieman Heads	Massive CL-bright luminescence, cut by numerous bifurcated CL-dark cracks	Locally observed in quartz from the Heemskirk Granite, but uncommon in the Pieman Heads Granite	Abundant CL-dark patches typically occur in the interior of the CL-bright quartz	Intermediately developed; cut the massive CL-bright quartz grains and connect the non-luminescent patches	Weakly developed, CL-dark fractures that have engulfed and offset CL-bright quartz cores
Tourmaline cavities	Heemskirk	Homogenously CL-bright response characterise the embayed quartz cores	Uncommon	Thick streaks (> 100 μm) with intermediate CL intensities locally developed	Commonly cut CL-bright quartz grains; intermediately to intensely developed	Weakly developed, associated with CL-dark patches and fractures
Tourmaline veins	Heemskirk, Pieman Heads	CL-bright quartz has been cut and separated by dark to gray luminescent patches and fractures	Fine-scale growth zones commonly developed, with orientations parallel to grain boundaries	Dark luminescent patches and bands have typically embayed and truncated the CL-bright and CL-gray quartz	Abundant thin, elongated non-luminescent cracks and streaks intensely developed	Gray to dark CL intensity, occur mostly where the quartz has been strongly fractured and offset
Pb-Zn veins	Heemskirk	CL-bright cores overprinted by euhedral, oscillatory CL-gray rims	Intensely developed euhedral oscillatory growth zones parallel to grain boundaries	Small CL-dark patches occur locally, much less abundant than in the tourmaline-rich textures	Thin fractures cut the CL-bright core, and are overprinted by the euhedral CL-gray overgrowths	Uncommonly developed

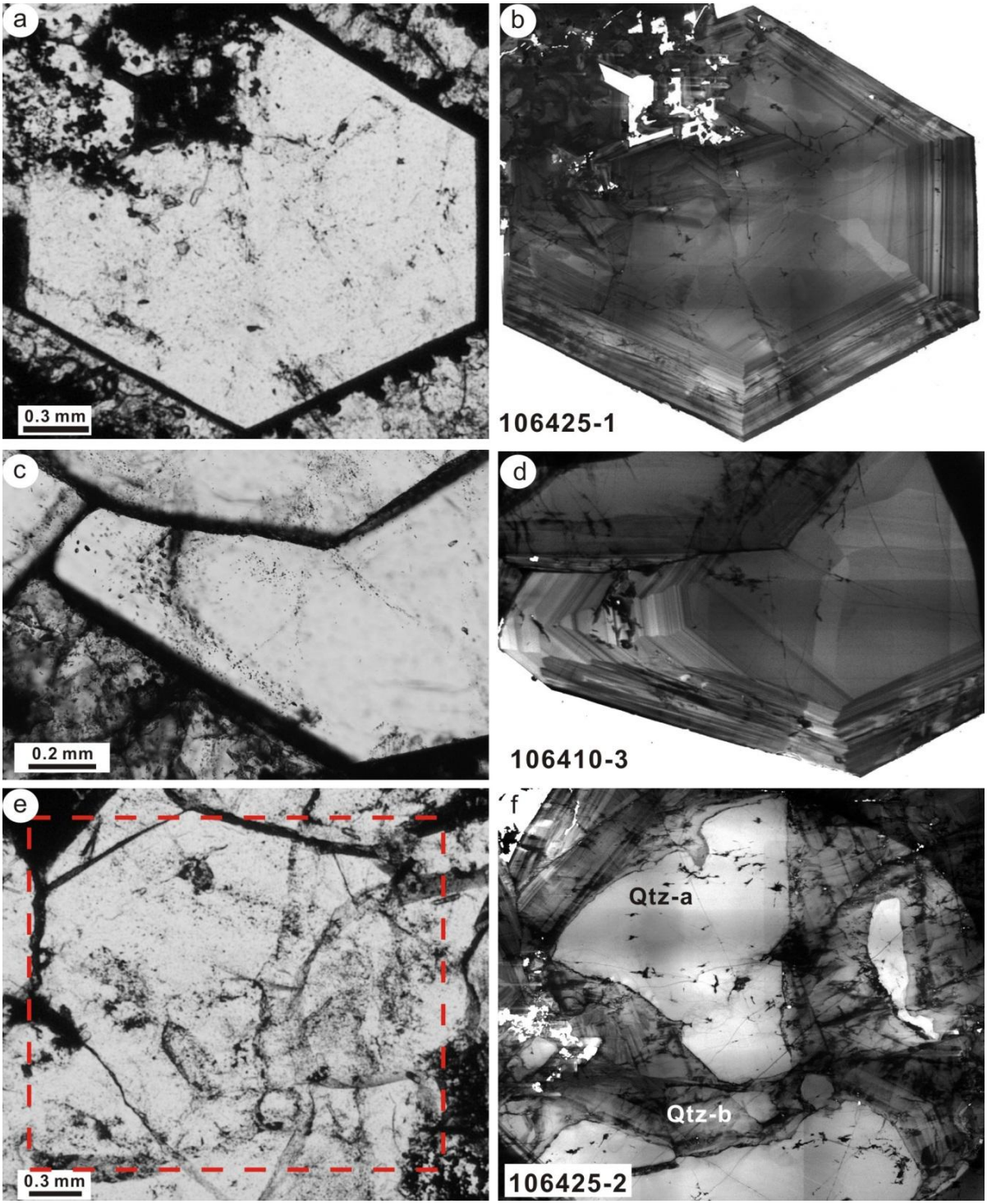

Figure 6.5 Contrasting internal features of quartz from Pb-Zn veins revealed by transmitted light (a, c, e) and SEM-CL imaging (b, d, f). Qtz = quartz. All sample details listed in Table 6.1 and Fig. 6.1.

In some quartz grains from the Pb-Zn veins, CL textures have distinctive irregular CL-bright cores overprinted by euhedral, oscillatory CL-gray rims (Table 6.2). These features cannot be discerned in plane polarised light images (Figs. 6.5e-f). Similar to quartz from tourmaline-rich features, the CL-bright cores contain irregular patches and thin fractures with weak or no CL intensity, and have been subsequently embayed and overprinted by the euhedral CL-gray overgrowths. These features provide evidence for two

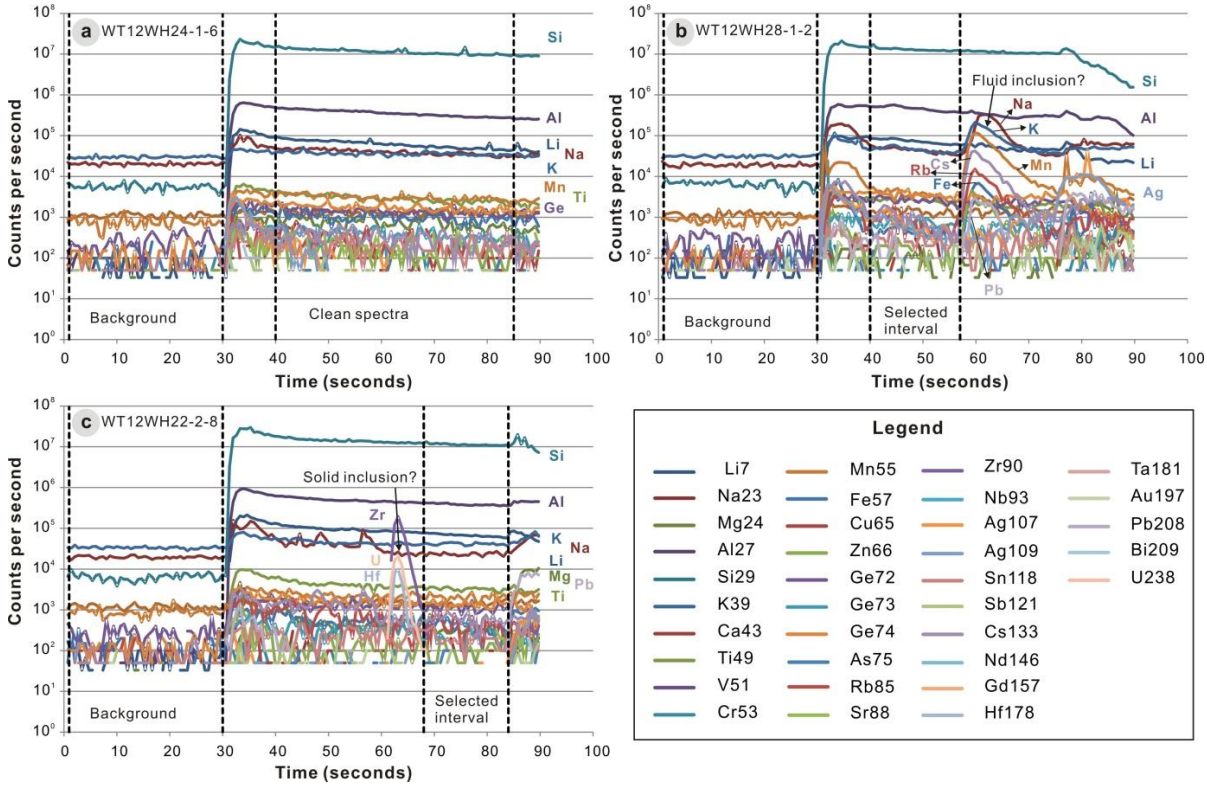

Figure 6.6 Time-resolved signals from LA-ICP-MS analysis of quartz, showing signal spectra for trace elements analysed. The background measurement starts at 1s and ends at 30s, when the laser is switched on. Subsequent laser ablation starts at 32s and ends at 90s. (a) Most quartz grains present smooth LA-ICP-MS spectral signals similar to the spot analysis of WT12WH24-1-6, and the chosen interval for data reduction varies from 40s to 85s. (b) Spot analysis of quartz WT12WH28-1-2 shows spiked spectra between 59s and 70s, and between 73s and 86s, due to ablating of two fluid inclusions containing higher Na, K, Mn, Cs, Rb, Fe, Ag, and Pb concentrations. The interval for data reduction was selected from 40s to 57s, avoiding the interference of the inclusions. (c) Spot analysis of quartz WT22WH22-2-8 shows spiked spectra between 60s and 66s, possibly ablating of a solid inclusion (zircon?) containing higher Zr, U, and Hf concentrations. The interval for data reduction was selected from 68s to 84s, avoiding the interference of the inclusion.

stages of quartz precipitation: an early-stage CL-bright quartz (Qtz-a) that is likely to have crystallised at higher temperature; and a late-stage CL-gray quartz (Qtz-b) that probably formed at lower pressures and temperatures (e.g., Rusk and Reed, 2002).

6.3.2 Trace elements in quartz

LA-ICP-MS analyses have revealed that Al is the most abundant trace element in quartz grains from western Tasmanian granites, ranging from 40.1 to 2266 ppm with a median of 258 ppm (Fig. 6.7; Table 6.3). The median values of Li, Ca, Ti, and Fe are in the tens of ppm level (Table 6.3), and concentrations of these trace elements commonly span from one to hundreds of ppm (Fig. 6.7). Sodium, K and Ge have mean concentrations of several ppm, whereas Mg, Mn, Zn, Rb, and Cs have mean values below 1 ppm (Table 6.3). Strontium and Sb typically have values ranging from below detection limit (bdl) to several ppm with medians below 0.01 ppm. Tin in quartz has low abundances from bdl to 0.389 ppm, and a mean of 0.096 ppm. Other trace elements, such as V, Cr, Cu, As, Zr, Nb, Ag, Nd, Gd, Hf, Ta, Au, Pb, Bi, and U have concentrations lower than 0.1 ppm, and largely below detection limits of the instrument (Table 6.3;

Appendix 6). Figure 6.5 shows the detailed ranges and median values of representative elements in all quartz types from the western Tasmanian granites.

6.3.2.1 Heemskirk Granite – UST quartz

Most of the trace elements in aplitic and UST quartz have similar concentrations and ranges to those in tourmaline orbicules and cavities from the Heemskirk Granite, and contrast from those from tourmaline-rich veins (Table 6.3; Fig. 6.7). Aluminium in quartz from the aplitic phase of the Heemskirk Granite ranges from 186 to 704 ppm, with a median of 215 ppm (Table 6.3; Fig. 6.7a), whereas Li has a range of 22.8 to 51.4 ppm (median = 31.7 ppm; Table 6.3). Titanium in aplitic quartz has concentrations of 21.7 to 81.0 ppm, and Ge contents fluctuate from 0.763 to 1.69 ppm (Table 6.3). Iron, Na, K, Mg, Zn, and Rb concentrations are mostly over their respective detection limits, with median values of 18.0, 3.58, 6.13, 1.49, 0.344 and 0.153 ppm (Table 6.3).

Aluminium, Li, Na, Mg, Ge, Zn, Sr, Pb, Rb and Cs concentrations in UST quartz are consistently higher than those in aplitic quartz in the Heemskirk Granite (Table 6.3; Fig. 6.7). Aluminium in UST quartz ranges from 101 to 1196 ppm (median = 302 ppm), a broader range than its counterparts in aplitic quartz (Table 6.3). The ranges of Li concentrations mostly overlap between UST and aplitic quartz (Fig. 6.7b), but the median value in UST quartz (39.6 ppm) is higher than aplitic quartz (31.7 ppm; Table 6.3). Titanium values in UST quartz mostly range from 11.0 to 68.0 ppm with a median of 26.7 ppm (Fig. 6.7c), lower than those in aplitic quartz (median = 40.5 ppm; Table 6.3). The median Fe content in UST quartz (34.6 ppm) is almost twice in aplitic quartz (17.9 ppm), with the highest value of 1240 ppm in all of the quartz samples (Table 6.3). Germanium has similar concentrations in aplitic and UST quartz (0.763 to 1.72 ppm; Fig. 6.7f), but its median in UST quartz (1.32 ppm) is higher than in aplitic quartz (0.906 ppm; Table 6.3). The Sn concentrations mostly overlap between UST and aplitic quartz grains, and are typically lower than 0.1 ppm, with medians of 0.090 and 0.061 ppm, respectively (Table 6.3; Fig. 6.7i).

6.3.2.2 Heemskirk Granite – tourmaline-rich features

Aluminium in quartz from tourmaline patches and orbicules in the Heemskirk Granite mostly ranges from 130 to 400 ppm, with median values of ca. 280 ppm (Table 6.3; Fig. 6.7a). An extreme value of 900 ppm Al was obtained in a grain from the tourmaline orbicules. Quartz from tourmaline cavities has a wider range of Al concentrations than those from tourmaline patches and orbicules, and a lower median value of 248 ppm (Table 6.3; Fig. 6.7a). Quartz in tourmaline veins has the lowest concentrations of Al overall, with a median of 107 ppm (Table 6.3; Fig. 6.7a).

Median concentrations of Li in quartz decrease progressively from tourmaline patches to tourmaline cavities (46.8, 38.7 and 34.6 ppm), and to 10.2 ppm in tourmaline veins (Table 6.3; Fig. 6.7b). The median Ti concentrations behave in a similar fashion with the highest value (27.9 ppm) from tourmaline patches, and the lowest value (3.35 ppm) from tourmaline veins (Table 6.3; Fig. 6.7c).

Germanium in quartz has a restricted range, mostly from 0.7 to 2.7 ppm (Table 6.3; Fig. 6.7f). Median values of Ge increase subtly from tourmaline patches to cavities (1.23, 1.33 and 1.63 ppm), but decrease to

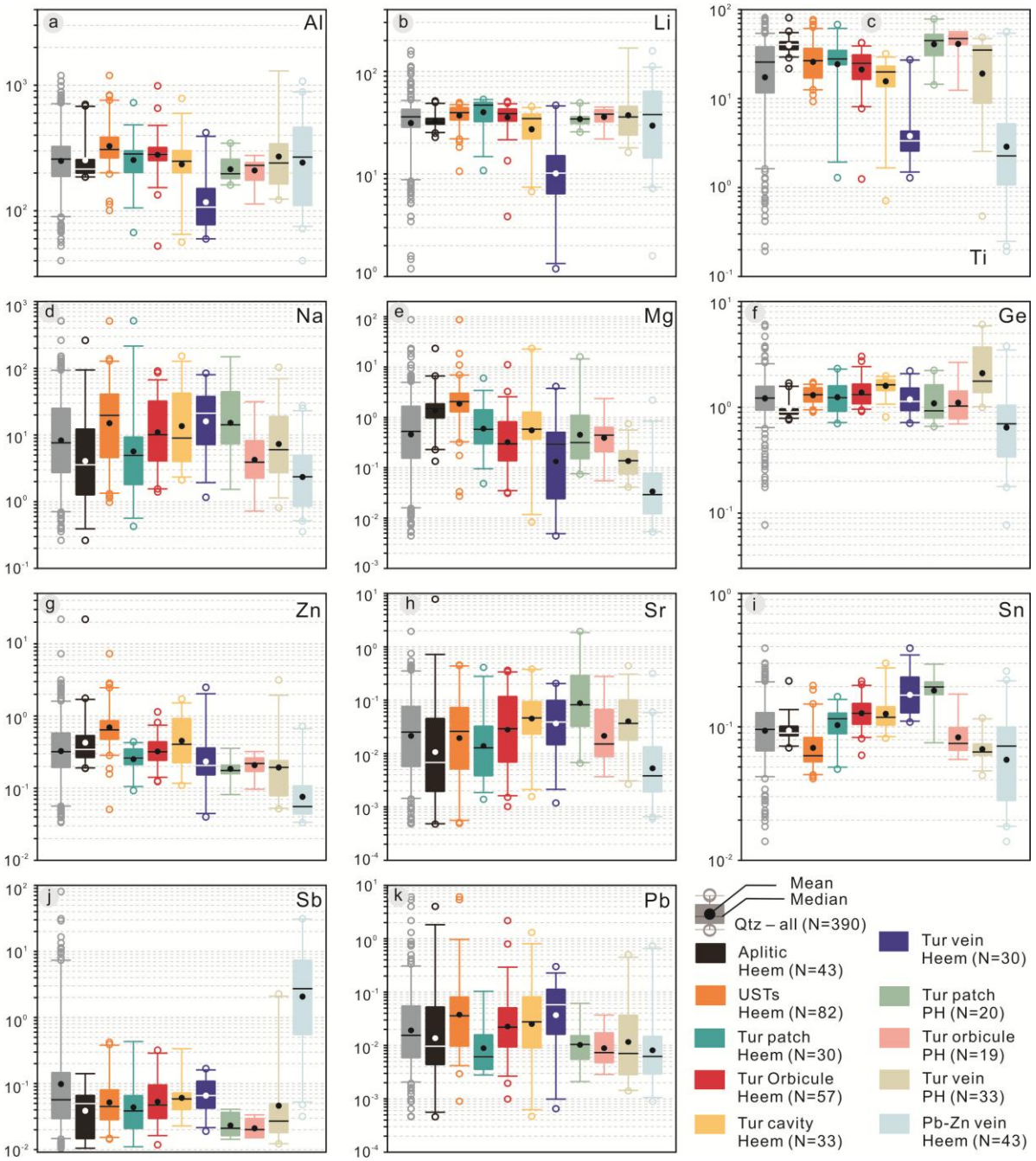

Figure 6.7 Percentile box and whisker plots showing ranges and average concentrations of representative trace elements in different quartz types from western Tasmanian granites. (a) Al, (b) Li, (c) Ti, (d) Na, (e) Mg, (f) Ge, (g) Zn, (h) Sr, (i) Sn, (j) Sb, and (k) Pb. Qtz = quartz, Tur = tourmaline, Heem = Heemskirk Granite, PH = Pieman Heads Granite. All data presented in Appendix 6, and sample details listed in Table 6.1.

1.14 ppm in quartz tourmaline veins. Similar compositional patterns can be found in Mn, Zn, and Sr concentrations from different tourmaline-rich features, except that these three trace elements are one or two orders of magnitude lower than the Ge concentrations (e.g., Figs. 6.7g-h; Table 6.3).

Quartz grains from tourmaline patches have Na concentrations ranging from 0.426 to 105 ppm that is wider than other tourmaline-rich features (Table 6.3; Fig. 6.7d). The median values of Na in quartz increase from tourmaline patches (4.94 ppm), to orbicules (10.1 ppm) and cavities (9.12 ppm), and to the veins (21.2 ppm). Tin concentrations in quartz have a narrow range from bdl to 0.389 ppm (Table 6.3), but

resemble the compositional pattern of Na values between tourmaline-rich features, with the highest median from tourmaline veins (0.174 ppm; Fig. 6.7i). The Sb and Pb contents of quartz commonly correlate with Sn in quartz from tourmaline patches, orbicules, cavities and veins, although their mean concentrations are typically one order of magnitude lower than the latter (Table 6.3; Figs. 6.7j-k).

6.3.2.3 Pieman Heads Granite – tourmaline-rich features

Aluminium concentrations in quartz from tourmaline-rich features of the Pieman Heads Granite are slightly lower than their counterparts from the Heemskirk Granite (Table 6.3; Fig. 6.7a). The highest Al values were detected in quartz from tourmaline veins (median = 240.4 ppm), higher than the median of 107 ppm obtained for the tourmaline veins from the Heemskirk Granite (Table 6.3). Quartz from the two granites mostly contains similar Li concentrations from 25 to 46 ppm (Table 6.3). Median Li values in quartz from Pieman Heads are similar for tourmaline patches (34.4 ppm), orbicules (38.3 ppm), and veins (35.9 ppm; Table 6.3; Fig. 6.7b).

Titanium concentrations in quartz show a decreasing trend from early tourmaline patches (median = 44.9 ppm) to late tourmaline veins (median = 35.1 ppm) in the Pieman Heads Granite (Table 6.3; Fig. 6.7c), whereas Ge values present the opposite pattern (Fig. 6.7f). The concentrations of these two elements are similar to those in the equivalent quartz textures from the Heemskirk Batholith.

Sodium and Mg concentrations in quartz appear to be higher in tourmaline patches than tourmaline veins at Pieman Heads (Table 6.3; Figs. 6.7d-e), whereas quartz from the tourmaline veins (median = 1.74 ppm) contains higher Ge than those from the tourmaline patches (median = 0.926 ppm; Figs. 6.7d-f).

Tin concentrations in quartz from Pieman Heads range from bdl to 0.295 ppm, with a median of 0.199 ppm, and the highest value was detected in tourmaline patches (Table 6.3). These results are similar to values from tourmaline veins in the Heemskirk Granite (Table 6.3; Fig. 6.7i). The median values of Sn in quartz decrease from tourmaline patches (0.199 ppm), to orbicules (0.075 ppm), and to veins (0.065 ppm) from Pieman Heads.

Many trace elements in quartz, including Sr, Rb, Sb, Cs, Nb, Ta and Pb, are typically below 0.1 ppm (Table 6.3), and have no clear variational trends between different tourmaline-rich textures. The highest Sr and Cs concentrations in quartz were detected in the tourmaline patches (Table 6.3; Fig. 6.7h).

6.3.2.4 Heemskirk Granite – Pb-Zn veins

Aluminium concentrations in quartz from Pb-Zn veins have the broadest range, from 40.1 to 1076 ppm (Table 6.3; Fig. 6.7a). The median value (268 ppm) is comparable to those in tourmaline patches, orbicules and cavities, and significantly higher than tourmaline-rich veins (107 ppm; Fig. 6.7a). Lithium contents in quartz from Pb-Zn veins (median = 37.9 ppm; Table 6.3) vary in a similar fashion to Al in the tourmaline-rich textures and Pb-Zn veins (Fig. 6.7b). Titanium in quartz from Pb-Zn veins range from 0.193 to 56.6 ppm, and the median value is similar to that from the tourmaline veins (Table 6.3; Fig. 6.7c).

Most of the trace elements in quartz from the Pb-Zn veins, including Na, Ca, Ge, Zn, Sr, Sn, Rb, and Cs, have concentrations lower than those from tourmaline-rich features in the Heemskirk Granite (Table

6.3; Fig. 6.7). Antimony concentrations in quartz from the Pb-Zn veins have a broad range, from 0.032 to 80.6 ppm with a median of 2.73 ppm, and are on average much higher than those in the tourmaline-rich features (medians < 0.1 ppm; Table 6.3).

6.4 Discussion

6.4.1 Trace element substitutions

Aluminium, Li, Ti and Ge are abundant trace elements analysed in quartz samples from the Heemskirk and Pieman Heads granites (Table 6.3). Aluminium, Ti and Ge preferentially substitute for Si in the quartz lattice, because they have similar ionic potentials (Götze et al., 2001, 2004; Müller and Koch-Müller, 2009). Aluminium concentrations correlate positively with Li in all quartz samples, with atomic Al: Li ratios typically below the 1:1 line (Fig. 6.8a). This linear correlation implies a coupled substitution of Al and Li for Si, defined as $[Al^{3+}O_4Li][Si^{4+}]_{-1}$, where Li contents compensate charge balance in the quartz lattice (Götze et al., 2001). Most of the quartz analyses cluster around the 2:1 Al: Li ratio (Fig. 6.8a), indicating the existence of other trace element exchanges in quartz's lattice, such as $[AlO_4/M^+][Si^{4+}]_{-1}$, $[GeO_4/M^+][Si^{4+}]_{-1}$, $[TiO_4/M^+][Si^{4+}]_{-1}$ and $[FeO_4/M^+][Si^{4+}]_{-1}$ vectors, with $M^+ = H^+$, Na^+, K^+, Rb^+ (e.g., Figs. 6.8c-d; Götze et al., 2004; Larsen et al., 2004; Müller and Koch-Müller, 2009). No linear correlations were detected between Al, and Ti and Ge in quartz (e.g., Fig. 6.8b), which all compete for the Si^{4+} crystallographic site (Götze et al., 2004).

6.4.2 Contamination by fluid inclusions

Quartz analysed from western Tasmanian granites, especially those from tourmaline orbicules, tourmaline-filled cavities, tourmaline veins and Pb-Zn veins, contain abundant clusters and trails of fluid inclusions (e.g., Figs. 7.2-7.3). All LA-ICP-MS analyses of quartz attempted to avoid fluid inclusions, but some analyses were contaminated by accidental ablation of fluid inclusions to varying degrees (e.g., Fig. 6.6b). Sodium and Ca (Figs. 6.9a-b) do not linearly correlate with Al, indicating that most of the Na and Ca contents incorporated into the quartz structure are not in the fashion of charge compensation for Al (cf. Götze et al., 2004). Approximately 12 % of K contents in quartz deviate from the linear trend ($r^2 = 0.61$) defined by Al and K (Fig. 6.8c), whereas 15 % of Rb values in quartz deviate from the linear trend ($r^2 = 0.53$) defined by Al and Rb (Fig. 6.8d). However, most of the K (up to 500 ppm) and Rb (up to 5.8 ppm) correlate positively with Na (up to 514 ppm) in quartz (Figs. 6.9c-d). These elements are probably the main components of sub-grain fluid inclusions hosted in quartz that were accidentally ablated, consistent with previous studies (e.g., Götze et al., 2004; Götze, 2009; Rusk et al., 2011). Anomalously high concentrations of other elements, including Mg, Mn, Fe, and Cs etc. (Fig. 6.7; Table 6.3), may be also due to accidental ablation of tiny fluid inclusions hosted in quartz that produced obvious spikes in the LA-ICP-MS spectra. Thereby, it is prudent to treat the Na, K, Ca, Mn, Fe, Rb and Cs data as having large uncertainties (e.g., Götze et al., 2004; Götze, 2009; Drivenes et al., 2016).

Table 6.3 Quartz trace element compositions from the Heemskirk and Pieman Heads granites analysed by LA-ICP-MS

Elements (ppm)	Aplite-Heem (n= 43)			USTs-Heem (n= 82)			Tur patch-Heem (n=30)			Tur orbicule-Heem (n=57)			Tur cavity-Heem (n=33)		
	Range	Median	% bdl	Range	Median	% bdl	Range	Median	% bdl	Range	Median	% bdl	Range	Median	% bdl
Li	22.8 - 51.4	31.7	0	10.6 - 49.6	39.6	0	10.8 - 53.3	46.8	0	3.85 - 50.9	38.7	0	6.74 - 45.3	34.6	0
Na	bdl - 262	3.58	9	bdl - 510	19.7	1	0.426 - 514	4.94	0	bdl- 91.2	10.1	2	bdl - 152	9.12	9
Mg	0.134 - 23.4	1.49	0	0.027 - 87.2	2.06	0	0.049 - 6.01	0.58	0	bdl - 11.1	0.299	2	bdl - 23.5	0.581	9
Al	186 - 704	215	0	101 - 1196	308	0	67.1 - 726	284	0	52.4 - 988	281	0	56.3 - 785	248	0
K	1.88 - 299	6.13	0	bdl - 302	26.5	2	1.11 - 31.0	4.57	0	1.96 - 507	9.67	0	bdl - 306	8.57	12
Ca	bdl - 22.7	13.9	58	bdl - 93.8	15.3	51	bdl - 20.8	12.8	60	bdl - 115	15.0	67	bdl - 90.9	20.3	67
Ti	21.7 - 81.0	40.5	0	9.26-77.1	26.7	0	1.29 - 67.9	27.9	0	1.25 - 42.5	24.9	0	0.711 - 31.9	19.9	0
V	bdl - 0.009	0.007	86	bdl - 0.067	0.003	95	bdl - 0.13	0.067	93	bdl - 0.082	0.018	93	bdl - 0.086	0.011	85
Cr	bdl - 0.135	0.102	74	bdl - 0.216	0.070	94	bdl - 0.19	0.134	43	bdl - 0.365	0.105	77	bdl - 0.277	0.110	82
Mn	0.241 - 94.4	0.610	0	0.118 - 17.8	1.70	0	0.071 - 1.54	0.589	0	bdl - 4.08	0.639	2	bdl - 31.2	0.951	9
Fe	4.62 - 252	18.0	0	0.903 - 1240	34.6	0	bdl - 137	12.4	3	bdl - 312	8.77	4	bdl - 481	21.2	18
Cu	bdl - 0.163	0.057	81	bdl - 0.403	0.054	89	bdl - 3.60	0.054	57	bdl - 1.14	0.080	42	bdl - 2.11	0.119	36
Zn	bdl - 21.9	0.344	2	bdl - 7.30	0.642	1	bdl - 0.438	0.262	3	bdl - 1.14	0.320	5	bdl - 1.72	0.406	12
Ge	0.763 - 1.69	0.906	0	0.902 - 1.72	1.32	0	0.703 - 2.32	1.23	0	0.915 - 3.02	1.32	0	0.812 - 1.98	1.63	0
As	bdl - 0.200	0.047	84	bdl - 0.913	0.072	63	bdl - 0.273	0.061	70	bdl - 0.568	0.103	33	bdl - 0.130	0.066	70
Rb	bdl - 4.94	0.153	5	bdl - 5.76	0.330	5	bdl - 0.681	0.147	3	0.041 - 5.12	0.265	0	bdl - 3.17	0.182	12
Sr	bdl - 7.79	0.007	21	bdl - 0.456	0.026	9	bdl - 0.411	0.013	7	bdl - 0.364	0.029	11	bdl - 0.383	0.046	9
Zr	bdl - 0.261	0.009	19	bdl - 0.464	0.017	12	bdl - 0.018	0.003	40	bdl - 9.85	0.019	40	bdl - 0.032	0.004	36
Nb	bdl - 0.098	0.003	37	bdl - 0.175	0.006	33	bdl - 0.008	0.002	27	bdl - 0.083	0.005	42	bdl - 0.027	0.003	42
Ag	bdl - 0.372	0.190	95	bdl - 0.021	0.021	99	bdl - 0.007	0.006	93	bdl - 36.5	0.051	40	bdl - 0.039	0.015	76
Sn	bdl - 0.221	0.090	9	bdl - 0.204	0.061	15	bdl - 0.168	0.115	7	bdl - 0.220	0.126	18	bdl - 0.300	0.118	18
Sb	bdl - 0.141	0.050	63	bdl - 0.421	0.045	32	bdl - 0.433	0.039	73	bdl - 0.320	0.047	33	bdl - 0.336	0.059	52
Cs	bdl - 5.01	0.081	12	bdl - 3.98	0.221	9	bdl - 1.08	0.115	10	bdl - 2.21	0.267	2	0.005 - 0.895	0.107	0
Nd	bdl - 0.873	0.003	72	bdl - 0.150	0.005	72	bdl - 0.004	0.003	60	bdl- 1.99	0.006	79	bdl - 0.074	0.005	76
Gd	bdl - 0.053	0.004	77	bdl - 0.139	0.004	83	bdl - 0.007	0.004	83	bdl - 0.236	0.007	79	bdl - 0.009	0.005	79
Hf	bdl - 0.019	0.003	67	bdl - 0.028	0.003	65	bdl - 0.004	0.002	77	bdl - 0.657	0.008	70	bdl - 0.011	0.004	79
Ta	bdl - 0.032	0.002	53	bdl - 0.108	0.002	50	bdl - 0.006	0.002	77	bdl - 0.102	0.002	44	bdl - 0.010	0.002	42
Pb	bdl - 4.02	0.010	42	bdl - 6.07	0.036	29	bdl - 0.103	0.006	43	bdl - 2.18	0.022	12	bdl - 1.31	0.028	24
Bi	bdl - 0.014	0.003	88	bdl - 0.087	0.005	67	bdl - 0.087	0.003	77	bdl - 0.663	0.004	63	bdl - 0.043	0.006	67
U	bdl - 0.089	0.000	53	bdl - 0.612	0.001	32	bdl - 0.003	0.000	60	bdl - 0.829	0.004	37	bdl - 0.013	0.001	36

Tur vein-Heem (n=30)			Tur patch-PH (n=20)			Tur orbicule-PH (n=19)			Tur vein-PH (n=33)			Pb-Zn vein (n=43)		
Range	Median	% bdl	Range	Median	% bdl	Range	Median	% bdl	Range	Median	% bdl	Range	Median	% bdl
1.19 - 46.7	10.2	0	25.6 - 49.2	34.4	0	21.9 - 44.8	38.3	0	16.2 - 146	35.9	0	1.59 - 158	37.9	0
bdl - 84.2	21.2	3	bdl - 14.2	14.2	5	bdl - 31.5	3.91	11	0.813 - 103	5.15	0	0.356 - 27.6	2.36	0
bdl - 4.11	0.292	3	0.074 - 15.9	0.32	0	0.055 - 2.36	0.444	0	0.041 - 0.745	0.141	0	bdl - 2.20	0.029	33
59.8 - 420	107	0	1601 - 346	198	0	113 - 276	230	0	122 - 1079	240	0	40.1- 1077	268	0
bdl - 33.0	4.49	7	bdl - 24.7	1.63	5	bdl - 5.18	1.72	32	bdl - 12.0	3.88	30	bdl - 5.68	1.76	79
bdl - 47.4	28.2	50	bdl - 185	38.9	25	bdl - 17.8	11.6	58	bdl - 21.9	13.5	64	bdl - 17.7	10.8	63
1.29 - 27.4	3.35	0	14.3 to 78.4	44.9	0	12.4 - 56.5	47.2	0	bdl - 48.7	35.1	9	0.193 - 56.6	2.27	0
bdl - 0.010	0.009	90	bdl - 0.020	0.020	95	bdl	bdl	100	bdl - 0.011	0.009	94	bdl - 0.090	0.011	79
bdl - 0.547	0.420	43	bdl - 0.324	0.158	75	bdl - 0.160	0.107	84	bdl - 0.098	0.095	94	bdl - 0.173	0.089	72
bdl - 9.86	0.443	33	bdl - 1.21	0.320	5	bdl - 1.22	0.281	95	bdl - 1.22	0.361	9	bdl - 3.86	0.481	86
bdl - 18.5	3.10	37	1.86 - 14.9	3.01	0	bdl - 14.0	3.78	95	bdl - 8.07	4.15	24	bdl - 44.9	2.68	74
bdl - 0.639	0.448	43	bdl - 0.541	0.076	65	bdl - 0.444	0.049	37	bdl - 0.476	0.063	73	bdl - 0.111	0.041	74
bdl - 2.49	0.206	27	bdl - 0.357	0.175	5	bdl - 0.322	0.220	11	bdl - 3.16	0.193	18	bdl - 0.718	0.056	47
0.708 - 2.21	1.14	0	0.659 - 2.23	0.926	0	0.696 - 2.66	1.03	0	0.997 - 5.82	1.75	0	0.077 - 3.79	0.699	0
bdl - 0.360	0.150	27	bdl - 0.097	0.056	75	bdl - 0.245	0.073	74	bdl - 0.217	0.068	58	bdl - 0.555	0.067	37
bdl - 0.865	0.077	10	bdl - 0.426	0.048	5	bdl - 0.145	0.030	37	bdl - 0.275	0.082	30	bdl - 0.114	0.032	67
bdl - 0.206	0.039	13	0.007 - 1.94	0.087	0	bdl - 0.278	0.015	16	bdl - 0.262	0.036	3	bdl - 0.317	0.004	7
bdl - 0.029	0.004	60	bdl - 0.04	0.008	50	bdl - 0.015	0.004	32	bdl - 5.50	0.003	55	bdl - 1.01	0.002	56
bdl - 0.002	0.002	80	bdl - 0.01	0.003	75	bdl - 0.022	0.002	53	bdl - 0.009	0.001	45	bdl - 0.581	0.002	84
bdl - 1.59	0.540	57	bdl - to 0.01	0.007	85	bdl - 0.006	0.006	95	bdl - 0.006	0.006	97	bdl - 0.037	0.009	93
bdl - 0.389	0.174	13	bdl - 0.295	0.199	20	bdl - 0.176	0.075	16	bdl - 0.116	0.065	9	bdl - 0.262	0.072	7
bdl - 0.168	0.066	13	bdl - 0.041	0.021	70	bdl - 0.034	0.020	74	bdl - 1.02	0.025	39	0.032 - 80.6	2.73	0
0.008 - 2.26	0.112	0	0.008 - 3.84	0.293	0	0.008 - 0.540	0.028	0	bdl - 0.601	0.085	6	bdl - 0.289	0.028	35
bdl - 0.009	0.007	83	bdl - 0.005	0.004	90	bdl - 0.004	0.003	84	bdl - 1.09	0.006	73	bdl - 0.051	0.007	74
bdl - 0.009	0.006	90	bdl - 0.008	0.006	90	bdl - 0.025	0.007	84	bdl - 0.085	0.004	79	bdl - 0.024	0.004	79
bdl - 0.003	0.003	93	bdl - 0.008	0.003	85	bdl - 0.003	0.002	79	bdl - 0.179	0.002	67	bdl - 0.089	0.004	86
bdl - 0.002	0.001	80	bdl - 0.015	0.003	70	bdl - 0.015	0.002	53	bdl - 0.112	0.002	42	bdl - 0.516	0.000	81
bdl - 0.300	0.058	13	bdl - 0.061	0.010	25	bdl - 0.037	0.007	37	bdl - 0.502	0.006	33	bdl - 0.733	0.006	47
bdl - 0.14	0.009	50	bdl - 0.012	0.002	65	bdl - 0.008	0.005	89	bdl - 0.372	0.003	70	bdl - 0.043	0.002	84
bdl - 0.152	0.057	30	bdl - 0.007	0.000	55	bdl - 0.037	0.000	37	bdl - 0.191	0.001	73	bdl - 0.715	0.004	37

Abbreviation: Tur = tourmaline, Heem = Heemskirk Granite, PH = Pieman Heads Granite, bdl = below detection limit.

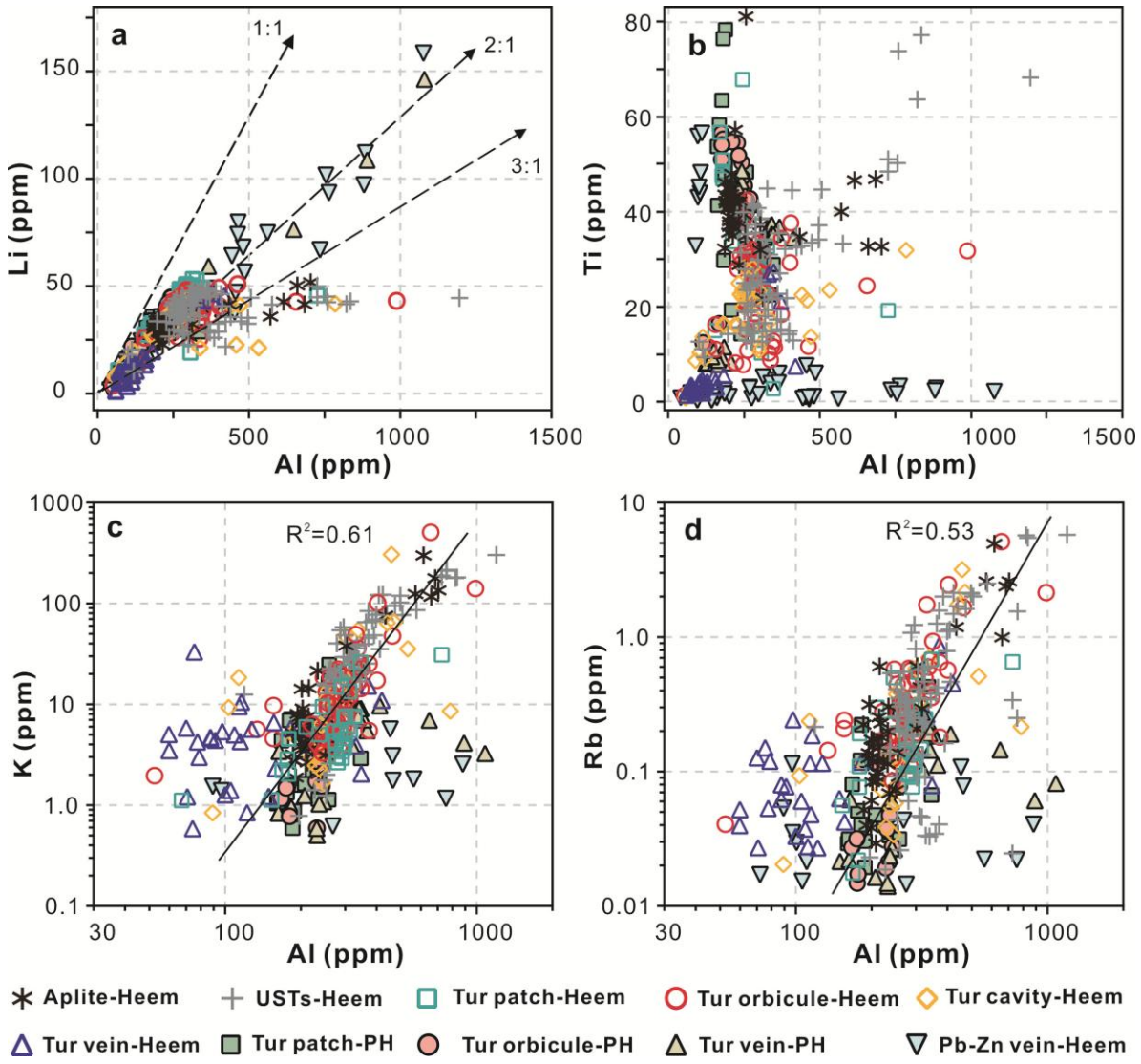

Figure 6.8 Plots showing representative trace element substitution in quartz from western Tasmanian granites. (a) Al versus Li, (b) Al versus Ti, (c) Al versus K, (d) Al versus Rb. Tur = tourmaline, Heem = Heemskirk, PH = Pieman Heads. All data presented in Appendix 6, and sample details listed in Table 6.1.

6.4.3 Implications for fluid evolution

Euhedral UST-quartz grains in the White phase of the Heemskirk Granite are characterised by higher abundances of Al, Li, Na, Mg, Fe, Mn, Ge, Zn, Sr, Pb, Rb and Cs than the intergrown aplitic quartz (Figs. 6.7-6.8; Table 6.3). The trace element contents and ratios in aplitic quartz mostly overlap with those in quartz intergrown with tourmaline patches in the Heemskirk Batholith (Figs. 6.8-6.10; Table 6.3), and they have similar CL-bright textures (Figs. 6.2d-e and 6.3a-b). The two types of quartz are considered to have a magmatic origin, which crystallised directly from the silicic magmas. In contrast, most of the trace elements in UST quartz from the comb-layered textures have similar ranges to those in quartz from tourmaline orbicules and cavities (Figs. 6.8-6.10), suggesting a magmatic – hydrothermal origin. High Ti concentrations (50–100 ppm) were reported from comb-layered quartz in felsic dykes associated with the Logtung W-Mo deposit (NW Canada; Lowenstern and Sinclair, 1996). These values contrast with low Ti concentrations in the UST quartz from Heemskirk Granite (median = 26.7 ppm; Fig. 6.8b), possibly due to

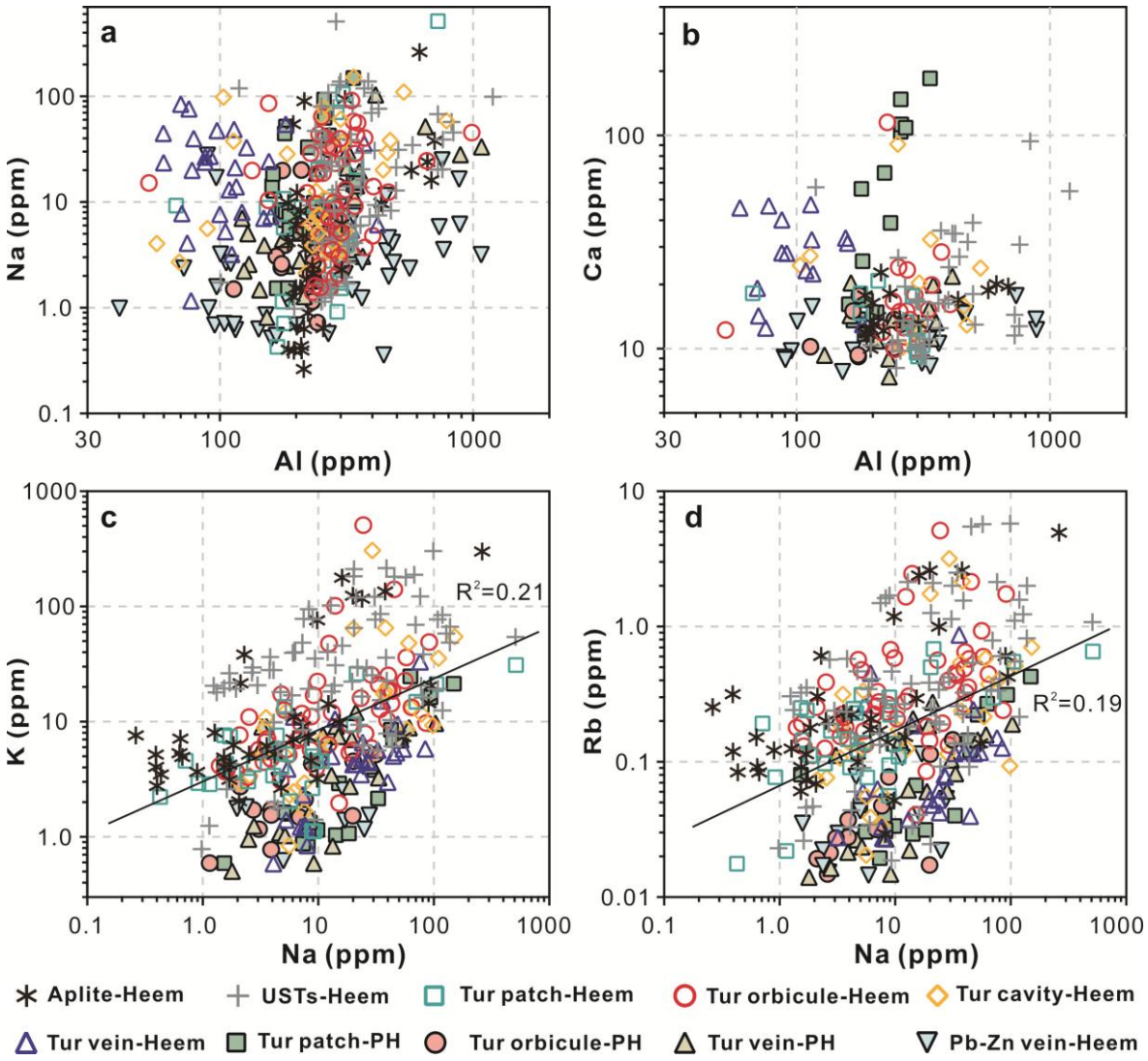

Figure 6.9 Plots showing trace element variations possibly caused by fluid inclusions in quartz from western Tasmanian granites. (a) Al versus Na, (b) Al versus Ca, (c) Na versus K, (d) Na versus Rb. Tur = tourmaline, Heem = Heemskirk, PH = Pieman Heads. All data presented in Appendix 6, and sample details listed in Table 6.1.

UST quartz precipitation occurring at lower temperatures in the Heemskirk Granite (e.g., Audétat et al., 2015).

Most of the quartz grains associated with different tourmaline assemblages have low Al (50–400 ppm) and various Ti (10–80 ppm) concentrations (Table 6.3; Fig. 6.8b). The Al and Ti concentrations in quartz from the Heemskirk and Pieman Heads granites are comparable to those from moderately to highly fractionated S-type granites from the Bohemian Massif, Czech (Breiter et al., 2013; Table 6.4), and Land's End Granite, SW England (Drivenes et al., 2016; Table 6.4). The western Tasmanian granites from which the quartz grains were analysed had probably undergone similar degrees of crystal fractionation.

Compared with tourmaline patches and orbicules, quartz grains in tourmaline veins from the Heemskirk Batholith have low Al (< 200 ppm) and extremely low Ti (< 10 ppm) concentrations (Fig. 6.8b). This characteristic is obvious on plots of Al/Ti against other trace elements (Figs. 6.10a-b). The extremely low Ti concentrations in quartz from the tourmaline veins are interpreted to indicate that they

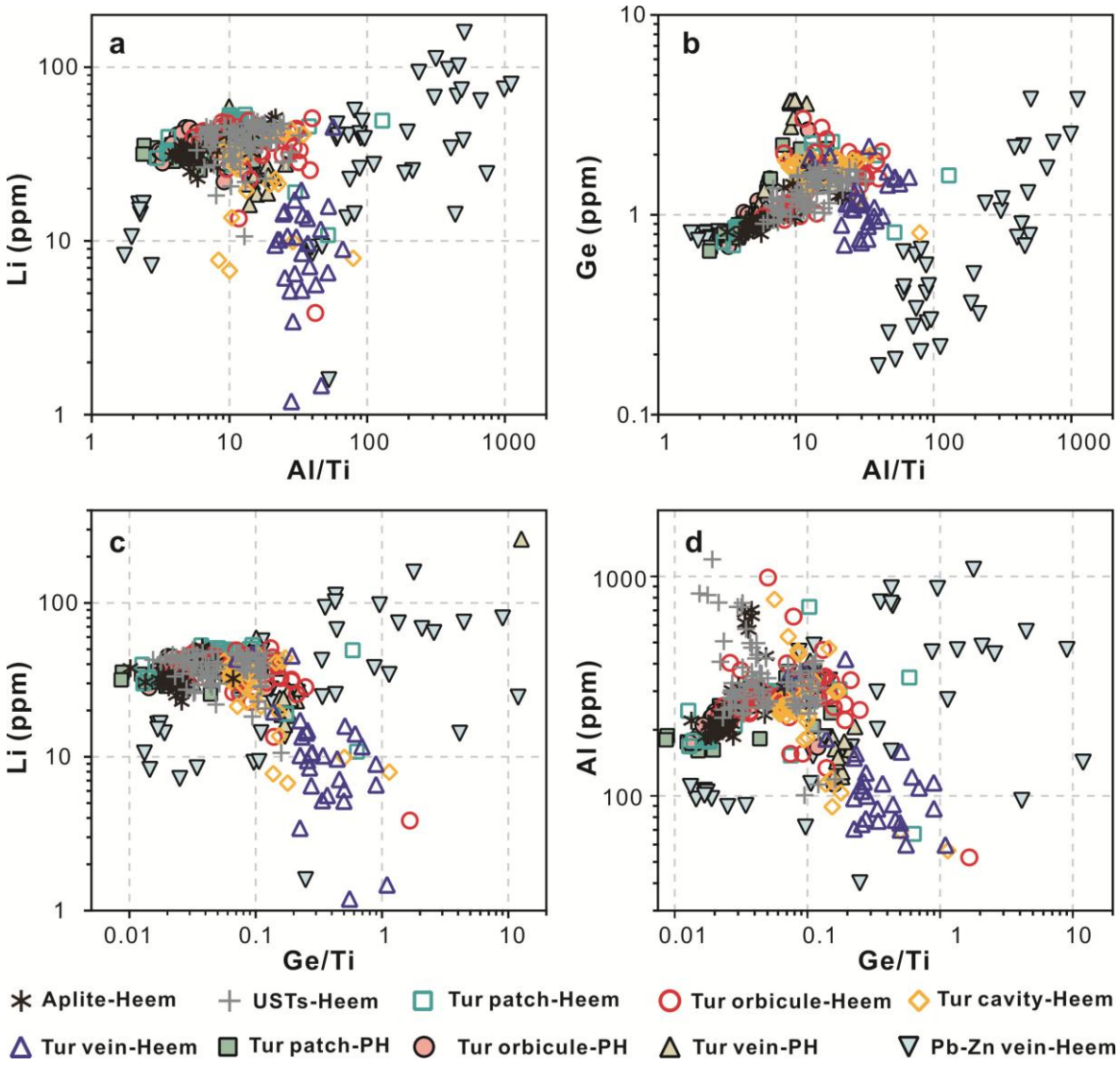

Figure 6.10 Plots showing variations of trace element ratios in quartz from western Tasmanian granites. (a) Al/Ti versus Li, (b) Al/Ti versus Ge, (c) Ge/Ti versus Li, (d) Ge/Ti versus Al. Tur = tourmaline, Heem = Heemskirk, PH = Pieman Heads. All data presented in Appendix 6, and sample details listed in Table 6.1.

formed at relatively low temperatures and pressures (350 °–400 ℃ and 0.2 kbars; e.g., Huang and Audétat, 2012). Intense muscovite-tourmaline alteration is associated with the tourmaline veins (Table 4.1), which most likely caused Al to partition into muscovite and tourmaline rather than quartz, consistent with Al's incompatible behaviour in the quartz lattice (cf. Larsen et al., 2004). The low Li concentrations in quartz veins from the Heemskirk Granite (Figs. 6.10a, c) may also relate to preferential deposition of Li in muscovite and tourmaline (cf. Breiter et al., 2013). Low Al, Li and Ti contents have also been detected in quartz associated with tourmaline from the Pieman Heads Granite, but their variations are not as low as for quartz in tourmaline veins from the Heemskirk Batholith (e.g., Fig. 6.8a-b, 6-10a and c).

Al/Ti and Ge/Ti ratios in quartz have been applied to estimate the degree of crystal fractionation in felsic melt systems (Larson et al., 2004; Jacamon and Larson, 2009; Breiter et al., 2013; Drivenes et al., 2016), because Al and Ge typically behave incompatibly in quartz (Larson et al., 2004). Titanium contents in quartz are independent from other trace elements according to analytical results of natural and synthetic

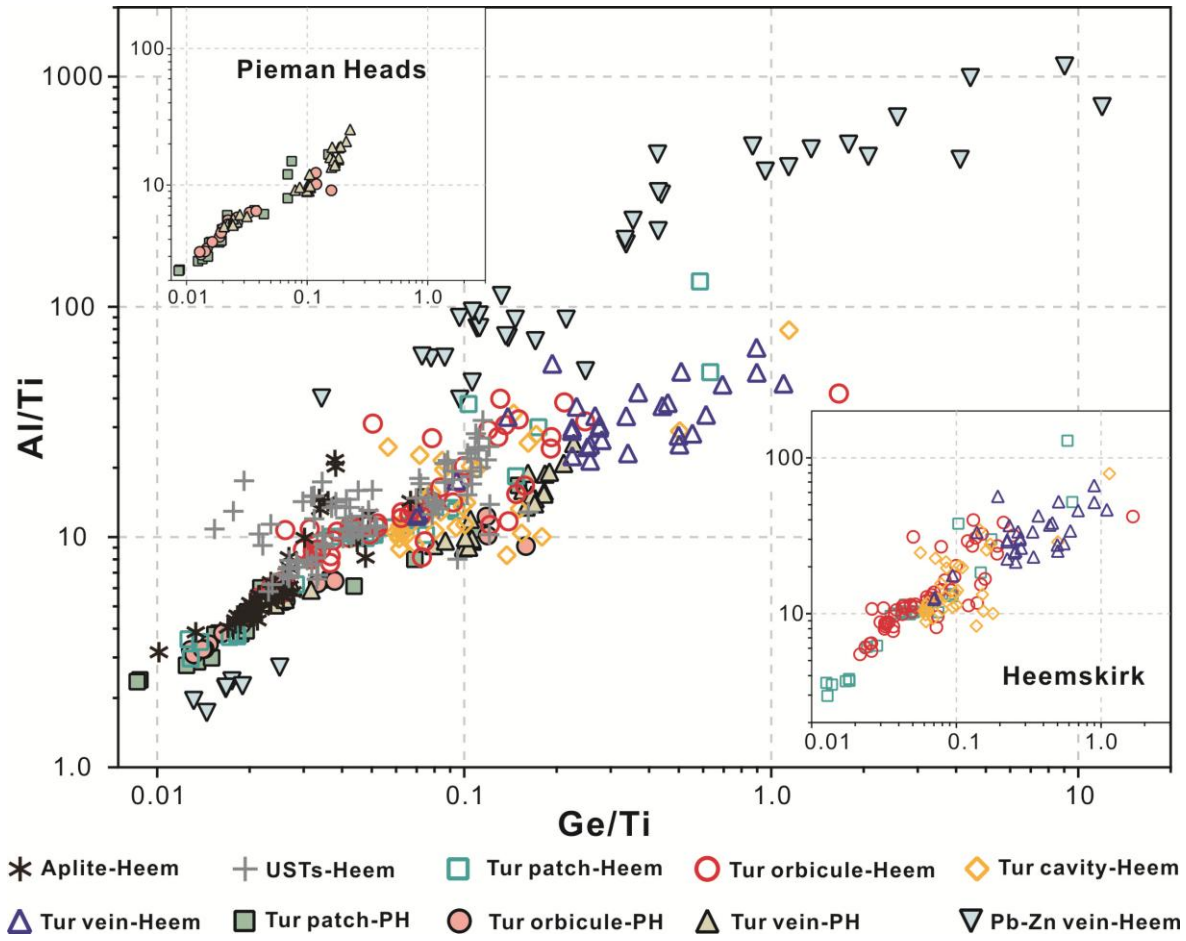

Figure 6.11 Ge/Ti versus Al/Ti plot of different quartz types from western Tasmanian granites. Inset plots are quartz from the Heemskirk (lower right) and Pieman Heads (upper left) granites, respectively. Tur = tourmaline, Heem = Heemskirk, PH = Pieman Heads. All data presented in Appendix 6, and sample details listed in Table 6.1.

quartz samples (Rusk et al., 2006; Huang and Audétat, 2012). For the western Tasmanian granites, plots of Al/Ti against Li and Ge, and Ge/Ti against Li and Al in quartz show remarkable variations in tourmaline veins, tourmaline patches, orbicules and/or cavities (Fig. 6.10), particularly for the samples from the Heemskirk Granite. The Al/Ti and Ge/Ti ratios in quartz increase by at least one order of magnitude from tourmaline patches, orbicules to cavities (Fig. 6.10), which may relate to increasing degrees of fractionation with time, as these tourmaline-rich features precipitated in the roof of the granitic sills.

The quartz samples display linear arrays on the Ge/Ti versus Al/Ti plot (Fig. 6.11), which magnifies the chemical differences in quartz between tourmaline-rich assemblages and Pb-Zn veins from the Heemskirk Granite. The quartz crystals from tourmaline-rich assemblages have distinctly lower Al/Ti ratios than quartz from the Pb-Zn quartz veins (Fig. 6.11). Overall, quartz samples from tourmaline patches have the lowest Ge/Ti and Al/Ti ratios (Fig. 6.11), with values down to 0.02 and 2, respectively. Their ranges mostly overlap with those from fine-grained S-type granites of SE Bohemia (Czech) and SW England (Table 6.4; Breiter et al., 2013; Drivenes et al., 2016), implying that the Heemskirk Granite may have experienced high degrees of crystal fractionation similar to these granites. The Ge/Ti and Al/Ti ratios of the tourmaline orbicules and cavities largely overlap, which are distributed intermediately in the district

between tourmaline patches and veins (Fig. 6.11). In contrast, the tourmaline veins within the Heemskirk Granite have the highest Ge/Ti (up to 1) and Al/Ti (up to 70) ratios (Fig. 6.11). Nevertheless, the Ge/Ti versus Al/Ti plot typically highlights chemical variations in quartz from the different tourmaline-rich features that probably result from exsolved magmatic – hydrothermal fluids from the Heemskirk Batholith.

The Ge/Ti and Al/Ti ratios in quartz from tourmaline-rich assemblages in the Pieman Heads Granite range from 0.01 to 0.2, and from 2 to 30, respectively (Fig. 6.11), narrower than their respective counterparts in the Heemskirk Batholith (Fig. 6.11). The discrepancies of these two ratios in quartz between the two granites may be due to lower degrees of fractional crystallisation of the Pieman Heads Granite (cf. Chapter 3). The Ge/Ti and Al/Ti ratios in quartz also increase in a linear fashion from tourmaline patches, via tourmaline orbicules, to tourmaline veins from the Pieman Heads Granite (Fig. 6.11).

6.4.4 Implications for Sn-Pb-Zn mineralisation

The highest tin concentrations in quartz from the Heemskirk Batholith (up to 0.39 ppm) were detected in tourmaline-quartz veins (Fig. 6.12a), consistent with the highest tin contents that were detected in tourmaline from quartz veins (Table 5.3). Prolonged fractionation of granitic magmas can enrich tin in late-stage magmatic – hydrothermal fluids (Lehmann, 1982; Blevin and Chappell, 1995). Most of the high-grade Sn-(W) greisen and skarn deposits within the south Heemskirk Batholith were hosted in tourmaline-quartz veins (Hajitaheri, 1985), consistent with the trace element geochemistry of tourmaline and quartz from these textures. An alternative interpretation is difficult to disprove that high tin concentrations in quartz from the tourmaline-quartz veins in this batholith might result from mixing of magmatic – hydrothermal fluids with oxidising, Sn^{4+}-rich formation waters derived from the neighbouring Oonah metasedimentary rocks (cf. Williamson et al., 2000).

In the Pieman Heads Granite, an opposite trend of decreasing tin concentrations was detected from tourmaline patches, via orbicules, to veins (Fig. 6.12a). Surprisingly, quartz grains from tourmaline patches in the Pieman Heads Granite have higher Sn concentrations than their counterparts in the Heemskirk Batholith (Table 6.3; Fig. 6.12a). It may be that Sn was trapped in the alteration patches of the Pieman Heads Granite, preventing Sn partitioning into the late stage fluids that produced muscovite-quartz-tourmaline veins at this locality. The tin concentrations in quartz from the Pb-Zn veins are lower than the tourmaline veins in the Heemskirk Batholith (Fig. 6.12a). This is unsurprising given the lower forming temperature of the Pb-Zn veins. Cassiterite probably precipitated at higher temperatures, before the sulphide-bearing veins formed.

Aluminium and Ti concentrations in quartz from Pb-Zn veins can be categorised into two groups, a minor cluster with high Ti and low Al concentrations, and a predominant group with low Ti and variable Al contents (Fig. 6.12b). The high Ti and low Al quartz grains have bright-CL intensity (Fig. 6.5f), which are consistent with quartz from tourmaline patches and orbicules from the Heemskirk Batholith (Fig. 6.3; Table 6.3). These CL-bright quartz cores were probably formed at relatively high temperatures (≈ 500 ℃), and were subsequently partially dissolved and overprinted by CL-gray, euhedral growth zoned quartz with

Table 6.4 Representative trace elements in quartz from granites, pegmatites and related magmatic-hydrothermal deposits

Location	Type	Al (ppm)		Li (ppm)		Ti (ppm)		Ge (ppm)		Sb (ppm)		References
		Range	Median	Range	Median	Range	Median	Range	Median	Range	Median	
Land's End, SW England	Granite	227-942	361	9.6-98.7	49.0	2.8-136	16.6	0.2-2.7	1.9	–	–	Drivenes et al. (2016)
Bohemian Massif, Czech Republic	Granite	10-1246	131	bdl-35.0	13.5	0.69-159	55.0	0.26-3.40	0.60	–	–	Breiter et al. (2013)
Drag, Evje-Iveland, Norway	Pegmatite	64-262	134	2.09-24.1	6.81	4.55-25.2	14.5	0.97-3.44	1.89	0.003-0.084	0.009	Götze et al. (2004)
Evje-Iveland, Norway; Rubicon, Namibia	Pegmatite related Nb-Ta, REE ores	36-636	118	2.96-166	17.3	0.34-4.45	4.45	1.24-7.12	4.20	0.012-0.114	0.038	
Creede, Colorado, USA	Epithermal Ag deposit	100-3000	–	< 5-1000	–	<10	–	–	–	< 5-120	–	Rusk et al. (2011)
Comstock Lode, Nevada, USA	Epithermal Ag deposit	100-2400	–	< 5-2000	–	< 10	–	–	–	< 5-80	–	
El Indio, Chile-Argentinia	High sulfidation Au-Ag-Cu deposit	211-3503	1149	24.8-333	101	bdl-11.6	11.3	bdl-6.3	4.1	bdl-9.01	3.30	Tanner et al. (2013)
Summitville, Colorado, USA	High sulfidation Au-Ag-Cu deposit	80.3-663	117	bdl-6.34	0.76	bdl-82.6	74.1	bdl-5.6	2.54	bdl-2.33	0.28	
Alter, San Juan, Argentina	High sulfidation Au-Ag-Cu deposit	254-2487	1298	4.1-214	18.9	0.10-14.0	4.35	2.30-9.70	4.6	1.2-116	23.6	Maydagán et al. (2015)
Alter, San Juan, Argentina	Porphyry Cu- (Au-Mo) deposit	40-1672	169	1.3-29	3.9	4.60-159	27	0.40-7.70	1.1	< 0.03-3.1	0.1	
El Teniente, Chile	Porphyry Cu-Mo deposit	100-300	–	< 5-100	–	<10-200	–	–	–	bdl (< 5)	–	Rusk et al. (2011)
North Parkes, NSW, Australia	Porphyry Cu-Au deposit	56.3-600	282	1.11-19.2	6.76	56.6-254	160	2.26-3.27	2.71	bdl (< 0.116)	–	Tanner et al. (2013)
Kingsgate, NSW, Australia	Granite-hosted Mo-Bi-W deposit	30.4-219	119	1.23-20.7	8.97	bdl-15.8	13.8	bdl-4.91	3.01	bdl-66.3	19.1	

Note: bdl = below detection limit, "–" = no data.

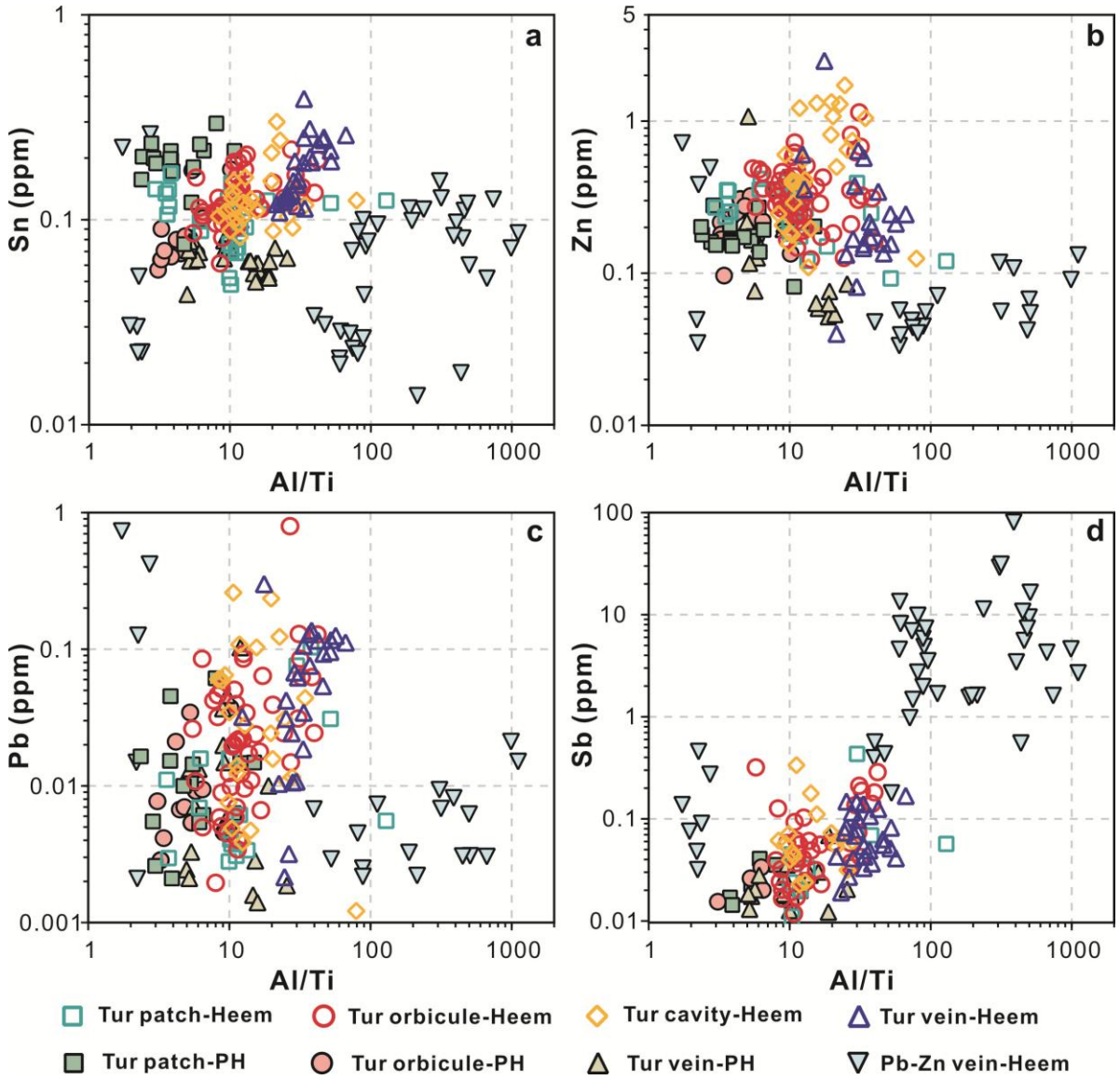

Figure 6.12 Compositional plots showing chemical variations in quartz between Pb-Zn veins and tourmaline-rich assemblages from western Tasmanian granites. Al/Ti versus Sn (a), Zn (b), Pb (c), and Sb (d). Tur = tourmaline, Heem = Heemskirk, PH = Pieman Heads. All data presented in Appendix 6, and sample details listed in Table 6.1.

low Ti and variable Al concentrations (Fig. 6.5f). Muscovite alteration of feldspar causes the extremely high Al concentrations (up to 1000 ppm) in hydrothermal quartz coexisting with Pb-Zn sulphides (cf. Fig. 6.8c).

Lead and Zn concentrations in quartz from Pb-Zn veins are generally lower than those of quartz from tourmaline patches, orbicules and veins (Figs. 6.12b-c), possibly because these two metal elements were preferentially incorporated into Pb-Zn sulphides rather than the associated quartz. The chemical variations of Pb and Zn in quartz are less noteworthy than Sb between the low temperature hydrothermal veins and high temperature tourmaline-rich assemblages (Figs. 6.12b-d). Quartz grains from tourmaline-rich assemblages have Sb concentrations typically lower than 0.1 ppm (Table 6.3), which are compatible with values of magmatic quartz from pegmatitic intrusions and porphyry deposits (Götze et al., 2004; Rusk et al., 2011; Tanner et al., 2013; Maydagán et al., 2015; Table 6.4). Low-Ti hydrothermal quartz crystals with

gray CL intensity are typically characterised by high Sb concentrations up to 100 ppm (Fig. 6.7j), which distinguishes them from the quartz intergrown with tourmaline-rich features on the Al/Ti versus Sb plot (Fig. 6.12d). The average Sb values of quartz associated with Pb-Zn veins in the Heemskirk Batholith overlap with those from high sulfidation epithermal Au-Ag veins and lodes (Table 6.4; Rusk et al., 2011; Tanner et al., 2013; Maydagán et al., 2015). Sb contents below detection limits are common in quartz from other low-temperature deposits such as Carlin-type and MVT Pb-Zn ores (Rusk et al., 2011). Antimony can occur as Sb^{5+}, and replace two Si^{4+}, incorporating into the lattice of quartz, with charge balance by $H^+ + Li^+ + Na^+ + K^+$ (Müller and Koch-Müller, 2009). The high Sb concentrations in quartz mostly reflect elevated Sb contents in the low temperature magmatic – hydrothermal fluids that produced the Pb-Zn veins within the Heemskirk Granite. Plotting Sb concentrations against Al/Ti (e.g., Fig. 6.12d) and other ratios in quartz may therefore be a useful tool to exploration for low-temperature base metal mineralisation related to granitic magmas (cf. Rusk et al., 2011; Tanner et al., 2013; Maydagán et al., 2015).

6.5 Conclusions

SEM-CL analysis reveals distinctive luminescent textures of quartz from different tourmaline-rich features, Pb-Zn veins and USTs in the Heemskirk and Pieman Heads granites, western Tasmania. Comb-layered quartz in USTs from the Heemskirk Granite present contrasting CL textures: thin CL-dark fractures cut across homogeneous CL-bright quartz on the base, whereas the trigonal quartz rims on the apex are defined by oscillatory growth zonings with gray to bright CL (Fig. 6.2; Table 6.2). Quartz in tourmaline patches, orbicules and cavities are characterised by homogeneous CL-bright intensity with minor concentric growth zoning, CL-dark patches, or planar CL-gray bands (Figs. 6.3-6.4; Table 6.2). Fractured streaks and cracks that do not show any luminescence have cut and/or offset the CL-bright quartz grains, and that are particularly abundant in quartz from the tourmaline veins (Figs. 6.3-6.4). Euhedral oscillatory luminescent zones orientated parallel to grain boundaries characterise the CL textures of quartz from the Pb-Zn mineralised veins of the Heemskirk Granite, in which embayed CL-bright cores are overgrown by CL-gray quartz (Fig. 6.5; Table 6.2).

LA-ICP-MS analyses show that Al, Li, Ti, Na, K, Fe, Ge, and Rb are the most abundant trace elements in quartz from the western Tasmanian granites (Table 6.3; Fig. 6.7). Trace element substitutions in quartz were mainly controlled by the $[AlO_4/M^+][Si^{4+}]_{-1}$ ($M^+ = H^+, Li^+, Na^+, K^+, Rb^+$) vector (Fig. 6.8), whereas sub-grain fluid inclusions in quartz can lead to variations of trace elements (especially Na, K, Rb, Ca) to different degrees (e.g., Fig. 6.9). Distinctive trace element variations have been detected in quartz between USTs, tourmaline-rich assemblages and Pb-Zn veins (Figs. 6.10-12). Concentrations and ratios of trace elements in UST quartz behave consistently with those from tourmaline orbicules and cavities, whereas aplitic quartz intergrown with UST quartz has similar trace element contents to quartz in tourmaline patches from the Heemskirk Granite (Figs. 6.10-11). Ge/Ti and Al/Ti ratios of quartz in the Heemskirk Granite (0.01–1.0 and 3.0–100) define wider ranges than those from the Pieman Heads Granite (0.01–0.2 and 2.0–30; Fig. 6.11), indicating that the Heemskirk Granite has experienced a higher extent of fractional crystallisation. The average Ge/Ti and Al/Ti ratios in quartz increase progressively from 0.04

and 9.79 in tourmaline patches, to 0.18 and 19.0 in tourmaline veins from the Heemskirk and Pieman granites (Fig. 6.11), indicating that evolved fluids were responsible for formation of these distinctive tourmaline-quartz features in the granite carapace.

Increasing Sn concentrations in quartz from tourmaline patches (median = 0.115 ppm) to tourmaline veins (median = 0.174 ppm) have been detected in the Sn-mineralised Heemskirk Granite (Table 6.3), consistent with Sn contents being gradually enriched in the evolved, late-stage magmatic – hydrothermal fluids, or due to mixing with oxidising stanniferous formation waters. Quartz associated with Pb-Zn sulphide veins has much higher Sb concentrations (median = 2.73 ppm) than other types of quartz (medians < 0.06 ppm) from the western Tasmanian granites (Fig. 6.12d), which may be useful to explore base metal mineralisation related to hydrothermal fluids from nearby granitic intrusions.

The temperatures, pressures and depths of the tourmaline-rich features and Pb-Zn veins will be constrained using Ti-in-quartz geothermometry and fluid inclusion data in Chapter 7.

Chapter 7 Fluid inclusions

7.1 Introduction

7.1.1 Preamble

Fluid inclusions are tiny samples of fluids trapped in minerals, which either form as a result of imperfect growth at crystal faces (primary inclusions) or by healing of microfractures within a crystal during later deformation (secondary or pseudosecondary inclusions; Roedder, 1984; Bodnar, 2003; Bodnar et al., 2014). They can contain liquid (typically H_2O, rarely CO_2, CH_4, or hydrocarbons), vapour and solid phases (commonly salts, and rarely sulphides, oxides, or silicates), with sizes mostly ranging from several to hundreds of microns (Roedder, 1984). Vein minerals such as quartz, calcite, dolomite and fluorite, as well as other translucent minerals (garnet, pyroxene, epidote), are the common objects of fluid inclusion study (Roedder, 1984).

Because a single mineral grain can contain multiple generations of fluid inclusions related to different geological events, it is crucial to identify temporal relationships between fluid inclusions prior to analysing them. A fluid inclusion assemblage is defined as a group of fluid inclusions that were all trapped at the same time, of which the fluid inclusions have similar sizes, shapes and compositions (Goldstein and Reynolds, 1994). An individual fluid inclusion assemblage represents the most finely discriminated fluid trapping event that can be recognised based on petrography (Goldstein and Reynolds, 1994).

Fluid inclusions can provide valuable information regarding the physicochemical characteristics of mineralising fluids, including temperature, pressure, salinity, density, and compositions, and help to document the hydrothermal evolution of a geological system (Roedder, 1984; Bodnar et al., 2014). Multiple methods have been used to analyse fluid inclusions in the past five decades, including petrographic observations, heating and cooling experiments, scanning electron microscope-electron microprobe analyses, Raman microspectrometry, proton-induced X-ray emission analyses, and LA-ICP-MS analyses (e.g., Roedder, 1984; Heinrich et al., 1992; Burke, 2001; Bodnar, 2003; Audétat et al., 1998; Pettke et al., 2012).

7.1.2 Previous work

Hajitaheri (1985) conducted fluid inclusion microthermometric study in quartz from the Heemskirk Granite, and related pegmatite, greisen dykes and tourmaline veins, and in fluorite from mineralised siderite-muscovite altered rocks. No fluid inclusions in quartz from tourmaline orbicules were analysed in Hajitaheri's (1985) study. Liquid-rich and halite-bearing inclusions in quartz were found to have homogenisation temperatures and salinities from 113 °to 503 ℃ and 0 to 12.5 wt % NaCl equiv, and 115 ° to 380 ℃ and 31 to 35.4 wt % NaCl equiv, respectively (Hajitaheri, 1985). CO_2-bearing fluid inclusions in quartz from tourmaline-muscovite veins were found to have CO_2 homogenisation temperatures of 2 ° to

26.9 ℃, liquid homogenisation temperatures of 300 ° to 430 ℃, and salt dissolution temperatures of 300 ° to 320 ℃. Hajitaheri (1985) proposed that a magmatic aqueous phase exsolved from the Heemskirk Granite separated into a coexisting hypersaline and a vapour phase at temperatures below 700 ℃ and pressures around1.2 kbars. A temperature range of 300 ° to 400 ℃ was calculated for the precipitation of cassiterite and sulphides associated with tourmaline + quartz + muscovite assemblage in the Heemskirk Granite at pressures from 50 to 200 bars (Hajitaheri, 1985). Low salinity fluids (0 to 12.5 wt % NaCl equiv) that have a temperature range of 110 ° to 270 ℃ were interpreted to be mixtures of magmatic – hydrothermal and meteoric water (Hajitaheri, 1985).

7.1.3 Aim of this study

The temperatures of tourmaline orbicule formation in granitic magmas has been estimated by previous studies to be between 550 ° to 720 ℃ based on crystallisation temperatures of near-solidus granitic magmas (e.g., Trumbull et al., 2008; Balen and Broska, 2011; Drivenes et al., 2015). The current study attempts to directly determine formation temperatures and pressures of tourmaline orbicules and other tourmaline-bearing features in the western Tasmanian granites through microthermometric measurements of fluid inclusions, combing with quartz trace element compositions.

When using microthermometric results of fluid inclusions to constrain physicochemical properties of a hydrothermal system, one of the challenges is to use homogenisation temperatures to calculate the trapping temperatures and pressures of the hydrothermal fluids, if critical fluid inclusion assemblages are absent (Roedder, 1984). A number of recent experiments (Wark and Watson, 2006; Ostapenko et al., 2007; Thomas et al., 2010) have revealed that Ti concentrations in quartz was fundamentally dependent on temperature, pressure and TiO_2 activity (i.e., the TitaniQ thermometer). This Ti-in-quartz geothermometer appears to overestimate pressure and/or temperature for quartz precipitated in hydrothermal environments, and thus Huang and Audétat (2012) calibrated the Ti-in-quartz thermobarometer being valid for hydrothermal quartz grown on variable growth rates. In combination with cathodoluminescence imaging and Ti-in-quartz geothermometry (Chapter 6), this chapter has used the technique of calculating intersections of isochores from microthermometric data and isopleths of Ti concentrations in quartz (e.g., Maydagán et al., 2015) to help constrain the P-T-X conditions of tourmaline-quartz-rich features in the Heemskirk and Pieman Heads granites. These data allow depositional mechanisms for the tourmaline-quartz-rich features and related mineralisation to be discussed.

7.2 Petrography and classification

7.2.1 Sample description

A total of 36 doubly polished thick sections (300 μm) that contain quartz and fluorite were prepared for petrographic investigations of fluid inclusions. The quartz grains selected for analysis are intergrown with tourmaline-rich patches, orbicules, cavities, and veins from the Heemskirk Granite at Trial Harbour, and from the Pieman Heads Granite. The textural features, mineralogy and corresponding analyses of each sample are listed in Table 7.1. Samples of Pb-Zn quartz veins from the Heemskirk Granite were collected

Table 7.1 Features of representative quartz-bearing samples used in the fluid inclusion study

Sample name	Coordinate	Location	Type	Mineralogy	Petro	CL	Microtherm	Source
WT12WH20-1	E145°09'23.93", S41°55'20.64", 3 m	Heemskirk	Tur patch	Qtz, Tur, Kfs	Yes	Yes		This study
WT12WH21-2	E145°09'23.93", S41°55'20.64", 3 m	Heemskirk	Tur patch	Qtz, Tur, Kfs	Yes	Yes		This study
WT12WH22	E145°09'23.93", S41°55'20.64", 3 m	Heemskirk	Tur orbicule	Qtz, Tur	Yes	Yes	Yes	This study
WT12WH28-6	E145°09'23.93", S41°55'20.64", 3 m	Heemskirk	Tur orbicule	Qtz, Tur	Yes	Yes	Yes	This study
WT12WH23	E145°09'23.93", S41°55'20.64", 3 m	Heemskirk	Tur vein	Qtz, Tur, Ms	Yes	Yes	Yes	This study
WT12WH24-3	E145°09'23.93", S41°55'20.64", 3 m	Heemskirk	Tur cavity	Qtz, Tur	Yes	Yes	Yes	This study
WT12WH33-3	E145°01'40.47", S41°48'34.80", 1 m	Heemskirk	Tur cavity	Qtz, Tur	Yes	Yes		This study
106405	E145°11'48.84", S41°54'22.65", -26 m	Heemskirk	Pb-Zn vein	Flu, Sp, Chl	Yes		Yes	Hajitaheri (1985)
106425	E145°11'48.84", S41°54'22.65", -36 m	Heemskirk	Pb-Zn vein	Qtz, Flu, Py	Yes	Yes	Yes	Hajitaheri (1985)
106410	E145°11'48.84", S41°54'22.65", -83 m	Heemskirk	Pb-Zn vein	Qtz, Py, Ga	Yes	Yes		Hajitaheri (1985)
WT14WH58	E145°09'23.93", S41°55'20.64", 3 m	Heemskirk	Porphyritic quartz in aplite	Qtz	Yes	Yes		This study
WT12WH03-1	E144°55'40.01", S41°43'15.00", 10 m	Pieman Heads	Tur patch	Qtz, Tur, Kfs	Yes	Yes		This study
WT12WH07-4	E144°55'40.01", S41°43'15.00", 10 m	Pieman Heads	Tur orbicule	Qtz, Tur, Kfs	Yes	Yes		This study
WT12WH13-4	E144°53'37.87", S41°43'13.75", 3 m	Pieman Heads	Tur vein	Qtz, Tur, Ms	Yes	Yes	Yes	This study

Abbreviation: Petro = petrography, Microtherm = microthermometry, Chl = chlorite, Flu = fluorite, Kfs = alkali feldspar, Qtz = quartz, Ms = muscovite, Tur = tourmaline, Ga = galena, Sp = sphalerite, Py = pyrite.

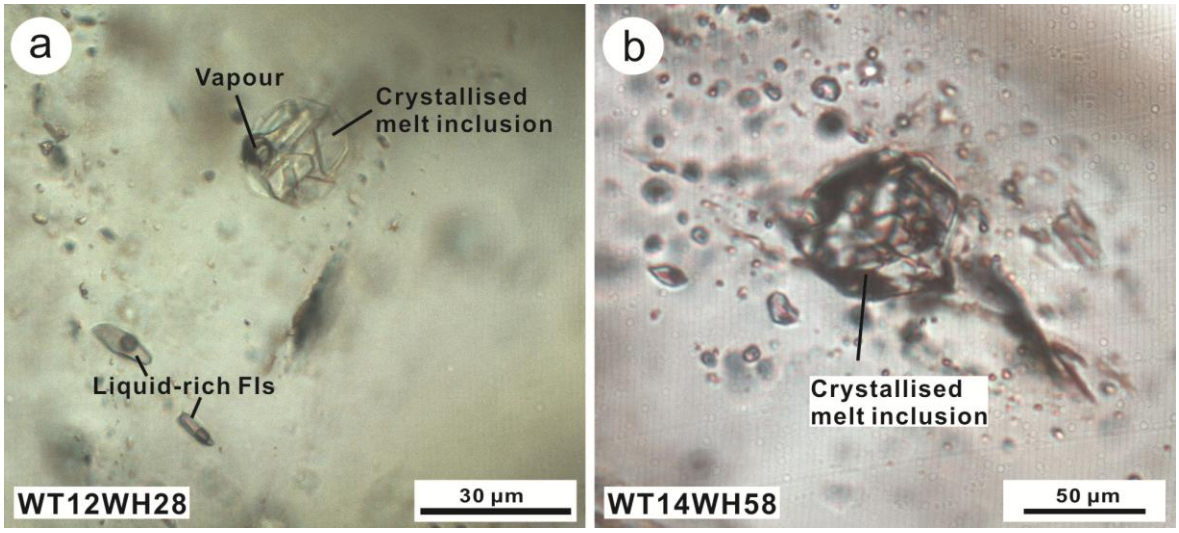

Figure 7.1 (a) Crystallised silicate melt inclusions coexisting with liquid-rich fluid inclusions in quartz from tourmaline orbicules in the Heemskirk Granite. (b) Crystallised silicate melt inclusions in quartz from an aplitic sill in the Heemskirk Granite. The silicate melt inclusion in Fig. 7.1b surrounded by clusters of fluid inclusions may have undergone decrepitation. FIs = fluid inclusions. Coordinates and samples listed in Table 7.1.

from the PhD thesis collection of Hajitaheri (1985), which is stored in the rock library at CODES, University of Tasmania. Quartz and fluorite in these vein samples are intimately intergrown with pyrite, sphalerite and galena that were collected from the historical Sweeney Mine (Table 7.1; Fig. 6.1).

7.2.2 Petrographic and cathodoluminescence observations

The quartz grains in this study were analysed by scanning electron microscope-cathodoluminescence (SEM-CL) prior to microthermometric measurements. CL images of the quartz grains were mostly presented in Chapter 6. Some representative CL images have been combined with transmitted light photomicrographs in this chapter in order to determine which fluid inclusions are primary or secondary in origin. Fluid inclusions that occur as individual inclusions and random groups, or that are aligned along growth zones in the CL-bright or CL-grey quartz were classified as primary in origin (Figs. 7.2a-d; cf. Roedder, 1984). Fluid inclusions that occur in trails associated with CL-dark microfractures in quartz were classified as secondary, and were not subjected to microthermometric analyses.

CL-bright quartz in tourmaline patches (e.g., WT12WH20-1, WT12WH21-2 and WT12WH07-4) and CL-bright phenocrystic quartz in an aplite dyke or sill (e.g., WT14WH58) rarely contain any fluid inclusions, but contain a few crystallised silicate melt inclusions. Fluid inclusions were only observed in CL-dark narrow fractures in quartz from tourmaline patches and aplites; those inclusions are undoubtedly secondary in origin.

Figure 7.2 (next page) (a-b) Photomicrograph and CL images showing distributions of fluid inclusions (FIs) in tourmaline orbicules from the Heemskirk Granite. (c) Liquid-rich FIs (type I) in tourmaline orbicules. (d) Halite-bearing FIs (type III) coexisting with liquid-rich FIs (type I) in tourmaline orbicules. (e) Vapour-rich (type II) and liquid-rich (type I) FIs in tourmaline orbicules from the Heemskirk Granite. (f) Multi-daughter-bearing FIs (type IIIc) in tourmaline orbicules. (g-h) Photomicrograph and CL image mapping FIs in tourmaline veins from the Heemskirk Granite. (i-j) Liquid-rich FIs (type I) in tourmaline veins in the Heemskirk Granite. (k) Liquid-rich and coexisting halite-bearing FIs (types I + III) in tourmaline veins from the Pieman Heads Granites. Tur = tourmaline, FIs = fluid inclusions. All sample details listed in Table 7.1.

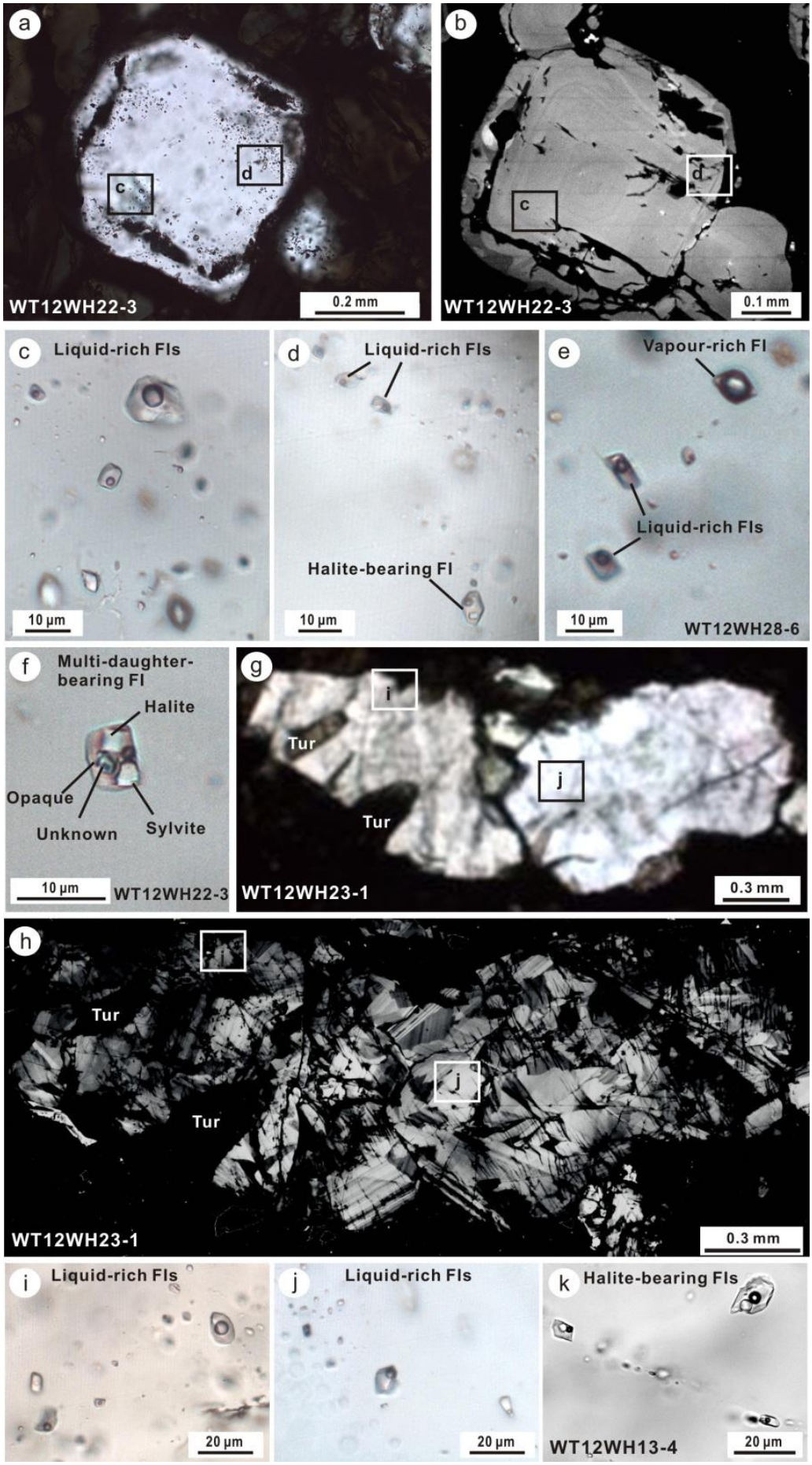
a
c
d
WT12WH22-3
0.2 mm
b
c
d
WT12WH22-3
0.1 mm
c Liquid-rich FIs
10 μm
d Liquid-rich FIs
Halite-bearing FI
10 μm
e Vapour-rich FI
Liquid-rich FIs
10 μm
WT12WH28-6
f Multi-daughter-bearing FI
Halite
Opaque
Unknown
Sylvite
10 μm
WT12WH22-3
g
i
Tur
j
Tur
WT12WH23-1
0.3 mm
h
Tur
j
Tur
WT12WH23-1
0.3 mm
i Liquid-rich FIs
20 μm
j Liquid-rich FIs
20 μm
k Halite-bearing FIs
WT12WH13-4
20 μm

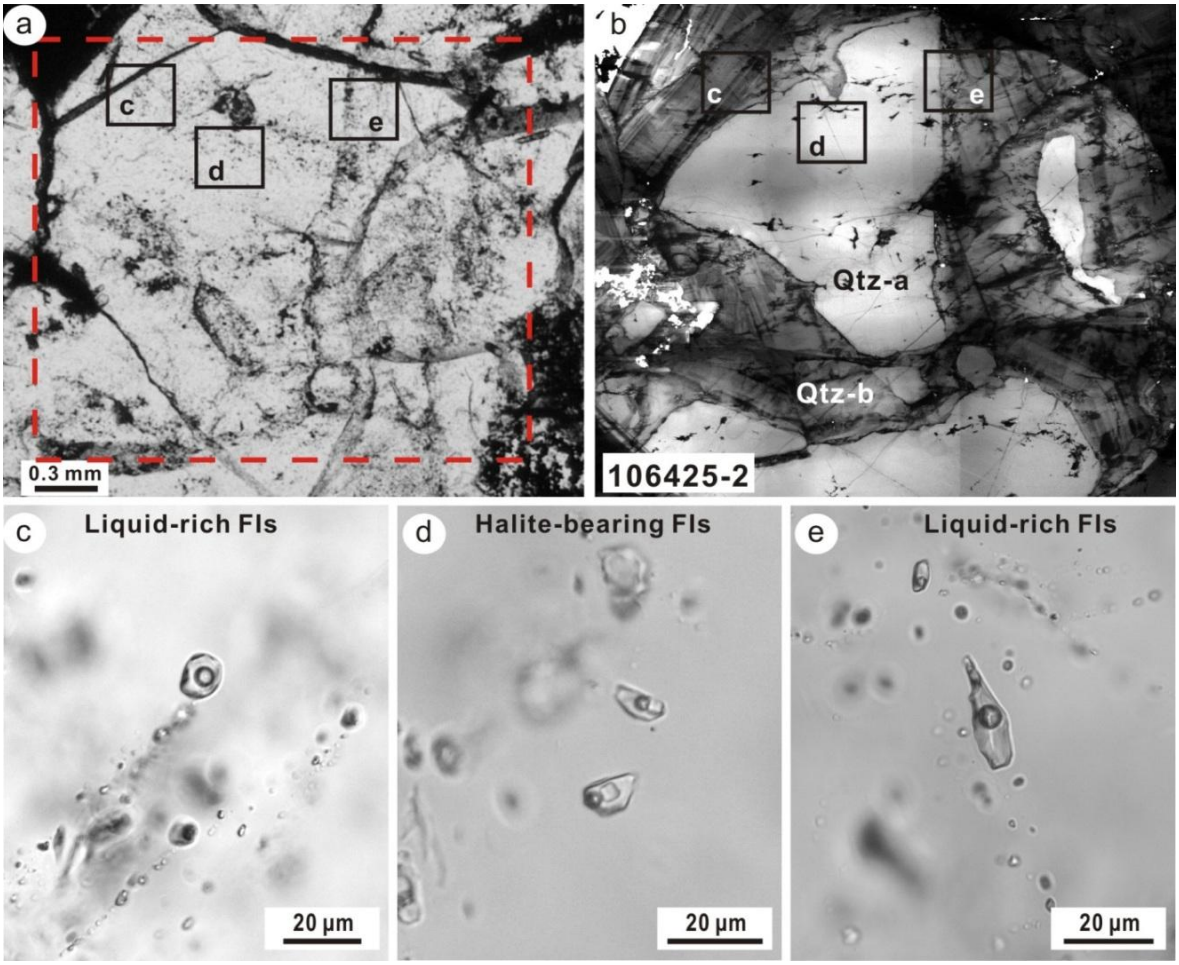

Figure 7.3 (a-b) Photomicrograph and CL images showing distributions of FIs in Pb-Zn veins from the Heemskirk Granite. (c) Type I liquid-rich FIs in CL-gray quartz with oscillatory zones. (d) Type III halite-bearing FIs in the CL-bright quartz. (e) Type I liquid-rich FIs in the CL-gray quartz with oscillatory zones. FIs = fluid inclusions. All sample details listed in Table 7.1.

Quartz grains in an aplite sill that hosts tourmaline orbicules in the Heemskirk Granite contain a number of what appear to be silicate melt inclusions. They have features comparable to what Audétat and Lowenstern (2014) defined as crystallised silicate melt inclusions in porphyritic intrusions (Fig. 7.1b). Planar halos of small fluid inclusions that immediately surround the crystallised melt inclusions possibly resulted from decrepitation of the primary silicate melt inclusions (Fig. 7.1b; cf. Audétat and Lowenstern, 2014). Some quartz grains in tourmaline orbicules from Trial Harbour of the Heemskirk Granite were also found to have a few similar crystallised melt inclusions (Fig. 7.1a). These individual crystallised melt inclusions coexist locally with liquid-rich and halite-bearing fluid inclusions in quartz intergrown with tourmaline in orbicules (e.g., Fig. 7.1a).

The tourmaline orbicules in the Pieman Heads Granite are hosted by an equigranular granitic phase rather than an aplitic dyke or sill. Crystallised melt inclusions were rare in equigranular quartz grains from the tourmaline orbicules. CL-bright quartz grains do not contain any primary fluid inclusions, but trails of secondary fluid inclusions have been observed along CL-dark microfractures in the equigranular quartz, a feature similar to those observed in quartz crystals from tourmaline patches both in the Heemskirk and Pieman Heads granites.

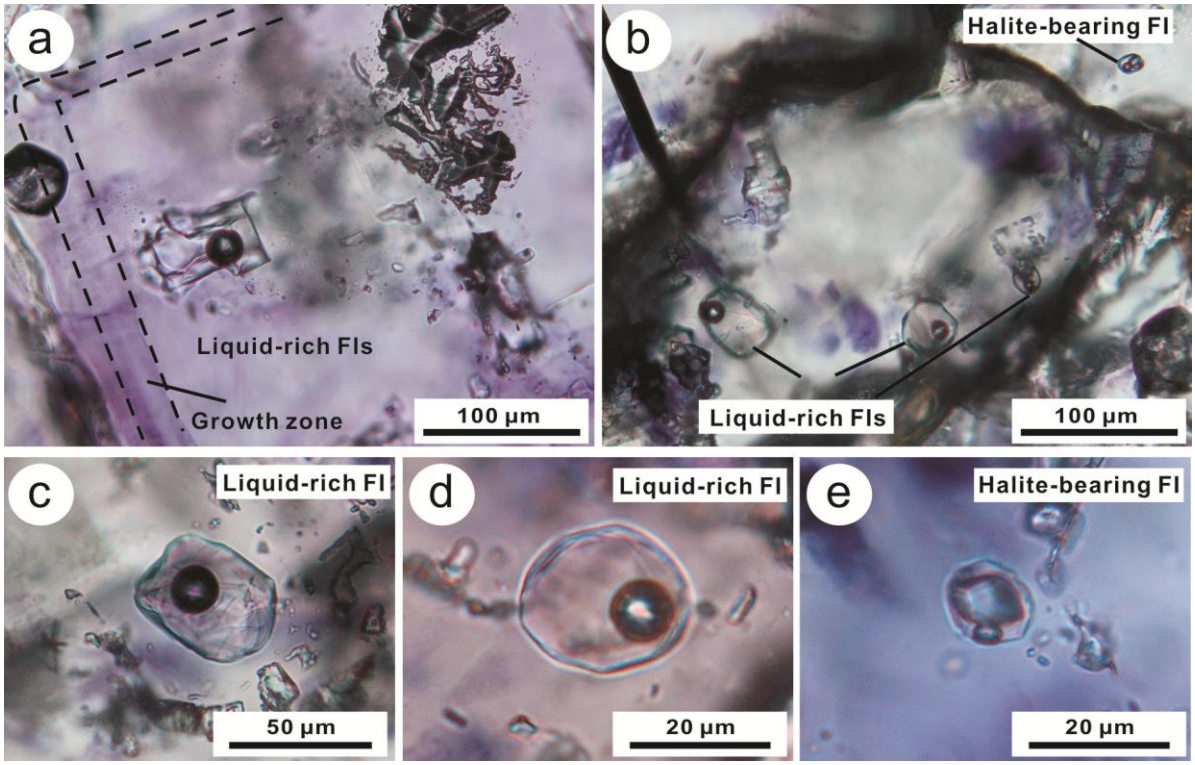

Figure 7.4 Characteristics of fluid inclusions hosted by fluorite in Pb-Zn veins from the Heemskirk Granite. (a) Type I liquid-rich FIs in growth zones in fluorite. (b) Type I liquid-rich and type III halite-bearing FIs in fluorite grain. (c-d) Isolated type I liquid-rich FI in a fluorite. (e) Rounded type III halite-bearing FI in fluorite cry. FI = fluid inclusion. All images are from Sample 106405, and sample details listed in Table 7.1.

Transmitted light and SEM-CL observations have revealed multiple quartz generations in the analysed tourmaline-quartz veins (e.g., Figs. 7.2g-h). Subround and negative fluid inclusions that occur individually and that are grouped as clusters, or decorate growth zones, are interpreted as primary in origin. They are hosted by CL-bright or CL-gray quartz from the tourmaline veins (Figs. 7.2i-j). CL-dark laminations within these quartz grains that cut the CL-bright or CL-gray quartz commonly contain trails of secondary two-phase liquid-rich fluid inclusions less than 10 μm in diameter.

The Pb-Zn veins contain CL-bright quartz cores overgrown by CL-gray quartz rim with oscillatory zones (Figs. 7.3a-b). The early-precipitated CL-bright quartz grains have similar CL textures and trace element contents to quartz in tourmaline patches and orbicules (Figs. 6.1 and 6.2). The CL-bright cores have been embayed and overgrown by the late-stage quartz with gray, oscillatory zoned luminescence. Fluid inclusions both in the CL-bright core and CL-gray oscillatory rims of quartz associated with Pb-Zn sulphides and fluorite are interpreted as primary in origin. Fluid inclusions in the CL-bright cores of quartz from the Pb-Zn veins are typically dominated by an assemblage of coexisting liquid-rich and halite-bearing inclusions in clusters (Fig. 7.3d). Only liquid-rich inclusions were observed in the CL-gray quartz rim, which typically occur along the oscillatory growth zones of the CL-gray quartz (Figs. 7.3c, e).

Primary fluid inclusions hosted by fluorite in the Pb-Zn veins commonly occur randomly, and locally are situated in the growth zones of a crystal (Fig. 7.4a). Individual fluid inclusions have equant to rounded shapes, and are commonly 20 to 50 μm in diameter (Figs. 7.4c-d). Liquid-rich fluid inclusions are dominant in the fluorite grains, but a few daughter-bearing inclusions (probably contain halite) were

Table 7.2 Summary of fluid inclusions in tourmaline-quartz features

Type	Morphology	Size	Phase (at 25°C)	Dominant	Homogenisation behaviour
I	Elongate, subround, elliptical, tabular negative, triangular, rhombic or irregular	< 5 to 40 μm	Liquid + vapour ± opaque	Liquid	Vapour disappearance
II	Elongate, elliptical, negative	5 to 35 μm	Liquid + vapour	Vapour	Liquid disappearance
IIIa	subround, elliptical, elongate, negative	< 5 to 25 μm	Liquid + vapour + halite	Liquid	Vapour disappearance
IIIb	subround, elliptical, negative	< 5 to 20 μm	Liquid + vapour + halite	Liquid	Salt dissolution
IIIc	subround, elliptical	< 5 to 20 μm	Liquid + vapour + halite + unknown	Liquid	Only halite dissolved, unknown crystals shrunk or did not homogenise by 550 °C

observed (< 5 %; Fig. 7.4b, e). Small fluid inclusions (< 10 μm) occur as trails along microfractures that locally truncate the growth zones in fluorite. This group of fluid inclusions are interpreted as secondary, and were not analysed microthermometrically.

7.2.3 Classification based on homogenisation features

Fluid inclusions hosted by quartz and fluorite from the Heemskirk and Pieman Heads granites can be classified into three types at room temperature (Table 7.2). Type I fluid inclusions have two main phases, liquid and vapour, although some contain opaque minerals in a few quartz grains (e.g., Figs. 7.2c, 7.3c and 7.3e). Type I fluid inclusions are commonly elongate, subround, elliptical, tabular, or negative in shape, and rarely triangular, rhombic or irregular, ranging from < 5 to 40 μm in size. They homogenise to liquid during heating experiments, although the opaque phases do not dissolve.

Type II fluid inclusions consist of liquid and vapour, but the vapour phase is dominant, and they homogenise to vapour. They mostly have equant shapes (Fig. 7.2e), but can be elongate, elliptical, and negative, ranging from 5 to 35 μm in size.

Type III fluid inclusions contain several phases, including liquid, vapour and salt daughter crystals (Table 7.2; Figs. 7.2d, k). They are dominated by the liquid phase. Type III fluid inclusions vary from < 5 to 25 μm in size, and typically have elliptical, elongate, negative or subrounded shapes. Depending on the number of daughter minerals and homogenisation behaviour, type III fluid inclusions are subdivided into three categories. Type IIIa and IIIb fluid inclusions contain liquid + vapour + halite, but have different homogenisation behaviours. Type IIIa homogenise to liquid by vapour disappearance, whereas type IIIb homogenise to liquid by salt dissolution (Figs. 7.3d, 7.8). These two subtypes are the most common halite-bearing fluid inclusions in quartz associated with tourmaline from western Tasmanian granites. Type IIIc fluid inclusions contain liquid + vapour + halite ± unknown daughter minerals (Fig. 7.2f). They commonly homogenised to liquid, but only one salt daughter crystal dissolved (mostly cubic halite), and the second

daughter mineral shrank or did not dissolve up to 550 ℃, making it difficult to record its dissolution temperatures.

7.3 Microthermometry

7.3.1 Method

Temperatures of liquid homogenisation, vapour homogenisation, dissolution of salt daughter minerals, and final ice melting were measured on a Linkam MD 600 heating/freezing stage at CODES, UTAS. The Linkam stage has a temperature range from -196 ° to 600 ℃. Synthetic fluid inclusions supplied by Synflinc Inc. were used to calibrate the Linkam stage prior to measurement, with precisions of ± 1.0 ℃ for heating and ± 0.3 ℃ for freezing. A total of 442 homogenisation temperatures were collected during heating and freezing experiments. Eutectic temperatures were not measured for the fluid inclusions in this study due to difficulties encountered in observing first ice melting temperatures. Melt inclusions hosted in quartz from the tourmaline orbicules and aplitic sill or dyke were not analysed microthermometrically, as their homogenisation temperatures are beyond the temperature range of the Linkam stage used in this study.

According to Bodnar and Vityk (1994)'s equations, salinities of halite-undersaturated fluid inclusions, reported as weight percent NaCl equivalent (wt % NaCl equiv), were calculated from the final ice melting temperatures. The salinities of halite-saturated fluid inclusions were calculated based on the temperatures of dissolution of salt daughter crystals using the equation from Bodnar and Vityk (1994). A total of 202 salinity results were acquired through collection and calculation of the freezing point depression and daughter salt dissolution temperatures.

7.3.2 Heating and freezing experiment results

For the Heemskirk Granite samples, fluid inclusions hosted in quartz from tourmaline-bearing orbicules, cavities and veins, and also inclusions in fluorite from Pb-Zn-bearing veins were analysed microthermometrically. For the Pieman Heads Granite, only fluid inclusions in quartz associated with tourmaline veins were measured. All fluid inclusion data are presented in Appendix 7.

7.3.2.1 Tourmaline-rich orbicules

Fluid inclusions in quartz from tourmaline orbicules of the Heemskirk Granite define two fluid assemblages: types I + IIIb, and types I + II + IIIa + IIIb + IIIc. The first fluid assemblage has a homogenisation temperature (to liquid) range from 170 °to 450 ℃, with a median of 265 ℃ (Fig. 7.5a). The final ice melting and final salt dissolution temperatures vary from -11.2 °to -1.2 ℃ (average = -5.8 ℃), and from 195 °to 312 ℃ (average = 248 ℃), respectively. This fluid inclusion assemblage has bimodal salinity ranges from 2.1 to 15.2 wt % and from 31.6 to 39.2 wt % NaCl equiv, respectively (Table 7.3; Fig. 7.5b).

The second fluid inclusion assemblage (I + II + IIIa + IIIb + IIIc) is the most common in the orbicules from the Heemskirk Granite. The fluid inclusions have a wide homogenisation temperature range, from

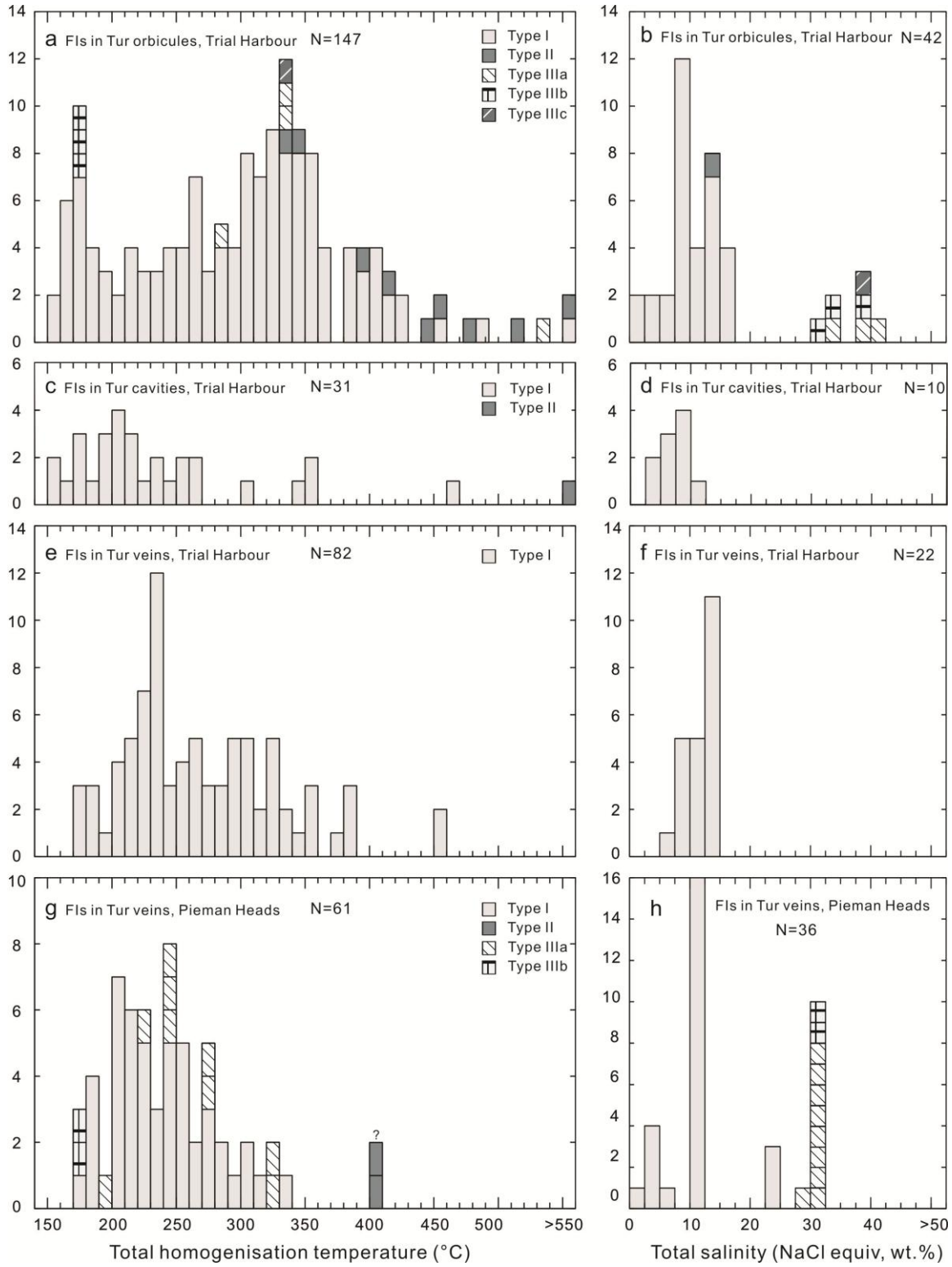

Figure 7.5 Histograms showing the ranges of homogenisation temperature and salinity of fluid inclusions hosted by quartz from tourmaline-rich assemblages of the Heemskirk (Trial Harbour) and Pieman Heads granites. Homogenisation temperatures (a, c, e) and salinities (b, d, f) for tourmaline orbicules, cavities and veins from the Heemskirk Granite. Homogenisation temperatures (g) and salinities (h) for tourmaline veins in the Pieman Heads Granite. FIs = fluid inclusions, Tur = tourmaline. All data listed in Appendix 7.

150 °to 550 ℃, with a median of 338 ℃ (Fig. 7.5a). The vapour-rich fluid inclusions in this assemblage have a higher homogenisation temperature than their liquid-rich counterparts, ranging from 334 ° up to

550 ℃, with a median of 448 ℃. The temperatures of final salt dissolution vary from 245 °to 471 ℃ with a median of 320 ℃ (Figs. 7.5a, 7.7a). This fluid inclusion assemblage has broader salinity ranges (3.1 to 16.0 wt % and 34.4 to 55.9 wt % NaCl equiv) and higher median salinity values than the fluid inclusion assemblage of type I + IIIb (Table 7.3; Fig. 7.5b).

7.3.2.2 Tourmaline-filled cavities

A fluid inclusion assemblage defined by type I ± II inclusions is common in quartz grains from tourmaline-filled cavities in the Heemskirk Granite (Table 7.3; Fig. 7.5c). Type I is the dominant fluid inclusion type in tourmaline-filled cavities. They have a homogenisation temperature range from 156 °to 461 ℃, with a median value of 213 ℃ (Fig. 7.5c). Type II fluid inclusions are rare in quartz from the miarolitic cavities, and have higher homogenisation temperatures (up to 550 ℃). Fluid inclusions in quartz from this tourmaline-filled association have final ice melting temperatures of -7.1 ° to -1.6 ℃, corresponding to a moderate salinity of 2.7 to 10.6 wt % NaCl equiv (median = 7.5 wt %). These salinities are lower than those obtained from tourmaline orbicules (Figs. 7.5d, 7.7a).

7.3.2.3 Tourmaline-quartz veins

Only type I fluid inclusions have been observed in tourmaline veins from the Heemskirk Granite at Trial Harbour. They have a similar homogenisation temperature range (172 ° to ~ 450 ℃) to fluid inclusions in the tourmaline cavities, with a median of 256 ℃ (Table 7.3; Fig. 7.5e). These fluid inclusions have final ice melting temperatures from -10.4 °to - 4.1 ℃, which corresponds to calculated salinities from 6.6 to 14.4 wt % NaCl equiv (median = 12.5 wt %; Table 7.3; Figs. 7.5f, 7.7a).

Fluid inclusions in quartz from tourmaline veins within the Pieman Heads Granite occur in two fluid inclusion assemblages: I + IIIa, and I + IIIa + IIIb. The type I + IIIa assemblage has a homogenisation temperature range of 203 °to 332 ℃ (average = 244 ℃; Fig. 7.5g). The final ice melting temperatures range from -8.4 ° to -1.5 ℃, whereas the halite dissolution temperatures change from 158 ° to 182 ℃. The calculated salinities of this fluid inclusion assemblage vary from 2.6 to 12.2 wt %, and 30.0 to 31.0 wt % NaCl equiv, respectively (Table 7.3; Fig. 7.5h). The second fluid inclusion assemblage (I + IIIa + IIIb) differs from the first population, in which it contains halite-bearing fluid inclusions that homogenise by salt dissolution (type IIIb; Table 7.3). The homogenisation temperatures of I + IIIa + IIIb assemblage range from 172 ° to ~ 400 ℃ (Fig. 7.5g). These fluid inclusions have final ice melting and salt dissolution temperatures from -22.4 ° to - 1.2 ℃, and from 176 ° to 205 ℃. Salinities calculated for saline and hypersaline fluid inclusions fluctuate from 2.1 to 23.9 wt %, and 31.4 to 32.1 wt % NaCl equiv (Table 7.3; Fig. 7.5h).

7.3.2.4 Pb-Zn veins in the Heemskirk Granite

The quartz grains intergrown with sphalerite, galena, and pyrite within the Heemskirk Granite have two fluid inclusion assemblages: type I-only, and type I + IIIa + IIIc, respectively (Table 7.3). The type I-only fluid inclusion assemblage is characterised by liquid-rich inclusions that homogenise to liquid

Table 7.3 Summary of fluid inclusion populations in quartz and fluorite from the Heemskirk and Pieman Heads granites

Mineral textures	Mineral assemblages	Inclusion types	Th (v→l) range (°C)	Th (v→l) median (°C)	Th (l→v) range (°C)	Th (l→v) median (°C)	Tsd range (°C)	Tsd mean (°C)	Salinity range (wt % NaCl equiv)	Salinity median (wt % NaCl equiv)
Tourmaline orbicules, Trial Harbour	Qtz, Kfs, Pl, Tur, Bi, Ms	I + IIIb	169 to 451	265	–	–	–	–	2.1 to 15.2	9
							195 to 312	248	31.6 to 39.1	35.1
		I + II + IIIa + IIIb + IIIc	153 to > 550	338	334 to > 550	448	–	–	3.1 to 16.0	12.3
							245 to 471	320	34.4 to 55.9	41.7
Tourmaline cavities, Trial Harbour	Qtz, Tur, Ms	I ± II	156 to 461	213	> 550	–	–	–	2.7 to 10.6	7.5
Tourmaline veins, Trial Harbour	Qtz, Tur, Ms	I	172 to > 450	256	–	–	–	–	6.6 to 14.36	12.5
Tourmaline veins, Pieman Heads	Qtz, Tur, Ms	I + IIIa	203 to 332	244	–	–	–	–	2.6 to 12.2	9.5
							158 to 182	173	30.0 to 31.0	30.6
		I ± II + IIIa + IIIb	172 to > 400	186	–	–	–	–	2.1 to 23.9	16.7
							176 to 205	198	31.4 to 32.1	31.6
Pb-Zn veins, Quartz	Qtz, Sp, Ga, Py	I	160 to 310	195	–	–	–	–	3.5 to 10.7	5.7
		I + IIIa + IIIc	158 to > 450	197	–	–	–	–	1.6 to 6.3	4.5
							220 to 400	240	32.9 to 47.2	36.1
Pb-Zn veins, Fluorite	Flu, Sph, Ga	I ± IIIc	140 to 206	169	–	–	–	–	7.5 to 12.7	9.6

Note: Th = homogenisation temperature, Tsd = salt dissolution temperature. Bi = biotite, Flu = fluorite, Kfs = alkali feldspar, Pl = plagioclase, Qtz = quartz, Ms = muscovite, Tur = tourmaline, Ga = galena, Sp = sphalerite, Py = pyrite

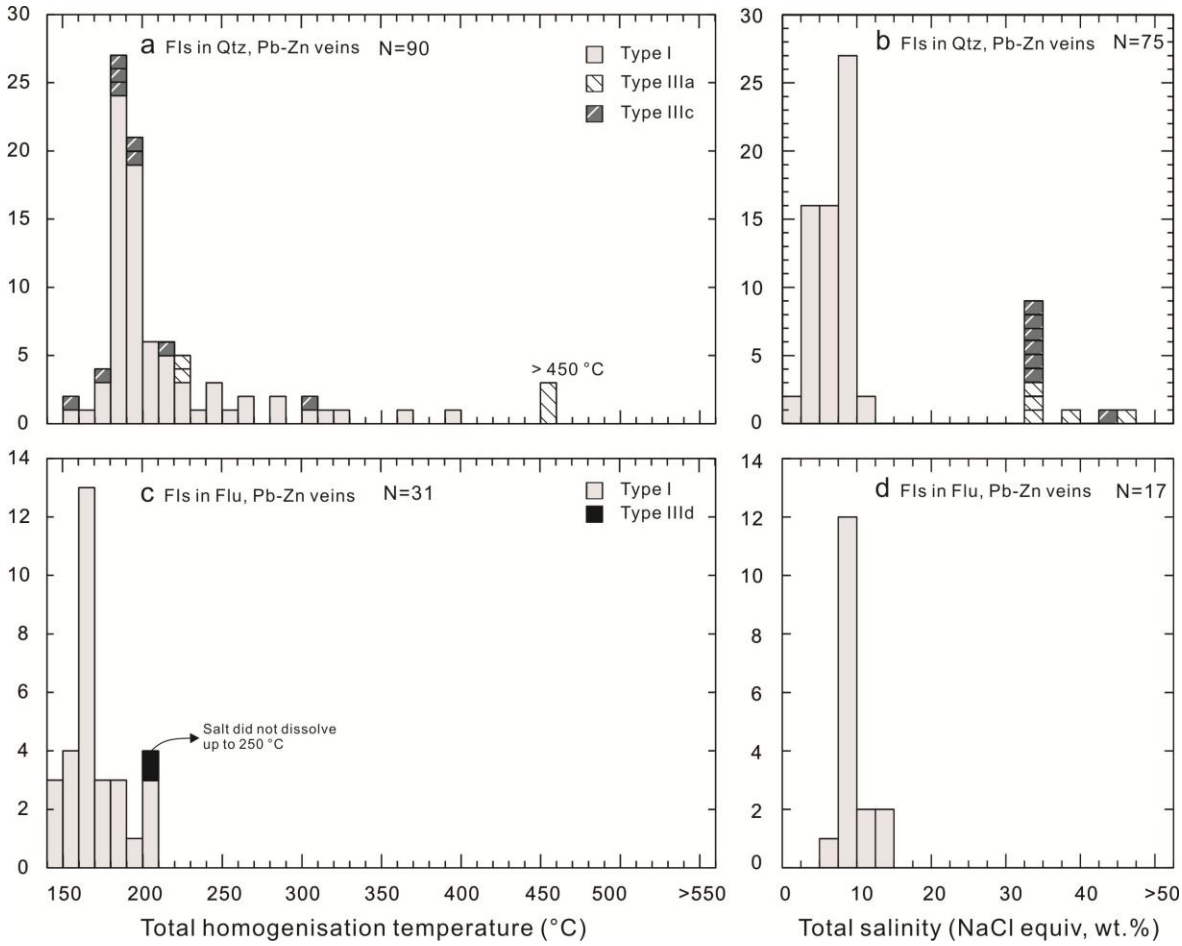

Figure 7.6 Histograms showing the ranges of homogenisation temperature and salinity of fluid inclusions hosted by quartz (a, b) and fluorite (c, d) from Pb-Zn veins within the Heemskirk Granite. FIs = fluid inclusions, Flu = fluorite, Qtz = quartz. All data listed in Appendix 7.

between 160 °and 310 ℃, with a median of 195 ℃ (Fig. 7.6a). These fluid inclusions have final ice melting temperatures that range from -7.2 °to -2.1 ℃, corresponding to moderate salinities from 3.5 to 10.7 wt % NaCl equiv (average = 5.7 wt %; Fig. 7.6b). The fluid inclusion assemblage consisting of I + IIIa + IIIc inclusions is less common than the type I-only fluid inclusion assemblage. Type I + IIIa + IIIc fluid inclusions have homogenisation temperatures from 158 °to 400 ℃ (Table 7.3; Figs. 7.6a, 7.7b). They have final ice melting and halite dissolution temperatures between -3.9 ° and -0.9 ℃, and between 220 ° and 400 ℃ (Table 7.3). Their salinities have a bimodal distribution, ranging from 1.6 to 6.3 wt %, and to 32.9 to 47.2 wt % NaCl equiv (Figs. 7.6b, 7.7b).

The fluid inclusions hosted in fluorite within Pb-Zn quartz veins from the Heemskirk Granite have a simple assemblage of type I + IIIc inclusions (Table 7.3; Fig. 7.6c). These fluid inclusions homogenise to liquid at temperatures of 140 ° to 206 ℃, with a median of 169 ℃ (Table 7.3). The final ice melting temperatures range from -8.9 ° to -4.7 ℃, corresponding moderate salinities between 7.5 and 12.7 wt % NaCl equiv, averaging at 9.6 wt % (Fig. 7.6d). Salt-bearing fluid inclusions were rarely observed in fluorite, and the salt crystals did not dissolve after heating to 500 ℃.

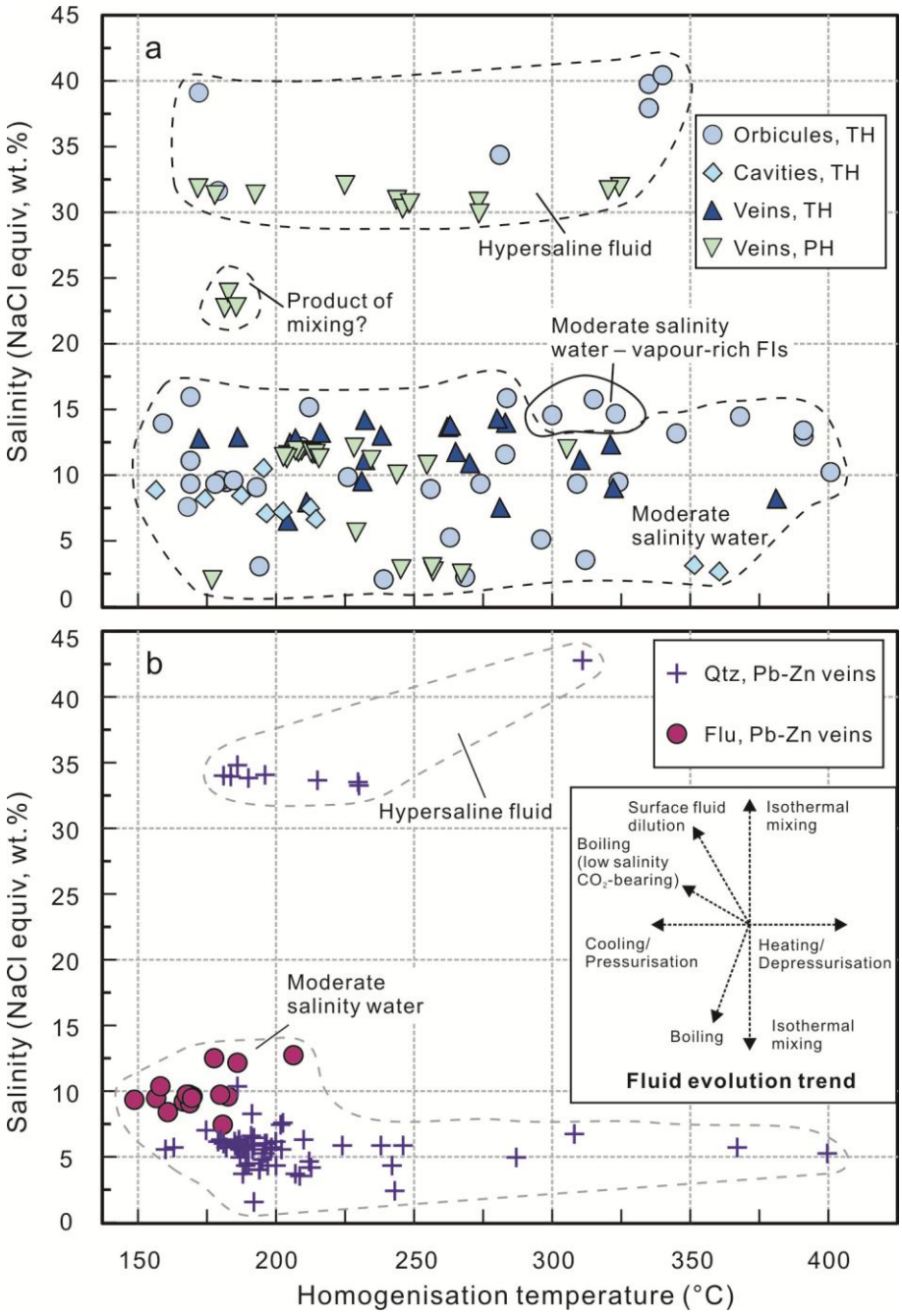

Figure 7.7 Salinity (wt % NaCl equiv) versus homogenisation temperature diagrams for fluid inclusion assemblages from tourmaline-rich features (a) and Pb-Zn veins (b) from the western Tasmanian granites. Inset plot showing fluid evolution trend after Wilkinson (2001). TH= Trial Harbour, Heemskirk Granite. PH = Pieman Heads Granite. Qtz = quartz, Flu = fluorite. All data listed in Appendix 7.

7.4 Discussion

7.4.1 Evidence for origins of tourmaline-rich features

Minor silicate melt inclusions were found in quartz grains from tourmaline patches in the Heemskirk Granite, as well as tourmaline patches and tourmaline orbicules in the Pieman Heads Granite. The quartz grains in these tourmaline-rich features have a similar equigranular texture to those in the granitic host rocks, and also have high Ti contents in quartz (up to 67.9 ppm; Table 6.3). Quartz in the tourmaline patches is therefore interpreted to have crystallised at magmatic conditions from a granitic melt. This interpretation also applies to tourmaline orbicules in the equigranular phase of the Pieman Heads Granite.

Crystallised silicate melt inclusions in quartz from the aplitic feeder dyke and sill, and tourmaline orbicules in the Heemskirk Granite at Trial Harbour (Fig. 7.1) imply that the aplitic phases and tourmaline orbicules may have crystallised at least in part directly from a silicate melt. However, abundant liquid-rich and salt-saturated fluid inclusions observed in quartz from the tourmaline orbicules at Trial Harbour (Figs. 7.2a-f) provide evidence that boron-rich hydrothermal fluids were also involved in the formation of the tourmaline-quartz orbicules. Silicate melt inclusions and primary fluid inclusions coexisting in quartz grains unequivocally demonstrate a magmatic – hydrothermal origin for tourmaline orbicules at Trial Harbour. This interpretation is consistent with the hydrothermal alteration halos surrounding tourmaline orbicules that were documented in Chapter 4 (Fig. 4.3D).

Coexisting hypersaline and low salinity primary fluid inclusions in quartz from the tourmaline-filled cavities prove that these textural features have a magmatic – hydrothermal origin. They are interpreted to have grown at the transition stage from magmatic to hydrothermal conditions in the granitic magmas (cf. Candela and Blevin, 1995).

Quartz grains in tourmaline-rich veins from both of the Heemskirk and Pieman Heads granites are enriched in liquid-rich and hypersaline fluid inclusions. These features, together with dark CL intensities and low Ti contents of the quartz (low to 1.3 ppm; Table 6.2) strengthen that tourmaline, quartz and muscovite in the tourmaline veins were precipitated from boron-rich magmatic – hydrothermal fluids sourced from the local intrusions.

CO_2-bearing fluid inclusions were reported in quartz from tourmaline-quartz veins, greisen dykes and pegmatite of the Heemskirk Granite (Hajitaheri, 1985). However, no CO_2-bearing fluid inclusions were observed in the current study, probably due to the small number of tourmaline-rich veins analysed. Hajitaheri (1985) reported that eutectic temperatures of fluid inclusions in the tourmaline orbicules range from -49 °to -35 ℃, which indicate the presence of KCl, $CaCl_2$ and $MgCl_2$ etc. (cf. Crawford, 1981).

7.4.2 Estimated trapping pressures and temperatures

Vapour-rich fluid inclusions (type II) coexist with liquid-rich inclusions (type I) in quartz from the tourmaline-filled orbicules and cavities of the Heemskirk Granite (e.g., Fig. 7.2e). The type II inclusions generally have higher homogenisation temperatures (average = 320 ℃) than the type I inclusions (average = 250 ℃; Table 7.3; Figs. 7.5a, c), which was also noted by Hajitaheri (1985) for fluid inclusions in tourmaline-quartz veins from the Heemskirk Granite. This implies that either these coexisting type I and type II inclusions were not simultaneously trapped during boiling (cf. Wilkinson, 2001), or that they experienced post-entrapment modification. In either case, the two groups of microthermometric results cannot be used to calculate trapping pressures and temperatures of the boron-rich magmatic – hydrothermal fluids.

In order to constrain the trapping pressures and temperatures of magmatic – hydrothermal fluids, isochores of fluid inclusion assemblages for each stage of quartz grains were combined with Ti-in-quartz data (Appendix 6) from the same quartz grain (Fig. 7.9). Isochores for each fluid inclusion assemblage were calculated using the equations of Steele-MacInnis et al. (2012), whereas median values of the Ti-in-

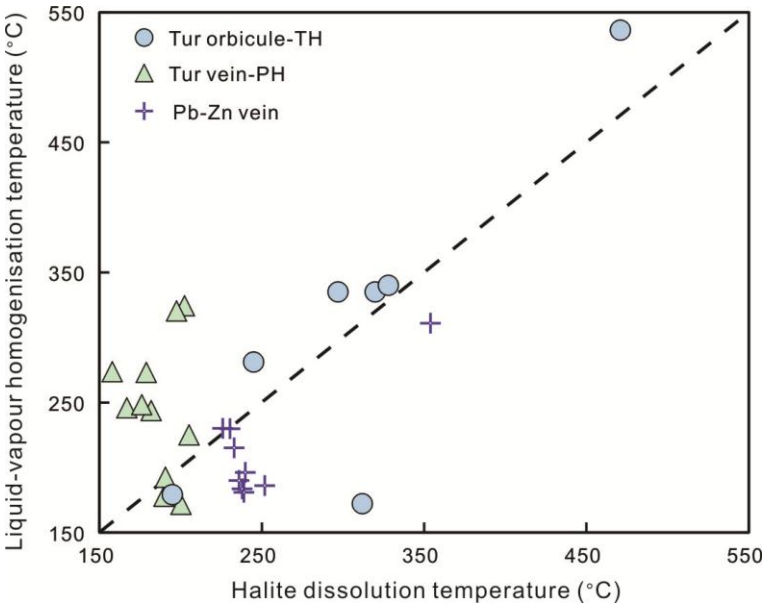

Figure 7.8 Halite dissolution temperature versus liquid-vapour homogenisation temperature for brine inclusions from tourmaline-rich features and Pb-Zn veins in the western Tasmanian granites. TH= Trial Harbour, Heemskirk Granite. PH = Pieman Heads Granite. All data listed in Appendix 7.

quartz data were used to depict Ti-in-quartz isopleths (Huang and Audétat, 2012). Where the fluid inclusion isochores intersect the corresponding Ti-in-quartz isopleths, the ranges of trapping pressures and temperatures under which each tourmaline-rich feature formed in the studied granites can be interpreted (Fig. 7.9). TiO_2 activity was assumed to equal 1.0 for all of the Ti-in-quartz geothermometric calculations, as titanite and/or rutile aggregates occur in both the tourmaline-rich features and Pb-Zn veins.

Type I fluid inclusions in homogeneous CL-bright quartz from tourmaline orbicules in the Heemskirk Granite have low salinities and high temperatures (Figs. 7.5a, b). The isochores of these liquid-rich fluid inclusions and Ti-in-quartz isopleths (median = 25 ppm) yield trapping temperatures of 520 °to 560 °C and lithostatic pressures of 0.75 to 1.3 kbars (Fig. 7.9) for the tourmaline orbicules in the Heemskirk Granite at Trial Harbour, equalising to depths of 2.8 to 5 km (assuming granite densities of ~2.7 g/cm^3).

The isochores of liquid-rich fluid inclusions in homogeneous CL-bright quartz from the tourmaline cavities in the Heemskirk Granite that intersect with the isopleth of median 20 ppm Ti concentration in the same quartz grains, imply a narrow temperature range of 495 °to 515 °C and lithostatic pressures of 0.6 to 0.95 kbars, corresponding to depths of 2.3 to 3.6 km (Fig. 7.9; Table 7.4).

CL-gray quartz grains in the tourmaline veins of the Heemskirk Granite contain liquid-rich fluid inclusions, and have relatively low Ti contents, ranging from 2.0 to 8.8 ppm (Table 6.3). The isochores of these liquid-rich inclusions intersect the 3.4 ppm Ti isopleth, giving a restricted trapping temperature around 310 ± 20 °C and a hydrostatic pressure of ~100 bars (Fig. 7.9; Table 7.4). The estimated trapping temperatures overlap with the liquid homogenisation temperatures (205 ° to 339 °C). The calculated hydrostatic pressure of ~100 bars equalises to depth of ca. 1.0 km, and is estimated for the tourmaline-quartz veins based on an assumed water density of 1 g/cm^3.

CL-gray quartz with oscillatory zoning in the Pb-Zn veins of the Heemskirk Granite has the lowest Ti concentrations, down to 0.19 ppm, with a median value of 2.3 ppm (Table 7.4). Over 70 % of the halite-bearing fluid inclusions in the Pb-Zn quartz veins homogenise by halite dissolution after vapour disappearance (Fig. 7.8). These halite-saturated fluid inclusions are interpreted to either have been

Table 7.4 Estimated pressures and temperatures for tourmaline-rich features and Pb-Zn veins

Textures	Granite	FI assemblage	Th (°C)	Salinity (wt % NaCl equiv)	Median Ti (ppm)	Temperature (°C)	Pressure (kbar)	Depth (km)
Quartz in aplite	Heemskirk	unavailable	unavailable	unavailable	40.5	[§] > 598	≥ 1.3	≥ 5
UST quartz	Heemskirk	unavailable	unavailable	unavailable	26.7	[§] > 561	≥ 1.3	≥ 5
Tur patch	Heemskirk	unavailable	unavailable	unavailable	27.9	[§] > 565	≥ 1.3	≥ 5
Tur orbicule	Heemskirk	Type I	178 to 389	3.7 to 15.1	25.0	520 to 560	0.75 to 1.3	2.8 to 5
Tur cavity	Heemskirk	Type I	173 to 343	3.2 to 9.1	20.0	495 to 515	0.6 to 0.95	2.3 to 3.6
Tur vein	Heemskirk	Type I	205 to 339	7.7 to 14.0	3.40	310 ± 20 [Ψ]	0.1	≈ 1.0
Pb-Zn vein	Heemskirk	Type I only	185 to 264	4.3 to 6.9	2.30	280 ± 40 [Ψ]	0.08	≈ 0.8
Tur patch	Pieman Heads	unavailable	unavailable	unavailable	44.9	[§] > 608	≥ 1.3	≥ 5
Tur orbicule	Pieman Heads	unavailable	unavailable	unavailable	47.2	[§] > 613	≥ 1.3	≥ 5
Tur vein	Pieman Heads	Type I only	206 to 286	11.0 to 12.0				
Tur vein	Pieman Heads	Type I + IIIa + IIIb + IIIc	178 to 320	30.4 to 32.0	*8.5	400 to 410	0.2 to 0.3	0.8 to 1.1

Note: Tur = tourmaline; FI = fluid inclusion; the homogenisation temperature and salinity ranges include microthermometric data between 10th and 90th percentile; Th = homogenisation temperature; median Ti = median Ti contents in corresponding quartz grains;

*The median Ti of quartz in tourmaline veins of the Pieman Heads Granite was calculated only by low temperature quartz with Ti < 10 ppm;

[§] The temperatures of quartz in aplite, UST quartz, tourmaline patches in the Heemskirk Granite, and tourmaline patches and orbicules in the Pieman Heads Granite were calculated by the equation of Huang and Audétat (2012) assuming minimum pressures of 1.3 kbars.

[Ψ] The errors for temperatures of tourmaline veins and Pb-Zn veins were calculated as standard deviations of Ti-in-quartz geothermometric temperatures.

entrapped heterogeneously or have undergone post-entrapment modification (e.g., Audétat and Günther, 1999), which cannot be used to estimate meaningful P-T conditions (e.g., Maydagán et al., 2015). Only the isochores of liquid-rich fluid inclusions were used to intersect the 2.3 ppm Ti isopleth, suggesting trapping temperatures of 280 ± 40 °C, hydrostatic pressures < 100 bars, and depths of approximately 0.8 km (Fig. 7.9; Table 7.4).

Titanium concentrations in quartz from tourmaline veins in the Pieman Head Granite range from 7.8 to 48.7 ppm (Table 6.3), much higher than Ti contents for quartz from tourmaline veins in the Heemskirk Granite at Trial Harbour (1.3 to 27.4 ppm; Table 6.3). High Ti quartz in tourmaline veins at Pieman Heads have similar bright CL intensity response to quartz from tourmaline patches and orbicules (Tables 6.2, 6.3), and fluid inclusions are rarely observed in these quartz grains. CL-gray quartz in the tourmaline veins commonly contain coexisting type I + III fluid inclusions (Fig. 7.2k), and most of the halite-bearing inclusions (type III) homogenise by vapour disappearance (Fig. 7.8). Both types of fluid inclusions have relatively narrow salinity ranges of 11 to 12 wt % and 30.4 to 32 wt % NaCl equiv (Table 7.3). The isochores of the type I + III fluid inclusions intersect the 8.5 Ti ppm isopleth, indicating a trapping temperature range of 400 ° to 410 °C, and a pressure range of 0.2 to 0.3 kbars (Fig. 7.9; Table 7.4). This corresponds to depths of 0.8 to 1.1 km under lithostatic pressure conditions, or 2.0 to 3.0 km under hydrostatic pressure conditions.

No microthermometric data are available for tourmaline patches from the Heemskirk Granite, and tourmaline patches and orbicules from the Pieman Heads Granite. A minimum pressure of 1.3 kbars is assumed for tourmaline patches and/or tourmaline orbicules from the Heemskirk and Pieman Heads granites, corresponding to a minimum depth of 5 km under lithostatic pressure conditions (Table 7.4). According to Huang and Audétat (2012)'s equation and median Ti concentrations in quartz, minimum trapping temperatures of 565 °, 608 ° and 613 °C are calculated for tourmaline orbicules in the Heemskirk Granite, and tourmaline patches and orbicules in the Pieman Heads Granite, respectively (Table 7.4). The minimum crystallisation temperatures of quartz in aplitic sills and USTs in the Heemskirk Granite are estimated to be 598 ° and 561 °C, respectively, based on the assumption of minimum pressures of 1.3 kbars and their median Ti-in-quartz concentrations (Table 7.4).

7.4.3 Depositional processes

Hajitaheri (1985) suggested that tourmaline crystallised at high pressures (up to 1.2 kbars) from halite-saturated fluids mixed with minor external waters, and this process is fundamental to the formation of tourmaline-rich textures and associated mineralisation in the Heemskirk Batholith. No fluid inclusion assemblages have been identified in the current study that have type I and type II inclusions with similar homogenisation temperatures. This feature illustrates that these fluid inclusions either were not trapped at the same time during boiling, or the fluid inclusions have undergone post-entrapment modifications that reset their homogenisation temperatures (cf. Wilkinson, 2001; Goldstein, 2003).

Broad ranges of homogenisation temperatures (150 ° to > 550 °C; Table 7.3) and salinities (2 to 16 wt %, and 31 to 56 wt % NaCl equiv; Table 7.3) in the current study indicate that tourmaline orbicules and

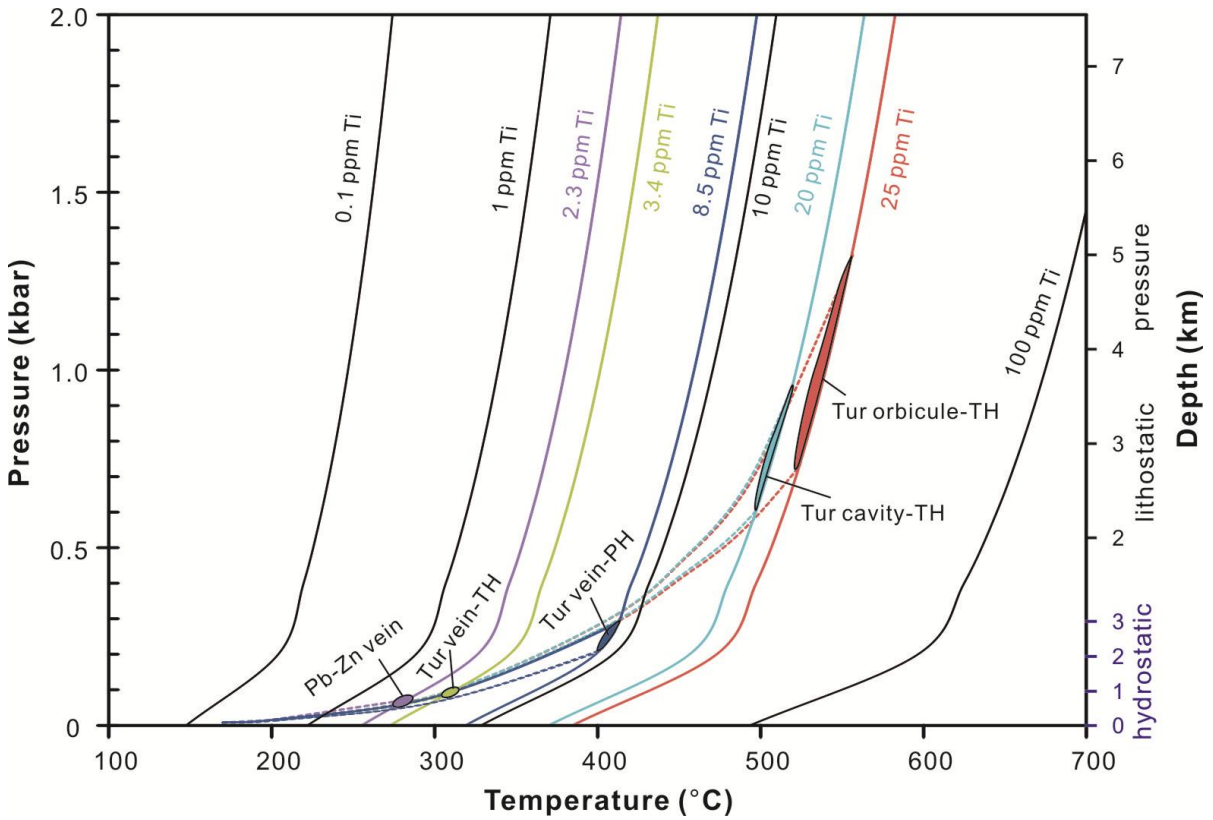

Figure 7.9 Pressure-temperature plot showing estimated formation conditions of tourmaline-rich features and Pb-Zn veins in western Tasmanian granites. The upper and lower isochores are calculated based on 10th percentile and 90th percentile microthermometric data of fluid inclusions assemblages, respectively, using the equation from Steele-MacInnis et al. (2012). The regions that isochores intersect with isopleths of median Ti-in-quartz concentrations (Huang and Audétat, 2012) represent estimated temperature and pressure ranges for corresponding quartz-rich features in the western Tasmanian granites. Tur = Tourmaline, TH= Trial Harbour, Heemskirk Granite. PH = Pieman Heads Granite.

cavities have experienced a prolonged history of depressurisation (e.g., Wilkinson, 2001; Fig. 7.7a). This argument is also evidenced by the calculated pressures that fluctuate widely, from 0.6 to 1.3 kbars for tourmaline orbicules and cavities from the Heemskirk Granite (Fig. 7.9; Table 7.4).

Halite dissolution preceding vapour disappearance was observed in type I + IIIa fluid inclusions from tourmaline orbicules of the Heemskirk Granite (Table 7.3; Fig. 7.8). The salinities of coexisting type I and type IIIa fluid inclusions in these tourmaline orbicules are 3.1 to 17.5 wt % and 35 to 55.9 wt % NaCl equiv, respectively (Fig. 7.5; Table 7.3). These variable salinities are commonly observed in magmatic – hydrothermal fluids, and are commonly explained by entrapment at high pressures (e.g., Hajitaheri, 1985; Cline and Bodnar, 1994; Becker et al., 2008). The entrapment of moderately saline liquid-rich fluid inclusions (2.5 to 12 wt % NaCl equiv) are interpreted to be due to fluctuating temperature and pressure at near-critical conditions, whereas the brine with salinity up to 56 wt % NaCl equiv may be directly exsolved from a crystallising felsic melt under lithostatic pressures (e.g., Cline and Bodnar, 1994), or the saline fluid and brine may be products of unmixing from supercritical fluids after exsolution (e.g., Bodnar et al., 1985).

Figure 7.9 and Table 7.4 show that temperatures and pressures decrease substantially from the early-formed tourmaline orbicules and cavities (500 °to 560 ℃ and 0.6 to 1.3 kbars), to the late-stage tourmaline

veins (310 ± 20 °C and 0.1 kbars). The estimated depths decrease from >5 km for the tourmaline orbicules to ~1 km for tourmaline veins, which may imply that uplift and/or exhumation of the host granites occurred during the lifespan of magmatic – hydrothermal activities. Furthermore, homogenisation temperatures and salinities display relatively coherent decreasing trends in tourmaline-vein quartz, possibly indicating the dilution of low salinity external water (e.g., Wilkinson, 2001; Fig. 7.7a).

Continuous decreasing of pressure (~ 0.08 kbars) and temperature (~ 280 ± 40 °C) of the hydrothermal fluids led to the precipitation of quartz-fluorite veins associated with sulphide mineralisation at Sweeney present in the Heemskirk Granite (Fig. 7.9; Table 7.4). More than 80 % measured salt-bearing fluid inclusions (type IIIb) in the Pb-Zn veins are characterised by homogenisation via halite dissolution (Fig. 7.8). This feature has been observed in a large number of magmatic – hydrothermal mineral deposits (Cline and Bodnar, 1994; Wilson et al., 2003; Masterman et al., 2005; Rusk et al., 2008; Maydagán et al., 2015). The trapping pressure for this type of fluid inclusions (type IIIb) is estimated to be about 80 bars (Table 7.4). The type IIIb inclusions are thus not the products of high trapping pressures (cf. Becker et al., 2008), and may result either from accidental salt crystals being heterogeneously entrapped in salt-saturated fluids, or from post-entrapment modification (e.g., Audétat and Günther, 1999; Wilson et al., 2003; Maydagán et al., 2015). Most of the salinities of types I + IIIa +IIIb inclusions gradually increase with decreasing homogenisation temperatures (Fig. 7.7b), suggesting that the magmatic – hydrothermal fluids could have been diluted by external (meteoric?) water (e.g., Wilkinson, 2001).

7.4.4 Sn-Pb-Zn mineralising fluids compared to barren fluids

The salinities and temperatures of fluid inclusions in tourmaline veins from the Pieman Heads Granite are similar to those from tourmaline orbicules, but higher than from tourmaline veins of the Heemskirk Granite (Table 7.4; Fig. 7.7a). The high salinity (up to 31 wt % NaCl equiv) of fluid inclusions in vein quartz from the Pieman Heads Granite is at odds with the argument that the absence of mineralisation in Sn granites is caused by a low salinity of exsolving fluids (e.g., Audétat and Pettke, 2003). Compositional analyses of fluid inclusions have shown that the fluid inclusions from Sn deposits commonly contain high Sn concentrations (Audétat et al., 2008), whereas comparable metal concentrations can be observed in fluid inclusions from both mineralised Cu-Mo porphyry intrusions and barren granites (cf. Lerchbaumer and Audétat, 2013). The metal contents of fluid inclusions have not been analysed for the Heemskirk and Pieman Heads granites in the current study, and so it is uncertain whether metal contents of hydrothermal fluids was a crucial factor to determine the mineralisation between the two western Tasmanian granites. However, based on whole-rock analytical results, the higher degree of crystal fractionation tends to indicate that the white Heemskirk Granite had the ability to exsolve fluids more enriched in Sn than the Pieman Heads Granite (Fig. 5.10).

7.5 Conclusions

Petrographic observations of melt and fluid inclusions provide unambiguous evidence that tourmaline patches, orbicules, cavities and veins precipitated from exsolved magmatic – hydrothermal fluids from the

associated granites. Liquid-rich (type I), vapour-rich (type II) and halite-bearing (type III) fluid inclusions have been recognised in quartz from these tourmaline-rich textural features. Microthermometric measurements reveal that type I, type II and type III fluid inclusions have homogenisation temperatures and salinities ranging from 156 °to 460 ℃ and 2 to 15 wt % NaCl equiv, 334 °up to 550 ℃ and 6 to 8 wt % NaCl equiv, and 170 °to 530 ℃ and 31 to 56 wt % NaCl equiv, respectively. Combined microthermometry and Ti-in-quartz geothermometry indicate that tourmaline patches, orbicules and cavities formed at temperatures of 500 ° to 565°C and lithostatic pressures of 0.6 to 1.3 kbars (depth of 2.8 to ≥ 5 km). Tourmaline veins formed at 310 ± 20 ℃ and 400 °to 410 ℃ for the Heemskirk and Pieman Heads granites, respectively, at hydrostatic pressures of 0.1 to 0.3 kbars (depth of ca. 1km). The estimated depths decreasing from ≥ 5 to 1 km may imply that the host granites have experienced uplift and/or exhumation events. Pb-Zn quartz veins with the Heemskirk Granite precipitated under lower temperature-pressure conditions (280 ± 40 ℃; hydrostatic pressure of 80 bars). Depositional mechanisms, including decompression, decreasing temperature, and/or mixing with external water could have played a positive role in the generation and precipitation of these tourmaline-quartz-rich features. These mechanisms will be assessed further in Chapter 8 using stable isotopic data.

Chapter 8 Boron, oxygen and strontium isotopes

8.1 Introduction

Boron isotopic studies have been developed as a powerful tool for deciphering complex geological phenomena during the past few decades (Marschall and Jiang, 2011), although the fractionation behaviour of B-isotopes is still poorly understood compared with other more traditional stable isotopes (e.g., H, O, C, and S). Boron isotopic compositions are particularly useful for discriminating magmatic, hydrothermal, or seawater fluid sources (e.g., Slack and Trumbull, 2011). Boron isotopic analyses of tourmalines can therefore supply valuable information to help constrain physicochemical conditions of igneous, metamorphic, and sedimentary events, as well as fluid evolution and genesis of tourmaline-bearing mineral deposits (Marschall and Jiang, 2011; Slack and Trumbull, 2011).

Oxygen isotopic studies of tourmaline have been widely used to trace fluid sources and to elucidate the ore genesis of a number of mineral deposit types, including massive sulphide deposits (e.g., Taylor and Slack, 1984; King, 1990), orogenic lode gold deposits (Ibrahim and Kyser, 1991; Ansdell and Kyser, 1992; Kotzer, 1993; Kontak and Kerrich, 1997; Beaudoin and Chiaradia, 2016), and magmatic – hydrothermal mineralisation associated with granites and pegmatites (e.g., Taylor et al., 1979, 1992; Skewes et al., 2003; Marks et al., 2013; Duncan et al., 2014; Siegel et al., 2016).

Because tourmaline contains low Rb and high Sr contents (e.g., Taylor and Slack, 1984; Griffin et al., 1996; Table 5.3), initial Sr isotopic compositions of hydrothermal fluids may be preserved in tourmaline (e.g., King and Kerrich, 1989; Jiang et al., 1999). Strontium isotope systematics of tourmaline have been used to constrain sources and evolution history of hydrothermal fluids related to ore-forming systems, particularly orogenic lode gold deposits (e.g., King and Kerrich, 1989; Ibrahim and Kyser, 1991; Mueller et al., 1991; Ansdell and Kyser, 1992; Kontak and Kerrich, 1997; Beaudoin and Chiaradia, 2016), and granite-related hydrothermal deposits (e.g., Jiang et al., 1999; Roberts et al., 2006).

Compared with traditional bulk isotopic measurement techniques (e.g., Palmer and Slack, 1989), in-situ microanalysis by secondary ion mass spectrometry (SIMS) makes it possible to determine the boron isotopic compositions of tourmaline at a sub-grain scale, which can effectively overcome the problem that tiny mineral inclusions within tourmaline contaminate the isotopic ratios (Chaussidon and Appel, 1997; Marschall et al., 2006, 2008; Trumbull et al., 2008; Shabaga et al., 2010; Marschall and Jiang, 2011; Duncan et al., 2014; Belley et al., 2015). In-situ SIMS microanalysis has a considerable advantage of revealing the isotopic variations between different growth zones within individual tourmaline grains.

This chapter documents the results of in-situ SIMS boron and oxygen isotopic analyses, and strontium isotopic measurements of tourmalines from western Tasmanian granites. These data are used to track fluid sources constrained by the paragenetic and chemical characteristics in other chapters, and to investigate

possible geological mechanisms for resulting in isotopic variations of tourmaline grains grouped in different textures from the western Tasmanian granites.

8.2 Methodology

8.2.1 Secondary ion mass spectrometry analyses

The boron and oxygen isotopic compositions for tourmaline and quartz samples were measured using a CAMECA ims7f secondary ion mass spectrometer (SIMS) at Department of Geological Sciences, University of Manitoba, Canada. Gold-coated samples and standard mounts were placed in stainless steel sample holders, and the whole assembly was put in the SIMS sample chamber airlock and held at high vacuum for a minimum of eight hours prior to the start of analysis, in order to reduce interference and increase accuracy.

The boron isotopic ratios were measured using a ~5 nA primary beam of O-ions accelerated at 12.5 kV with a spot size of ~30 μm, using a procedure similar to that described by Shabaga et al. (2010) and Belley et al. (2015). Sample-accelerating voltage and electrostatic analyser in the secondary column were both set up as +10 kV, and a ±50 volts energy window was used without application of a voltage offset. A 60 second pre-sputter was applied. The mass spectrometer was operated at a mass resolving power of 800. Ions were detected with a Balzers SEV 1217 electron multiplier coupled with an ion-counting system with an overall deadtime of 25ns. Entrance slit and exit slit were setup as 61.9 μm and 800 μm, respectively. Each spot analysis was operated over 50 cycles within 5 minutes. The species were detected as $^{11}B^{+}$ and $^{10}B^{+}$ during a separate session in order to obtain the B isotopic ratios when switching the magnetic field. The whole analysis was calibrated using external standard (elbaite) that has an $^{11}B/^{10}B$ ratio of 4.001162 (No.98114, Dyer et al., 2001). During the analytical period from September 30th to October 4th, 2013, the observed precisions for spot to spot reproducibility on the elbaite standard were 0.2 ‰, 0.2 ‰, 0.1 ‰, 0.2 ‰ and 0.3 ‰, respectively.

The parameters employed to measure oxygen isotopic ratios were different from those for B isotopes. A ~2 nA primary ion beam of Cs^{+} accelerated at 10 kV was focused to a 15-20 μm spot size. The sample-accelerating voltage and electrostatic analyser in the secondary column were set to -8.75 kV and -9 kV, respectively. The Balzers SEV 1217 electron detector has an overall dead time of 20ns. A ± 25 volts energy window was setup with 250 voltage offset. The entrance slit was set at 247 μm with a mass resolving power of 347. Species of $^{18}O^{-}$ and $^{16}O^{-}$ were collected successively in ~10 minutes which comprised 70 cycles with an eGun. The calculated precisions for individual spot reproducibility on the quartz standard were 0.1 ‰, 0.3 ‰ and 0.2 ‰ from January 7th to 9th, 2014, and 0.5 ‰ and 0.4 ‰ (January 10th, 13th) on the tourmaline standard. The oxygen isotope data ($\delta^{18}O$) were reported in ‰ units relative to Vienna-Standard Mean Ocean Water (V-SMOW).

Based on Ti-in-quartz geothermometry (Huang and Audétat, 2012) and microthermometric results of fluid inclusions, temperatures are calculated for the tourmaline-rich assemblages from the Heemskirk and Pieman Heads granites (Fig. 7.9; Table 8.3). Using the estimated temperatures, B- and O-isotopic compositions for the fluids are calculated according to the equations from Meyer et al. (2008), Clayton et

al. (1972; quartz) and Kotzer et al. (1993; tourmaline) respectively. These data are tabulated in Table 8.3, and their ranges are shown in Figures. 8.4 and 8.5. Isotopic values for measured tourmaline, quartz and calculated fluids are expressed as $\delta^{11}B_{Tur}$, $\delta^{18}O_{Tur}$, and $\delta^{18}O_{Qtz}$, and $\delta^{11}B_{H2O}$ and $\delta^{18}O_{H2O}$, respectively.

8.2.2 Strontium isotopic analyses

Whole rocks samples of collected granites were crushed into ~ 1 mm size with a Cr-steel mortar and pestle. Over 0.5g of tourmaline separates were hand-picked from the each crushed rocks, under a binocular microscope. Strontium isotope compositions of tourmaline were analysed in the Isotope Geochemistry Laboratory, School of Earth Sciences, University of Melbourne. Approximately 100 mg of tourmaline separates were weighed into Teflon beakers, cleaned with very dilute nitric acid and then digested with a 3:1 HF-HNO_3 mixture on a hot plate. After several days, most of the samples showed little sign of dissolution. After evaporating most of the acid, the remaining slurry was transferred to a Krogh-type PTFE high-pressure vessel. Pure HF was added, and the vessels were placed in an over at 160 ℃ for 4 days. The HF was then dried off, and the residue attacked with 2 x 1 ml of HNO_3 and returned to the oven with 6 M HCl overnight. The resulting HCl solutions still contained minor residues but most of the sample had dissolved. The solutions were then split for trace element and Sr isotopic measurements. Some of these samples (WT12WH20, 23, 24 and 28) yielded poor Sr isotope results, and so a second round analysis were conducted. The remaining tourmaline grains, in three samples, were ground to very fine sand size in an agate mortar and pestle. The entire material remaining for these separates was cleaned with dilute nitric acid and then digested in HF at high pressure for 1 week (e.g., Roberts et al., 2006). After removal of clear HF, fresh HF was added and the samples returned to the oven for another week. All HF was then combined, dried, evaporated twice with hot concentrated HNO_3 and returned to the oven with 6M HCL for another three days. As in the first round of dissolutions, the resulting HCl solutions were split for trace element and Sr isotopic analyses. Strontium was extracted using Eichrom Sr resin. Two or three passes over small (0.15 ml) beds of this resin were required to reduce levels of Rb and other impurities to allow high-quality isotopic analyses. Strontium isotopic ratios were measured on a Nu Plasma multi-collector ICP-MS at the University of Melbourne, with sample aspiration via a Glass Expansion Opal Mist PFA nebuliser (~0.07 ml/min uptake) and a CETAC Aridus desolvator (Woodhead, 2002; Maas et al., 2005).

Strontium isotopic data were acquired in static multi-collection mode on solutions containing 60–70 ppb Sr which produced total Sr signals of 8V. Instrumental mass bias was corrected by normalizing to $^{88}Sr/^{86}Sr$ = 8.37521 using the exponential law and data are reported relative to SRM987 = 0.710230. External reproducibility (2σ) of corrected $^{87}Sr/^{86}Sr$ is ± 0.000040. USGS basalt standard BCR-2 was measured with the tourmalines grains and yielded $^{87}Sr/^{86}Sr$ ratios (± 2σ) of 0.705016 ± 16 and 0.704963 ± 16, consistent with TIMS and MC-ICPMS reference values and with the laboratory's long-term average of 0.704997 ± 42 (2σ). $^{87}Rb/^{86}Sr$ ratios were constructed from trace element results for the same sample solutions, and they have a precision of 2 %.

Table 8.1 The measured $\delta^{11}B$ ranges and averages of tourmaline from the western Tasmanian granites

Sample	Area	Type	Range (‰)	Average (‰)	1σ (‰)	Number
WT12WH20	TH, Heemskirk	Patch	-21.7 to -0.6	−8.4	7.7	13
WT12WH28	TH, Heemskirk	Orbicule	-7.3 to -1.6	−4.5	1.7	15
WT12WH24	TH, Heemskirk	Cavity	-6.5 to +4.1	−2.3	2.4	22
WT12WH23	TH, Heemskirk	Vein	-7.5 to -0.3	−3.8	2.9	10
WT12WH35	GH, Heemskirk	Orbicule	-13.9 to -8.9	−11.4	1.0	7
WT12WH33	GH, Heemskirk	Cavity	-2.4 to + 0.6	−0.8	1.8	8
WT12WH04	Pieman Heads	Patch	-10.3 to -1.1	−5.7	3.0	7
WT12WH07	Pieman Heads	Orbicule	-6.6 to -1.1	−4.4	1.7	6
WT12WH13	Pieman Heads	Vein	-9.2 to -0.3	−4.5	1.9	39

Abbreviation: TH = Trial Harbour, GH = Granville Harbour.

8.3 Results

8.3.1 Boron isotopes

The samples analysed for boron isotopic compositions include tourmaline grains from patches, orbicules, cavities and veins associated with the Heemskirk and Pieman Heads granites. These tourmaline crystals were first analysed for their major element compositions using EMPA (Appendix 8.1) prior to boron isotope measurements. Samples mounts were re-polished and ultrasonically washed for trace element determinations by LA-ICP-MS. More than 120 spots of tourmaline crystals were determined for boron isotopes by in-situ SIMS. These results are tabulated in Appendix 8.1.

8.3.1.1 Heemskirk Granite

The boron isotopes ($\delta^{11}B_{Tur}$) for tourmalines associated with the Heemskirk Batholith range widely between -21.7 and +4.1 ‰ (Table 8.1; Fig. 8.1). The lowest and highest values were obtained from tourmaline patches and cavities from Trial Harbour, respectively. The Trial Harbour tourmaline patches have a relatively large range of $\delta^{11}B_{Tur}$ values, from -21.7 to -0.6 ‰ with an average of -8.4 ‰ (n = 13). Contrastingly, $\delta^{11}B_{Tur}$ ratios in orbicular tourmalines have a narrow range (-7.3 to -1.6 ‰, n = 15) with an average of -4.5 ‰. Boron isotopes in tourmaline veins range between -7.5 and -0.3‰ with an average of -3.8 ‰ (n = 10). The tourmalines in miarolitic cavities have a higher average $\delta^{11}B_{Tur}$ value (-2.3 ‰, n = 22), and more variable compositions than those in tourmaline orbicules.

For samples of the Heemskirk Granite from Granville Harbour, only tourmaline grains from orbicules and miarolitic textures were analysed for boron isotopic compositions (Table 8.1; Fig. 8.1). Tourmalines from orbicules have a range of $\delta^{11}B_{Tur}$ values, from -13.9 to -8.9 ‰ (average = -11.4 ‰, n = 7), which are lower values than their counterparts from Trial Harbour (average = -4.5 ‰). In contrast, boron isotopic ratios for tourmalines from miarolitic cavities have a narrow distribution of $\delta^{11}B_{Tur}$ values of -2.4 to +0.6‰ (average = -0.8 ‰, n = 8). They are higher on average than the values obtained in tourmaline cavities at Trial Harbour.

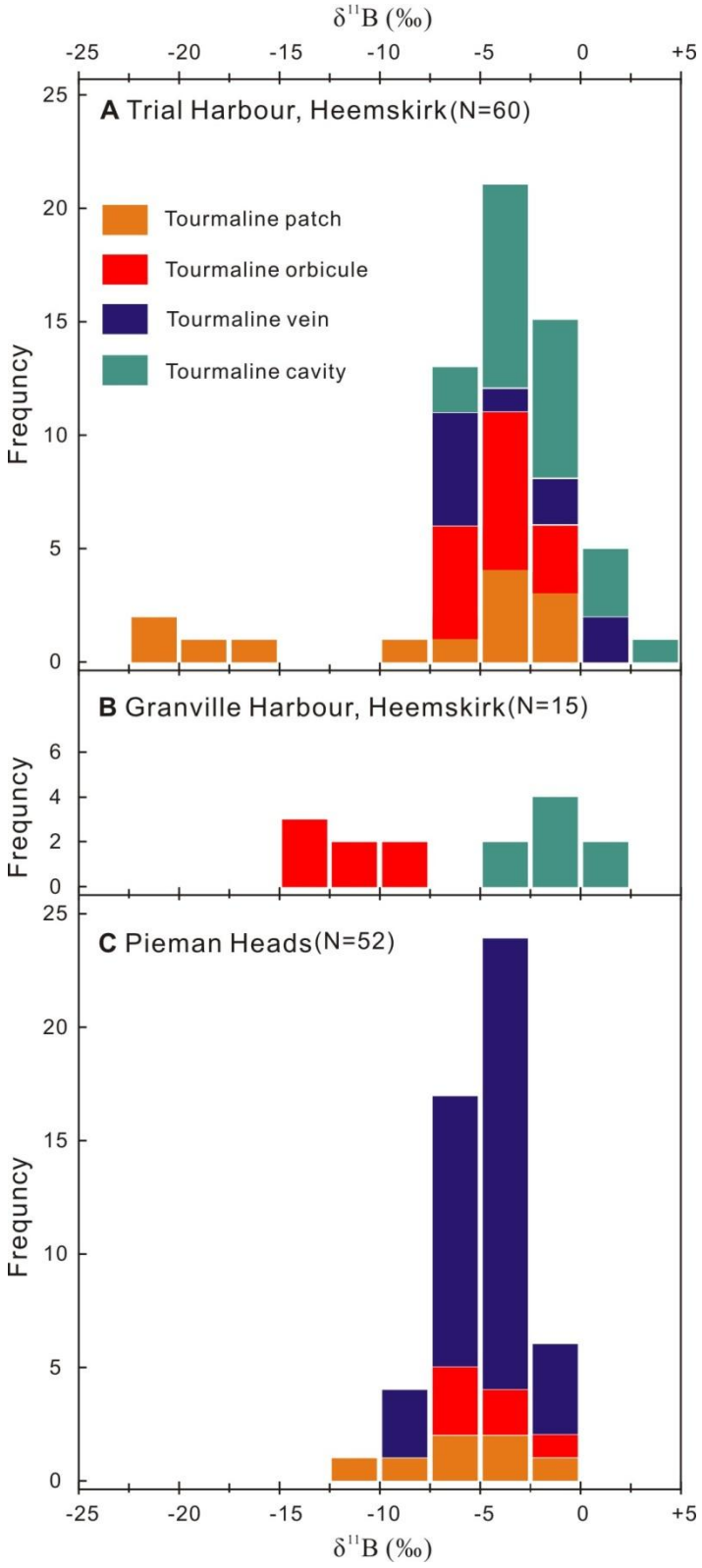

Figure 8.1 Histograms showing boron isotopic composition of tourmaline in different textural assemblages from (A) Trial Harbour, (B) Granville Harbour, Heemskirk Granite, and (C) the Pieman Heads Granite.

8.3.1.2 Pieman Heads Granite

The boron isotopes of tourmaline associated with the Pieman Heads Granite ($\delta^{11}B_{Tur}$ = -10.3 to -0.3‰; n = 52) have a more restricted range than those from the Heemskirk Batholith. More than 75% $\delta^{11}B_{Tur}$ data fall into the range of -6 to -2 ‰ (Table 8.1; Fig. 8.2). The lowest and highest boron isotopic

Table 8.2 The measured $\delta^{18}O$ ranges and averages of tourmaline and associated quartz

Sample	Area	Type	Mineral	Range (‰)	Average (‰)	1σ (‰)	Number
WT12WH20-3	TH, Heemskirk	Patch	Tourmaline	+9.8 to +11.3	10.5	0.6	4
WT12WH28-3-1	TH, Heemskirk	Orbicule	Tourmaline	+10.3 to +13.4	12.2	1.3	4
WT12WH28-3-2	TH, Heemskirk	Orbicule	Tourmaline	+8.9 to +14.9	11.3	2.2	4
WT12WH24-3	TH, Heemskirk	Cavity	Tourmaline	+9.7 to +13.3	11.6	1.3	5
WT12WH23-1	TH, Heemskirk	Vein	Tourmaline	+10.4 to +11.5	11.2	0.4	4
WT12WH04-1	Pieman Heads	Patch	Tourmaline	+8.6 to +13.3	10.8	1.7	4
WT12WH07-2	Pieman Heads	Orbicule	Tourmaline	+9.1 to +10.2	9.7	0.4	4
WT12WH13-1	Pieman Heads	Vein	Tourmaline	+6.5 to +11.9	9.4	1.8	9
WT12WH20-3	TH, Heemskirk	Patch	Quartz	+10.0 to +12.0	11.0	0.8	3
WT12WH28-3-1	TH, Heemskirk	Orbicule	Quartz	+7.9 to +11.6	10.0	1.3	5
WT12WH28-3-2	TH, Heemskirk	Orbicule	Quartz	+7.2 to +10.3	8.4	1.4	3
WT12WH24-3	TH, Heemskirk	Cavity	Quartz	+13.5 to +16.1	15.1	1.0	6
WT12WH23-1	TH, Heemskirk	Vein	Quartz	+10.5 to +10.8	10.6	0.1	4
WT12WH04-1	Pieman Heads	Patch	Quartz	+5.7 to +11.0	8.4	1.9	4
WT12WH07-2	Pieman Heads	Orbicule	Quartz	+5.0 to +8.8	7	1.8	4
WT12WH13-1	Pieman Heads	Vein	Quartz	+11.4 to 12.7	11.9	0.5	4

Abbreviation: TH = Trial Harbour, GH = Granville Harbour.

values from Pieman Heads were measured from a tourmaline patch (-10.3 ‰) and tourmaline vein (-0.3‰), respectively. Most of the boron isotopic data from the tourmaline veins that display distinctive compositional zones have $\delta^{11}B_{Tur}$ ratios between -9.2 and -0.3 ‰, with an average of -4.5 ‰ (n = 39). Tourmaline in patches show a broad range of $\delta^{11}B_{Tur}$ values (-10.3 to -1.1 ‰, n = 7), with an average of -5.7 ‰. In contrast, the $\delta^{11}B_{Tur}$ range is narrow for tourmaline orbicules from this granite, varying between -6.6 and -1.1 ‰ with an average of -4.4 ‰ (n = 6).

8.3.2 Oxygen isotopes

Oxygen isotopes were analysed for tourmaline and quartz from the Heemskirk and Pieman Heads granites. A total of 38 oxygen isotopic analyses of tourmalines, and 33 analyses of quartz were conducted. These data are presented in Appendix 8.2.

8.3.2.1 Tourmaline

The range of $\delta^{18}O_{Tur}$ values for tourmaline crystals from the Heemskirk and Pieman Heads granites vary from +6.5 to +14.9 ‰ (Table 8.2). The lowest value was obtained from a tourmaline vein from the Pieman Heads Granite. The highest $\delta^{18}O_{Tur}$ value was obtained from a tourmaline orbicule from the Heemskirk Batholith. The individual oxygen isotopic results, including ranges and averages are shown in Figs.8 .2A-B and Table 8.2 for each tourmaline assemblage from the two western Tasmanian granites.

In general, tourmalines from the Heemskirk Batholith at Trial Harbour have $\delta^{18}O_{Tur}$ ratios that increase subtly from tourmaline patches (+10.5 ± 0.6 ‰), through tourmaline orbicules (+11.8 ± 2.0 ‰) and tourmaline veins (+11.2 ± 0.4 ‰), to tourmaline cavities (+11.6 ± 1.3 ‰; Table 8.2). In contrast, the tourmalines from the Pieman Heads Granite have decreasing measured $\delta^{18}O_{V\text{-}SMOW}$ compositions from

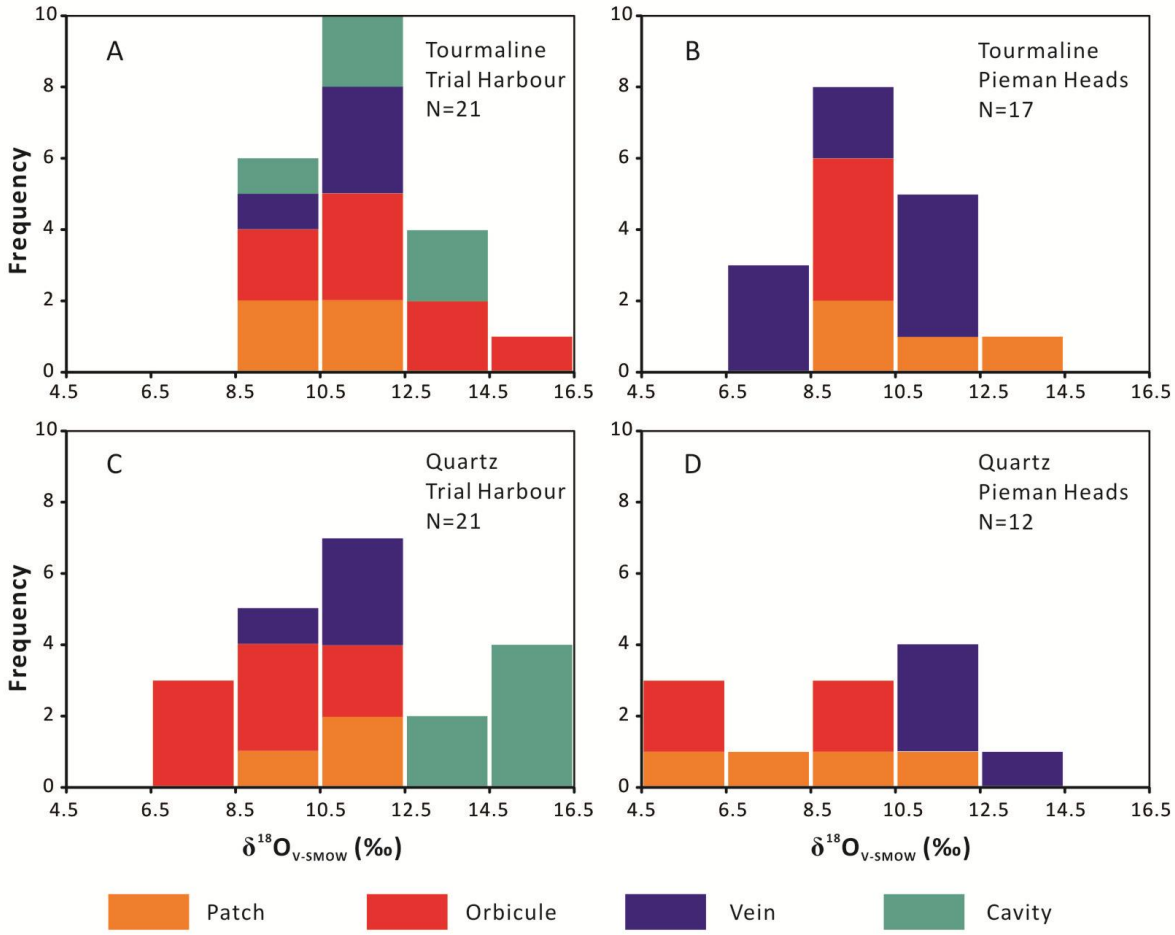

Figure 8.2 Histograms showing oxygen isotopic distributions in tourmaline and quartz from the Heemskirk and Pieman Heads granites, western Tasmania. (A) and (B) O-isotope values of tourmaline, (C) and (D) O-isotope values of quartz associated with tourmaline.

tourmaline patches (+10.8 ± 1.7 ‰), through tourmaline orbicules (+9.7 ± 0.4 ‰), to tourmaline-filled veins (+9.4 ± 1.8‰; Table 8.2; Fig. 8.2).

8.3.2.2 Quartz

In-situ SIMS measurement shows that quartz has a wider range of measured $\delta^{18}O_{V\text{-}SMOW}$ values (+5.0 to +16.1 ‰) than the associated tourmaline (+6.5 to +14.9 ‰) from the western Tasmanian granites (Table 8.2; Figs. 8.2C-D). The lowest $\delta^{18}O_{Qtz}$ value is from quartz grains associated with a tourmaline orbicule from Pieman Heads Granite, and the highest is from a tourmaline cavity in the Heemskirk Granite at Trial Harbour. The individual oxygen isotopic results, including ranges and averages are presented in Figs. 8.2C-D and Table 8.2 for quartz associated with each tourmaline assemblage.

The $\delta^{18}O_{Qtz}$ values detected from quartz intergrown with tourmaline from both Heemskirk and Pieman Heads granites generally increase from tourmaline patches and orbicules to tourmaline-filled cavities or veins (Figs. 8.2C, D), although there are a few exceptions, e.g., $\delta^{18}O_{V\text{-}SMOW}$ values in quartz from patches are higher than those from orbicules at Trial Harbour in the Heemskirk Granite.

Table 8.3 Temperature-calibrated B- and O-isotopic compositions for tourmaline grains

Sample	Area	Type	§Temper-ature (°C)	$\delta^{11}B$ (H_2O, ‰)	$\delta^{18}O_{V\text{-}SMOW}$ (H_2O, ‰)
WT12WH20	TH, Heemskirk	Patch	565	-20.2 to +0.8	+8.1 to +9.6
WT12WH28	TH, Heemskirk	Orbicule	550	-5.8 to -0.1	+7.2 to +13.2
WT12WH24	TH, Heemskirk	Cavity	500	-4.6 to +6.0	+7.7 to +11.3
WT12WH23	TH, Heemskirk	Vein	310	-3.9 to +4.0	+5.9 to +7.0
WT12WH35	GH, Heemskirk	Orbicule	550	-12.3 to -7.3	None
WT12WH33	GH, Heemskirk	Cavity	500	-0.5 to +2.5	None
WT12WH04	Pieman Heads	Patch	600	-9.0 to +0.1	+7.0 to +11.7
WT12WH07	Pieman Heads	Orbicule	600	-5.3 to +0.2	+7.5 to +8.6
WT12WH13	Pieman Heads	Vein	400	−6.5 to +2.4	+3.6 to +9.0

Note: §Temperatures are estimated based on Ti-in-quartz geothermometry (Huang and Audétat, 2012) and microthermometric results of fluid inclusions (Fig. 7.9); B- and O-isotopes for fluids are calibrated by the equations from Meyer et al. (2008) and Kotzer et al. (1993), respectively. Abbreviation: TH =Trial Harbour, GH = Granville Harbour.

8.3.3 Combined B-and O-isotopic variations across tourmaline growth zones

In-situ SIMS isotope analyses show that $\delta^{11}B_{Tur}$ and $\delta^{18}O_{Tur}$ variations are typically less than 2 ‰ across growth zones within a single tourmaline grain (e.g., Fig. 8.3). For most analysed tourmaline grains, both $\delta^{11}B_{Tur}$ and $\delta^{18}O_{Tur}$ values show increasing trends from core to rim. A tourmaline core from a patch at Trial Harbour, Heemskirk Batholith, has the lowest $\delta^{11}B_{Tur}$ values (-21‰), and also contains a relatively low $\delta^{18}O_{Tur}$value of +10.5 ‰. On the rim of this grain, the $\delta^{11}B_{Tur}$ and $\delta^{18}O_{Tur}$ ratios are -0.6 ‰ and +11.3‰, higher than the corresponding isotopic values at the core (WT12WH20; Fig. 8.3A). Similar isotopic variations have been detected in tourmaline grains from the quartz orbicules (Appendix 8.1 and 8.2). The highest $\delta^{11}B_{Tur}$ value (+4.1 ‰) is found on the oscillatory rim of a tourmaline grain from a miarolitic cavity, whereas the $\delta^{11}B_{Tur}$ value at the core is -0.8 ‰ (WT12WH24; Fig. 8.3B). The measured oxygen isotopes increase from +9.7 ‰ to +13.3 ‰ from core to rim of this tourmaline grain (Fig. 8.3B).

Substantial boron and oxygen isotopic variations (> up to 5 ‰) have been detected between core and rim in some tourmaline grains (e.g., Figs. 8.3C-D). A tourmaline grain from a patch in the Pieman Heads Granite comprises of a dark core and a grey massive zone overgrown by irregular bright rims (e.g., WT12WH04; Fig. 8.3C). The O-isotope values in the grain increase from +8.6 ‰ (massive tourmaline core) to +13.3 ‰ (bright selvage), whereas the B-isotope values increase from -10.3 to -1.1‰ (Fig. 8.3C). Distinctive growth zones have been identified in a tourmaline grain intergrown with quartz from a vein in the Pieman Heads Granite (i.e., WT12WH13-1-2; Fig. 8.3D). Measured B-isotopes vary between -7.6 and -4.6 ‰ in the Mn- and Al-rich tourmaline core, and increase from -6.2 to -1.6 ‰ across the Fe-rich inner rim to the Mg-rich outer rim (Fig. 8.3D). Measured O-isotopes have a restricted range from +10.8 to +11.5‰ in the Mn- and Al-rich core, but drop to +8.5 ‰ at the edge of the core (Fig. 8.3D). The $\delta^{18}O_{Tur}$ compositions increase to +11.9 ‰ on the inner rim, and then decrease from +7.3 to +6.5 ‰ on the outer rim (Fig. 8.3D).

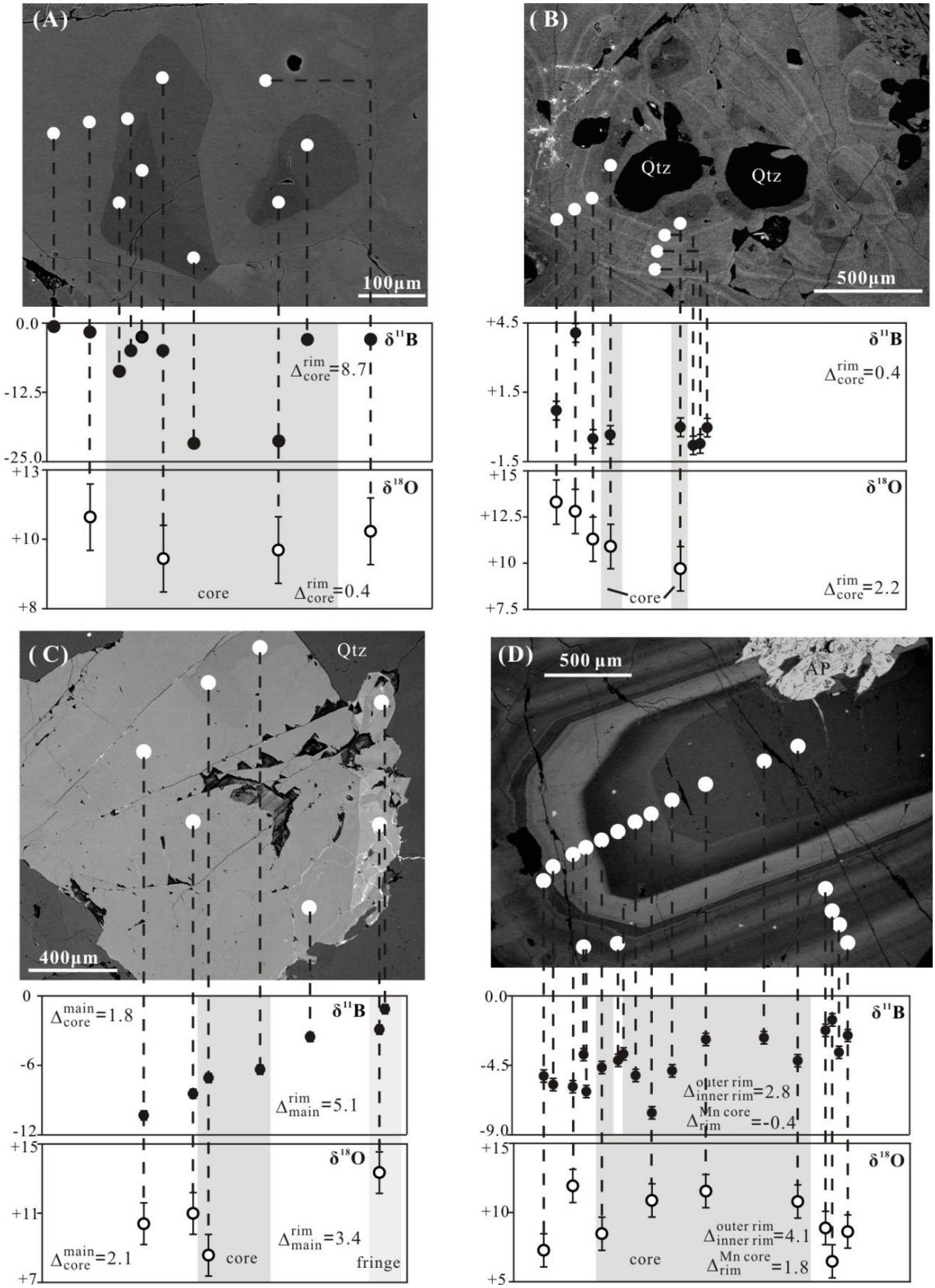

Figure 8.3 SIMS B- and O-isotope profiles plotted against their locations showing variations between different zonations of tourmaline from western Tasmanian granites. (A) Tourmaline patch (Samples WT12WH20) and (B) tourmaline cavity (Sample WT12WH24-3) from Trial Harbour, Heemskirk Batholith, (C) tourmaline patch (Sample WT12WH04) and (D) tourmaline vein (Sample WT12WH13-1-2) from Pieman Heads Granite.

Table 8.4 Strontium isotopes of tourmaline from the Heemskirk and Pieman Heads granites

Sample No.	Granite	Type	Age (Ma)	± 2σ	Rb (ppm)	Sr (ppm)	$^{87}Rb/^{86}Sr$	$^{87}Sr/^{86}Sr_m$	± 2σ	$^{87}Sr/^{86}Sr_i$
WT12WH07	Pieman Heads	Orbicule	366	4	0.91	8.38	0.32	0.751964	19	0.750317
WT12WH13	Pieman Heads	Vein	366	4	12.49	8.05	4.51	0.762240	17	0.738740
WT12WH20	TH, Heemskirk	Patch	364	7	18.78	1.89	29.21	0.870897	22	0.719525
WT12WH28	TH, Heemskirk	Orbicule	364	7	1.61	1.94	2.41	0.740361	26	0.727872
WT12WH24	TH, Heemskirk	Cavity	364	7	0.17	1.09	0.45	0.744964	21	0.742616
WT12WH23	TH, Heemskirk	Vein	364	7	29.69	7.85	11.04	0.801549	26	0.744338

Note: $^{87}Sr/^{86}Sr_m$ and $^{87}Sr/^{86}Sr_i$ represents measured and calculated initial strontium isotopes, respectively. TH = Trial Harbour.

8.3.4 Strontium isotopic results

The Sr isotopic compositions of tourmaline grains from tourmaline patches, orbicules, cavities and veins are tabulated in Table 8.4. The analysed tourmalines have very low Sr concentrations (1.09–8.4 ppm), variable Rb (0.17–29.7 ppm) and highly variable Rb/Sr (0.11–9.93). Six measured $^{87}Sr/^{86}Sr$ values of tourmaline separates range from 0.740361 to 0.870897 (Table 8.4). The initial $^{87}Sr/^{86}Sr$ compositions corrected to ages of the host granites (366 and 364 Ma), vary from 0.719525 to 0.750317. The highest $^{87}Sr/^{86}Sr$ value comes from a tourmaline orbicule from the Pieman Heads Granite, whereas a tourmaline patch within the Heemskirk Granite at Trial Harbour has the lowest value (Table 8.4).

8.4 Discussion

8.4.1 Boron and oxygen isotopic systematics in tourmaline

8.4.1.1 B-isotope fractionation and reservoirs

Boron isotopic compositions encompass an extensive range from -35 to +40 ‰ in geological environments (Fig. 8.4; van Hinsberg et al., 2011a). Boron isotopic data have potential to provide useful information that may reflect the geological processes of tourmaline formation, and could help to determine the sources of boron. The fractionation of boron isotopes can be affected by coordination between melts, waters, vapours, and minerals (Palmer and Swihart, 1996). Aqueous speciation can also influence boron fractionation. In aqueous solutions, boron can occur as trigonal and tetrahedral coordinated oxyanions, $B(OH)_3$ and $B(OH)_4^-$, respectively. Light boron (^{10}B) is preferentially incorporated into the tetrahedral species, whereas the heavy boron (^{11}B) tends to be absorbed into trigonal complex (Kakihana et al., 1977; Palmer and Swihart, 1996; Zeebe, 2005). Over the past three decades, the main factors that can affect the boron isotopic compositions of tourmalines have been determined to be (1) diversity of boron sources (e.g., fluid mixing), (2) isotopic fractionation induced by phase separation, (3) fluid/rock interaction, (4)

regional metamorphism, (5) prevailing temperature (and/or pH) conditions, and (6) secular variations in $\delta^{11}B$ of seawater (Palmer and Slack, 1989; Palmer et al., 1992; Chaussidon and Albarède, 1992; Barth,

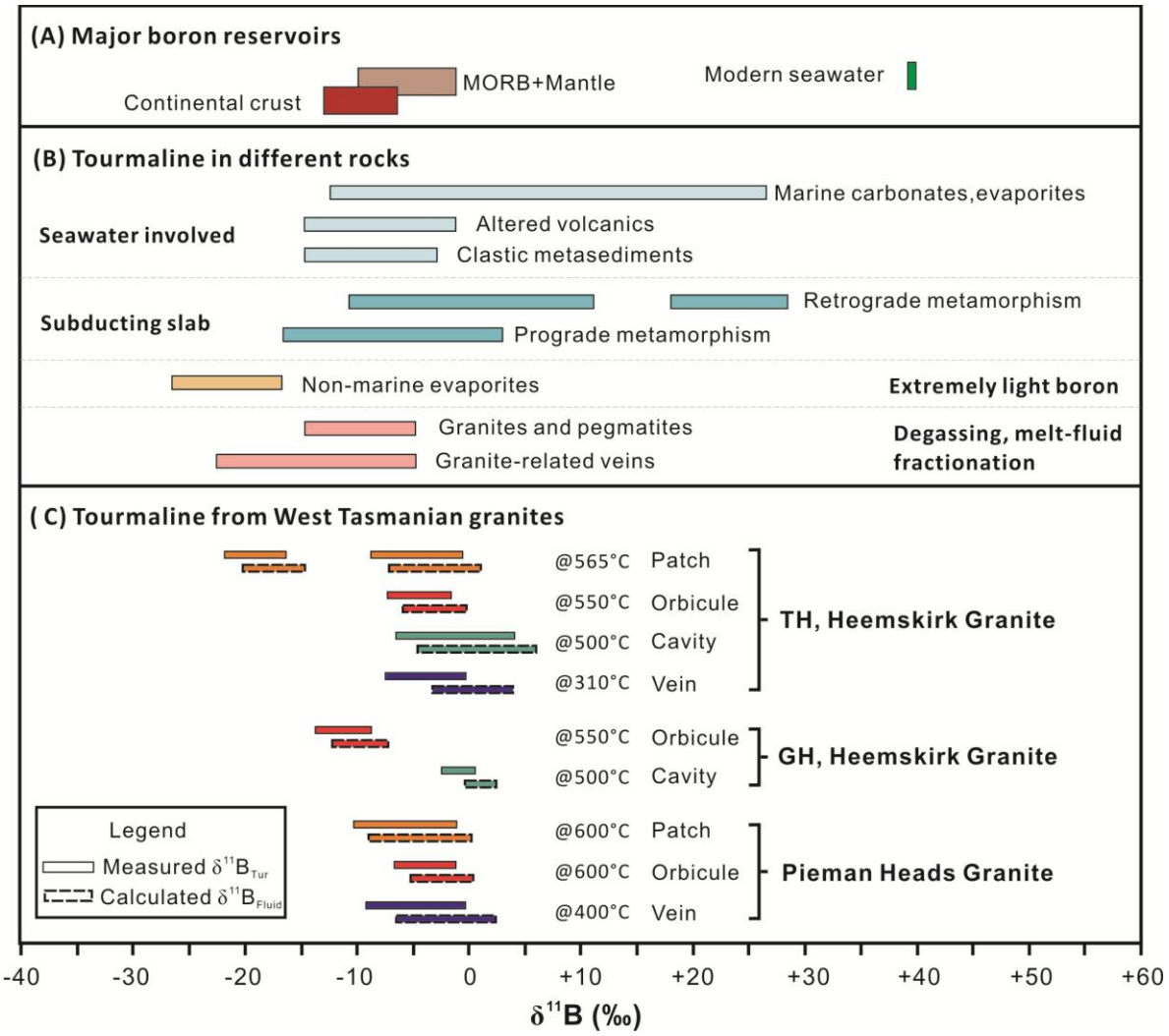

Figure 8.4 (A) Major boron reservoirs. (B) Ranges of boron isotopic compositions from different environment (Marschall and Jiang, 2011). (C) Comparison of measured and temperature-calibrated $\delta^{11}B$ compositions for tourmaline (Tur) and fluid, respectively; temperatures for each tourmaline-rich texture were estimated based on Ti-in-quartz geothermometry and microthermometric results of fluid inclusions from Table 8.3. $\delta^{11}B$ fluid values were calculated using the fractionation equation from Meyer et al. (2008). TH = Trial Harbour, GH = Granville Harbour.

1993; Slack et al., 1993; Smith and Yardley, 1996; Palmer and Swihart, 1996; Chaussidon and Appel, 1997; Jiang and Palmer, 1998; Herving et al., 2002; Marschall et al., 2006, 2008; Trumbull et al., 2008; Marschall and Jiang, 2011).

Tourmaline formed in different geological environments can have distinctive boron isotopic compositions (Fig. 8.4). $\delta^{11}B$ signatures of tourmaline from metamorphic rocks vary widely, typically between -22 and +22 ‰ (Swihart and Moore, 1989; Palmer and Slack, 1989; Chaussidon and Appel, 1997). Tourmaline related to non-marine evaporites have low $\delta^{11}B$ values (e.g., $\delta^{11}B$= -27 to -17 ‰ at Broken Hill; Palmer and Slack, 1989; Slack et al., 1993). Two of the most important boron isotope reservoirs are seawater and continental crust, with typical $\delta^{11}B$ values of +40 ‰ and -10 ± 3 ‰,

respectively (Marschall and Jiang, 2011; van Hinsberg et al., 2011a; Fig. 8.4).The $\delta^{11}B$ values of tourmaline from granites, pegmatites and associated hydrothermal veins mostly fall into the range of -22 to -5 ‰ (Swihart and Moore, 1989; Chaussidon and Albarède, 1992; Smith and Yardley, 1996; Jiang and Palmer, 1998; Trumbull et al., 2008). Tourmaline precipitated from subduction-related fluids has $\delta^{11}B$ values from -5 to +28 ‰, which overlaps with the $\delta^{11}B$ values of tourmaline associated with marine evaporites and carbonates (van Hinsberg et al., 2011a).

8.4.1.2 Boron sources

Boron isotopic compositions of tourmaline from western Tasmania mostly cluster between -14 and 0 ‰ (Fig. 8.4; Table 8.1). They largely overlap with the $\delta^{11}B$ range of granites-related tourmaline (-22 to -5 ‰; Jiang and Palmer, 1998; Marschall and Jiang, 2011; Fig. 8.4). The calculated $\delta^{11}B$ compositions for the fluids that precipitated tourmaline from western Tasmania mostly range from -12 to + 2 ‰, consistent with a magmatic origin derived from continental crust (-10 ± 3 ‰; Marschall and Jiang, 2011; Fig. 8.4). A few strongly depleted $\delta^{11}B_{Tur}$ values (-21.7 to -21.3 ‰) were obtained from a tourmaline grain in a tourmaline patch from the White phase of the Heemskirk Granite. Repeated analyses of the same growth zone yielded comparable values (-19 and -16.2 ‰) in the same repolished grain when analysed again on another day, showing that the results are within error for methodology (commonly < 2 ‰). The lower $\delta^{11}B_{Tur}$ values from the Heemskirk Granite are consistent with the range of tourmaline in granitic systems (Fig. 8.4). They could not have originated from a non-marine evaporite source (the major reservoir of ^{10}B; Marschall and Jiang, 2011), because there are no evaporites in western Tasmania (Corbett et al., 2014). This unusual tourmaline patch is suspected to have precipitated in a felsic melt that experienced more extreme B-isotopic fractionation compared to other tourmalines analysed.

Some boron isotopic analyses yielded positive $\delta^{11}B$ values for tourmaline crystals from miarolitic cavities and quartz-filled veins in the Heemskirk Granite ($\delta^{11}B_{Tur}$ = 0 to +4.1 ‰, $\delta^{11}B_{H2O}$ = 0 to +6.0 ‰; Fig. 8.4; Table 8.3). These results are the upper end of values for magmatic-hydrothermal fluids derived from adjacent granites (Fig. 8.4; Jiang and Palmer, 1998). Volatile exsolution during late stage granite crystallisation have drawn $\delta^{11}B$ compositions for tourmaline from cavities and quartz veins to positive values. However, the possibility remains that minor externally derived boron-rich fluids from the country rocks were involved in the formation of tourmaline-rich veins. The metasedimentary wall rocks (mainly quartzwacke turbidite or quartzite) are suspected to have elevated $\delta^{11}B$ values compared to the granites (Fig. 8.4). Fluid inclusions hosted in quartz from tourmaline veins have decreasing pattern of temperatures and salinities that are consistent with mixing (Fig. 7.7), and so the elevated $\delta^{11}B$ values could relate to meteoric waters entrapping a small component of ^{11}B from the wall rocks into the magmatic – hydrothermal system.

8.4.1.3 Oxygen sources

The O-isotopic compositions of tourmaline from the White phase of the Heemskirk Granite at Trial Harbour have a broader range ($\delta^{18}O_{Tur}$ = + 8.9 to + 14.9 ‰), and are on average slightly higher than those

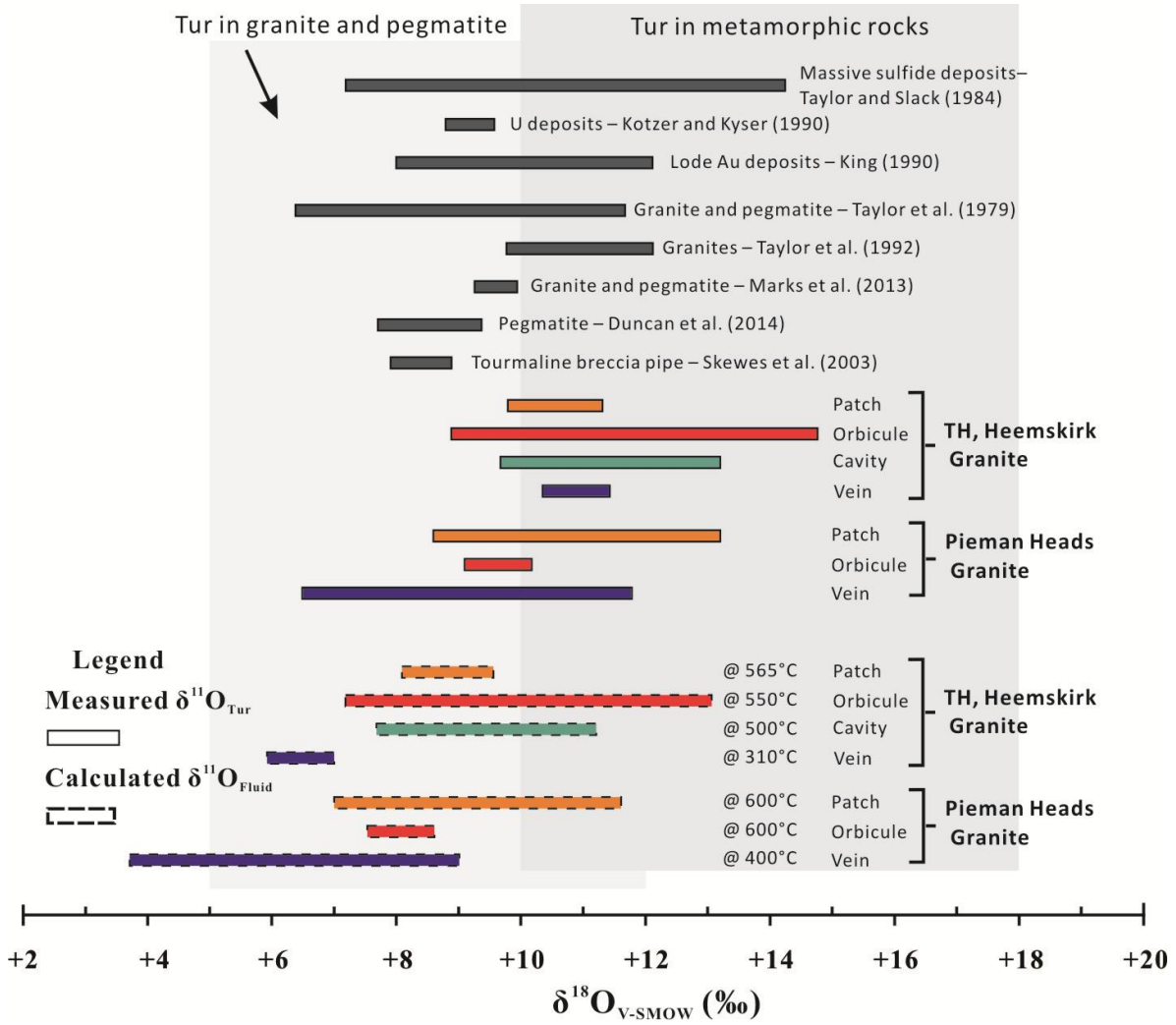

Figure 8.5 Oxygen isotopic compositions of tourmaline from different rocks, and O-isotopes for tourmaline (Tur) and calculated fluids from the Heemskirk Granite at Trial Harbour (TH), and Pieman Heads Granite. $\delta^{11}O$ fluid values were calculated using the equation from Kotzer et al. (1993).

of typical magmatic tourmaline in granites and pegmatites elsewhere (+9 to +12 ‰; Taylor et al., 1992; Jiang, 1998; Marks et al., 2013; Duncan et al., 2014; Fig. 8.5). They are lower than the O-isotopic values of metamorphic tourmaline from massive sulphide deposits (Taylor and Slack, 1984; Fig. 8.5). Similarly, quartz grains associated with tourmaline from the Heemskirk Granite have $\delta^{18}O_{Qtz}$ signatures of +7.2 to +16.1 ‰ (Fig. 8.2C), consistent with a magmatic – hydrothermal origin (e.g., Taylor, 1974). The calculated O-isotopic values for fluids related to tourmaline and quartz precipitation ($\delta^{18}O_{H2O}$ = +8 to +13‰; Table 8.3) are largely compatible with $\delta^{18}O$ values obtained from whole rocks of the White phase of the Heemskirk Granite (+10 to +11‰; Hajitaheri, 1985). Quartz and tourmaline are therefore interpreted to have precipitated from magmatic – hydrothermal fluids related to the Heemskirk Granite. The calculated $\delta^{18}O$ values for tourmaline in veins are lower ($\delta^{18}O_{H2O}$ = +5.9 to +7.0 ‰ at 310°C) than $\delta^{18}O$ values of whole rocks of host granite and country rocks (Hajitaheri, 1985). The tourmaline-quartz veins, which formed at lower temperatures, are predominantly magmatic – hydrothermal but have been mixed with small volumes of a non-magmatic low $\delta^{18}O$ fluid (e.g., meteoric water).

Compared to the White phase of the Heemskirk Granite, O-isotope signatures of tourmaline and quartz from the Pieman Heads Granite have a restricted range ($\delta^{18}O_{Tur}$ = + 6.5 to +13.3 ‰; $\delta^{18}O_{H2O}$ = + 3.6 to +11.7 ‰; Table 8.3). Although no O-isotopic composition has been defined for the Pieman Heads Granite, the range of calculated $\delta^{18}O$ values for fluids largely overlap with the O-isotope values of typical granitic rocks (+6 to +10 ‰; Taylor, 1978). This implies that the fluids responsible for tourmaline-quartz assemblages at Pieman Heads are mainly of magmatic origin. The O-isotopes for tourmaline veins in the Pieman Heads Granite ($\delta^{18}O_{H2O}$ = +7.3 to +9.0 ‰) are higher than those in the Heemskirk Granite (Fig. 8.5; Table 8.3), implying little or no involvement of meteoric water at Pieman Heads.

8.4.2 Isotopic fractionation by tourmaline growth

Rhythmic growth zones in tourmaline crystals can form due to variations in pressure, temperature and host rock chemistry. They result from the variations of growth surface morphology and charge, which allow for preferential incorporation of specific elements (Henry et al., 1999; van Hinsberg et al., 2006; van Hinsberg and Marschall, 2007). Growth (or sector) zones not only cause major and trace element variations, but also isotopic discrepancies. Isotopic partitioning between crystal and fluid (or melt) can give rise to boron isotopic variations, since the coordination of boron from trigonal to tetrahedral in various medium can significantly affect boron isotope fractionation (Palmer and Swihart, 1996; Sanchez-Valle et al., 2005; Meyer et al., 2008). B^{11} when coordinated as $B(OH)_3$ will selectively partition into fluids; in contrast, B^{11} when coordinated as $B(OH)_4^-$ will partition into minerals (Palmer and Swihart, 1996; Meyer et al., 2008). Dipolar surface charge may adsorb the negatively charged $B(OH)_4^-$ ligand to the c-sector (core) plane compared to the neutral a-sector rim (van Hinsberg and Marschall, 2007). The a-sector appears to preferentially take up ^{11}B and ^{18}O from fluids relative to the central c-sector, which could explain the observed increasing trend of boron and oxygen isotopes from core to rim within individual tourmaline grains (e.g., Figs. 8.3A-B).

Boron and oxygen isotopic fractionation between tourmaline and fluid are generally less than 3 ‰ at temperatures of 400 ° to 600 ℃ (Meyer et al., 2008; Kotzer et al., 1993). They cannot account for the substantial isotopic variations (up to 5 ‰) between core and rim detected in tourmaline grains in the current study (e.g., Figs. 8.3C-D). Abrupt variations of $\delta^{11}B_{Tur}$ and $\delta^{18}O_{Tur}$ compositions between different tourmaline growth zones coincide with distinctive textural and compositional differences across individual zones (Figs. 8.3C-D). The distinct and coincident isotopic and compositional variations between growth zones are interpreted to be due to processes such as phase separation or fluid mixing (cf. Marschall et al., 2008; Pal et al., 2010).

8.4.3 Isotopic fractionation due to volatile exsolution

Both the boron and oxygen isotopic compositions of tourmalines have increasing trends from tourmaline patches to orbicules, and/or to cavities, and veins in the Heemskirk and Pieman Heads granites (Figs.8.1, 8.2). These variations of $\delta^{11}B$ and $\delta^{18}O$ signatures are interpreted to be products of magmatic – hydrothermal volatile exsolution during the late crystallisation stage of the western Tasmanian granites.

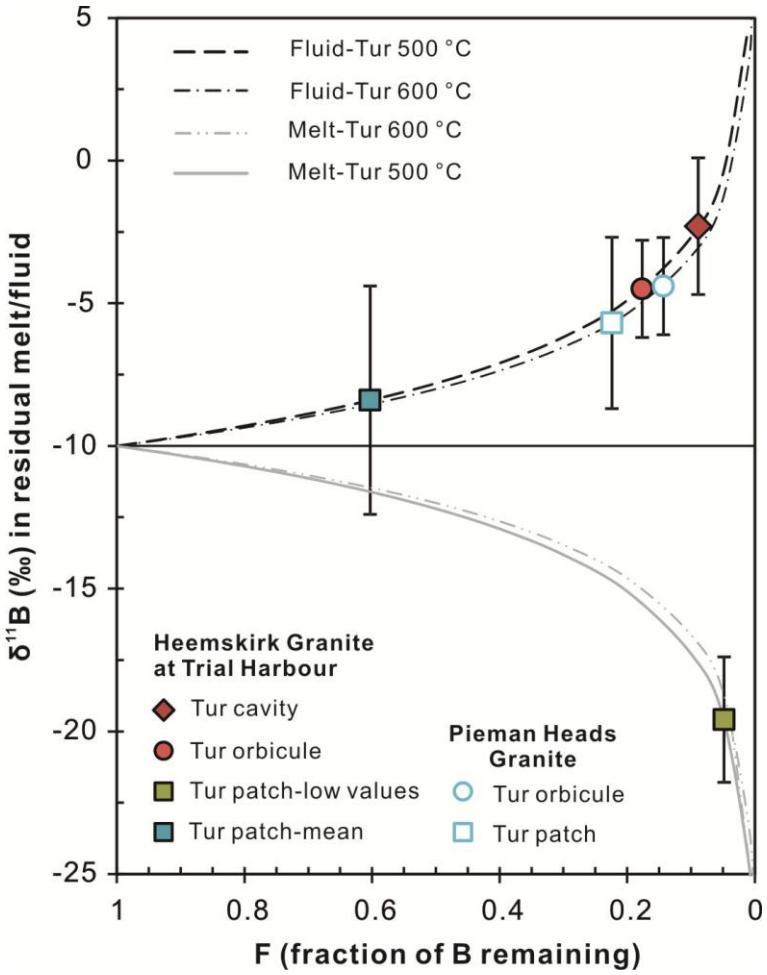

Figure 8.6 Rayleigh fractionation modelling of boron isotopes between melt/fluid and tourmaline for samples from the Heemskirk and Pieman Heads granites. A mean $\delta^{11}B$ composition of -10 ‰ for granites (Marschall and Jiang, 2011) is taken as the starting compositions. The temperatures of 500 °and 600 ℃ are assumed based on Ti-in-quartz geothermometry and microthermometry. The mean boron compositions of tourmaline-rich features are marked on the respective curves. The low boron composition of the tourmaline patch is calculated based on the isotopically lightest values analysed from the Heemskirk Granite (Table 8.1).

The relative sequence of ^{11}B fractionation in different phases is vapour > fluid > tourmaline > melt (Palmer et al., 1992; Barth, 1993; Herving et al., 2002; Meyer et al., 2008). Assuming an equivalent proportion of trigonal and tetrahedral boron in the melt (Kaliwoda et al., 2011; Trumbull et al., 2013), the combined fractionation factors between tourmaline and melt are calculated to be 2.91 ‰ at 600°C, and 3.2 ‰ at 500°C (Hervig et al., 2002; Meyer et al., 2008). The $\delta^{18}O$ compositions did not achieve equilibrium between quartz and tourmaline for the western Tasmanian granites, because negative oxygen isotopic fractionation values were commonly obtained (ΔQtz-Tur; Table 8.2). ^{18}O should preferentially partition into quartz rather than tourmaline under equilibrium conditions (Zheng, 1993; Kotzer et al., 1993). Nevertheless, Rayleigh fractionation can still be used to model the boron isotopic variations among the tourmaline-rich associations from the two western Tasmanian granites (Fig.8.6).

Peraluminous, volatile-rich (e.g., H_2O, B, F) S-type granitic magmas can be produced through anatexis and/or partial melting of pre-existing metapelitic rocks (London et al., 1996; Trumbull et al., 2008; Pesquera et al., 2013). With progressive fractional crystallisation of this type of felsic magmas, an immiscible B-Fe-Na-rich hydrous liquid has been shown experimentally to separate from the aluminosilicate-rich melt (Veksler et al., 2002; Veksler and Thomas, 2002; Veksler, 2004). The B-rich aqueous phase can ascend buoyantly as a bubble-laden plume (Candela, 1997) interstitially between grain boundaries within the siliceous melt due to the lower viscosity density of the volatiles (Dingwell et al.,

1996). For these western Tasmanian granites, ^{11}B and ^{18}O would have partitioned preferentially into the hydrous boron-bearing volatile fluids compared to the felsic melt enriched in ^{10}B and ^{16}O (cf. Kotzer et al., 1993; Herving et al., 2002; Meyer et al., 2008). This may have required approximately 60 % boron removal from the initial granitic melt ($\delta^{11}B \approx$ -10 ‰) to produce the tourmaline patches with an average $\delta^{11}B_{Tur}$ of –8.4 ‰ in the Heemskirk Granite, or ca.77 % boron removal for the tourmaline patches with an average $\delta^{11}B_{Tur}$ of –5.7 ‰ in the Pieman Heads Granite (Fig. 8.6). In contrast, the tourmaline patches with $\delta^{11}B_{Tur}$ values as low as –20 ‰ (Fig. 8.1) might have precipitated from a residual melt after approximately 95% of the boron had been removed from the initial melt (Fig. 8.6).

Continuous fractional crystallisation of granitic magmas can lead to abundant B-rich aqueous volatiles to coalesce and grow larger, advecting as spanning clusters (Candela, 1991), so that they can ascend to the shallow crust (4 -5 km). Various components, including Al, Mg, Fe, and Na etc., may adhere into the aqueous volatiles due to capillary forces. The hypersaline fluids were locally trapped together as pockets in the granitic melts (Shinohara and Kazahaya, 1995). The $\delta^{11}B_{Tur}$ and $\delta^{18}O_{Tur}$ compositions of tourmaline from orbicules and/or in the Heemskirk and Pieman Heads granites cavities are higher than those from tourmaline patches (Fig. 8.1; Table 8.1). Approximate 80 to 85 % boron removal would permit formation of the tourmaline orbicules with average $\delta^{11}B_{Tur}$ values of -4.5 ‰ (Fig. 8.6).

Miarolitic cavities in granitic rocks are generally considered to be products of magmatic (volatile-) fluid saturation (Candela and Blevin, 1995; Candela, 1997; Harris et al., 2004). The shift of $\delta^{11}B_{Tur}$ values from –10 ‰ to –2.3 ‰ for tourmaline-filled in miarolitic textures could have resulted from approximately 90 % boron separating from the initial melt at temperatures of 500 ° to 600 ℃ (Fig. 8.6). The results of Rayleigh isotopic fractionation modelling are consistent with the hypothesis that tourmaline-quartz orbicules and cavities precipitated at a later stage of boron-rich volatile exsolution than the tourmaline patches in the Heemskirk and Pieman Heads granites.

The boron and oxygen isotopic compositions of tourmaline in quartz veins from the Heemskirk batholith and the Pieman Heads Granite largely overlap with the $\delta^{11}B_{Tur}$ and $\delta^{18}O_{Tur}$ signatures of tourmaline from the orbicules and miarolitic cavities (Figs. 8.4, 8.5). However, the isotopic variations of tourmaline and quartz in veins cannot be simply modelled via Rayleigh fractionation. Since the tourmaline veins precipitated in sheeted brittle fractures that formed after the granites had crystallised, and also after the tourmaline orbicules and cavities, minor external sources (e.g., meteoric water, boron-bearing fluids from the country rocks) could have been incorporated into the tourmaline quartz veins, consistent with the observed fluid inclusion and isotopic variations (Figs. 7.7, 8.5).

8.4.4 Strontium isotopic variations

The unusually low Sr contents in tourmaline from the Heemskirk and Pieman Heads granites (Table 8.4) may relate to tourmaline precipitation from highly differentiated, Sr-poor melts. The Sr isotopic values for the four different tourmaline textures from the White Heemskirk Granite are lower than that of whole-rock values for the Red phase of the Heemskirk Granite ($^{87}Sr/^{86}Sr$ = 0.71142, corrected for 360 Ma; Black et al., 2010). The whole-rock $^{87}Sr/^{86}Sr$ ratio of the White phase of the Heemskirk Granite ($^{87}Sr/^{86}Sr$ =

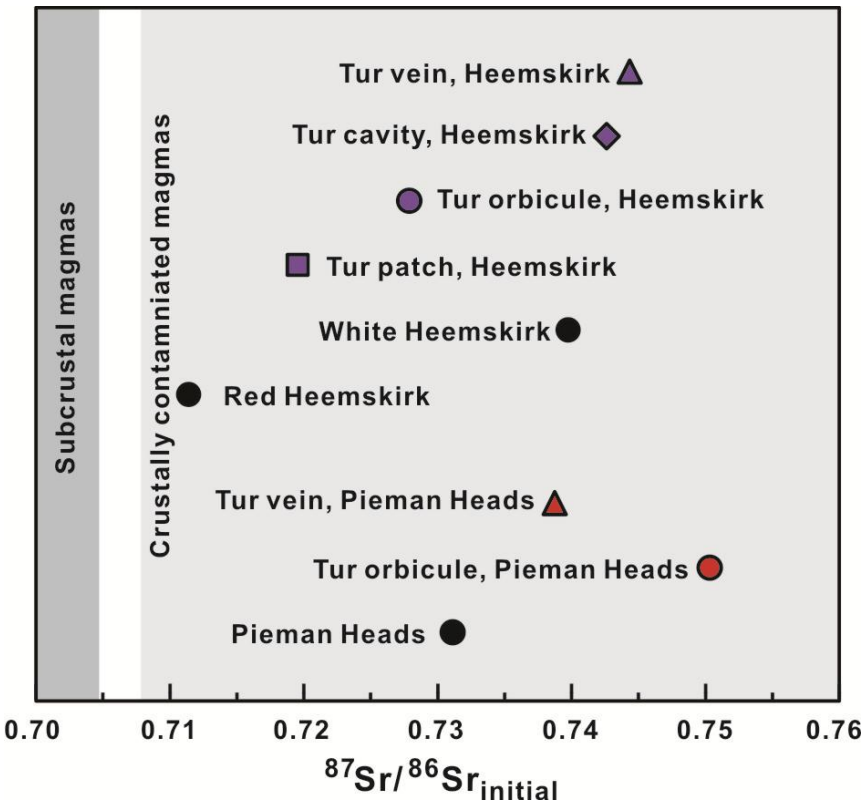

Figure 8.7 Strontium isotopic compositions of tourmaline (Tur) and whole-rocks from the Heemskirk and Pieman Heads granites. Whole-rock Sr isotopic data for of Heemskirk and Pieman Heads granites from Black et al. (2010) and Maas (unpublished data). $^{87}Sr/86^{Sr}$ ratios corrected to their U-Pb ages.

0.73974, corrected for 361 Ma; Black et al., 2010) overlaps with these tourmaline Sr isotopic values (Fig. 8.7). Similarly, Sr isotopes of tourmaline orbicule and vein from the Pieman Heads Granite are higher than that of their granitic host ($^{87}Sr/^{86}Sr$ = 0.731125, corrected for 366 Ma; Camacho and Maas, unpublished data; Fig. 8.7). All of these Sr isotopic results are much higher than the $^{87}Sr/^{86}Sr$ signature of sub-crustal magmas ($^{87}Sr/^{86}Sr < 0.7045$; DePaolo and Wasserburg, 1979), implying that the parental magmas for the tourmalines and granites might be contributed by a minor mantle source but were strongly contaminated by continental crust. Some metasedimentary rocks from western Tasmania, e.g., Upper Oonah Formation (0.76152 at 380 Ma) and Badger Head Group (0.78095 at 380 Ma; Black et al., 2010), have $^{87}Sr/^{86}Sr$ compositions higher than but close to those of the tourmaline and granites, and are most likely candidates for crustal components that were partially assimilated into the felsic magmas related to the tourmaline-rich features documented here.

A gradual increasing pattern in Sr isotopic values was detected paragenetically from tourmaline patches, orbicules, and cavities, to veins in the Heemskirk Granite (Fig. 8.7). Boron-rich magmatic – hydrothermal fluids exsolved from the fractionated granitic magmas were mixed with an increasing component of formation waters derived from the adjacent metasedimentary rocks (cf. Williamson et al., 2000), possibly leading to sequential precipitation of tourmaline patches, orbicules, cavities and veins that were progressively enriched in more radiogenic Sr isotopes. However, it shoud be noted that this interpretation is problematic due to the limited dataset of Sr compositions of tourmaline.

The opposite Sr isotopic pattern was discerned for tourmaline orbicules and veins from the Pieman Heads Granite – the tourmaline orbicules have higher $^{87}Sr/^{86}Sr$ ratios than the tourmaline veins (Fig. 8.7). This variation could relate to impurities of muscovite and/or alkali feldspar inclusions that have

contaminated the tourmaline separates, as indicated by lower Rb and Rb/Sr ratio of the tourmaline orbicule analysed than from their counterparts from the Heemskirk Granite (Table 8.4).

8.5 Conclusions

Boron and oxygen isotopic compositions of tourmaline and/or quartz from the western Tasmanian granites indicate that tourmaline-rich assemblages formed from magmatic – hydrothermal fluids sourced locally from their host intrusions. Strontium isotopic values of tourmaline reveal that these granitic magmas have been heavily contaminated by crustal components. Minor external components of boron and oxygen may have been drawn into the tourmaline-rich quartz veins, causing their isotopic compositions and salinities to deviate slightly from the typical ranges of magmatic – hydrothermal fluids (Figs. 7.7, 8.5).

A number of gradually increasing values of boron and oxygen isotopes from core to rim in individual tourmaline grains (generally < 2 ‰) are related to sector zoning during tourmaline crystallisation. The different paragenetic stages of tourmaline were precipitated from fluids that had isotopic variations more than 5 ‰.

Both B- and O-isotopic compositions of tourmaline increase sequentially from patches to orbicules and cavities in the Heemskirk and Pieman Heads granites. These isotopic variations among various tourmaline-rich textures were caused by magmatic – hydrothermal volatile exsolution during the final crystallisation stages of the granite intrusions. Volatile-rich hypersaline fluids separated from the crystallising aluminosilicate magmas due to liquid immiscibility, ascending and coalescing between grain boundaries of the crystallising melts in terms of tube plume or spanning clusters (Candela, 1991). Rayleigh fractionation modelling indicates that approximately 60 % to 77 % boron was removed from the initial felsic melt to produce tourmaline patches, whereas higher degrees of fractionation of the initial granitic melt (up to 90 %) led to exsolution of boron-rich hyperosaline fluids from which the tourmaline orbicules and miarolitic cavities precipitated (Fig. 8.6). This interpretation is consistent with the increasing Sr isotopic signatures of tourmalines from patches, orbicules, and cavities to veins (Fig. 8.7), possible implying an increasing volume of formation waters mixed with boron-rich magmatic – hydrothermal fluids from the parental felsic magmas.

Chapter 9 Synthesis and conclusions

9.1 Introduction

This chapter presents models for the geodynamic evolution of Tasmanian granites and for the formation of tourmaline-rich magmatic – hydrothermal features in two granites from western Tasmania. The geodynamic model is partly based on previous studies (e.g., Black et al., 2005, 2010), and integrates geological, geochemical, geochronological and radiogenic isotopic data for mid-Palaeozoic granites across Tasmania. The model for magmatic – hydrothermal processes is based on geological mapping, whole-rock geochemistry, mineral geochemistry (e.g., tourmaline, quartz), fluid inclusion microthermometry and stable isotopic data from the Heemskirk and Pieman Heads granites. Interpretation of the geological and geochemical controls on Sn-(W-Pb-Zn) mineralisation associated with Tasmanian granites is followed by recommendations for future work.

9.2 Geodynamic model

The Devonian-Carboniferous granite provinces in Tasmania belong to part of an enormous mid-Palaeozoic granite belt that formed along the easternmost margin of the Gondwana supercontinent (Fig. 9.1a; Gray, 1997; Foster et al., 2009). This belt records extensive Palaeozoic magmatic activity over a strike length of more than 3000 km, from the central portions of the Lachlan Orogen in southeastern Australia, to eastern and western Tasmania, the Western Province of the South Island of New Zealand, and to North Victoria Land and Marie Byrd Land in West Antarctica (Fig. 9.1a; Muir et al., 1994, 1996; Pankhurst et al., 1998; Keay et al., 1999; Wombacher and Münker et al., 2000; Kemp et al., 2005; Black et al., 2005, 2010; Collins and Richards, 2008; Tulloch et al., 2009; Cayley, 2011; Fergusson, 2014; Moresi et al., 2014; Yakymchuk et al., 2015; Turnbull et al., 2016). Because Tasmania lies between mainland Australia, Antarctica and New Zealand, understanding the geodynamic evolution of Tasmanian granites is essential for correlating magmatic events from the Silurian to Early Carboniferous across eastern Gondwana. Drawing on previous work (e.g., Black et al., 2005, 2010) and the results of the current study, a geodynamic model describing the evolution of Tasmanian granites is depicted in Figure 9.1.

Black et al. (2010) favoured a three-component mixing model for Tasmanian granites, including mantle-derived basaltic magmas, Neoproterozoic–Cambrian meta-igneous rocks in the lower-middle crust and Ordovician upper-crustal sedimentary rocks (Collins, 1996, 1998; Keay et al., 1997). Their model suggested that the compositional and isotopic variations between Tasmanian granites, particularly the eastern Tasmanian granites, are mostly due to these three components mixing in differing proportions, and the resultant magmas experiencing various extents of crystal fractionation (Black et al., 2010). Radiogenic isotopes from the current study and Black et al. (2010) imply that Sn-mineralised granites in Tasmania were produced by partial melting of mafic meta-igneous rocks (e.g., amphibolites) combined with

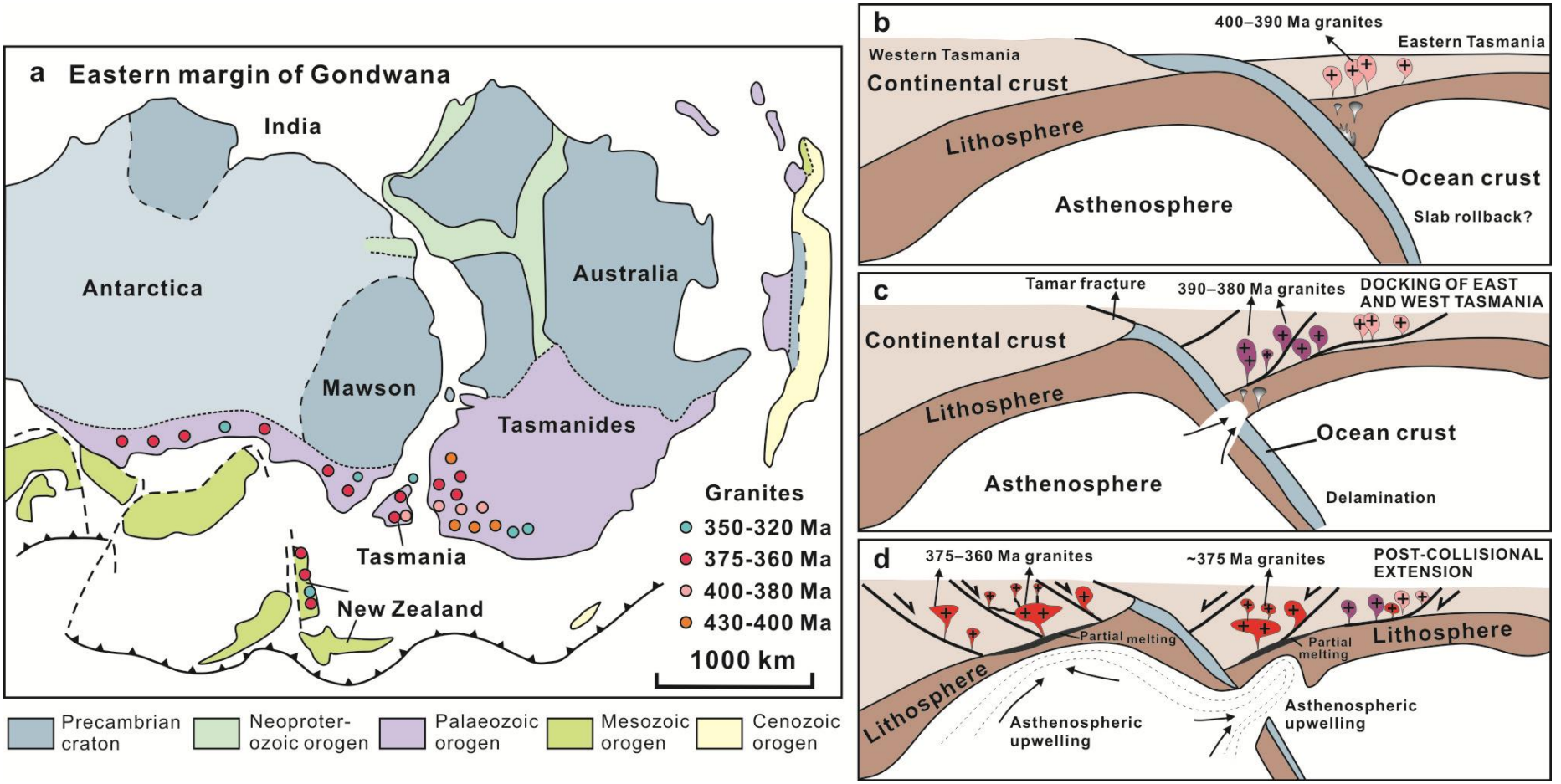

Figure 9.1 (a) Tectonic reconstruction of mid-Palaeozoic granite provinces in Tasmania and adjacent regions along the eastern margin of Gondwana (modified from Foster et al., 2009). Granite ages are compiled from Keay et al. (1999), Kemp et al. (2005), Fergusson (2014), Black et al. (2005), Kositcin and Everard (2013), Muir et al. (1994), Tulloch et al. (2009), Turnbull et al. (2016), Yakymchuk et al. (2015) and this study. (b–d) Simplified cartoons showing geodynamic evolution of Tasmanian granites (modified from Black et al., 2010). (b) 400–390 Ma granodiorites emplaced when eastern Tasmania subducted towards the western Tasmania. (c) Weakly fractionated 390-380 Ma granites intruded the eastern Tasmania during amalgamation of the two Tasmanian terraces. (d) Moderately to strongly fractionated 375–360 Ma granites emplaced into both western and eastern Tasmania in a post-collisional extension setting.

assimilation of abundant upper-crust sedimentary rocks (e.g., the Mathinna Supergroup or Oonah Formation). The Pb isotopic compositions of western Tasmanian granites do not, however, perfectly match their potential source rocks. Mantle-derived basaltic magmas may have mostly provided heat to melt the overlying rocks, rather than being a significant magmatic source. This conclusion is consistent with the argument that Phanerozoic granites genetically related to Sn mineralisation worldwide mostly originate from the melting of crustal rocks (e.g., Lehmann, 1982; Sato, 2012; Mao et al., 2013; Romer and Kroner, 2016).

The 400 Ma I-type granodiorites (including the George River) in northeastern Tasmania are mineralogically and chemically similar to those formed at subduction zones (cf. Barbarin, 1999). They are considered to have been generated above a west-dipping Palaeozoic subduction zone located east of the Australian portion of the active Gondwanan margin (Black et al., 2010; Cayley, 2011; Fig. 9.1a). Mafic basaltic magmas contaminated by abundant Ordovician turbidites and possible Proterozoic lower-crust components produced minor coeval S-type granites (e.g., the Grant Point Granite). Black et al. (2010) argued that slab rollback to the west allowed the continuation of I-type magmatism, producing the Blue Tier and Scottsdale Batholiths, and their extrusive correlates (e.g., St. Marys Porphyry), until 390 Ma (Fig. 9.1b).

The docking and collision of East and West Tasmanian terranes defined the Tabberabberan Orogeny in Tasmania (ca. 390 Ma; Black et al., 2005). Large amounts of I- and S-type monzogranites were produced when delamination allowed mantle-derived magmas to intrude the lower and upper crust, assimilating the Mathinna Supergroup turbidites (and Proterozoic lower-crust material?) in varying proportions. Syn-collisional granites were emplaced widely in eastern Tasmania from 390–385 Ma (Fig. 9.1c). Post-collisional slab breakoff may have triggered asthenospheric mantle upwelling, leading to lithospheric underplating by mafic magmas (cf. Crawford et al., 2003; Collins and Richards, 2008; Black et al., 2010; Fig. 9.1d). Eastern Tasmania probably evolved to an extensional regime around 375 Ma (e.g., Cayley, 2011; Moresi et al., 2014; Fig. 9.1d). The heat flow from lithospheric underplating resulted in different degrees of partial melting of Ordovician turbidites, generating the peraluminous S-type granites sporadical in eastern Tasmania (378–374 Ma), including the stanniferous Lottah, Mt Paris and Ben Lomond granites. Similar tectonic scenarios (slab rollback, delamination and asthenospheric upwelling in a backarc extensional setting) may have coevally occurred in neighbouring districts of eastern Gondwana margin, including the Melbourne Zone of Lachlan Orogen (Bierlein et al., 2001), the West Province of New Zealand (Tulloch et al., 2009; Turnbull et al., 2016), and the Marie Byrd Land of Antarctica (Yakymchuk et al., 2015).

The mineralogical and chemical compositions of western Tasmanian granites are comparable to those occurring in a within-plate setting (e.g., Barbarin, 1999). The upwelling of asthenospheric mantle may have been coeval in the East and West Tasmanian terranes, due to lithospheric delamination following crustal thickening after the Tabberabberan Orogeny (Black et al., 2010; Fig. 9.1d). During crust-mantle interaction, mafic magmas may have contributed sufficient heat to partially melt the overlying lower-crustal Proterozoic amphibolites, and to assimilate considerable amounts of upper-crustal sedimentary

rocks. These components mixed to different degrees in individual magma chambers, and may have experienced protracted stagnation and crystallisation prior to producing felsic, metaluminous I-type and peraluminous S-type granites from 374 to 360 Ma, including the Sn–W mineralised Housetop, Meredith, Pine Hill and Heemskirk granites (Fig. 9.1d). The granitic batholiths in northwestern Tasmania (Fig. 2.3) define distribution patterns similar to regional magmatism caused by lithospheric delamination (cf. Mahéo et al., 2009).

9.3 Genesis of magmatic – hydrothermal features

Distinctive magmatic – hydrothermal textural features, including unidirectional solidification textures, tourmaline patches, tourmaline orbicules, tourmaline cavities and tourmaline veins, together with cassiterite-Pb-Zn sulphide veins, have been developed in discrete layers of the Heemskirk and Pieman Heads granites of western Tasmania (Figs. 4.1, 6.1). Field mapping, mineral chemistry, fluid inclusion microthermometry and stable isotopic data have provided insights into the formation of these magmatic – hydrothermal features (Fig. 9.2).

When hydrous granitic magmas are emplaced into the shallow crust, a volatile-rich aqueous phase can exsolve from the crystallising melt due to phase separation (Burnham, 1979; Burnham and Ohmoto, 1980). For the western Tasmanian tin granites, a B-Fe-Na-rich aqueous phase separated from the initial aluminosilicate-rich and water-rich S-type melts (e.g., Veksler and Thomas 2002; Veksler 2004). Continuous decompression during crystallisation of the hydrous magmas gave rise to a spanning cluster of

Figure 9.2 (next page) Schematic genetic model showing the formation of magmatic – hydrothermal tourmaline- and quartz-rich features in western Tasmanian granites. (a) When S-type magmas emplaced into the shallow crust, spanning clusters of volatile bubbles (enriched in B, Fe, Na etc.) can ascend and accumulate in the roof of the crystallising granite, due to continuous decompression and crystallisation (Candela, 1991; Veksler, 2004): (a-i) buoyant boron-rich aqueous bubbles migrated upwards between grain boundaries as bubble-laden plumes at low degrees of crystallisation (Candela, 1991); (a-ii) at high degrees of crystallisation, the boron-rich bubbles are likely to be trapped into pockets of peripheral magma, because capillary forces can cause abundant water and volatiles adhering to the crystal mush of alumino-siliceous components (Shinohara and Kazahaya, 1995). (b) Quartz-rich unidirectional solidification textures precipitation in the crystallised carapace of the White phase of the Heemskirk Granite at temperatures of 600 ℃ and pressure 1.3 kbars: (b-i) bubbles of volatiles accumulated in the roof and quartz grew downwards as USTs, with minor magnetite, tourmaline, feldspar and biotite; (b-ii) when vapour pressure exceeded the lithostatic pressure, brittle fracturing occurred, resulting in the release of aqueous fluids into overlying cupolas and the next cycles of growth of UST and intercalated aplite. (c) Continuous decompression and crystallisation caused the precipitation of tourmaline patches and orbicules in the White phase of Heemskirk and Pieman Heads granites at temperatures of 600 °–550 ℃ and pressure 1.3 kbars: (c-i) the boron-rich bubbles interstitial to igneous crystals crystallised to be disseminated tourmaline patches when 60-77 % of the boron removed from the granitic melt; (c-ii) the spherical tourmaline orbicules and cavities in upper layers of the granites are remnants of large boron-rich volatile bubbles after ca. 80 to 90 % depletion of the boron of the initial granitic melts. (d) At the final stage of granite emplacement, boron-rich aqueous fluids migrated upwards along the brittle fractures and hydrothermally altered the host rocks, probably mixed with minor meteoric water, forming widespread tourmaline-quartz veins at temperature 300 °–330 ℃ and pressure 0.1 kbar; locally, these tourmaline-quartz veins host cassiterite ores in the Heemskirk Granite. (e) As the Heemskirk Granite experienced degrees of erosion or uplift, magmatic – hydrothermal fluids derived from the intrusion that were mixed with external waters precipitated fluorite-quartz Pb-Zn veins at temperature 280 ℃ and pressure 0.08 kbar, locally overprinting the cassiterite-tourmaline-quartz veins.

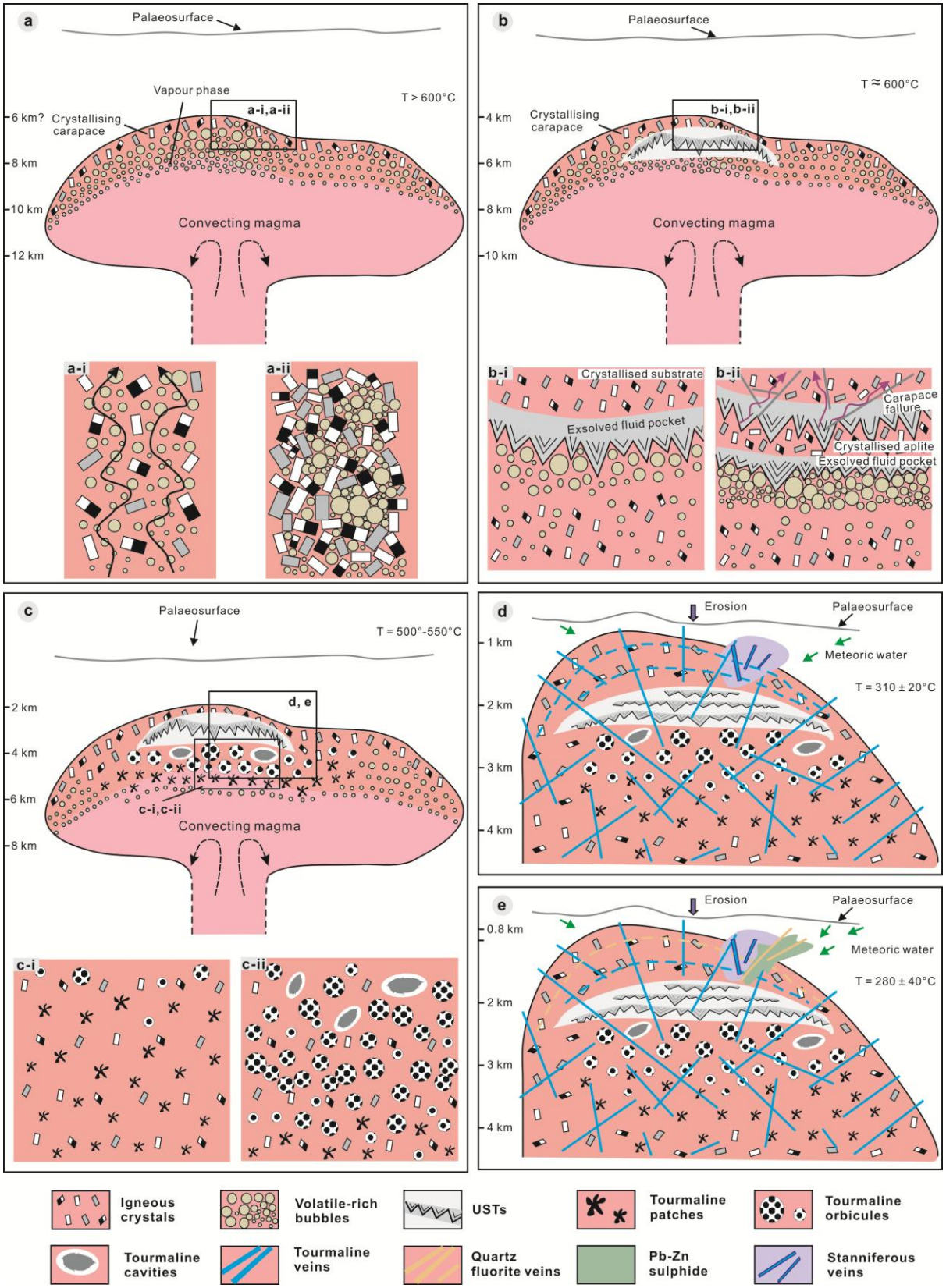

bubbles of volatiles (Burnham, 1979; Burnham and Ohmoto, 1980; Candela, 1991; Fig. 9.2a). Boron-rich buoyant bubbles were released from the crystallising hydrous melt phase at low degrees of crystallisation, and were transported upwards between grain boundaries in the manner of bubble-laden plumes or tubules

(Candela, 1991, 1997; Fig. 9.2a-i). As magma crystallisation proceeded and the viscosity increased, small bubbles may have coalesced to form tube flows during their journey to the apical regions. They would have crystallised as miarolitic cavities whereas volatile abundances were too low to form a spanning cluster of bubbles (Candela, 1991). When the volatile supply diminished, the bubble-laden plume ultimately collapsed, producing irregular patches coexisting with coarse-grained igneous crystals (Fig. 9.2c-i).

At high degrees of crystallisation, volatile bubbles were more likely to be trapped into pockets of peripheral magma, because capillary forces can make abundant water and volatiles adhere to the crystal mush of alumino-siliceous components (Shinohara and Kazahaya, 1995; Harris et al., 2004). These buoyant bubbles may gradually percolate upwards through a crystal mush. At higher degrees of magmas crystallisation, the bubbles can coalesce and grow larger, until they overcome the capillary force, typically developing spherical or elliptical shapes in order to minimise surface energy (Fig. 9.2a-ii). When the magma cooled down, large stagnant bubbles that contain significant alumino-siliceous elements would not collapse, unlike the small bubbles interstitial to grain boundaries, but instead the large bubbles would be trapped separately as spherical, subround or ellipsoidal bodies in the felsic intrusions (Fig. 9.2c-ii). Diffusion of fluids from the bubbles into the surrounding granite during crystallisation could have produced the altered rims commonly observed around most of the tourmaline orbicules and cavities (e.g., Figs. 4.3and 9b-d).

The bubble-laden plume theory (Candela 1991) can explain the transport of a buoyant Fe (Mg)-Na-(Al)-rich brine and B-rich vapour exsolved from a granitic melt. Petrographic observations have shown that primary salt-bearing fluid inclusions coexist with liquid-rich fluid inclusions in quartz from the tourmaline orbicules (Fig. 7.2). A hypersaline fluid exsolved from a granitic melt has the potential to transport significant concentrations of Fe, Mg and Na. Furthermore, Al can be highly soluble if the brine is acidic (e.g., Seedorff et al., 2005). Incompatible boron will have been transported preferentially in vapour bubbles, as the Fe-Na-rich brine and coexisting vapour ascended to the cupolas of the intrusion.

The aqueous bubbles of volatiles would ascend and accumulate in the roof zones of the magma chamber, along which initial comb quartz layers precipitated (Fig. 9.2b). These crenulated UST layers contain abundant quartz, and minor K-feldspar, plagioclase, biotite, magnetite and tourmaline (Fig. 4.7). The UST quartz grains are commonly enriched in Al, Na, K, Fe, and Mn relative to other types of quartz (e.g., Fig. 6.7; Table 6.3). As the magma progressively crystallised, a large amount of volatiles could be concentrated in the cupolas, increasing the volume of vapour accumulating in the roof zone. When vapour pressure exceeded the lithostatic load and tensile stress, the carapace underwent brittle fracturing (Burnham, 1979), resulting in the release of volatiles and fluids into adjacent wallrocks (Fig. 9.2b-ii). Microscopic fractures and associated K-feldspar-muscovite alteration (e.g., Fig. 4.7D) in euhedral comb quartz from the Heemskirk Batholith provide evidence of brittle fracturing and volatile fluxing after UST growth.

Multiple comb quartz layers and aplite interlayers in the Heemskirk Granite (Fig. 4.7) provide physical evidence for fluctuating pressure conditions, as the volatiles exsolving from the silicate melt

accumulated and escaped episodically during granite crystallisation. Brittle fracturing caused drastic pressure decrease and heat loss via phase separation. Rapid undercooling coupled with decompression caused crystallisation of the aplite substrate below each comb-quartz layer (cf. Kirkham and Sinclair, 1988; Lowenstern and Sinclair, 1996; Fig. 4.7). Open system conditions were transient, with minerals rapidly precipitating and sealing the brittle fractures that formed during decompression, allowing the next cycle of UST formation to commence (Figs. 4.7, 9.2b-ii). Cycles of pressure build-up and release were repeated several times until the vapour pressure decreased to the point at which the UST layers ceased growing in the granitic carapace.

As boron-rich granitic magmas intruded the shallow crust (~5 km) at 600 °–550 ℃, Mg, Na, Ti (Figs. 5.6), and minor amounts of transition elements (V, Co, Sc, Zn, and Ga; Fig. 5.15) were incorporated into small boron-rich volatile bubbles interstitial to coarse igneous crystals (Fig. 9.2c). Approximately 60 to 77 % of the boron may have been depleted from the initial granitic melt ($\delta^{11}B \approx -10$ ‰), yielding average $\delta^{11}B_{Tur}$ values of -5.7 to -8.4 ‰ (Fig. 8.6). These small boron-rich volatile bubbles altered the granite to produce irregular tourmaline patches (Figs. 4.1, 9.2c-i). The spherical tourmaline orbicules and cavities in uppermost portions of the granites are interpreted to be remnants of large boron-rich volatile bubbles that were enriched in Fe, volatiles (Li, Be, B), and incompatible elements (Nb, Ta, Th, U, and Pb; Figs. 5.15, 9.2c-ii). The crystallisation of tourmaline orbicules and cavities may have caused 80 to 90 % of boron removal from their parent granitic melts, with average $\delta^{11}B_{Tur}$ values of –4.5 and −0.8 ‰ at temperatures of 500 ° to 600 ℃ and lithostatic pressures of 1.3 to 0.6 kbars (Fig. 8.6; Table 7.4). The calculated boron and oxygen isotopic compositions ($\delta^{11}B_{H2O}$ = −20 to +6 %, $\delta^{18}O_{H2O}$ = +7 to +13‰; Table 8.3) are consistent with a dominantly magmatic – hydrothermal origin for the waters and boron (Fig. 9.2c-ii).

Pressures decrease from 0.6 to 0.1 kbars, and temperature decrease from 500 ° to 310 ℃ (Fig. 7.9) may have caused intense brittle failure and fluid exsolution from the cupolas of the intrusions (Fig. 9.2d), providing focus for magmatic – hydrothermal fluids that precipitated tourmaline-muscovite-quartz veins and associated Sn-sulphide mineralisation within and around the Heemskirk Granite (Figs. 3.5, 4.1). Vein tourmalines are characterised by higher Fe, Al, Be and incompatible elements (e.g., Nb, Ta, Pb, Sr, REEs) than tourmaline grains from patches, orbicules and cavities (Figs. 5.7 and 5.15). Lower Al, Ti, Li, Mg, and Ge contents were detected in quartz from the tourmaline veins than from tourmaline patches and orbicules (Fig. 6.7). The chemical evolution of tourmaline-rich textural features in space and time relates to the variations of exsolved boron-rich fluids from the intrusions during fractional crystallisation (Fig. 9.2d). Decreasing homogenisation temperatures and salinities in tourmaline-vein quartz from their respective granites (Fig. 7.7a), and low $\delta^{18}O$ signatures for tourmaline and quartz in veins ($\delta^{18}O_{H2O}$ = +3.6 to +9.0 ‰; Fig. 8.4C) provide evidence that small amounts of external water (e.g., meteoric water, fluids from the country rocks), interacted with the predominant magmatic – hydrothermal fluids from which the tourmaline-quartz veins precipitated (Fig. 9.2d). The tourmaline-quartz veins locally host economic cassiterite ores within the Heemskirk Granite and adjacent Neoproterozoic wallrocks (Hajitaheri, 1985).

The Heemskirk and Pieman Heads granites appears to have experienced uplift and/or exhumation during magmatic – hydrothermal activity, because depths estimated from fluid inclusions and Ti-in-quartz

geothermometry decrease from >5 km for the tourmaline orbicules to < 1 km for Pb-Zn sulphide quartz veins (Figs. 7.9, 9.2e; Table 7.4). The decreasing pressure (~0.08 kbars) and temperature (280 ℃) of the hydrothermal fluids ultimately favoured the precipitation of Pb-Zn-sulphide – fluorite –quartz veins in the Heemskirk Granite (Hajitaheri, 1985; Fig. 9.2e).

9.4 Implications for Sn (-W) mineralisation

Geological, geochemical and geochronological analyses of Tasmanian granites, and LA-ICP-MS analyses of tourmaline and quartz from the Heemskirk and Pieman Heads granites in this study, combined with previous studies (e.g., Kwak et al., 1983; Higgins et al., 1985; Mackenzie et al., 1988; Sawka et al., 1990; Bajwah et al., 1995; Black et al., 2005, 2010), have highlighted several outcomes relevant to the genesis of Sn-(W) mineralisation.

The Sn-mineralised granites in eastern and western Tasmania formed in a long-lived, post-collisional, extensional regime (Fig. 9.1). This has been shown to be the most favourable tectonic setting for formation of economical primary Sn deposits worldwide, including the Cornwall tin field in SW England (Williamson et al., 2010), Variscan Sn province in Erzgebirge–Vogtland (Breiter et al., 1999), Sn-bearing granites in the Central Asian Orogenic Belt (Konopelko et al., 2009), Late Triassic W–Sn–Nb–Ta province in South China (Mao et al., 2013), Japanese W–Sn Belt (Sato, 2012), Southeast Asian Tin Belt (Searle et al., 2012), and Rondônia Tin Province in Brazil (Bettencourt et al., 2005). In a post-collisional setting, Sn and W can be enriched residually in the protoliths through strong chemical weathering of sedimentary rocks, and this may be an essential prerequisite for the generation of economic Sn–W deposits (cf. Romer and Kroner, 2016).

Tasmanian granites associated with Sn-mineralisation are mostly characterised by high SiO_2 (Fig. 9.3a), Al_2O_3 and $Na_2O + K_2O$, as well as low FeO (Fig. 9.3c), MgO and TiO_2 contents, consistent with chemical characteristics of stanniferous granites worldwide (Olade, 1980; Lehmann, 1982; Blevin and Chappell, 1995; Dietrich et al., 2000). As an incompatible element, Sn preferentially remains in melts during granite crystallisation (Ishihara, 1977; Taylor and Wall, 1992). Therefore, prolonged fractionation of granitic magmas can facilitate progressive enrichment of tin in residual melts (Lehmann, 1982; Blevin and Chappell, 1995). Most Tasmanian Sn-mineralised granites have Rb/Sr ratios > 5 (Fig. 9.3b), implying high degrees of fractional crystallisation that could have promoted efficient Sn extraction from the parental magmas.

Tin accumulation in magmas is fundamentally dependent on the redox state of the melt, which determines whether Sn occurs as a bivalent or tetravalent cation (Ishihara, 1977; Lehmann, 1982). Low fO_2 conditions (below Ni-NiO or quartz-magnetite-fayalite [FMQ] buffer) allow Sn to occur predominantly as Sn^{2+}, so that it behaves incompatibly and can be progressively enriched in reduced felsic magmas during fractionation (Linnen et al., 1995). The Sn-mineralised Tasmanian granites have a much narrower range of Fe^{3+}/Fe^{2+} ratios (mostly < 0.5; Fig. 9.3d) than other Sn-bearing granites in the Lachlan Orogen (cf., Fig. 9a from Blevin and Chappell, 1995), indicating that they are highly reduced magmas.

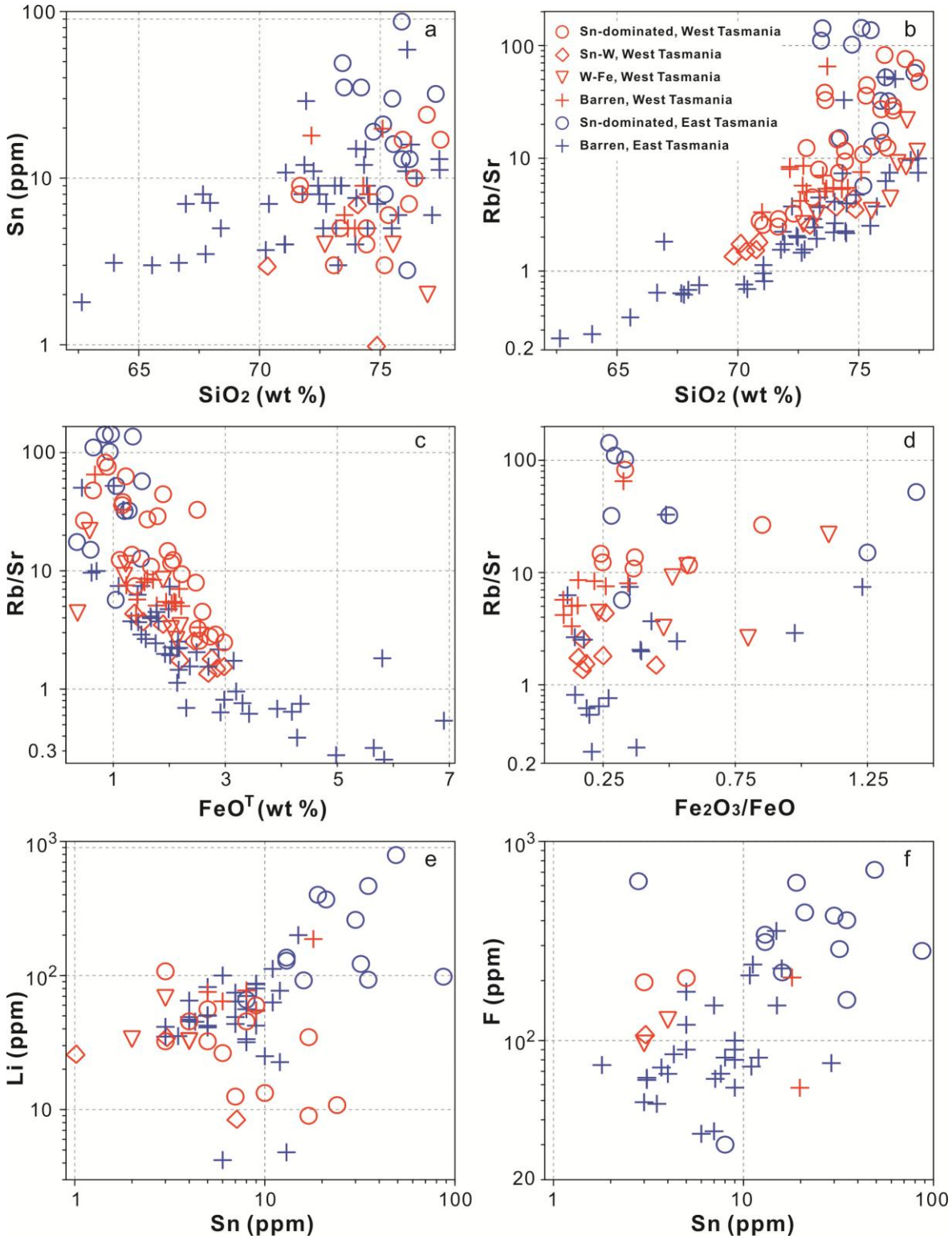

Figure 9.3 Element plots showing chemical variations between Sn-mineralised and barren granites in Tasmania. (a) SiO_2 versus Sn, (b) SiO_2 versus Rb/Sr, (c) FeO^T versus Rb/Sr, (d) Fe_2O_3 versus Rb/Sr, (e) Li versus Sn, (f) Sn versus F. Data sources: Kwak et al. (1983), Higgins et al. (1985), Mackenzie et al. (1988), Sawka et al. (1990), Bajwah et al. (1995), Black et al. (2010) and this study. All data listed in Appendix 3.1.

This characteristic may be one of the most critical factors leading to the formation of world-class Sn deposits in Tasmania. Deposits such as Renison Bell and Mt Bischoff (Table 2.1) are larger and richer than other Sn deposits in southeast Australia (e.g., Solomon and Groves, 2000).

High Li (> 20 ppm) and F abundances (> 1000 ppm; Higgins et al., 1985; Mackenzie et al., 1988; Bajwah et al., 1995; Black et al., 2010; this study) correlate positively with increasing Sn contents in Tasmanian granites, particularly the eastern Tasmanian Sn-mineralised granites (Figs. 9.3e, f). Positive correlations between high Sn concentrations and volatile components (e.g., B, F, Cl, Li) have been also determined in a felsic pluton from the Ehrenfridersdorf Sn–W district (Thomas and Webster, 2000) and Bolivian tin porphyry systems (Dietrich et al., 2000). Recent experimental investigations by Bhalla et al. (2005) have emphasised that volatile components can significantly enhance SnO_2 solubility in fractionated peraluminous melts that have $fO_2 \leq$ Ni-NiO buffer. All of these investigations tend to support that strong enrichment of magmatic volatiles can improve the efficiency of extracting and complexing Sn metal from crystallising felsic magmas and subsequent mineralisation (cf. Hedenquist and Lowenstern, 1994; Cooke et al., 2009).

Despite their differences in metal endowment, the Heemskirk and Pieman Heads granites have similar geological, geochemical, and geochronological signatures, and are characterised by distinctive tourmaline-rich magmatic – hydrothermal textural features. The higher degree of fractional crystallisation (e.g., high Rb/Sr values, Fig. 3.10) and abundant evidence for volatile exsolution (e.g., tourmaline-filled miarolitic cavities and USTs) that characterised the Heemskirk Granite, coupled with its strongly reduced state of the granitic magmas (e.g., Fig. 3.12) and higher contents of volatile elements (e.g., fluorine in tourmaline, Fig. 5.6), are concluded to have caused the Heemskirk Batholith to be highly fertile, producing world class Sn deposits and numerous Pb-Zn-Ag veins. The Pieman Heads produced lower amounts of volatiles, and never achieved the crucial volatile percolation threshold required to form the USTs and miarolitic cavities seated in the Heemskirk Granite, and so the volatiles were trapped mostly as tourmaline patches and orbicules, with only sparse tourmaline veins late in the formation of the Pieman Heads Granite. It is also possible that USTs and miarolitic cavities had formed in the Pieman Heads Granite, but they were not observed in the current study, or they were destroyed by subsequent erosion or uplift.

9.5 Implications for exploration

Chemical variations in trace element compositions of tourmaline and quartz grains from the Heemskirk and Pieman Heads granites imply that it is possible to discriminate granites with respect to their potential for Sn and base metal mineralisation. Element ratios of Zn/Nb, Co/Nb, Sr/Ta, and Co/La when plotted against Sn concentrations in tourmaline have shown potential to be useful discriminators for distinguishing Sn-mineralised granites from barren intrusions (Fig. 5.17). Variations of trace elements (e.g., Al, Li, Ti, and Ge) and element ratios (e.g., Al/Ti, Ge/Ti) in quartz can reflect the degree of crystal fractionation of the parent granites, evolution path of composition, pressure and temperature of relevant fluids. Quartz associated with Pb-Zn sulphide veins from the Heemskirk Granite has Sb concentrations as high as tens to hundreds of ppm (Fig. 6.12d), several orders of magnitude higher than high-temperature quartz (Sb < 0.1 ppm). The Sb content of quartz may therefore give guide to help identify the potential for base metal mineralisation associated with granite-related quartz veins.

9.6 Recommendations for future work

Although this study has conducted a regional geochemical and geochronological investigation of Tasmanian granites, many questions remain unresolved with regards granite geochronology, petrogenesis and hydrothermal phenomena. Recommendations for further research to understand Tasmanian granites and associated mineralisation include the follows.

Most of the mid-Palaeozoic granites across Tasmania have been dated precisely (Black et al., 2005; Kositcin and Everard, 2013; this study), but a few do not have U-Pb zircon ages, including the Maria Island granite from eastern Tasmania, and the Dolcoath, Granite Tor, Three Hummock Island, and Sea Elephant (King Island) granites from western Tasmania. Dating these granites may help to ascertain whether an N-directed subduction system occurred beneath southwestern Tasmania from 375 to 350 Ma, or if the Tasmanian granites formed along cross-arc structures in a post-subduction environment after the W-directed subduction system terminated beneath eastern Tasmania, as proposed in Figure 9.1.

Lead isotopic compositions of K-feldspar from the eastern Tasmanian granites are consistent with their respective whole-rock Pb isotopic compositions (cf. Black et al., 2010 and this study). Lead isotopic compositions of K-feldspar from the western Tasmanian granites in this study are very scattered, similar to previous whole-rock Pb isotopic analyses (Black et al., 2010), largely due to contamination by inclusions of Th-U-rich minerals in K-feldspar, and due to intense hydrothermal alteration. Consequently only a small dataset of meaningful Pb isotopic analyses were obtained by this study. It is recommended that future research of this nature should check K-feldspar grains using the SEM-BSE technique, and analyse Pb isotopes via LA-ICP-MS, especially for K-feldspar from such highly fractionated granites.

Distinctive multiple layers of biotite schlieren have been observed in the George River Granodiorite at Binalong Bay and granites from Freycinet Bay, eastern Tasmania (Cocker, 1971; Fig. 3.2), and in the Heemskirk Granite at Trial Harbour. The genesis of these biotite schlieren remains enigmatic. They may be petrologically significant with respect to understanding how volatiles and water interact with Mg-Fe components in felsic magmas. Detailed investigations of the schlieren are recommended.

Tourmaline crystals were discovered in coarse-grained USTs in the Heemskirk Granite at Trial Harbour in late 2016, after the completion of the current studies. Also, tourmaline grains have been reported in the country rocks (Oonah Formation) at the contact with the Heemskirk Granite (Hajitaheri, 1985). These two types of tourmaline should be analysed in order to understand their evolution in the framework of the results of the current study.

Trace element compositions of fluid inclusions should be analysed by LA-ICP-MS from the Sn-mineralised Heemskirk and barren Pieman Heads granites, and should be conducted to evaluate the metal contents in fertile and barren granites.

Abundant magnetite veins and magnesian iron skarn are developed along the coast at Trial Harbour in the Heemskirk Granite (Fig. 4.1). No detailed investigation of the Fe skarn has been conducted for over 50 years, since Green (1964). The Fe skarn at Trial Harbour consists of diopside, magnetite, serpentine,

chlorite, epidote, quartz, chalcedony and rare garnet. Magnetite veins occur in the country rocks, and locally extend a few tens to hundreds meters. Tertiary basalt appears to overprint these iron skarn and veins. The economic potential and genesis of the iron skarn at Trial Harbour should be assessed using modern research techniques.

References

Allègre, C.J., Provost, A., Jaupart, C., 1981, Oscillatory zoning: a pathological case of crystal growth: Nature, v. 294, p. 223–228.

Ansdell, K.M., Kyser, T.K., 1992, Mesothermal gold mineralization in a Proterozoic greenstone belt: Western Flin Flon Domain, Saskatchewan, Canada: Economic Geology, v. 87, p. 1496–1524.

Arne, D.C., Bierlein, F.P., Mcnaughton, M., Wilson, C.J.L., Morand, V.J., 1998, Timing of gold mineralisation in western and central Victoria: new constraints from SHRIMP II analysis of zircon grains from felsic intrusive rocks: Ore Geology Reviews, v.13, p. 251–273.

Audétat, A., Garbe-Schönberg, D., Kronz, A., Pettke, T., Rusk, B., Donovan, J.J., Lowers, H.A., 2015, Characterisation of a natural quartz crystal as a reference material for microanalytical determination of Ti, Al, Li, Fe, Mn, Ga and Ge: Geostandards and Geoanalytical Research, v. 39, p. 171–184.

Audétat, A., Günther, D., 1999, Mobilization and H_2O-loss from fluid inclusions in natural quartz crystals: Contributions to Mineralogy and Petrology, v. 137, p. 1−14.

Audétat, A., Günther, D., Heinrich, C.A., 1998, Formation of a magmatic–hydrothermal ore deposit: insights with LA-ICP-MS analysis of fluid inclusions: Science 279, p. 2091–2094.

Audétat, A., Lowenstern, J.B., 2014, Melt inclusions, in Scott, S.D., ed., Geochemistry of Mineral Deposits: Treatise on Geochemistry 13, 2nd edition, Elsevier, p. 143–173.

Audétat, A., Pettke, T., 2003, The magmatic-hydrothermal evolution of two barren granites: A melt and fluid inclusion study of the Rio del Medio and Cañada Pinabete plutons in northern New Mexico (USA): Geochimica et Cosmochimica Acta, v. 67, p. 91–121.

Audétat, A., Pettke, T., Heinrich, C.A., Bodnar, R.J., 2008, The composition of magmatic-hydrothermal fluids in barren and mineralized intrusions: Economic Geology, v. 103, p. 877–908.

Baillie, P.W., 1989, Jurassic – Cainozoic, in Burrett, C.F., and Martin, E.L., eds., Geology and mineral resources of Tasmania: Geological Society of Australia, Special Publication 15, p. 339–409.

Bajwah, Z.U., White, A.J.R., Kwak, T.A.P., Price, R.C., 1995, The Renison granite, northwestern Tasmania: A petrological, geochemical and fluid inclusion study of hydrothermal alteration: Economic Geology, v. 90, p. 1663–1675.

Baker, J., Peate, D., Waight, T., Meyzen, C., 2004, Pb isotopic analysis of standards and samples using a Pb-207-Pb-204 double spike and thallium to correct for mass bias with a double-focusing MC-ICP-MS: Chemical Geology, v. 211, p. 275–303.

Balen, D., Broska, I., 2011, Tourmaline nodules: products of devolatilization within the final evolutionary stage of granitic melt?: Geological Society, London, Special Publications, v. 350, p. 53–68.

Banks, M.R., and Baillie, P.W., 1989, Late Cambrian to Devonian, in Burrett, C.F., and Martin, E.L., eds., Geology and mineral resources of Tasmania: Geological Society of Australia, Special Publication 15, p. 182–237.

Barbarin, B., 1999, A review of the relationships between granitoid types, their origins and their geodynamic environments: Lithos, v. 46, p. 605–626.

Barth, S., 1993, Boron isotope variations in nature: a synthesis: Geol Rundsch, v. 82, p. 640–651.

Beaudoin, G., Chiaradia, M., 2016, Fluid mixing in orogenic gold deposits: Evidence from the H-O-Sr isotope composition of the Val-d'Or vein field (Abitibi, Canada): Chemical Geology, v. 437, p. 7–18.

Bebout, G.E., Nakamura, E., 2003, Record in metamorphic tourmalines of subduction-zone devolatilization and boron cycling: Geology, v. 31, p. 407–410.

Becker, S.P., Fall, A., Bodnar, R.J., 2008, Synthetic fluid inclusions: XVII. PVTX properties of high salinity H_2O-NaCl solutions (>30 wt% NaCl): Application to fluid inclusions that homogenized by halite disappearance from porphyry copper and other hydrothermal ore deposits: Economic Geology, v. 103, p. 539−554.

Belley, P.M., Grice, J.D., Fayek, M., Kowalski, P.M., Grew, E.S., 2015, A new occurrence of the borosilicate serendibite in tourmaline-bearing calc-silicate rocks, Portage-Du-Fort Marble, Grenville Province, Quebec: Evolution of boron isotope and tourmaline compositions in a metamorphic context: The Canadian Mineralogist, v. 52, p. 595–616.

Benard, F., Moutou, P., Pichavant, M., 1985, Phase relations of tourmaline leucogranites and the significance of tourmaline in silicic magmas: The Journal of Geology, v. 93, p. 271–291.

Berry, R.F., Bull, S.W., 2012, The pre-Carboniferous geology of Tasmania: Episodes, v. 35, p. 195–204.

Berry, R.F., Crawford, A.J., 1988, The tectonic significance of Cambrian allochthonous mafic-ultramafic complexes in Tasmania: Australian Journal of Earth Sciences, v. 35, p. 523–533.

Berry, R.F., Steele, D.A., Meffre, S., 2008, Proterozoic metamorphism in Tasmania: Implications for tectonic reconstructions: Precambrian Research, v. 166, p. 387–396.

Bettencourt, J.S., Leite, W.B., Goraieb, C.L., Sparrenberger, I., Bello, R.M., and Payolla, B.L., 2005, Sn-polymetallic greisen-type deposits associated with late-stage rapakivi granites, Brazil: fluid inclusion and stable isotope characteristics: Lithos, v. 80, p. 363–386.

Bhalla, P., Holtz, F., Linnen, R.L., Behrens, H., 2005, Solubility of cassiterite in evolved granitic melts: effect of T, fO_2, and additional volatiles: Lithos, v. 80, p. 387–400.

Bierlein, F.P., Arne, D.C., Keay, S.M., Mcnaughton, N.J., 2001, Timing relationships between felsic magmatism and mineralization in the central Victorian gold province, southeast Australia: Australian Journal of Earth Sciences, v. 48, p. 883–899.

Black, L.P., Calver, C.R., Seymour, D.B., Reed, A., 2004, SHRIMP U–Pb detrital zircon ages from Proterozoic and Early Palaeozoic sandstones and their bearing on the early geological evolution of Tasmania: Australian Journal of Earth Sciences, v. 51, p. 885–900.

Black, L.P., Everard, J.L., McClenaghan, M.P., Korsch, R.J., Calver, C.R., Fioretti, A.M., Brown, A.V., Foudoulis, C., 2010, Controls on Devonian–Carboniferous magmatism in Tasmania, based on inherited zircon age patterns, Sr, Nd and Pb isotopes, and major and trace element geochemistry: Australian Journal of Earth Sciences, v. 57, p. 933–968.

Black, L.P., Kamos, L., Allen, C.M., Aleinikoff, J.N., Davis, D.W., Korsch, R.J., Foudoulis, C., 2003, TEMORA 1: a new zircon standard for Phanerozoic U–Pb geochronology: Chemical Geology, v. 200, p. 155–170.

Black, L.P., McClenaghan, M.P., Korsch, R.J., Everard, J.L., Foudoulis, C., 2005, Significance of Devonian–Carboniferous igneous activity in Tasmania as derived from U–Pb SHRIMP dating of zircon: Australian Journal of Earth Sciences, v. 52, p. 807–829.

Blevin, P.L., Chappell, B.W., 1992, The role of magma sources, oxidation states and fractionation in determining the granite metallogeny of eastern Australia: Transactions of the Royal Society of Edinburgh: Earth Sciences, v. 83, p. 305–316.

Blevin, P.L., Chappell, B.W., 1995, Chemistry, origin and evolution of mineralized granites in the Lachlan Fold Belt, Australia: the metallogeny of I- and S-type granites: Economic Geology, v. 90, p. 1604–1619.

Blisset, A.H., 1962, Geological survey explanatory report, One Mile Geological Map Series: K/15-5-50, Zeehan, Tasmanian Department of Mines, p. 1–255.

Bodnar, R.B., Vityk, M.O., 1994, Interpretation of microthermometric data for H_2O-NaCl fluid inclusions, in De Vivo, B., and Frezzotti, M.L., eds., Fluid Inclusions in Minerals, Methods and Applications: Virginia Tech, Blacksburg, p. 117–130.

Bodnar, R.J., 2003, Introduction to fluid inclusions, in Samson, I., Anderson, A., and Marshall, D., eds., Fluid Inclusions: Analysis and Interpretation: Mineralogical Association of Canada, Short Course 32, p. 1–8.

Bodnar, R.J., Burnham, C.W., Sterner, S.M., 1985, Synthetic fluid inclusions in natural quartz III: Determination of phase equilibrium properties in the system H_2O-NaCl to 1000 °C and 1500 bars: Geochimica et Cosmochimica Acta, v. 49, p. 1861–1873.

Bodnar, R.J., Lecumberri-Sanchez, P., Moncada, D., Steele-MacInnis, M., 2014, Fluid Inclusions in Hydrothermal Ore Deposits, in Scott, S.D., ed., Geochemistry of Mineral Deposits: Treatise on Geochemistry 13, Elsevier, 2nd edition, p. 119–142.

Both, R.A., Rafter, T.A., Solomon, M., Jensen, M. L., 1969, Sulfur isotopes and zoning of the Zeehan Mineral Field, Tasmania: Economic Geology, v. 64, p. 618–628.

Both, R.A., Williams, K.L., 1968, Mineralogical zoning in the lead-zinc ores of the Zeehan field, Tasmania Part I: Introduction and review: Journal of the Geological Society of Australia, v. 15, p. 121–137.

Breiter, K., Ackerman, L., Svojtka, M., Müller, A., 2013, Behavior of trace elements in quartz from plutons of different geochemical signature: a case study from the Bohemian Massif, Czech Republic: Lithos, v. 175-176, p. 54–67.

Breiter, K., Förster, H.J., Seltmann, R., 1999, Variscan silicic magmatism and related tin– tungsten mineralization in the Erzgebirge-Slavkovský les metallogenic province: Mineralium Deposita, v. 34, p. 505–521.

Breiter, K., Müller, A., 2009, Evolution of rare-metal granitic magmas documented by quartz chemistry: European Journal of Mineralogy, v. 21, p. 335–346.

Brooks, C., 1966, The rubidium–strontium ages of some Tasmanian igneous rocks: Journal of the Geological Society of Australia, v. 13, p. 457–469.

Brooks, C., and Compston, W., 1965, The age and initial Sr^{87}/Sr^{86} of the Heemskirk Granite, Western Tasmania: Journal of Geophysical research, v. 70, p. 6249–6262.

Buriánek, D., Novák, M., 2007, Compositional evolution and substitutions in disseminated and nodular tourmaline from leucocratic granites: Examples from the Bohemian Massif, Czech Republic: Lithos, v. 95, p. 148–164.

Burke, E.A.J., 2001, Raman microspectrometry of fluid inclusions: Lithos, v. 55, p. 139–158.

Burnham, C.W., 1979, Magmas and hydrothermal fluids, in Barnes, H.L., ed., Geochemistry of hydrothermal ore deposits: 2nd edition, Wiley, New York, p.71-136.

Burnham, C.W., Ohmoto, H., 1980, Late-stage processes of felsic magmatism, in Ishihara, S. and Takenouchi, S., eds., Granitic magmatism and related mineralization: Mining Geology Special Issue, No.8, p. 1–11.

Callaghan, T., 2013, Heemskirk tin project – Tasmania: Tasmanian Geoscience Forum, Cradle Mountain, Tasmania, December 5-6th.

Calver, C.R., Everard, J.L., Berry, R.F., Bottrill, R.S., Seymour, D.B., 2014a, Proterozoic Tasmania, in Corbett, K.D., Quilty, P.G., Calver, C.R., eds., Geological Evolution of Tasmania: Geological Society of Australia, Special Publication 24, p. 34–94.

Calver, C.R., Baillie, P.W., Banks, M.R., Seymour, D.B., 2014b, Ordovician–Lower Devonian successions, in Corbett, K.D., Quilty, P.G., Calver, C.R., eds., Geological Evolution of Tasmania: Geological Society of Australia, Special Publication 24, p. 241–271.

Candela, P.A., 1991, Physics of aqueous phase evolution in plutonic environments: American Mineralogist, v. 76, p. 1081–1091.

Candela, P.A., 1997, A review of shallow, ore-related granites: textures, volatiles, and ore metals: Journal of Petrology, v. 38, p. 1619–1633.

Candela, P.A., Blevin, P.L., 1995, Do some miarolitic granites preserve evidence of magmatic volatile phase permeability?: Economic Geology, v. 90, p. 2310–2316.

Cannell, J., Cooke, D. R., Walshe, J. L., Stein, H., 2005, Geology, mineralization, alteration and structural evolution of the El Teniente porphyry Cu-Mo deposit: Economic Geology, v. 100, p. 979–1003.

Carr, G.R., Dean, J.A., Suppel, D.W., Heithersay, P.S., 1995, Precise lead isotope fingerprinting of hydrothermal activity associated with Ordovician to Carboniferous metallogenic events in the Lachlan Fold Belt of New South Wales: Economic Geology, v. 90, p. 1467–1505.

Cayley, R.A., 2011, Exotic crustal block accretion to the eastern Gondwanaland margin in the Late Cambrian–Tasmania, the Selwyn Block, and implications for the Cambrian–Silurian evolution of the Ross, Delamerian, and Lachlan orogens: Gondwana Research, v.19, p. 628–649.

Chappell, B.W, White, A.J.R., 2001, Two contrasting granite types: 25 years later: Australian Journal of Earth Sciences, v. 48, p. 489–499.

Chappell, B.W., 1999, Alumina saturation in I-type and S-type granites and the characteristics of fractionated haplogranites: Lithos, v. 46, p. 535–551.

Chappell, B.W., White, A.J.R., 1974, Two contrasting granite types: Pacific Geology, v.8, p. 173–174.

Chappell, B.W., White, A.J.R., 1992, I- and S-type granites in the Lachlan Fold Belt: Transactions of the Royal Society of Edinburgh: Earth Sciences, v. 83, p. 1–26.

Chappell, B.W., White, A.J.R., Hine, R., 1988, Granite provinces and basement terranes in the Lachlan Fold Belt, southeastern Australia: Australian Journal of Earth Sciences, v. 35, p. 505–521.

Chaussidon, M., Albarède, F., 1992, Secular boron isotope variations in the continental crust: an ion microprobe study: Earth and Planetary Science Letters, v.108, p. 229–241.

Chaussidon, M., Appel, P.W.U., 1997, Boron isotopic composition of tourmaline from the 3.8-Ga-old Isua supracrustals, West Greenland: Implications on the 11B values of early Archean seawater: Chemical Geology, v.136, p. 171–180.

Clarke, M.J., Forsyth, S.M., 1989, Late Carboniferous – Triassic, in Burrett, C.F., and Martin, E.L., eds., Geology and mineral resources of Tasmania: Geological Society of Australia, Special Publication 15, p. 292–338.

Clayton, R.N., O'Neil, J.R., Mayeda, T.K., 1972, Oxygen isotope exchange between quartz and water: Journal of Geophysical Research, v. 77, p. 3057–3067.

Cline, J.S., Bodnar, R.J., 1994, Direct evolution of brine from a crystallizing silicic melt at the Questa, New Mexico, Molybdenum Deposit: Economic Geology, v. 89, p. 1780–1802.

Cocker, J.D., 1971, The St. Helens pluton: petrology and structure: Unpublished B.Sc. (Hons) thesis, University of Tasmania, 115 p.

Cocker, J.D., 1977, Petrogenesis of the Tasmanian granitoids: Unpublished Ph.D. thesis, University of Tasmania, 300 p.

Cocker, J.D., 1982, Rb-Sr geochronology and Sr isotopic composition of Devonian granitoids, eastern Tasmania: Journal of the Geological Society of Australia, v. 29, p. 139–158.

Collins, P.L.F., 1981, Geology and genesis of the Cleveland tin deposit, Western Tasmania: Fluid inclusion and stable isotope studies: Economic Geology, v. 76, p. 365–392.

Collins, W.J., 1996, Lachlan Fold Belt granitoids: products of three component mixing: Transactions of the Royal Society of Edinburgh: Earth Sciences, v. 87, p. 171–179.

Collins, W.J., 1998, Evaluation of petrogenetic models for Lachlan Fold Belt granitoids: implications for crustal architecture and tectonic models: Australian Journal of Earth Sciences, v. 45, p. 483–500.

Collins, W.J., Richards, S.W., 2008, Geodynamic significance of S-type granites in circum-Pacific orogens: Geology, v. 36, p. 559–562.

Cooke, D.R, Kitto, P.A., Harris, A.C., Chang, Z., Wilkinson, J.J., Wilkinson, C.C., Hollings, P., Webster, J.D., 2009, Magma fertility and mineralisation, in Smart Science for Exploration and Mining-Proceedings of the 10th Biennial SGA Meeting, Townsville, Economic Geology Research Unit, Volume 1, p. 8–10.

Cooke, D.R., Baker, M., Hollings, P., Sweet, G., Chang, Z., Danyushevsky, L., Gilbert, S., Zhou, T., White, N., Gemmell, J.B., Inglis, S., 2014, New advances in detecting the distal geochemical footprints of porphyry systems—epidote mineral chemistry as a tool for vectoring and fertility assessments: Society of Economic Geologists, Special Publication 18, p. 127–152.

Corbett, K.D., Quilty, P.G., Calver, C.R., 2014, Geological Evolution of Tasmania: Geological Society of Australia, Special Publication 24, 660 p.

Corfu, F., Hanchar, J.M., Hoskin, P.W.O., Kinny, P., 2003, Atlas of zircon textures, in Hanchar, J.M., and Hoskin, P.W.O., eds., Reviews in Mineralogy and Geochemistry, v. 53, p. 469–500.

Crawford, A.J., Berry, R.F., 1992, Tectonic implication of Late Proterozoic-Early Paleozoic igneous rocks associations in western Tasmania: Tectonophysics, v. 214, p. 37–56.

Crawford, A.J., Corbett, K.D., Everard, J.L., 1992, Geochemistry of the Cambrian volcanic- hosted massive sulfide-rich Mount Read Volcanics, Tasmania, and some tectonic implications: Economic Geology, v. 87, p. 597–619.

Crawford, A.J., Meffre, S., Symonds, P.A., 2003, 120 to 0 Ma tectonic evolution of the southwest Pacific and analogous geological evolution of the 600 to 220 Ma Tasman Fold Belt System, in Hillis R.R. and Müller R.D.,eds., Evolution and Dynamics of the Australian Plate: Geological Society of Australia Special Publication 22, p. 383–403.

Crawford, M.L., 1981, Phase equilibria in aqueous fluid inclusions: Short course in fluid inclusions: applications to petrology, v. 6, p. 75–100.

Cumming, G.L., Richards, J.R., 1975, Ore lead isotope ratios in a continuously changing Earth: Earth and Planetary Science Letters, v. 28, p. 155–171.

DePaolo, D.J., Wasserburg, G.J., 1979, Petrogenetic mixing models and Nd-Sr isotopic patterns: Geochimica et Cosmochimica Acta, v. 43, p. 615–627.

DeWolf, C. P., Mezger, K., Lead isotope analyses of leached feldspars: Constraints on the early crustal history of the Grenville Orogen: Geochimica et Cosmochimica Acta, v. 58, p. 5537–5550.

Dick, L.A., 1980, A comprehensive study of the geology, mineralogy and conditions of formation of contact metasomatic mineral deposits in the Northeastern Canadian Cordillera: Unpublished Ph.D. thesis, Queen's University, Kingston, Ontario, 471 p.

Didier, J., 1973, Mineral nodules, in Didier, J., ed., Granites and their enclaves, The bearing of enclaves on the origin of granites: Elsevier, Amsterdam, Developments in Petrology 3, p. 357-368.

Dietrich, A., Lehmann, B., and Wallianos, A., 2000, Bulk rock and melt inclusion geochemistry of Bolivian Tin Porphyry systems: Economic Geology, v. 95, p. 313–326.

Dingwell, D.B., Pichavant, M., Holtz, F., 1996, Experimental studies of boron in granitic melts: Reviews in Mineralogy and Geochemistry, v. 33, p. 331–385.

Dini, A., Corretti, A., Innocenti, F., Rocchi, S., Westerman, S., 2007, Sooty sweat stains or tourmaline spots? The Argonauts on the Island of Elba (Tuscany) and the spread of Greek trading in the Mediterranean Sea, in Piccardi, L. and Masse, W.B., eds., Myth and Geology: Geological Society, London, Special Publications, v. 273, p. 227–243.

Dini, A., Mazzarini, F., Musumeci, G., Rocchi, S., 2008, Multiple hydro-fracturing by boron-rich fluids in the Late Miocene contact aureole of eastern Elba Island (Tuscany, Italy): Terra Nova, v. 20, p. 318–326.

Drivenes, K., Larsen, R.B., Müller, A., Sørensen, B.E., 2016, Crystallization and uplift path of late Variscan granites evidenced by quartz chemistry and fluid inclusions: Example from the Land's End granite, SW England: Lithos, v. 252, p. 57–75.

Drivenes, K., Larsen, R.B., Müller, A., Sørensen, B.E., Wiedenbeck, M., Raanes, M.P., 2015, Late-magmatic immiscibility during batholith formation: assessment of B isotopes and trace elements in tourmaline from the Land's End granite, SW England: Contributions to Mineralogy and Petrology, 169:56. doi: 10.1007/s00410-015-1151-6.

Duncan, R.J., Buick, I.S., Kobayashi, K., Wilde, A.R., 2014, Chemical and stable isotopic characteristics of syn-tectonic tourmaline from the Western fold belt, Mount Isa inlier, Queensland, Australia: Chemical Geology, v. 381, p. 131–143.

Dutrow, B.L., Henry, D.J., 2011, Tourmaline: A geologic DVD: Elements, v. 7, p. 301–306.

Dyer, M.D., Wiedenbeck, M., Robertson, D., Cross, L.R., Delaney, J.S., Ferguson, K., Francis, C.A., Grew, E.S., Guidotti, C.V., Hervig, R.L., Hughes, J.M., Husler, J., Leeman, W., Mcguire, A.V., Rhede, D., Rothe, H., Paul, R.L., Richards, I., Yates, M., 2001, Reference minerals for the microanalysis of light elements: Geostandards Newsletter, v. 25, p. 441–463.

Elburg, M.A., 1996, U–Pb ages and morphologies of zircon in micrograniteoid enclaves and peraluminous host granite: evidence for magma mingling: Contributions to Mineralogy and Petrology, v. 123, p. 177–189.

Everard, J.L. 2001, Intrusive relationships of granite and dolerite at Lagunta Creek, Freycinet Peninsula: Papers and Proceedings Royal Society of Tasmania, v.135, p. 63–74.

Fergusson, C.L., 2014, Late Ordovician to mid-Silurian Benambran subduction zones in the Lachlan Orogen, southeastern Australia: Australian Journal of Earth Sciences, v. 61, p. 587–606.

Foster, D.A., Gray, D.R., Spaggiari, C., Kamenov, G., Bierlein, F.P., 2009, Palaeozoic Lachlan Orogen, Australia; accretion and construction of continental crust in a marginal ocean setting: Isotopic evidence from Cambrian metavolcanic rocks: Geological Society of London Special Publication, v. 318, p. 329–349.

Glen, R. Stewart, I. R., Percival, I. G., 2004, Narooma Terrane: implications for the construction of the outboard part of the Lachlan Orogen: Australian Journal of Earth Sciences, v. 51, p. 859–884.

Goldstein, R.H., 2003, Petrographic analysis of fluid inclusions, in Samson, I., Anderson, A., and Marshall, D., eds., Fluid Inclusions: Analysis and Interpretation: Mineralogical Association of Canada, Short Course 32, p. 9–53.

Goldstein, R.H., Reynolds, T.J., 1994, Systematics of fluid inclusions in diagenetic minerals: Society for Sedimentary Geology Short Course 31, p. 1–199.

Götze, J., 2009, Chemistry, textures and physical properties of quartz – geological interpretation and technical application: Mineralogical Magazine, v. 73, p. 645–671.

Götze, J., Plötze, M., Graupner, T., Hallbauer, D.K., Bray, C.J., 2004, Trace element incorporation into quartz: a combined study by ICP-MS, electron spin resonance, cathodoluminescence, capillary ion analysis and gas chromatography: Geochimica et Cosmochimica Acta, v. 68, p. 3741–3759.

Götze, J., Plötze, M., Habermann, D., 2001, Origin, spectral characteristics and practical applications of the Cathodoluminescence (CL) of quartz – a review: Mineralogy and Petrology, v. 71, p. 225–250.

Gray, D.R., 1997, Tectonics of the southeastern Australian Lachlan Fold Belt: structural and thermal aspects: Geological Society, London, Special Publications, v. 121, p. 149–177.

Green, G.R., 2012, Ore deposits and metallogenesis of Tasmania: Episodes, News magazine of the International Union of Geological Sciences, v. 35, p. 205–215.

Green, T.H., 1964, Geology of the Trial Harbour district: Unpublished B.Sc. (Hons) thesis, University of Tasmania, 244 p.

Griffin, W.L., Slack, J.F., Ramsden A.R., Win, T.T., Ryan, C.G., 1996, Trace elements in tourmaline from massive sulfide deposits and tourmalinites: geochemical controls and exploration applications: Economic Geology, v. 91, p. 657–675.

Groves, D.I., 1972a, The geochemical evolution of tin-bearing granites in the Blue Tier Batholith, Tasmania: Economic Geology, v. 67, p. 445–457.

Groves, D.I., 1972b, The zoned mineral deposits of the Scamander-St. Helens district: Geological Survey of Tasmanian Bulletin, v. 53, p. 1–56.

Groves, D.I., McCarthy, T.S., 1978, Fractional crystallization and the origin of tin deposits in granitoids: Mineralium Deposita, v. 13, p. 11–26.Gulson, B.L, Porritt, P.M., 1987, Base metal exploration of the Mount Read Volcanics, Western Tasmania: Pt. II. Lead isotope signatures and genetic implications: Economic Geology, v. 82, p. 291–307.

Hajitaheri, J., 1985, The origin of mineralisation in South Heemskirk granite, Western Tasmania, Australia: Unpublished Ph.D. thesis, University of Tasmania, Hobart, 322 p.

Halley, S.W., 1982, A fluid inclusion study of the Lutwyche vein system, Rossarden: Unpublished B. Sc. Thesis, University of Tasmania, Hobart, 134 p.

Halley, S.W., Walshe, J.L., 1995, A reexamination of the Mount Bischoff cassiterite sulfide Skarn, Western Tasmania: Economic Geology, v. 90, p. 1676–1693.

Halpin, J. A., Jensen, T., McGoldrick, P., Meffre, S., Berry, R.F., Everard, J.L., Calver, C.R., Thompson, J., Goemann, K., Whittaker, J. M., 2014, Authigenic monazite and detrital zircon dating from the Proterozoic Rocky Cape Group, Tasmania: Links to the Belt-Purcell Supergroup, North America: Precambrian Research, v. 250, p. 50–67.

Hannah, J.L., Stein, H.J., 1990, Magmatic and hydrothermal processes in ore-bearing systems: Geological Society of America, Special Paper 246, p. 1–10.

Harris, A.C., Kamenetsky, V.S., White, N.C., Steele, D.A., 2004, Volatile phase separation in silicic magmas at Bajo de la Alumbrera porphyry Cu-Au deposit, NW Argentina: Resource Geology, v. 54, p. 341–356.

Hawthorne, F.C., Dirlam, D.M., 2011, Tourmaline the Indicator Mineral: From Atomic Arrangement to Viking Navigation: Elements, v. 7, p. 307–312.

Hawthorne, F.C., Henry, D.J., 1999, Classification of the minerals of the tourmaline group: European Journal of Mineralogy, v. 11, p. 201–215.

Hedenquist, J.W., Lowenstern, J.B., 1994, The role of magmas in the formation of hydrothermal ore deposits: Nature, v. 370, p. 519–527.

Heier, K.S., Brooks, C., 1966, Geochemistry and the genesis of the Heemskirk granite, West Tasmania: Geochimica et Cosmochimica Acta, v. 30, p. 633–643.

Heinrich, C.A., Ryan, C.G., Mernagh, T.P., Eadington, P.J., 1992, Segregation of ore metals between magmatic brine and vapor – a fluid inclusion study using PIXE microanalysis: Economic Geology, v. 87, p. 1566–1583.

Henry, D.J., Dutrow, B.L., 1996, Metamorphic tourmaline and its petrologic applications: Reviews in Mineralogy and Geochemistry, v. 33, p. 503–557.

Henry, D.J., Dutrow, B.L., 2001, Compositional zoning and element partitioning in nickeloan tourmaline from a metamorphosed karstbauxite from Samos, Greece: American Mineralogist, v. 86, p. 1130–1142.

Henry, D.J., Guidotti, C.V., 1985, Tourmaline as a petrogenetic indicator mineral: an example from the staurolite-grade metapelites of NW Maine: American Mineralogist, v. 70, p. 1–15.

Henry, D.J., Kirkland, B.L., Kirkland, D.W., 1999, Sector-zoned tourmaline from the cap rock of a salt dome: European Journal of Mineralogy, v. 11, p.263–280.

Henry, D.J., Novák, M., Hawthorne, F.C., Ertl, A., Dutrow, B.L., Uher, P., Pezzotta, F., 2011, Nomenclature of the tourmaline-supergroup minerals: American Mineralogist, v. 96, p. 895–913.

Herving, R.L., Moore, G.M., Williams, L.B., Peacock, S.M., Holloway, J.R., Roggensack, K., 2002, Isotopic and elemental partitioning of boron between hydrous fluid and silicate melt: American Mineralogist, v. 87, p. 769–774.

Higgins, N.C., Solomon, M., Varne, R., 1985, The genesis of the Blue Tier Batholith, northeastern Tasmania, Australia: Lithos, v. 18, p. 129–149.

Holm, O.H., Crawford, A.J., Berry, R.F., 2003, Geochemistry and tectonic settings of meta-igneous rocks in the Arthur Lineament and surrounding area, northwest Tasmania: Australian Journal of Earth Sciences, v. 50, p. 903–918.

Hoskin, P.W.O., 2005, Trace-element composition of hydrothermal zircon and the alteration of Hadean zircon from the Jack Hill, Australia: Geochimica et Cosmochimica Acta, v. 69, p. 637–648.

Huang, R., Audétat, A., 2012, The titanium-in-quartz (TitaniQ) thermobarometer: A critical examination and re-calibration: Geochimica et Cosmochimica Acta, v. 84, p. 75–89.

Hughes, P., 1995, The Exe River Sn-Pb-Zn-(Cu) prospect, NW Tasmania: Unpublished B. Sc. (Hons) thesis, University of Tasmania, 97 p.

Huston, D. L., Champion, D.C., Mernagh, T.P., Downes, P.M., Jones, P., Carr, G., Forster, D., Vladimir, D., 2016, Metallogenesis and geodynamics of the Lachlan Orogen: New (and old) insights from spatial and temporal variations in lead isotopes: Ore Geology Reviews, v. 76, p. 257–267.

Huston, D.L., Relvas, J.M.R.S., Gemmell, J.B., Drieberg, S., 2011, The role of granites in volcanic-hosted massive sulphide ore-forming systems: an assessment of magmatic–hydrothermal contributions: Mineralium Deposita, v. 46, p. 473–507.

Ibrahim, M.S., Kyser, T.K., 1991, Fluid inclusion and isotope systematics of the high-temperature Proterozoic Star Lake lode gold deposit, Northern Saskatchewan, Canada: Economic Geology, v. 86, p. 1468–1490.

Ickert, R.B., Williams, I.S., 2011, U–Pb zircon geochronology ofSilurian–Devonian granites in southeastern Australia: implications for the timing of the Benambran Orogeny and the I–S dichotomy: Australian Journal of Earth Sciences, v. 58, p. 501–516.

Innes, P.A., 1995, Geology and mineralization of the North Dundas mineral field, N-W Tasmania: Unpublished B.Sc. (Hons) thesis, University of Tasmania, 106 p.

Ishihara, S., 1977, The magnetite-series and ilmenite-series granitic rocks: Mining Geology, v. 27, p. 293–305.

Jacamon, F., Larsen, R.B., 2009, Trace element evolution of quartz in the charnockitic Kleivan granite, SW-Norway: the Ge/Ti ratio of quartz as an index of igneous differentiation: Lithos, v. 107, p. 281–291.

Jackson P.C.A., Krouse H.R., Gray J., 2000, The origin of greisen fluids of the Foley's zone, Cleveland tin deposit, Tasmania, Australia: Economic Geology, v. 95, p. 227–236.

Jiang, S.-Y., 1998, Stable and radiogenic isotope studies of tourmaline: An overview: Journal of the Czech Geological Society, v. 43, p. 75–90.

Jiang, S.-Y., Han, F., Shen, J.-Z., Palmer, M.R., 1999, Chemical and Rb–Sr, Sm–Nd isotopic systematics of tourmaline from the Dachang Sn-polymetallic ore deposit, Guangxi Province, P.R. China: Chemical Geology, v. 157, p. 49–67.

Jiang, S.-Y., Palmer, M.R., 1998, Boron isotope systematics of tourmaline in granites and pegmatites: a synthesis: European Journal of Mineralogy, v. 10, p. 1253–1265.

Jiang, S.-Y., Radvanec, M., Nakamura, E., Palmer, M., Kobayashi, K., Zhao, H.-X., Zhao, K.-D., 2008, Chemical and boron isotopic variations of tourmaline in the Hnilec granite-related hydrothermal system, Slovakia: Constraints on magmatic and metamorphic fluid evolution: Lithos, v. 106, p. 1–11.

Jiang, S.-Y., Yang, J.-H., Novák, M., Selway, J., 2003, Chemical and boron isotopic compositions of tourmaline from the Lavicky leucogranite, Czech Republic: Geochemical Journal, v. 37, p. 545–556.

Jones, A.T., 1993, The geology, geochemistry and structure of the Mount Darwin-South Darwin Peak area, western Tasmania: Unpublished B. Sc. (Hons) thesis, University of Tasmania, 106 p.

Jourdan, A.-L., Vennemann, T.W., Mullis, J., Ramseyer, K., Spiers, C.J., 2009, Evidence of growth and sector zoning in hydrothermal quartz from Alpine veins: European Journal of Mineralogy, v. 21, p. 219–231.

Kakihana, H., Kotaka, M., Satoh, S., Nomura, M., Okamoto, M., 1977, Fundamental studies on the ion-exchange separation of boron isotopes: Bulletin of the Chemical Society of Japan, v. 50, p. 158–163.

Kaliwoda, M., Marschall, H.R., Marks, M.A.H., Ludwig, T., Altherr, R., and Markl, G., 2011, Boron and boron isotope systematics in the peralkaline il ímaussaq intrusion (South Greenland) and its granitic country rocks: a record of magmatic and hydrothermal processes: Lithos, v. 125, p. 51–64.

Kamber, B.S., Gladu, A.H., 2009, Comparison of Pb purification by anion-exchnage resins methods and assessment of long-term reproducibility of Th/U/Pb ratio measurements by quadrupole ICP-MS: Geostandards and Geoanalytical Research, v. 33, p. 169–181.

Keay, S., Collins, W.J., Mcculloch, M.T., 1997, A three-component Sr–Nd isotopic mixing model for granitoid genesis, Lachlan Fold Belt eastern Australia: Geology, v.25, p. 307–310.

Keay, S., Steele, D., Compston, W., 1999, Identifying granite sources by SHRIMP U-Pb zircon geochronology:an application to the Lachlan foldbelt: Contributions to Mineralogy Petrology, v. 137, p. 323–341.

Keays, R.R., Jowitt, S.M., 2013, The Avebury Ni deposit, Tasmania: A case study of an unconventional nickel deposit: Ore Geology Reviews, v. 52, p. 4–17.

Kemp, A.I.S., Whitehouse, M.J., Hawkesworth, C.J., Alarcon, M.K., 2005, A zircon U-Pb study of metaluminous (I-type) granites of the Lachlan Fold Belt, southeastern Australia: implications for the high/low temperature classification and magma differentiation processes: Contributions to Mineralogy and Petrology, v. 150, p. 230–249.

King, R.W., 1990, Tourmaline from mesothermal gold deposits of the Superior Province, Canada: Textural, chemical, and isotopic relationships: Unpublished Ph.D. thesis, University Saskatchewan, 228 p.

King, R.W., Kerrich, R.W., 1989, Strontium isotope compositions of tourmaline from lode gold deposits of the Archean Abitibi greenstone belt (Ontario-Quebec, Canada): Implication for source reservoirs: Chemical Geology, v .79, p. 225–240.

Kirkham, R.V., Sinclair, W.D., 1988, Comb quartz layers in felsic intrusions and their relationship to porphyry deposits, in R.R.S. Taylor and Strong, D.F., eds., Recent advances in the geology of granite-related mineral deposits: Canadian Institute of Mining and Metallurgy, Special Volume 31, p. 50–71.

Kirwin, D.J., Seltmann, R. 2002, Unidirectional solidification textures associated with intrusion-related gold deposits: 11th Quadrennial IAGOD Symposium and GEO-CONGRESS, Nambia, p. 22–26.

Kitto, P. A., 1994, Structural and geochemical controls on mineralisation at Renison, Tasmania: Unpublished Ph.D. thesis, University of Tasmania, 484 p.

Klominsky, J., 1972, The Heemskirk granite massif, Western Tasmania: Unpublished Ph.D. thesis, University of Tasmania, 285 p.

Konopelko, D., Seltmann, R., Biske, G., Lepekhina, E., Sergeev, S., 2009, Possible source dichotomy of contemporaneous post-collisional barren I-type versus tin-bearing Atype granites, lying on opposite sides of the South Tien Shan suture: Ore Geology Reviews, v. 35, p. 206–216.

Kontak, D.J., Kerrich, R., 1997, An isotopic (C, O, Sr) study of vein gold deposits in the Meguma Terrane, Nova Scotia: Implication for source reservoirs: Economic Geology, v. 92, p. 161–180.

Kositcin, N., Everard, J. L., 2013, New SHRIMP U-Pb zircon ages from Tasmania: Mineral Resources Tasmania, Tasmanian Geological Survey Record 2013/02, p. 1–47.

Kosler, J., 2001, Laser-ablation ICPMS study of metamorphic minerals and processes, in Sylvester, P.J., ed., Laser-ablation-ICPMS in the Earth Sciences: principles and applications: Mineralogical Association of Canada Short Course Handbook 29, p. 185–202.

Kotzer, T.G., Kyser, T.K., King, R.W., Kerrich, R., 1993, An empirical oxygen- and hydrogen-isotope geothermometer for quartz-tourmaline and tourmaline-water: Geochimica et Cosmochimica Acta, v. 57, p. 3421–3426.

Kwak T.A.P., 1983, The geology and geochemistry of the zoned Sn-W-F-Be skarns at Mt. Lindsay, Tasmania, Australia: Economic Geology, v. 78, p. 1440–1465.

Kwak, T.A.P., Askins, P.W., 1981, Geology and genesis of the F-Sn-W (-Be-Zn) skarn (Wrigglite) at Moina, Tasmania: Economic Geology, v. 76, p. 439–467.

Kwak, T.A.P., Tan, T.H., 1981, The Geochemistry of zoning in skarn minerals at the King Island (Dolphin) Mine: Economic Geology, v. 76, p. 468–497.

Landtwing, M.R., Pettke, T., 2005, Relationships between SEM-cathodoluminescence response and trace- element composition of hydrothermal vein quartz: American Mineralogist, v. 90, p. 122–131.

Large, R., Doyle, M., Raymond, O., Cooke, D., Jones, A., Heasman, L., 1996, Evaluation of the role of Cambrian granites in the genesis of world class VHMS deposits in Tasmania: Ore Geology Reviews, v.10, p. 215–230.

Large, R.R., 1992, Australian volcanic-hosted massive sulphide deposits: features, styles, and genetic models: Economic Geology, v. 87, p. 471–510.

Larsen, R.B., Henderson, I., Ihlen, P.M., Jacamon, F., 2004, Distribution and petrogenetic behaviour of trace elements in granitic pegmatite quartz from South Norway: Contributions to Mineralogy and Petrology, v. 147, p. 615–628.

Larsen, R.B., Jacamon, F., Kronz, A., 2009, Trace element chemistry and textures of quartz during the magmatic hydrothermal transition of Oslo Rift granites: Mineralogical Magazine, v. 73, p. 691–707.

Le Ford, P., 1991, Enclaves of the Miocene Himalayan leucogranites, in Didier, J. and Barbarin, B., eds., Enclaves and Granite Petrology: Elsevier, Amsterdam, Developments in Petrology 13, p. 35–46.

Leaman, D.E., Richardson, R.G., 2003, A geophysical model of the major Tasmanian granitoids: Mineral Resources Tasmania, Tasmanian Geological Survey Record 2003/11, p.1–8.

Lehmann, B., 1982, Metallogeny of tin: Magmatic differentiation versus geochemical heritage: Economic Geology, v. 77, p. 50–59.

Lennox, P.G., Trzebski, R., Armstrong, R., Siebel, W., 2005, Structural evolution and granite chronology of the central Molong Zone, Eastern Lachlan fold belt, Australia: Australian Journal of Earth Sciences, v. 52, p. 79–99.

Lerchbaumer, L., Audétat, A., 2013, The metal content of silicate melts and aqueous fluids in subeconomically Mo mineralized granites: implications for porphyry Mo genesis: Economic Geology, v. 108, p. 987–1013.

Lickfold, V., Cooke, D.R., Crawford, A.J., Fanning, C.M., 2007, Shoshonitic magmatism and the formation of the Northparkes porphyry Cu – Au deposits, New South Wales: Australian Journal of Earth Sciences, v. 54, p. 417–444.

Lickfold, V., Cooke, D.R., Smith, S.G., Ullrich, T.D., 2003, Endeavour copper-gold porphyry deposits, Northparkes, New South Wales: intrusive history and fluid evolution: Economic Geology, v. 98, p. 1607–1636.

Linnen, R.L., Pichavant, M., Holtz, F., Burgess, S., 1995, The effect of fO_2 on the solubility, diffusion, and speciation of tin in haplogranitic melt at 850 ℃ and 2 kbar: Geochimica et Cosmochimica Acta, v. 59, p. 1579–1588.

London, D., 1999, Stability of tourmaline in peraluminous granite systems: the boron cycle from anatexis to hydrothermal aureoles: European Journal of Mineralogy, v. 11, p. 253–262.

London, D., Manning, D.A.C., 1995, Chemical variation and significance of tourmaline from Southwest England: Economic Geology, v. 90, p. 495–519.

London, D., Morgan VI, G.B., Wolf, M.B., 1996, Boron in granitic rocks and their contact aureoles: Reviews in Mineralogy and Geochemistry, v. 33, p. 299–330.

Lowenstern, J.B., Sinclair, W.D., 1996, Exsolved magmatic fluid and its role in the formation of comb-layered quartz at the Cretaceous Logtung W-Mo deposit, Yukon Territory, Canada: Transactions of the Royal Society of Edinburgh: Earth Sciences, v. 87, p. 291–303.

Ludwig, K. R., Silver, L. T., 1977, Lead-isotope inhomogeneity in Precambrian igneous K-feldspars: Geochimica et Cosmochimica Acta, v. 41, p. 1457–1471.

Lynch, G., Ortega, J., 1997, Hydrothermal alteration and tourmaline-albite equlibria at the Coxhealth porphyry Cu-Mo-Au deposit, Nova Scotia: The Canadian Mineralogist, v. 35, p. 79–94.

Lyons, P., Raymond, O.L., Duggan, M.B. (compiling editors), 2000, Forbes 1:250 000 geological sheet SI55-7, 2nd edition, Explanatory Notes: AGSO Record 2000/20, p. 230.

Maas, R., Kamenetsky, M.B., Sobolev, A.V., Kamenetsky, V.S., Sobolev, N.V., 2005, Sr-Nd-Pb isotopic evidence for a mantle origin of alkali chlorides and carbonates in the Udachnaya kimberlite, Siberia: Geology, v. 35, p. 549–552.

Mackenzie, D.E., Black, P.L., Sun, S.S., 1988, Origin of alkali-feldspar granites; an example from the Poimena Granite, northeastern Tasmania, Australia: Geochimica et Cosmochimica Acta, v. 52, p. 2507–2524.

Mahéo, G., Blichert-Toft, J., Pin, C., Guillot, S., Pecher, A., 2009, Partial melting of mantle and crustal sources beneath south Karakorum, Pakistan: implications for the miocene geodynamic evolution of the India-Asia convergence zone: Journal of Petrology, v. 50, p. 427–449.

Mao, J.W., Cheng, Y.B., Chen, M.H., Pirajno, F., 2013, Major types and time-space distribution of Mesozoic ore deposits in South China and their geodynamic settings: Mineralium Deposita, v. 48, p. 267–294.

Marks, M.A.W., Marschall, H.R., Schühle, P., Guth, A., Wenzel, T., Jacob, D.E., Barth, M., Gregor, M., 2013, Trace element systematics of tourmaline in pegmatitic and hydrothermal systems from the Variscan Schwarzwald (Germany): The importance of major element composition, sector zoning, and fluid or melt composition: Chemical Geology, v. 344, p. 73–90.

Marschall, H.R., Altherr, R., Kalt, A., Ludwig, T., 2008, Detrital, metamorphic and metasomatic tourmaline in high-pressure metasediments from Syros (Greece): intra-grain boron isotope patterns determined by secondary-ion mass spectrometry: Contributions to Mineralogy and Petrology, v. 155, p. 703–717.

Marschall, H.R., Jiang, S.-Y., 2011, Tourmaline isotopes: No element left behind: Elements, v. 7, p. 313–319.

Marschall, H.R., Ludwig, T., 2006, Re-examination of the boron isotopic composition of tourmaline from the Lavicky granite, Czech Republic, by secondary ion mass spectrometry: back to normal. Critical comment on "Chemical and boron isotopic compositions of tourmaline from the Lavicky leucogranite, Czech Repulic" by S.-Y. Jiang et al., Geochemical Journal, 37, 545-556, 2003: Geochemical Journal, v. 40, p.631–638.

Marschall, H.R., Ludwig, T., Altherr, R., Kalt, A., Tonarini, S., 2006, Syros metasomatic tourmaline: Evidence for very high-δ11B fluids in subduction zones: Journal of Petrology, v. 47, p. 1915–1942.

Masterman, G.J., Cooke, D.R., Berry, R.F., Walshe, J.L., Lee, A.W., Clark, A.H., 2005, Fluid chemistry, structural setting, and emplacement history of the Rosario Cu-Mo porphyry and Cu-Ag-Au epithermal veins, Collahuasi district, northern Chile: Economic Geology, v. 100, p. 835−862.

Maydagán, L., Franchini, M., Rusk, B., Lentz, D.R., McFarlane, C., Impiccini, A., Ríos, F.J., Rey, R., 2015, Porphyry to epithermal transition in the Altar Cu-(Au-Mo) deposit, Argentina, studied by Cathodoluminescence, LA-ICP-MS, and fluid inclusion analysis: Economic Geology, v. 110, p. 889–923.

McClenaghan, M.P., 2006a, The geochemistry of Tasmanian Devonian-Carboniferous granites and implications for the composition of their source rocks: Mineral Resources Tasmania, Tasmanian Geological Survey Record 2006/06, p.1–31.

McClenaghan, M.P., 2006b, Digital Geological Atlas 1:25 000 Scale Series, Mineral Resources Tasmania: Sheet 6041 Beaumaris, Sheet 6042 St Helens, and Sheet 6043 Binalong.

McClenaghan, M.P., Higgins, N.C., 1993, The age and intrusive relationships of granitoids of the Blue Tier Batholith, north-east Tasmania: Mineral Resources Tasmania Report 1993/33.

McClenaghan, M.P., Williams, P.R., 1982, Distribution and characterisation of granitoid intrusions in the Blue Tier area: Geological Survey of Tasmania Paper 4, p. 1–31.

Mcculloch, M.T., Woodhead, J.D., 1993, Lead isotope evidence for deep crustal-scale fluid transport during granite petrogenesis: Geochimica et Cosmochimica Acta, v. 57, p. 659–674.

McDonough, W. F., Sun, S.-S., 1995, The composition of the Earth: Chemical Geology, v. 120, p. 223–253.

McDougall, I., Leggo, P. J., 1965, Isotopic age determinations on granitic rocks from Tasmania: Journal of the Geological Society of Australia, v. 12, p. 295–332.

Meakin, N.S., Morgan, E.J. (compilers), 1999, Dubbo 1:250 000 geological sheet SI/55-4, 2nd edition, Explanatory Notes: Geological Survey of New South Wales, Sydney, p. 504.

Meffre, S., Direen, N.G., Crawford, A.J., Kamenetsky, V., 2004, Mafic volcanic rockson King Island, Tasmania: evidence for 579 Ma break-up in east Gondwana: Precambrian Research, v. 135, p. 177–191.

Mercadier, J., Richard, A., Cathelineau, M., 2012, Boron- and magnesium-rich marine brines at the origin of giant unconformity-related uranium deposits: $\delta^{11}B$ evidence from Mg-tourmalines: Geology, v. 40, p. 231–234.

Meyer, C., Wunder, B., Meixner, A., Romer, R., Heinrich, W., 2008, Boron-isotope fractionation between tourmaline and fluid: An experimental re-investigation: Contributions to Mineralogy and Petrology, v. 156, p. 259-267.

Mlynarczyk, M.S.J., Williams-Jones, A.E., 2006, Zoned tourmaline associated with cassiterite: Implications for fluid evolution and Tin mineralization in the San Rafeal Sn-Cu deposit, southeastern Peru: The Canadian Mineralogist, v. 44, p. 347–365.

Moresi, L., Betts, P.G., Miller, M.S., Cayley, R.A., 2014. Dynamics of continental accretion: Nature, v. 508, p. 245–248.

Morgan VI, G.B., 2016, A spreadsheet for calculating normative mole fractions of end-member species for Na-Ca-Li-Fe2+-Mg-Al tourmalines from electron microprobe data: American Mineralogist, v.101, p. 111–119.

Mortensen, J.K., Gemmell, J.B., McNeill, A.W., Friedman, R.M., 2015, High-Precision U-Pb Zircon Chronostratigraphy of the Mount Read Volcanic Belt in Western Tasmania, Australia: Implications for VHMS Deposit Formation: Economic Geology, v. 110, p. 445–468.

Mueller, A.G., De Laeter, J.R., Groves, D.I., 1991, Strontium isotope systematics of hydrothermal minerals from epigenetic Archean gold deposits in the Yilgarn Block, Western Australia: Economic Geology, v. 86, p. 780–809.

Muir, R.J., Ireland, T.R., Weaver, S.D., Bradshaw, J.D., 1994, Ion microprobe U-Pb zircon geochronology of granitic magmatism in the Western Province of the South Island, New Zealand: Chemical Geology, v. 113, p. 171–189.

Muir, R.J., Ireland, T.R., Weaver, S.D., Bradshaw, J.D., 1996, Ion microprobe dating of Paleozoic granitoids: Devonian magmatism in New Zealand and correlations with Australia and Antarctica: Chemical Geology, v. 127, p. 191–210.

Müller, A., Herrington, R., Armstrong, R., Seltmann, R., Kirwin, D., Stenina, N., Kronz, A., 2010, Trace elements and cathodoluminescence of quartz in stockwork veins of Mongolian porphyry-style deposits: Mineralium Deposita, v. 45, p. 707–727.

Müller, A., Koch-Müller, M., 2009, Hydrogen speciation and trace element contents of igneous, hydrothermal and metamorphic quartz from Norway: Mineralogical Magazine, v. 73, p. 569–583.

Münker, C., 2000, Pb-Nd isotopes indicate the origin of island arc terranes in the Early Paleozoic Pacific: The Journal of Geology, v. 108, p. 233–242.

Olade, A.M., 1980, Geochemical characteristics of tin-bearing and tin-barren granites, Northern Nigeria: Economic Geology, v.75, p. 71–82.

Ostapenko, G. T., Tarashchan, A. N., and Mitsyuk, B. M., 2007, Rutile-quartz geothermobarometer: Geochemistry International, v. 45, p. 506–508.

Pal, D.C, Trumbull, R.B., Wiedenbeck, M., 2010, Chemical and boron isotope compositions of tourmaline from the Jaduguda U (–Cu–Fe) deposit, Singhbhum shear zone, India: Implications for the sources and evolution of mineralizing fluids: Chemical Geology, v. 277, p. 245–260.

Palmer, M.R., London, D., Morgan, V.I.G.B., Babb, H.A., 1992, Experimental determination of fractionation of $^{11}B/^{10}B$ between tourmaline and aqueous vapor: Chemical Geology, v. 101, p. 123–129.

Palmer, M.R., Slack, J.F., 1989, Boron isotopic composition of tourmaline from massive sulfide deposits and tourmalinites: Contributions to Mineralogy and Petrology, v. 103, p. 434–451.

Palmer, M.R., Swihart, G.H., 1996, Boron isotope geochemistry: An overview: Reviews in Mineralogy and Geochemistry, v. 33, p. 709–744.

Pankhurst, R.J., Weaver, S.D., Bradshaw, J.D., Storey, B.C., Ireland, T.R., 1998, Geochronology and geochemistry of pre-Jurassic superterranes in Marie Byrd Land, Antarctica: Journal of Geophysical Research, v. 103, p. 2529–2547.

Paton, C., Woodhead, J.D., Hellstrom, J.C., Hergt, J.M, Greig, A., Maas, R., 2010, Improved laser ablation U-Pb zircon geochronology through robust down-hole fractionation correction: Geochemistry, Geophysics, Geosystems, v. 11, p. 1525–2027.

Patterson, D.J., Ohmoto, H., Solomon, M., 1981, Geologic setting and genesis of cassiterite-sulfide mineralization at Renison Bell, Western Tasmania: Economic Geology, v. 76, p. 393–438.

Peccerillo, A, Taylor, S.R., 1976, Geochemistry of Eocene calc-alkaline volcanic rocks from the Kastamonu area, Northern Turkey: Contributions to Mineralogy and Petrology, v. 58, p. 63–81.

Perkins, C., Walshe, J.L., 1993, Geochronology of the Mount Read Volcanics, Tasmania, Australia: Economic Geology, v. 88, p. 1176–1197.

Perugini, D., Poli, G., 2007, Tourmaline nodules from Capo Bianco aplite (Elba Island, Italy): an example of diffusion limited aggregation growth in a magmatic system: Contributions to Mineralogy and Petrology, v. 153, p. 493–508.

Pesquera, A., Torres-Ruiz, J., Garcia-Casco, A., Gil-Crespo, P.P., 2013, Evaluating the controls on tourmaline formation in granitic systems: A case study on peraluminous granites from the Central Iberian Zone (CIZ), Western Spain: Journal of Petrology, v. 54, p. 609–634.

Pesquera, A., Torres-Ruiz, J., Gil-Crespo, P., Jiang, S.-Y., 2005, Petrographic, Chemical and B-Isotopic Insights into the Origin of Tourmaline-Rich Rocks and Boron Recycling in the Martinamor Antiform (Central Iberian Zone, Salamanca, Spain): Journal of Petrology, v. 46, p. 1013–1044.

Pettke, T., Oberli, F., Audétat, A., Guillong, M., Simon, A.C., Hanley, J.J., Klemm, L.M., 2012, Recent developments in element concentration and isotope ratio analysis of individual fluid inclusions by laser ablation single and multiple collector ICP-MS: Ore Geology Reviews, v. 44, p. 10–38.

Plimer, I.R., Lees, T.C., 1988, Tourmaline-rich rocks associated with the submarine Hydrothermal Rosebery Zn-Pb-Cu-Ag-Au deposit and granites in Western Tasmania, Australia: Mineralogy and Petrology, v. 38, p. 81–103.

Powell, C.McA., 1992, New perspectives on Tasmanian geology: Bulletin of Geological Survey of Tasmania, v.70, p. 177–187.

Purvis, J.G., 1989, Tasmanian tin prospects part 1: West Tasmania Tin Province: Tasmanian Geological Survey Bulletin, p. 51–64.

Richards, J.R., Singleton, O.P., 1981, Palaeozoic Victoria, Australia: igneous rocks, ages and their interpretation: Journal of the Geological Society of Australia, v. 28, p. 395– 421.

Roberts, S., Palmer, M.R., Waller, L., 2006, Sm-Nd and REE charactcteristics of tourmaline and scheelite from the Björkdal gold deposit, northern Sweden: evidence for an intrusion-related gold deposit?: Economic Geology, v. 101, p. 1415–1425.

Roedder, E., 1984, Fluid inclusions: Reviews in Mineralogy, v. 12, 644 p.

Romer, R.L., Kroner, U., 2016, Phanerozoic tin and tungsten mineralization–Tectonic controls on the distribution of enriched protoliths and heat sources for crustal melting: Gondwana Research, v. 31, p. 60–95.

Rossiter, A.G., 2003, Granitic rocks of the Lachlan Fold Belt in Victoria, potential keys to the composition of the lower-middle crust, in Birch W. D., ed., Geology of Victoria: Geological Society of Australia Special Publication 23, p. 217–237.

Rozendaal, A., Bruwer, L., 1995, Tourmaline nodules: indicators of hydrothermal alteration and Sn-Zn-(W) mineralization in the Cape Granite Suite, South Africa: Journal of African Earth Sciences, v. 21, p.141–155.

Rusk, B., Koenig, A., Lowers, H., 2011, Visualizing trace element distribution in quartz using cathodoluminescence, electron microprobe, and laser ablation-inductively coupled plasma-mass spectrometry: American Mineralogist, v. 96, p. 703–708.

Rusk, B.G., Reed, M.H., 2002, Scanning electron microscope-cathodoluminescence of quartz reveals complex growth histories in veins from the Butte porphyry copper deposit, Montana: Geology, v. 30, p. 727–730.

Rusk, B.G., Reed, M.H., Dilles, J.H., 2008, Fluid inclusion evidence for magmatic- hydrothermal fluid evolution in the porphyry copper-molybdenum deposit at Butte, Montana: Economic Geology, v. 103, p. 307–334.

Rusk, B.G., Reed, M.H., Dilles, J.H., Kent, A.J.R., 2006, Intensity of quartz cathodoluminescence and trace-element content in quartz from the porphyry copper deposit at Butte, Montana: American Mineralogist, v. 91, p. 1300–1312.

Samson, I.M., Sinclair, W.D., 1992, Magmatic hydrothermal fluids and the origin of quartz-tourmaline orbicules in the Seagull Batholoth, Yukon Tertitory: The Canadian Mineralogist, v. 30, p. 937–954.

Sanchez-Valle, C., Reynard, B., Daniel, I., Lecuyer, C., Martinez, I., Chervin, J.C., 2005, Boron isotope fractionation between minerals and fluids: new insights from in situ high pressure–high temperature vibrational spectroscopic data: Geochimica et Cosmochimica Acta, v. 69, p. 4301–4313.

Sato, K., 2012, Sedimentary crust and metallogeny of granitoid affinity: implications from the geotectonic histories of the Circum-Japan Sea region, Central Andes and southeastern Australia: Resource Geology, v. 62, p. 329–351.

Sawka, W.N., Heizler, M.T., Kistler, R.W., Chappell, B.W., 1990, Geochemistry of highly fractionated I- and S-type granites from the tin–tungsten province of western Tasmania: Geological Society of America Special Paper 246, p. 161–179.

Scaillet, B., Pichavant, M, Roux, J., 1995, Experimental crystallization of leucogranite magmas: Journal of Petrology, v. 36, p. 663–705.

Schaltegger, U., Pettke, T., Audétat, A., Reusser, E., Heinrich, C.A., 2005, Magmatic-to-hydrothermal crystallization in the W–Sn mineralized Mole Granite (NSW, Australia) Part I: Crystallization of zircon and REE-phosphates over three million years—a geological and U-Pb geochronological study: Chemical Geology, v. 220, p. 215–235.

Schmitz, C., and Burt, D.M., 1990, The Black Pearl mine, Arizona; Wolframite veins and stockscheider pegmatite related to an albitic stock: Geological Society of America Special Papers 246, p. 221–232.

Searle, M.P., Whitehouse, M.J., Robb, L.J., Ghani, A.A., Hutchison, C.S., Sone, M., Ng, S.W.-P., Roselee, M.H., Chung, S.-L., Oliver, G.J.H., 2012, Tectonic evolution of the Sibumasu– Indochina terrane collision zone in Thailand and Malaysia: constraints from new U–Pb zircon chronology of SE Asian tin granitoids: Journal of the Geological Society, v. 169, p. 489–500.

Seedorff, E., Dilles, J.H., Proffett, J.M., Jr., Einaudi, M.T., Zurcher, L., Stavast, W.J.A., Johnson, D.A., Barton, M.D., 2005, Porphyry deposits: Characteristics and origin of hydrogen features: Economic Geology 100th Anniversary Volume, p. 251–298.

Seyedolali, A., Krinsley, D.H., Boggs, S., O'Hara, P.F., Dypvik, H., Goles, G.G., 1997, Provenance interpretation of quartz by scanning electron microscope-cathodoluminescence fabric analysis: Geology, v. 25, p. 787–790.

Seymour, D.B., 1989, Geological Atlas 1:50 000 Series, Sheet 36 (8015S), St Valentines: Explanatory Report Geological Survey Tasmania.

Seymour, D.B., Green, G.R., Calver, C.R., 2007, The geological and mineral deposits of Tasmania: a summary: Tasmanian Geological Survey Bulletin 72, p. 1–29.

Seymour, D.B., Woolward, I.R., McClenaghan, M.P., Bottrill, R.S., 2011, Stratigraphic revision and re-mapping of the Mathinna Supergroup between the River Tamar and the Scottsdale Batholith, northeast Tasmania, Explanatory report for parts of the 1:25 000 scale Low Head, Tam O'Shanter, Weymouth, Retreat, Lilydale,

Bridport, Bowood, Nabowla, Lisle and Patersonia map sheets. Explanatory Report 1:25 000 Scale Digital Geological Map Series Mineral Resources Tasmania 4, p. 1–82.

Shabaga, B.M., Fayek, M., Hawthorne, F.C., 2010, Boron and lithium isotopic compositions as provenance indicators of Cu-bearing tourmalines: Mineralogical Magazine, v. 74, p. 241–255.

Shannon, J. R., Walker, B. M., Carten, R. B., Geraghty, E. P., 1982, Unidirectional solidification textures and their significance in determining relative ages of intrusions at the Henderson Mine, Colorado: Geology, v. 10, p. 293–297.

Shewfelt, D., 2005, The nature and origin of Western Australian tourmaline nodules; A petrological, geochemical and isotopic study: Unpublished M.Sc. thesis, University of Saskatchewan, 146 p.

Shewfelt, D., Ansdell, K., Sheppard, K., 2005, The origin of tourmaline nodules in granites: preliminary findings from the Paleoproterozoic Scrubber Granite: Geological Survey of Western Australia Annual Review, p. 59–63.

Shinohara, H., Kazahaya, K., 1995, Degassing processes related to magma-chamber crystallization, in Thompson, J.F.H., ed., Magmas, Fluids, and Ore Deposits: Mineralogical Association of Canada Short Course 23, p. 47–70.

Shore, M., Fowler, A.D., 1996, Oscillatory zoning in minerals: a common phenomenon: The Canadian Mineralogist, v. 34, p.1111–1126.

Siegel, K., Wagner, T., Trumbull, R.B., Jonssond, E., Matalin, G., Wälle, M., Heinrich, C.A., 2016, Stable isotope (B, H, O) and mineral-chemistry constraints on the magmatic to hydrothermal evolution of the Varutträsk rare-element pegmatite (Northern Sweden): Chemical Geology, v. 421, p. 1–16.

Sillitoe, R. H., 2010, Porphyry copper systems: Economic Geology, v. 105, p. 3–41.

Sinclair, W.D., Richardson, J.M., 1992, Quartz-tourmaline orbicules in the Seagull Batholith, Yukon Territory: The Canadian Mineralogist, v. 30, p. 923–935.

Singoyi, B., Zaw, K., 2000, A petrological and fluid inclusion study of magnetite-scheelite skarn mineralization at Kara: implications for ore genesis: Chemical Geology, v. 173, p. 239–253.

Skewes, M.A., Holmgren, C., Stern, C.R., 2003, The Donoso copper-rich, tourmaline-bearing breccia pipe in central Chile: petrologic, fluid inclusion and stable isotope evidence for an origin from magmatic fluids: Mineralium Deposita, v. 38, p. 2–21.

Slack, J.F., 1996, Tourmaline associations with hydrothermal ore deposits: Reviews in Mineralogy and Geochemistry, v. 33, p. 559–664.

Slack, J.F., Palmer, M.R., Stevens, B.J., Branes, R.G., 1993, Origin and significance of tourmaline-rich rocks in the Broken Hill district, Australia: Economic Geology, v. 88, p. 505–541.

Slack, J.F., Trumbull, R.B., 2011, Tourmaline as a recorder of ore-forming processes: Elements, v.7, p. 321–326.

Sláma, J., Kosler, J., Condon, D.J., Crowley, J.L., Gerdes, A., Hanchar, J.M., Horstwood, M.S.A., Morris, G.A., Nasdala, L., Norberg, N., Schaltegger, U., Schoene, B., Tubrett, M.N., Whitehouse, M.J., 2008, Plesovice zircon - A new natural reference material for U-Pb and Hf isotopic microanalysis: Chemical Geology, v. 249, p. 1–35.

Smith, M.P., Yardley, B.W.D., 1996, The boron isotopic composition of tourmaline as a guide to fluid porcess in the southwestern English orefield: An ion microprobe study: Geochimica et Cosmochimica Acta, v. 60, p. 1415–1427.

Solomon, M., 1981, An introduction to the geology and metallic ore deposits of Tasmania: Economic Geology, v. 76, p. 194–208.

Solomon, M., Groves, D.I., 2000, The geology and origin of Australia's mineral deposits: Centre for Ore Deposits Research, University of Tasmania and Centre for Global Metallogeny, University of Western Australia, Publication No.32, p. 428–521.

Steele-MacInnisn, M., Lecumberri-Sanchez, P., Bodnar, R.J., 2012, HOKIEFLINCS_H_2O-NACL: A Microsoft Excel spreadsheet for interpreting microthermometric data from fluid inclusions based on the PVTX properties of H_2O–NaCl: Computers & Geosciences, v. 49, p. 334–337.

Sun, S.-S., Higgins, N.C., 1996, Neodymium and strontium isotope study of the Blue Tier Batholith, NE Tasmania, and its bearing on the origin of tin-bearing alkali feldspar granites: Ore Geology Reviews, v. 10, p. 339–365.

Sun, S.-S., McDonough, W. F., 1989, Chemical and isotopic systematics of oceanic basalts: implications for mantle composition and processes, in Saunders, D., and Norry, M.J., eds., Magmatism in the Ocean Basins: Geological Society, London, v. 42, p. 313–345.

Swihart, G.H., Moore, P.B., 1989, A reconnaissance of the boron isotopic composition of tourmaline: Geochimica et Cosmochimica Acta, v. 53, p. 911–916.

Tanner, D., Henley, R.W., Mavrogenes, J.A., Holden, P., 2013, Combining in situ isotopic, trace element and textural analyses of quartz from four magmatic-hydrothermal ore deposits: Contributions to Mineralogy and Petrology: v. 166, p. 1119–1142.

Taylor, B.E., Food, E.E., Friedrichsen, H., 1979, Stable isotope and fluid inclusion studies of gem-bearing pegmatite-aplite dikes, San Diego Co., California: Contributions to Mineralogy and Petrology, v. 68, p. 187–205.

Taylor, B.E., Slack, J.F., 1984, Tourmalines from Appalachian-Caledonian massive sulfide deposits: Textual, chemical, and isotopic relationships: Economic Geology, v. 79, p. 1703–1726.

Taylor, H.P., Jr., 1974, The application of oxygen and hydrogen isotope studies to problems of hydrothermal alteration and ore deposition: Economic Geology, v. 69, p. 843–883.

Taylor, H.P., Jr., 1978, Oxygen and hydrogen isotope studies of plutonic granitic rocks: Earth and Planetary Science Letters, v. 38, p. 177–210.

Taylor, J.R., and Wall, V.J., 1992, The behavior of tin in granitoid magmas: Economic Geology, v. 87, p. 403–420.

Taylor, R.P., Ikingura, J.R., Fallick, A.E., Huang, Y., Watkinson, D.H., 1992, Stable isotope compositions of tourmalines from granites and related hydrothermal rocks of the Karagwe-Ankolean belt, northwest Tanzania: Chemical Geology, v. 94, p. 215–227.

Thomas, J., Bruce Watson, E., Spear, F., Shemella, P., Nayak, S., Lanzirotti, A., 2010, TitaniQ under pressure: the effect of pressure and temperature on the solubility of Ti in quartz: Contributions to Mineralogy and Petrology, v. 160, p. 743–759.

Thomas, R., Förster, H.J., Heinrich, W., 2003, The behaviour of boron in a peraluminous granite-pegmatite system and associated hydrothermal solutions: a melt and fluid-inclusion study: Contributions to Mineralogy and Petrology, v. 144, p. 457–472.

Thomas, R., Webster, J.D., 2000, Strong tin enrichment in a pegmatite-forming melt: Mineralium Deposita, v. 35, p. 570–582.

Tornos, F., Wiedenbeck, M., Velasco, F., 2012, The boron isotope geochemistry of tourmaline-rich alteration in the IOCG systems of northern Chile: implications for a magmatic-hydrothermal origin: Mineralium Deposita, v. 47, p. 483–499.

Trumbull, R.B., Beurlen, H., Wiedenbeck, M., and Soares, D.R., 2013. The diversity of B-isotope variations in tourmaline from rare-element pegmatites in the Borborema Province of Brazil: Chemical Geology, v. 352, p. 47–62.

Trumbull, R.B., Chaussidon, M., 1999, Chemical and boron isotopic composition of magmatic and hydrothermal tourmalines from the Sinceni granite-pegmatite system in Swaziland: Chemical Geology, v. 153, p. 125–137.

Trumbull, R.B., Krienitz, M.S., Gottesmann, B., Wiedenbeck, M., 2008, Chemical and boron-isotope variations in tourmalines from an S-type granite and its source rocks: the Erongo granite and tourmalinites in the Damara Belt, Namibia: Contributions to Mineralogy and Petrology, v. 155, p. 1–18.

Tulloch, A.J., Ramezani, J., Kimbrough, D.L., Faure, K., Allibone, A.H., 2009, U-Pb geochronology of mid-Paleozoic plutonism in western New Zealand: Implications for S-type granite generation and growth of the east Gondwana margin: Geological Society of America Bulletin, v. 121, p. 1236–1261.

Turnbull, R., Tulloch, A., Ramezani, J., Jongens, R., 2016, Extension-facilitated pulsed S-I-A-type "flare-up" magmatism at 370 Ma along the southeast Gondwana margin in New Zealand: Insights from U-Pb geochronology and geochemistry: Geological Society of America Bulletin, v. 128, p. 1500–1520.

Turner, N.J., Black, L.P., Higgins, N.C., 1986, The St Marys Porphyrite—a Devonian ash-flow tuff and its feeder: Australian Journal of Earth Sciences, v. 33, p. 201–218.

Turner, N.J., Black, L.P., Kamperman, M., 1998, Dating of Neoproterozoic and Cambrian orogenies in Tasmania: Australian Journal of Earth Sciences, v. 45, p. 789–806.

van Hinsberg, V., Marschall, H., 2007, Boron isotope and light element sector zoning in tourmaline: Implications for the formation of B-isotopic signatures: Chemical Geology, v. 238, p. 141–148.

van Hinsberg, V.J., 2011, Preliminary experimental data on trace-element partitioning between tourmaline and silicate melt: The Canadian Mineralogist, v. 49, p. 153–163.

van Hinsberg, V.J., Henry, D.J., Marschall, H.R., 2011a, Tourmaline: an ideal indicator of its host environment: The Canadian Mineralogist, v. 49, p. 1–16.

van Hinsberg, V.J., Henry, D.J., Dutrow, B.L., 2011b, Tourmaline as a petrologic forensic mineral: A unique recorder of its geologic past: Elements, v. 7, p. 327–332.

van Hinsberg, V.J., Schumacher, J.C., Kearns, S., Mason, P.R.D., Franz, G., 2006, Hourglass sector zoning in metamorphic tourmaline and resultant major and trace-element fractionation: American Mineralogist, v. 91, p. 717–728.

Veksler, I., Thomas, R., Schmidt, C., 2002, Experimental evidence of three coexisting immiscible fluids in synthetic granitic pegmatite: American Mineralogist, v. 87, p. 775–779.

Veksler, I.V., 2004, Liquid immiscibility and its role at the magmatic-hydrothermal transition: a summary of experimental studies: Chemical Geology, v. 210, p. 7–31.

Veksler, I.V., Thomas, R., 2002, An experimental study of B-, P- and F-rich synthetic granite pegmatite at 0.1 and 0.2 GPa: Contributions to Mineralogy and Petrology, v. 143, p. 673–683.

Vicary, M.J., 2004, Digital geological atlas 1:25000 scale series, Sheet 3237 Ahrberg and Sheet 3238 Hardwicke: Mineral Resources Tasmania.

Walshe, J.L., Solomon, M., Whitford, D.J., Sun, S-S, Foden, J.D., 2011, The role of the mantle in the genesis of tin deposits and tin provinces of Eastern Australia: Economic Geology, v. 106, p. 297–305.

Wark, D.A., Watson, E.B., 2006, TitaniQ: a titanium-in-quartz geothermometer: Contributions to Mineralogy and Petrology, v. 152, p. 743–754.

Waterhouse, L.L., 1916, The South Heemskirk Tinfield: Tasmanian Geological Survey Bulletin, No. 21, 1–450.

Weil, J.A., 1993, A review of the EPR spectroscopy of the point defects in α-quartz: The decade 1982–1992: In Helms, C.R. and Deal, B.E. (Eds.), Physics and Chemistry of SiO_2 and the Si–SiO_2 interface 2: Plenum Press, New York, p. 131–144.

Weis, D., Kieffer, B., Maerschalk, C., Barling, J., de Jong., J., Williams, G. A., Hanano, D., Pretorius, W., Mattielli, N., Scoates, J.S., Goolaerts, A., Friedman, R.M., Mahoney, J.B., 2006, High-precision isotopic characterization

of USGS reference materials by TIMS and MC-ICP-MS: Geochemistry, Geophysics, Geosystems, v. 7, Q08006, doi:10.1029/2006GC001283.

Weston-Dunn J.G., 1922, The economic geology of the Mount Bischoff tin deposits, Tasmania: Economic Geology, v. 17, p. 153–193.

Wiedenbeck, M., Alle, P., Corfu, F., Griffin W.L., Meier, M., Oberli, F., Vonquadt A., Roddick, J.C., Speigel, W., 1995, 3 Natural Zircon Standards for U-Th-Pb, Lu-Hf, Trace-Element and REE Analyses: Geostandards Newsletter, v. 19, p. 1–23.

Wilkinson, J.J., 2001, Fluid inclusions in hydrothermal ore deposits: Lithos, v. 55, p. 229–272.

Wilkinson, J.J., Chang, Z., Cooke, D.R., Baker, M.J., Wilkinson, C.C., Inglis, S., Chen H., Gemmell, J.B., 2015, The chlorite proximitor: A new tool for detecting porphyry ore deposits: Journal of Geochemical Exploration, v.152, p. 10–26.

Williams, E., 1978, Tasman fold belt system in Tasmania: Tectonophysics, v. 48, p. 159–206.

Williams, E., McClenaghan, M.P., Collins, P.L.F., 1989, Mid-Palaeozoic deformation, granitoids and ore deposits, in Burrett, C.F., and Martin, E.L., eds., Geology and mineral resources of Tasmania: Geological Society of Australia, Special Publication 15, p. 238–292.

Williamson, B. J., Spratt, J., Adams, J. T., Tindle, A. G., and Stanley, C. J., 2000, Geochemical constraints from zoned hydrothermal tourmalines on fluid evolution and Sn mineralization: an example from fault breccias at Roche, SW England: Journal of Petrology, v. 41, p. 1439–1453.

Williamson, B.J., Müller, A., and Shail, R.K., 2010, Source and partitioning of B and Sn in the Cornubian batholith of southwest England: Ore Geology Reviews, v. 38, p. 1–8.

Wilson, A.J., Cooke, D.R., Happer, B.L., 2003, The Ridgeway gold-copper deposit: A high-grade alkalic porphyry deposit in the Lachlan Fold Belt, New South Wales, Australia: Economic Geology, v. 98, p. 1637–1666.

Wolf, M.B., London, D., 1997, Boron in granitic magmas: stability of tourmaline in equilibrium with biotite and cordierite: Contributions to Mineralogy and Petrology, v. 130, p. 12–30.

Wombacher, F., Muenker, C., 2000, Pb, Nd, and Sr isotopes and REE systematic of Cambrian sediments from New Zealand: Implications for the reconstruction of the early Paleozoic Gondwana margin along Australia and Antarctica: Journal of Geology, v. 108, p. 663–686.

Woodhead, J.D., 2002, A simple method for obtaining highly accurate Pb isotope data by MC-ICP-MS: Journal of Analytical Atomic Spectrometry, v. 17, p. 1381–1385.

Woodhead, J.D., Hergt, J.M., 2000, Pb-Isotope Analyses of USGS Reference Materials: Geostandards Newsletter, v. 24, p. 33–38.

Wormald, R.J., Price, R.C., Kemp, A.I.S., 2004, Geochemistry and Rb–Sr geochronology of the alkaline–peralkaline Narraburra Complex, central southern New South Wales; tectonic significance of Late Devonian granitic magmatism in the Lachlan Fold Belt: Australian Journal of Earth Sciences, v. 51, p. 369–384.

Wright, J.H., Kwak, T.A.P., 1989, Tin-bearing greisens of Mount Bisehoff, Northwestern Tasmania, Australia: Economic Geology, v. 84, p. 551–574.

Xavier, R.P., Wiedenbeck, M., Trumbull, R.B., Dreher, A.M., Monteiro, L.V.S., Rhede, D., de Araújo, C.E.G., Torresi, I., 2008, Tourmaline B-isotopes fingerprint marine evaporites as the source of high-salinity ore fluids in iron oxide copper-gold deposits, Carajás Mineral Province (Brazil): Geology, v. 36, p. 743–746.

Yakymchuk, C., Brown, C.R., Brown, M., Siddoway, C.S., Fanning, C.M., Korhonen, F.J., 2015, Paleozoic evolution of western Marie Byrd Land, Antarctica: Geological Society of America Bulletin, v. 127, p. 1464–1484.

Yavuz, F., Iskenderoglu, A., and Jiang, S.-Y., 1999, Tourmaline compositions from the Salikvan porphyry Cu-Mo deposit and vicinity, northeastern Turkey: The Canadian Mineralogist, v. 37, p. 1007–1023.

Yavuz, F., Jiang, S.-Y., Karakaya, N., Karakaya, M. Ç., Yavuz, R., 2011, Trace-element, rare-earth element and boron isotopic compositions of tourmaline from a vein-type Pb–Zn–Cu ± U deposit, NE Turkey: International Geology Review, v.53, p. 1–24.

Zaw, K., Singoyi, B., 2000, Formation of magnetite-scheelite skarn mineralization at Kara: evidence from mineral chemistry and stable isotopes: Economic Geology, v. 95, p. 1215–1230.

Zeebe, R.E., 2005, Stable boron isotope fractionation between dissolved $B(OH)_3$ and $B(OH)_4^-$: Geochimica et Cosmochimica Acta, v. 69, p. 2753–2766.

Zheng, Y.-F., 1993, Calculations of oxygen isotope fractionation in anhydrous silicate minerals: Geochimica et Cosmochimica Acta, v. 57, p. 1079–1091.

References

Appendices

Appendix 1 Rock catalogue

Sample NO.	District	Rock name	Easting	Southing	Elevation(m)	Datum	Rock Classification	Main Mineral and feature
WT12WH01	West Tasmania	Massive sulphides	none	none		WGS84	Massive sulphide	Mostly pyrite, quartz
WT12WH02	West Tasmania	Pieman Heads	144°55'40.01"	41°43'15.00"	10	WGS84	Fine-grained granite	Quartz and feldspar, biotite
WT12WH03	West Tasmania	Pieman Heads	144°55'40.01"	41°43'15.00"	10	WGS84	Coarse-grained granite	Quartz and feldspar
WT12WH04	West Tasmania	Pieman Heads	144°55'40.01"	41°43'15.00"	10	WGS84	Granite	Quartz, feldspar, tourmaline
WT12WH05	West Tasmania	Pieman Heads	144°55'40.01"	41°43'15.00"	10	WGS84	Granite	Quartz, feldspar, tourmaline
WT12WH06	West Tasmania	Pieman Heads	144°55'40.01"	41°43'15.00"	10	WGS84	Granite	Quartz, feldspar, tourmaline
WT12WH07	West Tasmania	Pieman Heads	144°55'40.01"	41°43'15.00"	10	WGS84	Granite	Quartz, feldspar, tourmaline
WT12WH08	West Tasmania	Pieman Heads	144°55'40.01"	41°43'15.00"	10	WGS84	Granite	Quartz, feldspar, tourmaline
WT12WH09	West Tasmania	Pieman Heads	144°55'40.01"	41°43'15.00"	10	WGS84	Granite	Quartz, feldspar, tourmaline
WT12WH10	West Tasmania	Pieman Heads	144°55'40.01"	41°43'15.00"	10	WGS84	Granite	Quartz, feldspar, tourmaline
WT12WH11	West Tasmania	Pieman Heads	144°53'37.87"	41°43'13.75"	3	WGS84	Coarse-grained granite	Quartz and feldspar
WT12WH12	West Tasmania	Pieman Heads	144°53'37.87"	41°43'13.75"	3	WGS84	Granite	Quartz, feldspar, tourmaline
WT12WH13	West Tasmania	Pieman Heads	144°53'37.87"	41°43'13.75"	3	WGS84	Granite	Quartz, feldspar, tourmaline
WT12WH14	West Tasmania	Pieman Heads	144°53'37.87"	41°43'13.75"	3	WGS84	Granite	Quartz and feldspar, biotite
WT12WH15	West Tasmania	Pieman Heads	144°53'37.87"	41°43'13.75"	3	WGS84	Granite	Quartz and feldspar, biotite
WT12WH16	West Tasmania	Pieman Heads	144°55'36.38"	41°43'06.20"	2	WGS84	Granite	Quartz, feldspar, tourmaline
WT12WH17	West Tasmania	Pieman Heads	144°55'36.38"	41°43'06.20"	2	WGS84	Granite	Quartz, feldspar, tourmaline
WT12WH18	West Tasmania	Pieman Heads	144°55'36.38"	41°43'06.20"	2	WGS84	Granite	Quartz, feldspar, tourmaline
WT12WH19	West Tasmania	Pieman Heads	144°56'51.36"	41°42'58.61"	4	WGS84	Granite	Quartz, feldspar, tourmaline
WT12WH20	West Tasmania	Trial Harbour, Heemskirk	145°09'23.93"	41°55'20.64"	3	WGS84	White granite	Quartz, feldspar, tourmaline
WT12WH21	West Tasmania	Trial Harbour, Heemskirk	145°09'23.93"	41°55'20.64"	3	WGS84	White granite	Quartz, feldspar, tourmaline
WT12WH22	West Tasmania	Trial Harbour, Heemskirk	145°09'23.93"	41°55'20.64"	3	WGS84	White granite	Quartz, feldspar, tourmaline
WT12WH23	West Tasmania	Trial Harbour, Heemskirk	145°09'23.93"	41°55'20.64"	3	WGS84	White granite	Quartz, feldspar, tourmaline
WT12WH24	West Tasmania	Trial Harbour, Heemskirk	145°09'23.93"	41°55'20.64"	3	WGS84	White granite	Tourmaline, quartz
WT12WH25	West Tasmania	Trial Harbour, Heemskirk	145°09'23.93"	41°55'20.64"	3	WGS84	White granite	Quartz, tourmaline
WT12WH26	West Tasmania	Trial Harbour, Heemskirk	145°09'23.93"	41°55'20.64"	3	WGS84	White granite	Quartz, tourmaline
WT12WH27	West Tasmania	Trial Harbour, Heemskirk	145°09'23.93"	41°55'20.64"	3	WGS84	White granite	Tourmaline
WT12WH28	West Tasmania	Trial Harbour, Heemskirk	145°09'23.93"	41°55'20.64"	3	WGS84	White granite	Tourmaline
WT12WH29	West Tasmania	Trial Harbour, Heemskirk	145°09'23.93"	41°55'20.64"	3	WGS84	White granite	Quartz, tourmaline
WT12WH30	West Tasmania	Trial Harbour, Heemskirk	145°09'23.93"	41°55'20.64"	3	WGS84	White granite	Quartz, tourmaline
WT12WH31	West Tasmania	Granville Harbour, Heemskirk	145°01'40.47"	41°48'34.80"	1	WGS84	White granite	Quartz, tourmaline, muscovite
WT12WH32	West Tasmania	Granville Harbour, Heemskirk	145°01'40.47"	41°48'34.80"	1	WGS84	White granite	Tourmaline, muscovite
WT12WH33	West Tasmania	Granville Harbour, Heemskirk	145°01'40.47"	41°48'34.80"	1	WGS84	White granite	Quartz, tourmaline, muscovite
WT12WH34	West Tasmania	Granville Harbour, Heemskirk	145°01'40.47"	41°48'34.80"	1	WGS84	White granite	Quartz, tourmaline
WT12WH35	West Tasmania	Granville Harbour, Heemskirk	145°01'40.47"	41°48'34.80"	1	WGS84	White granite	Quartz, tourmaline
WT12WH36	West Tasmania	Granville Harbour, Heemskirk	145°01'40.47"	41°48'34.80"	1	WGS84	White granite	Quartz, tourmaline

NT13WH01	East Tasmania	George River	148°18´23.51"	S41°15´05.28"	8	WGS84	Pegmatite	Quartz
NT13WH02	East Tasmania	George River	148°18´23.51"	S41°15´05.28"	8	WGS84	Granodiorite	Quartz, feldspar, biotite
NT13WH03	East Tasmania	George River	148°18´23.51"	S41°15´05.28"	8	WGS84	Granodiorite	Quartz, feldspar, biotite
NT13WH04	East Tasmania	George River	148°18´23.51"	S41°15´05.28"	8	WGS84	Pegmatite	Quartz, feldspar
NT13WH05	East Tasmania	George River	148°18´23.51"	S41°15´05.28"	8	WGS84	Pegmatite	Quartz, feldspar
NT13WH06	East Tasmania	George River	148°18´23.51"	S41°15´05.28"	8	WGS84	Pegmatite	Quartz, feldspar
NT13WH07	East Tasmania	George River	148°18´23.51"	S41°15´05.28"	8	WGS84	Pegmatite	Quartz, feldspar
NT13WH08	East Tasmania	George River	148°18´23.51"	S41°15´05.28"	8	WGS84	Sulphide in vein	Molybdenite, pyrrhotite, pyrite
NT13WH09	East Tasmania	George River	148°18´23.51"	S41°15´05.28"	8	WGS84	Granodiorite with veins	Quartz, feldspar, biotite and sulphide
NT13WH10	East Tasmania	George River	148°18´23.51"	S41°15´05.28"	8	WGS84	Granodiorite	Quartz, feldspar, biotite
NT13WH11	East Tasmania	George River	148°18´23.51"	S41°15´05.28"	8	WGS84	Granodiorite	Quartz, feldspar, biotite
NT13WH12	East Tasmania	George River	148°18´23.51"	S41°15´05.28"	8	WGS84	Quartz dyke	Quartz, feldspar
NT13WH13	East Tasmania	George River	148°18´23.51"	S41°15´05.28"	8	WGS84	Bi-rich granodiorite	Quartz, feldspar, biotite
NT13WH14	East Tasmania	George River	148°18´23.51"	S41°15´05.28"	8	WGS84	Bi-rich granodiorite	Quartz, feldspar, biotite
NT13WH15	East Tasmania	Grant Point	148°18'50.63"	41°14'58.97"	8	WGS84	Dyke	Quartz, feldspar, biotite
NT13WH16	East Tasmania	Grant Point	148°18'50.63"	41°14'58.97"	8	WGS84	Granite	Quartz, feldspar, biotite
NT13WH17	East Tasmania	Grant Point	148°18'50.63"	41°14'58.97"	8	WGS84	Granite	Quartz, feldspar, biotite
NT13WH18	East Tasmania	George River	148°18'50.63"	41°14'58.97"	8	WGS84	Granodiorite	Quartz, feldspar, biotite
NT13WH19	East Tasmania	Grant Point	148°18'50.63"	41°14'58.97"	8	WGS84	Granite	Quartz, feldspar, biotite
NT13WH20	East Tasmania	Grant Point	148°18'50.63"	41°14'58.97"	8	WGS84	Dyke (pegmatite?)	Quartz, feldspar, biotite
NT13WH21	East Tasmania	Grant Point	148°18'50.63"	41°14'58.97"	8	WGS84	Granite	Quartz, feldspar, biotite
NT13WH22	East Tasmania	George River	148°18´23.51"	S41°15´05.28"	8	WGS84	Bi-rich granodiorite	Quartz and feldspar, biotite
NT13WH23	East Tasmania	George River	148°18´23.51"	S41°15´05.28"	8	WGS84	Bi-rich granodiorite	Quartz and feldspar, biotite
NT13WH24	East Tasmania	George River	148°18´23.51"	S41°15´05.28"	8	WGS84	Bi-rich granodiorite	Quartz and feldspar, biotite
NT13WH25	East Tasmania	Mt. Pierson	148°17'32.57"	41°14'33.11"	15	WGS84	Coarse granite	Quartz and feldspar, biotite
NT13WH26	East Tasmania	Mt. Pierson	148°17'32.57"	41°14'33.11"	15	WGS84	Dyke (pegmatite)?	Quartz dominated
NT13WH27	East Tasmania	Mt. Pierson	148°17'32.57"	41°14'33.11"	15	WGS84	Dyke (pegmatite)?	Quartz dominated
NT13WH28	East Tasmania	Mt. Pierson	148°17'32.57"	41°14'33.11"	15	WGS84	Dyke (pegmatite)	Quartz dominated
NT13WH29	East Tasmania	Mt. Pierson	148°17'32.57"	41°14'33.11"	15	WGS84	Coarse granite	Quartz and feldspar, biotite
NT13WH30	East Tasmania	George River	148°18´23.51"	41°14'58.97"	8	WGS84	Granodiorite	Quartz and feldspar, biotite
NT13WH31	East Tasmania	George River	148°18´23.51"	S41°15´05.28"	8	WGS84	Granodiorite	Quartz and feldspar, biotite
NT13WH32	East Tasmania	George River	148°18´23.51"	S41°15´05.28"	8	WGS84	Bi-rich granodiorite	Quartz and feldspar, biotite
NT13WH33	East Tasmania	George River	148°18´23.51"	S41°15´05.28"	8	WGS84	Biotite granodiorite	Quartz and feldspar, biotite
NT13WH34	East Tasmania	Bicheno granite	148°18'46"	S41°52'30"	5	WGS84	Coarse-grained granite	Quartz and feldspar, biotite
NT13WH35	East Tasmania	Bicheno granite	148°18'46"	S41°52'30"	5	WGS84	Coarse-grained granite	Quartz, feldspar, tourmaline
NT13WH36	East Tasmania	Bicheno granite	148°18'46"	S41°52'30"	5	WGS84	Fine- to coarse-grained	Quartz and feldspar, biotite
NT13WH37	East Tasmania	Bicheno granite	148°18'46"	S41°52'30"	5	WGS84	Tourmaline cavity	Tourmaline

NT13WH38	East Tasmania	Bicheno granite	148°18’46”	S41°52’30”	5	WGS84	Coarse-grained granite	Contain biotite, tourmaline
NT13WH39	East Tasmania	Bicheno granite	148°18’46”	S41°52’30”	5	WGS84	Coarse-grained granite	Quartz and feldspar, biotite
NT13WH40	East Tasmania	Coles Bay	148°17’00.31”	42°01’23.43”	3	WGS84	Coarse-grained granite	Quartz and feldspar, biotite
NT13WH41	East Tasmania	Coles Bay	148°17’00.31”	42°01’23.43”	3	WGS84	Coarse-grained granite	Quartz and feldspar, biotite
NT13WH42	East Tasmania	Coles Bay	148°17’00.31”	42°01’23.43”	3	WGS84	Coarse-grained granite	Quartz and feldspar, biotite
WT14WH57	East Tasmania	Trial Harbour, Heemskirk	145°09’23.93”	41°55’20.64”	3	WGS84	White granite	Contain tourmaline patches
WT14WH58	East Tasmania	Trial Harbour, Heemskirk	145°09’23.93”	41°55’20.64”	3	WGS84	Aplitic White granite	Quartz, K-feldspar
WT14WH59	East Tasmania	Trial Harbour, Heemskirk	145°09’23.93”	41°55’20.64”	3	WGS84	Aplitic White granite	Quartz, K-feldspar and garnet
WT14WH64	West Tasmania	Heemskirk	145°14’38.92”	41°52’54.76”		WGS84	Red granite	Drill hole sample, tindh01, 110-116m
WT14WH65	West Tasmania	Heemskirk	145°14’38.92”	41°52’54.76”		WGS84	Red granite	Drill hole sample, tindh01, 131-146m
WT14WH66	West Tasmania	Heemskirk	145°14’38.92”	41°52’54.76”		WGS84	Red granite	Drill hole sample, tindh01, 148-156m
WT14WH67	West Tasmania	Heemskirk	145°14’38.92”	41°52’54.76”		WGS84	Red granite	Drill hole sample, tindh01, 157-169m
WT14WH68	West Tasmania	Heemskirk	145°14’38.92”	41°52’54.76”		WGS84	Red granite	Drill hole sample, tindh01, 176-191m
WT14WH69	West Tasmania	Heemskirk	145°14’38.92”	41°52’54.76”		WGS84	Red granite	Drill hole sample, tindh01, 227-266m
WT14WH70	West Tasmania	Meredith	145°22’10.80”	41°39’10.21”		WGS84	Felsic phase granite	Drill hole sample, bwdh07, 151m
WT14WH71	West Tasmania	Meredith	145°22’10.80”	41°39’10.21”		WGS84	Felsic phase granite	Drill hole sample, bwdh07, 267m
WT14WH72	West Tasmania	Meredith	145°22’10.80”	41°39’10.21”		WGS84	Felsic phase granite	Drill hole sample, bwdh07, 173m
WT14WH73	West Tasmania	Meredith	145°22’10.80”	41°39’10.21”		WGS84	Felsic phase granite	Drill hole sample, bwdh07, 181.4m
WT14WH74	West Tasmania	Meredith	145°22’10.80”	41°39’10.21”		WGS84	Felsic phase granite	Drill hole sample, bwdh07, 233m
WT14WH75	West Tasmania	Meredith	145°22’10.80”	41°39’10.21”		WGS84	Felsic phase granite	Drill hole sample, bwdh07, 241.5m

Appendix 3.1 Whole-rock geochemical results of investigated Tasmanian granites

Sample	Area	Lithology	SiO_2	Al_2O_3	Fe_2O_3	MgO	CaO	Na_2O	K_2O	TiO_2	P_2O_5	MnO	LOI	Sum	Ba	Sc	Cs	Ga	Hf
East Tasmania			%												ppm				
NT13WH10	George River	Granodiorite	71.04	13.81	3.55	0.87	2.54	2.65	4.31	0.44	0.11	0.06	0.4	99.81	553	10	8.4	16.6	4.8
NT13WH18	George River	Granodiorite	72.76	13.62	2.63	0.58	1.65	2.63	4.82	0.29	0.09	0.05	0.7	99.83	464	7	12.9	15	4.5
NT13WH02	George River	Granodiorite	68.40	14.32	4.83	1.09	3.36	2.77	3.36	0.68	0.18	0.08	0.7	99.81	539	13	12.5	19.5	4.9
NT13WH30	George River	Granodiorite	67.66	16.08	3.24	0.87	3.32	3.69	2.88	0.35	0.09	0.07	1.6	99.84	336	9	7.2	20.7	4.2
NT13WH32	George River	Granodiorite	66.95	13.84	6.45	1.62	1.72	2.49	4.98	0.74	0.21	0.11	0.6	99.72	746	18	13	21.1	6.5
NT13WH16	Grant Point	Granite	71.06	14.75	2.38	0.65	1.87	2.89	4.70	0.27	0.1	0.04	1.1	99.84	523	5	7.2	15.6	3.6
NT13WH17	Grant Point	Granite	71.78	14.28	3.00	0.83	1.91	3.02	3.80	0.35	0.15	0.06	0.7	99.83	429	7	16	17.4	4.4
NT13WH21	Grant Point	Granite	72.64	13.99	2.41	0.61	1.52	2.74	4.69	0.27	0.11	0.04	0.8	99.84	495	6	8.9	16.1	4
NT13WH25	Mt. Pierson	Granite	73.97	13.22	2.38	0.36	1.60	2.90	4.48	0.21	0.07	0.04	0.6	99.86	268	7	8.4	16.8	4.5
NT13WH29	Mt. Pierson	Granite	73.26	13.61	2.24	0.35	1.56	2.90	4.71	0.20	0.07	0.04	0.9	99.85	335	7	6.9	15.1	4.7
NT13WH34	Bicheno	Granite	74.50	13.14	1.86	0.18	0.82	2.48	5.52	0.15	0.17	0.02	1	99.85	454	2	15.8	18.7	3.8
NT13WH36	Bicheno	Granite	74.33	12.80	2.23	0.24	0.33	2.17	6.78	0.20	0.19	0.02	0.6	99.9	132	2	11.7	17.3	3.1
NT13WH39	Bicheno	Granite	73.37	14.02	1.97	0.17	0.84	2.64	5.95	0.15	0.18	0.02	0.5	99.85	491	2	18	18.7	3.6
NT13WH40	Coles Bay	Granite	77.15	12.85	0.68	0.04	0.24	2.84	5.46	0.10	0.03	< 0.01	0.5	99.88	140	3	5.5	20.6	4.6
NT13WH41	Coles Bay	Granite	77.45	12.65	0.78	0.03	0.23	2.95	5.27	0.08	0.02	< 0.01	0.4	99.89	125	3	7.1	19.2	3.8
West Tasmania																			
WT14WH73	Meredith	Coarse-grained	74.81	12.68	2.07	0.27	0.98	2.67	5.53	0.22	0.04	0.02	0.6	99.89	313	4	5.2	16.1	4.8
WT14WH74	Meredith	Coarse-grained	74.01	12.78	1.68	0.25	1.34	2.62	6.03	0.21	0.05	0.02	0.9	99.89	420	5	5.2	17.1	4.7
134229	Housetop	Coarse-grained	75.53	12.11	2.44	0.35	1.35	3.01	4.43	0.28	0.05	0.05	0.3	99.9	338	4	5.5	15.7	5.2
134237	Housetop	Coarse-grained	76.96	11.66	2.10	0.21	0.81	2.93	4.91	0.18	0.03	0.03	0.1	99.92	186	2	6.3	15.4	5.1
131415	Pine Hill	Porphyry	71.66	13.22	3.31	0.82	2.00	2.47	4.87	0.45	0.13	0.05	0.9	99.86	351	7	14	17.3	5.7
131241	Pine Hill	Porphyry	73.08	12.68	2.88	0.51	1.43	2.35	5.66	0.35	0.09	0.04	0.8	99.88	252	6	8.2	17.6	5.4
131414	Pine Hill	Porphyry	71.68	13.50	3.14	0.76	2.14	2.55	4.86	0.45	0.13	0.04	0.6	99.86	344	7	11.6	18.6	5.7
WT14WH67-3	Heemskirk	Red granite	74.43	12.32	2.47	0.31	0.93	3.04	5.22	0.27	0.06	0.03	0.8	99.89	196	5	16.3	18.5	6.8
WT14WH68-4	Heemskirk	Red granite	73.35	12.71	2.75	0.36	0.98	3.08	5.37	0.30	0.06	0.04	0.9	99.87	242	5	14.5	19.4	7.2
WT12WH20	Trial Harbour	White granite	75.93	12.98	1.79	0.14	0.13	2.70	5.18	0.11	0.06	0.03	0.9	99.9	64	4	12.2	19.2	3.1
WT12WH28-1	Trial Harbour	White granite, aplite	77.38	12.88	1.36	0.07	0.03	2.38	4.55	0.02	0.02	0.02	1.1	99.82	21	2	14.1	18.6	2.5
WT12WH30	Trial Harbour	Red granite, aplite	76.42	12.13	1.99	0.14	0.09	2.60	5.55	0.08	0.04	0.01	0.9	99.9	24	4	7.6	18.8	3
WT12WH34	Granville Harbour	White granite, aplite	75.34	12.60	2.10	0.09	0.22	2.83	5.76	0.07	0.04	0.02	0.8	99.91	17	5	7.5	19.5	3.2
WT12WH35	Granville Harbour	White granite	76.19	12.84	1.24	0.09	0.20	2.63	5.55	0.11	0.07	0.01	1	99.9	77	4	9.2	19.1	3.1
WT14WH08	Heemskirk, TH	White granite, aplite	77.50	12.38	0.71	0.06	0.08	2.58	5.72	0.09	0.04	< 0.01	0.8	99.96	23	3	11.6	19.6	3.3
WT14WH58	Heemskirk, TH	White granite, aplite	76.93	12.75	1.00	0.13	0.02	2.42	5.64	0.06	0.01	0.01	1	99.98	41	3	13.4	21.5	2.9
WT12WH02	Pieman Heads	Fine-grained	74.30	13.29	2.27	0.41	0.46	2.51	5.34	0.25	0.11	0.04	0.9	99.86	161	5	20.7	17.4	4.4
WT12WH11	Pieman Heads	Coarse-grained	74.55	13.12	2.16	0.35	0.69	2.69	5.01	0.23	0.13	0.04	0.9	99.88	260	4	17.5	16.7	4
WT12WH16-2	Pieman Heads	Coarse-grained	73.66	13.37	2.35	0.37	0.89	2.83	5.08	0.24	0.13	0.04	0.9	99.86	253	5	16	17.5	4
WT12WH16-2A	Pieman Heads	Granite, repeat	73.95	13.24	2.32	0.36	0.89	2.80	5.01	0.24	0.12	0.04	0	99.87	233	5	16.2	16.9	4.1
WT12WH19-1	Pieman Heads	Medium-grained	73.52	13.65	2.42	0.37	0.61	2.66	5.32	0.24	0.12	0.05	0.9	99.88	252	4	19.1	17.7	3.6
Detection limit			0.01	0.01	0.04	0.01	0.01	0.01	0.01	0.01	0.01	0.01			1	1	0.1	0.5	0.1

Nb	Rb	Sn	Sr	Ta	Th	U	V	W	Zr	Y	La	Ce	Pr	Nd	Sm	Eu	Gd	Tb	Dy	Ho	Er
10.3	171	4	179.4	1	19.2	3.9	40	0.7	173.7	34.8	38.5	81	9.21	33.2	6.89	0.87	6.62	1.11	6.49	1.46	4.05
9.5	213	7	136.9	1.1	20.9	5	29	0.7	131.2	28.5	34	84.9	9.07	34	6.49	0.71	5.48	0.91	5.26	1.1	3.21
10.8	163	5	217.2	1	17.4	3.3	54	0.7	185.6	31.1	38.5	83.1	9.42	36.7	6.91	1.28	6.36	1.04	6.14	1.33	3.72
10.6	163	8	257.1	1.2	14.1	5	47	0.6	133.7	45.1	19.3	36.6	4.37	16.7	4.01	1.03	5.1	1.11	7.27	1.62	4.97
19.5	265	7	145.3	1.7	42.8	4	67	0.7	244.9	59	97.8	213	23.3	86.7	16.04	0.75	14.31	2.08	10.9	2.09	5.75
9.1	195	4	172.8	1	13	2.7	23	1	126.7	22.2	25.6	53.1	6.01	21.9	4.6	0.79	4.09	0.66	3.89	0.84	2.53
12.6	236	8	152.4	1.8	18	4.7	37	4.1	155.5	30.7	34.6	79	8.42	32.1	6.27	0.71	5.5	0.92	5.21	1.17	3.07
10.1	228	5	156.5	1.5	14.9	4.6	31	0.6	138.4	29.6	29.2	63.5	7.22	26.1	4.76	0.75	4.61	0.85	4.88	1.04	3.31
9.9	213	4	96.5	1.1	29.8	4.4	18	0.7	138.6	45.8	37.1	84.2	9.75	35.1	7.97	0.59	7.8	1.32	8.06	1.69	5.01
9.7	215	3	111.4	1	33.7	5.5	22	0.6	130.6	45.6	38.1	82.2	9.56	35.6	7.7	0.54	7.63	1.39	8.55	1.73	5.07
9.7	303	8	76.2	1.2	18.5	4.4	19	3.8	128.1	17.1	25.1	57.5	6.31	22.5	5.11	0.84	4.61	0.78	4.03	0.68	1.53
9.3	362	12	49.2	0.9	15.1	4.2	17	1.9	99.2	11.8	17.6	38.3	4.26	14.7	4.01	0.43	3.71	0.63	3.13	0.43	0.9
9.8	350	9	78	1	15.5	3.5	21	3	117.2	17.3	21.2	47.2	5.14	19.2	4.77	0.85	4.37	0.71	3.65	0.57	1.16
13.5	339	6	35.2	1.6	33.4	7.4	11	5.7	105.2	70.4	33	79.3	9.31	36.1	8.14	0.4	8.81	1.65	10.84	2.36	7.18
9	329	13	33	1.2	34.1	8.4	9	1.5	94	40.3	21.5	55.3	6.3	23.2	5.96	0.28	5.48	1.11	7.13	1.54	4.86
12.5	216	1	60	0.9	31.3	5.9	14	1.2	152.8	59.6	57.8	120.2	13.85	51	10.06	0.49	9.61	1.81	10.3	2.18	5.94
13.3	273	7	72.3	1.4	25.3	7.2	11	3.5	152.7	57.7	56	114	13.34	48.7	10.19	0.51	9.81	1.72	10.13	1.93	5.69
14.2	245	4	71.7	1.3	28.1	8.4	20	0.7	159.5	34.5	48.1	89	9.52	33.6	5.87	0.66	5.62	0.94	5.66	1.2	3.49
16.6	328	2	38.9	1.9	50.1	15	8	1.1	135.7	44.5	62.2	116.4	11.97	37.5	6.74	0.43	6.19	1.09	6.84	1.45	4.59
18	291	8	117.3	2.1	34	12.3	37	2.4	205.5	45.4	57	115.2	13.02	46.5	9.51	1.06	8.6	1.35	8.09	1.6	4.54
19.2	325	3	72	4.1	35	19.1	29	12	164.9	71.4	42.4	88.1	10.42	39.6	9.29	0.77	10.06	1.94	11.87	2.47	7.32
18.1	341	9	117.8	2	33.6	13.3	39	1.3	204.9	48.2	58.8	119.7	13.09	48.3	9.27	1.12	8.91	1.46	8.2	1.6	5.06
22.3	363	4	38.8	2.3	34.9	11.3	15	1.7	228.4	50.8	60.4	120.8	13.42	46.3	8.93	0.61	8.27	1.43	8.28	1.66	5.04
24.6	362	5	45.6	2.7	37.2	12.3	23	3.5	232.3	70.9	64.4	129.3	14.39	53.9	11.09	0.68	10.96	2.04	11.86	2.49	7.7
18.9	492	17	18.1	3.6	22	4.2	<8	5.6	71.1	48.5	20.6	50.9	6.06	22	6.6	0.13	6.11	1.23	8.08	1.74	5.17
26.5	478	850	7.6	6.2	21.3	5	<8	3.4	40.9	30.1	8.2	23.1	2.81	10.5	3.59	0.05	3.36	0.89	5.77	1.15	3.59
17.3	379	10	13.1	2.9	22.4	10.1	<8	1	63	67.6	18.2	48.2	5.61	19.7	6.2	0.1	7.32	1.59	11.13	2.49	7.65
21.1	307	6	6.9	4.2	19.9	9.8	10	1.7	61.9	58	16.7	40.3	4.86	17.4	5.39	0.1	6.41	1.41	9.13	2.13	6.47
19.6	398	7	32.2	2.9	21	13.7	12	5	65	43.2	20.2	49.2	5.7	22	5.69	0.19	5.58	1.16	7.3	1.68	4.65
23.5	469	17	9.8	2.9	18.1	5.5	<8	1.9	72.2	70.7	21.6	49.1	5.86	20.4	6.05	0.09	7.23	1.72	11.34	2.49	7.84
24	561	24	7.4	4.4	5.7	2.9	<8	10.9	53.2	30.4	7.4	16.8	2.07	7.4	2.05	0.04	2.79	0.78	5.04	0.99	3.36
17.4	332	9	62.3	2.6	23.2	16.1	21	9.3	136.2	39.7	42.2	92.8	10.37	36.6	7.66	0.46	6.59	1.17	7.54	1.53	4.69
13.9	310	8	56.6	2	20.4	8.7	24	11	125.9	28.9	32.6	74.1	8.13	28.7	6.32	0.57	5.29	0.92	5.2	1.08	3.08
15.3	322	5	59.9	2.1	20.2	4.4	23	18.5	137.5	33.6	34.6	77.7	8.78	31.9	6.57	0.76	6.36	1.07	6.44	1.31	3.79
15	300	5	54.9	2	20.8	4.9	26	16.7	130.3	30.5	33.8	80.4	8.84	32.7	6.96	0.71	5.97	1.05	5.96	1.31	3.63
14.9	325	6	46.3	2	21.3	6.6	25	3.1	110	27.6	30.7	72	8.12	30.2	6.45	0.47	5.51	0.89	4.92	0.97	3.03
0.1	0.1	1	0.5	0.1	0.2	0.1	8	0.5	0.1	0.1	0.1	0.1	0.02	0.3	0.05	0.02	0.05	0.01	0.05	0.02	0.03

Tm	Yb	Lu	Mo	Cu	Pb	Zn	Ag	Ni	Co	Mn	As	Sb	Bi	Cr	B	Tl	Be	Li	ACNK	ANK	Ce/Ce*	Eu/Eu*
						ppm	ppb											ppm				
0.61	3.83	0.56	0.88	3.11	6.49	53.2	27	3.4	5.1	430	0.7	<0.02	0.21	11.8	2	0.61	0.4	49	1.02	1.54	1.06	0.39
0.49	3.37	0.51	0.39	3.58	8.46	45.7	12	2.2	3.5	397	1.7	<0.02	0.34	7.7	2	0.44	0.2	43.5	1.09	1.44	1.19	0.36
0.59	3.51	0.52	0.61	6.21	6.89	57	21	3.9	6.6	519	0.9	0.04	0.3	12.6	6	0.58	0.4	50.1	1.01	1.76	1.05	0.59
0.76	4.71	0.7	0.39	6.37	7.68	63.4	79	2.6	4.3	500	26.7	<0.02	1.6	13.8	4	0.25	0.9	33.5	1.06	1.77	0.95	0.70
0.84	4.9	0.71	0.98	2.77	6.55	88	<2	5.5	9.3	821	1.1	<0.02	0.14	18.4	2	1.05	<0.1	74.5	1.10	1.47	1.08	0.15
0.38	2.47	0.36	0.32	1.93	6.03	30.5	31	2.3	3.3	285	0.4	<0.02	0.05	8.5	2	0.37	0.2	45.5	1.12	1.51	1.04	0.56
0.47	3.24	0.45	0.2	1.84	4.44	41.2	14	2.5	3.6	432	< 0.1	<0.02	0.33	11.3	3	0.75	0.3	70.3	1.14	1.59	1.12	0.37
0.51	3.4	0.5	0.7	1.46	5.34	29.5	11	2.2	2.6	300	1	<0.02	0.05	9.4	<1	0.42	<0.1	42.3	1.14	1.47	1.08	0.49
0.76	4.78	0.7	0.25	1.61	6.97	42.1	12	1.9	2.6	326	1.3	0.12	0.13	7.2	4	0.49	0.1	46.9	1.06	1.39	1.11	0.23
0.73	4.82	0.7	0.19	2.05	6.64	35.2	<2	1.6	2.3	307	0.1	0.07	0.12	5.5	3	0.42	<0.1	41.4	1.08	1.39	1.06	0.22
0.2	1.08	0.13	0.48	2.7	8.39	23.9	21	1.5	1.1	130	3.4	0.07	0.26	6.1	4	0.23	1.1	31.8	1.14	1.32	1.14	0.53
0.09	0.55	0.05	0.65	0.96	14.03	34.8	14	1.6	1.2	161	1.4	0.04	0.06	3.5	2	0.1	0.3	22.6	1.12	1.18	1.10	0.34
0.15	0.69	0.08	0.61	1.67	11.99	36	9	1.5	1.3	145	2.2	0.04	0.47	5.1	4	0.24	1.1	42.3	1.15	1.31	1.10	0.57
1.11	7.66	1.07	0.24	0.69	7.42	3.9	9	1.1	<0.1	45	0.5	<0.02	0.72	3.5	1	0.08	0.4	4.2	1.17	1.22	1.11	0.14
0.72	4.73	0.7	0.25	1.48	6.3	3.4	13	1.1	0.3	54	< 0.1	0.02	0.81	3.8	1	0.16	0.2	4.8	1.16	1.21	1.20	0.15
0.9	5.76	0.83	0.66	1.57	8.64	22.6	57	1.2	1.8	185	1	0.11	0.11	3.1	7	0.17	0.6	26.3	1.05	1.23	1.04	0.15
0.85	5.37	0.8	0.47	1.57	7.77	14.4	192	1.3	1	137	4	0.13	0.13	3.1	8	0.08	2	8.6	0.97	1.19	1.02	0.16
0.55	3.87	0.59	0.92	1.83	7.19	19.7	7	2	2.8	337	1.6	0.17	0.11	5.4	6	0.18	1.1	32.3	1.00	1.25	1.00	0.35
0.78	5.34	0.82	0.53	1.34	8.66	18.5	7	1.4	1.9	202	2.3	0.45	0.1	3.9	5	0.15	1.4	33.5	1.01	1.16	1.06	0.20
0.69	4.5	0.71	1.21	2.19	5.67	17.7	<2	2.1	3.7	278	0.9	0.04	0.57	8.9	5	0.42	0.7	45.5	1.02	1.43	1.03	0.36
1.19	8.23	1.26	0.5	13.73	7.98	16.6	5	1.7	3.3	204	0.7	0.09	5.49	6.5	30	0.15	3.6	32.3	1.01	1.28	1.02	0.24
0.73	5.16	0.75	0.63	9.03	4.8	16.6	<2	2.3	3.7	233	0.9	0.04	2.45	7.4	7	0.42	1.3	59.8	1.02	1.44	1.04	0.38
0.77	5.29	0.76	1.32	1.99	18.99	30.9	14	1.2	1.9	198	0.8	0.16	0.57	3.8	14	0.24	3.3	45.5	1.00	1.17	1.04	0.22
1.22	8.1	1.13	2.37	2.09	25.34	46.5	35	1.3	1.8	242	1.1	0.18	0.63	4.2	11	0.17	5.6	32.3	1.01	1.18	1.02	0.19
0.93	6.37	0.89	0.47	2.93	10.36	10.2	17	1	0.3	156	3.2	0.42	2.57	3.6	5	0.18	1.1	34.7	1.27	1.30	1.16	0.06
0.65	4.7	0.69	0.08	1.67	11.47	11	24	0.6	0.2	65	0.3	0.08	1.35	4	8	0.34	0.9	22.6	1.46	1.47	1.24	0.04
1.25	8.16	1.14	0.55	1.85	13.55	26.9	8	1.3	0.6	103	0.6	0.38	0.55	5.5	6	0.11	0.7	13.3	1.17	1.19	1.23	0.05
1.05	6.99	1.07	2.49	2.37	9.74	15.2	8	0.5	0.7	161	0.6	0.06	0.9	4.4	4	0.07	0.9	26.4	1.12	1.16	1.14	0.05
0.8	5.16	0.73	2.21	29.21	8.91	3.5	7	0.5	0.3	63	1	0.23	5.72	4.2	3	0.09	0.2	12.5	1.21	1.25	1.13	0.10
1.17	8.32	1.2	1.79	3.2	18.18	10.7	<2	1	0.2	32	1.2	0.17	1.15	1.5	4	0.12	0.3	9	1.18	1.19	1.11	0.04
0.57	4.45	0.65	0.34	0.84	9.45	17.3	<2	0.6	<0.1	42	0.4	0.11	0.07	1.7	7	0.26	0.4	10.8	1.27	1.27	1.09	0.05
0.76	4.91	0.72	6.34	12.1	15.8	21.1	42	1.2	1.1	253	3.9	0.48	4.17	6.9	5	0.1	0.2	54.4	1.24	1.35	1.10	0.20
0.46	3.07	0.45	0.97	1.33	7	15.1	3	1.2	1.3	260	1.1	0.15	0.75	5.3	4	0.26	0.2	77.4	1.19	1.34	1.13	0.30
0.58	3.95	0.56	1.03	0.89	7.69	24.3	6	1.9	1.9	284	0.7	0.05	0.07	7.4	4	0.34	0.3	75.4	1.14	1.33	1.10	0.36
0.54	3.72	0.55	0	0	0	0	0	0	0	0	0	0	0	0	0	0	0	0	1.14	1.33	1.15	0.34
0.48	3.2	0.44	0.21	0.91	14.55	20.7	13	1.7	1.5	327	1.3	0.1	0.05	7.2	2	0.19	0.8	64.2	1.22	1.36	1.13	0.24
0.01	0.05	0.01	0.01	0.01	0.01	0.1	2	0.1	0.1	1	0.1	0.02	0.02	0.5	1	0.02	0.1	0.1				

Appendix 3.2 LA-ICP-MS zircon U-Pb chronological results of Tasmanian granites

Analytical No.	$^{206}Pb/^{238}U$ Age	+/-1 std. error	$^{206}Pb/^{238}U$	+/-1 RSE	$^{208}Pb/^{232}Th$	+/-1 RSE	$^{207}Pb/^{206}Pb$	+/-1 RSE	Pb^{204} (ppm)	Pb^{206} (ppm)	Pb^{207} (ppm)	Pb^{208} (ppm)	Th^{232} (ppm)	U^{238} (ppm)
NT13WH10	George River Granodiorite, East Tasmania													
NO26A073	340	6	0.0557	1.7%	0.0276	2.3%	0.0749	1.9%	0.08	48	4	7	241	809
NO26A080	351	7	0.0568	1.9%	0.0166	2.4%	0.0655	1.9%	0.01	21	1	5	327	409
NO26A079	**394**	**8**	0.0713	2.1%	0.0533	2.8%	0.1495	2.0%	0.09	13	2	5	100	212
NO26A077	**396**	**7**	0.0635	1.7%	0.0194	3.5%	0.0566	3.0%	0.00	14	1	2	85	227
NO26A068	**397**	**7**	0.0635	1.9%	0.0206	2.7%	0.0549	2.2%	0.00	19	1	3	170	315
NO26A075	**399**	**6**	0.0639	1.5%	0.0203	2.7%	0.0543	1.9%	0.01	20	1	2	79	309
NO26A071	**401**	**6**	0.0642	1.4%	0.0197	2.1%	0.0556	1.3%	0.00	44	2	8	369	653
NO26A072	**403**	**6**	0.0646	1.6%	0.0192	2.5%	0.0552	1.5%	0.03	48	3	5	245	694
NO26A078	404	8	0.0646	2.1%	0.0187	3.7%	0.0547	4.4%	0.00	19	1	2	120	278
NO26A066	**406**	**6**	0.0662	1.5%	0.0254	2.5%	0.0702	1.9%	0.04	22	2	5	188	333
NO26A069	**410**	**6**	0.0657	1.4%	0.0199	2.0%	0.0544	1.3%	0.00	24	1	4	215	372
NO26A074	**417**	**8**	0.0668	2.0%	0.0220	3.5%	0.0553	2.2%	0.00	21	1	2	78	338
NO26A070	**416**	**6**	0.0667	1.5%	0.0215	2.1%	0.0529	2.5%	0.01	24	1	5	232	349
NO26A067	**418**	**6**	0.0671	1.5%	0.0230	2.3%	0.0559	2.0%	0.01	17	1	2	96	248
NO26A076	425	7	0.0682	1.7%	0.0209	3.3%	0.0538	2.4%	0.01	10	1	1	56	155
NT13WH16	Grant Point Granite, East Tasmania													
NO26A087	**411**	**8**	0.0565	1.4%	0.0161	1.6%	0.0550	0.8%						
NO26A089	**394**	**6**	0.0630	1.5%	0.0200	2.0%	0.0553	1.4%	0.00	32	2	5	253	520
NO26A091	**398**	**6**	0.0639	1.5%	0.0209	2.1%	0.0578	1.2%	0.02	139	8	13	550	2051
NO26A094	**399**	**7**	0.0639	1.7%	0.0204	2.4%	0.0544	1.0%	0.01	99	5	4	213	1766
NO26A098	**400**	**5**	0.0646	1.4%	0.0227	1.9%	0.0620	1.2%	0.02	38	2	5	237	593
NO26A095	**400**	**6**	0.0643	1.4%	0.0204	1.8%	0.0577	0.9%	0.01	47	3	8	409	734
NO26A086	**402**	**6**	0.0644	1.5%	0.0198	2.1%	0.0560	1.7%	0.01	18	1	3	152	282
NO26A099	**402**	**7**	0.0647	1.9%	0.0238	4.1%	0.0588	3.4%	0.01	19	1	2	105	325
NO26A097	**405**	**8**	0.0649	1.9%	0.0198	2.4%	0.0551	2.3%	0.01	26	1	4	197	431
NO26A090	**410**	**7**	0.0671	1.6%	0.0311	2.3%	0.0728	1.5%	0.10	101	7	14	417	1400
NO26A088	**420**	**7**	0.0675	1.7%	0.0232	2.9%	0.0587	2.1%	0.00	15	1	2	99	222
NO26A093	443	8	0.0717	1.8%	0.0274	3.5%	0.0630	3.1%	0.02	24	1	3	101	314
NO26A085	921	31	0.1538	3.5%	0.0569	3.8%	0.0706	1.6%	0.00	23	2	1	22	160
NO26A092	1113	17	0.1885	1.5%	0.0565	2.0%	0.0764	0.7%	0.03	136	10	9	161	730
NO26A096	1273	17	0.2183	1.4%	0.0600	1.7%	0.0819	0.7%	0.02	98	8	15	253	447
NO26A084	356	11	0.0610	3.2%	0.0409	4.7%	0.1091	2.9%	0.33	90	9	21	577	1775
NT13WH25	Mt Pearson Granite, East Tasmania													
NO26A112	**384**	**6**	0.0620	1.7%	0.0216	2.2%	0.0630	2.5%	0.07	30	2	9	460	518
NO26A107	**388**	**6**	0.0621	1.6%	0.0188	3.0%	0.0543	2.4%	0.01	7	0	1	55	116
NO26A111	**388**	**7**	0.0630	1.9%	0.0208	2.3%	0.0661	2.2%	0.01	48	3	7	367	792
NO26A115	**391**	**6**	0.0625	1.5%	0.0188	2.0%	0.0555	1.2%	0.00	23	1	3	177	365
NO26A110	**393**	**7**	0.0629	1.7%	0.0192	3.0%	0.0559	2.8%	0.00	6	0	1	51	91
NO26A103	**396**	**6**	0.0640	1.4%	0.0208	2.0%	0.0618	1.2%	0.04	44	3	12	541	668
NO26A109	**398**	**9**	0.0636	2.2%	0.0197	3.7%	0.0544	4.2%	0.00	11	1	2	98	197
NO26A113	**398**	**6**	0.0642	1.6%	0.0241	2.4%	0.0607	1.9%	0.03	22	1	3	129	359
NO26A116	**402**	**6**	0.0646	1.6%	0.0220	3.1%	0.0576	2.5%	0.01	10	1	1	54	152
NO26A105	**404**	**6**	0.0649	1.5%	0.0214	2.4%	0.0572	1.8%	0.01	24	1	3	147	376
NO26A104	**406**	**6**	0.0651	1.4%	0.0212	1.9%	0.0548	1.0%	0.00	47	3	6	280	718
NO26A102	**407**	**9**	0.0653	2.2%	0.0206	3.6%	0.0567	4.0%	0.01	6	0	1	35	80
NO26A106	411	8	0.0660	1.9%	0.0222	2.1%	0.0576	1.7%	0.01	31	2	5	228	510
NO26A114	927	16	0.1548	1.8%	0.0486	2.3%	0.0703	1.9%	0.02	18	1	5	92	112
NO26A108	1707	25	0.3321	1.5%	0.0944	1.7%	0.1814	0.4%	0.01	192	35	14	154	586
NT13WH41	Coles Bay Granite, East Tasmania													
NO26A125	274	6	0.0434	2.0%	0.0106	2.1%	0.0517	2.1%	0.05	159	8	41	3856	3812
NO26A134	288	5	0.0459	1.7%	0.0140	1.9%	0.0557	1.3%	0.06	186	10	31	2010	4005
NO26A122	312	6	0.0501	1.9%	0.0136	3.1%	0.0616	2.3%	0.05	63	4	6	466	1402
NO26A130	**382**	**6**	0.0611	1.5%	0.0190	2.3%	0.0530	1.5%	0.01	23	1	3	145	393
NO26A131	**383**	**6**	0.0613	1.5%	0.0187	2.4%	0.0549	1.8%	0.00	13	1	2	104	208
NO26A121	**387**	**5**	0.0620	1.4%	0.0193	1.8%	0.0560	0.6%	0.04	346	19	61	3246	6126
NO26A123	**388**	**5**	0.0621	1.4%	0.0192	2.3%	0.0566	1.4%	0.02	23	1	3	130	363

NO26A128	**396**	**6**	0.0633	1.5%	0.0191	2.2%	0.0534	1.5%	0.01	18	1	3	140	285
NO26A129	**404**	**9**	0.0648	2.2%	0.0192	4.6%	0.0553	6.0%	0.04	17	1	2	87	246
NO26A120	528	7	0.0854	1.4%	0.0260	2.6%	0.0590	1.1%	0.01	35	2	1	50	406
NO26A126	554	9	0.0898	1.7%	0.0277	2.4%	0.0589	2.6%	0.00	14	1	4	150	164
NO26A127	566	9	0.0918	1.6%	0.0283	2.4%	0.0594	2.1%	0.00	8	0	2	57	90
NO26A124	579	8	0.0939	1.4%	0.0283	2.2%	0.0596	0.9%	0.00	61	4	2	72	655
NO26A133	835	14	0.1465	1.7%	0.0420	2.0%	0.1135	1.5%	0.00	19	2	8	183	126
NO26A132	353	9	0.0819	2.3%	0.1794	3.7%	0.3090	1.8%	4.49	234	77	210	1115	3006
WT14WH73	Meredith Granite, West Tasmania													
NO26A174	241	5	0.0383	2.2%	0.0066	6.3%	0.0547	2.0%	0.02	99	5	4	588	2682
NO26A179	**369**	**5**	0.0592	1.5%	0.0196	2.4%	0.0583	2.0%	0.00	12	1	2	102	198
NO26A173	**369**	**5**	0.0590	1.5%	0.0183	2.2%	0.0545	1.8%	0.01	13	1	2	111	218
NO26A184	**369**	**5**	0.0589	1.5%	0.0181	2.2%	0.0539	1.3%	0.00	25	1	2	110	433
NO26A172	**370**	**6**	0.0603	1.8%	0.0222	3.3%	0.0695	2.5%	0.03	27	2	8	391	494
NO26A178	**371**	**6**	0.0592	1.5%	0.0190	2.4%	0.0529	1.4%	0.02	42	2	3	173	759
NO26A186	**372**	**6**	0.0593	1.5%	0.0185	2.3%	0.0539	1.4%	0.03	31	2	3	176	533
NO26A175	**372**	**6**	0.0594	1.6%	0.0179	2.8%	0.0541	2.0%	0.00	14	1	2	118	253
NO26A182	**373**	**5**	0.0595	1.5%	0.0177	2.1%	0.0531	1.5%	0.00	18	1	3	162	300
NO26A176	**374**	**6**	0.0598	1.6%	0.0183	2.2%	0.0530	1.9%	0.00	18	1	3	175	315
NO26A180	**375**	**6**	0.0600	1.6%	0.0190	2.3%	0.0551	1.3%	0.02	28	2	4	192	490
NO26A177	**376**	**5**	0.0600	1.4%	0.0188	2.6%	0.0539	1.2%	0.00	25	1	1	79	417
NO26A181	**379**	**6**	0.0606	1.5%	0.0192	2.4%	0.0522	1.2%	0.00	40	2	4	200	708
NO26A187	**381**	**6**	0.0609	1.6%	0.0189	2.1%	0.0543	1.4%	0.00	37	2	9	491	623
NO26A185	**398**	**6**	0.0638	1.6%	0.0203	2.6%	0.0555	3.8%	0.00	19	1	2	111	313
NO26A183	304	12	0.0496	3.9%	0.0247	3.9%	0.0754	1.9%	0.09	78	5	11	582	2122
131414	Pine Hill Granite, West Tasmania													
NO26A192	340	5	0.0542	1.6%	0.0176	2.0%	0.0550	1.2%	0.01	106	6	17	910	1843
NO26A199	**358**	**6**	0.0575	1.6%	0.0181	2.1%	0.0595	1.1%	0.00	70	4	7	381	1159
NO26A191	**361**	**6**	0.0581	1.7%	0.0211	2.1%	0.0612	1.6%	0.03	79	5	13	579	1277
NO26A194	**362**	**7**	0.0579	1.8%	0.0231	2.4%	0.0547	1.4%	0.05	146	8	16	627	2334
NO26A202	**362**	**6**	0.0579	1.8%	0.0185	1.8%	0.0554	0.8%	0.03	144	8	26	1414	2740
NO26A195	**364**	**5**	0.0588	1.5%	0.0240	2.1%	0.0642	0.8%	0.12	190	12	24	1020	3476
NO26A204	**365**	**5**	0.0583	1.5%	0.0183	2.1%	0.0558	1.9%	0.02	16	1	3	168	287
NO26A196	**368**	**5**	0.0590	1.5%	0.0199	1.7%	0.0571	1.0%	0.03	60	3	17	869	1044
NO26A205	**368**	**5**	0.0588	1.4%	0.0180	1.8%	0.0539	0.9%	0.00	49	3	6	357	836
NO26A206	**371**	**6**	0.0592	1.5%	0.0185	2.0%	0.0539	1.5%	0.00	28	2	6	307	490
NO26A193	**377**	**6**	0.0603	1.6%	0.0193	2.3%	0.0547	1.6%	0.00	35	2	4	246	630
NO26A203	**379**	**7**	0.0607	1.9%	0.0200	2.5%	0.0560	1.2%	0.02	158	9	10	554	3074
NO26A198	387	6	0.0636	1.6%	0.0257	2.3%	0.0763	2.3%	0.11	82	6	18	644	1214
NO26A201	393	8	0.0630	2.2%	0.0182	4.1%	0.0557	3.0%	0.00	10	1	1	59	143
NO26A200	524	10	0.0855	1.9%	0.0958	1.9%	0.0653	0.6%	0.25	321	21	128	1421	4336
NO26A197	319	6	0.0540	2.0%	0.0256	3.4%	0.1019	1.7%	0.27	84	9	22	759	1437
WT12WH20	White Heemskirk Granite, West Tasmania													
NO26A160	177	3	0.0288	1.8%	0.0170	4.6%	0.0742	3.7%	0.26	137	11	15	851	5664
NO26A159	193	4	0.0334	1.7%	0.0281	5.5%	0.1213	4.5%	0.93	180	23	41	1215	5436
NO26A156	201	5	0.0337	2.6%	0.0117	4.3%	0.0955	2.4%	0.27	76	8	13	1057	2641
NO26A166	205	3	0.0329	1.6%	0.0054	2.3%	0.0626	1.1%	0.05	61	4	4	791	1776
NO26A157	234	4	0.0382	1.7%	0.0106	2.7%	0.0774	1.2%	0.17	106	8	12	1031	2720
NO26A158	**355**	**9**	0.0570	2.5%	0.0169	5.6%	0.0605	4.2%	0.00	18	1	2	88	299
NO26A169	**356**	**7**	0.0572	1.9%	0.0200	2.2%	0.0595	2.1%	0.00	38	2	7	363	723
NO26A161	**356**	**6**	0.0570	1.6%	0.0175	2.1%	0.0556	1.8%	0.02	23	1	7	420	424
NO26A163	**359**	**7**	0.0573	1.9%	0.0186	2.8%	0.0536	2.9%	0.00	12	1	2	97	218
NO26A168	**368**	**6**	0.0587	1.6%	0.0173	3.0%	0.0541	2.2%	0.00	7	0	1	56	124
NO26A165	**369**	**6**	0.0590	1.6%	0.0169	3.0%	0.0563	1.8%	0.01	60	3	6	319	950
NO26A164	**371**	**7**	0.0531	1.4%	0.0157	1.6%	0.0540	0.6%						
NO26A162	**378**	**7**	0.0604	1.9%	0.0191	3.5%	0.0553	3.7%	0.00	4	0	1	32	62
NO26A167	385	6	0.0618	1.7%	0.0183	2.8%	0.0578	2.9%	0.00	46	3	8	389	695
WT12WH11	Pieman Heads Granite, West Tasmania													
NO26A146	325	6	0.0525	1.7%	0.0198	2.3%	0.0662	2.0%	0.02	30	2	7	361	612
NO26A144	353	6	0.0565	1.6%	0.0194	2.5%	0.0571	1.5%	0.02	45	3	7	408	846

NO26A145	**362**	**6**	0.0587	1.7%	0.0197	2.3%	0.0669	2.1%	0.04	50	3	9	416	798
NO26A152	**362**	**5**	0.0579	1.5%	0.0187	2.5%	0.0561	1.6%	0.00	26	1	2	128	470
NO26A141	**362**	**7**	0.0579	1.9%	0.0202	3.4%	0.0558	2.2%	0.03	41	2	2	113	660
NO26A147	**362**	**5**	0.0578	1.4%	0.0176	1.9%	0.0535	0.9%	0.00	71	4	5	282	1235
NO26A151	**366**	**5**	0.0584	1.5%	0.0181	2.0%	0.0534	1.4%	0.00	23	1	3	191	403
NO26A140	**367**	**5**	0.0586	1.5%	0.0169	2.4%	0.0539	1.3%	0.00	51	3	4	237	837
NO26A138	**371**	**7**	0.0592	1.9%	0.0190	3.6%	0.0544	2.5%	0.00	13	1	1	46	246
NO26A143	**373**	**5**	0.0596	1.5%	0.0180	2.9%	0.0537	1.5%	0.00	28	2	2	108	501
NO26A150	387	6	0.0620	1.7%	0.0189	2.6%	0.0559	1.7%	0.01	60	3	6	270	910
NO26A139	390	8	0.0626	2.0%	0.0201	4.4%	0.0572	2.8%	0.03	18	1	1	63	267
NO26A148	397	7	0.0636	1.7%	0.0189	2.7%	0.0561	2.0%	0.01	27	1	4	197	395
NO26A149	1055	15	0.1833	1.5%	0.0580	2.0%	0.0996	0.8%	0.01	174	17	17	306	1021
NO26A142	382	9	0.0620	2.3%	0.0209	2.6%	0.0672	1.5%	0.01	34	2	4	193	543

Appendix 3.2 LA-ICP-MS zircon U-Pb chronological results of Tasmanian granites (continued)

Analytical No.	Ti49 (ppm)	Fe56 (ppm)	Hf178 (ppm)	$^{238}U/^{206}Pb$	+/-1 std err	$^{207}Pb/^{206}Pb$	+/-1 std err	common Pb	$^{206}Pb/^{238}U$	± 1 σ	$^{208}Pb/^{232}Th$	± 1 σ	$^{207}Pb/^{206}Pb$	± 1 σ
NT13WH10														
NO26A073	63	431	13637	17.95	0.30	0.0749	0.0014	0.859	350	6	551	13	1067	19
NO26A080	32	211	10214	17.62	0.33	0.0655	0.0013	0.859	356	7	332	8	791	20
NO26A079	24	496	9549	14.03	0.29	0.1495	0.0030	0.866	444	9	1049	29	2340	17
NO26A077	9	3	12098	15.75	0.26	0.0566	0.0017	0.862	397	7	389	14	477	33
NO26A068	4	3	11437	15.75	0.30	0.0549	0.0012	0.862	397	7	412	11	408	25
NO26A075	3	0	13329	15.65	0.24	0.0543	0.0010	0.862	399	6	407	11	385	21
NO26A071	9	22	10041	15.57	0.22	0.0556	0.0007	0.863	401	6	394	8	438	14
NO26A072	8	4	12944	15.48	0.24	0.0552	0.0008	0.863	404	6	385	10	419	17
NO26A078	8	36	10943	15.48	0.32	0.0547	0.0024	0.863	404	8	374	14	399	49
NO26A066	32	26	9903	15.09	0.22	0.0702	0.0013	0.864	414	6	506	13	935	19
NO26A069	10	2	10286	15.22	0.22	0.0544	0.0007	0.863	410	6	398	8	390	14
NO26A074	5	3	12794	14.96	0.30	0.0553	0.0012	0.864	417	8	440	15	425	25
NO26A070	5	4	11997	14.99	0.23	0.0529	0.0013	0.864	416	6	430	9	325	29
NO26A067	11	115	11123	14.90	0.23	0.0559	0.0011	0.864	419	6	461	11	449	23
NO26A076	10	0	11336	14.67	0.24	0.0538	0.0013	0.864	425	7	418	14	361	27
NT13WH16														
NO26A087				17.71	0.25	0.0550	0.0004	0.859	354	5	322	5	411	8
NO26A089	7	4	10680	15.87	0.24	0.0553	0.0008	0.862	394	6	400	8	424	16
NO26A091	6	97	13946	15.66	0.24	0.0578	0.0007	0.862	399	6	418	9	522	13
NO26A094	1	1	15449	15.64	0.27	0.0544	0.0005	0.863	399	7	408	10	387	11
NO26A098	6	1	12605	15.47	0.22	0.0620	0.0008	0.863	404	6	453	9	673	13
NO26A095	6	140	12224	15.55	0.22	0.0577	0.0005	0.863	402	6	408	7	520	10
NO26A086	9	0	10375	15.53	0.23	0.0560	0.0009	0.863	402	6	397	8	453	19
NO26A099	4	1	13146	15.46	0.29	0.0588	0.0020	0.863	404	8	475	19	559	37
NO26A097	7	0	11894	15.41	0.30	0.0551	0.0013	0.863	405	8	396	10	416	26
NO26A090	32	17035	13758	14.89	0.24	0.0728	0.0011	0.864	419	7	620	14	1008	15
NO26A088	47	119	10253	14.81	0.26	0.0587	0.0012	0.864	421	7	464	13	558	23
NO26A093	4	7	12128	13.95	0.26	0.0630	0.0019	0.866	446	8	546	19	707	33
NO26A085	16	0	11416	6.50	0.23	0.0706	0.0011	0.902	922	32	1118	43	946	16
NO26A092	5	10	14642	5.31	0.08	0.0764	0.0005	0.918	1113	17	1111	22	1105	7
NO26A096	7	3	12052	4.58	0.06	0.0819	0.0005	0.932	1273	18	1179	20	1242	6
NO26A084	56	379	12632	16.40	0.52	0.1091	0.0032	0.861	382	12	810	38	1785	26
NT13WH25														
NO26A112	10	865	8779	16.12	0.28	0.0630	0.0015	0.862	388	7	432	9	707	26
NO26A107	16	0	10390	16.11	0.26	0.0543	0.0013	0.862	388	6	376	11	383	27
NO26A111	15	28	12188	15.87	0.29	0.0661	0.0014	0.862	394	7	417	10	811	23
NO26A115	7	2	11997	15.99	0.23	0.0555	0.0007	0.862	391	6	377	8	431	14
NO26A110	18	3	9815	15.90	0.27	0.0559	0.0016	0.862	393	7	384	12	448	31
NO26A103	10	11	10215	15.63	0.22	0.0618	0.0007	0.863	400	6	417	8	666	12
NO26A109	13	6	10856	15.71	0.34	0.0544	0.0023	0.862	398	9	393	15	386	47
NO26A113	7	55	12930	15.57	0.24	0.0607	0.0012	0.863	401	6	481	11	630	21
NO26A116	17	2	10296	15.49	0.24	0.0576	0.0014	0.863	403	6	441	14	516	27
NO26A105	9	3	11261	15.41	0.23	0.0572	0.0010	0.863	405	6	429	10	500	20
NO26A104	3	5	13059	15.37	0.22	0.0548	0.0006	0.863	406	6	424	8	405	12
NO26A102	20	0	10486	15.31	0.33	0.0567	0.0022	0.863	408	9	413	15	478	44
NO26A106	11	8	11045	15.15	0.28	0.0576	0.0010	0.863	412	8	444	9	515	18
NO26A114	4	45	10770	6.46	0.12	0.0703	0.0014	0.903	928	17	960	22	937	20
NO26A108	7	4	9541	3.01	0.05	0.1814	0.0007	0.987	1848	28	1822	32	2665	3
NT13WH41														
NO26A125	290	2622	15074	23.06	0.47	0.0517	0.0011	0.854	274	6	213	5	270	24
NO26A134	146	3386	16180	21.79	0.37	0.0557	0.0007	0.855	289	5	282	5	440	14
NO26A122	9	523	13454	19.96	0.39	0.0616	0.0014	0.857	315	6	273	8	659	25
NO26A130	7	0	11772	16.37	0.25	0.0530	0.0008	0.861	382	6	381	9	328	17
NO26A131	14	9	9924	16.32	0.25	0.0549	0.0010	0.861	383	6	375	9	406	20
NO26A121	13	321	13394	16.13	0.23	0.0560	0.0003	0.862	388	6	387	7	451	6
NO26A123	6	1	11505	16.10	0.23	0.0566	0.0008	0.862	389	6	385	9	477	15

NO26A128	13	1	9861	15.79	0.24	0.0534	0.0008	0.862	396	6	383	8	347	17
NO26A129	7	0	12282	15.44	0.33	0.0553	0.0033	0.863	405	9	384	18	423	67
NO26A120	6	1	7639	11.71	0.16	0.0590	0.0006	0.872	528	7	519	14	567	12
NO26A126	16	0	10307	11.14	0.19	0.0589	0.0015	0.874	554	10	553	13	562	29
NO26A127	15	4	10537	10.89	0.18	0.0594	0.0013	0.875	566	9	563	13	581	23
NO26A124	8	4	11473	10.65	0.15	0.0596	0.0005	0.876	579	8	564	12	588	9
NO26A133	16	2	11415	6.83	0.12	0.1135	0.0018	0.899	881	15	832	17	1856	14
NO26A132	81	4356	14668	12.21	0.28	0.3090	0.0054	0.870	507	12	3336	122	3516	14
WT14WH73														
NO26A174	49	1410	17594	26.12	0.57	0.0547	0.0011	0.852	242	5	132	8	399	23
NO26A179	35	124	11778	16.90	0.25	0.0583	0.0012	0.860	371	6	392	9	542	22
NO26A173	9	3	11954	16.96	0.26	0.0545	0.0010	0.860	369	6	366	8	390	20
NO26A184	4	1	13569	16.97	0.25	0.0539	0.0007	0.860	369	5	363	8	365	15
NO26A172	8	108	9884	16.59	0.29	0.0695	0.0017	0.861	377	7	444	15	913	25
NO26A178	329	181	14183	16.88	0.26	0.0529	0.0007	0.861	371	6	380	9	326	16
NO26A186	5	0	12996	16.85	0.26	0.0539	0.0008	0.861	372	6	371	9	366	16
NO26A175	8	2	12062	16.84	0.27	0.0541	0.0011	0.861	372	6	360	10	374	22
NO26A182	8	1	11824	16.80	0.25	0.0531	0.0008	0.861	373	5	355	8	331	17
NO26A176	11	4	11352	16.73	0.26	0.0530	0.0010	0.861	374	6	366	8	329	22
NO26A180	5	26	13323	16.68	0.26	0.0551	0.0007	0.861	375	6	381	9	416	15
NO26A177	4	2	14095	16.66	0.24	0.0539	0.0007	0.861	376	5	377	10	366	14
NO26A181	3	2	13738	16.49	0.25	0.0522	0.0006	0.861	379	6	384	9	295	14
NO26A187	11	3	11193	16.43	0.27	0.0543	0.0008	0.861	381	6	379	8	382	16
NO26A185	13	1	10691	15.67	0.24	0.0555	0.0021	0.862	399	6	406	10	433	42
NO26A183	14	1193	13017	20.15	0.80	0.0754	0.0014	0.856	312	12	493	19	1079	19
131414														
NO26A192	24	199	10567	18.45	0.30	0.0550	0.0007	0.858	340	6	352	7	412	14
NO26A199	10	111	11275	17.38	0.28	0.0595	0.0007	0.860	361	6	362	8	587	12
NO26A191	16	104	10629	17.20	0.29	0.0612	0.0010	0.860	364	6	422	9	645	17
NO26A194	8	768	13252	17.28	0.32	0.0547	0.0008	0.860	363	7	462	11	399	16
NO26A202	9	264	10471	17.26	0.31	0.0554	0.0004	0.860	363	6	371	7	429	9
NO26A195	43	1048	12885	17.00	0.25	0.0642	0.0005	0.860	369	5	479	10	747	9
NO26A204	8	0	11670	17.14	0.26	0.0558	0.0010	0.860	365	6	366	8	443	21
NO26A196	7	36	10198	16.96	0.25	0.0571	0.0006	0.860	369	6	398	7	494	11
NO26A205	15	26106	10245	17.02	0.24	0.0539	0.0005	0.860	368	5	361	6	365	10
NO26A206	7	0	12099	16.88	0.26	0.0539	0.0008	0.861	371	6	370	7	366	16
NO26A193	9	14	9882	16.57	0.27	0.0547	0.0009	0.861	378	6	386	9	402	18
NO26A203	3	33	14085	16.48	0.32	0.0560	0.0007	0.861	380	7	400	10	452	13
NO26A198	64	10809	10279	15.73	0.25	0.0763	0.0018	0.862	397	6	514	12	1104	23
NO26A201	11	1	10440	15.87	0.34	0.0557	0.0017	0.862	394	9	365	15	440	34
NO26A200	5	129	12465	11.70	0.22	0.0653	0.0004	0.872	529	10	1848	35	783	6
NO26A197	12	10895	13531	18.52	0.36	0.1019	0.0018	0.858	339	7	512	18	1660	16
WT12WH20														
NO26A160	48	3554	19216	34.77	0.62	0.0742	0.0027	0.848	183	3	340	16	1046	37
NO26A159	70	2590	18555	29.98	0.50	0.1213	0.0055	0.849	211	4	561	31	1976	40
NO26A156	59	2335	16806	29.71	0.76	0.0955	0.0023	0.850	213	5	236	10	1539	23
NO26A166	27	583	14228	30.44	0.49	0.0626	0.0007	0.849	208	3	108	2	694	12
NO26A157	37	665	16310	26.16	0.44	0.0774	0.0009	0.852	242	4	213	6	1131	12
NO26A158	20	9	12092	17.53	0.44	0.0605	0.0025	0.860	358	9	339	19	621	45
NO26A169	11	31	12159	17.47	0.32	0.0595	0.0012	0.860	359	7	401	9	586	23
NO26A161	18	0	10852	17.55	0.28	0.0556	0.0010	0.860	357	6	351	7	435	20
NO26A163	28	3	11338	17.45	0.33	0.0536	0.0015	0.860	359	7	372	11	355	32
NO26A168	37	1	10423	17.03	0.28	0.0541	0.0012	0.860	368	6	346	10	374	25
NO26A165	12	212	13243	16.94	0.27	0.0563	0.0010	0.860	370	6	339	10	463	20
NO26A164				18.84	0.27	0.0540	0.0003	0.858	333	5	314	5	371	7
NO26A162	45	3	10276	16.55	0.31	0.0553	0.0020	0.861	378	7	382	13	424	41
NO26A167	215	7969	13076	16.17	0.27	0.0578	0.0017	0.862	387	6	367	10	522	32
WT12WH11														
NO26A146	12	1489	11881	19.04	0.33	0.0662	0.0013	0.858	330	6	395	9	813	21
NO26A144	5	43	12543	17.71	0.29	0.0571	0.0008	0.859	354	6	388	10	496	16

NO26A145	16	596	10012	17.05	0.30	0.0669	0.0014	0.860	367	6	394	9	835	22
NO26A152	26	404	10954	17.27	0.26	0.0561	0.0009	0.860	363	6	374	9	456	18
NO26A141	9	118	13683	17.26	0.33	0.0558	0.0012	0.860	363	7	404	14	444	24
NO26A147	5	2	13932	17.30	0.24	0.0535	0.0005	0.860	362	5	354	7	350	10
NO26A151	7	0	12781	17.12	0.25	0.0534	0.0008	0.860	366	5	364	7	346	16
NO26A140	4	15	14042	17.07	0.25	0.0539	0.0007	0.860	367	5	339	8	367	14
NO26A138	15	2	11766	16.89	0.32	0.0544	0.0013	0.860	371	7	381	14	386	28
NO26A143	4	1	13942	16.79	0.25	0.0537	0.0008	0.861	373	6	360	10	357	17
NO26A150	4	21	13997	16.13	0.27	0.0559	0.0009	0.862	388	7	379	10	449	19
NO26A139	18	11	12591	15.97	0.33	0.0572	0.0016	0.862	391	8	401	18	501	31
NO26A148	7	2	12960	15.73	0.26	0.0561	0.0011	0.862	397	7	379	10	456	22
NO26A149	10	477	13396	5.46	0.08	0.0996	0.0008	0.916	1085	16	1139	23	1617	7
NO26A142	724	732	12261	16.12	0.38	0.0672	0.0010	0.862	388	9	418	11	844	16

Appendix 5.1 Microprobe analytical data of tourmaline from the Heemskirk and Pieman Heads granites

Sample No.	Location	Texture type	Sector zone	wt.%	SiO_2	TiO_2	Al_2O_3	FeO	MgO	CaO	MnO	Na_2O	K_2O	F	H_2O	B_2O_3	TOTAL
WT12WH04-1-1	Pieman Heads Granite	Patch	c sector		35.11	0.26	36.14	10.29	2.57	0.08	0.04	1.54	0.06	0.40	3.60	10.44	100.54
WT12WH04-1-2	Pieman Heads Granite	Patch	a sector		34.41	0.56	34.88	10.95	3.13	0.27	0.07	1.72	0.01	0.67	3.56	10.32	100.56
WT12WH04-1-3	Pieman Heads Granite	Patch	a sector		34.44	0.09	35.27	13.00	1.60	0.11	0.11	1.90	0.04	0.51	3.54	10.26	100.86
WT12WH04-1-4	Pieman Heads Granite	Patch	later		34.85	0.02	35.57	14.65	0.29	0.04	0.09	1.15	0.04	0.48	3.53	10.24	100.96
WT12WH04-1-5	Pieman Heads Granite	Patch	later		34.35	0.00	35.51	14.73	0.26	0.04	0.09	1.31	0.03	0.53	3.53	10.22	100.59
WT12WH04-3-1	Pieman Heads Granite	Patch	a sector		34.64	0.92	33.35	11.72	3.48	0.36	0.09	2.12	0.02	0.86	3.53	10.22	101.30
WT12WH04-3-2	Pieman Heads Granite	Patch	a sector		34.24	0.66	34.62	11.24	3.37	0.30	0.10	1.73	0.04	0.76	3.55	10.28	100.89
WT12WH04-3-4	Pieman Heads Granite	Patch	a sector		34.55	0.58	34.58	11.30	3.07	0.29	0.08	1.95	0.05	0.73	3.55	10.28	101.00
WT12WH04-4-1	Pieman Heads Granite	Patch	a sector		34.88	0.34	36.15	10.49	2.66	0.22	0.06	1.74	0.04	0.33	3.59	10.42	100.92
WT12WH04-4-2	Pieman Heads Granite	Patch	a sector		34.54	0.58	34.94	11.09	3.14	0.27	0.12	1.99	0.05	0.75	3.55	10.29	101.31
WT12WH04-4-3	Pieman Heads Granite	Patch	a sector		34.55	0.51	35.66	11.21	2.81	0.28	0.08	1.88	0.04	0.68	3.55	10.30	101.56
WT12WH04-4-4	Pieman Heads Granite	Patch	a sector		34.21	0.39	35.65	10.56	2.95	0.22	0.09	1.71	0.04	0.58	3.58	10.36	100.33
WT12WH04-4-6	Pieman Heads Granite	Patch	a sector		34.58	0.34	36.01	10.85	2.63	0.19	0.07	1.62	0.02	0.33	3.59	10.40	100.64
WT12WH07-1-1-1	Pieman Heads Granite	Orbicule	c sector		34.59	0.30	35.91	10.53	2.60	0.11	0.06	1.63	0.04	0.61	3.58	10.38	100.35
WT12WH07-1-1-2	Pieman Heads Granite	Orbicule	c sector		34.20	0.72	34.39	11.33	3.10	0.24	0.10	1.80	0.05	0.72	3.55	10.28	100.48
WT12WH07-1-1-3	Pieman Heads Granite	Orbicule	a sector		33.81	0.48	33.80	13.15	2.31	0.28	0.12	1.86	0.09	0.78	3.51	10.18	100.39
WT12WH07-1-1-4	Pieman Heads Granite	Orbicule	c sector		34.53	0.21	36.42	11.94	1.79	0.11	0.06	1.59	0.04	0.36	3.57	10.35	100.98
WT12WH07-1-1-5	Pieman Heads Granite	Orbicule	a sector		33.96	0.69	34.64	12.80	2.41	0.29	0.07	1.94	0.06	0.80	3.52	10.19	101.38
WT12WH07-1-2-5	Pieman Heads Granite	Orbicule	c sector		34.11	0.84	33.41	11.66	2.79	0.31	0.09	1.74	0.06	0.74	3.54	10.27	99.58
WT12WH07-1-2-6	Pieman Heads Granite	Orbicule	a sector		34.09	0.81	33.92	12.20	2.61	0.32	0.09	1.77	0.03	0.69	3.54	10.24	100.32
WT12WH07-1-2-7	Pieman Heads Granite	Orbicule	c sector		34.00	0.46	35.42	11.52	2.53	0.25	0.08	1.77	0.05	0.58	3.56	10.31	100.51
WT12WH07-1-2-8	Pieman Heads Granite	Orbicule	a sector		33.99	0.76	34.49	12.30	2.36	0.33	0.10	1.93	0.03	0.67	3.53	10.24	100.75
WT12WH07-2-1	Pieman Heads Granite	Orbicule	c sector		34.12	0.40	34.77	10.56	2.68	0.22	0.13	1.72	0.05	0.29	3.59	10.41	98.93
WT12WH07-2-2	Pieman Heads Granite	Orbicule	a sector		34.06	0.94	33.91	11.01	3.07	0.39	0.04	1.83	0.05	0.58	3.55	10.29	99.72
WT12WH07-2-3	Pieman Heads Granite	Orbicule	c sector		33.83	0.42	35.02	10.65	2.87	0.21	0.08	1.75	0.03	0.37	3.58	10.38	99.19
WT12WH07-2-4	Pieman Heads Granite	Orbicule	a sector		33.25	0.68	33.82	11.28	3.21	0.31	0.07	1.84	0.03	0.59	3.55	10.29	98.92
WT12WH07-3-2-1	Pieman Heads Granite	Orbicule	c- sector		34.72	0.39	35.36	10.76	2.68	0.12	0.09	1.54	0.05	0.25	3.61	10.45	100.03
WT12WH07-3-2-2	Pieman Heads Granite	Orbicule	a sector		34.59	0.35	35.06	10.86	2.65	0.13	0.11	1.69	0.04	0.25	3.60	10.42	99.74
WT12WH07-3-2-3	Pieman Heads Granite	Orbicule	c- sector		34.06	0.50	34.67	11.39	3.16	0.28	0.10	1.75	0.05	0.50	3.57	10.34	100.37
WT12WH07-3-2-4	Pieman Heads Granite	Orbicule	a sector		33.13	0.71	34.09	11.51	3.21	0.39	0.09	2.04	0.03	0.62	3.55	10.29	99.68
WT12WH07-3-2-5	Pieman Heads Granite	Orbicule	a sector		33.98	0.44	35.38	11.10	2.83	0.24	0.10	1.75	0.03	0.35	3.58	10.39	100.17
WT12WH07-3-2-6	Pieman Heads Granite	Orbicule	c sector		34.33	0.37	35.55	10.74	2.71	0.18	0.09	1.66	0.05	0.28	3.59	10.42	99.97
WT12WH07-3-2-7	Pieman Heads Granite	Orbicule	a sector		33.69	0.68	34.41	11.28	3.15	0.34	0.08	1.88	0.05	0.57	3.56	10.32	100.01
WT12WH07-3-2-8	Pieman Heads Granite	Orbicule	c sector		33.45	0.50	34.75	11.06	3.05	0.32	0.08	1.79	0.03	0.49	3.57	10.35	99.45
WT12WH13-1-1-1	Pieman Heads Granite	Vein	c sector		32.90	0.81	32.89	14.99	0.88	0.20	0.10	1.70	0.04	0.65	3.49	10.11	98.76
WT12WH13-1-1-2	Pieman Heads Granite	Vein	a sector		33.32	0.65	34.87	12.83	1.53	0.12	0.06	1.67	0.05	0.63	3.53	10.24	99.51
WT12WH13-1-1-3	Pieman Heads Granite	Vein	a sector		34.00	0.24	35.62	11.17	1.88	0.05	0.03	1.31	0.06	0.28	3.59	10.42	98.67
WT12WH13-1-1-5	Pieman Heads Granite	Vein	a sector		33.62	0.78	34.25	11.43	2.72	0.25	0.10	1.89	0.02	0.72	3.54	10.26	99.59
WT12WH13-1-2-1-1	Pieman Heads Granite	Vein	a sector		32.67	0.65	34.34	13.74	1.29	0.21	0.12	1.76	0.04	0.68	3.51	10.17	99.19

WT12WH13-1-2-1-2	Pieman Heads Granite	Vein	a sector	33.33	0.58	34.24	11.35	3.00	0.21	0.09	1.90	0.08	0.72	3.54	10.26	99.29
WT12WH13-1-2-1-3	Pieman Heads Granite	Vein	a sector	33.26	0.53	34.23	11.27	2.96	0.24	0.05	1.96	0.03	0.71	3.54	10.27	99.07
WT12WH13-1-2-1-4	Pieman Heads Granite	Vein	a sector	33.19	0.57	34.27	12.14	2.33	0.19	0.08	1.92	0.07	0.74	3.53	10.23	99.25
WT12WH13-1-2-1-5	Pieman Heads Granite	Vein	a sector	33.11	0.47	35.45	12.90	1.37	0.13	0.07	1.59	0.04	0.66	3.53	10.24	99.56
WT12WH13-1-2-1-6	Pieman Heads Granite	Vein	a sector	33.18	0.41	35.18	11.66	2.36	0.22	0.07	1.75	0.05	0.65	3.55	10.28	99.36
WT12WH13-1-2-1-7	Pieman Heads Granite	Vein	a sector	32.95	0.50	35.09	11.93	2.20	0.18	0.04	1.73	0.06	0.81	3.53	10.25	99.26
WT12WH13-1-2-1-8	Pieman Heads Granite	Vein	a sector	33.24	0.51	35.66	11.88	2.10	0.20	0.07	1.63	0.03	0.73	3.54	10.27	99.85
WT12WH13-1-2-1-9	Pieman Heads Granite	Vein	a sector	33.27	0.65	35.45	11.02	2.71	0.33	0.10	1.74	0.03	0.70	3.55	10.28	99.84
WT12WH13-1-2-1-10	Pieman Heads Granite	Vein	a sector	32.62	0.53	36.27	12.78	1.04	0.13	0.12	1.72	0.02	0.84	3.52	10.20	99.77
WT12WH13-1-2-1-11	Pieman Heads Granite	Vein	a sector	32.55	0.40	35.69	13.67	0.48	0.13	0.34	1.70	0.00	0.98	3.50	10.14	99.57
WT12WH13-1-2-1-12	Pieman Heads Granite	Vein	a sector	32.38	0.47	35.50	14.10	0.39	0.11	0.22	1.84	0.07	0.98	3.48	10.10	99.64
WT12WH13-1-2-1-13	Pieman Heads Granite	Vein	core	32.42	0.36	40.42	7.80	0.35	0.19	2.42	1.59	0.01	0.53	3.59	10.42	100.09
WT12WH13-1-2-1-14	Pieman Heads Granite	Vein	core	32.12	0.50	39.53	8.41	0.25	0.17	2.36	1.69	0.04	0.58	3.57	10.36	99.61
WT12WH13-1-2-1-15	Pieman Heads Granite	Vein	core	31.74	0.56	38.59	9.36	0.22	0.15	1.99	1.74	0.04	0.63	3.56	10.33	98.91
WT12WH13-1-2-1-16	Pieman Heads Granite	Vein	core	32.14	0.48	38.30	10.27	0.28	0.14	1.62	1.63	0.00	0.70	3.55	10.28	99.40
WT12WH13-1-2-1-17	Pieman Heads Granite	Vein	core	33.45	0.38	38.20	10.33	0.25	0.02	1.41	1.40	0.01	0.66	3.57	10.35	100.02
WT12WH13-1-2-1-18	Pieman Heads Granite	Vein	core	32.89	0.40	37.96	10.15	0.25	0.09	1.46	1.46	0.02	0.64	3.57	10.35	99.25
WT12WH13-1-2-1-19	Pieman Heads Granite	Vein	core	33.22	0.41	38.08	10.42	0.24	0.08	1.33	1.47	0.02	0.58	3.57	10.35	99.77
WT12WH13-1-2-1-20	Pieman Heads Granite	Vein	core	33.21	0.32	38.50	9.17	0.19	0.04	1.83	1.40	0.01	0.56	3.59	10.40	99.23
WT12WH13-1-2-1-21	Pieman Heads Granite	Vein	a sector	33.28	0.50	34.98	10.90	2.92	0.22	0.07	1.88	0.02	0.73	3.55	10.30	99.35
WT12WH13-1-2-1-22	Pieman Heads Granite	Vein	a sector	33.12	0.44	35.02	14.31	0.47	0.10	0.27	1.90	0.01	0.91	3.49	10.11	100.15
WT12WH13-1-2-1-23	Pieman Heads Granite	Vein	c sector	33.30	0.35	36.20	13.39	0.15	0.03	0.29	1.46	0.04	0.69	3.53	10.23	99.65
WT12WH13-1-2-1-24	Pieman Heads Granite	Vein	c sector	33.40	0.30	35.92	13.64	0.15	0.08	0.28	1.62	0.04	0.56	3.53	10.23	99.76
WT12WH13-1-2-1-25	Pieman Heads Granite	Vein	a sector	33.04	0.58	35.28	14.17	0.41	0.10	0.22	1.78	0.06	0.98	3.49	10.11	100.21
WT12WH13-1-2-1-26	Pieman Heads Granite	Vein	a sector	33.66	0.57	35.05	10.67	2.90	0.27	0.05	1.73	0.04	0.76	3.55	10.30	99.55
WT12WH13-1-2-2-1	Pieman Heads Granite	Vein	a sector	33.27	0.47	34.59	13.13	1.70	0.17	0.08	1.81	0.03	0.60	3.53	10.22	99.59
WT12WH13-1-2-2-2	Pieman Heads Granite	Vein	a sector	33.39	0.65	34.41	12.02	2.54	0.20	0.07	1.78	0.06	0.77	3.53	10.24	99.67
WT12WH13-1-2-2-3	Pieman Heads Granite	Vein	a sector	33.20	0.60	34.64	11.29	2.96	0.20	0.04	1.90	0.04	0.70	3.54	10.27	99.39
WT12WH13-1-2-2-4	Pieman Heads Granite	Vein	a sector	33.86	0.52	34.53	11.04	2.99	0.21	0.07	1.90	0.04	0.71	3.55	10.30	99.73
WT12WH13-1-2-2-5	Pieman Heads Granite	Vein	a sector	33.48	0.38	35.05	11.28	2.70	0.20	0.08	1.73	0.02	0.62	3.56	10.31	99.41
WT12WH13-1-2-2-6	Pieman Heads Granite	Vein	a sector	33.24	0.56	34.88	11.76	2.63	0.18	0.09	1.84	0.05	0.78	3.53	10.25	99.77
WT12WH13-1-2-2-7	Pieman Heads Granite	Vein	a sector	33.31	0.55	34.89	11.83	2.41	0.19	0.05	1.77	0.04	0.74	3.54	10.26	99.59
WT12WH13-1-2-2-8	Pieman Heads Granite	Vein	a sector	33.07	0.52	35.01	11.84	2.25	0.22	0.12	1.76	0.04	0.83	3.53	10.23	99.42
WT12WH13-1-2-2-9	Pieman Heads Granite	Vein	a sector	33.24	0.49	35.28	12.63	1.77	0.16	0.12	1.91	0.04	0.90	3.52	10.19	100.24
WT12WH13-1-2-2-10	Pieman Heads Granite	Vein	a sector	33.09	0.48	35.38	12.54	1.51	0.13	0.08	1.57	0.04	0.75	3.53	10.24	99.35
WT12WH13-1-2-2-11	Pieman Heads Granite	Vein	c sector	33.74	0.49	35.39	11.62	2.48	0.23	0.06	1.78	0.04	0.71	3.55	10.28	100.36
WT12WH13-1-2-2-12	Pieman Heads Granite	Vein	c sector	34.06	0.26	36.48	10.43	2.14	0.08	0.06	1.37	0.04	0.44	3.60	10.43	99.38
WT12WH13-1-2-2-13	Pieman Heads Granite	Vein	c sector	34.07	0.26	36.83	10.27	2.10	0.06	0.05	1.28	0.03	0.33	3.60	10.45	99.36
WT12WH13-1-2-2-14	Pieman Heads Granite	Vein	c sector	32.96	0.58	35.31	11.46	2.53	0.19	0.09	1.80	0.03	0.71	3.55	10.28	99.48
WT12WH13-1-2-2-15	Pieman Heads Granite	Vein	a sector	33.06	0.48	34.73	11.61	2.30	0.16	0.07	1.77	0.04	0.75	3.54	10.27	98.79
WT12WH13-1-2-2-16	Pieman Heads Granite	Vein	a sector	33.10	0.47	34.73	11.63	2.63	0.14	0.07	1.81	0.04	0.77	3.54	10.26	99.17

WT12WH13-1-2-2-17	Pieman Heads Granite	Vein	a sector	33.59	0.62	34.99	11.59	2.67	0.23	0.06	1.83	0.03	0.76	3.54	10.26	100.17
WT12WH13-2-2-1	Pieman Heads Granite	Vein	a sector	32.22	0.56	35.48	14.00	0.39	0.20	0.44	1.74	0.06	0.90	3.49	10.11	99.58
WT12WH13-2-2-2	Pieman Heads Granite	Vein	a sector	33.85	0.32	35.50	13.46	0.54	0.03	0.30	1.47	0.03	0.66	3.53	10.23	99.93
WT12WH13-2-2-3	Pieman Heads Granite	Vein	a sector	33.78	0.32	35.70	13.15	0.57	0.04	0.33	1.46	0.02	0.64	3.53	10.23	99.77
WT12WH13-2-2-4	Pieman Heads Granite	Vein	a sector	34.05	0.33	35.61	13.15	0.51	0.05	0.36	1.36	0.04	0.57	3.54	10.26	99.84
WT12WH13-2-2-5	Pieman Heads Granite	Vein	a sector	33.55	0.42	36.03	13.21	0.60	0.04	0.38	1.56	0.02	0.79	3.52	10.21	100.32
WT12WH13-2-2-6	Pieman Heads Granite	Vein	a sector	32.18	0.64	35.29	14.11	0.36	0.15	0.51	1.78	0.06	0.93	3.48	10.08	99.56
WT12WH13-2-3-1-1	Pieman Heads Granite	Vein	a sector	33.87	0.14	33.99	13.69	1.54	0.09	0.15	1.59	0.00	0.55	3.52	10.21	99.36
WT12WH13-2-3-1-2	Pieman Heads Granite	Vein	a sector	33.88	0.09	34.48	13.83	1.44	0.07	0.12	1.59	0.05	0.56	3.52	10.22	99.85
WT12WH13-2-3-1-3	Pieman Heads Granite	Vein	a sector	33.83	0.12	34.63	12.97	1.93	0.07	0.08	1.57	0.03	0.52	3.54	10.27	99.54
WT12WH13-2-3-1-4	Pieman Heads Granite	Vein	a sector	34.26	0.15	34.29	12.09	2.50	0.07	0.10	1.68	0.01	0.57	3.55	10.30	99.56
WT12WH13-2-3-1-5	Pieman Heads Granite	Vein	a sector	33.93	0.15	34.36	11.67	2.65	0.08	0.11	1.65	0.06	0.55	3.56	10.32	99.07
WT12WH13-2-3-1-6	Pieman Heads Granite	Vein	c sector	33.97	0.04	34.41	14.63	0.82	0.07	0.12	1.57	0.03	0.47	3.52	10.20	99.85
WT12WH13-2-3-1-7	Pieman Heads Granite	Vein	c sector	33.44	0.01	34.57	15.31	0.34	0.04	0.12	1.60	0.03	0.51	3.50	10.16	99.63
WT12WH13-2-3-1-8	Pieman Heads Granite	Vein	c sector	34.25	0.03	34.98	14.74	0.66	0.04	0.09	1.74	0.04	0.44	3.51	10.19	100.71
WT12WH13-2-3-1-9	Pieman Heads Granite	Vein	c sector	34.20	0.04	34.08	14.74	0.88	0.06	0.11	1.66	0.04	0.64	3.51	10.17	100.13
WT12WH13-2-3-1-10	Pieman Heads Granite	Vein	c sector	33.63	0.06	33.92	15.63	0.49	0.11	0.15	1.87	0.01	0.66	3.48	10.10	100.10
WT12WH13-2-3-1-11	Pieman Heads Granite	Vein	c sector	34.08	0.04	35.18	14.71	0.22	0.02	0.11	1.43	0.03	0.18	3.54	10.26	99.80
WT12WH13-2-3-1-12	Pieman Heads Granite	Vein	c sector	33.89	0.04	33.87	15.49	0.33	0.10	0.15	1.73	0.06	0.68	3.49	10.12	99.95
WT12WH13-2-3-1-13	Pieman Heads Granite	Vein	c sector	34.08	0.00	34.38	14.72	0.80	0.09	0.11	1.87	0.03	0.59	3.51	10.16	100.36
WT12WH13-2-3-1-14	Pieman Heads Granite	Vein	a sector	33.85	0.13	33.85	12.40	2.47	0.07	0.08	1.87	0.02	0.67	3.54	10.25	99.18
WT12WH13-2-3-1-15	Pieman Heads Granite	Vein	a sector	33.78	0.18	34.04	11.93	2.76	0.08	0.13	1.93	0.01	0.75	3.53	10.25	99.37
WT12WH13-2-3-1-16	Pieman Heads Granite	Vein	a sector	34.14	0.14	33.57	13.54	2.02	0.09	0.15	1.94	0.01	0.71	3.51	10.19	100.03
WT12WH13-2-3-1-17	Pieman Heads Granite	Vein	a sector	34.02	0.21	33.77	13.69	2.00	0.05	0.11	1.77	0.01	0.78	3.51	10.18	100.09
WT12WH13-2-3-1-18	Pieman Heads Granite	Vein	a sector	33.57	0.08	32.92	14.53	1.12	0.06	0.16	1.88	0.07	0.68	3.50	10.15	98.71
WT12WH13-2-3-2-1	Pieman Heads Granite	Vein	a sector	33.31	0.01	34.10	16.06	0.11	0.12	0.21	1.70	0.02	0.47	3.49	10.11	99.72
WT12WH13-2-3-2-2	Pieman Heads Granite	Vein	a sector	32.37	0.65	35.42	13.86	0.36	0.13	0.61	1.65	0.00	0.92	3.49	10.12	99.59
WT12WH13-2-3-2-3	Pieman Heads Granite	Vein	c sector	33.67	0.32	35.49	13.62	0.22	0.03	0.41	1.31	0.02	0.67	3.53	10.23	99.53
WT12WH13-2-3-2-4	Pieman Heads Granite	Vein	c sector	33.34	0.49	35.59	13.85	0.27	0.07	0.47	1.46	0.02	0.93	3.50	10.15	100.14
WT12WH13-2-3-2-5	Pieman Heads Granite	Vein	c sector	33.18	0.45	35.62	13.70	0.23	0.05	0.50	1.57	0.01	0.98	3.50	10.15	99.95
WT12WH13-2-3-2-6	Pieman Heads Granite	Vein	a sector	32.63	0.64	35.41	14.28	0.35	0.16	0.52	1.71	0.04	0.93	3.48	10.08	100.22
WT12WH13-2-3-2-7	Pieman Heads Granite	Vein	a sector	33.90	0.07	34.97	12.38	2.05	0.10	0.11	1.68	0.06	0.66	3.54	10.26	99.78
WT12WH13-3-1-1	Pieman Heads Granite	Vein	a sector	33.48	0.57	35.17	11.32	2.76	0.35	0.12	1.79	0.07	0.66	3.54	10.27	100.12
WT12WH13-3-1-6	Pieman Heads Granite	Vein	a sector	33.58	0.62	34.51	11.28	3.01	0.32	0.06	1.90	0.04	0.72	3.54	10.28	99.85
WT12WH20-3-1	Trial Harbour, Heemskirk	Patch	a sector	33.16	0.54	32.79	14.88	1.33	0.20	0.15	2.02	0.08	1.19	3.46	10.02	99.82
WT12WH20-3-2	Trial Harbour, Heemskirk	Patch	c sector?	33.33	0.49	33.79	15.06	1.04	0.09	0.14	1.98	0.05	0.95	3.47	10.06	100.45
WT12WH20-3-3	Trial Harbour, Heemskirk	Patch	c sector?	33.32	0.54	33.58	14.74	1.12	0.11	0.11	2.07	0.04	0.96	3.48	10.07	100.14
WT12WH20-3-4	Trial Harbour, Heemskirk	Patch	c sector?	34.05	0.36	33.80	14.44	1.07	0.04	0.17	1.77	0.04	0.77	3.50	10.15	100.16
WT12WH20-3-5	Trial Harbour, Heemskirk	Patch	c sector?	33.80	0.37	33.70	14.45	1.10	0.06	0.13	1.85	0.00	0.89	3.49	10.12	99.96
WT12WH20-3-6	Trial Harbour, Heemskirk	Patch	c sector?	33.89	0.32	33.70	14.59	1.08	0.08	0.15	1.83	0.05	0.87	3.49	10.12	100.17
WT12WH20-3-7	Trial Harbour, Heemskirk	Patch	a sector	32.38	0.60	32.49	15.33	1.38	0.19	0.15	2.15	0.02	1.26	3.44	9.97	99.36

WT12WH20-3-8	Trial Harbour, Heemskirk	Patch	a sector	32.69	0.61	32.59	15.21	1.31	0.16	0.13	2.17	0.04	1.22	3.45	9.98	99.58
WT12WH20-4-8	Trial Harbour, Heemskirk	Patch	c sector	33.82	0.30	34.18	13.53	1.04	0.06	0.13	1.77	0.03	0.67	3.52	10.21	99.25
WT12WH20-4-9	Trial Harbour, Heemskirk	Patch	a sector	32.51	0.68	33.18	14.64	1.25	0.25	0.19	2.05	0.06	1.02	3.46	10.04	99.33
WT12WH20-3-11	Trial Harbour, Heemskirk	Patch	a sector	32.98	0.45	33.33	14.85	1.33	0.22	0.14	2.18	0.07	1.11	3.46	10.02	100.13
WT12WH20-4-10	Trial Harbour, Heemskirk	Patch	c sector	33.16	0.42	34.89	13.55	1.06	0.12	0.14	1.69	0.04	0.77	3.51	10.19	99.56
WT12WH20-4-11	Trial Harbour, Heemskirk	Patch	a sector	32.67	0.53	33.96	14.60	1.31	0.21	0.17	1.96	0.07	1.03	3.47	10.05	100.03
WT12WH20-4-12	Trial Harbour, Heemskirk	Patch	a sector	32.63	0.53	33.53	14.85	1.34	0.19	0.13	2.12	0.04	1.12	3.46	10.02	99.95
WT12WH20-4-13	Trial Harbour, Heemskirk	Patch	a sector	32.74	0.69	33.49	14.98	1.22	0.23	0.14	1.96	0.06	1.06	3.46	10.03	100.07
WT12WH20-4-14	Trial Harbour, Heemskirk	Patch	c sector	33.05	0.39	34.86	13.98	0.98	0.10	0.15	1.80	0.07	0.80	3.50	10.15	99.82
WT12WH21-1-1	Trial Harbour, Heemskirk	Patch	a sector	33.05	0.80	31.62	15.73	1.37	0.17	0.17	2.07	0.05	1.36	3.43	9.94	99.75
WT12WH21-1-2	Trial Harbour, Heemskirk	Patch	a sector	33.09	0.48	32.96	15.32	1.33	0.21	0.18	2.20	0.07	1.15	3.45	9.99	100.44
WT12WH21-1-3	Trial Harbour, Heemskirk	Patch	a sector	32.95	0.61	33.16	15.04	1.37	0.25	0.18	2.04	0.08	1.22	3.44	9.97	100.32
WT12WH21-1-4	Trial Harbour, Heemskirk	Patch	a sector	32.87	0.51	33.23	14.80	1.29	0.19	0.18	2.09	0.06	1.19	3.46	10.02	99.89
WT12WH21-1-5	Trial Harbour, Heemskirk	Patch	a sector	32.85	0.57	33.65	14.94	1.24	0.24	0.20	2.11	0.00	1.16	3.45	10.01	100.43
WT12WH21-1-6	Trial Harbour, Heemskirk	Patch	a sector	33.12	0.57	33.61	14.99	1.27	0.21	0.20	1.98	0.03	1.19	3.45	10.01	100.65
WT12WH21-1-7	Trial Harbour, Heemskirk	Patch	a sector	32.86	0.67	33.36	15.05	1.33	0.20	0.16	2.01	0.06	1.22	3.45	10.00	100.38
WT12WH21-1-8	Trial Harbour, Heemskirk	Patch	a sector	32.95	0.50	33.96	15.11	1.28	0.16	0.17	1.87	0.06	1.07	3.46	10.02	100.59
WT12WH21-1-9	Trial Harbour, Heemskirk	Patch	a sector	33.09	0.52	33.37	15.13	1.33	0.23	0.18	2.07	0.02	1.18	3.45	10.01	100.57
WT12WH21-3-3	Trial Harbour, Heemskirk	Patch	a sector	32.99	0.42	33.69	14.99	1.26	0.19	0.21	1.94	0.04	1.03	3.46	10.03	100.23
WT12WH21-3-4	Trial Harbour, Heemskirk	Patch	a sector	33.01	0.43	33.76	14.87	1.25	0.16	0.17	2.04	0.04	0.94	3.47	10.06	100.21
WT12WH21-3-5	Trial Harbour, Heemskirk	Patch	a sector	33.32	0.47	33.77	14.98	1.32	0.14	0.23	2.00	0.04	1.12	3.46	10.03	100.88
WT12WH21-5-3	Trial Harbour, Heemskirk	Patch	a sector	32.96	0.62	32.81	15.16	1.42	0.24	0.19	1.98	0.03	1.16	3.45	10.00	100.00
WT12WH21-5-4	Trial Harbour, Heemskirk	Patch	a sector	33.28	0.41	34.59	14.10	1.17	0.11	0.16	1.97	0.08	0.83	3.49	10.13	100.32
WT12WH21-5-5	Trial Harbour, Heemskirk	Patch	a sector	32.79	0.51	33.91	14.66	1.35	0.22	0.14	2.02	0.03	1.08	3.46	10.04	100.21
WT12WH21-5-6	Trial Harbour, Heemskirk	Patch	a sector	32.70	0.46	33.85	14.54	1.33	0.20	0.16	2.07	0.04	1.06	3.47	10.05	99.93
WT12WH21-5-7	Trial Harbour, Heemskirk	Patch	a sector	33.13	0.43	34.00	14.70	1.31	0.20	0.20	2.06	0.05	1.01	3.47	10.05	100.60
WT12WH21-5-8	Trial Harbour, Heemskirk	Patch	a sector	33.16	0.54	33.83	14.52	1.31	0.25	0.18	1.85	0.04	1.18	3.46	10.04	100.36
WT12WH23-2-3-1	Trial Harbour, Heemskirk	Vein	c sector	34.14	0.15	35.24	15.44	0.15	0.10	0.12	1.69	0.04	0.53	3.52	10.19	101.29
WT12WH23-2-3-2	Trial Harbour, Heemskirk	Vein	a sector	33.95	0.34	33.44	16.81	0.16	0.11	0.11	2.08	0.05	1.06	3.52	10.03	101.64
WT12WH23-2-3-3	Trial Harbour, Heemskirk	Vein	c sector	34.02	0.19	34.20	16.42	0.14	0.07	0.10	1.84	0.03	0.59	3.52	10.11	101.23
WT12WH23-2-3-4	Trial Harbour, Heemskirk	Vein	c sector	33.88	0.18	34.74	15.47	0.02	0.05	0.08	1.55	0.02	0.33	3.52	10.20	100.03
WT12WH23-2-3-5	Trial Harbour, Heemskirk	Vein	a sector	33.72	0.38	32.22	17.51	0.41	0.06	0.14	2.14	0.06	1.03	3.52	9.98	101.17
WT12WH23-2-3-6	Trial Harbour, Heemskirk	Vein	a sector	33.71	0.31	32.05	17.56	0.34	0.05	0.11	2.08	0.04	1.07	3.52	9.99	100.85
WT12WH23-2-3-7	Trial Harbour, Heemskirk	Vein	a sector	33.46	0.27	31.98	17.72	0.32	0.04	0.12	2.13	0.06	1.10	3.52	9.96	100.68
WT12WH23-2-5-1	Trial Harbour, Heemskirk	Vein	c sector	34.26	0.13	34.95	15.99	0.01	0.10	0.09	1.71	0.05	0.53	3.52	10.15	101.51
WT12WH23-2-5-2	Trial Harbour, Heemskirk	Vein	c sector	34.52	0.15	34.93	15.71	0.17	0.10	0.06	1.76	0.05	0.58	3.52	10.15	101.70
WT12WH23-2-5-3	Trial Harbour, Heemskirk	Vein	a sector	34.50	0.24	34.81	15.37	0.29	0.06	0.10	1.66	0.03	0.37	3.52	10.21	101.16
WT12WH23-2-5-4	Trial Harbour, Heemskirk	Vein	a sector	34.31	0.19	34.84	15.20	0.49	0.08	0.07	1.65	0.05	0.51	3.52	10.19	101.11
WT12WH23-2-5-5	Trial Harbour, Heemskirk	Vein	a sector	34.04	0.51	32.26	17.36	0.26	0.03	0.10	1.87	0.02	1.23	3.52	9.99	101.18
WT12WH23-2-5-6	Trial Harbour, Heemskirk	Vein	a sector	33.98	0.13	33.68	16.29	0.32	0.05	0.09	1.92	0.04	0.73	3.52	10.10	100.86
WT12WH23-2-5-7	Trial Harbour, Heemskirk	Vein	a sector	33.85	0.15	33.49	16.41	0.29	0.06	0.11	1.78	0.03	0.62	3.52	10.11	100.42

WT12WH23-2-5-8	Trial Harbour, Heemskirk	Vein	c sector	33.89	0.21	32.50	17.25	0.35	0.07	0.13	2.30	0.05	0.96	3.52	10.01	101.24
WT12WH23-2-5-9	Trial Harbour, Heemskirk	Vein	a sector	33.90	0.21	34.23	16.25	0.08	0.06	0.10	1.82	0.02	0.45	3.52	10.14	100.80
WT12WH23-2-5-10	Trial Harbour, Heemskirk	Vein	c sector	33.65	0.29	32.14	17.48	0.36	0.04	0.12	2.43	0.06	1.09	3.52	9.97	101.15
WT12WH24-1-1-1	Trial Harbour, Heemskirk	Cavity	c sector	33.23	0.01	34.33	14.78	0.57	0.16	0.11	1.78	0.03	0.70	3.50	10.14	99.32
WT12WH24-1-1-2	Trial Harbour, Heemskirk	Cavity	a sector	33.38	0.11	32.83	16.58	0.57	0.10	0.14	2.18	0.05	1.11	3.43	9.94	100.43
WT12WH24-1-1-3	Trial Harbour, Heemskirk	Cavity	a sector	33.78	0.04	34.28	15.33	0.27	0.02	0.03	1.75	0.05	0.38	3.51	10.17	99.62
WT12WH24-1-1-4	Trial Harbour, Heemskirk	Cavity	c sector	32.94	0.11	33.39	15.96	0.50	0.11	0.09	2.13	0.04	1.00	3.45	10.01	99.73
WT12WH24-1-2-1	Trial Harbour, Heemskirk	Cavity	a sector	32.38	0.00	33.30	16.90	0.02	0.22	0.13	1.97	0.01	0.90	3.44	9.98	99.26
WT12WH24-1-2-2	Trial Harbour, Heemskirk	Cavity	a sector	32.76	0.04	33.81	16.44	0.21	0.17	0.11	2.08	0.04	1.04	3.44	9.98	100.12
WT12WH24-1-2-3	Trial Harbour, Heemskirk	Cavity	c sector	33.68	0.00	33.74	15.87	0.14	0.04	0.14	1.71	0.04	0.27	3.51	10.17	99.30
WT12WH24-1-2-4	Trial Harbour, Heemskirk	Cavity	c sector	33.96	0.02	34.20	15.44	0.18	0.06	0.16	1.61	0.05	0.34	3.51	10.18	99.73
WT12WH24-1-3-1	Trial Harbour, Heemskirk	Cavity	a sector	32.66	0.30	32.18	17.06	0.65	0.26	0.08	1.95	0.04	1.06	3.43	9.93	99.59
WT12WH24-1-3-2	Trial Harbour, Heemskirk	Cavity	a sector	33.07	0.52	32.59	16.38	0.63	0.15	0.08	1.93	0.05	1.20	3.43	9.95	99.99
WT12WH24-1-3-3	Trial Harbour, Heemskirk	Cavity	a sector	32.93	0.57	32.89	15.98	0.66	0.17	0.13	2.00	0.04	1.15	3.44	9.98	99.95
WT12WH24-1-3-4	Trial Harbour, Heemskirk	Cavity	a sector	32.71	0.65	32.11	16.33	0.96	0.26	0.06	2.00	0.07	1.05	3.44	9.96	99.61
WT12WH24-1-3-5	Trial Harbour, Heemskirk	Cavity	a sector	32.91	0.57	32.44	16.59	0.69	0.24	0.09	2.18	0.06	1.18	3.43	9.93	100.30
WT12WH24-1-3-6	Trial Harbour, Heemskirk	Cavity	a sector	32.79	0.57	32.40	16.24	0.70	0.27	0.07	2.14	0.05	1.14	3.43	9.95	99.75
WT12WH24-2-3-1	Trial Harbour, Heemskirk	Cavity	a sector	33.01	0.47	33.57	15.30	0.85	0.16	0.11	1.87	0.06	0.98	3.47	10.05	99.90
WT12WH24-2-3-2	Trial Harbour, Heemskirk	Cavity	a sector	32.52	0.49	33.95	15.37	0.92	0.20	0.09	2.09	0.04	1.03	3.45	10.01	100.18
WT12WH24-2-3-3	Trial Harbour, Heemskirk	Cavity	c sector	32.98	0.31	34.73	14.17	0.75	0.16	0.08	1.80	0.05	0.71	3.51	10.16	99.41
WT12WH24-2-3-4	Trial Harbour, Heemskirk	Cavity	c sector	33.15	0.28	34.72	14.28	0.73	0.17	0.04	1.75	0.03	0.67	3.51	10.16	99.48
WT12WH24-2-3-5	Trial Harbour, Heemskirk	Cavity	c sector	33.17	0.33	34.46	14.22	0.75	0.18	0.08	1.79	0.06	0.68	3.51	10.17	99.39
WT12WH24-2-3-6	Trial Harbour, Heemskirk	Cavity	a sector	32.77	0.42	33.91	14.94	0.96	0.28	0.06	1.83	0.05	1.03	3.47	10.05	99.78
WT12WH24-2-3-7	Trial Harbour, Heemskirk	Cavity	a sector	32.80	0.32	33.40	16.44	0.67	0.29	0.04	2.12	0.02	0.89	3.45	9.99	100.43
WT12WH24-2-3-8	Trial Harbour, Heemskirk	Cavity	c sector	33.76	0.16	33.83	15.02	0.66	0.09	0.01	1.64	0.02	0.67	3.50	10.14	99.51
WT12WH24-2-3-9	Trial Harbour, Heemskirk	Cavity	c sector	33.69	0.24	34.24	14.71	0.50	0.03	0.07	1.63	0.06	0.58	3.51	10.18	99.45
WT12WH24-2-3-10	Trial Harbour, Heemskirk	Cavity	c sector	33.65	0.26	34.09	14.78	0.56	0.09	0.05	1.66	0.00	0.55	3.51	10.18	99.38
WT12WH24-2-3-11	Trial Harbour, Heemskirk	Cavity	c sector	34.01	0.23	34.19	14.75	0.60	0.03	0.07	1.55	0.00	0.55	3.52	10.19	99.69
WT12WH24-2-3-12	Trial Harbour, Heemskirk	Cavity	a sector	32.74	0.36	32.99	15.72	0.83	0.25	0.05	1.92	0.04	0.80	3.47	10.05	99.21
WT12WH24-2-3-13	Trial Harbour, Heemskirk	Cavity	a sector	32.73	0.40	32.97	16.11	0.53	0.18	0.06	1.93	0.02	0.85	3.46	10.03	99.26
WT12WH24-2-3-14	Trial Harbour, Heemskirk	Cavity	a sector	32.72	0.31	33.75	15.76	0.49	0.23	0.09	1.81	0.02	0.81	3.47	10.05	99.54
WT12WH24-2-3-15	Trial Harbour, Heemskirk	Cavity	a sector	32.76	0.30	33.81	15.43	0.61	0.25	0.07	1.91	0.05	0.85	3.47	10.06	99.58
WT12WH24-2-3-16	Trial Harbour, Heemskirk	Cavity	a sector	32.84	0.19	34.14	15.82	0.45	0.26	0.06	1.80	0.06	0.80	3.47	10.05	99.93
WT12WH24-2-3-17	Trial Harbour, Heemskirk	Cavity	a sector	33.03	0.07	32.82	17.07	0.08	0.12	0.06	1.98	0.02	0.79	3.45	9.99	99.47
WT12WH24-2-3-18	Trial Harbour, Heemskirk	Cavity	a sector	32.50	0.63	32.53	15.84	1.05	0.32	0.07	1.94	0.02	0.97	3.45	10.00	99.33
WT12WH24-2-3-19	Trial Harbour, Heemskirk	Cavity	a sector	32.57	0.38	32.28	16.42	0.79	0.29	0.07	2.03	0.05	0.90	3.44	9.98	99.20
WT12WH24-2-3-20	Trial Harbour, Heemskirk	Cavity	a sector	32.85	0.50	32.73	16.03	0.76	0.29	0.09	2.04	0.06	0.93	3.45	9.99	99.71
WT12WH24-2-4-1	Trial Harbour, Heemskirk	Cavity	a sector	32.27	0.52	33.06	15.42	0.75	0.21	0.12	1.99	0.09	1.07	3.45	10.01	98.97
WT12WH24-2-4-2	Trial Harbour, Heemskirk	Cavity	c sector	33.36	0.37	34.29	14.87	0.66	0.12	0.09	1.88	0.05	0.66	3.49	10.13	99.97
WT12WH24-2-4-3	Trial Harbour, Heemskirk	Cavity	c sector	32.92	0.32	33.85	15.16	0.68	0.16	0.09	1.75	0.04	0.75	3.48	10.09	99.29
WT12WH24-2-4-4	Trial Harbour, Heemskirk	Cavity	c sector	32.87	0.34	33.53	15.40	0.72	0.14	0.08	1.91	0.04	0.84	3.47	10.06	99.42

WT12WH24-2-4-5	Trial Harbour, Heemskirk	Cavity	c sector	33.65	0.29	34.06	15.27	0.76	0.09	0.06	1.88	0.05	0.81	3.48	10.09	100.50
WT12WH24-2-4-6	Trial Harbour, Heemskirk	Cavity	c sector	33.56	0.32	33.57	14.92	0.67	0.11	0.09	1.75	0.04	0.56	3.50	10.16	99.26
WT12WH24-2-4-7	Trial Harbour, Heemskirk	Cavity	c sector	34.07	0.28	33.89	15.21	0.65	0.05	0.02	1.54	0.02	0.55	3.51	10.16	99.94
WT12WH24-2-4-8	Trial Harbour, Heemskirk	Cavity	c sector	32.86	0.31	33.66	15.20	0.65	0.22	0.07	1.80	0.04	0.74	3.48	10.09	99.13
WT12WH24-2-4-9	Trial Harbour, Heemskirk	Cavity	c sector	34.03	0.26	33.93	15.03	0.63	0.07	0.07	1.83	0.03	0.60	3.50	10.14	100.11
WT12WH24-2-4-10	Trial Harbour, Heemskirk	Cavity	a sector	33.10	0.54	32.47	15.96	0.91	0.37	0.05	2.03	0.04	0.93	3.45	10.00	99.85
WT12WH24-3-1	Trial Harbour, Heemskirk	Cavity	a sector	32.63	0.20	32.57	17.03	0.41	0.21	0.09	1.80	0.04	0.95	3.44	9.96	99.34
WT12WH24-3-2	Trial Harbour, Heemskirk	Cavity	a sector	32.36	0.36	33.51	15.75	0.63	0.23	0.06	1.86	0.05	0.82	3.46	10.04	99.14
WT12WH24-3-3	Trial Harbour, Heemskirk	Cavity	a sector	32.26	0.36	33.29	15.80	0.74	0.27	0.06	1.85	0.04	0.93	3.46	10.02	99.08
WT12WH24-3-4	Trial Harbour, Heemskirk	Cavity	c sector	32.73	0.52	33.15	15.02	1.00	0.21	0.05	1.97	0.07	1.02	3.46	10.04	99.25
WT12WH24-3-5	Trial Harbour, Heemskirk	Cavity	c sector	33.89	0.31	34.63	14.21	0.84	0.04	0.04	1.76	0.01	0.62	3.52	10.19	100.05
WT12WH24-3-6	Trial Harbour, Heemskirk	Cavity	c sector	33.47	0.34	33.76	14.68	0.83	0.19	0.08	1.80	0.05	0.78	3.49	10.12	99.59
WT12WH24-3-7	Trial Harbour, Heemskirk	Cavity	c sector	32.62	0.46	33.29	15.46	0.93	0.30	0.04	1.93	0.04	1.01	3.46	10.02	99.57
WT12WH24-3-8	Trial Harbour, Heemskirk	Cavity	a sector	32.42	0.43	32.22	16.73	0.62	0.27	0.12	1.93	0.06	0.87	3.44	9.97	99.08
WT12WH24-3-9	Trial Harbour, Heemskirk	Cavity	a sector	32.91	0.54	32.78	15.88	0.73	0.33	0.09	1.90	0.06	0.97	3.45	10.00	99.65
WT12WH24-3-10	Trial Harbour, Heemskirk	Cavity	a sector	32.71	0.45	33.07	15.99	0.69	0.23	0.04	1.97	0.04	0.99	3.45	10.00	99.64
WT12WH24-3-11	Trial Harbour, Heemskirk	Cavity	a sector	32.54	0.36	32.40	16.54	0.49	0.29	0.06	2.01	0.06	0.96	3.44	9.96	99.11
WT12WH24-3-12	Trial Harbour, Heemskirk	Cavity	c sector	33.17	0.48	33.35	15.85	0.97	0.26	0.06	1.90	0.05	0.96	3.45	10.00	100.49
WT12WH24-3-13	Trial Harbour, Heemskirk	Cavity	c sector	33.12	0.37	34.42	14.34	0.89	0.20	0.08	1.86	0.05	0.79	3.50	10.13	99.75
WT12WH28-1-1-4	Trial Harbour, Heemskirk	Orbicule	a sector	32.75	0.40	33.28	15.46	0.72	0.14	0.10	1.91	0.09	1.05	3.46	10.02	99.38
WT12WH28-1-1-5	Trial Harbour, Heemskirk	Orbicule	a sector	33.10	0.29	34.30	15.11	0.58	0.17	0.14	1.82	0.03	0.96	3.47	10.07	100.05
WT12WH28-1-1-6	Trial Harbour, Heemskirk	Orbicule	a sector	32.48	0.47	33.92	15.40	0.77	0.14	0.16	1.86	0.04	0.92	3.47	10.05	99.66
WT12WH28-1-2-1	Trial Harbour, Heemskirk	Orbicule	a sector	32.73	0.63	33.79	15.48	0.70	0.17	0.09	1.95	0.08	0.97	3.46	10.03	100.06
WT12WH28-1-2-2	Trial Harbour, Heemskirk	Orbicule	a sector	32.97	0.42	34.20	15.23	0.64	0.14	0.09	1.97	0.02	0.83	3.48	10.08	100.07
WT12WH28-1-2-3	Trial Harbour, Heemskirk	Orbicule	a sector	32.80	0.53	33.84	15.13	0.61	0.22	0.09	1.87	0.06	0.90	3.47	10.07	99.60
WT12WH28-1-2-4	Trial Harbour, Heemskirk	Orbicule	a sector	32.64	0.58	32.73	16.06	0.75	0.22	0.08	1.94	0.08	1.04	3.44	9.97	99.53
WT12WH28-1-2-5	Trial Harbour, Heemskirk	Orbicule	a sector	32.45	0.45	33.40	15.86	0.64	0.16	0.10	2.05	0.05	0.99	3.45	10.00	99.60
WT12WH28-1-2-6	Trial Harbour, Heemskirk	Orbicule	a sector	32.61	0.27	34.24	15.44	0.56	0.22	0.09	1.91	0.05	1.00	3.46	10.04	99.89
WT12WH28-1-3-1	Trial Harbour, Heemskirk	Orbicule	a sector	32.77	0.13	35.03	14.55	0.62	0.17	0.08	1.87	0.07	0.87	3.49	10.11	99.76
WT12WH28-1-3-2	Trial Harbour, Heemskirk	Orbicule	a sector	33.27	0.25	34.47	15.00	0.70	0.12	0.06	1.74	0.05	0.81	3.48	10.09	100.04
WT12WH28-1-3-3	Trial Harbour, Heemskirk	Orbicule	a sector	32.94	0.20	34.94	14.51	0.57	0.08	0.12	1.72	0.07	0.66	3.50	10.16	99.48
WT12WH28-1-3-4	Trial Harbour, Heemskirk	Orbicule	a sector	33.29	0.18	34.90	14.65	0.67	0.14	0.07	1.94	0.05	0.90	3.48	10.10	100.38
WT12WH28-1-3-5	Trial Harbour, Heemskirk	Orbicule	a sector	32.61	0.17	33.97	15.53	0.64	0.15	0.08	1.78	0.09	0.94	3.47	10.05	99.48
WT12WH28-1-4-1	Trial Harbour, Heemskirk	Orbicule	a sector	31.99	0.46	34.40	15.64	0.48	0.29	0.21	2.05	0.05	1.03	3.45	9.99	100.04
WT12WH28-1-4-2	Trial Harbour, Heemskirk	Orbicule	a sector	32.76	0.21	35.09	14.99	0.39	0.22	0.18	1.98	0.04	0.77	3.48	10.09	100.21
WT12WH28-1-4-3	Trial Harbour, Heemskirk	Orbicule	a sector	33.01	0.26	34.10	15.09	0.34	0.11	0.22	1.89	0.08	0.68	3.48	10.10	99.35
WT12WH28-1-4-4	Trial Harbour, Heemskirk	Orbicule	a sector	32.35	0.45	33.68	15.74	0.43	0.28	0.22	2.05	0.11	0.99	3.45	9.99	99.74
WT12WH28-1-4-5	Trial Harbour, Heemskirk	Orbicule	a sector	33.30	0.23	34.79	14.80	0.38	0.10	0.20	1.78	0.03	0.65	3.49	10.13	99.88
WT12WH28-1-4-6	Trial Harbour, Heemskirk	Orbicule	a sector	32.68	0.32	34.20	15.37	0.48	0.22	0.21	2.03	0.06	0.91	3.46	10.04	99.96
WT12WH28-1-4-7	Trial Harbour, Heemskirk	Orbicule	c sector	32.47	0.23	34.86	14.63	0.42	0.17	0.20	1.90	0.13	0.85	3.48	10.09	99.44
WT12WH28-1-4-8	Trial Harbour, Heemskirk	Orbicule	c sector	32.21	0.38	34.09	15.46	0.41	0.22	0.24	2.09	0.07	0.97	3.46	10.02	99.62

WT12WH28-1-5-1	Trial Harbour, Heemskirk	Orbicule	a sector	33.21	0.27	32.79	16.03	0.88	0.16	0.13	1.90	0.06	1.06	3.45	10.00	99.92
WT12WH28-1-5-2	Trial Harbour, Heemskirk	Orbicule	a sector	33.79	0.17	34.39	14.45	0.61	0.06	0.16	1.82	0.00	0.65	3.51	10.17	99.79
WT12WH28-1-5-3	Trial Harbour, Heemskirk	Orbicule	a sector	33.11	0.17	34.20	15.10	0.77	0.16	0.16	1.91	0.05	0.95	3.47	10.06	100.12
WT12WH28-1-5-4	Trial Harbour, Heemskirk	Orbicule	a sector	32.83	0.23	33.92	15.35	0.74	0.21	0.13	1.93	0.07	1.08	3.46	10.02	99.97
WT12WH28-1-5-5	Trial Harbour, Heemskirk	Orbicule	a sector	33.17	0.14	34.47	14.70	0.69	0.13	0.14	1.89	0.04	0.85	3.49	10.11	99.80
WT12WH28-2-1-1	Trial Harbour, Heemskirk	Orbicule	c sector	32.29	0.31	34.85	14.80	0.52	0.30	0.20	1.95	0.05	1.00	3.47	10.05	99.78
WT12WH28-2-1-2	Trial Harbour, Heemskirk	Orbicule	a sector	32.46	0.44	33.63	15.94	0.52	0.32	0.16	1.86	0.08	1.01	3.45	10.00	99.87
WT12WH28-2-1-3	Trial Harbour, Heemskirk	Orbicule	c sector	32.76	0.24	35.08	14.51	0.50	0.20	0.17	1.89	0.08	0.91	3.48	10.10	99.93
WT12WH28-2-1-4	Trial Harbour, Heemskirk	Orbicule	a sector	32.76	0.32	34.48	15.40	0.53	0.26	0.24	2.03	0.04	1.03	3.46	10.02	100.55
WT12WH28-2-1-5	Trial Harbour, Heemskirk	Orbicule	a sector	32.47	0.41	33.74	15.58	0.53	0.26	0.17	1.98	0.09	1.00	3.45	10.01	99.68
WT12WH28-2-2-1	Trial Harbour, Heemskirk	Orbicule	a sector	32.65	0.29	34.94	14.45	0.49	0.21	0.22	1.79	0.04	0.97	3.48	10.09	99.62
WT12WH28-2-2-2	Trial Harbour, Heemskirk	Orbicule	a sector	33.01	0.22	34.95	14.96	0.52	0.21	0.20	1.96	0.03	0.96	3.47	10.07	100.55
WT12WH28-2-2-3	Trial Harbour, Heemskirk	Orbicule	c sector	33.20	0.38	32.53	16.70	0.54	0.15	0.26	1.98	0.03	1.12	3.43	9.95	100.27
WT12WH28-2-2-4	Trial Harbour, Heemskirk	Orbicule	c sector	32.34	0.39	34.06	15.57	0.48	0.26	0.22	2.04	0.08	1.04	3.45	10.00	99.94
WT12WH28-2-2-5	Trial Harbour, Heemskirk	Orbicule	c sector	33.21	0.21	34.62	15.04	0.40	0.14	0.17	1.88	0.05	0.72	3.49	10.11	100.04
WT12WH28-2-2-6	Trial Harbour, Heemskirk	Orbicule	a sector	32.59	0.23	35.02	14.63	0.46	0.20	0.21	1.83	0.04	0.95	3.48	10.09	99.72
WT12WH28-2-3-1	Trial Harbour, Heemskirk	Orbicule	a sector	32.86	0.36	34.27	16.05	0.61	0.21	0.21	2.26	0.10	1.22	3.43	9.94	101.53
WT12WH28-2-3-2	Trial Harbour, Heemskirk	Orbicule	c sector	32.25	0.17	35.32	14.44	0.53	0.26	0.21	1.95	0.06	1.00	3.48	10.08	99.73
WT12WH28-2-3-3	Trial Harbour, Heemskirk	Orbicule	a sector	33.19	0.29	33.10	16.15	0.45	0.09	0.21	2.07	0.03	0.77	3.46	10.03	99.82
WT12WH28-2-3-4	Trial Harbour, Heemskirk	Orbicule	c sector	32.53	0.16	35.74	14.55	0.53	0.20	0.17	2.00	0.05	0.94	3.48	10.08	100.42
WT12WH28-2-3-5	Trial Harbour, Heemskirk	Orbicule	a sector	32.54	0.29	34.24	15.18	0.55	0.17	0.18	1.97	0.02	1.25	3.45	10.01	99.85
WT12WH28-2-3-6	Trial Harbour, Heemskirk	Orbicule	c sector	32.15	0.19	35.42	14.62	0.52	0.21	0.20	1.87	0.02	1.13	3.47	10.05	99.85
WT12WH28-2-7-1	Trial Harbour, Heemskirk	Orbicule	c sector	33.14	0.23	35.26	14.31	0.52	0.20	0.20	1.94	0.04	1.06	3.48	10.09	100.48
WT12WH28-2-7-2	Trial Harbour, Heemskirk	Orbicule	a sector	33.40	0.25	33.96	15.50	0.42	0.12	0.21	2.01	0.04	0.77	3.47	10.07	100.23
WT12WH28-2-7-3	Trial Harbour, Heemskirk	Orbicule	c sector	32.56	0.18	35.66	14.52	0.46	0.23	0.19	1.78	0.02	1.04	3.48	10.08	100.19
WT12WH28-2-7-4	Trial Harbour, Heemskirk	Orbicule	a sector	32.31	0.34	34.57	15.58	0.46	0.25	0.22	2.18	0.07	1.17	3.44	9.98	100.57
WT12WH28-2-7-5	Trial Harbour, Heemskirk	Orbicule	c sector	33.15	0.16	35.48	14.58	0.46	0.17	0.19	1.93	0.05	0.98	3.48	10.09	100.71
WT12WH28-3-1-1	Trial Harbour, Heemskirk	Orbicule	a sector	33.16	0.47	34.21	15.60	0.71	0.16	0.09	2.01	0.03	1.18	3.45	9.99	101.05
WT12WH28-3-1-2	Trial Harbour, Heemskirk	Orbicule	a sector	33.43	0.50	33.74	15.30	0.79	0.10	0.16	1.99	0.05	1.10	3.46	10.03	100.63
WT12WH28-3-1-3	Trial Harbour, Heemskirk	Orbicule	a sector	32.92	0.44	33.79	15.35	0.80	0.09	0.12	1.99	0.05	1.10	3.46	10.02	100.13
WT12WH28-3-1-4	Trial Harbour, Heemskirk	Orbicule	c sector	34.42	0.21	35.21	14.07	0.57	0.06	0.11	1.62	0.04	0.78	3.51	10.19	100.77
WT12WH28-3-1-5	Trial Harbour, Heemskirk	Orbicule	a sector	33.61	0.41	34.18	15.23	0.78	0.13	0.13	1.95	0.05	1.06	3.46	10.05	101.06
WT12WH28-3-1-6	Trial Harbour, Heemskirk	Orbicule	c sector	33.84	0.33	34.79	14.65	0.62	0.03	0.09	1.72	0.04	0.91	3.49	10.13	100.63
WT12WH28-3-1-7	Trial Harbour, Heemskirk	Orbicule	c sector	33.88	0.31	34.84	14.27	0.58	0.04	0.07	1.69	0.02	0.87	3.50	10.15	100.22
WT12WH28-3-3-2	Trial Harbour, Heemskirk	Orbicule	a sector	33.10	0.39	33.44	15.90	0.59	0.21	0.11	2.09	0.07	1.24	3.44	9.97	100.55
WT12WH28-3-3-3	Trial Harbour, Heemskirk	Orbicule	c sector	32.79	0.23	34.61	15.14	0.62	0.11	0.04	1.89	0.05	1.00	3.47	10.06	100.00
WT12WH28-3-3-4	Trial Harbour, Heemskirk	Orbicule	c sector	34.33	0.16	35.02	14.53	0.49	0.04	0.11	1.82	0.02	0.70	3.51	10.17	100.89
WT12WH28-3-3-5	Trial Harbour, Heemskirk	Orbicule	a sector	33.60	0.29	34.41	15.55	0.63	0.13	0.10	1.91	0.06	1.15	3.46	10.02	101.30
WT12WH28-3-5-2	Trial Harbour, Heemskirk	Orbicule	c sector	33.27	0.31	34.33	15.23	0.51	0.05	0.13	1.86	0.07	0.76	3.48	10.10	100.10
WT12WH28-3-5-3	Trial Harbour, Heemskirk	Orbicule	a sector	32.61	0.45	33.51	15.69	0.70	0.18	0.05	1.93	0.07	1.28	3.44	9.98	99.89
WT12WH28-3-6-2	Trial Harbour, Heemskirk	Orbicule	a sector	32.87	0.27	33.38	16.14	0.60	0.13	0.19	1.96	0.06	0.69	3.46	10.04	99.79

WT12WH28-3-6-3	Trial Harbour, Heemskirk	Orbicule	c sector	31.98	0.21	36.07	14.11	0.53	0.26	0.16	1.91	0.05	0.94	3.48	10.10	99.80
WT12WH28-3-6-4	Trial Harbour, Heemskirk	Orbicule	a sector	32.10	0.23	35.39	14.91	0.58	0.22	0.18	1.98	0.04	1.09	3.46	10.04	100.22
WT12WH28-3-6-5	Trial Harbour, Heemskirk	Orbicule	c sector	32.15	0.16	35.93	14.31	0.56	0.28	0.17	2.02	0.02	0.99	3.48	10.08	100.15
WT12WH28-4-1-1	Trial Harbour, Heemskirk	Orbicule	a sector	33.33	0.16	33.68	16.59	0.37	0.19	0.13	1.91	0.05	1.18	3.43	9.95	100.98
WT12WH28-4-1-2	Trial Harbour, Heemskirk	Orbicule	a sector	32.86	0.13	34.91	15.73	0.31	0.30	0.13	1.78	0.02	1.09	3.46	10.02	100.74
WT12WH28-4-1-3	Trial Harbour, Heemskirk	Orbicule	a sector	32.59	0.08	34.85	15.72	0.21	0.21	0.12	1.82	0.07	1.04	3.46	10.02	100.17
WT12WH28-4-1-4	Trial Harbour, Heemskirk	Orbicule	c sector	34.16	0.01	35.59	14.72	0.05	0.01	0.42	1.02	0.00	0.10	3.54	10.28	99.92
WT12WH28-4-1-5	Trial Harbour, Heemskirk	Orbicule	a sector	32.05	0.15	34.77	15.47	0.34	0.24	0.07	1.84	0.06	1.13	3.45	10.01	99.60
WT12WH28-4-1-6	Trial Harbour, Heemskirk	Orbicule	a sector	31.99	0.14	35.24	15.35	0.34	0.31	0.08	1.71	0.05	1.06	3.46	10.03	99.76
WT12WH28-4-1-7	Trial Harbour, Heemskirk	Orbicule	a sector	32.32	0.07	34.78	15.90	0.30	0.23	0.10	1.81	0.05	1.12	3.45	10.00	100.12
WT12WH28-4-3-1	Trial Harbour, Heemskirk	Orbicule	c sector	33.34	0.45	34.32	15.20	0.93	0.32	0.12	1.86	0.03	1.15	3.46	10.02	101.19
WT12WH28-4-3-2	Trial Harbour, Heemskirk	Orbicule	a sector	33.24	0.16	34.79	15.91	0.33	0.27	0.12	1.90	0.02	1.09	3.45	10.00	101.27
WT12WH28-4-3-3	Trial Harbour, Heemskirk	Orbicule	c sector	33.52	0.29	34.58	14.87	0.66	0.16	0.02	1.80	0.08	0.79	3.49	10.11	100.36
WT12WH28-4-3-4	Trial Harbour, Heemskirk	Orbicule	a sector	33.03	0.37	34.13	15.96	0.75	0.28	0.12	1.90	0.05	1.10	3.44	9.98	101.12
WT12WH28-4-4-1	Trial Harbour, Heemskirk	Orbicule	a sector	32.67	0.38	34.49	15.15	0.75	0.29	0.11	1.77	0.04	1.12	3.46	10.03	100.26
WT12WH28-4-4-2	Trial Harbour, Heemskirk	Orbicule	c sector	32.60	0.19	35.71	14.75	0.60	0.26	0.09	1.75	0.04	0.92	3.48	10.09	100.49
WT12WH28-4-4-3	Trial Harbour, Heemskirk	Orbicule	c sector	32.47	0.30	35.57	14.31	0.66	0.28	0.06	1.77	0.07	1.03	3.48	10.09	100.10
WT12WH28-4-4-4	Trial Harbour, Heemskirk	Orbicule	a sector	33.06	0.38	34.14	15.72	0.54	0.36	0.13	1.91	0.03	1.07	3.45	10.00	100.80
WT12WH28-4-4-5	Trial Harbour, Heemskirk	Orbicule	a sector	32.44	0.21	35.15	15.46	0.53	0.31	0.08	1.86	0.02	1.08	3.46	10.02	100.63
WT12WH28-4-4-6	Trial Harbour, Heemskirk	Orbicule	a sector	32.73	0.36	34.32	15.67	0.62	0.32	0.12	1.87	0.07	1.08	3.45	10.00	100.61
WT12WH28-4-4-7	Trial Harbour, Heemskirk	Orbicule	c sector	32.92	0.21	34.71	15.36	0.62	0.27	0.10	1.98	0.07	0.88	3.47	10.05	100.64
WT12WH28-4-4-8	Trial Harbour, Heemskirk	Orbicule	c sector	32.40	0.31	34.53	15.30	0.62	0.30	0.08	1.93	0.02	1.12	3.45	10.01	100.07
WT12WH33-2-1-1	Granville Harbour, Heemskirk	Cavity	c sector	33.69	0.38	35.38	13.79	1.24	0.14	0.08	1.72	0.04	0.92	3.52	10.20	101.11
WT12WH33-2-1-2	Granville Harbour, Heemskirk	Cavity	c sector	33.70	0.56	34.91	14.52	1.06	0.20	0.10	1.77	0.04	1.03	3.52	10.15	101.55
WT12WH33-2-1-3	Granville Harbour, Heemskirk	Cavity	c sector	34.00	0.67	33.12	14.72	1.71	0.21	0.09	2.00	0.06	1.24	3.52	10.09	101.43
WT12WH33-2-1-4	Granville Harbour, Heemskirk	Cavity	a sector	34.42	0.74	32.60	15.76	0.96	0.23	0.10	2.04	0.04	1.11	3.52	10.06	101.58
WT12WH33-2-1-5	Granville Harbour, Heemskirk	Cavity	c sector	33.75	0.65	32.88	14.77	1.52	0.18	0.14	1.91	0.06	1.20	3.52	10.09	100.66
WT12WH33-2-1-6	Granville Harbour, Heemskirk	Cavity	c sector	34.16	0.59	33.45	14.43	1.74	0.18	0.13	2.07	0.03	1.27	3.52	10.11	101.66
WT12WH33-2-1-7	Granville Harbour, Heemskirk	Cavity	c sector	33.69	0.56	33.58	14.37	1.61	0.18	0.14	1.96	0.04	1.30	3.52	10.10	101.03
WT12WH33-2-1-8	Granville Harbour, Heemskirk	Cavity	a sector	33.94	0.46	32.95	16.09	0.93	0.22	0.12	1.86	0.04	1.18	3.52	10.04	101.35
WT12WH33-2-1-9	Granville Harbour, Heemskirk	Cavity	a sector	33.47	0.35	32.81	16.18	0.75	0.24	0.14	2.07	0.03	1.17	3.52	10.02	100.77
WT12WH33-2-1-10	Granville Harbour, Heemskirk	Cavity	a sector	33.60	0.45	32.93	15.69	0.92	0.25	0.12	2.14	0.04	1.26	3.52	10.04	100.94
WT12WH33-2-1-11	Granville Harbour, Heemskirk	Cavity	a sector	33.94	0.56	33.62	14.75	1.62	0.14	0.16	2.07	0.04	1.29	3.52	10.08	101.79
WT12WH33-2-1-12	Granville Harbour, Heemskirk	Cavity	a sector	33.53	0.40	32.77	16.25	0.84	0.23	0.15	1.91	0.05	1.18	3.52	10.03	100.86
WT12WH33-2-5-1	Granville Harbour, Heemskirk	Cavity	c sector	33.95	0.16	35.41	14.34	0.52	0.06	0.12	1.43	0.04	0.65	3.52	10.23	100.45
WT12WH33-2-5-2	Granville Harbour, Heemskirk	Cavity	c sector	34.22	0.17	35.54	14.30	0.55	0.08	0.12	1.50	0.05	0.60	3.52	10.23	100.87
WT12WH33-2-5-3	Granville Harbour, Heemskirk	Cavity	a sector	33.87	0.47	34.06	15.24	0.85	0.20	0.07	1.85	0.04	1.08	3.52	10.10	101.36
WT12WH33-2-5-4	Granville Harbour, Heemskirk	Cavity	a sector	33.64	0.32	35.66	13.50	1.41	0.13	0.11	1.81	0.05	0.96	3.52	10.20	101.31
WT12WH33-2-5-5	Granville Harbour, Heemskirk	Cavity	a sector	32.88	0.45	34.02	15.40	0.78	0.21	0.13	1.74	0.03	1.07	3.52	10.09	100.32
WT12WH33-2-5-6	Granville Harbour, Heemskirk	Cavity	a sector	33.49	0.35	34.81	14.80	1.16	0.18	0.13	2.04	0.04	0.97	3.52	10.12	101.61
WT12WH33-2-5-7	Granville Harbour, Heemskirk	Cavity	a sector	32.83	0.26	34.54	15.14	0.77	0.22	0.13	1.80	0.03	1.02	3.52	10.11	100.38

WT12WH33-2-5-8	Granville Harbour, Heemskirk	Cavity	a sector	33.82	0.41	35.05	13.87	1.38	0.12	0.08	1.94	0.02	0.94	3.52	10.19	101.33
WT12WH33-2-5-9	Granville Harbour, Heemskirk	Cavity	a sector	33.53	0.34	34.29	15.27	0.73	0.24	0.06	1.75	0.05	1.05	3.52	10.11	100.92
WT12WH33-2-5-10	Granville Harbour, Heemskirk	Cavity	a sector	33.65	0.31	34.57	14.34	1.04	0.17	0.08	1.82	0.03	0.97	3.52	10.17	100.67
WT12WH33-2-5-11	Granville Harbour, Heemskirk	Cavity	a sector	34.22	0.21	35.58	13.82	1.18	0.15	0.08	1.63	0.03	0.83	3.52	10.22	101.50
WT12WH33-2-5-12	Granville Harbour, Heemskirk	Cavity	a sector	34.16	0.16	35.27	14.14	0.98	0.16	0.08	1.74	0.04	0.80	3.52	10.22	101.26
WT12WH35-1-1-2	Granville Harbour, Heemskirk	Orbicule	a sector	34.09	0.73	32.07	14.65	1.71	0.15	0.05	2.12	0.08	1.10	3.47	10.05	100.05
WT12WH35-1-1-3	Granville Harbour, Heemskirk	Orbicule	a sector	34.30	0.62	32.88	14.10	1.79	0.17	0.11	1.98	0.03	1.00	3.49	10.11	100.35
WT12WH35-1-1-4	Granville Harbour, Heemskirk	Orbicule	a sector	34.10	0.51	33.59	13.99	1.67	0.10	0.11	1.86	0.05	0.97	3.50	10.13	100.32
WT12WH35-1-1-5	Granville Harbour, Heemskirk	Orbicule	a sector	34.69	0.51	33.57	14.32	1.70	0.17	0.07	1.98	0.04	1.13	3.48	10.09	101.47
WT12WH35-2-2-1	Granville Harbour, Heemskirk	Orbicule	a sector	33.24	0.60	34.75	14.45	1.01	0.30	0.23	1.94	0.02	1.13	3.52	10.12	101.31
WT12WH35-2-2-2	Granville Harbour, Heemskirk	Orbicule	a sector	32.79	0.43	35.78	13.81	1.04	0.27	0.19	1.83	0.06	1.13	3.52	10.15	101.00
WT12WH35-2-2-3	Granville Harbour, Heemskirk	Orbicule	c sector	33.47	0.28	35.91	13.47	0.90	0.21	0.15	1.79	0.06	0.82	3.52	10.22	100.80
WT12WH35-2-2-4	Granville Harbour, Heemskirk	Orbicule	c sector	33.25	0.42	36.12	13.72	1.02	0.22	0.14	1.82	0.04	1.01	3.52	10.18	101.47
WT12WH35-2-2-5	Granville Harbour, Heemskirk	Orbicule	a sector	33.01	0.51	35.01	14.23	1.07	0.23	0.17	1.95	0.05	1.09	3.52	10.13	100.98
WT12WH35-2-2-6	Granville Harbour, Heemskirk	Orbicule	a sector	33.14	0.50	35.14	14.36	1.07	0.30	0.17	1.84	0.08	1.14	3.52	10.12	101.38
WT12WH35-2-2-7	Granville Harbour, Heemskirk	Orbicule	c sector	34.00	0.29	35.80	13.64	1.03	0.21	0.21	1.86	0.06	0.90	3.52	10.20	101.72
WT12WH35-2-2-8	Granville Harbour, Heemskirk	Orbicule	c sector	33.88	0.32	35.61	13.41	0.85	0.17	0.17	1.77	0.04	0.67	3.52	10.25	100.66
WT12WH35-2-4-1	Granville Harbour, Heemskirk	Orbicule	c- sector	33.42	0.35	35.13	13.59	1.13	0.24	0.15	1.86	0.07	1.03	3.50	10.13	100.30
WT12WH35-2-4-2	Granville Harbour, Heemskirk	Orbicule	a sector	33.82	0.33	35.14	13.59	1.13	0.23	0.13	1.85	0.04	1.04	3.50	10.14	100.68
WT12WH35-2-4-3	Granville Harbour, Heemskirk	Orbicule	a sector	34.24	0.22	35.94	13.09	1.10	0.10	0.09	1.80	0.01	0.64	3.54	10.25	100.78
WT12WH35-2-4-4	Granville Harbour, Heemskirk	Orbicule	a sector	33.78	0.49	34.99	14.08	1.26	0.26	0.15	2.13	0.07	1.09	3.48	10.08	101.63

Appendix 5.1 Microprobe analytical data of tourmaline from the Heemskirk and Pieman Heads granites (continued)

Sample No.	apfu	Si	T Al	Z Al	Y Al	Al total	Ti	Mg	Mn	Fe^{2+}	Ca	Na	K	X vac.	OH	F	B
WT12WH04-1-1		5.79	0.21	6.00	0.81	7.02	0.03	0.63	0.01	1.42	0.01	0.49	0.01	0.48	3.79	0.21	3.00
WT12WH04-1-2		5.73	0.27	6.00	0.57	6.84	0.07	0.78	0.01	1.52	0.05	0.55	0.00	0.39	3.64	0.35	3.00
WT12WH04-1-3		5.75	0.25	6.00	0.69	6.94	0.01	0.40	0.02	1.82	0.02	0.62	0.01	0.36	3.73	0.27	3.00
WT12WH04-1-4		5.82	0.18	6.00	0.83	7.01	0.00	0.07	0.01	2.05	0.01	0.37	0.01	0.61	3.74	0.26	3.00
WT12WH04-1-5		5.78	0.22	6.00	0.82	7.04	0.00	0.06	0.01	2.07	0.01	0.43	0.01	0.56	3.72	0.28	3.00
WT12WH04-3-1		5.77	0.23	6.00	0.31	6.55	0.11	0.86	0.01	1.63	0.06	0.68	0.00	0.25	3.54	0.46	3.00
WT12WH04-3-2		5.70	0.30	6.00	0.49	6.79	0.08	0.84	0.01	1.56	0.05	0.56	0.01	0.38	3.60	0.40	3.00
WT12WH04-3-4		5.74	0.26	6.00	0.52	6.77	0.07	0.76	0.01	1.57	0.05	0.63	0.01	0.31	3.61	0.39	3.00
WT12WH04-4-1		5.74	0.26	6.00	0.75	7.01	0.04	0.65	0.01	1.44	0.04	0.55	0.01	0.40	3.83	0.17	3.00
WT12WH04-4-2		5.72	0.28	6.00	0.53	6.82	0.07	0.78	0.02	1.54	0.05	0.64	0.01	0.30	3.61	0.39	3.00
WT12WH04-4-3		5.69	0.31	6.00	0.62	6.92	0.06	0.69	0.01	1.55	0.05	0.60	0.01	0.34	3.65	0.35	3.00
WT12WH04-4-4		5.69	0.31	6.00	0.68	6.99	0.05	0.73	0.01	1.47	0.04	0.55	0.01	0.40	3.69	0.31	3.00
WT12WH04-4-6		5.72	0.28	6.00	0.73	7.02	0.04	0.65	0.01	1.50	0.03	0.52	0.00	0.44	3.83	0.17	3.00
WT12WH07-1-1-1		5.74	0.26	6.00	0.77	7.03	0.04	0.64	0.01	1.46	0.02	0.53	0.01	0.45	3.68	0.32	3.00
WT12WH07-1-1-2		5.72	0.28	6.00	0.50	6.78	0.09	0.77	0.01	1.58	0.04	0.59	0.01	0.36	3.62	0.38	3.00
WT12WH07-1-1-3		5.72	0.28	6.00	0.46	6.74	0.06	0.58	0.02	1.86	0.05	0.61	0.02	0.32	3.58	0.42	3.00
WT12WH07-1-1-4		5.71	0.29	6.00	0.81	7.10	0.03	0.44	0.01	1.65	0.02	0.51	0.01	0.46	3.81	0.19	3.00
WT12WH07-1-1-5		5.67	0.33	6.00	0.48	6.81	0.09	0.60	0.01	1.79	0.05	0.63	0.01	0.31	3.58	0.42	3.00
WT12WH07-1-2-5		5.78	0.22	6.00	0.45	6.67	0.11	0.71	0.01	1.65	0.06	0.57	0.01	0.36	3.60	0.40	3.00
WT12WH07-1-2-6		5.74	0.26	6.00	0.46	6.73	0.10	0.65	0.01	1.72	0.06	0.58	0.01	0.36	3.63	0.37	3.00
WT12WH07-1-2-7		5.68	0.32	6.00	0.64	6.97	0.06	0.63	0.01	1.61	0.04	0.57	0.01	0.37	3.69	0.31	3.00
WT12WH07-1-2-8		5.69	0.31	6.00	0.50	6.81	0.10	0.59	0.01	1.72	0.06	0.63	0.01	0.31	3.64	0.36	3.00
WT12WH07-2-1		5.76	0.24	6.00	0.67	6.92	0.05	0.67	0.02	1.49	0.04	0.56	0.01	0.39	3.85	0.15	3.00
WT12WH07-2-2		5.73	0.27	6.00	0.46	6.73	0.12	0.77	0.01	1.55	0.07	0.60	0.01	0.32	3.69	0.31	3.00
WT12WH07-2-3		5.70	0.30	6.00	0.66	6.95	0.05	0.72	0.01	1.50	0.04	0.57	0.01	0.39	3.80	0.20	3.00
WT12WH07-2-4		5.67	0.33	6.00	0.46	6.80	0.09	0.82	0.01	1.61	0.06	0.61	0.01	0.33	3.68	0.32	3.00
WT12WH07-3-2-1		5.78	0.22	6.00	0.71	6.93	0.05	0.67	0.01	1.50	0.02	0.50	0.01	0.47	3.87	0.13	3.00
WT12WH07-3-2-2		5.78	0.22	6.00	0.69	6.90	0.04	0.66	0.02	1.52	0.02	0.55	0.01	0.42	3.87	0.13	3.00
WT12WH07-3-2-3		5.70	0.30	6.00	0.53	6.83	0.06	0.79	0.01	1.59	0.05	0.57	0.01	0.37	3.73	0.27	3.00
WT12WH07-3-2-4		5.62	0.38	6.00	0.43	6.81	0.09	0.81	0.01	1.63	0.07	0.67	0.01	0.25	3.67	0.33	3.00
WT12WH07-3-2-5		5.67	0.33	6.00	0.64	6.96	0.06	0.70	0.01	1.55	0.04	0.57	0.01	0.38	3.81	0.19	3.00
WT12WH07-3-2-6		5.72	0.28	6.00	0.71	6.98	0.05	0.67	0.01	1.50	0.03	0.54	0.01	0.42	3.85	0.15	3.00
WT12WH07-3-2-7		5.67	0.33	6.00	0.49	6.82	0.09	0.79	0.01	1.59	0.06	0.61	0.01	0.32	3.70	0.30	3.00
WT12WH07-3-2-8		5.65	0.35	6.00	0.57	6.92	0.06	0.77	0.01	1.56	0.06	0.59	0.01	0.35	3.74	0.26	3.00
WT12WH13-1-1-1		5.72	0.28	6.00	0.45	6.74	0.11	0.23	0.01	2.18	0.04	0.57	0.01	0.38	3.64	0.36	3.00
WT12WH13-1-1-2		5.66	0.34	6.00	0.65	6.99	0.08	0.39	0.01	1.82	0.02	0.55	0.01	0.42	3.66	0.34	3.00
WT12WH13-1-1-3		5.75	0.25	6.00	0.85	7.10	0.03	0.47	0.00	1.58	0.01	0.43	0.01	0.55	3.85	0.15	3.00
WT12WH13-1-1-5		5.69	0.31	6.00	0.52	6.83	0.10	0.69	0.01	1.62	0.05	0.62	0.01	0.33	3.61	0.39	3.00

WT12WH13-1-2-1-1	5.62	0.38	6.00	0.58	6.96	0.08	0.33	0.02	1.98	0.04	0.59	0.01	0.37	3.63	0.37	3.00
WT12WH13-1-2-1-2	5.66	0.34	6.00	0.52	6.85	0.07	0.76	0.01	1.61	0.04	0.63	0.02	0.32	3.61	0.39	3.00
WT12WH13-1-2-1-3	5.66	0.34	6.00	0.53	6.87	0.07	0.75	0.01	1.60	0.04	0.65	0.01	0.30	3.62	0.38	3.00
WT12WH13-1-2-1-4	5.66	0.34	6.00	0.55	6.89	0.07	0.59	0.01	1.73	0.03	0.63	0.01	0.32	3.60	0.40	3.00
WT12WH13-1-2-1-5	5.63	0.37	6.00	0.72	7.10	0.06	0.35	0.01	1.83	0.02	0.52	0.01	0.44	3.65	0.35	3.00
WT12WH13-1-2-1-6	5.63	0.37	6.00	0.66	7.03	0.05	0.60	0.01	1.65	0.04	0.58	0.01	0.37	3.65	0.35	3.00
WT12WH13-1-2-1-7	5.61	0.39	6.00	0.65	7.04	0.06	0.56	0.01	1.70	0.03	0.57	0.01	0.38	3.56	0.44	3.00
WT12WH13-1-2-1-8	5.61	0.39	6.00	0.70	7.09	0.06	0.53	0.01	1.68	0.04	0.53	0.01	0.42	3.61	0.39	3.00
WT12WH13-1-2-1-9	5.60	0.40	6.00	0.63	7.03	0.08	0.68	0.01	1.55	0.06	0.57	0.01	0.37	3.63	0.37	3.00
WT12WH13-1-2-1-10	5.54	0.46	6.00	0.80	7.26	0.07	0.26	0.02	1.81	0.02	0.57	0.00	0.41	3.55	0.45	3.00
WT12WH13-1-2-1-11	5.58	0.42	6.00	0.78	7.21	0.05	0.12	0.05	1.96	0.02	0.56	0.00	0.41	3.47	0.53	3.00
WT12WH13-1-2-1-12	5.56	0.44	6.00	0.74	7.18	0.06	0.10	0.03	2.02	0.02	0.61	0.02	0.35	3.47	0.53	3.00
WT12WH13-1-2-1-13	5.38	0.62	6.00	1.28	7.90	0.05	0.09	0.34	1.08	0.03	0.51	0.00	0.45	3.72	0.28	3.00
WT12WH13-1-2-1-14	5.38	0.62	6.00	1.20	7.81	0.06	0.06	0.34	1.18	0.03	0.55	0.01	0.41	3.69	0.31	3.00
WT12WH13-1-2-1-15	5.39	0.61	6.00	1.11	7.72	0.07	0.06	0.29	1.33	0.03	0.57	0.01	0.39	3.66	0.34	3.00
WT12WH13-1-2-1-16	5.44	0.56	6.00	1.07	7.64	0.06	0.07	0.23	1.45	0.02	0.54	0.00	0.44	3.62	0.38	3.00
WT12WH13-1-2-1-17	5.59	0.41	6.00	1.12	7.53	0.05	0.06	0.20	1.44	0.00	0.45	0.00	0.54	3.65	0.35	3.00
WT12WH13-1-2-1-18	5.55	0.45	6.00	1.11	7.55	0.05	0.06	0.21	1.43	0.02	0.48	0.00	0.50	3.66	0.34	3.00
WT12WH13-1-2-1-19	5.57	0.43	6.00	1.10	7.53	0.05	0.06	0.19	1.46	0.01	0.48	0.00	0.50	3.69	0.31	3.00
WT12WH13-1-2-1-20	5.58	0.42	6.00	1.20	7.62	0.04	0.05	0.26	1.29	0.01	0.46	0.00	0.53	3.70	0.30	3.00
WT12WH13-1-2-1-21	5.63	0.37	6.00	0.61	6.98	0.06	0.74	0.01	1.54	0.04	0.62	0.00	0.34	3.61	0.39	3.00
WT12WH13-1-2-1-22	5.65	0.35	6.00	0.69	7.04	0.06	0.12	0.04	2.04	0.02	0.63	0.00	0.35	3.51	0.49	3.00
WT12WH13-1-2-1-23	5.66	0.34	6.00	0.90	7.25	0.04	0.04	0.04	1.90	0.00	0.48	0.01	0.51	3.63	0.37	3.00
WT12WH13-1-2-1-24	5.67	0.33	6.00	0.86	7.19	0.04	0.04	0.04	1.94	0.01	0.53	0.01	0.44	3.70	0.30	3.00
WT12WH13-1-2-1-25	5.63	0.37	6.00	0.71	7.08	0.07	0.10	0.03	2.02	0.02	0.59	0.01	0.38	3.47	0.53	3.00
WT12WH13-1-2-1-26	5.67	0.33	6.00	0.63	6.96	0.07	0.73	0.01	1.50	0.05	0.56	0.01	0.38	3.59	0.41	3.00
WT12WH13-1-2-2-1	5.66	0.34	6.00	0.60	6.94	0.06	0.43	0.01	1.87	0.03	0.60	0.01	0.37	3.68	0.32	3.00
WT12WH13-1-2-2-2	5.66	0.34	6.00	0.54	6.88	0.08	0.64	0.01	1.70	0.04	0.58	0.01	0.37	3.59	0.41	3.00
WT12WH13-1-2-2-3	5.63	0.37	6.00	0.55	6.92	0.08	0.75	0.01	1.60	0.04	0.63	0.01	0.33	3.62	0.38	3.00
WT12WH13-1-2-2-4	5.71	0.29	6.00	0.56	6.86	0.07	0.75	0.01	1.56	0.04	0.62	0.01	0.33	3.62	0.38	3.00
WT12WH13-1-2-2-5	5.66	0.34	6.00	0.64	6.98	0.05	0.68	0.01	1.60	0.04	0.57	0.00	0.39	3.67	0.33	3.00
WT12WH13-1-2-2-6	5.62	0.38	6.00	0.58	6.96	0.07	0.66	0.01	1.66	0.03	0.60	0.01	0.35	3.58	0.42	3.00
WT12WH13-1-2-2-7	5.64	0.36	6.00	0.61	6.97	0.07	0.61	0.01	1.68	0.04	0.58	0.01	0.37	3.61	0.39	3.00
WT12WH13-1-2-2-8	5.62	0.38	6.00	0.63	7.01	0.07	0.57	0.02	1.68	0.04	0.58	0.01	0.37	3.55	0.45	3.00
WT12WH13-1-2-2-9	5.62	0.38	6.00	0.65	7.03	0.06	0.45	0.02	1.78	0.03	0.63	0.01	0.34	3.52	0.48	3.00
WT12WH13-1-2-2-10	5.63	0.37	6.00	0.73	7.10	0.06	0.38	0.01	1.79	0.02	0.52	0.01	0.45	3.60	0.40	3.00
WT12WH13-1-2-2-11	5.65	0.35	6.00	0.64	6.99	0.06	0.62	0.01	1.63	0.04	0.58	0.01	0.37	3.62	0.38	3.00
WT12WH13-1-2-2-12	5.70	0.30	6.00	0.90	7.20	0.03	0.53	0.01	1.46	0.01	0.45	0.01	0.53	3.77	0.23	3.00
WT12WH13-1-2-2-13	5.69	0.31	6.00	0.94	7.25	0.03	0.52	0.01	1.43	0.01	0.41	0.01	0.57	3.82	0.18	3.00
WT12WH13-1-2-2-14	5.58	0.42	6.00	0.63	7.05	0.07	0.64	0.01	1.62	0.03	0.59	0.01	0.37	3.62	0.38	3.00
WT12WH13-1-2-2-15	5.65	0.35	6.00	0.64	6.99	0.06	0.59	0.01	1.66	0.03	0.59	0.01	0.37	3.60	0.40	3.00

WT12WH13-1-2-2-16	5.63	0.37	6.00	0.60	6.97	0.06	0.67	0.01	1.66	0.03	0.60	0.01	0.37	3.59	0.41	3.00
WT12WH13-1-2-2-17	5.65	0.35	6.00	0.58	6.93	0.08	0.67	0.01	1.63	0.04	0.60	0.01	0.36	3.60	0.40	3.00
WT12WH13-2-2-1	5.54	0.46	6.00	0.72	7.18	0.07	0.10	0.06	2.01	0.04	0.58	0.01	0.37	3.51	0.49	3.00
WT12WH13-2-2-2	5.73	0.27	6.00	0.81	7.08	0.04	0.14	0.04	1.91	0.01	0.48	0.01	0.50	3.65	0.35	3.00
WT12WH13-2-2-3	5.72	0.28	6.00	0.84	7.12	0.04	0.14	0.05	1.86	0.01	0.48	0.00	0.51	3.66	0.34	3.00
WT12WH13-2-2-4	5.75	0.25	6.00	0.84	7.09	0.04	0.13	0.05	1.86	0.01	0.44	0.01	0.54	3.69	0.31	3.00
WT12WH13-2-2-5	5.66	0.34	6.00	0.82	7.16	0.05	0.15	0.05	1.86	0.01	0.51	0.01	0.48	3.58	0.42	3.00
WT12WH13-2-2-6	5.54	0.46	6.00	0.69	7.16	0.08	0.09	0.07	2.03	0.03	0.59	0.01	0.37	3.49	0.51	3.00
WT12WH13-2-3-1-1	5.78	0.22	6.00	0.62	6.84	0.02	0.39	0.02	1.95	0.02	0.53	0.00	0.46	3.70	0.30	3.00
WT12WH13-2-3-1-2	5.75	0.25	6.00	0.65	6.90	0.01	0.36	0.02	1.96	0.01	0.52	0.01	0.45	3.70	0.30	3.00
WT12WH13-2-3-1-3	5.74	0.26	6.00	0.66	6.92	0.01	0.49	0.01	1.84	0.01	0.52	0.01	0.46	3.72	0.28	3.00
WT12WH13-2-3-1-4	5.79	0.21	6.00	0.62	6.83	0.02	0.63	0.01	1.71	0.01	0.55	0.00	0.43	3.70	0.30	3.00
WT12WH13-2-3-1-5	5.76	0.24	6.00	0.63	6.87	0.02	0.67	0.02	1.66	0.01	0.54	0.01	0.43	3.71	0.29	3.00
WT12WH13-2-3-1-6	5.78	0.22	6.00	0.68	6.90	0.00	0.21	0.02	2.08	0.01	0.52	0.01	0.46	3.74	0.26	3.00
WT12WH13-2-3-1-7	5.73	0.27	6.00	0.71	6.98	0.00	0.09	0.02	2.19	0.01	0.53	0.01	0.46	3.72	0.28	3.00
WT12WH13-2-3-1-8	5.77	0.23	6.00	0.71	6.94	0.00	0.17	0.01	2.08	0.01	0.57	0.01	0.42	3.77	0.23	3.00
WT12WH13-2-3-1-9	5.81	0.19	6.00	0.64	6.83	0.00	0.22	0.02	2.10	0.01	0.55	0.01	0.43	3.66	0.34	3.00
WT12WH13-2-3-1-10	5.76	0.24	6.00	0.60	6.84	0.01	0.12	0.02	2.24	0.02	0.62	0.00	0.36	3.64	0.36	3.00
WT12WH13-2-3-1-11	5.78	0.22	6.00	0.80	7.03	0.01	0.06	0.02	2.08	0.00	0.47	0.01	0.52	3.90	0.10	3.00
WT12WH13-2-3-1-12	5.80	0.20	6.00	0.64	6.83	0.00	0.09	0.02	2.22	0.02	0.58	0.01	0.39	3.63	0.37	3.00
WT12WH13-2-3-1-13	5.78	0.22	6.00	0.65	6.87	0.00	0.20	0.02	2.09	0.02	0.62	0.01	0.36	3.69	0.31	3.00
WT12WH13-2-3-1-14	5.77	0.23	6.00	0.57	6.80	0.02	0.63	0.01	1.77	0.01	0.62	0.00	0.37	3.64	0.36	3.00
WT12WH13-2-3-1-15	5.74	0.26	6.00	0.56	6.82	0.02	0.70	0.02	1.70	0.01	0.63	0.00	0.35	3.60	0.40	3.00
WT12WH13-2-3-1-16	5.80	0.20	6.00	0.51	6.72	0.02	0.51	0.02	1.92	0.02	0.64	0.00	0.34	3.62	0.38	3.00
WT12WH13-2-3-1-17	5.77	0.23	6.00	0.53	6.75	0.03	0.51	0.02	1.94	0.01	0.58	0.00	0.41	3.58	0.42	3.00
WT12WH13-2-3-1-18	5.82	0.18	6.00	0.54	6.72	0.01	0.29	0.02	2.11	0.01	0.63	0.02	0.34	3.63	0.37	3.00
WT12WH13-2-3-2-1	5.73	0.27	6.00	0.64	6.91	0.00	0.03	0.03	2.31	0.02	0.57	0.00	0.41	3.74	0.26	3.00
WT12WH13-2-3-2-2	5.56	0.44	6.00	0.72	7.17	0.08	0.09	0.09	1.99	0.02	0.55	0.00	0.43	3.50	0.50	3.00
WT12WH13-2-3-2-3	5.73	0.27	6.00	0.85	7.12	0.04	0.06	0.06	1.94	0.01	0.43	0.00	0.56	3.64	0.36	3.00
WT12WH13-2-3-2-4	5.66	0.34	6.00	0.79	7.13	0.06	0.07	0.07	1.97	0.01	0.48	0.00	0.50	3.50	0.50	3.00
WT12WH13-2-3-2-5	5.65	0.35	6.00	0.80	7.15	0.06	0.06	0.07	1.95	0.01	0.52	0.00	0.47	3.47	0.53	3.00
WT12WH13-2-3-2-6	5.57	0.43	6.00	0.69	7.12	0.08	0.09	0.07	2.04	0.03	0.56	0.01	0.40	3.50	0.50	3.00
WT12WH13-2-3-2-7	5.73	0.27	6.00	0.69	6.96	0.01	0.52	0.02	1.75	0.02	0.55	0.01	0.42	3.65	0.35	3.00
WT12WH13-3-1-1	5.63	0.37	6.00	0.59	6.96	0.07	0.69	0.02	1.59	0.06	0.58	0.01	0.34	3.65	0.35	3.00
WT12WH13-3-1-6	5.66	0.34	6.00	0.52	6.86	0.08	0.76	0.01	1.59	0.06	0.62	0.01	0.31	3.62	0.38	3.00
WT12WH20-3-1	5.73	0.27	6.00	0.40	6.67	0.07	0.34	0.02	2.15	0.04	0.68	0.02	0.27	3.35	0.65	3.00
WT12WH20-3-2	5.69	0.31	6.00	0.49	6.80	0.06	0.27	0.02	2.15	0.02	0.65	0.01	0.32	3.49	0.51	3.00
WT12WH20-3-3	5.71	0.29	6.00	0.49	6.78	0.07	0.28	0.02	2.11	0.02	0.69	0.01	0.28	3.48	0.52	3.00
WT12WH20-3-4	5.79	0.21	6.00	0.57	6.78	0.05	0.27	0.02	2.05	0.01	0.58	0.01	0.40	3.59	0.41	3.00
WT12WH20-3-5	5.77	0.23	6.00	0.56	6.79	0.05	0.28	0.02	2.06	0.01	0.61	0.00	0.38	3.52	0.48	3.00
WT12WH20-3-6	5.78	0.22	6.00	0.55	6.77	0.04	0.28	0.02	2.08	0.01	0.60	0.01	0.37	3.53	0.47	3.00

WT12WH20-3-7	5.65	0.35	6.00	0.33	6.68	0.08	0.36	0.02	2.24	0.04	0.73	0.00	0.23	3.30	0.70	3.00
WT12WH20-3-8	5.68	0.32	6.00	0.35	6.67	0.08	0.34	0.02	2.21	0.03	0.73	0.01	0.23	3.33	0.67	3.00
WT12WH20-4-8	5.78	0.22	6.00	0.67	6.89	0.04	0.26	0.02	1.93	0.01	0.59	0.01	0.40	3.64	0.36	3.00
WT12WH20-4-9	5.64	0.36	6.00	0.42	6.78	0.09	0.32	0.03	2.12	0.05	0.69	0.01	0.25	3.44	0.56	3.00
WT12WH20-3-11	5.67	0.33	6.00	0.43	6.76	0.06	0.34	0.02	2.14	0.04	0.73	0.02	0.22	3.40	0.60	3.00
WT12WH20-4-10	5.66	0.34	6.00	0.68	7.02	0.05	0.27	0.02	1.94	0.02	0.56	0.01	0.41	3.59	0.41	3.00
WT12WH20-4-11	5.61	0.39	6.00	0.49	6.87	0.07	0.34	0.02	2.10	0.04	0.65	0.02	0.29	3.44	0.56	3.00
WT12WH20-4-12	5.62	0.38	6.00	0.44	6.81	0.07	0.34	0.02	2.14	0.03	0.71	0.01	0.25	3.39	0.61	3.00
WT12WH20-4-13	5.63	0.37	6.00	0.43	6.79	0.09	0.31	0.02	2.16	0.04	0.65	0.01	0.29	3.42	0.58	3.00
WT12WH20-4-14	5.64	0.36	6.00	0.66	7.02	0.05	0.25	0.02	2.00	0.02	0.60	0.02	0.37	3.57	0.43	3.00
WT12WH21-1-1	5.75	0.25	6.00	0.24	6.49	0.11	0.36	0.02	2.29	0.03	0.70	0.01	0.26	3.25	0.75	3.00
WT12WH21-1-2	5.69	0.31	6.00	0.37	6.68	0.06	0.34	0.03	2.20	0.04	0.73	0.01	0.21	3.38	0.62	3.00
WT12WH21-1-3	5.66	0.34	6.00	0.38	6.72	0.08	0.35	0.03	2.16	0.05	0.68	0.02	0.26	3.34	0.66	3.00
WT12WH21-1-4	5.67	0.33	6.00	0.43	6.76	0.07	0.33	0.03	2.14	0.04	0.70	0.01	0.25	3.35	0.65	3.00
WT12WH21-1-5	5.63	0.37	6.00	0.43	6.80	0.07	0.32	0.03	2.14	0.04	0.70	0.00	0.25	3.37	0.63	3.00
WT12WH21-1-6	5.66	0.34	6.00	0.44	6.77	0.07	0.32	0.03	2.14	0.04	0.66	0.01	0.30	3.36	0.64	3.00
WT12WH21-1-7	5.65	0.35	6.00	0.40	6.75	0.09	0.34	0.02	2.16	0.04	0.67	0.01	0.28	3.33	0.67	3.00
WT12WH21-1-8	5.63	0.37	6.00	0.47	6.84	0.06	0.33	0.02	2.16	0.03	0.62	0.01	0.34	3.42	0.58	3.00
WT12WH21-1-9	5.67	0.33	6.00	0.41	6.74	0.07	0.34	0.03	2.17	0.04	0.69	0.00	0.27	3.36	0.64	3.00
WT12WH21-3-3	5.66	0.34	6.00	0.47	6.81	0.05	0.32	0.03	2.15	0.03	0.64	0.01	0.31	3.44	0.56	3.00
WT12WH21-3-4	5.66	0.34	6.00	0.47	6.82	0.05	0.32	0.02	2.13	0.03	0.68	0.01	0.28	3.49	0.51	3.00
WT12WH21-3-5	5.67	0.33	6.00	0.45	6.78	0.06	0.33	0.03	2.13	0.03	0.66	0.01	0.30	3.40	0.60	3.00
WT12WH21-5-3	5.69	0.31	6.00	0.36	6.67	0.08	0.36	0.03	2.19	0.04	0.66	0.01	0.29	3.37	0.63	3.00
WT12WH21-5-4	5.66	0.34	6.00	0.59	6.93	0.05	0.30	0.02	2.00	0.02	0.65	0.02	0.31	3.55	0.45	3.00
WT12WH21-5-5	5.62	0.38	6.00	0.47	6.85	0.07	0.35	0.02	2.10	0.04	0.67	0.01	0.28	3.41	0.59	3.00
WT12WH21-5-6	5.62	0.38	6.00	0.48	6.86	0.06	0.34	0.02	2.09	0.04	0.69	0.01	0.26	3.43	0.57	3.00
WT12WH21-5-7	5.65	0.35	6.00	0.48	6.83	0.05	0.33	0.03	2.10	0.04	0.68	0.01	0.27	3.45	0.55	3.00
WT12WH21-5-8	5.67	0.33	6.00	0.49	6.82	0.07	0.33	0.03	2.08	0.05	0.61	0.01	0.33	3.36	0.64	3.00
WT12WH23-2-3-1	5.74	0.26	6.00	0.72	6.98	0.02	0.04	0.02	2.17	0.02	0.55	0.01	0.42	3.72	0.28	3.00
WT12WH23-2-3-2	5.77	0.23	6.00	0.48	6.70	0.04	0.04	0.02	2.39	0.02	0.68	0.01	0.29	3.43	0.57	3.00
WT12WH23-2-3-3	5.76	0.24	6.00	0.59	6.83	0.02	0.03	0.01	2.32	0.01	0.60	0.01	0.38	3.68	0.32	3.00
WT12WH23-2-3-4	5.76	0.24	6.00	0.73	6.96	0.02	0.01	0.01	2.20	0.01	0.51	0.00	0.48	3.82	0.18	3.00
WT12WH23-2-3-5	5.80	0.20	6.00	0.32	6.53	0.05	0.11	0.02	2.52	0.01	0.71	0.01	0.26	3.44	0.56	3.00
WT12WH23-2-3-6	5.82	0.18	6.00	0.34	6.52	0.04	0.09	0.02	2.53	0.01	0.70	0.01	0.29	3.41	0.59	3.00
WT12WH23-2-3-7	5.80	0.20	6.00	0.33	6.53	0.03	0.08	0.02	2.57	0.01	0.72	0.01	0.26	3.40	0.60	3.00
WT12WH23-2-5-1	5.76	0.24	6.00	0.68	6.92	0.02	0.00	0.01	2.25	0.02	0.56	0.01	0.42	3.72	0.28	3.00
WT12WH23-2-5-2	5.78	0.22	6.00	0.67	6.89	0.02	0.04	0.01	2.20	0.02	0.57	0.01	0.40	3.69	0.31	3.00
WT12WH23-2-5-3	5.79	0.21	6.00	0.68	6.89	0.03	0.07	0.01	2.16	0.01	0.54	0.01	0.44	3.80	0.20	3.00
WT12WH23-2-5-4	5.77	0.23	6.00	0.67	6.90	0.02	0.12	0.01	2.14	0.01	0.54	0.01	0.44	3.73	0.27	3.00
WT12WH23-2-5-5	5.84	0.16	6.00	0.37	6.53	0.07	0.07	0.01	2.49	0.01	0.62	0.00	0.37	3.33	0.67	3.00
WT12WH23-2-5-6	5.79	0.21	6.00	0.55	6.76	0.02	0.08	0.01	2.32	0.01	0.64	0.01	0.35	3.61	0.39	3.00

WT12WH23-2-5-7	5.79	0.21	6.00	0.54	6.75	0.02	0.07	0.02	2.35	0.01	0.59	0.01	0.39	3.66	0.34	3.00
WT12WH23-2-5-8	5.81	0.19	6.00	0.37	6.57	0.03	0.09	0.02	2.47	0.01	0.76	0.01	0.21	3.48	0.52	3.00
WT12WH23-2-5-9	5.76	0.24	6.00	0.61	6.85	0.03	0.02	0.01	2.31	0.01	0.60	0.01	0.38	3.76	0.24	3.00
WT12WH23-2-5-10	5.80	0.20	6.00	0.32	6.52	0.04	0.09	0.02	2.52	0.01	0.81	0.01	0.17	3.41	0.59	3.00
WT12WH24-1-1-1	5.72	0.28	6.00	0.68	6.96	0.00	0.15	0.02	2.13	0.03	0.59	0.01	0.37	3.62	0.38	3.00
WT12WH24-1-1-2	5.76	0.24	6.00	0.43	6.67	0.01	0.15	0.02	2.39	0.02	0.73	0.01	0.24	3.39	0.61	3.00
WT12WH24-1-1-3	5.78	0.22	6.00	0.69	6.91	0.01	0.07	0.00	2.19	0.00	0.58	0.01	0.40	3.80	0.20	3.00
WT12WH24-1-1-4	5.71	0.29	6.00	0.52	6.82	0.01	0.13	0.01	2.31	0.02	0.72	0.01	0.25	3.45	0.55	3.00
WT12WH24-1-2-1	5.66	0.34	6.00	0.53	6.87	0.00	0.00	0.02	2.47	0.04	0.67	0.00	0.29	3.50	0.50	3.00
WT12WH24-1-2-2	5.66	0.34	6.00	0.55	6.89	0.00	0.05	0.02	2.38	0.03	0.70	0.01	0.26	3.43	0.57	3.00
WT12WH24-1-2-3	5.80	0.20	6.00	0.64	6.84	0.00	0.04	0.02	2.29	0.01	0.57	0.01	0.41	3.85	0.15	3.00
WT12WH24-1-2-4	5.80	0.20	6.00	0.69	6.89	0.00	0.05	0.02	2.21	0.01	0.53	0.01	0.44	3.81	0.19	3.00
WT12WH24-1-3-1	5.71	0.29	6.00	0.34	6.63	0.04	0.17	0.01	2.49	0.05	0.66	0.01	0.28	3.41	0.59	3.00
WT12WH24-1-3-2	5.73	0.27	6.00	0.39	6.66	0.07	0.16	0.01	2.38	0.03	0.65	0.01	0.31	3.34	0.66	3.00
WT12WH24-1-3-3	5.70	0.30	6.00	0.42	6.71	0.07	0.17	0.02	2.31	0.03	0.67	0.01	0.29	3.37	0.63	3.00
WT12WH24-1-3-4	5.70	0.30	6.00	0.30	6.60	0.09	0.25	0.01	2.38	0.05	0.68	0.02	0.26	3.42	0.58	3.00
WT12WH24-1-3-5	5.70	0.30	6.00	0.32	6.62	0.07	0.18	0.01	2.40	0.04	0.73	0.01	0.21	3.35	0.65	3.00
WT12WH24-1-3-6	5.71	0.29	6.00	0.35	6.65	0.07	0.18	0.01	2.36	0.05	0.72	0.01	0.22	3.37	0.63	3.00
WT12WH24-2-3-1	5.69	0.31	6.00	0.50	6.81	0.06	0.22	0.02	2.20	0.03	0.63	0.01	0.33	3.46	0.54	3.00
WT12WH24-2-3-2	5.60	0.40	6.00	0.48	6.89	0.06	0.24	0.01	2.21	0.04	0.70	0.01	0.26	3.44	0.56	3.00
WT12WH24-2-3-3	5.66	0.34	6.00	0.68	7.02	0.04	0.19	0.01	2.03	0.03	0.60	0.01	0.36	3.61	0.39	3.00
WT12WH24-2-3-4	5.68	0.32	6.00	0.69	7.01	0.04	0.19	0.01	2.05	0.03	0.58	0.01	0.38	3.64	0.36	3.00
WT12WH24-2-3-5	5.69	0.31	6.00	0.66	6.97	0.04	0.19	0.01	2.04	0.03	0.60	0.01	0.36	3.63	0.37	3.00
WT12WH24-2-3-6	5.65	0.35	6.00	0.53	6.89	0.05	0.25	0.01	2.15	0.05	0.61	0.01	0.33	3.44	0.56	3.00
WT12WH24-2-3-7	5.65	0.35	6.00	0.43	6.78	0.04	0.17	0.01	2.37	0.05	0.71	0.01	0.23	3.52	0.48	3.00
WT12WH24-2-3-8	5.79	0.21	6.00	0.63	6.84	0.02	0.17	0.00	2.15	0.02	0.55	0.01	0.43	3.64	0.36	3.00
WT12WH24-2-3-9	5.77	0.23	6.00	0.68	6.91	0.03	0.13	0.01	2.11	0.01	0.54	0.01	0.44	3.68	0.32	3.00
WT12WH24-2-3-10	5.77	0.23	6.00	0.66	6.89	0.03	0.14	0.01	2.12	0.02	0.55	0.00	0.43	3.70	0.30	3.00
WT12WH24-2-3-11	5.80	0.20	6.00	0.67	6.87	0.03	0.15	0.01	2.10	0.01	0.51	0.00	0.48	3.70	0.30	3.00
WT12WH24-2-3-12	5.69	0.31	6.00	0.45	6.76	0.05	0.21	0.01	2.29	0.05	0.65	0.01	0.30	3.56	0.44	3.00
WT12WH24-2-3-13	5.70	0.30	6.00	0.46	6.76	0.05	0.14	0.01	2.35	0.03	0.65	0.00	0.31	3.53	0.47	3.00
WT12WH24-2-3-14	5.66	0.34	6.00	0.54	6.88	0.04	0.13	0.01	2.28	0.04	0.61	0.01	0.34	3.55	0.45	3.00
WT12WH24-2-3-15	5.66	0.34	6.00	0.55	6.89	0.04	0.16	0.01	2.23	0.05	0.64	0.01	0.30	3.53	0.47	3.00
WT12WH24-2-3-16	5.65	0.35	6.00	0.58	6.93	0.03	0.12	0.01	2.28	0.05	0.60	0.01	0.34	3.57	0.43	3.00
WT12WH24-2-3-17	5.75	0.25	6.00	0.49	6.74	0.01	0.02	0.01	2.49	0.02	0.67	0.00	0.31	3.57	0.43	3.00
WT12WH24-2-3-18	5.66	0.34	6.00	0.35	6.68	0.08	0.27	0.01	2.31	0.06	0.66	0.01	0.28	3.47	0.53	3.00
WT12WH24-2-3-19	5.70	0.30	6.00	0.35	6.66	0.05	0.21	0.01	2.40	0.05	0.69	0.01	0.25	3.50	0.50	3.00
WT12WH24-2-3-20	5.70	0.30	6.00	0.39	6.69	0.07	0.20	0.01	2.33	0.05	0.69	0.01	0.25	3.49	0.51	3.00
WT12WH24-2-4-1	5.64	0.36	6.00	0.46	6.81	0.07	0.20	0.02	2.26	0.04	0.68	0.02	0.27	3.41	0.59	3.00
WT12WH24-2-4-2	5.70	0.30	6.00	0.61	6.91	0.05	0.17	0.01	2.12	0.02	0.62	0.01	0.34	3.64	0.36	3.00
WT12WH24-2-4-3	5.69	0.31	6.00	0.58	6.89	0.04	0.17	0.01	2.19	0.03	0.59	0.01	0.38	3.59	0.41	3.00

WT12WH24-2-4-4	5.69	0.31	6.00	0.53	6.84	0.04	0.19	0.01	2.23	0.03	0.64	0.01	0.32	3.54	0.46	3.00
WT12WH24-2-4-5	5.73	0.27	6.00	0.57	6.84	0.04	0.19	0.01	2.18	0.02	0.62	0.01	0.35	3.56	0.44	3.00
WT12WH24-2-4-6	5.78	0.22	6.00	0.59	6.81	0.04	0.17	0.01	2.15	0.02	0.58	0.01	0.39	3.69	0.31	3.00
WT12WH24-2-4-7	5.81	0.19	6.00	0.62	6.81	0.04	0.17	0.00	2.17	0.01	0.51	0.00	0.48	3.70	0.30	3.00
WT12WH24-2-4-8	5.69	0.31	6.00	0.57	6.87	0.04	0.17	0.01	2.20	0.04	0.60	0.01	0.35	3.59	0.41	3.00
WT12WH24-2-4-9	5.80	0.20	6.00	0.61	6.81	0.03	0.16	0.01	2.14	0.01	0.60	0.01	0.38	3.68	0.32	3.00
WT12WH24-2-4-10	5.73	0.27	6.00	0.35	6.62	0.07	0.23	0.01	2.31	0.07	0.68	0.01	0.24	3.49	0.51	3.00
WT12WH24-3-1	5.71	0.29	6.00	0.42	6.71	0.03	0.11	0.01	2.49	0.04	0.61	0.01	0.34	3.47	0.53	3.00
WT12WH24-3-2	5.63	0.37	6.00	0.51	6.87	0.05	0.16	0.01	2.29	0.04	0.63	0.01	0.32	3.55	0.45	3.00
WT12WH24-3-3	5.63	0.37	6.00	0.48	6.85	0.05	0.19	0.01	2.31	0.05	0.63	0.01	0.32	3.48	0.52	3.00
WT12WH24-3-4	5.68	0.32	6.00	0.46	6.78	0.07	0.26	0.01	2.18	0.04	0.66	0.01	0.28	3.44	0.56	3.00
WT12WH24-3-5	5.75	0.25	6.00	0.68	6.93	0.04	0.21	0.01	2.02	0.01	0.58	0.00	0.41	3.67	0.33	3.00
WT12WH24-3-6	5.75	0.25	6.00	0.58	6.83	0.04	0.21	0.01	2.11	0.04	0.60	0.01	0.35	3.58	0.42	3.00
WT12WH24-3-7	5.65	0.35	6.00	0.45	6.80	0.06	0.24	0.01	2.24	0.06	0.65	0.01	0.29	3.44	0.56	3.00
WT12WH24-3-8	5.69	0.31	6.00	0.35	6.66	0.06	0.16	0.02	2.45	0.05	0.66	0.01	0.28	3.52	0.48	3.00
WT12WH24-3-9	5.71	0.29	6.00	0.41	6.70	0.07	0.19	0.01	2.30	0.06	0.64	0.01	0.29	3.47	0.53	3.00
WT12WH24-3-10	5.68	0.32	6.00	0.44	6.76	0.06	0.18	0.01	2.32	0.04	0.66	0.01	0.28	3.46	0.54	3.00
WT12WH24-3-11	5.70	0.30	6.00	0.39	6.69	0.05	0.13	0.01	2.42	0.05	0.68	0.01	0.25	3.47	0.53	3.00
WT12WH24-3-12	5.69	0.31	6.00	0.42	6.74	0.06	0.25	0.01	2.27	0.05	0.63	0.01	0.31	3.48	0.52	3.00
WT12WH24-3-13	5.67	0.33	6.00	0.62	6.95	0.05	0.23	0.01	2.05	0.04	0.62	0.01	0.33	3.57	0.43	3.00
WT12WH28-1-1-4	5.69	0.31	6.00	0.50	6.81	0.05	0.19	0.01	2.25	0.03	0.64	0.02	0.31	3.42	0.58	3.00
WT12WH28-1-1-5	5.68	0.32	6.00	0.61	6.93	0.04	0.15	0.02	2.17	0.03	0.61	0.01	0.36	3.48	0.52	3.00
WT12WH28-1-1-6	5.61	0.39	6.00	0.52	6.91	0.06	0.20	0.02	2.23	0.03	0.62	0.01	0.34	3.50	0.50	3.00
WT12WH28-1-2-1	5.63	0.37	6.00	0.49	6.86	0.08	0.18	0.01	2.23	0.03	0.65	0.02	0.30	3.47	0.53	3.00
WT12WH28-1-2-2	5.65	0.35	6.00	0.56	6.91	0.05	0.16	0.01	2.18	0.03	0.65	0.00	0.32	3.55	0.45	3.00
WT12WH28-1-2-3	5.66	0.34	6.00	0.54	6.88	0.07	0.16	0.01	2.18	0.04	0.63	0.01	0.32	3.51	0.49	3.00
WT12WH28-1-2-4	5.68	0.32	6.00	0.39	6.71	0.08	0.19	0.01	2.34	0.04	0.65	0.02	0.29	3.43	0.57	3.00
WT12WH28-1-2-5	5.63	0.37	6.00	0.47	6.83	0.06	0.17	0.01	2.30	0.03	0.69	0.01	0.27	3.46	0.54	3.00
WT12WH28-1-2-6	5.62	0.38	6.00	0.58	6.96	0.04	0.14	0.01	2.23	0.04	0.64	0.01	0.31	3.46	0.54	3.00
WT12WH28-1-3-1	5.62	0.38	6.00	0.70	7.08	0.02	0.16	0.01	2.09	0.03	0.62	0.01	0.33	3.53	0.47	3.00
WT12WH28-1-3-2	5.69	0.31	6.00	0.63	6.94	0.03	0.18	0.01	2.14	0.02	0.58	0.01	0.39	3.56	0.44	3.00
WT12WH28-1-3-3	5.65	0.35	6.00	0.71	7.06	0.03	0.15	0.02	2.08	0.01	0.57	0.02	0.40	3.64	0.36	3.00
WT12WH28-1-3-4	5.67	0.33	6.00	0.67	7.00	0.02	0.17	0.01	2.09	0.02	0.64	0.01	0.32	3.52	0.48	3.00
WT12WH28-1-3-5	5.65	0.35	6.00	0.58	6.93	0.02	0.17	0.01	2.25	0.03	0.60	0.02	0.35	3.48	0.52	3.00
WT12WH28-1-4-1	5.53	0.47	6.00	0.53	7.01	0.06	0.12	0.03	2.26	0.05	0.69	0.01	0.25	3.43	0.57	3.00
WT12WH28-1-4-2	5.60	0.40	6.00	0.67	7.07	0.03	0.10	0.03	2.14	0.04	0.66	0.01	0.29	3.58	0.42	3.00
WT12WH28-1-4-3	5.70	0.30	6.00	0.63	6.93	0.03	0.09	0.03	2.18	0.02	0.63	0.02	0.33	3.63	0.37	3.00
WT12WH28-1-4-4	5.61	0.39	6.00	0.49	6.88	0.06	0.11	0.03	2.28	0.05	0.69	0.02	0.23	3.46	0.54	3.00
WT12WH28-1-4-5	5.69	0.31	6.00	0.69	7.00	0.03	0.10	0.03	2.11	0.02	0.59	0.01	0.38	3.65	0.35	3.00
WT12WH28-1-4-6	5.63	0.37	6.00	0.57	6.94	0.04	0.12	0.03	2.21	0.04	0.68	0.01	0.27	3.51	0.49	3.00
WT12WH28-1-4-7	5.60	0.40	6.00	0.68	7.09	0.03	0.11	0.03	2.11	0.03	0.64	0.03	0.30	3.54	0.46	3.00

WT12WH28-1-4-8	5.58	0.42	6.00	0.55	6.97	0.05	0.11	0.04	2.24	0.04	0.70	0.02	0.24	3.47	0.53	3.00
WT12WH28-1-5-1	5.74	0.26	6.00	0.43	6.68	0.04	0.23	0.02	2.32	0.03	0.64	0.01	0.32	3.42	0.58	3.00
WT12WH28-1-5-2	5.76	0.24	6.00	0.68	6.92	0.02	0.16	0.02	2.06	0.01	0.60	0.00	0.39	3.65	0.35	3.00
WT12WH28-1-5-3	5.68	0.32	6.00	0.59	6.91	0.02	0.20	0.02	2.17	0.03	0.64	0.01	0.32	3.48	0.52	3.00
WT12WH28-1-5-4	5.66	0.34	6.00	0.55	6.89	0.03	0.19	0.02	2.21	0.04	0.64	0.02	0.30	3.41	0.59	3.00
WT12WH28-1-5-5	5.69	0.31	6.00	0.65	6.96	0.02	0.18	0.02	2.11	0.02	0.63	0.01	0.34	3.54	0.46	3.00
WT12WH28-2-1-1	5.56	0.44	6.00	0.64	7.08	0.04	0.13	0.03	2.13	0.06	0.65	0.01	0.28	3.46	0.54	3.00
WT12WH28-2-1-2	5.62	0.38	6.00	0.49	6.86	0.06	0.13	0.02	2.31	0.06	0.62	0.02	0.30	3.45	0.55	3.00
WT12WH28-2-1-3	5.61	0.39	6.00	0.69	7.08	0.03	0.13	0.02	2.08	0.04	0.63	0.02	0.32	3.50	0.50	3.00
WT12WH28-2-1-4	5.61	0.39	6.00	0.57	6.96	0.04	0.13	0.03	2.21	0.05	0.68	0.01	0.27	3.44	0.56	3.00
WT12WH28-2-1-5	5.63	0.37	6.00	0.51	6.89	0.05	0.14	0.02	2.26	0.05	0.67	0.02	0.27	3.45	0.55	3.00
WT12WH28-2-2-1	5.61	0.39	6.00	0.70	7.08	0.04	0.12	0.03	2.08	0.04	0.60	0.01	0.36	3.47	0.53	3.00
WT12WH28-2-2-2	5.63	0.37	6.00	0.65	7.02	0.03	0.13	0.03	2.13	0.04	0.65	0.01	0.31	3.48	0.52	3.00
WT12WH28-2-2-3	5.74	0.26	6.00	0.38	6.64	0.05	0.14	0.04	2.42	0.03	0.66	0.01	0.30	3.39	0.61	3.00
WT12WH28-2-2-4	5.59	0.41	6.00	0.53	6.94	0.05	0.12	0.03	2.25	0.05	0.68	0.02	0.25	3.43	0.57	3.00
WT12WH28-2-2-5	5.68	0.32	6.00	0.66	6.98	0.03	0.10	0.03	2.15	0.03	0.62	0.01	0.34	3.61	0.39	3.00
WT12WH28-2-2-6	5.60	0.40	6.00	0.70	7.09	0.03	0.12	0.03	2.10	0.04	0.61	0.01	0.34	3.48	0.52	3.00
WT12WH28-2-3-1	5.60	0.40	6.00	0.48	6.88	0.05	0.15	0.03	2.29	0.04	0.75	0.02	0.19	3.34	0.66	3.00
WT12WH28-2-3-2	5.55	0.45	6.00	0.71	7.16	0.02	0.14	0.03	2.08	0.05	0.65	0.01	0.29	3.46	0.54	3.00
WT12WH28-2-3-3	5.73	0.27	6.00	0.47	6.74	0.04	0.12	0.03	2.33	0.02	0.69	0.01	0.28	3.58	0.42	3.00
WT12WH28-2-3-4	5.54	0.46	6.00	0.72	7.18	0.02	0.13	0.02	2.07	0.04	0.66	0.01	0.29	3.49	0.51	3.00
WT12WH28-2-3-5	5.62	0.38	6.00	0.59	6.97	0.04	0.14	0.03	2.19	0.03	0.66	0.00	0.30	3.32	0.68	3.00
WT12WH28-2-3-6	5.53	0.47	6.00	0.71	7.18	0.02	0.13	0.03	2.10	0.04	0.63	0.00	0.33	3.38	0.62	3.00
WT12WH28-2-7-1	5.64	0.36	6.00	0.71	7.07	0.03	0.13	0.03	2.04	0.04	0.64	0.01	0.31	3.43	0.57	3.00
WT12WH28-2-7-2	5.72	0.28	6.00	0.57	6.85	0.03	0.11	0.03	2.22	0.02	0.67	0.01	0.30	3.58	0.42	3.00
WT12WH28-2-7-3	5.56	0.44	6.00	0.74	7.18	0.02	0.12	0.03	2.07	0.04	0.59	0.00	0.36	3.44	0.56	3.00
WT12WH28-2-7-4	5.55	0.45	6.00	0.55	7.00	0.04	0.12	0.03	2.24	0.05	0.73	0.02	0.21	3.36	0.64	3.00
WT12WH28-2-7-5	5.63	0.37	6.00	0.72	7.10	0.02	0.12	0.03	2.07	0.03	0.63	0.01	0.32	3.47	0.53	3.00
WT12WH28-3-1-1	5.65	0.35	6.00	0.52	6.87	0.06	0.18	0.01	2.22	0.03	0.67	0.01	0.30	3.37	0.63	3.00
WT12WH28-3-1-2	5.71	0.29	6.00	0.50	6.79	0.06	0.20	0.02	2.19	0.02	0.66	0.01	0.31	3.40	0.60	3.00
WT12WH28-3-1-3	5.66	0.34	6.00	0.51	6.85	0.06	0.20	0.02	2.21	0.02	0.66	0.01	0.31	3.40	0.60	3.00
WT12WH28-3-1-4	5.79	0.21	6.00	0.76	6.98	0.03	0.14	0.02	1.98	0.01	0.53	0.01	0.46	3.58	0.42	3.00
WT12WH28-3-1-5	5.70	0.30	6.00	0.54	6.84	0.05	0.20	0.02	2.16	0.02	0.64	0.01	0.32	3.43	0.57	3.00
WT12WH28-3-1-6	5.73	0.27	6.00	0.68	6.94	0.04	0.16	0.01	2.07	0.00	0.57	0.01	0.42	3.51	0.49	3.00
WT12WH28-3-1-7	5.75	0.25	6.00	0.72	6.97	0.04	0.15	0.01	2.02	0.01	0.56	0.00	0.43	3.53	0.47	3.00
WT12WH28-3-3-2	5.69	0.31	6.00	0.47	6.78	0.05	0.15	0.02	2.29	0.04	0.70	0.01	0.25	3.33	0.67	3.00
WT12WH28-3-3-3	5.63	0.37	6.00	0.63	7.00	0.03	0.16	0.01	2.17	0.02	0.63	0.01	0.34	3.46	0.54	3.00
WT12WH28-3-3-4	5.78	0.22	6.00	0.72	6.94	0.02	0.12	0.02	2.05	0.01	0.59	0.00	0.40	3.63	0.37	3.00
WT12WH28-3-3-5	5.70	0.30	6.00	0.57	6.88	0.04	0.16	0.01	2.20	0.02	0.63	0.01	0.34	3.39	0.61	3.00
WT12WH28-3-5-2	5.69	0.31	6.00	0.61	6.92	0.04	0.13	0.02	2.18	0.01	0.62	0.02	0.36	3.59	0.41	3.00
WT12WH28-3-5-3	5.65	0.35	6.00	0.49	6.84	0.06	0.18	0.01	2.27	0.03	0.65	0.02	0.30	3.30	0.70	3.00

WT12WH28-3-6-2	5.68	0.32	6.00	0.48	6.80	0.04	0.15	0.03	2.33	0.02	0.66	0.01	0.31	3.62	0.38	3.00
WT12WH28-3-6-3	5.48	0.52	6.00	0.77	7.29	0.03	0.14	0.02	2.02	0.05	0.63	0.01	0.31	3.49	0.51	3.00
WT12WH28-3-6-4	5.51	0.49	6.00	0.67	7.16	0.03	0.15	0.03	2.14	0.04	0.66	0.01	0.29	3.41	0.59	3.00
WT12WH28-3-6-5	5.50	0.50	6.00	0.74	7.24	0.02	0.14	0.02	2.05	0.05	0.67	0.00	0.28	3.46	0.54	3.00
WT12WH28-4-1-1	5.71	0.29	6.00	0.51	6.80	0.02	0.09	0.02	2.38	0.03	0.63	0.01	0.32	3.36	0.64	3.00
WT12WH28-4-1-2	5.61	0.39	6.00	0.64	7.03	0.02	0.08	0.02	2.25	0.06	0.59	0.00	0.35	3.41	0.59	3.00
WT12WH28-4-1-3	5.60	0.40	6.00	0.67	7.06	0.01	0.05	0.02	2.26	0.04	0.61	0.02	0.34	3.44	0.56	3.00
WT12WH28-4-1-4	5.77	0.23	6.00	0.86	7.09	0.00	0.01	0.06	2.08	0.00	0.34	0.00	0.66	3.95	0.05	3.00
WT12WH28-4-1-5	5.55	0.45	6.00	0.65	7.10	0.02	0.09	0.01	2.24	0.05	0.62	0.01	0.32	3.38	0.62	3.00
WT12WH28-4-1-6	5.52	0.48	6.00	0.69	7.17	0.02	0.09	0.01	2.22	0.06	0.57	0.01	0.36	3.42	0.58	3.00
WT12WH28-4-1-7	5.57	0.43	6.00	0.64	7.07	0.01	0.08	0.01	2.29	0.04	0.61	0.01	0.34	3.39	0.61	3.00
WT12WH28-4-3-1	5.66	0.34	6.00	0.52	6.86	0.06	0.24	0.02	2.16	0.06	0.61	0.01	0.32	3.38	0.62	3.00
WT12WH28-4-3-2	5.65	0.35	6.00	0.61	6.96	0.02	0.08	0.02	2.26	0.05	0.62	0.01	0.32	3.41	0.59	3.00
WT12WH28-4-3-3	5.70	0.30	6.00	0.64	6.93	0.04	0.17	0.00	2.12	0.03	0.59	0.02	0.36	3.58	0.42	3.00
WT12WH28-4-3-4	5.63	0.37	6.00	0.49	6.86	0.05	0.19	0.02	2.28	0.05	0.63	0.01	0.31	3.41	0.59	3.00
WT12WH28-4-4-1	5.60	0.40	6.00	0.58	6.97	0.05	0.19	0.02	2.17	0.05	0.59	0.01	0.35	3.39	0.61	3.00
WT12WH28-4-4-2	5.55	0.45	6.00	0.71	7.16	0.02	0.15	0.01	2.10	0.05	0.58	0.01	0.37	3.51	0.49	3.00
WT12WH28-4-4-3	5.55	0.45	6.00	0.72	7.17	0.04	0.17	0.01	2.05	0.05	0.59	0.01	0.35	3.44	0.56	3.00
WT12WH28-4-4-4	5.65	0.35	6.00	0.53	6.88	0.05	0.14	0.02	2.25	0.07	0.63	0.01	0.29	3.42	0.58	3.00
WT12WH28-4-4-5	5.55	0.45	6.00	0.63	7.08	0.03	0.14	0.01	2.21	0.06	0.62	0.01	0.32	3.41	0.59	3.00
WT12WH28-4-4-6	5.61	0.39	6.00	0.54	6.93	0.05	0.16	0.02	2.24	0.06	0.62	0.01	0.31	3.41	0.59	3.00
WT12WH28-4-4-7	5.62	0.38	6.00	0.59	6.98	0.03	0.16	0.01	2.19	0.05	0.65	0.02	0.28	3.52	0.48	3.00
WT12WH28-4-4-8	5.58	0.42	6.00	0.59	7.01	0.04	0.16	0.01	2.20	0.06	0.64	0.01	0.30	3.39	0.61	3.00
WT12WH33-2-1-1	5.66	0.34	6.00	0.67	7.01	0.05	0.31	0.01	1.94	0.03	0.56	0.01	0.41	3.51	0.49	3.00
WT12WH33-2-1-2	5.67	0.33	6.00	0.58	6.92	0.07	0.27	0.01	2.04	0.04	0.58	0.01	0.38	3.45	0.55	3.00
WT12WH33-2-1-3	5.76	0.24	6.00	0.37	6.61	0.09	0.43	0.01	2.08	0.04	0.66	0.01	0.29	3.33	0.67	3.00
WT12WH33-2-1-4	5.83	0.17	6.00	0.35	6.51	0.09	0.24	0.01	2.23	0.04	0.67	0.01	0.28	3.41	0.59	3.00
WT12WH33-2-1-5	5.77	0.23	6.00	0.39	6.62	0.08	0.39	0.02	2.11	0.03	0.63	0.01	0.32	3.35	0.65	3.00
WT12WH33-2-1-6	5.76	0.24	6.00	0.41	6.65	0.07	0.44	0.02	2.03	0.03	0.68	0.01	0.29	3.32	0.68	3.00
WT12WH33-2-1-7	5.72	0.28	6.00	0.45	6.72	0.07	0.41	0.02	2.04	0.03	0.64	0.01	0.31	3.30	0.70	3.00
WT12WH33-2-1-8	5.78	0.22	6.00	0.40	6.61	0.06	0.24	0.02	2.29	0.04	0.61	0.01	0.34	3.36	0.64	3.00
WT12WH33-2-1-9	5.75	0.25	6.00	0.40	6.65	0.05	0.19	0.02	2.33	0.04	0.69	0.01	0.26	3.36	0.64	3.00
WT12WH33-2-1-10	5.75	0.25	6.00	0.40	6.65	0.06	0.23	0.02	2.25	0.04	0.71	0.01	0.24	3.32	0.68	3.00
WT12WH33-2-1-11	5.73	0.27	6.00	0.41	6.68	0.07	0.41	0.02	2.08	0.03	0.68	0.01	0.29	3.31	0.69	3.00
WT12WH33-2-1-12	5.76	0.24	6.00	0.39	6.63	0.05	0.21	0.02	2.33	0.04	0.64	0.01	0.31	3.36	0.64	3.00
WT12WH33-2-5-1	5.73	0.27	6.00	0.78	7.05	0.02	0.13	0.02	2.03	0.01	0.47	0.01	0.51	3.65	0.35	3.00
WT12WH33-2-5-2	5.74	0.26	6.00	0.78	7.03	0.02	0.14	0.02	2.01	0.01	0.49	0.01	0.49	3.68	0.32	3.00
WT12WH33-2-5-3	5.73	0.27	6.00	0.52	6.79	0.06	0.21	0.01	2.16	0.04	0.61	0.01	0.35	3.42	0.58	3.00
WT12WH33-2-5-4	5.64	0.36	6.00	0.68	7.04	0.04	0.35	0.02	1.89	0.02	0.59	0.01	0.38	3.49	0.51	3.00
WT12WH33-2-5-5	5.65	0.35	6.00	0.53	6.89	0.06	0.20	0.02	2.21	0.04	0.58	0.01	0.37	3.42	0.58	3.00
WT12WH33-2-5-6	5.64	0.36	6.00	0.55	6.91	0.04	0.29	0.02	2.09	0.03	0.67	0.01	0.29	3.49	0.51	3.00

WT12WH33-2-5-7	5.62	0.38	6.00	0.60	6.97	0.03	0.20	0.02	2.17	0.04	0.60	0.01	0.35	3.45	0.55	3.00
WT12WH33-2-5-8	5.68	0.32	6.00	0.61	6.93	0.05	0.34	0.01	1.95	0.02	0.63	0.00	0.34	3.50	0.50	3.00
WT12WH33-2-5-9	5.70	0.30	6.00	0.57	6.87	0.04	0.18	0.01	2.17	0.04	0.58	0.01	0.37	3.44	0.56	3.00
WT12WH33-2-5-10	5.71	0.29	6.00	0.62	6.91	0.04	0.26	0.01	2.03	0.03	0.60	0.01	0.36	3.48	0.52	3.00
WT12WH33-2-5-11	5.71	0.29	6.00	0.71	7.00	0.03	0.29	0.01	1.93	0.03	0.53	0.01	0.44	3.56	0.44	3.00
WT12WH33-2-5-12	5.73	0.27	6.00	0.69	6.97	0.02	0.25	0.01	1.98	0.03	0.56	0.01	0.40	3.58	0.42	3.00
WT12WH35-1-1-2	5.84	0.16	6.00	0.31	6.47	0.09	0.44	0.01	2.10	0.03	0.70	0.02	0.25	3.40	0.60	3.00
WT12WH35-1-1-3	5.82	0.18	6.00	0.40	6.58	0.08	0.45	0.02	2.00	0.03	0.65	0.01	0.31	3.46	0.54	3.00
WT12WH35-1-1-4	5.78	0.22	6.00	0.49	6.71	0.07	0.42	0.02	1.98	0.02	0.61	0.01	0.36	3.48	0.52	3.00
WT12WH35-1-1-5	5.81	0.19	6.00	0.44	6.63	0.06	0.43	0.01	2.01	0.03	0.64	0.01	0.32	3.40	0.60	3.00
WT12WH35-2-2-1	5.62	0.38	6.00	0.55	6.93	0.08	0.25	0.03	2.04	0.05	0.64	0.01	0.30	3.40	0.60	3.00
WT12WH35-2-2-2	5.55	0.45	6.00	0.68	7.13	0.06	0.26	0.03	1.95	0.05	0.60	0.01	0.34	3.40	0.60	3.00
WT12WH35-2-2-3	5.63	0.37	6.00	0.76	7.12	0.04	0.23	0.02	1.90	0.04	0.58	0.01	0.36	3.57	0.43	3.00
WT12WH35-2-2-4	5.58	0.42	6.00	0.71	7.14	0.05	0.26	0.02	1.92	0.04	0.59	0.01	0.36	3.46	0.54	3.00
WT12WH35-2-2-5	5.60	0.40	6.00	0.59	7.00	0.06	0.27	0.03	2.02	0.04	0.64	0.01	0.31	3.41	0.59	3.00
WT12WH35-2-2-6	5.60	0.40	6.00	0.59	7.00	0.06	0.27	0.02	2.03	0.05	0.60	0.02	0.33	3.39	0.61	3.00
WT12WH35-2-2-7	5.67	0.33	6.00	0.71	7.04	0.04	0.26	0.03	1.90	0.04	0.60	0.01	0.35	3.53	0.47	3.00
WT12WH35-2-2-8	5.70	0.30	6.00	0.75	7.05	0.04	0.21	0.02	1.89	0.03	0.58	0.01	0.39	3.64	0.36	3.00
WT12WH35-2-4-1	5.66	0.34	6.00	0.66	7.01	0.04	0.28	0.02	1.92	0.04	0.61	0.01	0.33	3.45	0.55	3.00
WT12WH35-2-4-2	5.70	0.30	6.00	0.67	6.97	0.04	0.28	0.02	1.91	0.04	0.60	0.01	0.34	3.45	0.55	3.00
WT12WH35-2-4-3	5.71	0.29	6.00	0.78	7.07	0.03	0.27	0.01	1.83	0.02	0.58	0.00	0.40	3.66	0.34	3.00
WT12WH35-2-4-4	5.66	0.34	6.00	0.56	6.91	0.06	0.31	0.02	1.97	0.05	0.69	0.01	0.25	3.42	0.58	3.00

Appendix 5.2 Trace element data of tourmaline from the Heemskirk and Pieman Heads granites analysed by LA-ICP-MS

Abbreviation: bdl = below detection limit

Sample No.	Corresponding EMPA No.	Location	Texture type	ppm	Li	Be	P	Sc	V	Co	Cr	Ni	Zn	Ga	Pb	Sr	Y	Cu	As	Rb	^{95}Mo
WT12WH04-1-1	WT12WH04-1-1	Pieman Head	Patch		42.33	1.97	142.82	53.60	77.93	29.04	3.20	11.62	194.66	135.46	0.98	2.28	0.02	1.91	2.91	bdl	bdl
WT12WH04-1-2		Pieman Head	Patch		70.62	bdl	86.41	43.54	82.58	28.12	bdl	11.12	200.55	154.66	3.12	8.50	bdl	bdl	bdl	bdl	bdl
WT12WH04-1-3	WT12WH04-1-3	Pieman Head	Patch		62.47	1.06	bdl	42.96	77.88	28.45	6.40	11.12	206.06	147.66	3.09	7.30	0.05	bdl	bdl	bdl	bdl
WT12WH04-1-4		Pieman Head	Patch		65.97	bdl	bdl	42.14	80.60	27.94	3.70	11.72	200.51	146.07	3.02	7.90	0.15	bdl	bdl	bdl	bdl
WT12WH04-1-5		Pieman Head	Patch		72.88	2.90	bdl	34.33	54.97	28.01	bdl	7.77	209.12	136.49	2.41	8.28	bdl	bdl	bdl	0.10	bdl
WT12WH04-1-6	WT12WH04-1-6	Pieman Head	Patch		46.37	2.85	bdl	0.88	bdl	29.08	bdl	1.04	190.51	90.50	0.38	4.53	0.02	bdl	0.36	bdl	0.16
WT12WH04-1-7	WT12WH04-1-7	Pieman Head	Patch		82.47	8.15	103.10	2.99	1.93	28.53	bdl	1.85	181.18	96.97	1.32	7.87	0.21	bdl	3.03	0.72	bdl
WT12WH04-3-1	WT12WH04-3-1	Pieman Head	Patch		54.59	9.80	bdl	59.08	107.66	27.83	bdl	12.31	175.86	131.16	2.36	6.62	0.06	bdl	bdl	bdl	bdl
WT12WH04-3-2	WT12WH04-3-2	Pieman Head	Patch		64.19	bdl	52.41	51.15	115.25	25.79	3.99	10.29	185.01	135.77	3.04	8.25	bdl	bdl	0.97	bdl	bdl
WT12WH04-3-3	WT12WH04-3-3	Pieman Head	Patch		65.65	1.54	bdl	37.00	90.51	27.56	4.71	8.57	206.14	136.14	2.89	7.73	0.05	bdl	0.34	bdl	bdl
WT12WH07-1-1-1	WT12WH07-1-1-1	Pieman Head	Orbicule		135.00	bdl	64.53	31.42	70.59	29.77	34.73	10.46	181.53	131.58	0.76	2.58	bdl	bdl	bdl	bdl	bdl
WT12WH07-1-1-2	WT12WH07-1-1-2	Pieman Head	Orbicule		89.41	bdl	bdl	41.29	78.21	27.53	17.73	7.96	208.03	139.17	2.29	6.72	0.07	bdl	bdl	bdl	bdl
WT12WH07-1-1-3	WT12WH07-1-1-3	Pieman Head	Orbicule		79.14	6.53	69.11	10.12	17.01	30.62	bdl	7.63	256.46	170.20	1.80	12.23	0.04	bdl	bdl	bdl	bdl
WT12WH07-1-1-4	WT12WH07-1-1-4	Pieman Head	Orbicule		39.69	3.58	171.01	13.35	17.34	27.62	bdl	6.96	233.72	229.46	0.57	3.85	bdl	bdl	bdl	bdl	bdl
WT12WH07-1-1-5	WT12WH07-1-1-5	Pieman Head	Orbicule		78.71	20.43	121.03	35.07	43.00	25.10	bdl	7.45	245.18	196.46	15.25	18.20	0.54	0.71	bdl	bdl	bdl
WT12WH07-2-1	WT12WH07-2-1	Pieman Head	Orbicule		36.72	bdl	111.67	66.51	117.06	26.70	14.75	10.63	217.31	160.17	1.55	3.67	0.02	bdl	bdl	bdl	bdl
WT12WH07-2-2	WT12WH07-2-2	Pieman Head	Orbicule		43.03	3.04	98.10	53.25	119.91	26.33	14.99	10.52	202.10	145.05	3.22	7.70	0.09	bdl	0.82	bdl	bdl
WT12WH07-2-3	WT12WH07-2-3	Pieman Head	Orbicule		37.38	bdl	86.79	67.66	141.91	26.52	14.83	10.40	203.96	153.08	2.13	4.26	bdl	bdl	bdl	bdl	bdl
WT12WH07-2-4	WT12WH07-2-4	Pieman Head	Orbicule		55.92	1.56	65.35	54.67	180.58	30.97	40.65	14.86	197.48	143.46	3.16	5.34	bdl	bdl	bdl	bdl	bdl
WT12WH07-3-1	WT12WH07-3-1	Pieman Head	Orbicule		41.65	1.67	94.70	55.57	144.28	28.63	18.74	10.91	207.70	152.60	2.97	7.58	0.06	bdl	bdl	0.13	bdl
WT12WH07-3-2	WT12WH07-3-2	Pieman Head	Orbicule		18.80	bdl	189.07	102.80	156.10	25.86	22.27	11.04	176.31	157.41	4.87	3.06	0.43	bdl	1.34	bdl	bdl
WT12WH07-3-3	WT12WH07-3-3	Pieman Head	Orbicule		35.91	bdl	92.90	55.49	126.61	28.14	12.46	12.44	192.66	149.04	2.39	6.77	bdl	bdl	bdl	bdl	bdl
WT12WH07-3-4	WT12WH07-3-4	Pieman Head	Orbicule		42.34	1.56	153.78	77.89	117.27	25.31	5.85	10.35	166.64	151.59	1.45	3.94	0.10	bdl	bdl	0.19	bdl
WT12WH13-1-2-1-1	WT12WH13-1-2-1-1	Pieman Head	Vein		97.32	3.80	88.30	20.23	30.52	30.36	2.50	6.04	237.88	122.72	2.46	9.55	0.00	bdl	bdl	bdl	bdl
WT12WH13-1-2-1-2	WT12WH13-1-2-1-2	Pieman Head	Vein		82.06	1.93	53.56	48.70	114.97	27.27	4.25	10.96	186.48	110.64	2.14	5.57	0.04	bdl	bdl	bdl	bdl
WT12WH13-1-2-1-3	WT12WH13-1-2-1-3	Pieman Head	Vein		131.34	8.77	bdl	36.62	53.04	27.56	bdl	8.95	200.05	101.86	1.97	2.94	bdl	bdl	bdl	bdl	bdl
WT12WH13-1-2-1-4	WT12WH13-1-2-1-4	Pieman Head	Vein		89.62	5.55	57.56	52.79	66.06	25.41	2.70	9.28	198.39	103.65	1.99	3.00	bdl	bdl	0.66	bdl	bdl
WT12WH13-1-2-1-5	WT12WH13-1-2-1-5	Pieman Head	Vein		259.02	20.54	114.41	41.65	4.81	4.88	bdl	bdl	298.76	403.93	1.32	0.72	bdl	bdl	bdl	bdl	0.10
WT12WH13-1-2-1-6	WT12WH13-1-2-1-6	Pieman Head	Vein		968.35	7.80	78.55	109.89	0.06	3.02	bdl	bdl	361.09	792.82	1.56	0.84	0.10	bdl	bdl	bdl	bdl
WT12WH13-1-2-1-7	WT12WH13-1-2-1-7	Pieman Head	Vein		712.38	5.11	55.15	87.54	0.55	3.22	bdl	bdl	374.59	585.00	0.67	0.42	bdl	bdl	bdl	0.11	bdl
WT12WH13-1-2-1-8	WT12WH13-1-2-1-8	Pieman Head	Vein		481.00	5.86	81.59	101.99	0.24	3.81	bdl	0.55	344.58	493.10	0.24	0.17	bdl	bdl	0.70	bdl	bdl
WT12WH13-1-2-1-9	WT12WH13-1-2-1-9	Pieman Head	Vein		765.80	3.97	65.33	91.78	0.25	2.21	bdl	0.28	374.07	599.68	0.28	0.19	bdl	bdl	0.71	0.15	bdl
WT12WH13-1-2-2-1	WT12WH13-1-2-2-1	Pieman Head	Vein		119.41	2.15	bdl	24.18	33.78	31.33	bdl	5.94	214.04	125.75	1.64	7.05	0.17	bdl	bdl	bdl	0.17
WT12WH13-1-2-2-2	WT12WH13-1-2-2-2	Pieman Head	Vein		106.80	0.60	99.86	56.71	130.51	26.98	bdl	12.06	194.10	114.20	1.95	4.75	0.01	bdl	bdl	bdl	bdl
WT12WH13-1-2-2-3	WT12WH13-1-2-2-3	Pieman Head	Vein		78.77	1.30	74.42	57.93	148.38	27.78	bdl	10.10	188.03	123.53	2.53	5.45	0.04	0.79	bdl	bdl	bdl
WT12WH13-1-2-2-4	WT12WH13-1-2-2-4	Pieman Head	Vein		80.53	2.46	87.00	70.69	127.37	27.92	7.16	10.50	188.08	120.94	2.28	3.72	bdl	bdl	bdl	0.10	bdl
WT12WH13-1-2-2-5	WT12WH13-1-2-2-5	Pieman Head	Vein		102.82	5.53	55.72	60.97	94.94	27.81	4.84	10.81	209.54	112.37	2.35	3.73	0.06	1.44	0.87	bdl	bdl
WT12WH13-1-2-2-6	WT12WH13-1-2-2-6	Pieman Head	Vein		58.07	6.42	93.11	99.16	76.01	26.46	bdl	13.50	182.50	110.81	1.08	1.32	0.03	bdl	bdl	bdl	0.07
WT12WH13-2-2-1	WT12WH13-2-2-1	Pieman Head	Vein		183.70	bdl	86.01	58.00	0.65	4.48	bdl	bdl	429.95	235.78	0.33	0.47	bdl	bdl	bdl	bdl	0.44

WT12WH13-2-2-2	WT12WH13-2-2-2	Pieman Head	Vein	60.31	0.89	149.00	91.59	2.87	5.22	bdl	3.62	373.28	231.34	0.06	bdl	0.01	bdl	bdl	bdl	bdl
WT12WH13-2-2-3	WT12WH13-2-2-3	Pieman Head	Vein	138.35	2.86	76.86	70.43	4.33	5.36	bdl	3.00	387.98	219.36	0.21	0.15	0.03	bdl	bdl	bdl	bdl
WT12WH13-2-2-4	WT12WH13-2-2-4	Pieman Head	Vein	358.13	bdl	76.09	62.30	0.48	2.25	bdl	bdl	378.48	268.92	0.44	0.38	bdl	bdl	bdl	bdl	bdl
WT12WH13-2-3-1	WT12WH13-2-3-1	Pieman Head	Vein	82.16	3.94	bdl	3.95	5.01	11.66	bdl	1.52	202.57	69.20	1.84	8.24	bdl	1.01	bdl	bdl	bdl
WT12WH13-2-3-2	WT12WH13-2-3-2	Pieman Head	Vein	70.43	5.40	48.15	12.55	30.97	16.56	bdl	bdl	179.59	76.30	2.39	10.07	0.40	8.80	bdl	bdl	bdl
WT12WH13-2-3-3	WT12WH13-2-3-3	Pieman Head	Vein	91.12	2.97	54.62	3.96	10.85	21.46	bdl	1.96	250.33	88.39	1.32	8.85	bdl	1.38	bdl	bdl	bdl
WT12WH13-2-3-4	WT12WH13-2-3-4	Pieman Head	Vein	46.23	22.32	71.41	0.84	2.43	21.00	bdl	bdl	215.75	102.21	1.03	6.71	bdl	bdl	bdl	bdl	bdl
WT12WH13-2-3-5	WT12WH13-2-3-5	Pieman Head	Vein	88.16	5.37	56.46	1.07	1.98	21.33	bdl	bdl	241.67	93.25	1.45	8.49	0.19	bdl	bdl	bdl	bdl
WT12WH13-2-3-6	WT12WH13-2-3-6	Pieman Head	Vein	86.96	5.42	69.54	1.38	1.00	21.36	bdl	bdl	240.87	97.91	2.17	9.79	0.24	1.65	bdl	bdl	bdl
WT12WH13-2-3-7	WT12WH13-2-3-7	Pieman Head	Vein	84.93	2.01	64.61	14.66	25.59	20.64	bdl	1.52	225.58	87.33	2.00	8.64	0.16	1.84	bdl	bdl	bdl
WT12WH13-2-3-8	WT12WH13-2-3-8	Pieman Head	Vein	94.37	1.09	bdl	5.28	2.76	9.89	1.05	1.05	244.00	75.79	1.62	9.81	0.30	2.20	bdl	bdl	bdl
WT12WH20-3-1	WT12WH20-3-1	Trial Harbour	Patch	114.80	8.65	51.47	75.47	53.26	11.74	9.68	5.47	211.51	189.10	0.39	0.89	bdl	1.19	bdl	bdl	bdl
WT12WH20-3-2	WT12WH20-3-2	Trial Harbour	Patch	155.42	7.48	46.06	59.10	57.17	12.65	11.89	4.35	244.06	181.21	0.73	1.37	0.20	3.04	bdl	0.19	bdl
WT12WH20-3-3	WT12WH20-3-3	Trial Harbour	Patch	174.91	7.15	60.66	56.39	62.97	14.23	17.30	5.44	260.15	174.43	0.79	1.20	0.04	7.58	bdl	bdl	bdl
WT12WH20-3-4	WT12WH20-3-4	Trial Harbour	Patch	96.73	6.09	bdl	58.43	57.96	14.06	14.69	4.91	185.25	184.38	0.43	0.51	0.02	7.16	bdl	0.18	bdl
WT12WH20-3-5	WT12WH20-3-5	Trial Harbour	Patch	78.56	4.08	67.06	56.25	58.29	14.73	13.19	6.54	196.55	177.64	0.59	0.49	0.07	10.31	bdl	0.16	0.14
WT12WH20-3-6	WT12WH20-3-6	Trial Harbour	Patch	89.69	bdl	bdl	50.92	59.77	14.73	19.29	5.00	199.03	182.87	0.55	0.53	bdl	10.00	bdl	bdl	bdl
WT12WH20-3-7	WT12WH20-3-7	Trial Harbour	Patch	160.78	10.23	65.07	52.51	55.26	12.03	14.60	2.93	200.33	162.57	0.94	1.47	bdl	6.82	bdl	bdl	bdl
WT12WH20-4-1	WT12WH20-4-1	Trial Harbour	Patch	68.07	13.86	135.86	66.50	29.95	11.42	8.10	2.29	186.69	170.33	0.38	0.63	bdl	0.90	bdl	0.17	bdl
WT12WH20-4-2	WT12WH20-4-2	Trial Harbour	Patch	126.16	9.91	80.68	41.42	27.22	10.52	18.79	3.03	204.44	151.10	1.42	1.53	0.09	bdl	1.32	3.01	0.50
WT12WH20-4-3	WT12WH20-4-3	Trial Harbour	Patch	119.81	12.88	91.77	45.61	30.49	10.34	9.98	3.53	205.08	160.05	1.34	1.76	bdl	1.14	bdl	bdl	bdl
WT12WH20-4-4	WT12WH20-4-4	Trial Harbour	Patch	127.87	8.95	147.30	64.01	30.52	10.08	bdl	3.85	203.74	164.67	1.18	1.52	bdl	bdl	bdl	bdl	0.18
WT12WH23-1-1	WT12WH23-2-3-1	Trial Harbour	Vein	128.44	9.10	93.89	46.34	34.86	10.42	10.00	3.51	189.91	161.09	1.25	1.52	bdl	7.68	bdl	0.56	bdl
WT12WH23-1-2	WT12WH23-2-3-2	Trial Harbour	Vein	144.21	7.08	82.30	46.33	31.77	9.71	3.49	2.76	197.42	166.78	1.16	1.55	bdl	6.25	bdl	bdl	0.27
WT12WH23-1-3	WT12WH23-2-3-3	Trial Harbour	Vein	142.17	10.49	89.65	42.56	31.67	11.81	7.71	2.70	199.79	160.90	0.87	1.40	0.03	bdl	bdl	bdl	bdl
WT12WH23-1-4	WT12WH23-2-5-1	Trial Harbour	Vein	135.83	7.89	96.46	64.64	40.51	11.62	8.39	2.38	216.32	174.80	3.23	1.55	0.03	bdl	bdl	11.12	0.49
WT12WH23-1-5	WT12WH23-2-5-2	Trial Harbour	Vein	129.74	8.09	63.49	60.97	40.67	10.82	6.03	3.71	183.70	173.19	0.93	1.19	0.02	bdl	bdl	bdl	0.31
WT12WH23-2-3-1	WT12WH23-2-5-3	Trial Harbour	Vein	57.34	36.26	bdl	3.73	4.01	2.83	bdl	0.38	91.70	68.95	3.03	7.14	1.15	8.45	bdl	bdl	0.36
WT12WH23-2-3-2	WT12WH23-2-5-4	Trial Harbour	Vein	22.82	64.51	73.96	3.88	3.27	3.16	0.00	bdl	75.01	77.80	0.65	5.34	6.69	bdl	2.45	bdl	bdl
WT12WH23-2-3-3	WT12WH23-2-5-5	Trial Harbour	Vein	65.01	16.14	40.69	12.33	10.61	3.23	bdl	bdl	71.49	78.28	1.05	5.59	0.12	5.93	bdl	bdl	0.15
WT12WH23-2-5-1	WT12WH23-2-5-6	Trial Harbour	Vein	60.68	12.48	bdl	5.34	6.76	2.79	2.23	bdl	91.04	94.08	1.37	9.12	3.45	bdl	3.63	0.31	bdl
WT12WH23-2-5-2	WT12WH24-1-1	Trial Harbour	Vein	26.87	30.78	78.00	25.76	17.67	1.35	bdl	0.24	70.72	138.01	0.82	4.57	5.95	2.44	bdl	bdl	bdl
WT12WH23-2-5-3	WT12WH24-1-2	Trial Harbour	Vein	131.23	44.16	bdl	6.16	4.39	2.60	bdl	bdl	108.00	46.34	0.63	3.27	0.05	bdl	bdl	bdl	bdl
WT12WH23-2-5-4	WT12WH24-1-3	Trial Harbour	Vein	50.55	12.81	82.95	12.07	7.08	3.66	bdl	bdl	103.17	65.92	1.22	7.24	bdl	bdl	bdl	bdl	bdl
WT12WH23-2-5-5	WT12WH24-1-4	Trial Harbour	Vein	31.41	33.09	47.69	17.36	10.73	2.60	2.56	0.00	61.57	93.45	0.66	5.01	3.94	1.09	4.59	bdl	bdl
WT12WH23-2-5-6	WT12WH24-2-3-1	Trial Harbour	Vein	65.84	16.25	bdl	12.93	8.54	3.01	0.23	bdl	81.92	75.02	1.21	7.98	0.07	2.38	bdl	bdl	bdl
WT12WH24-1-1	WT12WH24-2-3-2	Trial Harbour	Cavity	107.44	5.54	71.78	7.97	0.49	9.37	0.61	bdl	152.35	128.09	1.36	0.95	0.08	bdl	2.92	bdl	bdl
WT12WH24-1-2	WT12WH24-2-3-3	Trial Harbour	Cavity	79.73	17.10	112.45	31.21	1.23	10.11	bdl	0.48	172.96	149.25	2.19	1.72	bdl	bdl	1.42	bdl	bdl
WT12WH24-1-3	WT12WH24-2-3-4	Trial Harbour	Cavity	84.27	14.98	bdl	1.22	bdl	4.45	bdl	bdl	124.58	64.28	1.78	7.41	0.06	bdl	0.81	bdl	bdl
WT12WH24-1-4	WT12WH24-2-3-5	Trial Harbour	Cavity	35.21	54.36	61.86	4.31	bdl	3.53	bdl	bdl	126.86	92.07	3.33	1.80	8.77	bdl	3.97	0.20	bdl
WT12WH24-2-3-1	WT12WH24-2-3-6	Trial Harbour	Cavity	98.13	7.23	55.34	71.10	13.17	8.78	bdl	1.40	242.77	196.27	1.10	0.74	0.05	bdl	bdl	bdl	bdl

WT12WH24-2-3-2	WT12WH24-2-3-7	Trial Harbour	Cavity	44.94	9.62	bdl	73.95	29.47	10.65	bdl	bdl	220.88	241.38	0.65	0.64	0.07	bdl	bdl	0.32	bdl
WT12WH24-2-3-3	WT12WH24-2-3-8	Trial Harbour	Cavity	46.53	14.35	bdl	69.36	30.20	10.09	bdl	bdl	208.21	225.23	0.72	0.69	bdl	bdl	bdl	bdl	bdl
WT12WH24-2-3-4	WT12WH24-2-4-1	Trial Harbour	Cavity	25.91	1.79	59.80	46.69	11.61	11.35	bdl	1.09	239.79	251.41	0.23	0.39	0.02	bdl	bdl	0.04	bdl
WT12WH24-2-3-5	WT12WH24-2-4-2	Trial Harbour	Cavity	86.80	6.98	bdl	44.68	7.38	8.65	bdl	bdl	250.22	230.31	0.91	0.97	bdl	bdl	bdl	bdl	bdl
WT12WH24-2-3-6	WT12WH24-2-4-3	Trial Harbour	Cavity	73.62	7.19	bdl	72.48	25.82	11.75	1.41	1.23	259.58	215.84	1.25	1.08	0.14	0.84	0.30	bdl	0.22
WT12WH24-2-3-7	WT12WH24-2-4-4	Trial Harbour	Cavity	102.58	4.96	43.97	42.98	11.14	8.66	bdl	1.43	253.57	265.46	0.76	1.20	0.12	bdl	bdl	0.24	bdl
WT12WH24-2-3-8	WT12WH28-1-3-1	Trial Harbour	Cavity	91.78	5.45	57.50	71.31	17.56	10.41	bdl	1.41	251.98	225.98	1.18	1.41	bdl	bdl	0.69	0.50	0.19
WT12WH24-2-4-1	WT12WH28-1-3-2	Trial Harbour	Cavity	112.38	4.07	bdl	52.79	16.31	10.85	bdl	1.19	246.52	187.92	0.88	1.16	0.08	bdl	bdl	bdl	bdl
WT12WH24-2-4-2	WT12WH28-1-4-1	Trial Harbour	Cavity	68.34	29.73	80.06	97.92	10.67	9.70	bdl	2.12	194.57	212.75	0.56	1.34	0.07	bdl	bdl	bdl	0.50
WT12WH24-2-4-3	WT12WH28-1-4-2	Trial Harbour	Cavity	24.31	2.78	71.17	84.50	15.71	11.72	bdl	1.77	221.79	225.51	0.17	0.36	0.04	bdl	0.81	bdl	bdl
WT12WH24-2-4-4		Trial Harbour	Cavity	78.25	5.94	51.83	118.63	17.53	10.73	bdl	bdl	251.86	212.34	1.15	1.14	bdl	bdl	1.27	bdl	bdl
WT12WH28-1-3-1		Trial Harbour	Orbicule	162.99	13.08	61.73	48.04	3.02	8.48	bdl	bdl	236.08	282.60	0.85	0.18	0.07	bdl	bdl	0.57	bdl
WT12WH28-1-3-2		Trial Harbour	Orbicule	139.51	7.33	bdl	52.68	5.71	9.35	bdl	0.50	241.27	170.74	1.32	0.60	0.12	bdl	1.18	0.76	0.16
WT12WH28-1-4-1		Trial Harbour	Orbicule	202.18	15.49	178.61	34.11	4.15	4.69	2.32	0.49	217.50	200.99	1.23	0.27	0.09	bdl	3.46	0.32	0.76
WT12WH28-1-4-2		Trial Harbour	Orbicule	141.31	27.23	246.46	65.14	5.57	5.22	3.55	bdl	209.74	213.87	1.27	0.33	0.23	bdl	2.71	bdl	1.71
WT12WH28-2-3-1	WT12WH28-2-3-1	Trial Harbour	Orbicule	134.10	36.26	370.65	28.78	2.98	5.00	bdl	0.94	216.29	199.77	1.60	0.26	0.09	bdl	2.33	0.10	0.73
WT12WH28-2-3-2	WT12WH28-2-3-2	Trial Harbour	Orbicule	203.90	22.19	512.07	33.87	3.25	4.98	bdl	0.89	225.47	208.69	3.25	1.80	0.25	bdl	5.39	2.62	1.58
WT12WH28-2-3-3	WT12WH28-2-3-3	Trial Harbour	Orbicule	262.28	15.74	153.53	28.34	4.52	5.87	bdl	bdl	217.87	202.94	2.00	1.17	bdl	bdl	2.48	1.08	0.68
WT12WH28-2-3-4	WT12WH28-2-3-4	Trial Harbour	Orbicule	205.15	17.76	254.34	27.70	4.04	4.34	bdl	0.47	201.46	192.49	1.79	0.82	0.10	bdl	4.65	0.91	0.72
WT12WH28-3-1-1	WT12WH28-3-1-1	Trial Harbour	Orbicule	131.72	6.09	39.26	51.22	11.26	9.45	bdl	0.78	236.68	183.31	1.52	0.26	bdl	2.16	bdl	0.61	0.21
WT12WH28-3-1-2	WT12WH28-3-1-2	Trial Harbour	Orbicule	149.13	7.25	10.32	49.58	10.73	10.05	bdl	1.17	243.21	194.62	1.39	0.40	bdl	1.79	bdl	0.50	bdl
WT12WH28-3-1-3	WT12WH28-3-1-3	Trial Harbour	Orbicule	134.46	8.57	73.99	54.33	8.56	9.22	bdl	0.23	229.34	189.87	1.17	0.14	bdl	3.14	bdl	1.41	bdl
WT12WH28-3-1-4	WT12WH28-3-1-4	Trial Harbour	Orbicule	107.41	6.78	65.62	46.70	12.02	10.58	bdl	1.90	222.21	184.52	0.65	0.06	0.01	1.75	1.00	0.37	0.08
WT12WH28-3-6-1		Trial Harbour	Orbicule	164.91	17.10	451.74	45.01	2.78	4.57	bdl	bdl	188.12	205.53	3.82	0.51	0.70	bdl	10.59	2.70	1.03
WT12WH28-3-6-2	WT12WH28-3-6-2	Trial Harbour	Orbicule	155.06	24.39	398.66	35.22	2.88	6.19	bdl	0.24	221.77	221.73	2.88	0.64	0.45	1.63	5.79	13.64	0.63
WT12WH28-3-6-3	WT12WH28-3-6-3	Trial Harbour	Orbicule	167.77	19.62	340.88	34.32	2.44	5.51	bdl	bdl	187.63	216.03	2.66	0.12	0.45	2.03	5.89	4.41	0.54
WT12WH28-3-6-4	WT12WH28-3-6-4	Trial Harbour	Orbicule	169.31	21.78	309.95	32.20	2.72	5.71	bdl	1.04	207.87	226.93	2.35	0.14	0.29	bdl	4.82	2.02	0.51
WT12WH28-4-1-1	WT12WH28-4-1-1	Trial Harbour	Orbicule	135.02	4.89	107.36	8.57	3.35	11.51	bdl	bdl	201.86	242.17	0.89	2.50	0.08	bdl	bdl	bdl	0.24
WT12WH28-4-1-3	WT12WH28-4-1-3	Trial Harbour	Orbicule	155.29	5.10	97.00	6.04	3.10	10.73	bdl	bdl	222.71	242.72	0.83	1.58	0.13	bdl	bdl	0.36	bdl
WT12WH28-4-4-1	WT12WH28-4-4-1	Trial Harbour	Orbicule	120.91	8.86	122.39	63.61	10.48	13.12	bdl	0.93	220.92	200.82	1.07	2.23	0.07	bdl	1.17	0.38	0.31
WT12WH28-4-4-2	WT12WH28-4-4-2	Trial Harbour	Orbicule	153.30	4.78	bdl	27.82	8.79	10.23	0.96	bdl	208.10	194.85	0.84	1.30	0.05	bdl	0.46	bdl	bdl
WT12WH28-4-4-3	WT12WH28-4-4-3	Trial Harbour	Orbicule	115.92	7.05	107.69	42.52	10.80	11.80	bdl	0.83	234.17	210.12	1.09	2.33	0.07	bdl	bdl	bdl	bdl
WT12WH28-4-4-4	WT12WH28-4-4-4	Trial Harbour	Orbicule	137.33	6.23	bdl	36.13	9.20	11.69	1.63	0.91	213.33	198.98	1.09	1.97	0.07	bdl	bdl	bdl	bdl
WT12WH33-2-1-1	WT12WH33-2-1-1	Granville Harbour	Cavity	128.05	9.71	22.35	23.63	78.04	20.52	74.28	8.53	211.00	149.40	1.61	5.10	0.14	1.49	bdl	bdl	bdl
WT12WH33-2-1-2	WT12WH33-2-1-2	Granville Harbour	Cavity	121.26	37.03	26.19	29.53	54.86	22.39	69.16	8.44	216.96	146.66	0.79	3.30	0.03	bdl	0.30	bdl	bdl
WT12WH33-2-1-3	WT12WH33-2-1-3	Granville Harbour	Cavity	111.84	62.09	75.24	25.62	38.63	21.32	27.45	8.47	215.21	138.52	0.67	4.52	bdl	bdl	bdl	bdl	bdl
WT12WH33-2-1-4	WT12WH33-2-1-4	Granville Harbour	Cavity	126.42	36.15	63.23	5.10	3.96	21.98	3.62	3.49	220.99	155.17	0.78	3.47	0.04	bdl	bdl	0.10	bdl
WT12WH33-2-1-5	WT12WH33-2-1-5	Granville Harbour	Cavity	126.97	29.75	66.72	19.50	34.39	21.11	14.64	8.81	222.23	153.61	0.84	3.92	bdl	bdl	bdl	bdl	bdl
WT12WH33-2-1-6	WT12WH33-2-1-6	Granville Harbour	Cavity	136.20	16.62	32.48	24.47	48.18	20.33	45.44	9.06	204.64	145.63	0.90	3.77	bdl	1.91	0.97	0.08	bdl
WT12WH33-2-5-1	WT12WH33-2-5-1	Granville Harbour	Cavity	145.92	8.35	20.65	11.24	32.49	21.99	26.85	9.69	222.63	171.33	1.37	4.36	bdl	2.33	bdl	0.08	bdl
WT12WH33-2-5-2	WT12WH33-2-5-2	Granville Harbour	Cavity	132.46	4.06	13.18	14.47	40.09	19.78	31.32	7.40	224.89	180.63	1.18	4.24	bdl	2.13	bdl	bdl	bdl

WT12WH33-2-5-3	WT12WH33-2-5-3	Granville Harbour	Cavity	131.41	5.87	41.37	13.83	36.55	20.42	33.74	7.33	211.54	181.34	1.06	4.17	bdl	bdl	0.54	bdl	bdl
WT12WH33-2-5-4	WT12WH33-2-5-4	Granville Harbour	Cavity	132.65	6.12	44.50	15.89	36.19	19.40	30.70	6.10	202.41	189.57	1.21	4.57	0.02	bdl	0.63	bdl	bdl
WT12WH33-2-5-5	WT12WH33-2-5-5	Granville Harbour	Cavity	127.57	4.88	51.08	14.38	39.44	22.05	28.87	6.05	231.61	193.70	1.17	4.49	bdl	1.23	bdl	bdl	bdl
WT12WH33-2-5-6	WT12WH33-2-5-6	Granville Harbour	Cavity	131.83	7.75	95.39	29.37	26.90	18.44	12.65	3.87	205.91	194.46	1.53	4.94	0.04	1.82	0.66	bdl	bdl
WT12WH35-2-2-2	WT12WH35-2-2-2	Granville Harbour	Orbicule	116.58	22.09	154.54	25.01	18.89	11.14	4.65	2.77	200.10	188.83	2.04	3.50	bdl	bdl	bdl	0.14	0.09
WT12WH35-2-2-3	WT12WH35-2-2-3	Granville Harbour	Orbicule	133.67	10.49	70.97	23.51	17.35	10.84	5.23	2.90	200.36	196.81	1.46	2.59	0.08	bdl	bdl	0.18	bdl
WT12WH35-2-2-4	WT12WH35-2-2-4	Granville Harbour	Orbicule	134.56	9.37	284.74	46.88	21.72	10.11	4.07	2.01	197.34	196.43	1.82	3.18	0.06	bdl	bdl	0.37	bdl
WT12WH35-2-4-1	WT12WH35-2-4-1	Granville Harbour	Orbicule	154.27	3.46	70.10	12.40	2.42	20.36	bdl	2.97	271.77	154.40	2.07	6.03	0.07	9.86	bdl	bdl	bdl
WT12WH35-2-4-2	WT12WH35-2-4-2	Granville Harbour	Orbicule	151.47	15.62	177.41	56.23	16.54	12.91	2.59	bdl	211.04	203.88	1.67	2.70	0.11	4.75	bdl	bdl	bdl
WT12WH35-2-4-3	WT12WH35-2-4-3	Granville Harbour	Orbicule	108.73	7.56	211.36	83.05	18.86	12.52	5.01	2.43	199.31	218.97	2.22	2.18	0.04	bdl	1.22	bdl	bdl
WT12WH35-2-4-4	WT12WH35-2-4-4	Granville Harbour	Orbicule	74.64	54.21	138.07	44.00	13.83	14.36	4.61	3.52	189.50	193.91	0.73	1.47	bdl	bdl	bdl	bdl	bdl

Appendix 5.2 Trace element data of tourmaline from the Heemskirk and Pieman Heads granites analysed by LA-ICP-MS (continued)

Sample No.	^{98}Mo	Ag	Cd	Sb	Cs	Ba	La	Ce	Pr	Nd	Sm	Eu	Gd	Dy	Er	Yb	Σ REE	W	Au	Tl	Bi	Sn	Ta	Nb	Zr	Hf	Th	U
WT12WH04-1-1	0.24	bdl	bdl	bdl	bdl	bdl	0.45	0.83	bdl	bdl	bdl	bdl	bdl	bdl	bdl	bdl	1.28	13.00	bdl	bdl	2.12	6.65	0.54	0.50	0.52	0.21	0.09	0.11
WT12WH04-1-2	0.31	bdl	bdl	bdl	bdl	bdl	3.30	5.65	0.56	0.99	bdl	0.23	bdl	bdl	bdl	bdl	10.74	14.07	bdl	bdl	1.54	10.13	0.60	1.67	bdl	bdl	bdl	0.15
WT12WH04-1-3	bdl	bdl	bdl	bdl	bdl	0.28	2.33	3.86	0.36	1.15	0.19	0.09	0.06	bdl	0.01	bdl	8.07	0.77	bdl	bdl	0.13	7.60	0.63	1.13	0.18	bdl	0.00	0.03
WT12WH04-1-4	bdl	bdl	bdl	bdl	0.09	0.23	2.38	4.16	0.46	1.62	0.21	bdl	bdl	0.02	0.03	bdl	8.88	2.12	bdl	bdl	0.30	6.15	0.46	1.17	0.11	bdl	bdl	0.02
WT12WH04-1-5	bdl	bdl	bdl	bdl	bdl	bdl	2.95	5.37	0.43	1.14	bdl	0.09	0.10	0.09	bdl	bdl	10.16	0.20	bdl	bdl	0.04	8.92	0.76	1.42	0.21	0.06	0.01	0.02
WT12WH04-1-6	bdl	bdl	bdl	bdl	bdl	bdl	0.09	0.19	bdl	bdl	0.10	bdl	0.10	bdl	0.00	0.00	0.49	bdl	bdl	bdl	bdl	6.40	0.49	0.25	0.02	bdl	0.00	bdl
WT12WH04-1-7	0.24	0.06	bdl	0.19	0.31	bdl	1.00	1.22	0.14	0.27	bdl	0.06	bdl	bdl	bdl	0.02	2.71	13.18	bdl	bdl	0.90	17.39	3.12	3.49	0.28	bdl	0.07	0.13
WT12WH04-3-1	bdl	bdl	0.19	bdl	bdl	0.16	1.71	3.80	0.39	1.19	bdl	0.11	0.25	0.05	bdl	0.02	7.53	1.53	bdl	bdl	0.10	3.75	0.86	1.32	0.24	bdl	0.04	0.02
WT12WH04-3-2	bdl	bdl	bdl	bdl	bdl	0.11	2.67	4.76	0.48	1.75	bdl	bdl	bdl	bdl	bdl	bdl	9.66	bdl	10.90	bdl	bdl	5.54	0.73	1.87	0.21	0.00	bdl	bdl
WT12WH04-3-3	bdl	bdl	bdl	bdl	bdl	0.06	2.32	5.04	0.48	1.34	0.10	0.14	0.00	bdl	bdl	0.04	9.47	0.10	bdl	bdl	bdl	6.68	0.45	0.85	0.15	0.01	0.01	bdl
WT12WH07-1-1-1	bdl	bdl	bdl	bdl	bdl	0.22	0.22	0.33	0.03	bdl	bdl	bdl	bdl	0.05	bdl	bdl	0.63	bdl	0.02	bdl	0.03	7.74	0.45	0.20	bdl	0.05	0.01	0.01
WT12WH07-1-1-2	bdl	bdl	bdl	bdl	bdl	bdl	2.10	3.09	0.32	0.76	0.18	0.08	bdl	bdl	bdl	0.02	6.54	bdl	bdl	bdl	bdl	11.52	0.70	1.06	0.14	bdl	bdl	0.00
WT12WH07-1-1-3	bdl	bdl	bdl	bdl	0.01	0.05	2.37	3.86	0.35	0.88	0.06	0.13	bdl	bdl	0.02	bdl	7.67	0.06	bdl	bdl	bdl	12.33	0.70	0.96	bdl	bdl	0.01	0.01
WT12WH07-1-1-4	bdl	bdl	0.13	bdl	bdl	0.17	0.28	0.41	0.04	bdl	0.07	bdl	0.03	bdl	0.08	bdl	0.91	bdl	bdl	bdl	bdl	30.86	2.57	1.26	1.63	0.24	bdl	bdl
WT12WH07-1-1-5	0.09	bdl	bdl	bdl	0.08	0.34	6.48	8.83	0.78	1.79	0.22	0.25	bdl	bdl	bdl	bdl	18.36	1.17	bdl	bdl	14.26	35.05	4.20	5.16	1.23	bdl	1.87	0.09
WT12WH07-2-1	bdl	bdl	0.33	bdl	bdl	0.06	1.34	2.56	0.24	0.34	0.03	0.11	bdl	bdl	bdl	bdl	4.63	bdl	bdl	bdl	bdl	18.43	1.55	1.87	1.16	0.20	0.04	0.01
WT12WH07-2-2	bdl	bdl	bdl	bdl	bdl	bdl	3.85	6.27	0.66	1.55	bdl	0.13	bdl	bdl	bdl	0.00	12.46	0.26	0.07	bdl	0.15	13.68	1.49	3.00	0.66	0.17	0.03	0.03
WT12WH07-2-3	bdl	bdl	bdl	bdl	0.25	bdl	1.84	3.23	0.25	0.80	0.09	bdl	0.03	bdl	bdl	0.02	6.26	bdl	0.07	bdl	0.40	16.04	1.23	1.55	0.58	bdl	0.03	0.02
WT12WH07-2-4	bdl	bdl	bdl	bdl	0.59	0.14	2.94	5.85	0.52	1.32	0.26	bdl	bdl	0.09	0.01	0.00	10.98	0.16	0.04	bdl	0.03	9.95	0.67	1.12	0.21	0.05	bdl	bdl
WT12WH07-3-1	bdl	bdl	bdl	bdl	bdl	bdl	4.13	6.51	0.61	1.54	bdl	bdl	0.12	0.03	bdl	bdl	12.95	bdl	bdl	0.02	bdl	12.83	1.02	2.20	bdl	bdl	bdl	0.01
WT12WH07-3-2	bdl	bdl	bdl	bdl	bdl	0.36	1.31	2.81	0.22	0.81	0.15	bdl	bdl	0.16	0.11	bdl	5.57	0.69	bdl	bdl	4.77	17.50	3.77	2.27	3.46	0.79	2.49	0.14
WT12WH07-3-3	bdl	bdl	bdl	bdl	0.01	0.16	3.22	6.14	0.47	1.97	0.09	0.11	bdl	bdl	0.02	bdl	12.03	bdl	bdl	bdl	0.04	13.63	0.96	1.65	0.31	bdl	bdl	bdl
WT12WH07-3-4	bdl	bdl	bdl	0.07	0.69	0.10	0.93	1.68	0.20	0.49	bdl	bdl	0.14	0.02	0.01	bdl	3.47	bdl	bdl	0.01	0.04	18.19	3.37	2.36	1.95	0.50	0.03	0.01
WT12WH13-1-2-1-1	bdl	bdl	bdl	bdl	bdl	bdl	1.56	2.36	0.12	0.54	bdl	0.12	0.18	0.00	bdl	bdl	4.89	bdl	bdl	bdl	bdl	5.69	4.16	2.46	0.17	0.03	bdl	0.00
WT12WH13-1-2-1-2	bdl	bdl	0.23	bdl	0.18	0.10	1.09	1.77	0.12	0.33	bdl	0.08	0.03	bdl	bdl	bdl	3.43	bdl	bdl	bdl	0.04	4.80	3.46	1.63	0.16	bdl	0.01	bdl
WT12WH13-1-2-1-3	bdl	bdl	bdl	bdl	bdl	bdl	0.65	1.18	0.08	0.13	bdl	bdl	bdl	bdl	0.01	bdl	2.05	bdl	bdl	bdl	0.09	3.50	1.64	1.31	bdl	bdl	bdl	bdl
WT12WH13-1-2-1-4	bdl	bdl	bdl	bdl	bdl	bdl	0.75	1.20	0.16	0.51	0.13	bdl	bdl	bdl	bdl	bdl	2.75	0.10	bdl	bdl	bdl	6.78	3.47	2.05	0.13	0.09	0.01	bdl
WT12WH13-1-2-1-5	bdl	bdl	bdl	bdl	bdl	bdl	bdl	0.11	bdl	0.03	0.06	0.01	bdl	0.00	bdl	0.04	0.25	bdl	bdl	bdl	bdl	15.43	7.01	3.57	0.13	0.15	0.12	bdl
WT12WH13-1-2-1-6	bdl	bdl	bdl	bdl	0.35	0.17	0.12	0.07	bdl	0.03	0.00	0.01	bdl	bdl	0.01	bdl	0.24	0.04	bdl	bdl	0.63	94.77	0.91	0.76	0.98	0.06	0.14	0.15
WT12WH13-1-2-1-7	bdl	bdl	0.45	bdl	bdl	bdl	bdl	bdl	0.04	bdl	0.10	0.00	0.06	bdl	bdl	bdl	0.20	bdl	bdl	0.02	bdl	78.51	0.51	0.87	0.28	bdl	0.02	bdl
WT12WH13-1-2-1-8	bdl	bdl	bdl	bdl	0.20	bdl	bdl	bdl	0.01	bdl	0.03	bdl	0.06	bdl	bdl	bdl	0.11	bdl	bdl	bdl	bdl	79.81	1.01	0.93	bdl	0.14	0.04	bdl
WT12WH13-1-2-1-9	bdl	bdl	bdl	bdl	bdl	bdl	0.04	bdl	bdl	bdl	bdl	bdl	bdl	0.04	0.04	bdl	0.11	bdl	bdl	bdl	bdl	98.18	0.80	0.48	bdl	bdl	0.02	0.00
WT12WH13-1-2-2-1	bdl	bdl	bdl	bdl	bdl	0.16	1.24	1.86	0.16	0.46	bdl	0.05	0.09	0.05	bdl	0.05	3.95	bdl	bdl	bdl	0.07	6.30	4.74	2.05	0.06	0.02	0.02	0.00
WT12WH13-1-2-2-2	bdl	bdl	bdl	bdl	0.01	bdl	0.78	1.67	0.17	0.41	bdl	0.05	0.03	bdl	bdl	bdl	3.09	bdl	bdl	0.05	bdl	5.38	3.05	1.52	bdl	bdl	0.00	bdl
WT12WH13-1-2-2-3	bdl	bdl	bdl	bdl	bdl	bdl	1.08	2.05	0.20	0.41	bdl	bdl	bdl	bdl	0.00	0.00	3.75	bdl	bdl	bdl	0.31	6.26	2.63	1.86	bdl	0.06	bdl	bdl
WT12WH13-1-2-2-4	bdl	bdl	bdl	bdl	bdl	0.14	0.93	1.69	0.18	bdl	0.28	bdl	bdl	0.01	bdl	bdl	3.10	bdl	0.07	bdl	bdl	5.96	1.78	1.53	0.04	0.06	bdl	bdl
WT12WH13-1-2-2-5	bdl	0.03	bdl	0.13	0.03	0.05	0.78	1.36	0.08	0.21	bdl	bdl	0.05	0.03	bdl	0.03	2.53	bdl	bdl	0.02	0.50	4.99	1.79	1.41	0.28	0.08	0.04	0.02
WT12WH13-1-2-2-6	bdl	bdl	bdl	bdl	bdl	0.16	0.24	0.47	0.04	0.06	bdl	bdl	bdl	0.00	bdl	0.05	0.87	bdl	bdl	0.01	0.29	5.36	4.11	1.02	bdl	0.21	0.02	bdl

WT12WH13-2-2-1	bdl	bdl	bdl	bdl	0.08	bdl	0.67	2.49	0.32	0.63	bdl	0.02	bdl	bdl	0.00	bdl	4.12	0.08	bdl	bdl	bdl	28.58	0.69	2.71	0.36	bdl	bdl	bdl
WT12WH13-2-2-2	bdl	bdl	0.17	bdl	bdl	bdl	0.06	0.21	0.04	0.15	bdl	bdl	0.03	0.03	bdl	bdl	0.51	bdl	bdl	bdl	bdl	29.93	2.18	2.02	0.82	0.43	0.01	0.00
WT12WH13-2-2-3	bdl	bdl	bdl	bdl	bdl	bdl	0.22	1.10	0.11	0.39	0.14	0.01	bdl	bdl	0.01	bdl	1.98	0.05	bdl	bdl	bdl	29.41	1.23	2.56	0.25	0.19	0.02	bdl
WT12WH13-2-2-4	bdl	bdl	bdl	bdl	bdl	bdl	0.14	0.43	0.06	bdl	0.03	bdl	0.11	bdl	bdl	bdl	0.77	bdl	bdl	bdl	0.06	29.36	0.83	1.31	bdl	bdl	bdl	0.00
WT12WH13-2-3-1	bdl	bdl	bdl	bdl	bdl	bdl	0.29	0.38	0.03	bdl	bdl	0.07	bdl	0.00	bdl	0.03	0.80	bdl	bdl	bdl	0.82	19.53	1.30	0.90	0.67	0.06	0.13	0.04
WT12WH13-2-3-2	bdl	bdl	bdl	bdl	0.15	0.75	0.30	0.48	bdl	bdl	bdl	0.15	0.05	0.06	bdl	0.08	1.12	0.07	18.70	bdl	2.99	17.72	2.42	1.80	1.15	bdl	0.16	0.14
WT12WH13-2-3-3	bdl	bdl	bdl	bdl	bdl	bdl	0.22	0.24	0.03	0.07	bdl	0.12	bdl	bdl	0.03	0.03	0.74	0.06	0.66	bdl	0.18	15.26	1.67	1.57	0.07	0.01	0.01	bdl
WT12WH13-2-3-4	bdl	bdl	bdl	bdl	0.07	bdl	0.06	0.07	0.01	bdl	bdl	bdl	0.02	bdl	bdl	0.03	0.20	0.05	0.22	bdl	0.41	38.52	1.95	4.42	2.38	0.41	bdl	0.01
WT12WH13-2-3-5	bdl	bdl	bdl	bdl	0.13	bdl	0.11	0.14	bdl	bdl	bdl	bdl	0.00	0.03	0.04	bdl	0.33	0.09	0.62	bdl	0.20	21.49	1.57	2.73	bdl	0.07	bdl	0.02
WT12WH13-2-3-6	bdl	bdl	bdl	0.19	0.04	0.47	0.15	0.24	bdl	bdl	bdl	0.02	bdl	0.05	0.05	bdl	0.51	0.18	0.16	bdl	1.74	23.32	1.62	2.95	0.87	0.09	0.17	0.08
WT12WH13-2-3-7	bdl	bdl	0.15	bdl	bdl	0.08	0.21	0.40	0.04	0.14	0.05	0.09	0.02	0.06	0.03	bdl	1.04	bdl	0.11	bdl	0.91	22.27	5.18	2.14	0.71	0.09	0.06	0.07
WT12WH13-2-3-8	bdl	bdl	bdl	bdl	bdl	0.23	0.40	0.48	0.09	0.24	0.05	0.12	0.10	0.04	bdl	0.03	1.55	bdl	bdl	0.02	0.85	35.57	3.67	1.97	1.19	0.13	0.12	0.16
WT12WH20-3-1	bdl	bdl	bdl	bdl	bdl	bdl	0.97	1.48	0.18	0.35	bdl	0.02	0.08	bdl	0.02	bdl	3.10	0.03	bdl	bdl	bdl	58.34	2.76	4.23	0.43	0.19	bdl	bdl
WT12WH20-3-2	bdl	bdl	bdl	0.12	0.46	0.05	1.83	3.69	0.39	0.96	bdl	bdl	0.13	0.09	0.05	0.07	7.21	0.08	bdl	bdl	0.04	37.57	1.32	3.27	0.24	bdl	0.06	bdl
WT12WH20-3-3	bdl	bdl	bdl	bdl	0.16	0.13	1.63	3.46	0.30	0.77	0.15	0.03	bdl	0.09	bdl	bdl	6.44	bdl	0.03	bdl	bdl	37.46	1.53	2.84	0.15	0.06	0.05	0.02
WT12WH20-3-4	bdl	bdl	bdl	bdl	0.03	bdl	0.35	0.73	bdl	0.17	0.05	bdl	0.00	0.01	0.00	0.03	1.35	bdl	bdl	bdl	bdl	48.47	1.74	2.17	bdl	0.14	bdl	bdl
WT12WH20-3-5	0.08	0.07	bdl	0.10	bdl	0.13	0.24	0.55	0.03	0.20	0.07	bdl	bdl	0.01	bdl	bdl	1.12	bdl	0.09	bdl	0.09	41.87	1.67	1.91	0.23	0.08	0.38	0.04
WT12WH20-3-6	bdl	bdl	bdl	bdl	0.12	0.17	0.13	0.29	bdl	bdl	0.05	bdl	bdl	bdl	0.03	bdl	0.50	bdl	0.04	bdl	bdl	40.84	1.47	1.51	0.25	bdl	0.02	0.01
WT12WH20-3-7	bdl	bdl	bdl	bdl	0.12	bdl	1.79	3.54	0.28	0.81	bdl	bdl	0.21	bdl	0.02	0.04	6.68	0.14	2.30	bdl	0.05	34.67	1.21	2.58	0.15	bdl	0.06	bdl
WT12WH20-4-1	bdl	bdl	bdl	bdl	0.12	0.05	0.30	0.51	0.03	bdl	bdl	bdl	bdl	0.02	bdl	bdl	0.85	bdl	bdl	bdl	bdl	61.73	2.70	3.35	0.68	0.21	bdl	0.01
WT12WH20-4-2	0.34	bdl	bdl	bdl	6.42	bdl	1.85	3.10	0.34	0.84	0.16	bdl	0.08	0.04	bdl	bdl	6.41	0.87	bdl	bdl	0.07	43.09	1.26	4.07	0.29	bdl	0.07	bdl
WT12WH20-4-3	0.36	bdl	bdl	bdl	0.14	bdl	2.04	3.64	0.27	1.03	bdl	0.04	0.10	bdl	0.01	0.04	7.18	0.13	0.04	0.03	0.04	49.16	1.80	5.47	0.40	0.06	0.06	bdl
WT12WH20-4-4	0.30	bdl	bdl	bdl	bdl	0.00	2.04	4.13	0.34	0.96	0.23	0.04	bdl	0.09	bdl	0.00	7.83	bdl	bdl	bdl	0.04	60.58	4.60	7.36	0.28	bdl	0.07	0.02
WT12WH23-1-1	0.26	bdl	bdl	bdl	3.47	bdl	1.81	3.42	0.25	0.68	0.15	0.00	0.11	bdl	bdl	0.03	6.45	0.23	bdl	0.06	0.18	42.80	1.27	3.59	0.39	0.07	0.13	0.65
WT12WH23-1-2	bdl	bdl	bdl	bdl	0.06	0.00	1.97	3.14	0.28	0.83	bdl	bdl	0.14	bdl	bdl	bdl	6.35	bdl	0.06	0.02	0.24	43.77	1.16	3.65	0.31	0.07	0.13	1.63
WT12WH23-1-3	bdl	bdl	bdl	bdl	0.02	bdl	1.95	3.09	0.30	0.89	bdl	bdl	0.20	bdl	0.00	bdl	6.44	bdl	0.03	bdl	0.03	42.86	1.46	4.03	0.17	0.14	0.05	bdl
WT12WH23-1-4	0.42	bdl	bdl	0.24	19.38	0.05	1.81	3.26	0.30	0.84	bdl	bdl	0.12	0.02	bdl	bdl	6.34	0.47	bdl	0.15	0.34	51.11	1.35	4.20	0.34	bdl	0.11	0.05
WT12WH23-1-5	0.27	bdl	bdl	bdl	0.11	bdl	2.01	3.57	0.30	0.91	bdl	0.02	0.19	bdl	bdl	0.02	7.02	0.06	bdl	bdl	0.04	48.21	1.35	4.58	0.26	bdl	0.10	0.01
WT12WH23-2-3-1	0.21	bdl	bdl	0.21	bdl	0.05	1.17	1.52	0.08	0.19	bdl	bdl	bdl	bdl	0.37	2.13	5.47	0.44	0.14	bdl	0.51	63.40	5.41	5.62	1.11	0.40	0.37	1.06
WT12WH23-2-3-2	0.10	bdl	bdl	bdl	bdl	bdl	0.75	0.87	0.06	bdl	0.04	0.01	0.00	0.64	2.14	9.49	14.00	1.41	0.08	bdl	0.09	151.88	17.36	14.29	4.64	0.77	0.05	0.22
WT12WH23-2-3-3	0.24	bdl	bdl	bdl	bdl	0.18	0.75	1.34	0.13	0.23	bdl	bdl	bdl	bdl	bdl	0.16	2.61	0.10	0.07	bdl	0.20	50.76	3.03	4.48	0.55	bdl	0.15	0.60
WT12WH23-2-5-1	bdl	bdl	bdl	bdl	0.41	bdl	2.36	3.11	0.24	0.42	bdl	bdl	0.15	0.51	1.21	4.18	12.18	0.59	bdl	0.01	bdl	121.75	17.72	11.91	3.23	0.59	0.11	0.13
WT12WH23-2-5-2	bdl	bdl	bdl	bdl	bdl	bdl	1.13	1.46	0.10	bdl	0.03	0.05	0.11	0.49	1.59	5.75	10.71	0.79	0.09	0.03	0.27	164.00	19.82	18.32	6.64	1.05	0.18	0.34
WT12WH23-2-5-3	bdl	bdl	bdl	bdl	0.18	0.05	0.23	0.32	0.03	bdl	bdl	bdl	bdl	bdl	0.02	0.05	0.65	bdl	bdl	bdl	bdl	21.18	1.72	1.43	0.12	0.04	0.03	bdl
WT12WH23-2-5-4	bdl	bdl	bdl	bdl	bdl	bdl	0.59	0.86	0.11	0.17	bdl	0.07	bdl	0.02	0.03	0.05	1.90	bdl	bdl	bdl	bdl	71.18	4.59	7.59	0.17	bdl	bdl	0.03
WT12WH23-2-5-5	bdl	bdl	bdl	bdl	0.04	0.15	0.96	1.42	0.10	0.13	0.09	bdl	0.03	0.48	1.26	4.90	9.35	0.74	bdl	bdl	bdl	117.00	10.90	17.13	3.19	0.47	0.21	0.15
WT12WH23-2-5-6	bdl	bdl	bdl	bdl	0.07	bdl	0.74	1.22	0.05	0.29	bdl	0.08	0.03	0.02	bdl	bdl	2.42	0.21	bdl	bdl	0.49	56.01	4.32	5.85	0.37	0.07	0.33	0.63
WT12WH24-1-1	bdl	bdl	bdl	1.09	bdl	0.12	1.10	1.67	0.10	bdl	0.26	0.04	bdl	bdl	bdl	0.04	3.21	bdl	0.06	bdl	0.08	42.19	0.51	0.86	bdl	bdl	0.22	bdl
WT12WH24-1-2	bdl	bdl	bdl	0.14	bdl	bdl	1.67	1.72	0.09	0.16	0.18	0.03	bdl	bdl	bdl	0.07	3.92	0.38	bdl	bdl	0.08	86.58	4.71	6.12	0.35	bdl	0.08	bdl
WT12WH24-1-3	bdl	bdl	bdl	bdl	bdl	0.05	2.46	4.20	0.31	0.90	bdl	0.10	bdl	bdl	bdl	bdl	7.96	0.49	bdl	0.02	bdl	150.57	6.20	3.66	0.34	0.08	0.05	0.00
WT12WH24-1-4	bdl	0.09	0.51	bdl	0.16	bdl	0.92	1.80	0.11	0.44	0.03	0.01	0.29	0.75	2.06	6.68	13.11	2.06	bdl	0.02	0.39	289.16	9.00	7.98	4.26	0.47	0.33	0.07

WT12WH24-2-3-1	0.15	bdl	bdl	bdl	0.01	0.00	4.45	9.20	0.84	2.30	0.37	bdl	0.24	bdl	0.01	bdl	17.39	0.07	bdl	bdl	bdl	28.85	2.17	4.51	0.35	0.10	0.15	bdl
WT12WH24-2-3-2	bdl	bdl	bdl	bdl	0.17	0.10	2.63	6.06	0.55	1.49	0.30	bdl	0.13	bdl	bdl	0.05	11.21	bdl	bdl	bdl	bdl	44.80	7.81	6.17	0.82	0.21	0.05	0.01
WT12WH24-2-3-3	bdl	bdl	bdl	bdl	bdl	0.14	3.15	7.40	0.71	1.79	0.26	0.02	bdl	0.04	0.01	0.06	13.45	bdl	bdl	bdl	bdl	42.52	6.76	6.05	0.78	0.20	0.11	bdl
WT12WH24-2-3-4	bdl	bdl	0.38	bdl	bdl	bdl	0.61	1.45	0.12	0.45	bdl	bdl	bdl	0.00	0.02	bdl	2.65	bdl	bdl	bdl	bdl	38.61	3.05	2.73	0.53	0.30	0.01	bdl
WT12WH24-2-3-5	0.14	bdl	bdl	bdl	bdl	bdl	7.80	17.96	1.63	4.27	0.80	0.01	0.33	bdl	0.06	0.02	32.89	bdl	bdl	bdl	bdl	43.37	5.30	7.17	0.23	0.07	0.25	0.01
WT12WH24-2-3-6	0.15	bdl	bdl	bdl	bdl	0.19	11.39	25.04	2.42	7.94	1.48	0.02	0.35	0.06	0.01	bdl	48.71	bdl	bdl	bdl	bdl	39.18	6.00	5.33	0.44	0.08	0.07	bdl
WT12WH24-2-3-7	bdl	bdl	0.21	0.10	0.14	0.09	5.63	13.48	1.17	3.42	0.80	0.02	bdl	bdl	0.01	bdl	24.53	0.11	0.87	bdl	bdl	39.35	2.64	4.80	0.25	bdl	0.05	bdl
WT12WH24-2-3-8	bdl	bdl	bdl	bdl	0.61	bdl	6.18	12.98	1.28	3.68	0.84	bdl	0.29	bdl	bdl	bdl	25.25	0.12	0.22	0.04	0.05	40.77	4.55	5.67	0.34	0.11	0.07	0.01
WT12WH24-2-4-1	bdl	bdl	bdl	bdl	0.01	0.10	6.25	13.41	1.31	3.34	0.71	bdl	bdl	0.05	bdl	bdl	25.07	bdl	bdl	bdl	0.02	29.29	2.30	2.90	0.22	bdl	0.04	bdl
WT12WH24-2-4-2	0.50	bdl	0.44	bdl	bdl	0.00	2.23	4.30	0.33	1.17	0.21	bdl	bdl	bdl	0.00	bdl	8.23	0.12	bdl	0.03	0.03	71.95	11.51	11.12	2.42	0.44	0.29	bdl
WT12WH24-2-4-3	bdl	bdl	0.67	bdl	bdl	bdl	0.63	1.56	0.18	0.44	bdl	0.00	0.03	bdl	0.02	0.05	2.92	bdl	bdl	bdl	bdl	57.53	7.13	3.07	1.11	0.32	0.01	bdl
WT12WH24-2-4-4	bdl	0.07	bdl	bdl	bdl	0.20	11.60	25.35	2.43	7.29	0.97	bdl	0.34	0.08	bdl	bdl	48.05	0.01	bdl	bdl	0.03	55.01	13.97	11.53	0.58	bdl	0.06	bdl
WT12WH28-1-3-1	bdl	bdl	bdl	bdl	bdl	0.11	3.68	11.43	1.25	3.66	0.83	0.02	0.27	0.15	bdl	bdl	21.29	0.00	bdl	bdl	0.02	31.86	5.43	8.18	0.41	bdl	0.32	bdl
WT12WH28-1-3-2	bdl	bdl	bdl	bdl	0.08	0.11	3.88	9.46	0.97	2.55	0.62	0.03	0.29	bdl	bdl	bdl	17.80	bdl	bdl	bdl	0.03	20.23	2.61	4.64	0.19	bdl	0.14	0.00
WT12WH28-1-4-1	0.47	bdl	bdl	bdl	bdl	bdl	3.12	6.34	0.47	1.86	0.37	bdl	0.22	0.11	bdl	bdl	12.49	0.09	bdl	bdl	bdl	54.15	10.12	20.05	1.12	0.56	0.87	0.10
WT12WH28-1-4-2	1.21	bdl	4.60	bdl	0.04	0.04	3.15	6.52	0.64	1.88	0.26	0.03	0.15	bdl	0.07	bdl	12.68	0.32	0.11	bdl	0.08	89.95	31.60	57.60	2.99	1.60	0.97	0.13
WT12WH28-2-3-1	0.55	bdl	bdl	bdl	bdl	bdl	2.34	6.03	0.50	1.46	0.64	0.01	0.32	0.07	bdl	0.04	11.41	0.80	29.48	bdl	0.09	83.36	24.92	44.20	1.68	0.89	0.93	0.08
WT12WH28-2-3-2	1.34	bdl	bdl	bdl	3.63	bdl	3.87	9.69	1.10	2.75	1.06	bdl	0.43	0.14	bdl	bdl	19.04	6.77	bdl	bdl	0.31	104.76	34.14	59.41	2.73	1.34	3.00	0.47
WT12WH28-2-3-3	0.72	bdl	bdl	0.26	1.52	0.22	2.72	6.00	0.60	1.31	0.36	bdl	0.24	bdl	0.01	bdl	11.24	1.60	bdl	bdl	0.20	54.64	6.77	16.58	0.98	0.37	1.14	0.08
WT12WH28-2-3-4	0.66	bdl	bdl	bdl	1.22	0.05	2.96	6.52	0.67	1.88	0.70	bdl	0.35	bdl	0.04	0.10	13.23	1.45	bdl	bdl	0.16	65.46	10.10	22.49	1.68	0.90	1.65	0.21
WT12WH28-3-1-1	bdl	0.06	bdl	bdl	0.15	bdl	3.02	6.60	0.70	1.93	0.30	bdl	bdl	bdl	0.01	bdl	12.57	bdl	bdl	bdl	bdl	19.33	1.08	2.66	0.19	bdl	0.06	0.01
WT12WH28-3-1-2	0.13	bdl	bdl	bdl	0.09	0.09	3.00	7.06	0.71	2.04	0.33	0.01	bdl	bdl	bdl	bdl	13.15	0.07	bdl	bdl	bdl	20.43	1.53	2.86	0.19	bdl	0.14	bdl
WT12WH28-3-1-3	0.11	0.06	bdl	bdl	0.21	bdl	3.06	6.88	0.64	2.21	0.48	bdl	0.13	bdl	bdl	bdl	13.39	bdl	bdl	bdl	0.01	26.60	2.15	4.08	0.30	bdl	0.13	0.01
WT12WH28-3-1-4	bdl	bdl	bdl	bdl	0.18	bdl	0.69	1.41	0.23	0.44	bdl	bdl	0.13	0.01	bdl	0.03	2.95	bdl	4.32	bdl	bdl	24.99	1.30	2.50	0.24	0.09	0.03	0.01
WT12WH28-3-6-1	1.19	0.09	bdl	0.29	2.78	bdl	6.53	25.32	3.36	9.78	4.52	bdl	1.79	0.47	0.07	bdl	51.84	2.89	0.47	bdl	0.66	114.81	40.21	70.38	5.22	1.78	22.43	4.22
WT12WH28-3-6-2	0.72	bdl	0.23	bdl	4.59	0.80	3.84	15.13	1.47	5.12	2.06	bdl	0.74	0.31	bdl	bdl	28.67	1.48	0.49	0.11	0.29	89.58	27.79	50.99	2.47	1.34	6.98	1.04
WT12WH28-3-6-3	0.71	bdl	bdl	bdl	2.94	bdl	4.36	16.94	1.94	6.15	2.49	0.00	0.99	0.25	bdl	bdl	33.13	1.05	0.35	0.08	0.29	87.10	22.17	44.61	1.87	0.80	6.83	0.97
WT12WH28-3-6-4	0.61	bdl	bdl	0.17	3.89	bdl	4.07	15.49	1.81	5.28	2.02	bdl	0.80	0.24	0.03	bdl	29.75	0.91	0.45	0.03	0.23	89.95	23.79	46.78	1.68	0.76	6.34	0.88
WT12WH28-4-1-1	0.06	bdl	bdl	bdl	0.01	0.00	4.89	9.06	0.74	2.44	0.72	0.02	0.28	bdl	bdl	0.02	18.18	0.10	bdl	bdl	bdl	30.39	4.10	9.67	0.17	bdl	0.14	0.00
WT12WH28-4-1-3	bdl	bdl	bdl	bdl	0.23	bdl	4.37	9.29	0.94	3.03	0.72	bdl	bdl	bdl	bdl	bdl	18.36	0.12	bdl	0.03	0.06	34.96	5.22	8.92	0.29	bdl	0.17	0.01
WT12WH28-4-4-1	bdl	bdl	bdl	bdl	0.32	0.05	5.33	7.92	0.61	1.98	0.30	bdl	0.06	bdl	0.01	bdl	16.21	0.32	bdl	bdl	0.05	42.86	8.25	17.36	0.52	0.10	0.31	0.07
WT12WH28-4-4-2	0.16	bdl	bdl	bdl	bdl	bdl	3.65	6.61	0.56	1.23	0.27	0.04	bdl	0.03	bdl	0.02	12.42	0.08	bdl	bdl	bdl	26.12	1.84	5.87	bdl	0.04	0.23	bdl
WT12WH28-4-4-3	bdl	bdl	bdl	bdl	bdl	0.05	4.20	7.03	0.53	1.16	0.26	0.04	0.26	bdl	bdl	0.06	13.56	0.15	0.09	bdl	0.03	32.96	5.13	12.63	0.47	0.13	0.10	bdl
WT12WH28-4-4-4	bdl	0.08	bdl	0.15	bdl	bdl	4.27	6.79	0.45	1.28	bdl	0.04	bdl	bdl	bdl	0.03	12.86	0.14	bdl	0.01	0.02	30.91	2.77	8.28	0.27	bdl	0.14	bdl
WT12WH33-2-1-1	bdl	bdl	bdl	bdl	0.06	bdl	2.35	3.67	0.34	1.02	0.24	bdl	bdl	bdl	0.02	0.07	7.71	bdl	bdl	0.02	2.25	5.71	0.85	2.24	0.38	bdl	0.86	0.03
WT12WH33-2-1-2	bdl	bdl	bdl	bdl	0.04	bdl	0.93	1.77	0.14	0.39	0.06	0.09	bdl	bdl	bdl	0.05	3.44	bdl	bdl	bdl	bdl	3.42	0.78	1.61	bdl	bdl	bdl	bdl
WT12WH33-2-1-3	bdl	bdl	bdl	bdl	bdl	bdl	1.07	1.63	0.14	0.43	bdl	0.10	0.03	0.10	bdl	bdl	3.48	0.06	bdl	0.01	0.08	3.59	0.65	1.39	0.24	bdl	bdl	0.00
WT12WH33-2-1-4	bdl	bdl	bdl	bdl	bdl	bdl	1.26	2.09	0.19	0.35	0.11	0.09	0.05	0.00	bdl	0.00	4.14	bdl	bdl	bdl	0.63	4.97	1.22	1.62	0.13	bdl	0.21	0.02
WT12WH33-2-1-5	bdl	bdl	bdl	bdl	bdl	0.12	1.21	2.07	0.14	0.57	0.22	0.05	bdl	bdl	bdl	0.10	4.36	bdl	bdl	bdl	bdl	4.37	1.24	2.03	0.16	0.03	0.01	bdl
WT12WH33-2-1-6	bdl	bdl	bdl	bdl	bdl	0.00	1.36	2.49	0.25	0.64	0.05	0.06	bdl	0.09	0.01	0.02	4.98	bdl	bdl	bdl	0.12	3.87	0.78	1.17	0.09	0.01	0.01	0.01
WT12WH33-2-5-1	bdl	bdl	bdl	bdl	bdl	0.14	1.96	3.90	0.34	0.79	bdl	0.04	bdl	bdl	bdl	0.02	7.05	0.06	bdl	bdl	0.35	6.17	0.73	1.77	0.21	bdl	0.09	bdl

WT12WH33-2-5-2	0.04	bdl	0.19	bdl	0.02	bdl	2.02	4.01	0.35	0.87	0.16	0.10	bdl	0.01	bdl	bdl	7.53	bdl	bdl	bdl	0.01	4.76	0.68	1.82	bdl	bdl	bdl	0.01
WT12WH33-2-5-3	bdl	bdl	bdl	bdl	bdl	bdl	2.12	4.30	0.37	0.97	0.05	0.07	bdl	0.03	bdl	bdl	7.90	bdl	bdl	bdl	bdl	4.81	0.63	1.51	0.03	0.02	bdl	bdl
WT12WH33-2-5-4	bdl	bdl	0.30	bdl	0.04	bdl	2.24	3.98	0.31	0.77	0.19	0.14	0.20	0.02	bdl	0.02	7.87	bdl	bdl	bdl	0.02	4.64	0.74	1.31	bdl	bdl	0.02	bdl
WT12WH33-2-5-5	bdl	0.08	bdl	bdl	bdl	0.18	2.29	4.40	0.31	0.88	0.16	bdl	bdl	0.03	bdl	0.04	8.11	bdl	bdl	bdl	0.09	4.80	0.64	1.68	bdl	0.00	bdl	bdl
WT12WH33-2-5-6	bdl	bdl	bdl	bdl	bdl	0.09	2.65	4.50	0.32	0.61	0.10	0.09	bdl	0.05	0.04	bdl	8.36	0.07	bdl	0.01	0.48	8.06	2.32	3.22	0.25	bdl	0.18	0.01
WT12WH35-2-2-2	bdl	bdl	bdl	bdl	0.10	bdl	2.83	4.85	0.41	1.40	0.28	0.03	0.06	bdl	0.01	bdl	9.88	0.38	0.35	bdl	bdl	22.23	5.31	14.04	0.69	0.13	0.09	bdl
WT12WH35-2-2-3	bdl	bdl	bdl	bdl	bdl	0.11	2.66	5.18	0.50	0.96	0.13	bdl	bdl	bdl	bdl	bdl	9.43	bdl	bdl	bdl	bdl	23.06	2.44	7.37	0.33	0.07	0.15	bdl
WT12WH35-2-2-4	bdl	bdl	bdl	bdl	0.20	bdl	3.28	6.23	0.44	1.23	bdl	bdl	0.11	bdl	bdl	bdl	11.30	0.32	bdl	bdl	0.03	35.29	13.15	27.52	0.79	0.34	0.19	0.02
WT12WH35-2-4-1	bdl	bdl	bdl	bdl	0.02	0.24	1.08	1.58	0.17	0.30	bdl	bdl	0.10	bdl	bdl	bdl	3.23	0.16	1.11	bdl	1.20	3.51	0.70	1.25	0.53	bdl	2.85	3.44
WT12WH35-2-4-2	bdl	bdl	bdl	0.19	0.26	bdl	2.75	5.02	0.48	1.08	bdl	0.07	0.11	0.02	0.02	0.05	9.60	0.29	0.10	bdl	0.23	20.12	18.03	16.51	1.51	0.59	0.94	1.49
WT12WH35-2-4-3	0.12	bdl	bdl	bdl	bdl	0.00	3.39	6.23	0.59	1.52	0.39	bdl	0.18	bdl	bdl	bdl	12.29	0.14	0.10	0.03	bdl	23.55	30.83	27.15	0.94	0.39	0.09	0.02
WT12WH35-2-4-4	bdl	bdl	bdl	bdl	bdl	bdl	0.48	0.87	0.08	0.19	0.06	0.02	0.09	bdl	0.02	bdl	1.81	bdl	bdl	bdl	0.01	13.26	10.22	7.98	1.16	0.45	0.04	bdl

Appendix 6 Trace element data of quartz from the Heemskirk and Pieman Heads granite analysed by LA-ICP-MS

Abbreviation: UST = unidirectional solidification texture, bdl = below detection limit

Sample Name	Granite	Type	ppm	Na	Mg	Al	Li	Ti	K	Ca	V	Cr	Mn	Fe	Cu
WT12WH03-1-1	Pieman Head	patch		93.22	0.14	257.72	33.29	48.37	16.23	104.04	bdl	bdl	0.44	3.98	0.07
WT12WH03-1-2	Pieman Head	patch		32.91	0.44	222.38	34.32	46.96	2.15	66.69	bdl	0.10	0.21	2.76	0.07
WT12WH03-1-3	Pieman Head	patch		44.49	1.13	180.18	31.65	76.51	6.94	56.12	bdl	0.11	0.32	2.76	bdl
WT12WH03-1-4	Pieman Head	patch		5.53	1.00	187.97	35.46	78.42	1.58	bdl	bdl	bdl	0.25	6.63	bdl
WT12WH03-1-5	Pieman Head	patch		1.53	2.49	167.57	30.43	58.36	4.36	13.55	bdl	0.29	0.46	14.87	0.08
WT12WH03-1-6	Pieman Head	patch		8.40	1.29	176.08	34.39	63.54	1.33	13.74	bdl	bdl	0.27	7.04	bdl
WT12WH03-1-7	Pieman Head	patch		14.21	0.64	160.73	30.66	53.78	1.03	16.15	bdl	bdl	0.17	3.02	bdl
WT12WH03-1-8	Pieman Head	patch		8.09	0.70	181.28	35.82	47.65	0.82	bdl	bdl	bdl	0.23	4.37	bdl
WT12WH03-2-1	Pieman Head	patch		51.71	0.11	182.17	25.58	29.76	7.15	25.70	bdl	bdl	0.53	2.52	0.18
WT12WH03-2-2	Pieman Head	patch		42.61	0.37	269.46	39.15	41.29	8.48	108.66	bdl	bdl	0.58	8.79	0.06
WT12WH03-2-3	Pieman Head	patch		62.66	2.48	258.98	36.02	32.35	24.69	112.61	bdl	bdl	0.60	13.04	0.54
WT12WH03-2-4	Pieman Head	patch		4.99	0.14	207.16	36.08	19.26	1.63	14.81	bdl	bdl	0.27	2.44	bdl
WT12WH03-2-5	Pieman Head	patch		1.53	0.14	185.37	33.62	48.45	0.59	11.68	bdl	bdl	0.23	2.14	bdl
WT12WH03-2-6	Pieman Head	patch		7.36	0.27	187.81	34.20	49.78	0.87	16.87	bdl	0.16	0.21	2.65	bdl
WT12WH03-2-7	Pieman Head	patch		18.37	0.18	162.00	28.75	41.37	1.07	bdl	bdl	bdl	0.34	1.86	bdl
WT12WH03-2-8	Pieman Head	patch		9.82	0.21	234.75	36.28	42.66	1.15	38.87	bdl	bdl	0.22	3.01	bdl
WT12WH04-1-1	Pieman Head	patch		bdl	0.07	239.08	37.19	14.27	bdl	bdl	bdl	bdl	bdl	2.77	0.16
WT12WH04-1-2	Pieman Head	patch		8.25	0.20	257.72	41.48	42.83	1.13	147.56	bdl	bdl	0.33	2.54	bdl
WT12WH04-1-3	Pieman Head	patch		148.87	15.92	336.24	28.80	22.50	21.31	184.98	bdl	bdl	1.21	10.15	bdl
WT12WH04-1-4	Pieman Head	patch		15.11	0.26	345.85	49.20	28.88	2.91	bdl	0.02	0.32	0.82	4.52	bdl
WT12WH07-1-1	Pieman Head	orbicule		3.07	0.24	166.94	27.79	16.45	1.17	15.01	bdl	bdl	0.15	1.84	bdl
WT12WH07-1-2	Pieman Head	orbicule		1.50	0.06	113.39	21.94	12.41	bdl	10.21	bdl	bdl	bdl	bdl	0.06
WT12WH07-1-3	Pieman Head	orbicule		3.91	0.13	230.07	38.74	42.62	1.73	bdl	bdl	bdl	0.44	3.10	bdl
WT12WH07-1-4	Pieman Head	orbicule		1.15	0.47	231.55	41.57	51.88	0.59	bdl	bdl	bdl	0.26	4.04	0.05
WT12WH07-1-5	Pieman Head	orbicule		0.72	0.41	242.62	44.56	47.21	bdl	13.69	bdl	bdl	0.30	4.30	0.04
WT12WH07-1-6	Pieman Head	orbicule		3.91	0.51	242.05	44.81	50.37	1.55	10.06	bdl	bdl	0.36	4.05	0.04
WT12WH07-1-7	Pieman Head	orbicule		20.07	1.10	209.82	36.21	54.76	4.52	bdl	bdl	bdl	0.41	9.24	bdl
WT12WH07-1-8	Pieman Head	orbicule		2.11	2.36	227.78	40.73	54.54	2.73	bdl	bdl	bdl	0.35	9.05	bdl
WT12WH07-2-1	Pieman Head	orbicule		bdl	0.24	276.08	43.10	22.48	bdl	bdl	bdl	bdl	0.28	3.52	bdl
WT12WH07-2-1	Pieman Head	orbicule		2.74	0.29	233.87	42.27	40.36	1.72	bdl	bdl	bdl	0.18	3.51	0.04
WT12WH07-2-2	Pieman Head	orbicule		2.60	0.77	175.30	32.23	54.16	bdl	9.18	bdl	0.07	0.19	3.34	0.04
WT12WH07-2-2	Pieman Head	orbicule		31.47	0.44	268.99	40.13	42.78	5.18	bdl	bdl	bdl	0.36	4.19	bdl
WT12WH07-2-3	Pieman Head	orbicule		19.83	0.63	176.61	28.17	54.13	1.52	17.76	bdl	0.11	0.18	3.01	0.05
WT12WH07-2-4	Pieman Head	orbicule		bdl	1.83	251.23	38.31	45.52	bdl	bdl	bdl	bdl	0.23	13.97	bdl
WT12WH07-2-4	Pieman Head	orbicule		8.80	0.21	257.70	42.24	39.96	4.31	13.03	bdl	0.11	0.44	5.10	0.05
WT12WH07-2-5	Pieman Head	orbicule		7.66	0.17	235.57	37.20	44.68	2.11	bdl	bdl	0.16	1.22	9.16	0.44
WT12WH07-2-6	Pieman Head	orbicule		6.87	0.20	174.79	29.52	51.03	1.48	9.34	bdl	bdl	0.28	1.34	0.06
WT12WH07-2-7	Pieman Head	orbicule		2.40	0.48	174.66	33.04	56.52	bdl	bdl	bdl	bdl	0.14	3.07	0.03
WT12WH07-2-8	Pieman Head	orbicule		3.91	0.44	180.33	32.18	55.36	0.77	bdl	bdl	bdl	0.17	2.94	0.11
WT12WH13-1-1	Pieman Head	vein		3.26	0.16	333.93	45.26	37.12	9.00	15.35	bdl	bdl	0.76	3.82	bdl
WT12WH13-1-2	Pieman Head	vein		21.08	0.15	317.87	41.73	35.13	12.03	bdl	bdl	bdl	0.74	5.10	0.48
WT12WH13-1-2	Pieman Head	vein		33.28	0.09	1079.70	146.31	bdl	3.26	bdl	bdl	bdl	bdl	bdl	bdl
WT12WH13-1-3	Pieman Head	vein		11.01	0.08	340.89	47.54	37.35	7.64	bdl	bdl	bdl	0.81	5.66	bdl
WT12WH13-1-3	Pieman Head	vein		28.09	0.51	890.43	108.67	bdl	4.13	bdl	bdl	bdl	bdl	3.48	bdl
WT12WH13-1-4	Pieman Head	vein		3.07	0.37	366.39	59.29	36.86	5.48	bdl	bdl	bdl	1.22	5.82	0.06
WT12WH13-1-4	Pieman Head	vein		51.66	0.74	647.93	76.46	bdl	6.96	bdl	bdl	bdl	0.72	5.35	0.24
WT12WH13-1-5	Pieman Head	vein		14.94	0.22	337.59	41.54	35.11	7.45	bdl	bdl	bdl	0.93	4.47	0.04
WT12WH13-1-6	Pieman Head	vein		14.25	0.31	346.68	44.05	35.26	9.11	19.90	bdl	bdl	1.04	4.15	bdl
WT12WH13-1-7	Pieman Head	vein		103.30	0.24	411.98	39.46	34.45	9.67	21.86	bdl	bdl	0.97	5.35	0.08
WT12WH13-1-8	Pieman Head	vein		19.48	0.28	355.53	49.03	35.65	7.01	13.27	bdl	bdl	1.11	4.54	bdl
WT12WH13-3-1	Pieman Head	vein		5.02	0.05	128.88	18.61	8.15	bdl	9.33	bdl	bdl	bdl	bdl	bdl
WT12WH13-3-2	Pieman Head	vein		7.02	0.04	122.31	19.21	7.94	bdl	bdl	bdl	bdl	0.07	bdl	bdl
WT12WH13-3-3	Pieman Head	vein		1.48	0.07	143.61	23.96	9.42	bdl	bdl	bdl	bdl	0.09	bdl	bdl
WT12WH13-3-4	Pieman Head	vein		2.23	0.05	124.52	21.27	9.21	bdl	bdl	bdl	bdl	0.06	bdl	bdl
WT12WH13-3-5	Pieman Head	vein		2.58	0.04	130.26	21.85	8.86	bdl	bdl	0.01	bdl	0.06	1.23	bdl
WT12WH13-3-6	Pieman Head	vein		0.81	0.04	153.28	27.10	8.15	bdl	bdl	bdl	bdl	0.07	1.17	0.05
WT12WH13-3-7	Pieman Head	vein		13.33	0.05	162.65	23.15	7.78	0.83	14.31	bdl	bdl	0.11	2.25	bdl
WT12WH13-3-8	Pieman Head	vein		4.44	0.13	176.57	23.81	9.22	bdl	bdl	bdl	bdl	0.13	bdl	bdl
WT12WH13-4-1	Pieman Head	vein		13.01	0.13	163.88	18.87	8.66	3.41	20.35	0.01	bdl	0.13	bdl	0.08
WT12WH13-4-2	Pieman Head	vein		5.15	0.13	236.47	35.46	41.77	1.03	bdl	bdl	bdl	0.25	2.63	0.03
WT12WH13-4-3	Pieman Head	vein		18.82	0.17	239.82	36.01	39.52	2.74	bdl	bdl	0.10	0.31	2.88	bdl
WT12WH13-4-4	Pieman Head	vein		3.55	0.19	340.43	47.23	35.37	9.05	11.16	bdl	bdl	0.89	6.84	bdl
WT12WH13-4-5	Pieman Head	vein		8.26	0.14	240.95	37.62	46.37	1.56	13.67	bdl	bdl	0.27	3.26	0.04
WT12WH13-4-6	Pieman Head	vein		1.95	0.18	241.80	34.41	48.65	bdl	bdl	bdl	bdl	0.28	2.53	bdl
WT12WH13-5-1	Pieman Head	vein		3.89	0.05	149.69	16.20	10.71	bdl	bdl	bdl	bdl	0.09	bdl	bdl
WT12WH13-5-2	Pieman Head	vein		2.78	0.12	206.95	27.73	8.10	1.24	10.90	bdl	bdl	0.19	2.26	bdl
WT12WH13-5-3	Pieman Head	vein		2.49	0.11	183.24	24.17	11.48	0.95	bdl	bdl	bdl	0.17	1.91	bdl
WT12WH13-5-4	Pieman Head	vein		30.58	0.43	319.13	41.14	34.69	3.88	bdl	bdl	0.09	0.62	8.07	bdl
WT12WH13-5-5	Pieman Head	vein		4.64	0.20	246.69	30.37	41.89	1.08	bdl	bdl	bdl	0.41	3.96	bdl
WT12WH13-5-6	Pieman Head	vein		1.79	0.15	232.03	37.13	44.68	0.50	7.38	bdl	bdl	0.54	5.75	bdl
WT12WH13-5-7	Pieman Head	vein		9.13	0.22	231.18	35.90	43.07	0.59	8.96	bdl	bdl	0.53	5.45	bdl

WT12WH13-5-8	Pieman Head	vein	1.28	0.13	215.05	30.06	42.29	bdl	bdl	bdl	bdl	0.49	4.39	bdl
WT12WH20-1-1	Heemskirk	patch	1.53	0.31	301.20	49.86	27.35	7.62	9.19	bdl	bdl	0.65	8.47	0.05
WT12WH20-1-2	Heemskirk	patch	1.83	0.59	297.61	50.26	29.29	3.68	9.57	bdl	0.08	0.71	12.69	bdl
WT12WH20-1-3	Heemskirk	patch	8.87	0.56	280.33	47.59	28.31	2.64	bdl	bdl	0.13	0.59	13.24	bdl
WT12WH20-1-4	Heemskirk	patch	1.72	1.38	297.00	49.32	26.06	7.42	10.74	bdl	0.19	0.94	27.46	bdl
WT12WH20-1-5	Heemskirk	patch	2.47	0.75	276.02	46.35	27.80	3.02	bdl	bdl	0.13	0.69	14.59	bdl
WT12WH20-1-6	Heemskirk	patch	0.92	0.51	290.44	49.85	28.40	2.93	12.36	bdl	0.19	0.65	12.36	0.07
WT12WH20-1-7	Heemskirk	patch	5.37	0.31	286.87	48.68	25.64	5.21	17.66	bdl	0.18	0.51	9.11	bdl
WT12WH20-2-1	Heemskirk	patch	9.02	1.53	236.50	40.07	38.62	5.00	bdl	bdl	0.15	0.59	16.49	0.05
WT12WH20-2-2	Heemskirk	patch	20.30	1.86	244.29	39.70	67.91	9.45	bdl	bdl	0.19	0.79	18.91	bdl
WT12WH20-2-2	Heemskirk	patch	105.38	6.01	306.24	19.04	10.21	21.13	bdl	0.13	bdl	1.54	136.45	3.60
WT12WH20-2-3	Heemskirk	patch	8.89	1.13	209.91	32.25	33.69	5.96	20.81	bdl	bdl	0.54	11.76	bdl
WT12WH20-2-3	Heemskirk	patch	513.80	0.33	726.00	45.61	19.19	30.98	bdl	bdl	bdl	0.80	6.88	bdl
WT12WH20-2-4	Heemskirk	patch	4.60	1.07	270.68	48.66	27.99	5.42	bdl	bdl	bdl	0.56	12.93	0.11
WT12WH20-2-5	Heemskirk	patch	5.10	0.20	312.58	50.42	23.38	13.41	bdl	bdl	0.13	0.65	7.13	0.21
WT12WH20-2-6	Heemskirk	patch	70.63	0.30	289.07	42.51	15.73	14.86	bdl	bdl	bdl	0.54	6.49	0.04
WT12WH20-2-7	Heemskirk	patch	21.48	0.17	346.24	49.27	2.69	26.06	bdl	bdl	0.15	0.68	7.63	bdl
WT12WH20-2-8	Heemskirk	patch	8.82	0.05	152.74	27.42	14.95	1.13	bdl	bdl	0.17	0.19	bdl	bdl
WT12WH20-2-9	Heemskirk	patch	9.24	0.20	67.14	10.80	1.29	1.11	18.18	bdl	0.09	0.07	5.74	0.10
WT12WH20-3-1	Heemskirk	patch	0.71	1.58	178.85	32.34	46.98	4.57	bdl	bdl	bdl	0.36	14.39	bdl
WT12WH20-3-2	Heemskirk	patch	10.72	2.16	178.66	31.84	48.52	4.53	18.15	bdl	bdl	0.48	15.63	bdl
WT12WH20-3-3	Heemskirk	patch	0.43	1.60	168.49	30.01	56.78	2.22	bdl	bdl	0.10	0.46	14.67	bdl
WT12WH20-3-4	Heemskirk	patch	1.14	1.81	176.62	31.97	47.64	2.86	bdl	bdl	0.11	0.50	15.22	bdl
WT12WH20-3-5	Heemskirk	patch	5.73	1.23	178.50	32.54	50.95	2.04	14.70	bdl	0.14	0.31	10.80	bdl
WT12WH20-4-1	Heemskirk	patch	1.59	0.29	273.71	45.90	27.42	4.31	13.33	bdl	0.12	0.39	5.70	bdl
WT12WH20-4-2	Heemskirk	patch	2.77	0.65	275.50	47.33	26.59	4.24	bdl	bdl	bdl	0.46	12.90	bdl
WT12WH20-4-3	Heemskirk	patch	4.79	0.63	292.97	50.80	29.06	4.03	bdl	0.00	bdl	0.63	15.45	0.05
WT12WH20-4-4	Heemskirk	patch	4.07	0.43	291.36	50.86	28.10	3.40	bdl	bdl	bdl	0.58	11.13	0.05
WT12WH20-4-5	Heemskirk	patch	9.55	0.49	300.79	49.74	25.41	4.57	10.95	bdl	bdl	0.60	10.01	0.04
WT12WH20-4-6	Heemskirk	patch	3.89	0.29	314.14	53.30	24.22	5.55	10.35	bdl	0.09	0.66	9.69	0.05
WT12WH20-4-7	Heemskirk	patch	4.36	0.20	327.22	53.00	32.62	7.60	bdl	bdl	bdl	0.62	7.02	0.05
WT12WH22-2-1	Heemskirk	orbicule	5.54	1.11	291.96	40.51	23.24	5.15	bdl	0.01	bdl	0.56	15.40	0.17
WT12WH22-2-2	Heemskirk	orbicule	3.04	0.80	295.26	45.59	33.45	5.71	10.01	bdl	bdl	0.79	13.98	0.08
WT12WH22-2-3	Heemskirk	orbicule	1.61	0.45	237.69	37.17	30.79	3.80	bdl	bdl	bdl	0.57	11.42	bdl
WT12WH22-2-4	Heemskirk	orbicule	2.46	0.94	243.63	40.93	38.00	3.29	9.91	bdl	0.08	0.71	13.91	bdl
WT12WH22-2-5	Heemskirk	orbicule	1.56	1.21	249.58	42.92	38.62	3.68	bdl	bdl	bdl	0.66	17.63	0.25
WT12WH22-2-6	Heemskirk	orbicule	1.40	1.81	232.18	39.47	42.35	4.13	bdl	bdl	bdl	0.66	21.06	0.09
WT12WH22-2-7	Heemskirk	orbicule	9.60	0.53	241.02	39.86	29.16	3.96	16.63	bdl	bdl	0.37	7.84	0.07
WT12WH22-2-8	Heemskirk	orbicule	1.55	0.26	272.46	41.63	27.48	3.77	bdl	bdl	0.10	0.52	6.29	bdl
WT12WH22-3-1	Heemskirk	orbicule	12.37	0.09	462.35	50.87	11.59	47.54	bdl	bdl	0.09	1.04	8.63	0.06
WT12WH22-3-2	Heemskirk	orbicule	91.19	0.08	331.15	33.25	10.21	49.01	15.22	bdl	bdl	1.37	7.35	0.08
WT12WH22-3-3	Heemskirk	orbicule	9.11	0.42	341.27	45.60	20.80	16.93	bdl	bdl	bdl	1.19	19.56	0.05
WT12WH22-3-4	Heemskirk	orbicule	5.10	0.28	301.41	45.23	27.08	12.59	12.36	bdl	bdl	0.86	13.00	bdl
WT12WH22-3-5	Heemskirk	orbicule	7.04	0.40	268.85	42.43	30.46	9.67	11.35	bdl	bdl	0.55	12.30	bdl
WT12WH22-3-6	Heemskirk	orbicule	3.62	0.53	273.42	44.73	32.14	7.09	23.40	bdl	0.11	0.57	11.56	0.04
WT12WH22-3-7	Heemskirk	orbicule	2.08	0.82	293.00	48.21	33.27	7.64	17.80	bdl	0.11	0.60	11.94	bdl
WT12WH22-3-8	Heemskirk	orbicule	2.52	0.61	303.20	47.76	31.31	10.96	bdl	bdl	bdl	0.68	12.31	0.03
WT12WH22-3-9	Heemskirk	orbicule	3.50	0.22	278.61	44.67	27.16	6.66	bdl	bdl	0.16	0.56	7.77	bdl
WT12WH22-5-1	Heemskirk	orbicule	56.08	0.26	349.99	44.28	11.42	22.64	bdl	bdl	bdl	1.10	6.34	bdl
WT12WH22-5-2	Heemskirk	orbicule	33.38	0.14	280.47	42.32	25.00	20.97	13.68	0.01	0.10	0.53	4.72	bdl
WT12WH22-5-3	Heemskirk	orbicule	7.22	0.24	272.23	44.96	31.29	11.74	14.99	bdl	bdl	0.46	7.54	0.05
WT12WH22-5-4	Heemskirk	orbicule	64.15	0.34	252.67	39.27	31.62	13.31	24.09	bdl	0.10	0.63	7.55	0.09
WT12WH22-5-5	Heemskirk	orbicule	10.37	0.07	155.37	25.97	16.21	4.58	bdl	bdl	bdl	0.23	3.02	bdl
WT12WH22-5-6	Heemskirk	orbicule	24.50	1.49	655.97	42.72	24.40	507.15	bdl	0.02	bdl	0.48	33.17	0.57
WT12WH22-5-7	Heemskirk	orbicule	28.67	3.26	341.54	34.50	11.68	25.50	19.88	0.08	bdl	0.59	87.10	1.14
WT12WH28-1-1	Heemskirk	orbicule	4.72	0.04	253.78	32.47	15.19	3.07	bdl	bdl	bdl	0.83	3.52	0.05
WT12WH28-1-10	Heemskirk	orbicule	9.84	0.03	281.07	30.37	24.91	22.30	bdl	bdl	bdl	0.49	5.93	0.18
WT12WH28-1-2	Heemskirk	orbicule	8.57	0.05	284.16	38.77	18.47	5.71	bdl	bdl	bdl	1.08	6.80	bdl
WT12WH28-1-3	Heemskirk	orbicule	12.20	0.03	221.11	31.77	8.14	6.31	bdl	bdl	0.09	3.30	8.77	0.03
WT12WH28-1-4	Heemskirk	orbicule	39.47	0.32	255.74	33.34	21.13	10.30	bdl	bdl	bdl	0.60	7.62	0.06
WT12WH28-1-5	Heemskirk	orbicule	39.65	0.83	297.85	36.41	27.51	18.59	bdl	bdl	0.16	0.96	11.81	0.05
WT12WH28-1-6	Heemskirk	orbicule	25.57	0.53	305.37	43.36	27.18	7.87	bdl	bdl	bdl	0.65	12.03	bdl
WT12WH28-1-7	Heemskirk	orbicule	19.85	0.22	133.95	13.47	11.44	5.64	bdl	bdl	bdl	0.66	5.96	0.08
WT12WH28-1-8	Heemskirk	orbicule	13.09	0.28	313.75	38.40	29.73	11.95	bdl	bdl	bdl	1.11	10.04	0.11
WT12WH28-1-9	Heemskirk	orbicule	8.67	0.16	288.91	36.40	21.94	11.06	bdl	bdl	0.21	1.34	9.36	0.09
WT12WH28-2-1	Heemskirk	orbicule	6.55	0.15	286.95	36.96	22.41	6.87	bdl	bdl	bdl	0.40	4.89	0.08
WT12WH28-2-2	Heemskirk	orbicule	1.94	0.12	283.34	38.68	24.71	3.68	bdl	bdl	0.09	0.37	5.70	0.19
WT12WH28-2-3	Heemskirk	orbicule	15.14	0.42	52.43	3.85	1.25	1.96	12.23	bdl	bdl	0.10	4.64	0.05
WT12WH28-2-4	Heemskirk	orbicule	18.79	0.18	255.63	30.36	20.58	9.33	14.91	bdl	bdl	0.42	5.10	bdl
WT12WH28-2-5	Heemskirk	orbicule	5.36	1.19	217.13	31.99	37.74	5.73	11.91	bdl	bdl	0.52	14.34	bdl
WT12WH28-2-6	Heemskirk	orbicule	3.88	0.14	265.08	39.47	24.01	4.76	12.54	bdl	bdl	0.42	5.93	bdl
WT12WH28-2-7	Heemskirk	orbicule	40.74	0.13	261.33	31.08	10.78	18.91	bdl	bdl	bdl	0.35	4.86	0.08
WT12WH28-3-1	Heemskirk	orbicule	3.72	0.16	373.39	42.59	34.39	5.49	bdl	bdl	bdl	0.44	5.31	bdl
WT12WH28-3-1	Heemskirk	orbicule	40.29	0.94	372.90	36.68	18.36	25.20	28.40	bdl	bdl	1.70	8.31	bdl

WT12WH28-3-2	Heemskirk	orbicule	23.28	0.07	285.91	31.12	16.61	15.97	bdl	bdl	bdl	0.78	9.18	bdl
WT12WH28-3-2	Heemskirk	orbicule	6.88	0.17	293.87	37.33	25.74	7.18	bdl	bdl	bdl	0.55	6.69	0.03
WT12WH28-3-3	Heemskirk	orbicule	34.12	0.45	266.09	26.21	21.18	12.78	bdl	bdl	bdl	1.15	3.66	bdl
WT12WH28-3-3	Heemskirk	orbicule	14.00	2.46	403.78	40.56	37.65	101.10	16.14	bdl	bdl	1.53	45.65	0.08
WT12WH28-3-4	Heemskirk	orbicule	3.35	1.34	257.35	37.75	42.45	4.45	bdl	bdl	bdl	0.68	17.51	0.08
WT12WH28-3-4	Heemskirk	orbicule	43.74	0.06	246.17	28.35	7.74	18.46	bdl	bdl	bdl	3.28	22.75	bdl
WT12WH28-3-5	Heemskirk	orbicule	57.82	0.77	336.76	25.54	8.76	36.06	bdl	bdl	bdl	1.10	7.13	bdl
WT12WH28-3-5	Heemskirk	orbicule	18.59	0.79	242.35	32.89	29.33	5.37	bdl	bdl	bdl	0.59	9.15	0.07
WT12WH28-3-6	Heemskirk	orbicule	42.90	0.14	346.39	38.04	12.73	14.31	bdl	bdl	bdl	0.63	8.85	0.50
WT12WH28-3-8	Heemskirk	orbicule	45.39	11.09	987.93	43.14	31.76	140.47	bdl	bdl	bdl	4.08	312.01	0.54
WT12WH35-2-1	Heemskirk	orbicule	28.93	bdl	228.08	34.94	27.91	5.88	115.07	bdl	0.36	bdl	bdl	0.85
WT12WH35-2-2	Heemskirk	orbicule	4.79	1.67	401.39	49.19	29.28	17.27	bdl	bdl	bdl	0.73	9.37	bdl
WT12WH35-2-3	Heemskirk	orbicule	bdl	0.08	325.74	43.27	22.87	15.37	bdl	bdl	bdl	0.68	3.96	bdl
WT12WH35-2-4	Heemskirk	orbicule	85.72	0.07	155.68	22.70	11.01	9.72	bdl	bdl	bdl	0.25	bdl	bdl
WT12WH24-1-1	Heemskirk	orbicule	4.05	bdl	56.28	7.94	0.71	bdl	bdl	bdl	bdl	0.06	bdl	bdl
WT12WH24-1-2	Heemskirk	orbicule	2.70	0.01	69.11	9.89	2.40	bdl	bdl	bdl	0.11	bdl	bdl	0.08
WT12WH24-1-3	Heemskirk	orbicule	5.60	0.02	89.14	13.63	8.59	0.84	bdl	bdl	bdl	bdl	1.00	0.20
WT12WH24-1-4	Heemskirk	orbicule	5.65	0.51	236.25	35.06	22.58	2.30	bdl	bdl	0.08	0.84	18.23	0.12
WT12WH24-1-5	Heemskirk	orbicule	7.57	0.60	248.28	37.77	23.79	2.93	bdl	bdl	bdl	0.99	21.23	0.41
WT12WH24-1-6	Heemskirk	orbicule	7.59	0.59	244.30	37.57	23.48	1.68	bdl	bdl	bdl	1.03	22.86	0.73
WT12WH24-1-7	Heemskirk	orbicule	3.34	0.65	267.17	38.41	21.53	5.29	bdl	bdl	bdl	0.97	25.35	0.45
WT12WH24-2-1	Heemskirk	orbicule	6.13	0.40	228.55	32.32	16.19	2.47	bdl	bdl	0.11	0.46	9.37	bdl
WT12WH24-2-2	Heemskirk	orbicule	2.11	0.13	218.76	34.64	16.13	2.95	bdl	bdl	bdl	0.32	7.30	bdl
WT12WH24-2-3	Heemskirk	orbicule	2.55	0.57	246.40	38.50	19.94	3.39	bdl	bdl	bdl	0.73	17.87	0.06
WT12WH24-2-4	Heemskirk	orbicule	20.12	1.25	441.00	40.90	22.48	64.09	bdl	bdl	bdl	2.08	37.56	0.06
WT12WH24-2-5	Heemskirk	orbicule	5.04	0.45	244.39	34.76	21.90	5.22	bdl	bdl	bdl	0.48	10.94	0.04
WT12WH24-2-6	Heemskirk	orbicule	10.66	0.29	262.05	38.36	23.05	6.87	10.16	bdl	bdl	0.47	8.79	bdl
WT12WH24-3-1	Heemskirk	orbicule	78.30	0.51	255.78	30.77	21.74	11.65	bdl	bdl	bdl	2.76	20.25	bdl
WT12WH24-3-2	Heemskirk	orbicule	58.72	23.47	785.08	41.80	31.91	8.57	bdl	0.09	bdl	6.92	480.71	bdl
WT12WH24-3-2	Heemskirk	orbicule	36.79	0.66	304.66	39.10	19.56	17.40	20.33	bdl	bdl	3.66	35.19	bdl
WT12WH24-3-3	Heemskirk	orbicule	3.52	1.26	297.69	41.59	11.62	10.82	bdl	bdl	bdl	1.60	39.03	bdl
WT12WH24-3-4	Heemskirk	orbicule	3.42	1.30	299.06	43.87	10.74	8.87	12.83	bdl	bdl	1.59	34.00	0.05
WT12WH24-3-5	Heemskirk	orbicule	5.30	2.12	312.08	45.36	15.39	12.46	bdl	bdl	bdl	1.66	37.21	0.12
WT12WH24-3-6	Heemskirk	orbicule	38.13	1.50	470.05	40.94	13.66	65.02	12.91	0.01	bdl	4.15	51.42	0.05
WT12WH24-3-7	Heemskirk	orbicule	3.88	0.47	232.20	35.00	24.95	4.51	bdl	bdl	0.06	1.30	14.76	bdl
WT12WH24-4-1	Heemskirk	orbicule	60.63	0.45	299.47	31.87	23.28	48.01	11.65	0.00	bdl	0.65	16.83	0.08
WT12WH24-4-2	Heemskirk	orbicule	37.60	0.75	113.15	7.75	13.57	18.43	27.24	bdl	bdl	0.75	4.69	0.32
WT12WH24-4-3	Heemskirk	orbicule	29.34	22.19	457.97	22.62	21.31	305.53	15.82	0.01	bdl	0.97	28.66	2.11
WT12WH24-4-5	Heemskirk	orbicule	109.64	9.45	531.87	21.29	23.47	35.45	23.87	0.02	bdl	31.23	447.94	0.33
WT12WH24-4-6	Heemskirk	orbicule	12.66	2.18	239.52	28.99	22.47	6.24	bdl	bdl	bdl	0.93	63.28	0.67
WT12WH24-4-7	Heemskirk	orbicule	151.62	0.88	337.93	21.23	17.11	54.61	32.48	bdl	bdl	4.03	51.67	0.06
WT12WH24-4-8	Heemskirk	orbicule	98.10	0.42	103.27	6.74	10.30	9.28	24.56	bdl	bdl	0.45	19.15	0.06
WT12WH33-2-1	Heemskirk	orbicule	bdl	0.09	277.92	37.29	28.21	7.02	bdl	bdl	bdl	0.37	bdl	0.12
WT12WH33-2-2	Heemskirk	orbicule	64.48	bdl	250.85	32.40	28.21	13.16	90.85	bdl	bdl	0.49	4.14	0.52
WT12WH33-2-3	Heemskirk	orbicule	28.48	0.04	184.22	25.99	16.23	5.11	bdl	bdl	0.19	0.23	bdl	bdl
WT12WH33-2-4	Heemskirk	orbicule	bdl	bdl	119.79	19.47	9.03	bdl	bdl	bdl	0.28	0.17	bdl	bdl
WT12WH33-2-5	Heemskirk	orbicule	bdl	0.06	180.05	27.17	16.34	bdl	bdl	bdl	bdl	bdl	bdl	bdl
WT12WH23-1-1	Heemskirk	vein	bdl	0.32	347.54	43.20	27.38	2.04	bdl	bdl	bdl	0.77	10.14	bdl
WT12WH23-1-1	Heemskirk	vein	44.63	3.44	59.76	1.47	1.29	5.03	45.72	bdl	0.54	0.09	1.96	0.58
WT12WH23-1-10	Heemskirk	vein	23.85	0.57	87.40	5.21	2.61	4.72	28.16	0.01	0.26	0.80	1.62	0.51
WT12WH23-1-11	Heemskirk	vein	13.93	0.66	116.05	8.50	3.46	10.53	22.48	bdl	0.37	0.15	7.52	0.42
WT12WH23-1-2	Heemskirk	vein	5.43	0.33	331.39	43.53	26.83	3.88	bdl	bdl	bdl	2.06	10.90	bdl
WT12WH23-1-2	Heemskirk	vein	13.05	0.42	108.85	11.67	2.37	4.99	23.26	bdl	0.55	0.06	1.53	0.42
WT12WH23-1-3	Heemskirk	vein	35.79	0.35	371.01	46.71	21.06	15.15	bdl	bdl	bdl	9.86	18.53	bdl
WT12WH23-1-3	Heemskirk	vein	7.34	0.34	158.79	15.85	3.03	2.32	31.26	bdl	0.45	bdl	bdl	0.49
WT12WH23-1-4	Heemskirk	vein	21.17	0.62	114.82	8.98	1.73	4.27	32.42	0.01	0.45	bdl	1.57	0.61
WT12WH23-1-4	Heemskirk	vein	6.12	0.19	419.55	45.39	7.41	10.97	bdl	bdl	bdl	1.34	7.95	bdl
WT12WH23-1-5	Heemskirk	vein	26.63	0.45	87.48	6.58	1.69	4.57	40.18	bdl	0.46	0.13	1.28	0.43
WT12WH23-1-6	Heemskirk	vein	19.97	0.29	77.62	7.13	2.03	4.24	46.74	bdl	0.50	bdl	bdl	0.45
WT12WH23-1-7	Heemskirk	vein	27.09	0.33	91.46	9.70	2.47	4.41	28.01	bdl	0.45	0.16	1.06	0.37
WT12WH23-1-8	Heemskirk	vein	48.62	4.11	113.73	5.62	2.68	9.50	47.36	bdl	0.42	0.48	5.92	0.56
WT12WH23-1-9	Heemskirk	vein	24.18	0.61	156.13	13.50	4.24	6.59	33.03	bdl	0.50	0.07	1.27	0.45
WT12WH23-2-1	Heemskirk	vein	7.65	0.05	99.96	10.67	3.79	1.27	bdl	bdl	0.09	bdl	bdl	bdl
WT12WH23-2-2	Heemskirk	vein	1.16	0.01	76.88	10.17	3.32	bdl	bdl	bdl	0.07	0.05	bdl	bdl
WT12WH23-2-3	Heemskirk	vein	4.08	0.01	74.27	9.47	3.46	0.59	bdl	bdl	bdl	bdl	bdl	bdl
WT12WH23-2-4	Heemskirk	vein	3.19	0.00	111.41	14.34	4.53	bdl	bdl	bdl	bdl	bdl	bdl	bdl
WT12WH23-2-5	Heemskirk	vein	7.02	0.01	148.93	17.23	5.00	1.22	bdl	bdl	0.11	bdl	bdl	bdl
WT12WH23-2-6	Heemskirk	vein	5.25	0.02	105.09	14.83	4.17	1.40	bdl	bdl	0.08	bdl	bdl	bdl
WT12WH23-2-7	Heemskirk	vein	7.78	0.01	70.74	10.21	3.15	1.21	14.26	bdl	bdl	bdl	bdl	0.03
WT12WH23-2-8	Heemskirk	vein	76.07	0.75	75.46	5.16	2.73	33.04	12.50	bdl	bdl	0.38	3.10	bdl
WT12WH23-2-9	Heemskirk	vein	84.21	0.10	70.03	6.14	2.77	5.80	19.21	bdl	0.08	0.41	0.92	bdl
WT12WH23-3-1	Heemskirk	vein	47.44	bdl	97.40	3.44	3.37	5.36	bdl	0.01	bdl	1.79	4.82	0.09
WT12WH23-3-2	Heemskirk	vein	23.54	0.09	59.90	1.19	2.13	3.47	bdl	bdl	bdl	1.15	10.82	0.12
WT12WH23-3-3	Heemskirk	vein	39.85	0.08	78.79	6.49	2.64	2.98	bdl	bdl	0.17	0.23	bdl	0.06

WT12WH23-3-4	Heemskirk	vein	54.44	0.07	181.92	19.62	5.46	5.79	12.98	bdl	bdl	0.72	2.35	0.64
WT12WH23-3-5	Heemskirk	vein	32.77	0.04	127.39	10.54	4.16	5.66	bdl	bdl	bdl	0.68	3.10	0.48
WT12WH23-3-6	Heemskirk	vein	7.99	0.01	122.19	14.12	3.59	0.84	bdl	bdl	bdl	bdl	bdl	bdl
106425-1-1	Heemskirk	Pb-Zn vein	0.69	bdl	95.30	14.21	0.22	bdl	9.76	bdl	bdl	bdl	bdl	bdl
106425-1-10	Heemskirk	Pb-Zn vein	0.85	0.03	151.88	14.30	1.88	bdl	7.80	bdl	bdl	bdl	bdl	bdl
106425-1-2	Heemskirk	Pb-Zn vein	0.51	0.01	159.78	25.38	0.75	bdl	bdl	bdl	bdl	bdl	bdl	bdl
106425-1-3	Heemskirk	Pb-Zn vein	4.98	0.01	267.98	39.12	2.99	0.62	bdl	bdl	bdl	bdl	bdl	bdl
106425-1-4	Heemskirk	Pb-Zn vein	0.54	2.20	166.96	26.16	1.89	bdl	9.84	bdl	0.10	bdl	bdl	0.02
106425-1-5	Heemskirk	Pb-Zn vein	2.09	0.02	312.35	38.83	5.22	bdl	8.55	bdl	bdl	bdl	bdl	bdl
106425-1-6	Heemskirk	Pb-Zn vein	3.44	0.01	455.47	47.06	7.55	bdl	bdl	bdl	bdl	bdl	bdl	0.04
106425-1-7	Heemskirk	Pb-Zn vein	2.68	0.03	365.02	40.43	5.98	bdl	bdl	bdl	0.08	bdl	bdl	bdl
106425-1-8	Heemskirk	Pb-Zn vein	1.32	0.02	185.74	22.61	2.49	bdl	bdl	bdl	bdl	bdl	bdl	bdl
106425-1-9	Heemskirk	Pb-Zn vein	0.62	bdl	115.22	13.56	1.62	bdl	15.73	bdl	bdl	bdl	bdl	bdl
106425-2-1	Heemskirk	Pb-Zn vein	11.50	0.11	452.76	37.93	0.91	5.67	14.76	bdl	bdl	0.49	bdl	bdl
106425-2-10	Heemskirk	Pb-Zn vein	0.99	0.01	90.31	8.46	2.25	bdl	8.89	bdl	bdl	bdl	bdl	bdl
106425-2-11	Heemskirk	Pb-Zn vein	0.70	bdl	113.74	9.30	2.42	bdl	bdl	bdl	bdl	bdl	bdl	bdl
106425-2-12	Heemskirk	Pb-Zn vein	2.62	bdl	110.30	10.57	56.62	bdl	bdl	bdl	bdl	bdl	bdl	bdl
106425-2-2	Heemskirk	Pb-Zn vein	0.99	bdl	40.11	1.59	0.76	bdl	bdl	bdl	bdl	bdl	bdl	bdl
106425-2-3	Heemskirk	Pb-Zn vein	1.58	bdl	97.09	14.27	43.02	bdl	bdl	0.02	0.09	0.47	2.27	bdl
106425-2-4	Heemskirk	Pb-Zn vein	2.66	bdl	105.94	16.31	48.28	bdl	bdl	bdl	bdl	0.09	1.53	bdl
106425-2-5	Heemskirk	Pb-Zn vein	0.71	bdl	104.13	16.45	43.95	bdl	bdl	bdl	0.08	bdl	bdl	bdl
106425-2-6	Heemskirk	Pb-Zn vein	3.21	bdl	100.58	15.10	45.22	bdl	13.43	bdl	0.08	bdl	bdl	bdl
106425-2-7	Heemskirk	Pb-Zn vein	27.62	0.33	89.30	7.21	32.85	1.54	9.11	0.09	0.07	2.19	44.91	0.04
106425-2-8	Heemskirk	Pb-Zn vein	16.97	bdl	96.65	8.26	55.94	1.39	bdl	bdl	bdl	3.86	12.21	bdl
106425-2-9	Heemskirk	Pb-Zn vein	2.36	0.01	72.00	9.19	1.82	bdl	bdl	bdl	bdl	bdl	bdl	bdl
106425-3-1	Heemskirk	Pb-Zn vein	3.17	bdl	1076.61	158.45	2.12	bdl	bdl	0.01	0.11	bdl	bdl	bdl
106425-3-2	Heemskirk	Pb-Zn vein	4.13	bdl	480.62	68.11	1.07	bdl	bdl	bdl	bdl	bdl	bdl	bdl
106425-3-3	Heemskirk	Pb-Zn vein	3.54	bdl	764.22	93.47	3.22	bdl	bdl	bdl	bdl	bdl	bdl	bdl
106425-3-4	Heemskirk	Pb-Zn vein	0.69	0.01	200.99	24.54	1.07	bdl	bdl	bdl	0.17	bdl	bdl	0.05
106425-3-5	Heemskirk	Pb-Zn vein	5.82	0.13	734.76	66.94	2.39	bdl	17.70	bdl	0.15	bdl	bdl	0.05
106425-3-6	Heemskirk	Pb-Zn vein	6.15	0.05	884.97	112.05	2.80	bdl	12.28	bdl	bdl	bdl	bdl	bdl
106425-3-7	Heemskirk	Pb-Zn vein	4.58	0.01	463.01	74.02	0.96	3.08	bdl	bdl	bdl	0.12	bdl	bdl
106425-3-8	Heemskirk	Pb-Zn vein	0.63	0.08	142.36	24.38	0.19	bdl	bdl	0.01	bdl	bdl	bdl	0.04
106425-4-1	Heemskirk	Pb-Zn vein	1.98	0.24	464.35	79.74	0.42	1.76	14.62	0.03	bdl	bdl	23.23	0.03
106425-4-10	Heemskirk	Pb-Zn vein	2.68	0.03	485.68	56.50	5.99	bdl	bdl	0.01	bdl	bdl	1.08	0.04
106425-4-11	Heemskirk	Pb-Zn vein	1.23	0.03	363.80	48.95	3.95	bdl	10.58	bdl	0.11	bdl	1.15	bdl
106425-4-12	Heemskirk	Pb-Zn vein	0.57	0.01	268.02	38.79	2.80	bdl	bdl	bdl	bdl	bdl	bdl	bdl
106425-4-13	Heemskirk	Pb-Zn vein	1.47	0.01	332.99	40.64	4.53	bdl	11.07	bdl	bdl	bdl	bdl	bdl
106425-4-2	Heemskirk	Pb-Zn vein	2.36	0.04	561.43	74.82	0.57	1.82	bdl	0.01	bdl	bdl	18.23	0.04
106425-4-3	Heemskirk	Pb-Zn vein	0.36	0.08	443.65	64.10	0.67	bdl	bdl	bdl	bdl	bdl	2.68	bdl
106425-4-4	Heemskirk	Pb-Zn vein	5.88	0.05	274.40	34.24	0.68	bdl	bdl	bdl	0.08	bdl	2.37	bdl
106425-4-5	Heemskirk	Pb-Zn vein	16.47	0.08	880.12	97.15	2.27	2.55	13.73	0.01	0.08	bdl	3.71	0.11
106425-4-6	Heemskirk	Pb-Zn vein	24.97	0.05	754.35	101.60	1.64	1.16	bdl	bdl	bdl	bdl	bdl	0.03
106425-4-7	Heemskirk	Pb-Zn vein	9.08	0.01	297.29	42.31	1.52	bdl	bdl	bdl	bdl	bdl	bdl	bdl
106425-4-8	Heemskirk	Pb-Zn vein	1.18	bdl	184.70	27.52	1.65	bdl	bdl	bdl	bdl	bdl	bdl	bdl
106425-4-9	Heemskirk	Pb-Zn vein	7.37	0.02	336.70	41.44	3.82	bdl	8.29	0.01	bdl	bdl	bdl	bdl
WT12WH30-2-1-1	Heemskirk	UST	34.51	2.64	576.19	41.17	33.18	85.95	bdl	bdl	bdl	2.83	20.35	bdl
WT12WH30-2-1-1	Heemskirk	UST	31.16	2.42	506.29	44.32	44.56	76.74	12.96	bdl	bdl	3.45	55.21	bdl
WT12WH30-2-1-2	Heemskirk	UST	7.35	1.14	318.32	45.22	34.08	8.47	bdl	bdl	0.22	1.58	26.51	bdl
WT12WH30-2-1-2	Heemskirk	UST	39.41	1.67	294.43	39.02	25.49	7.87	10.08	bdl	bdl	1.66	45.44	bdl
WT12WH30-2-1-3	Heemskirk	UST	77.57	1.31	280.82	28.54	26.43	20.47	bdl	bdl	bdl	0.63	10.03	bdl
WT12WH30-2-1-3	Heemskirk	UST	5.90	1.85	343.53	48.51	21.46	16.90	bdl	bdl	bdl	2.03	39.96	bdl
WT12WH30-2-1-4	Heemskirk	UST	24.60	0.82	251.37	32.44	24.89	6.19	bdl	bdl	bdl	0.61	11.08	bdl
WT12WH30-2-1-4	Heemskirk	UST	29.26	2.22	367.33	47.41	26.94	25.27	12.47	bdl	bdl	2.27	43.27	bdl
WT12WH30-2-1-5	Heemskirk	UST	30.68	1.42	408.24	46.03	44.41	121.10	bdl	bdl	bdl	1.60	31.06	bdl
WT12WH30-2-1-5	Heemskirk	UST	13.76	2.29	360.30	48.51	22.64	20.61	bdl	bdl	bdl	2.27	44.68	bdl
WT12WH30-2-1-6	Heemskirk	UST	4.70	1.58	324.58	45.85	31.96	18.03	bdl	bdl	bdl	1.70	38.23	bdl
WT12WH30-2-1-6	Heemskirk	UST	45.44	3.65	835.27	42.69	77.06	180.91	93.82	bdl	bdl	5.19	117.51	bdl
WT12WH30-2-1-7	Heemskirk	UST	24.15	2.17	276.09	38.65	41.53	6.24	bdl	bdl	bdl	0.73	17.66	bdl
WT12WH30-2-2-1	Heemskirk	UST	80.08	1.49	251.80	29.43	27.80	16.18	26.66	bdl	bdl	3.04	19.94	bdl
WT12WH30-2-2-1	Heemskirk	UST	57.15	2.04	822.15	41.41	63.53	178.67	bdl	bdl	bdl	4.83	62.80	bdl
WT12WH30-2-2-2	Heemskirk	UST	98.92	18.47	1195.67	44.24	68.13	302.26	54.75	bdl	bdl	10.03	482.05	bdl
WT12WH30-2-2-2	Heemskirk	UST	22.56	0.38	258.23	37.28	23.45	9.37	bdl	bdl	bdl	0.93	14.63	bdl
WT12WH30-2-2-3	Heemskirk	UST	43.70	2.07	326.34	44.25	44.79	6.10	bdl	bdl	bdl	2.02	30.98	0.10
WT12WH30-2-2-3	Heemskirk	UST	108.18	1.31	268.16	39.53	24.01	19.23	19.54	bdl	bdl	6.65	27.61	0.04
WT12WH30-2-2-4	Heemskirk	UST	12.04	0.56	278.16	38.98	40.70	40.14	bdl	bdl	bdl	0.50	7.81	bdl
WT12WH30-2-2-4	Heemskirk	UST	138.21	2.72	385.08	25.98	32.09	66.53	16.25	bdl	bdl	11.36	81.33	bdl
WT12WH30-2-2-5	Heemskirk	UST	42.59	0.60	270.51	29.92	24.45	10.32	bdl	bdl	bdl	0.70	13.91	bdl
WT12WH30-2-2-5	Heemskirk	UST	4.18	0.93	253.05	41.07	34.24	2.00	bdl	bdl	bdl	0.88	21.12	bdl
WT12WH30-2-2-6	Heemskirk	UST	32.58	0.32	236.25	26.56	35.99	5.63	bdl	bdl	bdl	0.77	9.34	bdl
WT12WH30-2-2-6	Heemskirk	UST	47.05	0.52	238.59	36.87	31.35	7.51	10.50	bdl	bdl	1.93	20.09	bdl
WT12WH30-2-3-1	Heemskirk	UST	5.23	2.98	303.07	45.51	38.29	12.02	bdl	bdl	bdl	1.80	40.69	bdl
WT12WH30-2-3-2	Heemskirk	UST	1.61	2.30	260.10	43.82	35.18	2.59	bdl	bdl	bdl	1.28	29.09	0.03
WT12WH30-2-3-3	Heemskirk	UST	4.48	2.53	280.05	45.33	41.15	5.78	bdl	bdl	bdl	1.60	35.85	bdl

WT12WH30-2-3-4	Heemskirk	UST	4.46	2.02	247.36	40.78	39.78	1.77	8.12	bdl	bdl	1.16	25.89	bdl
WT12WH30-2-3-5	Heemskirk	UST	1.14	2.05	251.91	42.30	36.54	1.25	bdl	bdl	bdl	1.24	27.82	bdl
WT12WH30-2-3-6	Heemskirk	UST	9.28	1.69	227.05	33.28	39.16	1.41	bdl	bdl	bdl	1.04	25.35	bdl
WT12WH34-4-1-1	Heemskirk	UST	8.27	0.43	473.57	33.55	33.39	94.61	31.62	bdl	bdl	3.42	34.32	bdl
WT12WH34-4-1-2	Heemskirk	UST	21.22	3.45	496.74	35.15	37.06	119.08	18.03	0.00	bdl	3.49	72.05	bdl
WT12WH34-4-1-3	Heemskirk	UST	7.46	1.02	422.78	33.41	34.91	77.90	34.60	bdl	bdl	3.39	39.24	bdl
WT12WH34-4-1-4	Heemskirk	UST	8.93	2.15	439.29	35.51	32.68	77.43	26.98	bdl	bdl	3.50	51.04	bdl
WT12WH34-4-1-5	Heemskirk	UST	12.84	1.50	496.33	32.41	34.04	101.93	38.95	bdl	bdl	3.93	58.86	bdl
WT12WH34-4-1-6	Heemskirk	UST	76.22	2.15	423.09	21.87	32.41	121.97	bdl	bdl	bdl	4.80	62.32	bdl
WT12WH34-4-1-7	Heemskirk	UST	20.40	0.57	362.86	29.57	35.37	65.04	16.33	bdl	bdl	2.05	17.87	bdl
WT12WH34-4-2-1	Heemskirk	UST	509.60	1.65	287.51	27.32	37.15	54.22	12.92	bdl	bdl	1.00	30.26	bdl
WT12WH34-4-2-2	Heemskirk	UST	21.81	1.86	295.57	34.74	40.68	29.45	bdl	bdl	bdl	1.17	31.31	bdl
WT12WH34-4-2-3	Heemskirk	UST	6.30	2.56	305.65	36.86	38.47	39.99	16.56	bdl	bdl	1.41	48.57	bdl
WT12WH34-4-2-4	Heemskirk	UST	13.04	2.44	287.99	40.71	35.49	18.24	bdl	bdl	bdl	1.17	34.67	bdl
WT12WH34-4-2-5	Heemskirk	UST	128.16	2.23	295.79	34.00	29.75	58.10	17.02	bdl	bdl	17.78	56.62	bdl
WT12WH34-4-2-6	Heemskirk	UST	81.13	2.77	334.40	35.87	30.88	38.32	11.07	bdl	bdl	1.69	34.62	bdl
WT12WH34-4-2-7	Heemskirk	UST	26.17	2.69	312.59	41.14	31.59	29.07	bdl	0.00	bdl	1.28	42.98	bdl
WT12WH34-4-3-1	Heemskirk	UST	118.96	3.90	119.06	10.61	9.26	12.48	57.08	bdl	bdl	1.11	4.05	bdl
WT12WH34-4-3-2	Heemskirk	UST	19.66	0.89	263.94	35.52	15.53	22.24	13.53	bdl	0.07	0.79	18.64	bdl
WT12WH34-4-3-3	Heemskirk	UST	0.98	0.17	196.54	33.57	14.18	0.78	10.35	bdl	0.07	0.33	3.89	bdl
WT12WH34-4-3-4	Heemskirk	UST	23.88	0.83	276.16	36.76	12.61	16.50	bdl	bdl	bdl	0.94	19.61	bdl
WT12WH34-4-3-5	Heemskirk	UST	137.75	3.74	299.38	22.83	16.34	48.48	16.64	bdl	bdl	4.62	46.87	bdl
WT12WH34-4-3-6	Heemskirk	UST	2.66	3.60	318.63	42.90	17.93	26.66	bdl	bdl	bdl	1.40	40.62	bdl
WT12WH34-4-4-1	Heemskirk	UST	4.11	1.59	237.18	37.36	15.56	9.83	bdl	bdl	bdl	1.27	22.29	bdl
WT12WH34-4-4-2	Heemskirk	UST	9.99	1.22	256.77	37.93	12.81	12.80	9.78	bdl	bdl	0.75	21.70	bdl
WT12WH34-4-4-3	Heemskirk	UST	8.24	1.08	283.42	36.94	14.68	19.24	11.64	bdl	bdl	1.00	15.96	bdl
WT12WH34-4-4-4	Heemskirk	UST	118.74	0.86	371.21	28.44	15.17	84.16	35.77	bdl	bdl	2.75	18.36	0.08
WT12WH34-4-4-5	Heemskirk	UST	108.08	1.68	399.11	28.77	14.82	77.09	24.09	bdl	0.05	1.69	23.45	bdl
WT12WH34-4-4-6	Heemskirk	UST	69.58	1.93	397.28	32.48	14.13	69.19	16.94	bdl	bdl	1.97	24.65	bdl
WT12WH34-5-1-1	Heemskirk	UST	3.83	2.72	318.48	41.00	16.48	36.36	10.44	bdl	bdl	1.97	34.65	bdl
WT12WH34-5-1-2	Heemskirk	UST	9.36	87.19	412.12	40.45	12.84	35.25	34.66	0.07	bdl	2.64	1240.48	0.40
WT12WH34-5-1-3	Heemskirk	UST	1.53	2.55	271.71	40.67	12.56	19.39	bdl	bdl	bdl	1.16	39.71	bdl
WT12WH34-5-1-4	Heemskirk	UST	bdl	0.03	112.70	20.60	11.01	bdl	bdl	0.00	bdl	0.12	0.90	bdl
WT12WH34-5-1-5	Heemskirk	UST	1.73	0.03	100.69	18.26	12.57	bdl	bdl	bdl	0.07	0.12	1.00	bdl
WT12WH34-5-1-6	Heemskirk	UST	2.71	1.76	305.37	41.27	24.79	29.51	10.45	bdl	bdl	1.73	35.01	bdl
WT12WH34-5-2-1	Heemskirk	UST	1.71	0.97	257.92	36.12	14.94	21.68	bdl	bdl	bdl	0.96	17.51	bdl
WT12WH34-5-2-2	Heemskirk	UST	39.10	2.18	262.06	36.54	18.76	22.63	bdl	bdl	bdl	1.90	31.40	bdl
WT12WH34-5-2-3	Heemskirk	UST	34.76	1.65	251.09	36.82	18.95	15.36	10.94	bdl	bdl	1.43	20.77	bdl
WT12WH34-5-2-4	Heemskirk	UST	2.97	3.15	273.84	41.62	19.18	20.67	bdl	bdl	bdl	2.03	38.23	bdl
WT12WH34-5-2-5	Heemskirk	UST	1.32	2.68	275.47	43.74	20.11	17.92	bdl	bdl	bdl	1.68	35.16	bdl
WT12WH34-5-2-6	Heemskirk	UST	1.24	1.87	259.73	39.60	20.73	20.47	bdl	bdl	bdl	1.14	27.54	bdl
WT12WH34-5-3-1	Heemskirk	UST	6.02	5.87	358.94	45.29	17.20	39.50	bdl	bdl	bdl	2.20	59.14	bdl
WT12WH34-5-3-2	Heemskirk	UST	14.07	4.72	328.03	46.68	19.23	30.84	bdl	bdl	bdl	1.59	48.04	bdl
WT12WH34-5-3-3	Heemskirk	UST	16.11	5.18	370.84	44.69	17.24	45.55	bdl	bdl	bdl	3.12	60.63	0.05
WT12WH34-5-3-4	Heemskirk	UST	4.09	4.46	339.44	46.96	14.69	27.98	bdl	bdl	bdl	1.89	47.40	bdl
WT12WH34-5-3-5	Heemskirk	UST	1.94	4.30	309.75	47.33	12.53	19.22	9.08	bdl	bdl	1.56	41.41	bdl
WT12WH34-5-3-6	Heemskirk	UST	3.79	1.94	323.64	44.37	13.57	28.02	9.16	bdl	bdl	1.43	25.23	bdl
WT12WH34-5-3-7	Heemskirk	UST	7.27	5.55	390.50	47.18	21.72	48.40	bdl	bdl	bdl	2.74	53.82	bdl
WT12WH34-5-4-1	Heemskirk	UST	1.70	4.84	316.27	47.15	21.33	26.27	bdl	bdl	bdl	2.05	50.86	bdl
WT12WH34-5-4-2	Heemskirk	UST	38.57	4.59	329.15	45.93	22.32	35.90	13.65	bdl	bdl	2.72	54.11	bdl
WT12WH34-5-4-3	Heemskirk	UST	67.73	6.68	725.91	44.58	50.95	188.14	14.41	bdl	bdl	7.08	111.69	0.09
WT12WH34-5-4-4	Heemskirk	UST	20.24	6.99	725.36	49.56	48.35	182.45	11.53	bdl	bdl	6.70	108.65	bdl
WT12WH34-5-4-5	Heemskirk	UST	20.37	6.42	756.67	44.90	50.14	210.52	12.74	bdl	bdl	6.85	105.72	0.05
WT12WH34-5-4-6	Heemskirk	UST	38.95	10.95	759.65	42.28	73.68	214.75	30.73	bdl	bdl	7.25	149.67	0.03
WT12WH30-1-1	Heemskirk	Aplite	94.32	1.16	311.79	32.29	21.74	20.54	bdl	bdl	bdl	0.94	13.04	bdl
WT12WH30-1-2	Heemskirk	Aplite	37.90	2.95	704.04	51.43	32.57	134.64	bdl	bdl	bdl	6.30	61.03	bdl
WT12WH30-1-3	Heemskirk	Aplite	23.92	3.00	659.83	49.96	32.59	116.50	bdl	bdl	bdl	5.45	60.12	bdl
WT12WH30-1-4	Heemskirk	Aplite	15.30	0.73	317.02	44.01	31.98	9.73	bdl	bdl	bdl	1.12	18.68	bdl
WT12WH34-3-1-1	Heemskirk	Aplite	12.23	0.27	201.57	25.05	38.83	14.21	13.01	0.01	bdl	0.46	4.61	bdl
WT12WH34-3-1-2	Heemskirk	Aplite	54.47	0.26	194.77	31.39	44.83	7.33	12.47	0.01	bdl	0.40	4.76	bdl
WT12WH34-3-1-3	Heemskirk	Aplite	9.78	0.24	186.17	31.88	46.09	3.20	17.79	0.01	bdl	0.24	4.80	bdl
WT12WH34-3-1-4	Heemskirk	Aplite	6.08	0.77	199.79	34.82	44.77	7.03	bdl	bdl	bdl	0.50	15.09	bdl
WT12WH34-3-1-5	Heemskirk	Aplite	7.37	0.97	203.19	33.66	41.43	9.08	bdl	bdl	bdl	0.44	16.52	bdl
WT12WH34-3-1-6	Heemskirk	Aplite	1.27	0.96	194.18	33.94	42.85	8.02	bdl	bdl	bdl	0.47	19.53	bdl
WT12WH34-3-1-7	Heemskirk	Aplite	8.20	0.90	208.07	31.65	37.18	7.33	bdl	bdl	bdl	0.33	5.16	bdl
WT12WH34-3-2-1	Heemskirk	Aplite	19.93	1.22	570.79	35.72	39.90	123.76	18.78	bdl	bdl	3.40	39.64	bdl
WT12WH34-3-2-2	Heemskirk	Aplite	16.07	6.55	684.25	41.32	46.76	177.60	19.56	bdl	bdl	6.45	105.26	bdl
WT12WH34-3-2-3	Heemskirk	Aplite	262.00	6.65	614.48	42.50	46.53	299.32	20.07	bdl	bdl	94.44	250.79	bdl
WT12WH34-3-2-4	Heemskirk	Aplite	9.77	2.78	433.57	41.25	34.64	75.69	16.94	bdl	bdl	3.79	42.05	bdl
WT12WH34-3-2-5	Heemskirk	Aplite	2.28	3.58	303.05	40.16	31.84	38.17	bdl	bdl	bdl	1.72	59.91	bdl
WT12WH34-3-2-6	Heemskirk	Aplite	2.12	0.13	233.44	33.02	28.67	21.50	18.13	bdl	bdl	0.68	8.11	bdl
WT14WH58-1-1	Heemskirk	Aplite	bdl	1.38	190.83	30.80	41.65	1.88	11.75	bdl	bdl	0.45	16.07	bdl
WT14WH58-1-2	Heemskirk	Aplite	0.40	1.42	186.43	31.21	43.48	2.76	11.82	bdl	0.10	0.58	16.91	0.03
WT14WH58-1-3	Heemskirk	Aplite	bdl	1.27	189.21	31.72	42.20	2.74	11.23	bdl	0.09	0.61	16.08	bdl

WT14WH58-1-4	Heemskirk	Aplite	1.53	1.68	199.61	30.99	40.87	4.87	16.39	bdl	0.14	0.63	19.19	0.02
WT14WH58-1-5	Heemskirk	Aplite	0.66	1.66	201.25	31.20	37.87	4.93	bdl	bdl	0.11	0.66	20.18	0.06
WT14WH58-1-6	Heemskirk	Aplite	0.26	1.85	214.29	28.89	37.70	7.59	bdl	bdl	bdl	0.47	19.26	0.06
WT14WH58-2-1	Heemskirk	Aplite	4.19	1.47	185.58	29.94	32.18	5.20	bdl	bdl	0.13	0.68	16.03	0.05
WT14WH58-2-2	Heemskirk	Aplite	0.39	1.49	195.95	32.74	40.48	5.17	9.99	bdl	bdl	0.64	18.33	0.03
WT14WH58-2-3	Heemskirk	Aplite	bdl	1.72	201.74	34.80	36.71	4.22	bdl	0.01	0.08	0.66	18.95	bdl
WT14WH58-2-4	Heemskirk	Aplite	bdl	1.94	198.96	31.33	35.51	3.85	bdl	bdl	bdl	0.69	18.07	bdl
WT14WH58-2-5	Heemskirk	Aplite	1.53	1.95	208.19	31.16	47.85	4.03	bdl	bdl	0.10	0.63	18.14	bdl
WT14WH58-4-1	Heemskirk	Aplite	8.61	1.48	254.11	28.52	34.81	4.57	bdl	bdl	0.09	0.55	9.59	0.15
WT14WH58-4-2	Heemskirk	Aplite	1.84	1.82	220.33	30.49	57.11	6.25	12.13	bdl	bdl	0.56	17.95	bdl
WT14WH58-4-3	Heemskirk	Aplite	3.58	1.60	217.73	28.24	43.02	6.13	bdl	bdl	bdl	0.56	18.55	bdl
WT14WH58-4-4	Heemskirk	Aplite	0.63	1.68	214.73	29.72	42.75	5.32	bdl	bdl	0.11	0.53	19.26	bdl
WT14WH58-4-5	Heemskirk	Aplite	0.39	1.45	210.21	29.61	46.07	4.04	14.08	bdl	0.09	0.46	15.32	bdl
WT14WH58-4-6	Heemskirk	Aplite	0.43	1.60	209.30	30.82	43.59	3.48	bdl	bdl	bdl	0.53	16.92	bdl
WT14WH58-4-7	Heemskirk	Aplite	0.64	3.18	255.91	37.66	80.97	7.12	13.69	bdl	0.07	0.97	31.29	bdl
WT14WH58-4-8	Heemskirk	Aplite	1.70	1.73	231.57	32.54	41.52	4.23	bdl	bdl	bdl	0.62	20.01	bdl
WT14WH58-4-9	Heemskirk	Aplite	0.89	1.73	222.80	32.08	43.06	3.66	bdl	bdl	bdl	0.52	17.79	bdl
WT14WH58-5-1	Heemskirk	Aplite	6.19	23.42	303.04	26.51	37.06	10.99	13.12	0.00	bdl	0.66	27.19	0.16
WT14WH58-5-2	Heemskirk	Aplite	1.70	1.77	250.38	33.47	39.27	3.12	bdl	bdl	bdl	0.31	6.84	bdl
WT14WH58-5-3	Heemskirk	Aplite	4.77	0.28	212.41	27.59	34.82	2.65	bdl	0.00	bdl	0.37	6.03	bdl
WT14WH58-5-4	Heemskirk	Aplite	2.06	0.23	235.06	32.46	42.14	2.04	bdl	bdl	bdl	0.36	4.93	bdl
WT14WH58-5-5	Heemskirk	Aplite	89.98	1.20	215.34	22.82	36.62	14.45	22.75	bdl	bdl	0.82	12.22	bdl
WT14WH58-5-6	Heemskirk	Aplite	2.51	1.19	231.96	31.27	37.64	5.16	bdl	bdl	bdl	0.45	12.54	bdl

Appendix 6 Trace element data of quartz from the Heemskirk and Pieman Heads granite analysed by LA-ICP-MS (continued)

Sample Name	Zn	Ge	As	Rb	Sr	Zr	Nb	Ag	Sn	Sb	Cs	Nd	Gd	Hf	Ta	Au	Pb	Bi	U
WT12WH03-1-1	0.16	1.06	bdl	0.31	0.37	bdl	0.00	bdl	0.12	0.02	1.18	0.01	bdl	0.00	bdl	bdl	0.01	bdl	0.00
WT12WH03-1-2	0.17	0.92	bdl	0.04	0.17	0.01	bdl	0.01	0.08	bdl	0.79	bdl	bdl	bdl	bdl	bdl	0.01	bdl	bdl
WT12WH03-1-3	0.20	0.66	bdl	0.12	0.35	0.02	bdl	bdl	0.16	bdl	1.02	bdl	0.01	bdl	0.01	bdl	0.02	0.01	0.00
WT12WH03-1-4	0.18	0.69	bdl	0.03	0.02	bdl	bdl	bdl	0.20	bdl	0.08	bdl	bdl	bdl	0.00	bdl	bdl	bdl	0.00
WT12WH03-1-5	0.28	0.79	bdl	0.08	0.01	0.02	bdl	bdl	0.20	bdl	0.01	bdl	bdl	bdl	bdl	bdl	0.01	bdl	0.00
WT12WH03-1-6	0.16	0.79	bdl	0.05	0.04	0.00	0.00	bdl	0.24	bdl	0.20	bdl	bdl	0.00	bdl	bdl	bdl	bdl	bdl
WT12WH03-1-7	0.15	0.81	0.05	0.03	0.04	0.01	bdl	bdl	0.19	bdl	0.20	bdl	bdl	bdl	bdl	bdl	0.00	0.00	bdl
WT12WH03-1-8	0.16	0.89	bdl	0.04	0.06	0.01	bdl	bdl	0.22	bdl	0.27	bdl	bdl	bdl	bdl	bdl	0.02	bdl	bdl
WT12WH03-2-1	0.14	1.30	bdl	0.22	0.13	bdl	bdl	bdl	0.23	0.04	1.43	bdl	bdl	bdl	bdl	bdl	0.01	bdl	bdl
WT12WH03-2-2	0.19	1.51	0.06	0.14	0.75	bdl	0.01	bdl	0.22	bdl	1.03	bdl	bdl	bdl	0.00	bdl	0.01	bdl	0.00
WT12WH03-2-3	0.36	2.23	0.08	0.27	0.54	0.00	0.01	bdl	0.30	0.04	1.31	bdl	0.00	0.00	0.00	bdl	0.06	0.01	0.00
WT12WH03-2-4	0.08	2.13	0.10	0.05	0.06	bdl	bdl	bdl	0.22	bdl	0.17	bdl	bdl	bdl	bdl	bdl	0.01	0.00	0.00
WT12WH03-2-5	0.16	0.77	bdl	bdl	0.01	bdl	bdl	bdl	0.20	bdl	0.05	bdl	bdl	bdl	0.00	bdl	0.05	bdl	0.00
WT12WH03-2-6	0.21	0.77	bdl	0.02	0.03	0.01	bdl	0.01	0.20	0.02	0.27	0.00	bdl	bdl	bdl	bdl	bdl	0.00	bdl
WT12WH03-2-7	0.15	0.81	0.05	0.03	0.04	0.00	bdl	bdl	0.17	0.01	0.23	bdl	bdl	bdl	bdl	bdl	0.00	0.00	bdl
WT12WH03-2-8	0.18	0.93	bdl	0.03	0.12	bdl	0.00	bdl	0.18	bdl	0.43	bdl	bdl	bdl	bdl	bdl	0.01	bdl	bdl
WT12WH04-1-1	bdl	2.14	bdl	0.04	0.02	bdl	bdl	bdl	bdl	bdl	0.11	bdl	bdl	0.01	bdl	bdl	bdl	bdl	bdl
WT12WH04-1-2	0.27	0.93	bdl	0.03	0.12	bdl	bdl	0.01	bdl	bdl	0.31	bdl	bdl	bdl	bdl	bdl	bdl	bdl	bdl
WT12WH04-1-3	0.20	1.67	bdl	0.43	1.94	0.04	bdl	bdl	bdl	bdl	3.84	bdl	bdl	bdl	0.01	bdl	0.01	0.01	0.01
WT12WH04-1-4	0.29	1.99	bdl	0.07	0.12	bdl	bdl	bdl	bdl	0.02	0.55	bdl	bdl	bdl	bdl	bdl	0.01	bdl	bdl
WT12WH07-1-1	0.13	1.96	bdl	0.03	0.08	0.00	0.00	bdl	0.18	0.02	0.02	bdl	bdl	0.00	0.02	bdl	0.04	bdl	0.00
WT12WH07-1-2	bdl	1.97	bdl	bdl	0.01	bdl	bdl	bdl	0.10	bdl	0.01	bdl	bdl	bdl	0.00	bdl	0.00	bdl	0.00
WT12WH07-1-3	0.23	1.06	0.07	0.04	0.01	bdl	0.00	bdl	0.17	bdl	0.09	bdl	bdl	bdl	bdl	bdl	0.01	bdl	bdl
WT12WH07-1-4	0.31	1.00	0.05	bdl	0.01	0.00	bdl	bdl	0.07	bdl	0.01	bdl	bdl	bdl	0.00	bdl	0.01	bdl	0.00
WT12WH07-1-5	0.28	1.03	bdl	bdl	bdl	0.01	bdl	bdl	0.08	bdl	0.03	0.00	bdl	bdl	bdl	bdl	bdl	bdl	bdl
WT12WH07-1-6	0.28	1.01	0.04	0.03	0.04	0.01	0.00	bdl	0.08	bdl	0.06	0.00	bdl	0.00	0.01	bdl	0.01	bdl	0.00
WT12WH07-1-7	0.23	0.90	bdl	0.11	0.12	0.00	bdl	bdl	0.07	bdl	0.23	bdl	bdl	bdl	0.00	bdl	bdl	bdl	0.00
WT12WH07-1-8	0.25	1.03	bdl	0.02	0.01	0.00	0.00	bdl	0.08	bdl	0.02	bdl	bdl	bdl	bdl	bdl	0.02	bdl	0.00
WT12WH07-2-1	bdl	2.66	bdl	bdl	bdl	bdl	bdl	bdl	bdl	bdl	0.02	bdl	bdl	bdl	bdl	bdl	bdl	bdl	bdl
WT12WH07-2-1	0.17	1.06	bdl	0.02	0.01	bdl	bdl	bdl	0.07	bdl	0.03	bdl	bdl	bdl	bdl	bdl	0.01	bdl	bdl
WT12WH07-2-2	0.22	0.70	bdl	0.01	0.00	0.00	bdl	bdl	0.06	bdl	0.02	bdl	bdl	bdl	bdl	bdl	bdl	bdl	0.00
WT12WH07-2-2	0.21	1.42	bdl	0.15	0.28	bdl	bdl	bdl	bdl	0.03	0.54	bdl	bdl	bdl	bdl	bdl	bdl	bdl	bdl
WT12WH07-2-3	0.17	0.77	bdl	0.02	0.10	0.01	0.02	bdl	0.09	bdl	0.11	0.00	0.00	bdl	0.01	0.01	bdl	bdl	0.00
WT12WH07-2-4	0.23	1.00	bdl	bdl	bdl	bdl	bdl	bdl	bdl	bdl	0.02	bdl	0.03	bdl	bdl	bdl	bdl	bdl	0.04
WT12WH07-2-4	0.22	1.51	0.11	0.08	0.04	0.00	0.00	bdl	0.10	0.02	0.20	bdl	bdl	0.00	bdl	bdl	0.01	0.00	0.00
WT12WH07-2-5	0.32	1.17	0.25	0.05	0.01	0.00	bdl	bdl	0.07	0.03	0.12	bdl	bdl	bdl	bdl	bdl	0.03	0.01	0.00
WT12WH07-2-6	0.10	0.75	bdl	0.03	0.02	0.00	0.00	bdl	0.07	bdl	0.06	bdl	bdl	0.00	0.00	bdl	0.00	bdl	0.00
WT12WH07-2-7	0.16	0.74	bdl	bdl	0.02	0.01	0.00	0.01	0.06	0.02	0.02	bdl	0.01	bdl	0.00	bdl	0.01	bdl	bdl
WT12WH07-2-8	0.18	0.78	bdl	bdl	0.01	0.01	0.00	bdl	0.06	bdl	0.01	bdl	bdl	bdl	0.00	bdl	0.00	bdl	bdl
WT12WH13-1-1	0.19	3.70	0.12	0.21	0.03	bdl	0.00	bdl	0.11	0.02	0.38	0.00	0.00	bdl	0.00	bdl	0.04	bdl	bdl
WT12WH13-1-2	0.43	3.63	0.12	0.28	0.04	bdl	0.00	bdl	0.08	0.02	0.37	bdl	0.00	bdl	0.00	bdl	0.02	0.00	bdl
WT12WH13-1-2	0.95	3.71	bdl	0.08	0.15	bdl	bdl	bdl	bdl	1.02	0.20	bdl	bdl	bdl	bdl	0.07	0.19	0.04	bdl
WT12WH13-1-3	0.21	3.72	0.07	0.14	0.04	bdl	0.00	bdl	0.06	0.03	0.16	bdl	bdl	bdl	0.00	bdl	0.00	bdl	0.00
WT12WH13-1-3	bdl	4.68	bdl	0.06	0.26	0.04	bdl	bdl	bdl	0.71	0.20	bdl	bdl	0.01	0.09	0.52	bdl	0.06	0.00
WT12WH13-1-4	0.22	3.72	0.04	0.11	0.08	bdl	0.00	bdl	0.07	bdl	0.05	bdl	bdl	bdl	bdl	bdl	0.01	0.00	0.00
WT12WH13-1-4	3.16	5.82	0.22	0.14	0.25	bdl	bdl	bdl	bdl	0.48	0.60	bdl	bdl	bdl	0.02	1.08	0.50	0.37	0.00
WT12WH13-1-5	0.21	3.73	bdl	0.19	0.08	0.00	0.00	bdl	0.08	0.04	0.30	bdl	bdl	0.00	bdl	bdl	0.01	0.01	bdl
WT12WH13-1-6	0.19	3.74	0.04	0.21	0.15	0.06	0.01	bdl	0.07	bdl	0.41	0.00	0.00	0.01	0.11	bdl	bdl	bdl	bdl
WT12WH13-1-7	0.38	3.61	0.06	0.19	0.11	0.01	0.00	0.01	0.10	0.02	0.54	0.00	bdl	0.00	0.00	bdl	0.10	bdl	bdl
WT12WH13-1-8	0.24	3.72	0.06	0.18	0.07	0.00	0.01	bdl	0.07	0.01	0.32	bdl	bdl	0.00	0.00	bdl	0.01	0.00	bdl
WT12WH13-3-1	bdl	1.48	bdl	bdl	0.01	0.04	bdl	bdl	0.06	bdl	0.02	bdl	bdl	0.00	bdl	bdl	0.00	bdl	bdl
WT12WH13-3-2	0.06	1.44	bdl	bdl	0.03	bdl	0.00	bdl	0.06	bdl	0.04	bdl	0.00	bdl	0.00	bdl	bdl	bdl	0.00
WT12WH13-3-3	bdl	1.56	bdl	bdl	0.02	bdl	bdl	bdl	0.05	bdl	0.02	bdl	bdl	bdl	0.00	bdl	0.00	0.00	0.00
WT12WH13-3-4	bdl	1.46	bdl	bdl	0.00	0.00	bdl	bdl	0.06	bdl	bdl	bdl	bdl	0.00	bdl	bdl	bdl	bdl	bdl
WT12WH13-3-5	bdl	1.51	bdl	bdl	0.01	bdl	0.00	bdl	0.05	bdl	0.01	bdl	bdl	bdl	bdl	bdl	0.00	bdl	bdl
WT12WH13-3-6	0.05	1.49	0.04	bdl	bdl	0.00	bdl	bdl	0.05	0.01	bdl	0.00	bdl	bdl	bdl	bdl	bdl	0.00	bdl
WT12WH13-3-7	0.05	1.64	bdl	0.02	0.02	bdl	bdl	bdl	0.07	bdl	0.09	bdl	bdl	bdl	0.00	bdl	bdl	bdl	bdl
WT12WH13-3-8	0.08	1.75	bdl	bdl	0.02	0.00	bdl	bdl	0.06	bdl	0.02	0.01	bdl	bdl	0.00	bdl	bdl	bdl	0.00
WT12WH13-4-1	0.06	1.40	0.09	0.06	0.12	bdl	bdl	bdl	0.05	0.07	0.15	bdl	bdl	bdl	0.01	bdl	0.01	bdl	bdl
WT12WH13-4-2	0.08	1.02	bdl	0.02	0.05	bdl	0.00	bdl	0.08	0.02	0.05	bdl	bdl	bdl	0.00	bdl	0.01	bdl	bdl
WT12WH13-4-3	0.16	1.09	bdl	0.06	0.09	0.01	0.00	bdl	0.07	0.03	0.14	bdl	bdl	bdl	0.00	bdl	0.01	bdl	bdl
WT12WH13-4-4	0.24	3.07	0.18	0.19	0.03	0.00	0.01	bdl	0.12	0.04	0.54	1.09	0.09	0.00	0.01	bdl	0.05	bdl	bdl
WT12WH13-4-5	0.19	1.02	0.07	0.03	0.02	0.00	0.00	bdl	0.06	0.01	0.22	0.11	0.02	bdl	bdl	bdl	0.01	bdl	0.01
WT12WH13-4-6	0.22	1.00	bdl	bdl	0.01	0.00	bdl	bdl	0.04	bdl	0.06	bdl	bdl	bdl	bdl	bdl	0.00	bdl	bdl
WT12WH13-5-1	bdl	1.82	bdl	0.02	0.03	bdl	bdl	bdl	0.06	0.03	0.07	bdl	bdl	bdl	bdl	bdl	bdl	bdl	bdl
WT12WH13-5-2	0.08	1.84	bdl	0.02	0.03	bdl	0.00	bdl	0.06	0.02	0.05	bdl	bdl	bdl	0.00	bdl	0.00	bdl	bdl
WT12WH13-5-3	0.06	1.78	bdl	bdl	0.08	bdl	0.00	bdl	0.06	0.03	0.05	bdl	bdl	bdl	0.01	bdl	bdl	bdl	bdl
WT12WH13-5-4	0.22	2.76	0.07	0.10	0.06	bdl	0.01	bdl	0.07	bdl	0.47	bdl	bdl	0.00	bdl	bdl	0.01	bdl	bdl
WT12WH13-5-5	0.13	1.33	bdl	0.03	0.16	bdl	bdl	bdl	0.06	bdl	0.07	bdl	bdl	0.00	0.00	bdl	bdl	bdl	bdl
WT12WH13-5-6	0.12	1.07	0.05	0.01	0.01	bdl	bdl	bdl	0.08	bdl	0.03	bdl	bdl	bdl	bdl	bdl	0.00	bdl	bdl

WT12WH13-5-7	0.19	1.12	bdl	0.01	0.04	0.00	0.00	bdl	0.06	0.02	0.06	0.01	bdl	bdl	bdl	bdl	0.00	0.00	bdl
WT12WH13-5-8	1.07	1.03	bdl	bdl	0.00	5.50	bdl	bdl	0.07	0.02	0.02	0.01	0.01	0.18	bdl	bdl	bdl	bdl	0.19
WT12WH20-1-1	0.25	1.58	bdl	0.25	0.00	bdl	0.00	bdl	0.07	bdl	0.12	bdl	bdl	bdl	bdl	bdl	bdl	bdl	0.00
WT12WH20-1-2	0.27	1.44	0.04	0.11	0.02	0.01	0.00	bdl	0.05	bdl	0.04	bdl	0.00	bdl	0.00	bdl	0.00	bdl	bdl
WT12WH20-1-3	0.37	1.35	bdl	0.09	0.01	0.00	0.00	bdl	0.05	bdl	0.11	bdl	bdl	0.00	bdl	bdl	bdl	bdl	bdl
WT12WH20-1-4	0.44	1.15	bdl	0.24	0.01	0.01	0.00	bdl	0.07	bdl	0.05	bdl	bdl	bdl	0.00	bdl	bdl	bdl	bdl
WT12WH20-1-5	0.21	1.24	bdl	0.10	0.00	0.00	0.00	bdl	0.08	bdl	0.01	bdl	bdl	bdl	bdl	bdl	0.00	bdl	0.00
WT12WH20-1-6	0.33	1.45	bdl	0.08	0.00	0.00	0.00	bdl	0.07	bdl	bdl	0.00	bdl	0.00	bdl	bdl	0.00	bdl	0.00
WT12WH20-1-7	0.22	1.65	bdl	0.14	0.01	bdl	0.00	bdl	0.10	bdl	0.04	bdl	bdl	0.00	bdl	bdl	0.00	bdl	bdl
WT12WH20-2-1	0.36	0.93	bdl	0.22	0.00	bdl	0.00	bdl	0.10	bdl	0.23	0.00	bdl	bdl	bdl	bdl	0.01	bdl	0.00
WT12WH20-2-2	0.35	0.86	bdl	0.50	0.04	0.01	bdl	bdl	0.11	bdl	0.30	bdl	bdl	bdl	bdl	bdl	0.01	bdl	bdl
WT12WH20-2-2	0.39	1.78	bdl	0.55	0.41	bdl	bdl	bdl	bdl	0.43	1.08	bdl	bdl	bdl	0.01	0.97	0.08	0.09	bdl
WT12WH20-2-3	0.42	0.95	bdl	0.30	0.01	0.00	bdl	bdl	0.09	bdl	0.24	bdl	bdl	bdl	bdl	bdl	0.02	bdl	bdl
WT12WH20-2-3	0.25	1.98	0.27	0.65	0.13	0.02	bdl	0.01	bdl	0.07	0.90	bdl	bdl	bdl	bdl	0.19	0.10	0.01	0.00
WT12WH20-2-4	0.40	0.98	bdl	0.23	0.02	bdl	bdl	bdl	0.13	bdl	0.18	bdl	bdl	bdl	bdl	bdl	bdl	bdl	bdl
WT12WH20-2-5	0.12	2.10	0.10	0.31	0.02	bdl	0.00	bdl	0.11	0.03	0.87	bdl	bdl	bdl	bdl	bdl	0.00	0.00	0.00
WT12WH20-2-6	0.15	2.32	0.06	0.30	0.11	0.00	0.00	bdl	0.12	bdl	0.77	bdl	bdl	bdl	bdl	bdl	bdl	bdl	bdl
WT12WH20-2-7	0.12	1.57	0.27	0.68	0.02	0.00	0.00	bdl	0.12	0.06	0.76	bdl	bdl	0.00	0.00	bdl	0.01	0.00	0.00
WT12WH20-2-8	bdl	1.12	bdl	0.06	0.02	bdl	bdl	bdl	0.15	0.04	0.24	bdl	bdl	0.00	bdl	bdl	bdl	0.00	bdl
WT12WH20-2-9	0.09	0.82	0.06	bdl	0.04	0.00	0.00	bdl	0.12	bdl	0.08	0.00	0.00	0.00	bdl	bdl	0.03	bdl	bdl
WT12WH20-3-1	0.25	0.85	bdl	0.19	bdl	0.01	0.00	bdl	0.17	bdl	0.03	bdl	0.00	bdl	bdl	bdl	bdl	bdl	0.00
WT12WH20-3-2	0.35	0.84	bdl	0.11	0.12	0.00	0.00	bdl	0.14	bdl	0.03	bdl	bdl	bdl	bdl	0.01	bdl	0.00	bdl
WT12WH20-3-3	0.27	0.73	0.03	0.02	0.00	0.01	0.00	bdl	0.14	bdl	bdl	bdl	0.00	0.00	bdl	bdl	bdl	bdl	bdl
WT12WH20-3-4	0.25	0.87	bdl	0.02	0.00	0.01	0.00	bdl	0.12	bdl	bdl	0.00	bdl	bdl	bdl	0.01	0.00	bdl	bdl
WT12WH20-3-5	0.24	0.70	bdl	0.08	bdl	0.00	0.00	bdl	0.13	bdl	0.06	bdl	bdl	bdl	bdl	bdl	bdl	0.00	bdl
WT12WH20-4-1	0.22	1.22	0.05	0.15	0.00	bdl	0.00	bdl	0.12	bdl	0.11	bdl	bdl	bdl	0.00	bdl	0.02	bdl	0.00
WT12WH20-4-2	0.31	1.13	bdl	0.17	0.00	bdl	bdl	bdl	0.13	0.01	0.08	bdl	bdl	bdl	bdl	bdl	0.00	bdl	bdl
WT12WH20-4-3	0.26	1.29	bdl	0.12	0.00	bdl	bdl	bdl	0.12	bdl	0.11	bdl	bdl	bdl	bdl	bdl	bdl	bdl	bdl
WT12WH20-4-4	0.31	1.42	bdl	0.09	0.01	bdl	0.00	bdl	0.13	bdl	0.07	bdl	bdl	bdl	0.00	0.01	bdl	bdl	0.00
WT12WH20-4-5	0.17	1.68	bdl	0.14	0.17	bdl	0.01	0.01	0.09	0.02	0.33	bdl	0.01	bdl	0.00	bdl	0.01	bdl	0.00
WT12WH20-4-6	0.26	2.28	bdl	0.15	0.01	0.00	0.00	bdl	0.09	bdl	0.08	bdl	bdl	bdl	bdl	bdl	bdl	bdl	bdl
WT12WH20-4-7	0.18	1.21	0.12	0.25	0.01	0.00	0.00	bdl	0.10	0.02	0.22	0.00	bdl	bdl	bdl	bdl	0.02	bdl	0.00
WT12WH22-2-1	0.24	1.68	0.15	0.13	0.02	bdl	0.01	0.02	0.11	bdl	0.14	bdl	bdl	bdl	0.00	bdl	0.09	0.02	0.00
WT12WH22-2-2	0.46	1.00	bdl	0.19	0.01	0.02	0.01	0.02	0.12	0.02	0.28	bdl	bdl	bdl	0.00	bdl	0.05	0.01	0.01
WT12WH22-2-3	0.35	1.13	bdl	0.13	0.01	bdl	0.01	0.03	0.11	bdl	0.09	bdl	bdl	bdl	bdl	bdl	0.04	bdl	bdl
WT12WH22-2-4	0.46	0.96	bdl	0.13	0.00	bdl	bdl	bdl	0.10	bdl	0.07	1.99	0.24	0.00	bdl	bdl	0.09	bdl	0.13
WT12WH22-2-5	0.36	1.00	bdl	0.19	0.00	bdl	0.00	bdl	0.11	bdl	0.10	bdl	0.01	bdl	bdl	bdl	0.00	bdl	bdl
WT12WH22-2-6	0.49	0.91	bdl	0.18	0.00	0.00	bdl	0.01	0.09	bdl	0.04	0.00	bdl	bdl	bdl	bdl	0.03	bdl	0.00
WT12WH22-2-7	0.32	0.94	bdl	0.13	0.08	0.01	0.00	bdl	0.11	bdl	0.09	bdl	0.01	bdl	bdl	bdl	0.03	bdl	bdl
WT12WH22-2-8	0.26	1.16	0.10	0.14	0.02	0.03	bdl	bdl	0.09	bdl	0.12	bdl	bdl	bdl	bdl	bdl	0.01	0.00	bdl
WT12WH22-3-1	0.16	1.52	0.57	1.66	0.05	0.00	0.02	bdl	0.14	0.18	1.86	bdl	0.01	bdl	0.01	bdl	0.02	0.00	0.01
WT12WH22-3-2	0.32	1.54	0.43	1.74	0.31	0.00	0.02	0.01	0.14	0.19	2.21	bdl	bdl	bdl	0.02	bdl	0.06	bdl	0.01
WT12WH22-3-3	0.29	1.73	0.23	0.67	0.01	0.00	0.01	0.02	0.12	0.06	0.76	0.00	bdl	bdl	0.01	bdl	0.02	0.01	0.00
WT12WH22-3-4	0.32	1.15	0.16	0.48	0.01	9.85	0.02	0.03	0.09	0.06	0.48	0.01	0.02	0.66	0.01	bdl	0.04	0.00	0.83
WT12WH22-3-5	0.27	1.04	0.09	0.33	0.00	1.39	0.00	0.03	0.10	0.02	0.27	0.00	bdl	0.05	0.00	bdl	0.01	bdl	0.08
WT12WH22-3-6	0.41	1.06	0.07	0.21	0.01	0.76	0.00	0.04	0.06	0.02	0.17	bdl	0.00	0.04	0.00	bdl	0.01	0.00	0.07
WT12WH22-3-7	0.36	1.10	0.06	0.25	bdl	0.32	0.00	0.06	0.08	bdl	0.18	bdl	bdl	0.02	0.00	bdl	0.01	0.00	0.05
WT12WH22-3-8	0.43	1.17	0.09	0.39	0.00	0.24	bdl	0.05	0.10	bdl	0.28	0.00	0.00	0.01	0.00	bdl	0.00	bdl	0.03
WT12WH22-3-9	0.28	1.34	0.08	0.22	bdl	0.04	0.01	0.03	0.10	0.02	0.31	bdl	bdl	bdl	0.00	0.01	0.01	bdl	0.01
WT12WH22-5-1	0.30	1.55	0.44	0.93	0.28	bdl	0.01	bdl	0.14	0.07	1.02	bdl	bdl	bdl	0.01	bdl	0.03	0.01	0.00
WT12WH22-5-2	0.22	1.21	0.14	0.45	0.03	bdl	0.01	0.01	0.09	0.04	0.41	0.01	bdl	bdl	0.00	bdl	bdl	bdl	0.00
WT12WH22-5-3	0.29	1.01	0.11	0.28	0.00	bdl	0.00	bdl	0.11	0.03	0.48	bdl	bdl	bdl	0.00	bdl	bdl	bdl	0.00
WT12WH22-5-4	0.28	1.01	0.10	0.45	0.36	bdl	0.00	bdl	0.10	0.04	1.23	bdl	0.01	bdl	0.00	bdl	0.00	0.00	bdl
WT12WH22-5-5	0.17	1.21	0.11	0.21	0.04	bdl	0.00	bdl	0.10	0.06	0.57	0.01	bdl	bdl	0.00	bdl	bdl	0.00	bdl
WT12WH22-5-6	0.35	1.92	0.16	5.12	0.10	0.06	0.04	bdl	0.12	0.06	0.36	bdl	bdl	0.02	0.10	bdl	0.80	0.24	0.01
WT12WH22-5-7	0.62	1.40	0.50	0.40	0.13	0.07	0.08	bdl	0.16	0.14	0.18	0.03	0.01	bdl	0.03	bdl	2.18	0.66	0.03
WT12WH28-1-1	0.17	2.39	bdl	0.12	0.01	0.00	0.00	2.09	0.11	0.02	0.12	bdl	bdl	bdl	0.00	bdl	0.01	0.00	0.00
WT12WH28-1-10	0.15	3.02	0.20	0.58	0.01	0.01	0.00	1.25	0.16	0.04	0.49	bdl	bdl	bdl	bdl	bdl	0.02	bdl	0.00
WT12WH28-1-2	0.37	2.73	bdl	0.23	0.00	0.00	bdl	0.46	0.13	0.03	0.16	bdl	bdl	bdl	bdl	bdl	0.02	bdl	0.00
WT12WH28-1-3	0.81	1.56	0.06	0.28	0.00	bdl	bdl	0.11	0.13	0.04	bdl	bdl	bdl	0.00	bdl	bdl	bdl	bdl	0.00
WT12WH28-1-4	0.29	1.32	bdl	0.27	0.20	0.00	bdl	0.10	0.14	bdl	0.40	bdl	bdl	bdl	0.00	bdl	0.01	bdl	0.00
WT12WH28-1-5	0.62	1.20	0.05	0.49	0.34	0.00	0.03	0.61	0.15	0.09	0.42	bdl	bdl	bdl	0.00	bdl	0.05	bdl	0.01
WT12WH28-1-6	0.48	1.18	bdl	0.19	0.09	bdl	bdl	0.22	0.13	0.02	0.28	bdl	bdl	bdl	0.00	bdl	0.01	bdl	bdl
WT12WH28-1-7	0.24	1.59	bdl	0.14	0.06	bdl	0.00	0.14	0.14	0.06	0.21	bdl	bdl	bdl	bdl	bdl	0.02	bdl	0.00
WT12WH28-1-8	0.58	1.15	0.04	0.30	0.01	0.01	0.00	0.51	0.15	bdl	0.22	bdl	bdl	0.00	0.00	bdl	0.02	0.00	bdl
WT12WH28-1-9	0.51	1.49	0.08	0.26	0.03	bdl	bdl	0.97	0.21	0.02	0.19	0.01	bdl	bdl	0.00	bdl	0.03	bdl	bdl
WT12WH28-2-1	0.20	1.40	0.07	0.22	0.02	0.00	0.00	bdl	0.18	0.02	0.26	bdl	bdl	0.00	bdl	bdl	0.01	bdl	0.00
WT12WH28-2-2	0.27	1.29	0.05	0.11	0.00	bdl	0.00	0.03	0.19	bdl	0.09	bdl	0.01	bdl	bdl	bdl	0.00	bdl	bdl
WT12WH28-2-3	bdl	2.07	0.05	0.04	0.15	0.04	0.00	bdl	0.20	0.29	0.12	0.00	bdl	bdl	bdl	bdl	0.13	0.00	0.06
WT12WH28-2-4	0.19	1.49	0.04	0.18	0.21	0.02	0.00	bdl	0.20	0.04	0.23	bdl	0.01	bdl	0.00	bdl	0.02	bdl	0.01
WT12WH28-2-5	0.27	0.98	0.04	0.17	0.03	0.04	bdl	0.03	0.16	0.32	0.05	bdl	bdl	0.00	bdl	bdl	0.01	bdl	0.01
WT12WH28-2-6	0.24	1.26	0.06	0.15	bdl	bdl	bdl	bdl	0.12	bdl	0.12	bdl	bdl	bdl	0.00	bdl	0.01	bdl	0.00
WT12WH28-2-7	0.13	2.06	0.12	0.33	0.12	0.10	bdl	0.03	0.13	bdl	0.41	0.01	bdl	0.00	bdl	bdl	0.02	bdl	0.00
WT12WH28-3-1	0.72	1.08	bdl	0.18	bdl	0.02	bdl	bdl	bdl	bdl	0.13	bdl	bdl	bdl	bdl	0.01	bdl	bdl	bdl

WT12WH28-3-1	0.18	1.83	0.14	0.65	0.34	bdl	0.01	6.52	0.15	0.06	0.44	bdl	bdl	0.00	bdl	bdl	0.04	0.00	0.00
WT12WH28-3-2	0.43	1.61	bdl	0.56	0.04	bdl	bdl	bdl	bdl	bdl	0.38	bdl	bdl	bdl	bdl	0.01	0.06	bdl	bdl
WT12WH28-3-2	0.20	1.25	0.10	0.26	0.01	0.00	bdl	8.27	0.13	0.05	0.16	bdl	bdl	bdl	0.00	bdl	0.00	bdl	bdl
WT12WH28-3-3	0.39	1.40	0.10	0.44	0.09	0.05	bdl	bdl	bdl	0.10	0.29	bdl	bdl	0.02	0.01	0.02	0.09	bdl	bdl
WT12WH28-3-3	0.43	0.98	0.11	2.45	0.05	0.00	0.06	3.97	0.19	0.01	0.24	bdl	bdl	bdl	0.01	bdl	0.02	bdl	bdl
WT12WH28-3-4	0.48	1.00	bdl	0.15	0.01	0.01	bdl	3.40	0.11	bdl	0.03	bdl	bdl	bdl	0.00	bdl	0.00	bdl	0.00
WT12WH28-3-4	0.68	1.92	0.21	0.58	bdl	bdl	bdl	bdl	bdl	0.04	0.41	bdl	bdl	bdl	bdl	bdl	0.09	0.06	0.00
WT12WH28-3-5	0.31	1.85	bdl	0.60	0.21	bdl	bdl	0.03	bdl	0.14	0.58	bdl	bdl	0.01	bdl	bdl	0.06	bdl	bdl
WT12WH28-3-5	0.32	1.08	bdl	0.09	0.05	0.02	0.00	2.63	0.13	0.13	0.14	bdl	bdl	0.01	0.00	bdl	0.05	0.04	0.00
WT12WH28-3-6	0.21	1.64	0.08	0.36	0.02	0.01	0.00	36.49	0.22	0.03	0.36	bdl	bdl	bdl	bdl	bdl	0.01	0.00	bdl
WT12WH28-3-8	1.14	1.60	bdl	2.14	bdl	0.02	bdl	bdl	bdl	0.21	0.13	bdl	bdl	0.01	0.04	0.83	0.13	bdl	0.01
WT12WH35-2-1	bdl	2.03	bdl	0.13	0.14	bdl	bdl	bdl	bdl	bdl	0.18	bdl	bdl	bdl	bdl	bdl	bdl	bdl	bdl
WT12WH35-2-2	0.34	2.05	0.16	0.57	0.06	bdl	bdl	0.02	bdl	0.06	0.74	bdl	0.02	bdl	bdl	0.01	0.02	bdl	bdl
WT12WH35-2-3	bdl	1.80	bdl	0.50	0.03	bdl	bdl	bdl	bdl	0.05	0.75	bdl	bdl	bdl	bdl	0.02	0.01	0.00	bdl
WT12WH35-2-4	0.12	1.01	0.13	0.24	0.27	bdl	bdl	bdl	bdl	bdl	0.94	bdl	bdl	bdl	bdl	bdl	bdl	bdl	bdl
WT12WH24-1-1	0.12	0.81	bdl	bdl	0.01	0.01	bdl	bdl	0.12	bdl	0.02	bdl	bdl	bdl	bdl	bdl	0.00	bdl	0.00
WT12WH24-1-2	bdl	1.21	bdl	bdl	0.00	bdl	bdl	0.02	0.14	bdl	0.00	bdl	0.00	bdl	0.00	bdl	bdl	bdl	0.00
WT12WH24-1-3	0.18	1.32	bdl	0.02	0.02	bdl	0.00	bdl	0.13	bdl	0.05	bdl	bdl	bdl	bdl	bdl	bdl	bdl	0.00
WT12WH24-1-4	0.39	1.40	bdl	0.06	0.04	0.00	bdl	bdl	0.14	0.05	0.07	bdl	bdl	bdl	0.00	bdl	bdl	bdl	0.00
WT12WH24-1-5	0.41	1.42	0.03	0.06	0.05	0.00	0.00	0.03	0.11	bdl	0.07	0.00	bdl	bdl	bdl	bdl	bdl	bdl	bdl
WT12WH24-1-6	0.40	1.49	bdl	0.03	0.06	0.00	0.00	0.04	0.13	bdl	0.04	bdl	0.00	bdl	0.00	bdl	0.00	bdl	bdl
WT12WH24-1-7	0.38	1.62	bdl	0.11	0.02	bdl	0.00	0.02	0.12	bdl	0.04	bdl	bdl	bdl	bdl	bdl	0.00	bdl	0.00
WT12WH24-2-1	0.20	1.65	bdl	0.04	0.02	bdl	bdl	bdl	0.13	0.18	0.03	bdl	bdl	bdl	bdl	bdl	0.00	bdl	0.01
WT12WH24-2-2	0.11	1.59	bdl	0.07	0.00	bdl	0.00	bdl	0.12	bdl	0.04	bdl	bdl	bdl	bdl	bdl	0.00	bdl	0.00
WT12WH24-2-3	0.55	1.46	bdl	0.08	0.03	bdl	0.00	0.01	0.10	bdl	0.03	bdl	bdl	bdl	0.00	bdl	bdl	bdl	bdl
WT12WH24-2-4	0.81	1.93	0.04	1.74	0.02	0.02	0.03	bdl	0.15	bdl	0.47	0.00	bdl	0.01	0.00	bdl	0.02	0.01	0.01
WT12WH24-2-5	0.40	1.35	bdl	0.13	0.05	0.00	0.00	0.01	0.10	0.34	0.08	0.00	bdl	bdl	0.00	bdl	bdl	bdl	0.00
WT12WH24-2-6	0.37	1.54	bdl	0.17	0.03	0.01	0.00	0.01	0.09	bdl	0.16	bdl	bdl	bdl	0.00	bdl	0.01	bdl	0.00
WT12WH24-3-1	1.22	1.38	bdl	0.40	0.17	0.00	0.00	bdl	0.08	0.02	0.54	bdl	bdl	bdl	0.00	bdl	0.11	bdl	0.00
WT12WH24-3-2	1.72	1.80	0.13	0.22	bdl	bdl	bdl	bdl	bdl	bdl	0.36	bdl	bdl	bdl	0.01	bdl	0.03	0.04	bdl
WT12WH24-3-2	1.31	1.53	0.06	0.54	0.05	bdl	0.01	bdl	0.11	0.11	0.89	bdl	bdl	bdl	bdl	bdl	0.10	bdl	0.00
WT12WH24-3-3	0.65	1.88	bdl	0.31	0.03	0.00	0.00	bdl	0.10	0.03	0.10	bdl	0.00	0.00	0.00	bdl	0.01	bdl	0.00
WT12WH24-3-4	0.74	1.84	bdl	0.18	0.05	0.01	0.00	bdl	0.09	0.06	0.04	bdl	bdl	bdl	0.00	bdl	0.01	bdl	0.00
WT12WH24-3-5	1.08	1.61	bdl	0.33	0.05	0.01	0.01	bdl	0.09	bdl	0.11	bdl	bdl	bdl	0.00	bdl	0.02	0.00	0.00
WT12WH24-3-6	1.05	1.98	0.08	2.16	0.09	0.03	0.02	bdl	0.12	bdl	0.90	0.01	0.00	bdl	0.00	bdl	0.04	0.00	0.01
WT12WH24-3-7	0.60	1.72	bdl	0.14	0.04	0.02	0.00	bdl	0.11	0.06	0.08	bdl	0.01	bdl	0.00	bdl	0.06	bdl	0.00
WT12WH24-4-1	0.41	1.95	0.06	0.58	0.30	0.00	0.01	bdl	0.16	0.02	0.36	0.00	bdl	0.00	0.01	bdl	0.03	bdl	0.00
WT12WH24-4-2	0.25	1.87	bdl	0.24	0.11	bdl	bdl	bdl	0.10	0.06	0.27	bdl	bdl	bdl	bdl	bdl	0.06	0.01	bdl
WT12WH24-4-3	0.50	1.81	0.08	3.17	0.37	0.01	0.01	bdl	0.30	0.05	0.24	bdl	bdl	0.00	0.01	bdl	1.31	0.01	0.01
WT12WH24-4-5	1.29	1.68	0.07	0.51	0.37	0.00	bdl	bdl	0.24	0.06	0.58	0.01	0.00	0.00	0.00	bdl	0.12	0.01	bdl
WT12WH24-4-6	0.29	1.81	0.06	0.12	0.07	0.00	bdl	bdl	0.15	0.04	0.11	0.07	bdl	bdl	0.00	bdl	0.26	0.01	0.00
WT12WH24-4-7	1.33	1.88	0.11	0.70	0.38	0.00	0.00	0.01	0.21	0.07	0.86	0.01	bdl	bdl	0.00	bdl	0.24	0.04	bdl
WT12WH24-4-8	0.18	1.85	bdl	0.09	0.18	0.00	bdl	bdl	0.09	0.04	0.46	bdl	bdl	bdl	bdl	bdl	0.03	0.00	0.00
WT12WH33-2-1	0.16	1.73	bdl	0.20	0.01	0.02	bdl	bdl	bdl	0.07	0.31	bdl	bdl	0.00	bdl	bdl	0.01	0.00	bdl
WT12WH33-2-2	0.21	1.74	bdl	0.38	0.09	bdl	bdl	bdl	bdl	bdl	0.85	bdl	bdl	0.01	bdl	bdl	0.06	bdl	bdl
WT12WH33-2-3	bdl	1.63	bdl	0.11	0.04	0.03	bdl	bdl	bdl	bdl	0.21	bdl	bdl	bdl	bdl	bdl	0.01	bdl	bdl
WT12WH33-2-4	bdl	1.37	bdl	bdl	bdl	bdl	bdl	bdl	bdl	bdl	0.01	bdl	bdl	bdl	bdl	bdl	bdl	bdl	bdl
WT12WH33-2-5	bdl	1.54	bdl	bdl	bdl	bdl	bdl	bdl	bdl	bdl	0.03	bdl	0.01	bdl	bdl	bdl	bdl	bdl	bdl
WT12WH23-1-1	0.36	1.95	0.12	0.08	0.01	bdl	bdl	bdl	bdl	bdl	0.03	bdl	bdl	bdl	bdl	bdl	bdl	bdl	bdl
WT12WH23-1-1	0.14	1.41	0.15	0.04	0.04	0.01	bdl	0.54	0.25	0.06	0.19	bdl	bdl	bdl	bdl	0.10	0.09	0.01	0.15
WT12WH23-1-10	0.57	0.88	0.05	0.06	0.04	0.00	bdl	0.60	0.39	0.03	0.10	bdl	bdl	bdl	bdl	0.02	0.11	0.01	0.10
WT12WH23-1-11	0.15	0.92	bdl	0.19	0.02	0.01	bdl	0.33	0.25	0.05	0.08	0.01	bdl	bdl	bdl	0.04	0.03	0.01	0.08
WT12WH23-1-2	0.60	1.88	bdl	0.27	bdl	bdl	bdl	bdl	bdl	bdl	0.39	bdl	bdl	bdl	bdl	bdl	0.03	bdl	bdl
WT12WH23-1-2	0.16	1.64	bdl	0.04	0.02	0.01	bdl	0.86	0.24	0.06	0.02	0.01	bdl	bdl	bdl	0.07	0.05	0.01	0.11
WT12WH23-1-3	2.49	1.98	0.15	0.87	bdl	bdl	bdl	bdl	bdl	bdl	2.26	bdl	bdl	bdl	bdl	bdl	0.30	bdl	bdl
WT12WH23-1-3	0.16	1.54	0.08	bdl	0.01	bdl	bdl	0.56	0.19	0.08	0.01	bdl	bdl	bdl	bdl	0.06	0.12	0.01	0.08
WT12WH23-1-4	0.24	1.55	0.07	0.05	0.11	0.00	0.00	1.59	0.26	0.17	0.12	bdl	bdl	bdl	0.00	0.04	0.11	0.01	0.13
WT12WH23-1-4	0.21	1.43	0.31	0.45	0.03	bdl	bdl	bdl	bdl	0.04	0.70	bdl	bdl	bdl	bdl	bdl	0.13	0.00	bdl
WT12WH23-1-5	0.24	1.51	bdl	0.08	0.07	bdl	bdl	0.48	0.22	0.05	0.15	bdl	bdl	0.00	0.00	0.03	0.10	0.01	0.06
WT12WH23-1-6	0.20	0.93	bdl	0.05	0.09	0.00	bdl	0.31	0.19	0.04	0.10	bdl	bdl	bdl	0.00	0.03	0.14	0.01	0.07
WT12WH23-1-7	0.17	1.09	bdl	0.08	0.10	bdl	bdl	0.27	0.20	0.11	0.16	bdl	bdl	bdl	bdl	0.05	0.08	0.01	0.07
WT12WH23-1-8	0.34	0.99	0.25	0.12	0.20	0.03	bdl	0.95	0.23	0.13	0.33	bdl	0.01	bdl	0.00	0.04	0.12	0.01	0.13
WT12WH23-1-9	0.22	0.98	0.08	0.04	0.01	0.01	bdl	0.60	0.28	0.05	0.09	0.01	bdl	bdl	0.00	0.05	0.13	0.01	0.13
WT12WH23-2-1	bdl	1.06	0.09	0.03	0.03	0.00	0.00	0.01	0.13	0.03	0.06	bdl	bdl	bdl	bdl	bdl	0.00	0.00	0.01
WT12WH23-2-2	bdl	1.13	bdl	bdl	bdl	bdl	0.00	bdl	0.12	0.02	0.01	bdl	bdl	bdl	bdl	bdl	bdl	bdl	bdl
WT12WH23-2-3	0.04	0.89	0.06	bdl	0.01	0.00	0.00	bdl	0.12	0.04	0.03	bdl	0.00	bdl	bdl	0.01	bdl	bdl	0.00
WT12WH23-2-4	bdl	1.14	0.17	0.03	0.00	bdl	bdl	bdl	0.13	0.07	0.02	0.01	0.01	bdl	bdl	bdl	0.00	bdl	bdl
WT12WH23-2-5	bdl	1.12	0.20	0.06	bdl	bdl	bdl	bdl	0.12	0.15	0.07	bdl	bdl	bdl	bdl	bdl	bdl	bdl	0.01
WT12WH23-2-6	bdl	1.07	0.07	0.06	0.02	0.00	bdl	bdl	0.13	0.08	0.04	bdl	bdl	bdl	bdl	0.01	0.03	bdl	0.00
WT12WH23-2-7	bdl	0.71	bdl	0.03	0.01	bdl	bdl	bdl	0.11	bdl	0.06	bdl	bdl	bdl	bdl	bdl	0.01	bdl	bdl
WT12WH23-2-8	bdl	1.36	0.36	0.15	0.14	0.00	0.00	bdl	0.14	0.12	0.21	bdl	bdl	bdl	bdl	bdl	0.02	0.01	0.00
WT12WH23-2-9	0.13	1.39	0.20	0.13	0.21	bdl	bdl	bdl	0.13	0.15	0.62	bdl	bdl	bdl	0.00	bdl	0.04	0.00	0.00
WT12WH23-3-1	0.38	0.75	0.21	0.24	0.12	bdl	bdl	bdl	0.19	0.07	0.36	bdl	bdl	bdl	bdl	bdl	0.07	bdl	0.00
WT12WH23-3-2	0.17	1.18	0.09	0.05	0.06	bdl	bdl	bdl	0.15	0.04	0.17	bdl	bdl	bdl	bdl	0.01	0.01	bdl	bdl

WT12WH23-3-3	0.08	0.73	0.16	0.12	0.11	bdl	bdl	bdl	0.15	0.08	0.23	bdl	bdl	bdl	bdl	bdl	0.01	bdl	bdl
WT12WH23-3-4	0.15	0.76	0.15	0.12	0.09	bdl	0.00	0.01	0.19	0.14	0.32	bdl	bdl	0.00	bdl	bdl	0.02	bdl	0.00
WT12WH23-3-5	0.64	1.15	0.32	0.12	0.04	bdl	bdl	bdl	0.16	0.10	0.12	bdl	bdl	bdl	bdl	bdl	0.06	bdl	0.00
WT12WH23-3-6	bdl	2.20	0.06	0.03	0.03	bdl	bdl	bdl	0.11	0.04	0.05	0.00	bdl	bdl	bdl	bdl	0.00	bdl	0.00
106425-1-1	bdl	0.90	bdl	bdl	0.00	bdl	bdl	bdl	0.02	0.55	0.01	0.01	bdl	bdl	bdl	bdl	bdl	bdl	bdl
106425-1-10	bdl	0.21	bdl	bdl	0.00	bdl	bdl	bdl	0.02	2.73	bdl	bdl	bdl	bdl	bdl	bdl	bdl	bdl	bdl
106425-1-2	bdl	0.32	0.05	bdl	0.00	bdl	bdl	bdl	0.01	1.62	bdl	0.01	bdl	bdl	bdl	bdl	0.00	bdl	0.00
106425-1-3	bdl	0.29	0.07	0.04	0.01	bdl	bdl	bdl	0.04	4.87	0.09	bdl	bdl	bdl	bdl	bdl	bdl	bdl	bdl
106425-1-4	0.04	0.41	bdl	bdl	0.00	0.00	bdl	bdl	0.03	1.97	bdl	0.00	0.00	bdl	bdl	bdl	0.00	bdl	bdl
106425-1-5	0.03	0.41	0.04	bdl	0.02	bdl	bdl	bdl	0.02	4.57	0.02	0.00	bdl	bdl	0.00	bdl	bdl	bdl	0.01
106425-1-6	0.06	0.65	bdl	bdl	0.00	0.00	bdl	bdl	0.02	13.45	0.01	bdl	bdl	bdl	0.00	bdl	bdl	bdl	0.00
106425-1-7	0.04	0.44	bdl	bdl	0.00	bdl	bdl	bdl	0.03	8.17	0.01	bdl	bdl	bdl	0.00	bdl	bdl	bdl	bdl
106425-1-8	0.04	0.34	bdl	bdl	0.01	bdl	bdl	bdl	0.02	1.48	0.02	0.00	bdl	0.00	bdl	bdl	bdl	bdl	bdl
106425-1-9	bdl	0.28	bdl	bdl	0.01	bdl	bdl	bdl	0.03	0.98	0.01	bdl	0.00	bdl	bdl	bdl	bdl	0.00	0.00
106425-2-1	0.07	0.79	bdl	0.11	0.32	0.00	bdl	bdl	0.06	9.46	0.19	bdl	bdl	bdl	bdl	bdl	0.01	bdl	bdl
106425-2-10	0.05	0.08	0.03	bdl	0.00	bdl	0.00	bdl	bdl	0.57	0.01	bdl	0.00	0.00	bdl	bdl	bdl	bdl	0.01
106425-2-11	bdl	0.26	0.04	bdl	0.00	bdl	bdl	bdl	0.03	0.43	bdl	bdl	bdl	bdl	bdl	bdl	bdl	bdl	bdl
106425-2-12	bdl	0.74	0.07	0.02	0.01	0.01	bdl	0.01	0.03	0.08	0.03	bdl	bdl	bdl	bdl	bdl	bdl	bdl	bdl
106425-2-2	bdl	0.19	0.06	bdl	0.00	bdl	bdl	bdl	bdl	0.18	bdl	0.01	0.00	bdl	bdl	bdl	0.00	bdl	bdl
106425-2-3	0.38	0.82	0.08	0.04	bdl	bdl	0.01	bdl	0.05	0.46	0.03	bdl	bdl	bdl	bdl	bdl	0.13	bdl	0.00
106425-2-4	0.05	0.81	0.05	0.02	0.00	0.00	bdl	bdl	0.03	0.05	0.04	bdl	0.00	bdl	bdl	bdl	0.01	bdl	0.00
106425-2-5	bdl	0.77	0.04	bdl	0.00	0.00	bdl	bdl	0.02	0.09	0.01	bdl	bdl	bdl	bdl	bdl	bdl	bdl	0.00
106425-2-6	0.03	0.76	0.04	0.03	0.00	0.00	bdl	bdl	0.02	0.03	0.05	bdl	bdl	bdl	bdl	bdl	0.00	0.00	bdl
106425-2-7	0.49	0.82	0.21	0.05	0.03	bdl	bdl	0.04	0.26	0.27	0.24	bdl	bdl	bdl	0.00	bdl	0.42	0.02	0.00
106425-2-8	0.72	0.81	0.15	0.11	0.03	1.01	0.58	bdl	0.23	0.14	0.29	0.05	0.02	0.09	0.52	bdl	0.73	0.04	0.72
106425-2-9	bdl	0.18	0.06	0.02	0.00	bdl	0.00	bdl	0.03	0.40	0.03	bdl	bdl	bdl	bdl	bdl	0.01	0.00	0.00
106425-3-1	0.05	3.79	bdl	bdl	0.00	bdl	bdl	bdl	bdl	16.52	bdl	bdl	bdl	bdl	bdl	bdl	0.00	bdl	bdl
106425-3-2	bdl	2.21	bdl	bdl	bdl	bdl	bdl	bdl	0.08	10.77	bdl	bdl	bdl	bdl	bdl	bdl	0.00	bdl	bdl
106425-3-3	bdl	1.14	0.08	bdl	0.00	0.00	bdl	bdl	0.11	11.34	bdl	bdl	bdl	bdl	bdl	bdl	bdl	bdl	0.00
106425-3-4	bdl	0.36	0.07	bdl	bdl	bdl	bdl	bdl	0.11	1.55	bdl	bdl	bdl	bdl	bdl	bdl	0.00	bdl	bdl
106425-3-5	0.12	1.05	0.05	bdl	0.00	0.00	bdl	0.01	0.15	29.09	0.01	bdl	bdl	bdl	bdl	bdl	0.01	bdl	0.00
106425-3-6	0.06	1.20	bdl	bdl	0.00	0.00	bdl	bdl	0.13	31.17	0.01	bdl	bdl	bdl	bdl	bdl	0.01	0.00	bdl
106425-3-7	0.04	1.29	0.03	0.08	0.01	bdl	bdl	bdl	0.12	7.36	0.13	bdl	bdl	bdl	bdl	bdl	bdl	0.00	0.00
106425-3-8	bdl	2.30	0.34	bdl	0.00	bdl	bdl	bdl	0.13	1.61	0.01	bdl	bdl	bdl	bdl	bdl	bdl	bdl	0.00
106425-4-1	0.13	3.77	0.54	bdl	0.01	0.13	0.00	bdl	0.09	2.69	bdl	0.02	0.01	0.00	bdl	bdl	0.02	bdl	0.04
106425-4-10	0.04	0.67	0.15	bdl	0.00	bdl	bdl	bdl	0.09	9.85	bdl	bdl	bdl	bdl	bdl	bdl	0.00	bdl	0.04
106425-4-11	0.06	0.44	0.07	bdl	0.00	0.00	bdl	bdl	0.07	7.37	bdl	bdl	bdl	bdl	bdl	bdl	bdl	bdl	0.02
106425-4-12	bdl	0.30	0.05	bdl	0.00	0.00	bdl	bdl	0.08	3.53	bdl	bdl	bdl	bdl	bdl	bdl	bdl	bdl	0.01
106425-4-13	0.05	0.63	bdl	bdl	0.00	bdl	0.00	bdl	0.07	6.94	bdl	bdl	bdl	bdl	0.00	0.01	bdl	bdl	0.00
106425-4-2	0.09	2.53	0.56	0.02	0.01	0.10	0.00	bdl	0.07	4.62	0.01	0.01	bdl	0.00	bdl	bdl	0.02	bdl	0.02
106425-4-3	bdl	1.71	0.19	bdl	0.00	0.00	bdl	bdl	0.05	4.28	bdl	bdl	0.01	bdl	bdl	bdl	0.00	bdl	0.02
106425-4-4	bdl	0.77	0.17	0.01	0.04	bdl	bdl	bdl	0.10	3.44	0.06	bdl	bdl	bdl	0.00	bdl	bdl	bdl	0.02
106425-4-5	0.11	2.17	0.43	0.04	0.03	0.00	bdl	bdl	0.08	80.55	0.09	0.02	bdl	bdl	bdl	bdl	0.01	bdl	0.03
106425-4-6	bdl	0.70	bdl	0.02	0.06	0.00	bdl	bdl	0.11	5.58	0.14	bdl	bdl	0.00	bdl	bdl	0.00	bdl	0.00
106425-4-7	bdl	0.51	bdl	bdl	0.04	bdl	bdl	bdl	0.10	1.61	0.05	bdl	bdl	bdl	bdl	bdl	bdl	bdl	0.00
106425-4-8	0.07	0.22	bdl	bdl	0.01	0.00	bdl	bdl	0.10	1.68	0.01	bdl	bdl	bdl	0.00	bdl	0.01	bdl	bdl
106425-4-9	bdl	0.56	bdl	bdl	0.03	bdl	bdl	bdl	0.10	5.84	0.06	0.01	0.00	bdl	bdl	bdl	0.00	bdl	0.01
WT12WH30-2-1-1	0.43	1.14	bdl	2.50	0.45	0.09	bdl	bdl	bdl	0.38	3.98	bdl	bdl	bdl	0.04	bdl	0.08	0.01	0.01
WT12WH30-2-1-1	0.87	1.04	bdl	2.00	0.09	0.07	0.01	bdl	0.09	0.08	0.19	0.01	0.00	0.00	0.00	bdl	0.05	0.00	0.00
WT12WH30-2-1-2	0.67	1.19	bdl	0.13	bdl	0.03	bdl	bdl	bdl	bdl	0.02	bdl	bdl	bdl	bdl	bdl	bdl	bdl	bdl
WT12WH30-2-1-2	0.59	1.09	bdl	0.13	0.17	0.02	0.00	bdl	0.06	0.10	0.15	bdl	bdl	bdl	0.00	bdl	0.03	bdl	bdl
WT12WH30-2-1-3	0.52	1.19	bdl	0.34	0.39	bdl	bdl	bdl	bdl	0.12	3.24	bdl	bdl	0.01	0.00	0.50	0.02	bdl	bdl
WT12WH30-2-1-3	0.74	1.08	bdl	0.34	0.01	0.02	bdl	bdl	0.05	0.02	0.01	0.01	bdl	bdl	0.00	0.00	0.01	bdl	0.00
WT12WH30-2-1-4	0.28	1.16	bdl	0.09	0.21	0.03	bdl	bdl	bdl	0.23	0.28	bdl	bdl	bdl	0.04	0.00	0.03	bdl	0.00
WT12WH30-2-1-4	0.67	1.03	bdl	0.42	0.03	0.01	0.00	bdl	0.06	0.03	0.14	bdl	bdl	bdl	bdl	bdl	bdl	bdl	0.00
WT12WH30-2-1-5	0.87	0.98	bdl	1.13	0.04	bdl	bdl	bdl	bdl	bdl	0.05	bdl	bdl	bdl	0.00	0.05	bdl	bdl	0.00
WT12WH30-2-1-5	0.81	1.02	bdl	0.38	0.04	0.01	bdl	bdl	0.05	0.04	0.05	bdl	bdl	bdl	0.00	bdl	0.01	bdl	0.00
WT12WH30-2-1-6	0.56	1.10	bdl	0.47	0.00	0.02	0.00	bdl	0.04	bdl	0.06	bdl	bdl	0.00	bdl	bdl	0.00	bdl	0.00
WT12WH30-2-1-6	1.07	1.18	bdl	5.47	0.03	0.13	bdl	bdl	bdl	0.03	0.32	bdl	bdl	0.01	bdl	bdl	0.10	0.01	0.04
WT12WH30-2-1-7	0.47	1.12	bdl	0.19	0.05	0.01	0.01	bdl	0.06	bdl	0.13	bdl	0.00	bdl	0.00	bdl	0.01	bdl	0.00
WT12WH30-2-2-1	1.31	0.98	bdl	0.41	0.46	0.00	0.01	bdl	0.06	0.07	0.51	bdl	bdl	bdl	0.00	bdl	0.18	0.00	0.01
WT12WH30-2-2-1	0.79	1.12	0.18	5.70	0.06	0.07	bdl	bdl	bdl	0.07	1.00	bdl	bdl	bdl	bdl	0.02	0.08	0.01	0.01
WT12WH30-2-2-2	1.93	1.31	0.91	5.76	0.14	0.15	bdl	bdl	bdl	0.11	3.16	bdl	bdl	0.02	0.03	0.08	0.89	0.09	0.26
WT12WH30-2-2-2	0.61	1.16	bdl	0.20	0.03	0.00	0.00	bdl	0.05	0.04	0.24	bdl	bdl	0.00	0.00	bdl	0.04	bdl	0.00
WT12WH30-2-2-3	0.75	1.22	bdl	0.09	0.04	bdl	bdl	bdl	bdl	bdl	0.53	bdl	bdl	bdl	bdl	bdl	bdl	bdl	bdl
WT12WH30-2-2-3	2.85	1.23	bdl	0.55	0.11	0.00	0.01	bdl	0.06	0.03	1.24	0.00	bdl	0.00	0.00	bdl	0.38	bdl	0.00
WT12WH30-2-2-4	0.56	1.36	bdl	0.27	bdl	bdl	bdl	bdl	bdl	bdl	0.02	bdl	bdl	bdl	bdl	bdl	0.05	bdl	bdl
WT12WH30-2-2-4	2.47	1.04	0.09	2.00	0.44	0.02	0.03	bdl	0.08	0.39	1.78	0.02	0.01	bdl	0.01	bdl	0.33	0.02	0.01
WT12WH30-2-2-5	0.40	1.27	bdl	0.16	0.12	0.02	bdl	bdl	bdl	bdl	0.22	bdl	bdl	bdl	bdl	0.02	bdl	bdl	bdl
WT12WH30-2-2-5	0.42	0.92	bdl	0.04	0.03	0.01	0.00	bdl	0.06	0.02	0.03	bdl	bdl	bdl	bdl	bdl	bdl	bdl	bdl
WT12WH30-2-2-6	0.48	1.19	bdl	0.14	0.05	bdl	bdl	bdl	bdl	0.13	0.78	bdl	bdl	bdl	bdl	bdl	0.02	bdl	bdl
WT12WH30-2-2-6	1.22	1.00	bdl	0.54	0.02	0.00	0.00	bdl	0.04	0.03	0.57	bdl	bdl	bdl	bdl	bdl	0.10	bdl	bdl
WT12WH30-2-3-1	0.68	1.03	bdl	0.09	0.00	0.02	0.00	bdl	0.05	0.03	bdl	0.00	bdl	0.00	bdl	bdl	0.01	0.00	0.00
WT12WH30-2-3-2	0.58	1.02	0.04	0.03	0.03	0.00	bdl	bdl	0.05	0.42	0.02	bdl	bdl	0.00	0.00	bdl	bdl	bdl	0.00

WT12WH30-2-3-3	0.62	1.09	0.03	0.06	0.01	0.01	0.00	bdl	0.05	0.16	0.01	bdl	bdl	bdl	bdl	bdl	bdl	bdl	0.00
WT12WH30-2-3-4	0.60	0.94	0.04	bdl	0.02	0.02	bdl	bdl	0.06	0.08	0.02	0.00	bdl	0.00	0.00	bdl	0.00	bdl	bdl
WT12WH30-2-3-5	0.52	0.94	bdl	bdl	0.01	0.01	0.00	bdl	0.05	0.02	0.01	bdl	bdl	bdl	bdl	0.00	bdl	0.00	bdl
WT12WH30-2-3-6	0.41	0.90	bdl	0.02	0.03	bdl	0.00	bdl	0.05	bdl	0.02	bdl	bdl	0.00	bdl	bdl	bdl	bdl	bdl
WT12WH34-4-1-1	0.44	1.28	0.17	1.62	0.01	0.04	0.01	bdl	0.20	0.08	1.36	bdl	bdl	bdl	bdl	bdl	0.06	0.01	0.00
WT12WH34-4-1-2	1.63	1.37	bdl	2.10	0.01	0.03	0.02	bdl	0.13	0.03	0.26	0.00	bdl	bdl	0.00	bdl	0.10	0.00	0.00
WT12WH34-4-1-3	0.46	1.43	0.07	1.49	0.01	0.03	0.01	bdl	0.15	0.03	0.79	bdl	0.00	bdl	bdl	bdl	0.07	0.01	0.00
WT12WH34-4-1-4	0.36	1.39	0.04	1.70	0.01	0.02	0.01	bdl	0.11	0.02	0.45	bdl	bdl	0.00	bdl	bdl	0.06	0.01	0.00
WT12WH34-4-1-5	0.36	1.41	0.09	2.13	0.01	0.04	0.02	bdl	0.15	bdl	0.99	0.01	bdl	bdl	0.00	bdl	0.07	0.01	0.00
WT12WH34-4-1-6	2.39	1.58	0.29	2.13	0.06	0.05	0.03	0.02	0.19	0.07	1.17	0.02	bdl	bdl	bdl	bdl	5.37	0.04	0.00
WT12WH34-4-1-7	0.30	1.55	bdl	1.26	0.01	0.01	0.01	bdl	0.12	bdl	0.43	0.02	bdl	0.00	bdl	bdl	0.28	0.01	0.00
WT12WH34-4-2-1	0.46	1.06	bdl	1.08	0.15	0.01	bdl	bdl	0.15	0.06	3.25	0.01	bdl	bdl	bdl	bdl	0.02	bdl	bdl
WT12WH34-4-2-2	0.53	1.08	0.09	0.25	0.00	0.01	0.00	bdl	0.07	0.04	0.04	bdl	0.01	0.00	0.00	bdl	0.01	bdl	0.00
WT12WH34-4-2-3	0.60	1.19	bdl	0.41	0.01	0.02	0.01	bdl	0.05	0.04	0.06	0.00	0.01	bdl	bdl	bdl	bdl	bdl	0.00
WT12WH34-4-2-4	0.58	1.17	bdl	0.18	0.01	0.01	bdl	bdl	0.06	0.03	0.06	bdl	bdl	bdl	bdl	bdl	bdl	0.00	0.00
WT12WH34-4-2-5	7.30	1.27	0.12	1.23	0.05	0.02	0.00	bdl	0.12	0.06	1.96	bdl	bdl	bdl	bdl	0.00	0.78	0.01	0.00
WT12WH34-4-2-6	0.63	1.28	0.05	0.60	0.09	0.03	0.00	bdl	0.06	0.03	1.02	bdl	0.00	0.00	bdl	0.00	0.02	bdl	0.00
WT12WH34-4-2-7	0.71	1.27	bdl	0.39	0.04	bdl	0.00	bdl	0.06	bdl	0.27	bdl	bdl	bdl	bdl	bdl	0.01	bdl	bdl
WT12WH34-4-3-1	0.16	1.50	0.05	0.21	0.44	0.01	0.01	bdl	0.07	0.08	0.61	0.01	bdl	bdl	0.01	bdl	0.03	bdl	0.00
WT12WH34-4-3-2	0.29	1.64	0.05	0.38	0.07	0.00	0.01	bdl	0.07	0.06	0.38	bdl	bdl	bdl	0.00	bdl	0.01	bdl	0.00
WT12WH34-4-3-3	0.19	1.72	bdl	0.02	0.00	0.00	0.00	bdl	0.08	0.04	0.02	bdl	bdl	0.00	0.00	bdl	bdl	bdl	bdl
WT12WH34-4-3-4	0.74	1.33	bdl	0.34	0.01	bdl	0.01	bdl	0.09	0.06	0.44	bdl	bdl	0.00	0.01	bdl	0.05	bdl	0.00
WT12WH34-4-3-5	2.46	1.72	0.07	0.82	0.13	0.03	0.04	bdl	0.12	0.08	1.50	0.01	bdl	0.00	0.02	bdl	0.30	bdl	bdl
WT12WH34-4-3-6	0.66	1.64	bdl	0.19	0.01	0.01	0.00	bdl	0.07	0.03	bdl	bdl	bdl	0.00	0.00	bdl	bdl	bdl	0.00
WT12WH34-4-4-1	0.51	1.59	0.05	0.15	0.00	0.00	0.00	bdl	0.09	0.05	0.05	bdl	bdl	bdl	0.00	0.00	0.05	bdl	bdl
WT12WH34-4-4-2	0.41	1.45	bdl	0.22	0.00	0.00	0.01	bdl	0.06	0.10	0.12	bdl	bdl	bdl	bdl	bdl	0.00	bdl	0.00
WT12WH34-4-4-3	0.33	1.56	0.15	0.28	0.05	0.05	0.06	bdl	0.08	0.15	0.25	0.00	bdl	bdl	0.05	bdl	0.02	0.00	0.06
WT12WH34-4-4-4	0.48	1.69	0.53	1.57	0.37	0.05	0.05	bdl	0.14	0.16	1.80	bdl	bdl	bdl	0.03	bdl	0.11	0.01	0.02
WT12WH34-4-4-5	0.62	1.65	0.07	1.10	0.16	0.01	bdl	bdl	0.08	0.03	1.05	bdl	bdl	bdl	bdl	bdl	0.04	bdl	bdl
WT12WH34-4-4-6	0.64	1.54	bdl	0.79	0.19	0.06	0.04	bdl	0.10	0.04	0.58	0.00	bdl	0.00	0.04	bdl	0.03	0.00	0.03
WT12WH34-5-1-1	0.48	1.51	bdl	0.58	0.00	0.02	0.01	bdl	0.07	bdl	0.04	bdl	bdl	bdl	bdl	bdl	0.01	bdl	0.00
WT12WH34-5-1-2	2.71	1.48	0.52	0.46	0.28	0.46	0.18	bdl	0.09	0.05	0.08	0.15	0.14	0.03	0.11	bdl	6.07	0.08	0.61
WT12WH34-5-1-3	0.71	1.49	bdl	0.32	0.00	0.02	0.00	bdl	0.06	bdl	0.07	bdl	bdl	bdl	0.00	bdl	0.05	bdl	0.01
WT12WH34-5-1-4	0.05	1.33	0.14	bdl	0.00	bdl	bdl	bdl	0.06	0.05	bdl	bdl	bdl	bdl	bdl	bdl	0.01	bdl	bdl
WT12WH34-5-1-5	bdl	1.19	0.14	bdl	0.00	bdl	0.00	bdl	0.06	0.07	0.00	bdl	bdl	bdl	bdl	bdl	bdl	bdl	0.00
WT12WH34-5-1-6	0.75	1.16	bdl	0.57	bdl	0.02	0.00	bdl	0.08	bdl	0.22	bdl	0.01	bdl	bdl	bdl	0.01	0.00	0.00
WT12WH34-5-2-1	0.41	1.29	bdl	0.35	bdl	0.00	0.00	bdl	0.10	0.01	0.18	bdl	bdl	bdl	bdl	bdl	0.01	bdl	0.00
WT12WH34-5-2-2	0.57	1.52	bdl	0.32	0.04	0.01	bdl	bdl	0.06	bdl	0.97	bdl	bdl	bdl	0.00	bdl	0.04	bdl	0.00
WT12WH34-5-2-3	0.66	1.57	bdl	0.26	0.03	0.00	bdl	bdl	0.06	0.02	0.83	0.00	bdl	bdl	bdl	bdl	0.01	bdl	0.00
WT12WH34-5-2-4	1.15	1.53	bdl	0.24	0.00	0.00	bdl	bdl	0.08	bdl	0.13	bdl	bdl	bdl	0.00	bdl	0.00	bdl	0.00
WT12WH34-5-2-5	0.96	1.59	bdl	0.24	0.00	0.00	bdl	bdl	0.06	bdl	0.04	bdl	bdl	0.00	bdl	bdl	bdl	bdl	0.00
WT12WH34-5-2-6	0.66	1.63	0.05	0.30	0.00	0.01	0.00	bdl	0.06	0.01	0.07	0.00	bdl	bdl	bdl	bdl	bdl	bdl	0.00
WT12WH34-5-3-1	0.86	1.49	bdl	0.03	0.00	0.02	bdl	bdl	0.06	bdl	bdl	0.00	bdl	0.00	0.00	bdl	bdl	bdl	0.00
WT12WH34-5-3-2	0.67	1.39	0.07	0.03	bdl	0.02	bdl	bdl	0.06	0.02	0.07	0.01	bdl	0.00	bdl	bdl	bdl	0.00	0.00
WT12WH34-5-3-3	0.76	1.52	0.16	0.04	bdl	0.03	0.01	bdl	0.07	0.03	0.06	bdl	0.01	0.00	bdl	bdl	0.01	bdl	0.00
WT12WH34-5-3-4	0.60	1.51	bdl	0.03	0.00	0.03	0.00	bdl	0.05	bdl	0.00	bdl	0.00	bdl	bdl	bdl	bdl	0.00	bdl
WT12WH34-5-3-5	0.53	1.51	bdl	0.05	bdl	0.01	0.00	bdl	0.06	bdl	bdl	0.00	0.00	bdl	0.00	bdl	bdl	bdl	bdl
WT12WH34-5-3-6	0.67	1.47	bdl	0.23	0.00	0.02	bdl	bdl	0.06	bdl	0.02	bdl	0.00	bdl	0.00	bdl	bdl	bdl	bdl
WT12WH34-5-3-7	0.74	1.55	0.03	0.16	0.00	0.04	0.01	bdl	0.05	bdl	bdl	bdl	bdl	0.00	0.00	bdl	bdl	0.00	bdl
WT12WH34-5-4-1	0.80	1.63	bdl	0.05	0.01	0.02	0.00	bdl	0.04	bdl	bdl	bdl	bdl	bdl	bdl	bdl	0.00	bdl	bdl
WT12WH34-5-4-2	1.53	1.56	0.07	0.22	0.02	0.01	0.01	bdl	0.05	0.03	0.73	0.00	bdl	bdl	bdl	bdl	0.05	bdl	bdl
WT12WH34-5-4-3	2.23	1.52	0.07	0.34	0.04	0.06	0.03	bdl	0.04	0.02	0.97	bdl	bdl	0.00	0.00	bdl	0.03	0.00	bdl
WT12WH34-5-4-4	2.13	1.54	bdl	0.02	0.00	0.10	0.02	bdl	0.05	bdl	0.08	bdl	0.00	0.00	0.00	0.00	bdl	bdl	0.00
WT12WH34-5-4-5	1.76	1.63	bdl	0.25	0.01	0.06	0.03	bdl	0.05	bdl	0.08	bdl	bdl	bdl	0.00	bdl	0.02	bdl	0.00
WT12WH34-5-4-6	1.76	1.58	bdl	1.55	0.04	0.07	0.02	bdl	0.06	bdl	0.50	bdl	bdl	0.01	0.00	bdl	0.07	bdl	0.00
WT12WH30-1-1	0.58	1.45	bdl	0.42	0.32	0.03	bdl	bdl	bdl	0.05	0.72	bdl	bdl	bdl	0.00	bdl	0.07	bdl	bdl
WT12WH30-1-2	0.86	1.24	bdl	2.60	0.02	0.13	bdl	bdl	bdl	0.14	0.14	bdl	bdl	0.01	bdl	0.08	0.03	bdl	0.01
WT12WH30-1-3	1.76	1.24	bdl	1.00	bdl	0.05	bdl	bdl	bdl	bdl	0.02	bdl	bdl	bdl	bdl	bdl	0.01	bdl	0.00
WT12WH30-1-4	0.79	0.97	bdl	0.29	0.01	bdl	bdl	bdl	bdl	bdl	0.30	bdl	0.03	bdl	bdl	bdl	bdl	bdl	0.00
WT12WH34-3-1-1	0.19	0.91	0.07	0.15	0.02	0.01	0.01	bdl	0.10	0.06	0.18	bdl	bdl	bdl	0.00	bdl	0.01	bdl	0.00
WT12WH34-3-1-2	0.24	0.95	bdl	0.14	0.10	0.00	0.00	bdl	0.13	0.02	0.34	bdl	bdl	bdl	bdl	bdl	bdl	bdl	bdl
WT12WH34-3-1-3	0.20	0.78	bdl	0.05	0.02	0.01	0.08	bdl	0.08	bdl	0.14	bdl	bdl	bdl	0.02	bdl	bdl	bdl	0.01
WT12WH34-3-1-4	0.19	0.83	bdl	0.17	0.01	bdl	0.10	bdl	0.08	bdl	0.10	0.01	bdl	0.00	0.02	bdl	bdl	bdl	bdl
WT12WH34-3-1-5	0.25	0.89	bdl	0.17	0.03	0.01	0.00	bdl	0.10	0.01	0.08	0.00	bdl	0.00	bdl	bdl	bdl	0.00	bdl
WT12WH34-3-1-6	0.30	0.89	bdl	0.13	0.00	bdl	bdl	bdl	0.07	bdl	0.03	bdl	0.00	0.00	0.00	0.00	bdl	bdl	0.00
WT12WH34-3-1-7	bdl	0.80	bdl	0.03	0.05	0.26	0.02	bdl	0.09	0.05	0.04	bdl	bdl	0.02	0.00	bdl	0.00	bdl	bdl
WT12WH34-3-2-1	0.52	1.44	bdl	2.59	0.00	0.05	0.01	bdl	0.22	bdl	0.50	0.01	bdl	0.01	0.00	bdl	0.06	0.01	bdl
WT12WH34-3-2-2	1.37	1.58	0.05	2.38	bdl	0.10	0.02	bdl	0.07	bdl	bdl	bdl	bdl	bdl	0.00	bdl	0.05	bdl	bdl
WT12WH34-3-2-3	21.88	1.58	bdl	4.94	0.05	0.03	0.02	bdl	0.10	0.01	5.01	0.00	bdl	0.00	0.00	bdl	4.02	0.00	0.00
WT12WH34-3-2-4	1.08	1.69	bdl	1.18	0.00	0.03	0.02	bdl	0.08	bdl	0.08	bdl	bdl	bdl	0.00	bdl	0.06	bdl	bdl
WT12WH34-3-2-5	0.71	1.43	0.04	0.61	bdl	0.02	0.02	bdl	0.09	bdl	0.10	bdl	bdl	bdl	0.00	bdl	0.01	0.00	bdl
WT12WH34-3-2-6	0.24	1.37	0.20	0.30	0.00	0.01	0.00	bdl	0.10	0.07	0.34	0.00	bdl	0.00	0.03	bdl	0.02	bdl	0.00
WT14WH58-1-1	0.27	0.84	bdl	0.04	0.00	bdl	bdl	0.01	0.09	bdl	bdl	bdl	bdl	bdl	bdl	bdl	bdl	bdl	bdl
WT14WH58-1-2	0.24	0.81	bdl	bdl	0.00	0.01	bdl	bdl	0.09	bdl	bdl	bdl	bdl	bdl	bdl	bdl	bdl	bdl	bdl

WT14WH58-1-3	0.27	0.86	0.07	bdl	0.00	bdl	0.00	bdl	0.09	bdl	bdl	0.00	0.00	bdl	0.00	bdl	bdl	bdl	bdl
WT14WH58-1-4	0.25	0.83	bdl	0.06	0.12	0.01	0.00	bdl	0.09	0.06	0.03	bdl	bdl	bdl	0.00	0.01	0.00	bdl	bdl
WT14WH58-1-5	0.34	0.88	bdl	0.08	0.00	0.01	bdl	bdl	0.07	0.01	0.00	bdl	0.00	bdl	0.00	bdl	bdl	bdl	0.00
WT14WH58-1-6	0.36	0.94	bdl	0.25	bdl	0.00	0.00	bdl	0.11	bdl	0.03	0.00	0.00	bdl	bdl	bdl	bdl	bdl	0.00
WT14WH58-2-1	0.48	0.89	bdl	0.22	bdl	0.01	bdl	bdl	0.07	bdl	0.14	bdl	bdl	0.00	bdl	bdl	0.04	bdl	bdl
WT14WH58-2-2	0.37	0.88	bdl	0.32	0.00	0.00	0.00	bdl	0.09	bdl	0.02	bdl	bdl	bdl	bdl	bdl	0.00	bdl	bdl
WT14WH58-2-3	0.30	0.95	bdl	0.12	0.00	0.00	0.00	bdl	0.09	bdl	0.00	bdl	bdl	bdl	bdl	bdl	bdl	bdl	0.00
WT14WH58-2-4	0.31	0.91	bdl	0.04	bdl	0.01	0.00	bdl	0.09	bdl	bdl	bdl	0.01	bdl	bdl	bdl	bdl	bdl	bdl
WT14WH58-2-5	0.31	0.86	bdl	0.09	0.04	0.00	0.00	bdl	0.10	bdl	0.03	bdl	bdl	bdl	bdl	bdl	bdl	bdl	0.00
WT14WH58-4-1	0.39	0.95	0.04	0.14	0.06	0.01	bdl	bdl	0.11	0.05	0.09	bdl	bdl	0.00	bdl	bdl	0.01	bdl	bdl
WT14WH58-4-2	0.35	0.76	bdl	0.18	bdl	0.00	bdl	bdl	0.09	bdl	0.04	bdl	bdl	bdl	bdl	bdl	0.01	bdl	bdl
WT14WH58-4-3	0.28	0.88	bdl	0.23	0.04	bdl	0.00	bdl	0.12	0.04	0.08	bdl	bdl	bdl	0.00	bdl	bdl	bdl	0.00
WT14WH58-4-4	0.35	0.88	bdl	0.15	bdl	0.00	bdl	bdl	0.09	bdl	0.01	bdl	bdl	bdl	bdl	bdl	0.00	bdl	bdl
WT14WH58-4-5	0.34	0.84	bdl	0.12	0.00	0.00	0.00	bdl	0.08	bdl	0.01	0.00	0.01	bdl	bdl	bdl	bdl	bdl	bdl
WT14WH58-4-6	0.39	0.88	0.03	0.08	0.00	0.01	bdl	bdl	0.10	bdl	0.01	bdl	bdl	bdl	bdl	bdl	0.00	bdl	0.00
WT14WH58-4-7	0.49	0.82	bdl	0.09	0.00	0.01	0.00	bdl	0.09	bdl	0.00	0.00	bdl	0.00	bdl	bdl	bdl	bdl	bdl
WT14WH58-4-8	0.39	0.95	bdl	0.11	0.00	0.01	0.00	bdl	0.08	bdl	0.01	0.00	bdl	bdl	0.00	bdl	bdl	bdl	0.00
WT14WH58-4-9	0.36	0.87	bdl	0.12	0.00	bdl	0.00	bdl	0.11	bdl	0.01	bdl	0.00	bdl	bdl	bdl	0.00	0.00	0.00
WT14WH58-5-1	0.87	1.00	bdl	0.21	0.07	0.02	0.01	bdl	0.12	0.12	0.09	bdl	bdl	0.01	0.00	bdl	0.01	bdl	0.00
WT14WH58-5-2	0.26	0.92	bdl	0.07	0.01	0.01	bdl	bdl	0.09	0.02	0.32	bdl	bdl	bdl	bdl	bdl	0.05	bdl	bdl
WT14WH58-5-3	0.30	0.94	bdl	0.10	0.00	0.02	0.00	bdl	0.10	bdl	0.24	0.01	bdl	bdl	0.00	bdl	0.01	bdl	bdl
WT14WH58-5-4	0.23	0.90	bdl	0.07	bdl	0.00	bdl	bdl	0.09	0.01	0.15	bdl	bdl	0.00	0.00	bdl	0.01	bdl	0.00
WT14WH58-5-5	0.69	0.95	bdl	0.61	7.79	0.01	bdl	0.37	0.10	0.13	1.70	0.87	0.05	bdl	bdl	bdl	0.29	bdl	0.09
WT14WH58-5-6	0.32	0.91	bdl	0.20	0.04	bdl	0.00	bdl	0.09	bdl	0.08	bdl	0.00	0.00	bdl	bdl	0.01	bdl	0.01

Appendix 7 Fluid inclusion microthermometric data from the Heemskirk and Pieman Heads granites

Abbreviation: Qtz = quartz, Flu = fluorite; L = liquid, V = vapour; Tm = final ice melting temperature, T_hL = temperature of liquid homogenisation; T_hV = temperature of vapour disappearance; T_hd = temperature of dissolution of daughter minerals; Salinity-Tm = salinity calculated on temperature of final ice melting; Salinity-Td = salinity calculated on temperature of daughter mineral dissolution.

Sample NO.	Granite	Sample type	Host mineral	Shape	Size	Phases	Homogenisation	Tm (°C)	T_hL (°C)	T_hV (°C)	T_hd(°C)	Salinity-Tm (%)	Salinity-Td (%)
WT12WH24-3-1	Heemskirk	Cavity	Qtz	negative	19.7	L > V	L	-5.3	174			8.28	
WT12WH24-3-3	Heemskirk	Cavity	Qtz	subround	16	L > V	L	-4.8	212			7.59	
WT12WH24-3-4	Heemskirk	Cavity	Qtz	irregular	23	L > V	L	-7.1	195			10.61	
WT12WH24-3-5	Heemskirk	Cavity	Qtz	irregular	18	L > V	L	-5.5	187			8.55	
WT12WH24-3-6	Heemskirk	Cavity	Qtz	negative	8	L > V	L	-5.8	156			8.95	
WT12WH24-3-7	Heemskirk	Cavity	Qtz	subround	8	L > V	L		215				
WT12WH24-3-8	Heemskirk	Cavity	Qtz	irregular	12	L > V	L		223				
WT12WH24-3-9	Heemskirk	Cavity	Qtz	subround	7	L > V	L		177				
WT12WH24-3-10	Heemskirk	Cavity	Qtz	elongate	39	L > V	L	-1.9	351			3.23	
WT12WH24-3-11	Heemskirk	Cavity	Qtz	subround	18	L > V	L	-1.6	360			2.74	
WT12WH24-3-12	Heemskirk	Cavity	Qtz		12	L > V	L		158				
WT12WH24-3-13	Heemskirk	Cavity	Qtz			L > V	L		163				
WT12WH24-3-14	Heemskirk	Cavity	Qtz	negative		L < V	V			> 550			
WT12WH24-3-15	Heemskirk	Cavity	Qtz			L > V	L		461				
WT12WH24-4-1	Heemskirk	Cavity	Qtz	elongate	23	L > V	L	-4.6	202			7.31	
WT12WH24-4-2	Heemskirk	Cavity	Qtz			L > V	L		201				
WT12WH24-4-3	Heemskirk	Cavity	Qtz			L > V	L		203				
WT12WH24-4-4	Heemskirk	Cavity	Qtz	irregular	17	L > V	L	-4.5	196			7.17	
WT12WH24-4-5	Heemskirk	Cavity	Qtz	irregular	15	L > V	L		255				
WT12WH24-4-6	Heemskirk	Cavity	Qtz	irregular	13	L > V	L	-4.2	214			6.74	
WT12WH24-4-7	Heemskirk	Cavity	Qtz			L > V	L		177				
WT12WH24-4-8	Heemskirk	Cavity	Qtz			L > V	L		198				
WT12WH24-4-9	Heemskirk	Cavity	Qtz			L > V	L		201				
WT12WH24-4-10	Heemskirk	Cavity	Qtz	irregular	17	L > V	L		269				
WT12WH24-4-11	Heemskirk	Cavity	Qtz	elongate	15	L > V	L		236				
WT12WH24-4-12	Heemskirk	Cavity	Qtz	negative	10	L > V	L		244				

WT12WH24-4-13	Heemskirk	Cavity	Qtz	tabular	15	L > V	L		342			
WT12WH24-4-14	Heemskirk	Cavity	Qtz	elongate	19	L > V	L		258			
WT12WH24-4-15	Heemskirk	Cavity	Qtz	elongate	11	L > V	L		261			
WT12WH24-4-16	Heemskirk	Cavity	Qtz		10	L > V	L		303			
WT12WH24-4-17	Heemskirk	Cavity	Qtz		8	L > V	L		239			
WT12WH22-0-1	Heemskirk	Orbicule	Qtz	subround	18	L + V + H				248		34.56
WT12WH22-0-4	Heemskirk	Orbicule	Qtz	subround	10	L + V	L		173			
WT12WH22-0-5	Heemskirk	Orbicule	Qtz	subround	20	L + V + H	H		172	312		39.11
WT12WH22-0-6	Heemskirk	Orbicule	Qtz	subround	18	L + V + H	H		179	195		31.63
WT12WH22-0-7	Heemskirk	Orbicule	Qtz	negative	14	L + V	L		302			
WT12WH22-0-8	Heemskirk	Orbicule	Qtz	round	9	L + V	L		338			
WT12WH22-0-9	Heemskirk	Orbicule	Qtz	elliptical	9	L + V	L		266			
WT12WH22-0-10	Heemskirk	Orbicule	Qtz	irregular	12	L + V	L		237			
WT12WH22-0-11	Heemskirk	Orbicule	Qtz		9	L + V	L		243			
WT12WH22-0-12	Heemskirk	Orbicule	Qtz	irregular	20	L + V	L		331			
WT12WH22-0-13	Heemskirk	Orbicule	Qtz	tabular	17	L + V	L		279			
WT12WH22-0-14	Heemskirk	Orbicule	Qtz	triangular	13	L + V	L		291			
WT12WH22-0-15	Heemskirk	Orbicule	Qtz	irregular	16	L + V	L		335			
WT12WH22-0-16	Heemskirk	Orbicule	Qtz	elongate	12	L + V	L		248			
WT12WH22-0-17	Heemskirk	Orbicule	Qtz	subround	10	L + V	L		306			
WT12WH22-0-18	Heemskirk	Orbicule	Qtz	tabular	20	L + V	L		322			
WT12WH22-0-19	Heemskirk	Orbicule	Qtz	subround	8	L + V	L		324			
WT12WH22-0-20	Heemskirk	Orbicule	Qtz	tabular	18	L + V	L		315			
WT12WH22-0-21	Heemskirk	Orbicule	Qtz	irregular	16	L + V	L		360			
WT12WH22-0-22	Heemskirk	Orbicule	Qtz	elongate	15	L + V	L		359			
WT12WH28-6-1-1	Heemskirk	Orbicule	Qtz	subround	18	L > V	L	-4.8	168		7.59	
WT12WH28-6-1-2	Heemskirk	Orbicule	Qtz	irregular	17	L > V	L	-12.0	169		15.96	
WT12WH28-6-1-3	Heemskirk	Orbicule	Qtz	tabular	14	L > V	L	-1.8	194		3.06	
WT12WH28-6-1-4	Heemskirk	Orbicule	Qtz	irregular	15	L > V	L		177			
WT12WH28-6-1-5	Heemskirk	Orbicule	Qtz	elongate	11	L > V	L		185			
WT12WH28-6-1-6	Heemskirk	Orbicule	Qtz	round	8	L > V	L		153			
WT12WH28-6-1-7	Heemskirk	Orbicule	Qtz	round	7	L > V	L	-7.5	169		11.10	
WT12WH28-6-1-8	Heemskirk	Orbicule	Qtz	elongate	8	L > V	L		172			
WT12WH28-6-1-9	Heemskirk	Orbicule	Qtz	negative	47	L > V	L		404			
WT12WH28-6-1-10	Heemskirk	Orbicule	Qtz	round	10	L > V	L		305			
WT12WH28-6-1-11	Heemskirk	Orbicule	Qtz	elliptical	18	L > V	L		270			
WT12WH28-6-1-12	Heemskirk	Orbicule	Qtz	subround	12	L > V	L		356			
WT12WH28-6-1-13	Heemskirk	Orbicule	Qtz	irregular	11	L > V	L		342			
WT12WH28-6-1-14	Heemskirk	Orbicule	Qtz	elongate	15	L > V	L		308			
WT12WH28-6-1-15	Heemskirk	Orbicule	Qtz	irregular	14	L > V	L		330			
WT12WH28-6-1-16	Heemskirk	Orbicule	Qtz	triangular	12	L > V	L		354			

WT12WH28-6-1-17	Heemskirk	Orbicule	Qtz	subround	15	L < V	V			400			
WT12WH28-6-1-18	Heemskirk	Orbicule	Qtz	triangular	23	L > V	L		386				
WT12WH28-6-1-19	Heemskirk	Orbicule	Qtz	negative	12	L < V	V			484			
WT12WH28-6-1-20	Heemskirk	Orbicule	Qtz	negative	18	L < V	V			458			
WT12WH28-6-1-22	Heemskirk	Orbicule	Qtz	negative	17	L < V	V			> 550			
WT12WH28-6-1-23	Heemskirk	Orbicule	Qtz	elliptical	14	L > V	L		339				
WT12WH28-6-1-24	Heemskirk	Orbicule	Qtz	elongate	22	L > V	L		317				
WT12WH28-6-1-25	Heemskirk	Orbicule	Qtz	irregular	9	L > V	L		318				
WT12WH28-6-1-26	Heemskirk	Orbicule	Qtz	negative	18	L > V	L		340				
WT12WH28-6-1-27	Heemskirk	Orbicule	Qtz	negative	13	L > V	L		422				
WT12WH28-6-2-1	Heemskirk	Orbicule	Qtz	elongate	20	L > V	L	-10.0	159			13.94	
WT12WH28-6-2-2	Heemskirk	Orbicule	Qtz	round	15	L > V	L		165				
WT12WH28-6-2-3	Heemskirk	Orbicule	Qtz	triangular	14	L > V	L		162				
WT12WH28-6-2-4	Heemskirk	Orbicule	Qtz	negative	18	L > V	L		222				
WT12WH28-6-2-5	Heemskirk	Orbicule	Qtz	elongate	20	L > V	L		217				
WT12WH28-6-2-6	Heemskirk	Orbicule	Qtz	subround	35	L < V	V			334			
WT12WH28-6-2-7	Heemskirk	Orbicule	Qtz	negative	10	L > V	L	-6.8	401			10.24	
WT12WH28-6-2-8	Heemskirk	Orbicule	Qtz	negative	11	L > V	L		386				
WT12WH28-6-2-9	Heemskirk	Orbicule	Qtz	elongate	26	L > V	L	-9.3	345			13.18	
WT12WH28-6-2-10	Heemskirk	Orbicule	Qtz	subround	15	L + V + H	L		335		320		39.76
WT12WH28-6-2-11	Heemskirk	Orbicule	Qtz	elongate	14	L > V	L		338				
WT12WH28-6-2-12	Heemskirk	Orbicule	Qtz	subround	16	L > V	L		298				
WT12WH28-6-2-13	Heemskirk	Orbicule	Qtz	irregular	17	L > V	L		305				
WT12WH28-6-2-14	Heemskirk	Orbicule	Qtz	irregular	12.5	L > V	L		311				
WT12WH28-6-2-15	Heemskirk	Orbicule	Qtz	elliptical	13	L < V	L		414				
WT12WH28-6-2-16	Heemskirk	Orbicule	Qtz	tabular	19	L > V	L		363				
WT12WH28-6-2-17	Heemskirk	Orbicule	Qtz	irregular	10	L > V	L		327				
WT12WH28-6-2-18	Heemskirk	Orbicule	Qtz	elongate	17	L > V	L		335				
WT12WH28-6-2-19	Heemskirk	Orbicule	Qtz	tabular	14	L ≈ V	L		351				
WT12WH28-6-2-20	Heemskirk	Orbicule	Qtz	elongate	13	L > V	L		346				
WT12WH28-6-2-21	Heemskirk	Orbicule	Qtz	elliptical	13	L > V	L		305				
WT12WH28-6-2-22	Heemskirk	Orbicule	Qtz	triangular	20	L > V	L		370				
WT12WH28-6-2-23	Heemskirk	Orbicule	Qtz	negative	20	L > V 20%	L	-11.8	315			15.76	
WT12WH28-6-2-24	Heemskirk	Orbicule	Qtz	negative	8.5	L > V 30%	L		282				
WT12WH28-6-2-25	Heemskirk	Orbicule	Qtz	round	10	L > V 30%	L		312				
WT12WH28-6-2-26	Heemskirk	Orbicule	Qtz	round	13	L > V 30%	L		351				
WT12WH28-6-2-27	Heemskirk	Orbicule	Qtz	irregular	19	L > V 10%	L	-11.9	284			15.86	
WT12WH28-6-2-28	Heemskirk	Orbicule	Qtz	tabular	22	L < V 60%	V			414			
WT12WH28-6-2-29	Heemskirk	Orbicule	Qtz	elongate	19	L < V 55%	V			343			
WT12WH28-6-2-30	Heemskirk	Orbicule	Qtz	triangular	20	L > V 15%	L	-9.1	391			12.96	
WT12WH28-6-2-31	Heemskirk	Orbicule	Qtz	tabular	17	L > V 25%	L		342				

WT12WH28-6-2-32	Heemskirk	Orbicule	Qtz	round	6.7	L > V 40%	L		328				
WT12WH28-6-2-33	Heemskirk	Orbicule	Qtz	round	13.6	L < V 55%	L		401				
WT12WH28-6-2-34	Heemskirk	Orbicule	Qtz	elongate	15	L > V	L		> 500				
WT12WH28-6-2-35	Heemskirk	Orbicule	Qtz		8	L > V	L		344				
WT12WH28-6-2-36	Heemskirk	Orbicule	Qtz	subround	10	L > V	L		349				
WT12WH28-6-2-37	Heemskirk	Orbicule	Qtz	round	6	L > V	L		356				
WT12WH28-6-2-38	Heemskirk	Orbicule	Qtz	irregular	13	L > V	L		354				
WT12WH28-6-2-39	Heemskirk	Orbicule	Qtz	tabular	12	L > V	L		387				
WT12WH28-6-2-40	Heemskirk	Orbicule	Qtz	elongate	12	L > V	L		412				
WT12WH28-6-2-41	Heemskirk	Orbicule	Qtz	round	10	L > V	L		421				
WT12WH28-6-3-1	Heemskirk	Orbicule	Qtz	elliptical	18	L + V + H	L		340		328		40.44
WT12WH28-6-3-2	Heemskirk	Orbicule	Qtz	elliptical	9.8	L + V + H	L		335		297		37.93
WT12WH28-6-3-4	Heemskirk	Orbicule	Qtz	elliptical	5.2	L > V	L		344				
WT12WH28-6-3-5	Heemskirk	Orbicule	Qtz	elongate	10	L > V	L		223				
WT12WH28-6-3-6	Heemskirk	Orbicule	Qtz	negative	15	L > V 20%	L		567				
WT12WH28-6-3-7	Heemskirk	Orbicule	Qtz	subround	9.6	L + V + H			536		471		55.91
WT12WH28-6-3-8	Heemskirk	Orbicule	Qtz	elongate	9.9	L + V + H 10%	L		281		245		34.37
WT12WH28-6-3-9	Heemskirk	Orbicule	Qtz	elliptical	7.6	L > V 10%	L		392				
WT12WH28-6-3-10	Heemskirk	Orbicule	Qtz	elongate	8	L > V 5%	L		344				
WT12WH28-6-3-11	Heemskirk	Orbicule	Qtz	round	5	L > V 5%	L		324				
WT12WH28-6-3-12	Heemskirk	Orbicule	Qtz	elongate	15.5	L > V 40%	V	-10.8		530		14.77	
WT12WH28-6-3-13	Heemskirk	Orbicule	Qtz	elliptical	8.9	L > V 20%	L	-9.5	391			13.40	
WT12WH22-3-1	Heemskirk	Orbicule	Qtz	elongate	28	L> V 20%	L	-6.2	182			9.47	
WT12WH22-3-2	Heemskirk	Orbicule	Qtz	tabular	17.7	L> V 15%	L		189				
WT12WH22-3-3	Heemskirk	Orbicule	Qtz	elliptical	13	L> V 10%	L	-6.3	180			9.60	
WT12WH22-3-4	Heemskirk	Orbicule	Qtz	irregular	11	L> V 10%	L	-6.1	178			9.34	
WT12WH22-3-5	Heemskirk	Orbicule	Qtz	tabular	10	L> V 15%	L		219				
WT12WH22-3-6	Heemskirk	Orbicule	Qtz	negative	10 *5	L> V 15%	L	-5.8	256			8.95	
WT12WH22-3-7	Heemskirk	Orbicule	Qtz	elongate	7 * 4	L> V 15%	L	-6.3	185			9.60	
WT12WH22-3-8	Heemskirk	Orbicule	Qtz	subround	12 * 11	L> V 20%	L	-6.1	169			9.34	
WT12WH22-3-9	Heemskirk	Orbicule	Qtz	tabular	6 * 5	L> V 10%	L		178				
WT12WH22-3-10	Heemskirk	Orbicule	Qtz	negative	9 * 6	L> V 10%	L	-5.9	193			9.08	
WT12WH22-3-11	Heemskirk	Orbicule	Qtz	tabular	13	L> V 15%	L	-8.4	209			12.16	
WT12WH22-3-13	Heemskirk	Orbicule	Qtz	elongate	4	L> V 5 %	L		194				
WT12WH22-3-14	Heemskirk	Orbicule	Qtz	subround	3 * 3	L> V 5 %	L		180				
WT12WH22-3-15	Heemskirk	Orbicule	Qtz	rhombic	8 * 7	L > V	L		257				
WT12WH22-3-17	Heemskirk	Orbicule	Qtz	irregular	13 * 10	L > V	L		265				
WT12WH22-3-18	Heemskirk	Orbicule	Qtz	elongate	12* 2	L> V 10%	L	-1.2	239			2.07	
WT12WH22-3-19	Heemskirk	Orbicule	Qtz	elliptical	10 * 8	L> V 10%	L	-1.3	269			2.24	
WT12WH22-3-20	Heemskirk	Orbicule	Qtz	elliptical	9* 8	L> V 10%	L	-2.1	312			3.55	
WT12WH22-3-21	Heemskirk	Orbicule	Qtz	negative	5 * 3	L> V 15%	L		267				

WT12WH22-3-22	Heemskirk	Orbicule	Qtz	tabular	9 * 5	L> V 25%	V			448	
WT12WH22-3-23	Heemskirk	Orbicule	Qtz	elliptical	10 * 8	L> V 15%	L	-3.2	263		5.26
WT12WH22-3-24	Heemskirk	Orbicule	Qtz	elliptical	11 * 6	L> V 15%	L	-3.1	296		5.11
WT12WH22-3-25	Heemskirk	Orbicule	Qtz	elliptical	9 * 5	L> V 15%	L		340		
WT12WH22-5-1	Heemskirk	Orbicule	Qtz	elliptical	17.8	L> V 15%	L	-6.5	226		9.86
WT12WH22-5-2	Heemskirk	Orbicule	Qtz	negative	10	L> V 20%	L	-6.2	324		9.47
WT12WH22-5-3	Heemskirk	Orbicule	Qtz	tabular	12	L> V 20%	L	-6.1	309		9.34
WT12WH22-5-4	Heemskirk	Orbicule	Qtz	negative	11	L> V 20%	L	-6.1	274		9.34
WT12WH22-5-5	Heemskirk	Orbicule	Qtz	subround	5	L> V 10%	L		208		
WT12WH22-5-6	Heemskirk	Orbicule	Qtz	elongate	10	L> V 15%	L		254		
WT12WH22-5-7	Heemskirk	Orbicule	Qtz	elliptical	6	L> V 20%	L		262		
WT12WH22-5-8	Heemskirk	Orbicule	Qtz	negative	13	L> V 20%	L		256		
WT12WH22-5-9	Heemskirk	Orbicule	Qtz	irregular	14	L> V 20%	L		248		
WT12WH22-5-10	Heemskirk	Orbicule	Qtz	tabular	16	L> V 15%	L		327		
WT12WH22-2-1	Heemskirk	Orbicule	Qtz	tabular	17	L> V 10%	L	-10.6	300		14.57
WT12WH22-2-2	Heemskirk	Orbicule	Qtz	irregular	12	L> V 10%	L		234		
WT12WH22-2-4	Heemskirk	Orbicule	Qtz	elliptical	10	L> V 10%	L	-7.9	283		11.58
WT12WH22-2-5	Heemskirk	Orbicule	Qtz	elliptical	16	L> V 10%	L	-10.7	323		14.67
WT12WH22-2-7	Heemskirk	Orbicule	Qtz	elliptical	10	L> V 10%	L	-10.5	368		14.46
WT12WH22-2-10	Heemskirk	Orbicule	Qtz	negative	11	L> V 10%	L	-11.2	212		15.17
WT12WH22-2-11	Heemskirk	Orbicule	Qtz	triangular	10	L> V 10%	L		216		
WT12WH22-2-12	Heemskirk	Orbicule	Qtz	elongate	11	L> V 10%	L		246		
WT12WH22-2-13	Heemskirk	Orbicule	Qtz	elliptical	14	L> V 15%	L		271		
WT12WH22-2-14	Heemskirk	Orbicule	Qtz	tabular	12	L> V 10%	L		288		
WT12WH22-2-15	Heemskirk	Orbicule	Qtz	elongate	14	L> V 10%	L		305		
WT12WH22-2-16	Heemskirk	Orbicule	Qtz	subround	13	L> V 15%	L		362		
WT12WH22-2-17	Heemskirk	Orbicule	Qtz	elongate	18	L> V 15%	L		390		
WT12WH22-2-18	Heemskirk	Orbicule	Qtz	negative	14	L> V 20%	L		451		
WT12WH22-2-19	Heemskirk	Orbicule	Qtz	tabular	20	L> V 25%	L		409		
WT12WH23-4-1	Heemskirk	Vein	Qtz	irregular	12	L> V 10%	L		236		
WT12WH23-4-2	Heemskirk	Vein	Qtz	triangular	9	L> V 10%	L		194		
WT12WH23-4-3	Heemskirk	Vein	Qtz	elliptical	5	L> V 10%	L		223		
WT12WH23-4-4	Heemskirk	Vein	Qtz	elongate	11	L> V 10%	L	-7.6	232		11.22
WT12WH23-4-6	Heemskirk	Vein	Qtz	tabular	8	L> V 10%	L		228		
WT12WH23-4-7	Heemskirk	Vein	Qtz	elliptical	6	L> V 10%	L		175		
WT12WH23-4-8	Heemskirk	Vein	Qtz	elongate	5	L> V 5%	L	-4.1	204		6.59
WT12WH23-4-9	Heemskirk	Vein	Qtz	negative	7	L> V 10%	L		187		
WT12WH23-4-10	Heemskirk	Vein	Qtz	elliptical	9	L> V 10%	L		233		
WT12WH23-4-11	Heemskirk	Vein	Qtz	elliptical	8	L> V 10%	L		235		
WT12WH23-4-12	Heemskirk	Vein	Qtz	triangular	9	L> V 10%	L		258		
WT12WH23-4-13	Heemskirk	Vein	Qtz	elliptical	6	L> V 20%	L	-10.1	283		14.04

WT12WH23-4-14	Heemskirk	Vein	Qtz	negative	5.8	L> V 15%	L		189	
WT12WH23-4-15	Heemskirk	Vein	Qtz	tabular	11.5	L> V 15%	L	-10.3	232	14.25
WT12WH23-4-16	Heemskirk	Vein	Qtz	tabular	8.3	L> V 15%	L		231	
WT12WH23-4-17	Heemskirk	Vein	Qtz	triangular	9	L> V 15%	L		230	
WT12WH23-4-18	Heemskirk	Vein	Qtz	tabular	8	L> V 15%	L		207	
WT12WH23-4-19	Heemskirk	Vein	Qtz	rhombic	9	L> V 15%	L		235	
WT12WH23-4-20	Heemskirk	Vein	Qtz	tabular	11	L> V 10%	L		244	
WT12WH23-4-21	Heemskirk	Vein	Qtz	tabular	13.3	L> V 20%	L		324	
WT12WH23-4-22	Heemskirk	Vein	Qtz	tabular	11	L> V 10%	L		238	
WT12WH23-4-23	Heemskirk	Vein	Qtz	negative	8	L> V 10%	L		216	
WT12WH23-4-24	Heemskirk	Vein	Qtz	subround	12	L> V 15%	L	-6.3	231	9.60
WT12WH23-4-25	Heemskirk	Vein	Qtz	tabular	13	L> V 15%	L	-7.4	270	10.98
WT12WH23-4-26	Heemskirk	Vein	Qtz	elongate	10	L> V 15%	L		304	
WT12WH23-4-27	Heemskirk	Vein	Qtz	elongate	9	L> V 10%	L		211	
WT12WH23-4-28	Heemskirk	Vein	Qtz	elongate	12	L> V 10%	L		233	
WT12WH23-4-29	Heemskirk	Vein	Qtz	elongate	13	L> V 10%	L		251	
WT12WH23-4-30	Heemskirk	Vein	Qtz	subround	8	L> V 15%	L		316	
WT12WH23-3-1	Heemskirk	Vein	Qtz	elliptical	15	L> V 20%	L	-4.8	281	7.59
WT12WH23-3-2	Heemskirk	Vein	Qtz	tabular	17	L> V 20%	L	-9.2	238	13.07
WT12WH23-3-3	Heemskirk	Vein	Qtz	irregular	14.5	L> V 10%	L	-9.0	172	12.85
WT12WH23-3-4	Heemskirk	Vein	Qtz	elongate	12	L> V 20%	L		179	
WT12WH23-3-5-1	Heemskirk	Vein	Qtz	tabular	11	L> V 10%	L	-9.1	186	12.96
WT12WH23-3-5	Heemskirk	Vein	Qtz	elongate	8	L> V 10%	L	-4.6	160 ?	7.31
WT12WH23-3-6	Heemskirk	Vein	Qtz	elongate	9	L> V 10%	L	-8.7	205	12.51
WT12WH23-3-7	Heemskirk	Vein	Qtz	elongate	18	L> V 10%	L	-9.4	216	13.29
WT12WH23-3-8	Heemskirk	Vein	Qtz	irregular	8	L> V 10%	L	-9.0	207	12.85
WT12WH23-3-9	Heemskirk	Vein	Qtz	rhombic	10	L> V 10%	L		230	
WT12WH23-3-10	Heemskirk	Vein	Qtz	elongate	11	L> V 10%	L	-10.4	280	14.36
WT12WH23-3-11	Heemskirk	Vein	Qtz	elliptical	10	L> V 20%	L		329	
WT12WH23-3-12	Heemskirk	Vein	Qtz	elliptical	11	L> V 25%	L		244	
WT12WH23-3-13	Heemskirk	Vein	Qtz	negative	9	L> V 20%	L	-8.6	321	12.39
WT12WH23-3-15	Heemskirk	Vein	Qtz	negative	16.2	L> V 20%	L		292	
WT12WH23-3-16	Heemskirk	Vein	Qtz	negative	6.2	L> V 30%	L		224	
WT12WH23-3-17	Heemskirk	Vein	Qtz	negative	8	L> V 15%	L		221	
WT12WH23-3-18	Heemskirk	Vein	Qtz	negative	11	L> V 20%	L		303	
WT12WH23-3-21	Heemskirk	Vein	Qtz	negative	8	L> V 15%	L		248	
WT12WH23-3-22	Heemskirk	Vein	Qtz	subround	10	L> V 25%	L		332	
WT12WH23-3-23	Heemskirk	Vein	Qtz	elongate	12	L> V 20%	L		320	
WT12WH23-3-24	Heemskirk	Vein	Qtz	elongate	11	L> V 20%	L	-9.8	262	13.72
WT12WH23-3-25	Heemskirk	Vein	Qtz	elliptical	7	L> V 20%	L		219	
WT12WH23-3-26	Heemskirk	Vein	Qtz	elongate	13.6	L> V 20%	L		293	

WT12WH23-3-27	Heemskirk	Vein	Qtz	elliptical	9	L> V 30%	L		343	
WT12WH23-3-28	Heemskirk	Vein	Qtz	elliptical	9.2	L> V 20%	L		274	
WT12WH23-3-29	Heemskirk	Vein	Qtz	elongate	16.3	L> V 20%	L		> 450	
WT12WH23-3-30	Heemskirk	Vein	Qtz	tabular	12.7	L> V 20%	L		339	
WT12WH23-3-32	Heemskirk	Vein	Qtz	elliptical	7.6	L> V 20%	L	-8.1	265	11.81
WT12WH23-3-33	Heemskirk	Vein	Qtz	elliptical	11	L> V 20%	L	-5.1	211	8.00
WT12WH23-3-34	Heemskirk	Vein	Qtz	elliptical	8.3	L> V 20%	L		254	
WT12WH23-3-35	Heemskirk	Vein	Qtz	elongate	11	L> V 20%	L		252	
WT12WH23-3-36	Heemskirk	Vein	Qtz	elliptical	6.4	L> V 20%	L		271	
WT12WH23-3-37	Heemskirk	Vein	Qtz	elliptical	12	L> V 30%	L	-7.6	310	11.22
WT12WH23-3-38	Heemskirk	Vein	Qtz	elliptical	7.6	L> V 10%	L		229	
WT12WH23-3-39	Heemskirk	Vein	Qtz	elongate	12.4	L> V 20%	L		264	
WT12WH23-3-40	Heemskirk	Vein	Qtz	elongate	10.8	L> V 20%	L		294	
WT12WH23-3-41	Heemskirk	Vein	Qtz	elongate	8	L> V 20%	L	-9.9	263	13.83
WT12WH23-3-42	Heemskirk	Vein	Qtz	elliptical	9	L> V 20%	L		233	
WT12WH23-3-43	Heemskirk	Vein	Qtz	elongate	10	L> V 15%	L		283	
WT12WH23-3-44	Heemskirk	Vein	Qtz	elliptical	10	L> V 20%	L		302	
WT12WH23-3-45	Heemskirk	Vein	Qtz	elongate	12	L> V 15%	L		309	
WT12WH23-3-46	Heemskirk	Vein	Qtz	elliptical	10	L> V 20%	L	-5.9	322	9.08
WT12WH23-3-47	Heemskirk	Vein	Qtz	elliptical	9	L> V 20%	L		328	
WT12WH23-3-48	Heemskirk	Vein	Qtz	elliptical	8	L> V 60%	L		351	
WT12WH23-3-49	Heemskirk	Vein	Qtz	elliptical	9	L> V 50%	L		371	
WT12WH23-3-50	Heemskirk	Vein	Qtz	triangular	14	L> V 15%	L		387	
WT12WH23-3-51	Heemskirk	Vein	Qtz	elliptical	5.8	L> V 30%	L		295	
WT12WH23-3-52	Heemskirk	Vein	Qtz	elliptical	6	L> V 30%			> 450	
WT12WH23-3-53	Heemskirk	Vein	Qtz	elliptical	5.4	L> V 30%	L		383	
WT12WH23-3-54	Heemskirk	Vein	Qtz	triangular	8.2	L> V 30%	L		354	
WT12WH23-3-55	Heemskirk	Vein	Qtz	elliptical	7	L> V 20%	L	-5.3	381	8.28
WT12WH23-3-56	Heemskirk	Vein	Qtz	elliptical	8	L> V 20%	L		292	
WT12WH23-3-57	Heemskirk	Vein	Qtz	elliptical	9	L> V 20%	L		357	
106425-3-1	Heemskirk	Pb-Zn vein	Qtz	negative	19	L> V 15%	L	-6.9	186	10.36
106425-3-2	Heemskirk	Pb-Zn vein	Qtz	elongate	15	L> V 15%	L	-3.7	181	6.01
106425-3-3	Heemskirk	Pb-Zn vein	Qtz	elongate	38	L> V 10%	L	-3.4	160	5.56
106425-3-4	Heemskirk	Pb-Zn vein	Qtz	elliptical	12	L> V 10%	L	-3.5	182	5.71
106425-3-5	Heemskirk	Pb-Zn vein	Qtz	negative	16	L> V 10%	L	-3.6	187	5.86
106425-3-6	Heemskirk	Pb-Zn vein	Qtz	elongate	18	L> V 10%	L	-3.2	196	5.26
106425-3-7	Heemskirk	Pb-Zn vein	Qtz	negative	14	L> V 10%	L	-3.4	202	5.56
106425-3-8	Heemskirk	Pb-Zn vein	Qtz	negative	10	L> V 10%	L		195	
106425-3-9	Heemskirk	Pb-Zn vein	Qtz	quadrangular	18.2	L> V 10%	L	-3.6	190	5.86
106425-3-10	Heemskirk	Pb-Zn vein	Qtz	quadrangular	25	L> V 10%	L	-3.8	185	6.16
106425-3-11	Heemskirk	Pb-Zn vein	Qtz	quadrangular	20	L> V 10%	L	-3.5	186	5.71

106425-3-12	Heemskirk	Pb-Zn vein	Qtz	negative	9	L> V 10%	L	-3.7	197	6.01
106425-3-14	Heemskirk	Pb-Zn vein	Qtz	negative	15	L> V 10%	L	-3.6	186	5.86
106425-3-15	Heemskirk	Pb-Zn vein	Qtz	subround	16	L> V 10%	L	-7.2	?	10.73
106425-3-16	Heemskirk	Pb-Zn vein	Qtz	negative	10	L> V 10%	L	-3.4	198	5.56
106425-3-17	Heemskirk	Pb-Zn vein	Qtz	negative	12	L> V 15%	L	-3.8	187	6.16
106425-3-18	Heemskirk	Pb-Zn vein	Qtz	subround	38	L> V 10%	L	-4.0	192	6.45
106425-3-19	Heemskirk	Pb-Zn vein	Qtz	quadrangular	37	L> V 10%	L		184	
106425-3-20	Heemskirk	Pb-Zn vein	Qtz	tabular	17	L> V 10%	L	-3.9	210	6.30
106425-3-21	Heemskirk	Pb-Zn vein	Qtz	negative	25	L> V 10%	L	-4.1	191	6.59
106425-3-22	Heemskirk	Pb-Zn vein	Qtz	tabular	22	L> V 10%	L	-3.5	188	5.71
106425-3-23	Heemskirk	Pb-Zn vein	Qtz	tabular	18	L> V 10%	L	-3.8	179	6.16
106425-3-24	Heemskirk	Pb-Zn vein	Qtz	negative	15	L> V 10%	L	-3.6	246	5.86
106425-1-1	Heemskirk	Pb-Zn vein	Qtz	elongate	17.5	L> V 10%	L	-2.9	195	4.80
106425-1-2	Heemskirk	Pb-Zn vein	Qtz	negative	16.3	L> V 15%	L	-2.6	189	4.34
106425-1-3	Heemskirk	Pb-Zn vein	Qtz	elongate	15	L> V 20%	L	-4.2	308	6.74
106425-1-4	Heemskirk	Pb-Zn vein	Qtz	subround	13.6	L> V 15%	L	-2.4	194	4.03
106425-1-5	Heemskirk	Pb-Zn vein	Qtz	subround	9	L> V 20%	L	-2.6	200	4.34
106425-1-6	Heemskirk	Pb-Zn vein	Qtz	subround	7.8	L> V 15%	L		227	
106425-1-7	Heemskirk	Pb-Zn vein	Qtz	elongate	16.9	L> V 10%	L	-2.8	212	4.65
106425-1-8	Heemskirk	Pb-Zn vein	Qtz	elongate	8	L> V 10%	L	-2.1	209	3.55
106425-1-9	Heemskirk	Pb-Zn vein	Qtz	subround	15	L> V 15%	L	-2.6	310?	4.34
106425-1-10	Heemskirk	Pb-Zn vein	Qtz	elongate	24	L> V 10%	L	-3.0	187	4.96
106425-1-11	Heemskirk	Pb-Zn vein	Qtz	subround	14.5	L> V 30%		-3.5	367	5.71
106425-1-12	Heemskirk	Pb-Zn vein	Qtz	subround	11	L> V 10%	L	-2.4	194	4.03
106425-1-13	Heemskirk	Pb-Zn vein	Qtz	subround	9	L> V 10%	L	-2.2	207	3.71
106425-1-14	Heemskirk	Pb-Zn vein	Qtz	subround	8	L> V 20%	L	-2.6	242	4.34
106425-1-16	Heemskirk	Pb-Zn vein	Qtz	subround	10.5	L> V 15%	L	-2.5	213	4.18
106425-1-17	Heemskirk	Pb-Zn vein	Qtz	negative	7.5	L> V 15%	L	-2.7	190	4.49
106425-1-18	Heemskirk	Pb-Zn vein	Qtz	negative	7	L> V 15%	L		195	
106425-1-19	Heemskirk	Pb-Zn vein	Qtz	elongate	14	L> V 10%	L		214	
106425-1-20	Heemskirk	Pb-Zn vein	Qtz	subround	7	L> V 15%	L		217	
106425-1-21	Heemskirk	Pb-Zn vein	Qtz	triangular	25.2	L> V 15%	L	-3.2	400	5.26
106425-1-22	Heemskirk	Pb-Zn vein	Qtz	negative	13	L> V 15%	L	-3.0	287	4.96
106425-1-23	Heemskirk	Pb-Zn vein	Qtz	elongate	13.1	L> V 15%	L		328	
106425-1-24	Heemskirk	Pb-Zn vein	Qtz	subround	8	L> V 15%	L		284	
106425-1-25	Heemskirk	Pb-Zn vein	Qtz	negative	7	L> V 15%	L		268	
106425-1-26	Heemskirk	Pb-Zn vein	Qtz	elongate	11	L> V 15%	L		256	
106425-1-27	Heemskirk	Pb-Zn vein	Qtz	triangular	15	L> V 10%	L		261	
106425-2-1	Heemskirk	Pb-Zn vein	Qtz	subround	12.4	L> V 15%	L	-3.6	224	5.86
106425-2-2	Heemskirk	Pb-Zn vein	Qtz	subround	10.1	L> V 15%	L	-3.6	238	5.86
106425-2-4	Heemskirk	Pb-Zn vein	Qtz	tabular	9	L> V 15%	L	-0.9	192	1.57

106425-2-5	Heemskirk	Pb-Zn vein	Qtz	subround	14.1	L> V 20%	L	-1.4	243		2.41	
106425-2-6	Heemskirk	Pb-Zn vein	Qtz	triangular	22	L> V 10%	L	-2.2	188		3.71	
106425-2-7	Heemskirk	Pb-Zn vein	Qtz	negative	8.3	L> V 10%	L	-2.6	197		4.34	
106425-2-8	Heemskirk	Pb-Zn vein	Qtz	negative	8.2	L> V 10%	L	-3.9	180		6.30	
106425-2-9	Heemskirk	Pb-Zn vein	Qtz	triangular	11	L> V 10%	L	-3.5	163		5.71	
106425-2-11	Heemskirk	Pb-Zn vein	Qtz	negative	11	L> V 10%	L		230			
106425-2-12	Heemskirk	Pb-Zn vein	Qtz	negative	11.5	L+ V (10%) + H	L		196	240		34.07
106425-2-13	Heemskirk	Pb-Zn vein	Qtz	negative	11	L+ V (10%) + H	L		181	239		34.01
106425-2-14	Heemskirk	Pb-Zn vein	Qtz	elongate	10.5	L+ V (10%) + H	L		184	238		33.95
106425-2-16	Heemskirk	Pb-Zn vein	Qtz	negative	6	L+ V (15%) + H	L		186	252		34.81
106425-2-17	Heemskirk	Pb-Zn vein	Qtz	subround	9.5	L+ V (15%) + H	L		190	236		33.83
106425-2-18	Heemskirk	Pb-Zn vein	Qtz	elongate	10	L+ V (15%) + H	L		> 450	220		32.92
106425-2-19	Heemskirk	Pb-Zn vein	Qtz	negative	6	L+ V (15%) + H	L		158	> 270		
106425-2-20	Heemskirk	Pb-Zn vein	Qtz	subround	11	L+ V (10%) + H	L		215	233		33.65
106425-2-21	Heemskirk	Pb-Zn vein	Qtz	elliptical	12.3	L+ V (10%) + H	L		230	226		33.25
106425-2-22	Heemskirk	Pb-Zn vein	Qtz	elongate	10	L+ V (10%) + H	L		180	> 400		
106425-2-23	Heemskirk	Pb-Zn vein	Qtz	elongate	12.4	L+ V (10%) + H	L		311	354		42.78
106425-2-24	Heemskirk	Pb-Zn vein	Qtz	elongate	10	L+ V (10%) + H			> 450	310		38.95
106425-2-25	Heemskirk	Pb-Zn vein	Qtz	negative	10.5	L+ V (15%) + H	L		230	230.6		33.52
106425-2-26	Heemskirk	Pb-Zn vein	Qtz	negative	11.3	L+ V (15%) + H			> 450	398		47.22
106425-4-1	Heemskirk	Pb-Zn vein	Qtz	negative	13.7	L+ V (15%)	L	-3.6	185		5.86	
106425-4-2	Heemskirk	Pb-Zn vein	Qtz	negative	10.4	L+ V (15%)	L	-3.5	182		5.71	
106425-4-3	Heemskirk	Pb-Zn vein	Qtz	negative	8	L+ V (15%)	L	-3.5	189		5.71	
106425-4-4	Heemskirk	Pb-Zn vein	Qtz	negative	9.7	L+ V (15%)	L	-4.7	202		7.45	
106425-4-5	Heemskirk	Pb-Zn vein	Qtz	negative	9	L+ V (15%)	L	-4.8	203		7.59	
106425-4-6	Heemskirk	Pb-Zn vein	Qtz	negative	9.7	L+ V (15%)	L	-3.6	190		5.86	
106425-4-7	Heemskirk	Pb-Zn vein	Qtz	negative	9.2	L+ V (15%)	L	-3.8	200		6.16	
106425-4-8	Heemskirk	Pb-Zn vein	Qtz	negative	8.9	L+ V (15%)	L	-3.5	198		5.71	
106425-4-9	Heemskirk	Pb-Zn vein	Qtz	negative	8.6	L+ V (15%)	L	-3.4	192		5.56	
106425-4-10	Heemskirk	Pb-Zn vein	Qtz	negative	12.2	L+ V (15%)	L	-3.5	186		5.71	
106425-4-11	Heemskirk	Pb-Zn vein	Qtz	negative	8.4	L+ V (15%)	L	-4.4	175		7.02	
106425-4-13	Heemskirk	Pb-Zn vein	Qtz	tabular	9.2	L+ V (15%)	L	-3.6	192		5.86	
106425-4-14	Heemskirk	Pb-Zn vein	Qtz	negative	8.1	L+ V (15%)	L	-3.4	187		5.56	
106425-4-15	Heemskirk	Pb-Zn vein	Qtz	negative	16.3	L+ V (15%)	L	-5.3	191		8.28	
106425-4-16	Heemskirk	Pb-Zn vein	Qtz	negative	9.4	L+ V (15%)	L	-3.6	190		5.86	
106425-4-17	Heemskirk	Pb-Zn vein	Qtz	negative	21.2	L+ V (15%)	L	-3.9	187		6.30	
106425-4-18	Heemskirk	Pb-Zn vein	Qtz	elongate	18.5	L+ V (15%)	L	-3.7	196		6.01	
106425-4-19	Heemskirk	Pb-Zn vein	Qtz	elliptical	11	L+ V (15%)	L		195			
106425-4-20	Heemskirk	Pb-Zn vein	Qtz	elliptical	8	L+ V (15%)	L		217			
106405-1-1	Heemskirk	Pb-Zn vein	Flu	elliptical	28	L+ V (15%)	L	-6.0	167		9.21	
106405-1-2	Heemskirk	Pb-Zn vein	Flu	elliptical	81	L+ V (15%)	L	-6.3	170		9.60	

106405-1-3	Heemskirk	Pb-Zn vein	Flu	elliptical	17.4	L+ V (15%)	L		201			
106405-1-4	Heemskirk	Pb-Zn vein	Flu	elliptical	43.3	L+ V (15%)	L	-6.4	169		9.73	
106405-1-5	Heemskirk	Pb-Zn vein	Flu	elliptical	18.8	L+ V (15%)	L	-5.9	169		9.08	
106405-1-6	Heemskirk	Pb-Zn vein	Flu	tabular	32	L+ V (10%)	L		203			
106405-1-7	Heemskirk	Pb-Zn vein	Flu	tabular	11.1	L+ V (10%)	L	-6.4	168		9.73	
106405-1-8	Heemskirk	Pb-Zn vein	Flu	elliptical	12.4	L+ V (10%)	L	-6.2	150 ?		9.47	
106405-1-9	Heemskirk	Pb-Zn vein	Flu	elliptical	9	L+ V (10%)	L	-8.4	186		12.16	
106405-1-10	Heemskirk	Pb-Zn vein	Flu	elliptical	8.8	L+ V (15%)	L		202			
106405-1-11	Heemskirk	Pb-Zn vein	Flu	elliptical	15.1	L+ V (15%) + H	L	-8.9	206		12.73	
106405-1-12	Heemskirk	Pb-Zn vein	Flu	elliptical	17.5	L+ V (15%)	L		140			
106405-1-13	Heemskirk	Pb-Zn vein	Flu	elliptical	21.9	L+ V (10%)	L	-8.7	178		12.51	
106405-2-1	Heemskirk	Pb-Zn vein	Flu	tabular	20.6	L+ V (10%)	L		169			
106405-2-2	Heemskirk	Pb-Zn vein	Flu	elliptical	18.9	L+ V (10%)	L	-6.2	157		9.47	
106405-2-3	Heemskirk	Pb-Zn vein	Flu	elongate	8.1	L+ V (5%)	L		162			
106405-2-4	Heemskirk	Pb-Zn vein	Flu	tabular	15	L+ V (10%)	L		199			
106405-2-5	Heemskirk	Pb-Zn vein	Flu	tabular	27	L+ V (5%)	L	-6.3	183		9.60	
106405-2-6	Heemskirk	Pb-Zn vein	Flu	elongate	26	L+ V (5%)	L	-6.4	180		9.73	
106405-2-7	Heemskirk	Pb-Zn vein	Flu	elongate	14.3	L+ V (10%)	L	-4.7	181		7.45	
106405-2-8	Heemskirk	Pb-Zn vein	Flu	elongate	7.5	L+ V (5%)	L		159			
106405-2-9	Heemskirk	Pb-Zn vein	Flu	elongate	8	L+ V (5%)	L		170			
106405-2-10	Heemskirk	Pb-Zn vein	Flu	triangular	20.5	L+ V (5%)	L		<130			
106405-2-11	Heemskirk	Pb-Zn vein	Flu	negative	7	L+ V (5%)	L		164			
106405-2-13	Heemskirk	Pb-Zn vein	Flu	elliptical	28	L+ V (10%)	L	-5.4	161		8.41	
106405-2-14	Heemskirk	Pb-Zn vein	Flu	triangular	22.2	L+ V (10%)	L		167			
106405-3-1	Heemskirk	Pb-Zn vein	Flu	tabular	10.2	L+ V (5%)	L		172			
106405-3-2	Heemskirk	Pb-Zn vein	Flu	elliptical	13.1	L+ V (10%)	L	-6.1	149		9.34	
106405-3-3	Heemskirk	Pb-Zn vein	Flu	elliptical	16.6	L+ V (10%)	L	-6.9	158		10.36	
106405-3-4	Heemskirk	Pb-Zn vein	Flu	tabular	9.9	L+ V (5%)	L	-6.2	170		9.47	
106405-3-5	Heemskirk	Pb-Zn vein	Flu	elongate	11.5	L+ V (5%)	L		169			
106405-3-6	Heemskirk	Pb-Zn vein	Flu	elliptical	13.7	L+ V (5%)	L		156			
WT12WH13-1-1	Pieman Heads	Vein	Qtz	tabular	10.1	L+ V (10%)	L	-1.6	256.8		2.74	
WT12WH13-1-2	Pieman Heads	Vein	Qtz	rhombic	7.4	L+ V (5%)	L		241.7			
WT12WH13-1-3	Pieman Heads	Vein	Qtz	irregular	19.4	L+ V (5%) +H	L		243.5	182		31.01
WT12WH13-1-4	Pieman Heads	Vein	Qtz	negative	8	L+ V (10%)	L		282.3			
WT12WH13-1-5	Pieman Heads	Vein	Qtz	negative	10	L+ V (10%)	L		255.1			
WT12WH13-1-6	Pieman Heads	Vein	Qtz	elongate	7	L+ V (10%)	L	-1.7	245.1		2.90	
WT12WH13-1-7	Pieman Heads	Vein	Qtz	negative	6	L+ V (10%)	L		319.8			
WT12WH13-1-8	Pieman Heads	Vein	Qtz	negative	14	L+ V (10%)	L		255.6			
WT12WH13-1-9	Pieman Heads	Vein	Qtz	elongate	11	L+ V (10%)	L		280.6			
WT12WH13-1-10	Pieman Heads	Vein	Qtz	elongate	10	L+ V (10%)	L	-1.8	256.3		3.06	
WT12WH13-1-11	Pieman Heads	Vein	Qtz	elliptical	6	L+ V (10%)	L		308.6			

WT12WH13-1-12	Pieman Heads	Vein	Qtz	elongate	15.5	L+ V (10%) + H	L		273.1	179		30.88
WT12WH13-1-13	Pieman Heads	Vein	Qtz	elongate	5.3	L+ V (10%)	L		234,1			
WT12WH13-1-14	Pieman Heads	Vein	Qtz	elongate	12.3	L+ V (10%)	L	-1.5	267		2.57	
WT12WH13-1-15	Pieman Heads	Vein	Qtz	irregular	16.4	L+ V (10%) + H	L		273.4	158		29.98
WT12WH13-1-16	Pieman Heads	Vein	Qtz	irregular	20	L+ V (5%) + H	L		245.8	167		30.35
WT12WH13-1-17	Pieman Heads	Vein	Qtz	negative	5.1	L+ V (5%)	L		276.2			
WT12WH13-1-18	Pieman Heads	Vein	Qtz	negative	15.4	L+ V (10%)	L	-3.5	228.8		5.71	
WT12WH13-1-19	Pieman Heads	Vein	Qtz	elliptical	5	L+ V (10%)	L		276.8			
WT12WH13-1-20	Pieman Heads	Vein	Qtz	elongate	6.9	L+ V (5%)	L		239.4			
WT12WH13-1-22	Pieman Heads	Vein	Qtz	elliptical	5.1	L+ V (10%)	L		228.8			
WT12WH13-2-1	Pieman Heads	Vein	Qtz	elliptical	11.5	L+ V (10%)	L	-8.2	209.2		11.93	
WT12WH13-2-2	Pieman Heads	Vein	Qtz	elliptical	8	L+ V (5%)	L	-8.0	213.2		11.70	
WT12WH13-2-3	Pieman Heads	Vein	Qtz	elliptical	7.6	L+ V (5%)	L	-7.9	204.2		11.58	
WT12WH13-2-4	Pieman Heads	Vein	Qtz	elliptical	5.7	L+ V (5%)	L	-8.1	208.1		11.81	
WT12WH13-2-5	Pieman Heads	Vein	Qtz	negative	7.4	L+ V (10%)	L	-8.3	305.2		12.05	
WT12WH13-2-6	Pieman Heads	Vein	Qtz	tabular	13.7	L+ V (10%)	L	-8.2	207.1		11.93	
WT12WH13-2-7	Pieman Heads	Vein	Qtz	tabular	10.6	L+ V (10%)	L	-8.1	212.6		11.81	
WT12WH13-2-8	Pieman Heads	Vein	Qtz	elliptical	10.5	L+ V (10%)	L	-7.7	203.9		11.34	
WT12WH13-2-9	Pieman Heads	Vein	Qtz	elliptical	9	L+ V (10%)	L	-7.8	202.6		11.46	
WT12WH13-2-10	Pieman Heads	Vein	Qtz	tabular	10.1	L+ V (10%)	L	-8.4	228.2		12.16	
WT12WH13-2-11	Pieman Heads	Vein	Qtz	elliptical	10	L+ V (10%)	L	-8.0	214.1		11.70	
WT12WH13-2-12	Pieman Heads	Vein	Qtz	elongate	12	L+ V (10%)	L		218.6			
WT12WH13-2-13	Pieman Heads	Vein	Qtz	elliptical	8	L+ V (5%)	L		214.8			
WT12WH13-2-14	Pieman Heads	Vein	Qtz	elliptical	6	L+ V (5%)	L		241.3			
WT12WH13-2-15	Pieman Heads	Vein	Qtz	elliptical	5	L+ V (5%)	L		208.7			
WT12WH13-2-16	Pieman Heads	Vein	Qtz	elliptical	7.6	L+ V (10%)	L		245.5			
WT12WH13-2-17	Pieman Heads	Vein	Qtz	elliptical	7.5	L+ V (30%)	L		296.2			
WT12WH13-2-18	Pieman Heads	Vein	Qtz	elongate	6.7	L+ V (10%)	L		332.4			
WT12WH13-2-19	Pieman Heads	Vein	Qtz	elliptical	7.4	L+ V (15%)	L		276.3			
WT12WH13-2-20	Pieman Heads	Vein	Qtz	elliptical	6.5	L+ V (10%)	L	-6.7	243.7		10.11	
WT12WH13-2-21	Pieman Heads	Vein	Qtz	elliptical	7.3	L+ V (10%)	L		228.3			
WT12WH13-2-22	Pieman Heads	Vein	Qtz	negative	6.1	L+ V (10%)	L	-7.6	234.2		11.22	
WT12WH13-2-23	Pieman Heads	Vein	Qtz	negative	5	L+ V (10%)	L		220.8			
WT12WH13-2-24	Pieman Heads	Vein	Qtz	negative	6.7	L+ V (10%)	L	-7.3	254.6		10.86	
WT12WH13-2-25	Pieman Heads	Vein	Qtz	negative	4.9	L+ V (10%)	L	-7.7	215.5		11.34	
WT12WH13-2-26	Pieman Heads	Vein	Qtz	negative	6.5	L+ V (10%)	L		266.7			
WT12WH13-5-1	Pieman Heads	Vein	Qtz	negative	16.6	L+ V (10%) + H	L		224.8	205.2		32.14
WT12WH13-5-3	Pieman Heads	Vein	Qtz	negative	10.7	L+ V (10%)	L		182.5			
WT12WH13-5-4	Pieman Heads	Vein	Qtz	elongate	9.8	L+ V (5%)	L	-1.2	176.7		2.07	
WT12WH13-5-5	Pieman Heads	Vein	Qtz	elongate	21.1	L+ V (10%)	L	-7.5	> 400		11.10	
WT12WH13-5-6	Pieman Heads	Vein	Qtz	rhombic	8.3	L+ V (5%) + H	L		324.3	202.4		31.99

WT12WH13-5-7	Pieman Heads	Vein	Qtz	negative	7	L+ V (5%) + H	L		320.2	197.6		31.75
WT12WH13-4-1	Pieman Heads	Vein	Qtz	negative	8.5	L+ V (5%) + H	L		171.6	200.4		31.89
WT12WH13-4-2	Pieman Heads	Vein	Qtz	negative	6.6	L+ V (5%) + H	L		177.8	189.9		31.38
WT12WH13-4-3	Pieman Heads	Vein	Qtz	elongate	13.1	L+ V (5%) + H	L		192.3	190.8		31.42
WT12WH13-4-4	Pieman Heads	Vein	Qtz	tabular	7	L+ V (5%) + H	L		248.2	176.1		30.75
WT12WH13-4-5	Pieman Heads	Vein	Qtz	elliptical	7.1	L+ V (10%)	L	-20.6	181.3		22.78	
WT12WH13-4-6	Pieman Heads	Vein	Qtz	negative	10.4	L+ V (10%)	L	-22.4	182.6		23.95	
WT12WH13-4-7	Pieman Heads	Vein	Qtz	tabular	6.8	L+ V (10%)	L	-20.7	185.5		22.85	

Appendix 8.1 SIMS boron isotopic results of tourmaline from the Heemskirk and Pieman Heads granites

Sample	Location	Type	Zones	$\delta^{11}B$	2σ
WT12WH04-1	Pieman Heads	patch	dark	-6.4	0.4
WT12WH04-2	Pieman Heads	patch	dark	-7.1	0.4
WT12WH04-3	Pieman Heads	patch	grey	-10.3	0.4
WT12WH04-4	Pieman Heads	patch	grey	-8.5	0.4
WT12WH04-5	Pieman Heads	patch	light	-3.6	0.4
WT12WH04-6	Pieman Heads	patch	light	-2.9	0.4
WT12WH04-7	Pieman Heads	patch	light	-1.1	0.4
WT12WH07-2-1	Pieman Heads	orbicule	grey	-5.4	0.4
WT12WH07-2-2	Pieman Heads	orbicule	dark	-3.5	0.4
WT12WH07-2-3	Pieman Heads	orbicule	dark	-4.7	0.4
WT12WH07-2-4	Pieman Heads	orbicule	grey	-5.2	0.4
WT12WH07-2-5	Pieman Heads	orbicule	dark	-1.1	0.4
WT12WH07-2-6	Pieman Heads	orbicule	grey	-6.6	0.4
WT12WH13-1-1-2	Pieman Heads	vein	rim	-3.1	0.4
WT12WH13-1-1-3	Pieman Heads	vein	rim	-3.7	0.4
WT12WH13-1-1-4	Pieman Heads	vein	core	-5.3	0.4
WT12WH13-1-2-1-1	Pieman Heads	vein	outer rim	-2.6	0.4
WT12WH13-1-2-1-2	Pieman Heads	vein	outer rim	-3.7	0.4
WT12WH13-1-2-1-3	Pieman Heads	vein	outer rim	-1.6	0.4
WT12WH13-1-2-1-4	Pieman Heads	vein	outer rim	-2.2	0.4
WT12WH13-1-2-1-5	Pieman Heads	vein	outer rim	-4.2	0.4
WT12WH13-1-2-1-6	Pieman Heads	vein	outer rim	-3.8	0.4
WT12WH13-1-2-1-8	Pieman Heads	vein	inner rim	-5.2	0.4
WT12WH13-1-2-1-9	Pieman Heads	vein	inner rim	-5.7	0.4
WT12WH13-1-2-1-10	Pieman Heads	vein	inner rim	-5.9	0.4
WT12WH13-1-2-1-11	Pieman Heads	vein	inner rim	-6.2	0.4
WT12WH13-1-2-1-12	Pieman Heads	vein	core	-4.6	0.4
WT12WH13-1-2-1-13	Pieman Heads	vein	core	-3.8	0.4
WT12WH13-1-2-1-14	Pieman Heads	vein	core	-5.2	0.4
WT12WH13-1-2-1-15	Pieman Heads	vein	core	-7.6	0.4
WT12WH13-1-2-1-16	Pieman Heads	vein	core	-4.9	0.4
WT12WH13-1-2-1-17	Pieman Heads	vein	core	-2.8	0.4
WT12WH13-1-2-1-18	Pieman Heads	vein	core	-2.7	0.4
WT12WH13-1-2-1-19	Pieman Heads	vein	core	-4.2	0.4
WT12WH13-1-2-1-20	Pieman Heads	vein	inner rim	-4.6	0.4
WT12WH13-1-2-1-21	Pieman Heads	vein	inner core	-3.5	0.4
WT12WH13-1-2-1-22	Pieman Heads	vein	inner core	-3.3	0.4
WT12WH13-1-2-1-23	Pieman Heads	vein	inner rim	-3.8	0.4
WT12WH13-1-2-2-1	Pieman Heads	vein	core	-0.3	0.4
WT12WH13-1-2-2-2	Pieman Heads	vein	middle	-2.8	0.4
WT12WH13-1-2-2-3	Pieman Heads	vein	middle	-5.2	0.4
WT12WH13-1-2-2-4	Pieman Heads	vein	rim	-3.1	0.4
WT12WH13-1-2-2-5	Pieman Heads	vein	rim	-2.3	0.4
WT12WH13-2-2-1	Pieman Heads	vein	rim	-9.2	0.4
WT12WH13-2-2-2	Pieman Heads	vein	rim	-9.0	0.4
WT12WH13-2-2-3	Pieman Heads	vein	core	-5.9	0.4
WT12WH13-2-2-4	Pieman Heads	vein	middle	-7.4	0.4
WT12WH13-2-3-1	Pieman Heads	vein	rim	-5.4	0.4
WT12WH13-2-3-2	Pieman Heads	vein	rim	-5.4	0.4
WT12WH13-2-3-3	Pieman Heads	vein	core	-4.3	0.4
WT12WH13-2-3-4	Pieman Heads	vein	core	-4.6	0.4
WT12WH13-2-3-5	Pieman Heads	vein	rim	-7.5	0.4
WT12WH20-1	TH, Heemskirk	patch	rim	-3.0	0.3
WT12WH20-1a	TH, Heemskirk	patch	rim	-4.3	0.3
WT12WH20-2	TH, Heemskirk	patch	middle	-1.7	0.3
WT12WH20-3	TH, Heemskirk	patch	middle	-3.0	0.3
WT12WH20-4	TH, Heemskirk	patch	core	-21.3	0.3
WT12WH20-5	TH, Heemskirk	patch	core	-21.7	0.3
WT12WH20-6	TH, Heemskirk	patch	middle	-2.3	0.3
WT12WH20-7	TH, Heemskirk	patch	rim	-0.6	0.3
WT12WH20-8	TH, Heemskirk	patch	middle	-2.6	0.3
WT12WH20-9	TH, Heemskirk	patch	middle	-5.1	0.3
WT12WH20-10	TH, Heemskirk	patch	middle	-8.8	0.3
WT12WH20-12	TH, Heemskirk	patch	core	-19.0	0.3
WT12WH20-13	TH, Heemskirk	patch	core	-16.2	0.3
WT12WH20-1	TH, Heemskirk	patch	rim	-3.0	0.3
WT12WH20-1a	TH, Heemskirk	patch	rim	-4.3	0.3
WT12WH20-2	TH, Heemskirk	patch	middle	-3.0	0.3
WT12WH20-3	TH, Heemskirk	patch	core	-21.3	0.3
WT12WH20-4	TH, Heemskirk	patch	core	-21.7	0.3

Sample	Location	Type	Zones	$\delta^{11}B$	2σ
WT12WH20-5	TH, Heemskirk	patch	middle	-2.3	0.3
WT12WH20-6	TH, Heemskirk	patch	middle	-2.6	0.3
WT12WH20-7	TH, Heemskirk	patch	middle	-5.1	0.3
WT12WH20-8	TH, Heemskirk	patch	middle	-8.8	0.3
WT12WH20-9	TH, Heemskirk	patch	middle	-1.7	0.3
WT12WH20-10	TH, Heemskirk	patch	rim	-0.6	0.3
WT12WH20-12	TH, Heemskirk	patch	core	-19.0	0.3
WT12WH20-13	TH, Heemskirk	patch	core	-16.2	0.3
WT12WH23-1-1	TH, Heemskirk	vein	out	-7.5	0.3
WT12WH23-1-2	TH, Heemskirk	vein	out	-6.6	0.3
WT12WH23-1-3	TH, Heemskirk	vein	out	-6.8	0.3
WT12WH23-1-4	TH, Heemskirk	vein	out	-5.7	0.3
WT12WH23-1-5	TH, Heemskirk	vein	out	-5.3	0.3
WT12WH23-2-1	TH, Heemskirk	vein	in	-1.3	0.5
WT12WH23-2-2	TH, Heemskirk	vein	in	-0.8	0.5
WT12WH23-2-3	TH, Heemskirk	vein	in	-4.2	0.5
WT12WH23-2-4	TH, Heemskirk	vein	in	0.3	0.5
WT12WH23-2-5	TH, Heemskirk	vein	in	0.1	0.5
WT12WH24-1-1	TH, Heemskirk	cavity	core	-2.3	0.4
WT12WH24-1-2	TH, Heemskirk	cavity	rim	-2.4	0.4
WT12WH24-1-3	TH, Heemskirk	cavity	rim	-4.4	0.4
WT12WH24-1-4	TH, Heemskirk	cavity	core	-3.2	0.4
WT12WH24-2-1	TH, Heemskirk	cavity	rim	-6.5	0.4
WT12WH24-2-2	TH, Heemskirk	cavity	core	-3.7	0.4
WT12WH24-2-3	TH, Heemskirk	cavity	core	-4.0	0.4
WT12WH24-2-4	TH, Heemskirk	cavity	core	-5.1	0.4
WT12WH24-2-5	TH, Heemskirk	cavity	core	-3.9	0.4
WT12WH24-2-6	TH, Heemskirk	cavity	middle	-4.8	0.4
WT12WH24-2-7	TH, Heemskirk	cavity	middle	-3.5	0.4
WT12WH24-2-8	TH, Heemskirk	cavity	rim	-2.7	0.4
WT12WH24-2-9	TH, Heemskirk	cavity	rim	-4.4	0.4
WT12WH24-3-1	TH, Heemskirk	cavity	core	-0.3	0.4
WT12WH24-3-2	TH, Heemskirk	cavity	middle	-0.5	0.4
WT12WH24-3-3	TH, Heemskirk	cavity	middle	4.1	0.4
WT12WH24-3-4	TH, Heemskirk	cavity	rim	0.7	0.4
WT12WH24-3-5	TH, Heemskirk	cavity	core	0.0	0.4
WT12WH24-3-6	TH, Heemskirk	cavity	middle	-0.8	0.4
WT12WH24-3-7	TH, Heemskirk	cavity	middle	-0.7	0.4
WT12WH24-3-8	TH, Heemskirk	cavity	rim	0.0	0.4
WT12WH24-3-9	TH, Heemskirk	cavity	rim	-1.4	0.4
WT12WH28-3-1	TH, Heemskirk	orbicule	grey	-2.9	0.3
WT12WH28-3-2	TH, Heemskirk	orbicule	dark	-4.8	0.3
WT12WH28-3-3	TH, Heemskirk	orbicule	grey	-3.5	0.3
WT12WH28-3-4	TH, Heemskirk	orbicule	dark	-4.7	0.3
WT12WH28-3-5	TH, Heemskirk	orbicule	grey	-3.5	0.3
WT12WH28-3-6	TH, Heemskirk	orbicule	grey	-4.9	0.3
WT12WH28-3-7	TH, Heemskirk	orbicule	dark	-5.8	0.3
WT12WH28-3-8	TH, Heemskirk	orbicule	dark	-4.6	0.3
WT12WH28-3-9	TH, Heemskirk	orbicule	grey	-7.3	0.3
WT12WH28-3-10	TH, Heemskirk	orbicule	dark	-5.9	0.3
WT12WH28-4-1	TH, Heemskirk	orbicule	grey	-2.5	0.3
WT12WH28-4-2	TH, Heemskirk	orbicule	grey	-2.5	0.3
WT12WH28-4-3	TH, Heemskirk	orbicule	dark	-7.0	0.3
WT12WH28-4-4	TH, Heemskirk	orbicule	dark	-6.4	0.3
WT12WH28-4-5	TH, Heemskirk	orbicule	grey	-1.6	0.3
WT12WH33-2-1	GH, Heemskirk	cavity	core	-1.6	0.5
WT12WH33-2-2	GH, Heemskirk	cavity	core	-0.2	0.5
WT12WH33-2-3	GH, Heemskirk	cavity	rim-1	0.6	0.5
WT12WH33-2-4	GH, Heemskirk	cavity	middle	-2.4	0.5
WT12WH33-2-5	GH, Heemskirk	cavity	middle	-0.3	0.5
WT12WH33-2-6	GH, Heemskirk	cavity	rim-2	-0.5	0.5
WT12WH33-2-7	GH, Heemskirk	cavity	rim-2	0.1	0.5
WT12WH33-2-8	GH, Heemskirk	cavity	rim-3	-2.2	0.5
WT12WH35-2-1	GH, Heemskirk	orbicule	grey	-10.1	0.4
WT12WH35-2-2	GH, Heemskirk	orbicule	dark	-9.6	0.4
WT12WH35-2-3	GH, Heemskirk	orbicule	grey	-8.9	0.4
WT12WH35-2-4	GH, Heemskirk	orbicule	dark	-13.9	0.4
WT12WH35-2-5	GH, Heemskirk	orbicule	dark	-13.0	0.4
WT12WH35-2-6	GH, Heemskirk	orbicule	grey	-11.5	0.4
WT12WH35-2-7	GH, Heemskirk	orbicule	dark	-12.7	0.4

Abbreviation: TH = Trial Harbour, GH= Granville Harbour.

Appendix 8.2 SIMS oxygen isotopic results of tourmaline and quartz from the Heemskirk and Pieman Heads granites

Sample	Location	Type	Mineral	$\delta^{18}O_{V\text{-}SMOW}$ (‰)	1σ
WT12WH04-1-1	Pieman Heads	patch	Tur	8.6	1.2
WT12WH04-1-2	Pieman Heads	patch	Tur	10.4	1.2
WT12WH04-1-3	Pieman Heads	patch	Tur	11.0	1.2
WT12WH04-1-4	Pieman Heads	patch	Tur	13.3	1.2
WT12WH04-1-1	Pieman Heads	patch	Qtz	8.9	1.2
WT12WH04-1-2	Pieman Heads	patch	Qtz	8.1	1.2
WT12WH04-1-3	Pieman Heads	patch	Qtz	5.7	1.2
WT12WH04-1-4	Pieman Heads	patch	Qtz	11.0	1.2
WT12WH07-2-1	Pieman Heads	orbicule	Qtz	8.8	1.2
WT12WH07-2-2	Pieman Heads	orbicule	Qtz	8.8	1.2
WT12WH07-2-3	Pieman Heads	orbicule	Qtz	5.0	1.2
WT12WH07-2-4	Pieman Heads	orbicule	Qtz	5.2	1.2
WT12WH07-2-1	Pieman Heads	orbicule	Tur	9.1	1.2
WT12WH07-2-2	Pieman Heads	orbicule	Tur	9.6	1.2
WT12WH07-2-3	Pieman Heads	orbicule	Tur	10.2	1.2
WT12WH07-2-4	Pieman Heads	orbicule	Tur	9.8	1.2
WT12WH013-1-1	Pieman Heads	vein	Qtz	11.5	1.2
WT12WH013-1-2	Pieman Heads	vein	Qtz	11.4	1.2
WT12WH013-1-3	Pieman Heads	vein	Qtz	12.7	1.2
WT12WH013-1-4	Pieman Heads	vein	Qtz	11.9	1.2
WT12WH013-1-2-1-1	Pieman Heads	vein	Tur	8.6	1.2
WT12WH013-1-2-1-2	Pieman Heads	vein	Tur	6.5	1.2
WT12WH013-1-2-1-3	Pieman Heads	vein	Tur	8.9	1.2
WT12WH013-1-2-1-4	Pieman Heads	vein	Tur	7.3	1.2
WT12WH013-1-2-1-5	Pieman Heads	vein	Tur	11.9	1.2
WT12WH013-1-2-1-6	Pieman Heads	vein	Tur	8.5	1.2
WT12WH013-1-2-1-7	Pieman Heads	vein	Tur	10.9	1.2
WT12WH013-1-2-1-8	Pieman Heads	vein	Tur	11.5	1.2
WT12WH013-1-2-1-9	Pieman Heads	vein	Tur	10.8	1.2
WT12WH020-3-1	TH, Heemskirk	patch	Tur	10.8	1.2
WT12WH020-3-2	TH, Heemskirk	patch	Tur	10.1	1.2
WT12WH020-3-3	TH, Heemskirk	patch	Tur	11.3	1.2
WT12WH020-3-4	TH, Heemskirk	patch	Tur	9.8	1.2
WT12WH020-3-1	TH, Heemskirk	patch	Qtz	10.9	1.2
WT12WH020-3-2	TH, Heemskirk	patch	Qtz	10.0	1.2
WT12WH020-3-3	TH, Heemskirk	patch	Qtz	12.0	1.2
WT12WH023-1-1-1	TH, Heemskirk	vein	Qtz	10.5	1.2
WT12WH023-1-1-2	TH, Heemskirk	vein	Qtz	10.6	1.2
WT12WH023-1-1-3	TH, Heemskirk	vein	Qtz	10.7	1.2
WT12WH023-1-1-4	TH, Heemskirk	vein	Qtz	10.8	1.2
WT12WH023-1-1-1	TH, Heemskirk	vein	Tur	10.4	1.2
WT12WH023-1-1-2	TH, Heemskirk	vein	Tur	11.2	1.2
WT12WH023-1-1-3	TH, Heemskirk	vein	Tur	11.5	1.2
WT12WH023-1-1-4	TH, Heemskirk	vein	Tur	11.5	1.2
WT12WH024-3-1	TH, Heemskirk	cavity	Tur	10.9	1.2
WT12WH024-3-2	TH, Heemskirk	cavity	Tur	11.3	1.2
WT12WH024-3-3	TH, Heemskirk	cavity	Tur	12.8	1.2
WT12WH024-3-4	TH, Heemskirk	cavity	Tur	13.3	1.2
WT12WH024-3-5	TH, Heemskirk	cavity	Tur	9.7	1.2
WT12WH024-3-1	TH, Heemskirk	cavity	Qtz	15.6	1.2
WT12WH024-3-2	TH, Heemskirk	cavity	Qtz	15.6	1.2
WT12WH024-3-3	TH, Heemskirk	cavity	Qtz	16.1	1.2
WT12WH024-3-4	TH, Heemskirk	cavity	Qtz	14.1	1.2
WT12WH024-3-5	TH, Heemskirk	cavity	Qtz	15.7	1.2
WT12WH024-3-6	TH, Heemskirk	cavity	Qtz	13.5	1.2
WT12WH028-3-1-1	TH, Heemskirk	orbicule	Tur	13.4	1.2
WT12WH028-3-1-2	TH, Heemskirk	orbicule	Tur	13.4	1.2
WT12WH028-3-1-3	TH, Heemskirk	orbicule	Tur	10.3	1.2
WT12WH028-3-1-4	TH, Heemskirk	orbicule	Tur	11.9	1.2
WT12WH028-3-1-1	TH, Heemskirk	orbicule	Qtz	11.1	1.2
WT12WH028-3-1-2	TH, Heemskirk	orbicule	Qtz	10.0	1.2
WT12WH028-3-1-3	TH, Heemskirk	orbicule	Qtz	7.9	1.2
WT12WH028-3-1-4	TH, Heemskirk	orbicule	Qtz	9.4	1.2
WT12WH028-3-1-5	TH, Heemskirk	orbicule	Qtz	11.6	1.2
WT12WH028-3-2-1	TH, Heemskirk	orbicule	Tur	8.9	1.2
WT12WH028-3-2-2	TH, Heemskirk	orbicule	Tur	10.8	1.2
WT12WH028-3-2-3	TH, Heemskirk	orbicule	Tur	10.7	1.2
WT12WH028-3-2-4	TH, Heemskirk	orbicule	Tur	14.9	1.2
WT12WH028-3-2-1	TH, Heemskirk	orbicule	Qtz	10.3	1.2
WT12WH028-3-2-2	TH, Heemskirk	orbicule	Qtz	7.7	1.2
WT12WH028-3-2-3	TH, Heemskirk	orbicule	Qtz	7.2	1.2

Abbreviation: TH = Trial Harbour, GH= Granville Harbour, Tur = tourmaline, Qtz = quartz.